Physik-Department

Exploring the Strange-Meson Spectrum with COMPASS in the Reaction $K^- + p \to K^-\pi^-\pi^+ + p$

Dissertation

Stefan Wallner

Technische Universität München

Technische Universität München

Fakultät für Physik

Exploring the Strange-Meson Spectrum with COMPASS in the Reaction $K^- + p \to K^-\pi^-\pi^+ + p$

Stefan Wallner

Vollständiger Abdruck der von der Fakultät für Physik der Technischen Universität München zur Erlangung des akademischen Grades eines

Doktors der Naturwissenschaften (Dr. rer. nat.)

genehmigten Dissertation.

Vorsitzende(r):		apl. Prof. Dr. Norbert Kaiser
Prüfer der Dissertation:	1.	Prof. Dr. Stephan Paul
	2.	Hon.-Prof. Allen C. Caldwell, Ph.D.

Die Dissertation wurde am 15.11.2021 bei der Technischen Universität München eingereicht und durch die Fakultät für Physik am 24.01.2022 angenommen.

Updated version with minor corrections. The original version is accessible via the university library of the Technical University of Munich.

22 # Abstract

In the naïve quark-model picture, strange mesons consist of a strange and an up or down (anti)quark, which are bound by the strong interaction. Although strange mesons have been studied since more than 70 years, many parts of their excitation spectrum are still unexplored.

The COMPASS experiment at CERN collected the so far world's largest sample of 720 494 exclusive events for the diffractive-scattering reaction $K^- + p \to K^-\pi^-\pi^+ + p$. This sample allows us to study strange mesons decaying into the $K^-\pi^-\pi^+$ final state. In this thesis, we present the analysis of this data sample, starting from the event selection, up to an elaborate partial-wave analysis (PWA), with which we extract the strange-meson resonances. We develop a novel method for the identification of beam kaons using the full experimentally available information, which doubles the efficiency for kaon identification compared to the previously used method. We extend the classical PWA approach by employing model-selection techniques in order to construct the partial-wave model, and by applying Bootstrapping techniques in order to improve the parameter and uncertainty estimates. Furthermore, we develop a novel approach to treat incoherent background contributions to
23 our $K^-\pi^-\pi^+$ sample in the PWA. We perform extensive systematic studies as well as Monte Carlo studies in order to validate the analysis results. Finally, we perform a first study of the amplitudes of light mesons appearing in the $\pi^-\pi^+$ and $K^-\pi^+$ subsystems of the $K^-\pi^-\pi^+$ final state.

Our analysis yields the so far most complete picture of the strange-meson spectrum coming from a single analysis. In total, we study 14 strange mesons. We find signals from well-known strange mesons, as well as indications for states that are not yet established. For example, we find indications for the $K_2(2250)$, $K_3(2320)$, and $K_4(2500)$ for the first time in a PWA of a final state other than $\Lambda\bar{p}$ or $\bar{\Lambda}p$. In addition, we find indications for three excited pseudoscalar kaons; i.e. the $K(1460)$, the $K(1630)$, and the $K(1830)$; while quark-model calculations predict only two excited states in this mass region. This hints towards an exotic nature of one of these three states. Our estimates for the masses and widths of the 14 strange mesons mostly agree with previous measurements and with quark-model calculations. Our uncertainties for most of the measured masses and widths are competitive with the corresponding so far best measurements of these parameters by previous measurements.

24 # Kurzzusammenfassung

Entsprechend dem Quarkmodell bestehen leichte Mesonen mit Strangeness aus einem Strange und einem Up (Anti-)Quark, welche durch die starke Wechselwirkung gebunden sind. Seit mehr als 70 Jahren werden diese Mesonen studiert und dennoch sind Teile ihres Anregungsspektrums bis heute unbekannt.

Das COMPASS Experiment am CERN hat den bisher weltweit größten Datensatz für die diffraktive Streureaktion $K^- + p \to K^-\pi^-\pi^+ + p$, bestehend aus 720 494 exklusiven Ereignissen gemessen. Dieser Datensatz erlaubt es, leichte Mesonen mit Strangeness in deren Zerfall in den $K^-\pi^-\pi^+$ Endzustand zu studieren. In dieser Arbeit präsentieren wir die zugehörige Analyse, von der Ereignisauswahl bis hin zu einer umfangreichen Partialwellenanalyse (PWA). Hierfür entwickeln wir eine neuartige Methode zur Identifikation von Kaonen im Strahl, die eine doppelt so hohe Effizienz verglichen mit der zuvor verwendete Methode aufweist. Zudem erweitern wir den klassischen PWA Ansatz um eine Methode zur systematischen Konstruktion des Partialwellenmodells mittels Modellselektionsverfahren, sowie um Bootstrapping-Verfahren zur Verbesserung der Parameter- und Unsicherheitsbestimmung. Des Weiteren entwickeln wir einen neuartigen Ansatz zur Modellierung inko-
25 härenter Untergründe und führen weitreichende systematische sowie Monte Carlo Studien zur Verifizierung unserer Ergebnisse durch. Abschließend messen wir erstmals die quantenmechanischen Amplituden von leichten Mesonen in den $\pi^-\pi^+$ und $K^-\pi^+$ Subsystemen des $K^-\pi^-\pi^+$ Endzustandes.

In dieser Arbeit präsentieren wir das bisher umfassendste Bild des Spektrums leichter Mesonen mit Strangeness, welches aus einer einzigen Analyse stammt. Wir studieren insgesamt 14 leichte Mesonen mit Strangeness, wobei wir sowohl Signale von wohlbekannten Zuständen, als auch Anzeichen für bisher nicht etablierte Zustände finden. Beispielsweise beobachten wir Anzeichen für die Zustände $K_2(2250)$, $K_3(2320)$ und $K_4(2500)$. In dieser Arbeit werden sie das erste Mal in einer PWA in einem anderen Endzustand als $\Lambda\bar{p}$ oder $\bar{\Lambda}p$ beobachtet. Des Weiteren finden wir Anzeichen für drei pseudoskalare Kaonen. Da das Quarkmodell nur zwei Zustände in dieser Massenregion vorhersagt, deuten unsere Beobachtungen auf eine exotische Natur eines dieser Zustände hin. Unsere Messung der Massen und Breiten der 14 Zustände stimmt mit vorherigen Messungen überein. Die Unsicherheiten unserer Messung sind meist ähnlich gut, wie die Unsicherheiten der bisher besten Messungen dieser Parameter.

Contents

List of Todos

1 Introduction

Our current understanding of nature is that there are four fundamental interactions: (i) gravitation, which, e.g., binds planets and stars to solar systems and solar systems together with other components to galaxies; (ii) the electromagnetic interaction, which, e.g., binds electrons and nuclei to atoms and atoms to molecules; (iii) the strong interaction, which, e.g., binds quarks to hadrons, such as strange mesons, and hadrons to nuclei; and (iv) the weak interaction, which, e.g., is responsible for radioactive decays of nuclei.[a] Often, the study of bound systems allows us to gain more knowledge about the respective interaction. For example, the high-precision measurements of the fine and hyper-fine structure of the hydrogen atom, one of the simplest electromagnetically bound systems, contributed greatly to the development of Quantum Electrodynamics (QED), the fundamental theory of the electromagnetic interaction [1, 2]. For certain bound systems, their composition is not completely known, but the study of the properties of such bound systems gives access to their composition. For example, the density of dark matter in galaxies can be studied based on observations of the distribution and movement of the visible matter [3–5]. Similarly, the composition of strongly bound systems, i.e. hadrons, is not completely understood as we cannot study the individual components of hadrons separately due to the confinement. In the same spirit as the studies of systems bound by the electromagnetic interaction or gravitation, the goal of hadron spectroscopy programs, such as the strange-meson spectroscopy program at COMPASS, is to gain a better understanding of the strong interaction and its fundamental theory the Quantum Chromodynamics (QCD) by studying strongly bound systems.

In the naïve quark-model picture [6–8], mesons are states build up from a constituent quark and antiquark pair ($q\bar{q}'$). Hence, they are the simplest strongly bound system. Light mesons are build up from up, down, or strange (anti)quarks. Strange mesons are light mesons with strangeness ± 1, i.e. they are build up from a strange (anti)quark and an up or down (anti)quark.

Important properties of light mesons are their quantum numbers, i.e. their isospin I, their total spin J, and their parity P. The latter two are often written as J^P.[b] In the quark model, light mesons form for each J^P a SU(3) flavor nonet. Each nonet consists of two isoscalar mesons with $I = 0$, three isovector mesons with $I = 1$, and four strange mesons with $I = 1/2$.

[a] We list the four fundamental interactions as they appear after electroweak symmetry breaking.

[b] In addition, neutral non-strange light mesons are characterized by their charge parity quantum number C. By convention, the C parity of a neutral meson is often also assigned to its charged partners. Furthermore, one can extend the idea of charge conjugation to charged mesons by introducing the G parity. Strange mesons are not eigenstates of the C- or G-parity operators and hence do not have C-or G-parity quantum numbers.

In the quark-model picture, the total spin J of the meson is given by the coupling of the total intrinsic spin $S_{q\bar{q}'}$ of the $q\bar{q}'$ system and the relative orbital angular momentum $L_{q\bar{q}'}$ between the two constituent quarks. The half-integer spins of the two quarks can couple to a total intrinsic spin of

$$S_{q\bar{q}'} = 0 \text{ or } 1. \tag{1.1}$$

The relative orbital angular momentum can take values of

$$L_{q\bar{q}'} = 0, 1, 2, \ldots \tag{1.2}$$

The total spin of the meson is in the range

$$|S_{q\bar{q}'} - L_{q\bar{q}'}| \leq J \leq (S_{q\bar{q}'} + L_{q\bar{q}'}). \tag{1.3}$$

The parity of the meson can be expressed as

$$P = (-1)^{L_{q\bar{q}'}+1}. \tag{1.4}$$

Finally, the so-called naturality of the meson is defined as

$$\eta \equiv (-1)^J P = (-1)^{J+L_{q\bar{q}'}+1}. \tag{1.5}$$

Strange mesons are grouped into two families: (i) states with positive naturality called K_J^* and (ii) states with negative naturality called K_J.[c]

Besides their quantum numbers, another important property of mesons is their mass. For light mesons, a large fraction of the meson mass is dynamically generated by the strong interaction. Hence, understanding the emergence of the meson masses by measuring the masses of a wide variety of mesons and comparing them to theory predictions leads to a better understanding of the strong interaction and its fundamental theory QCD. Furthermore, all strange mesons, except for the lightest strange meson, i.e. the kaon, quickly decay via the strong interaction to final-state hadrons such as pions, kaons, protons, or lambda baryons.[d] Hence, they have an extremely short lifetime and thus appear as resonances in the final states. The width of these resonances is another important property. Measuring the masses and widths of mesons is a major task of meson spectroscopy.

For fixed J^P, there are K_J^* states with $L_{q\bar{q}'} = J - 1$ and with $L_{q\bar{q}'} = J + 1$. K_J states always have $L_{q\bar{q}'} = J$.[e] In addition, there are radial excitations of the $q\bar{q}'$ system. Hence, there is not only one state for a given J^P, but we expect from angular and radial excitations a whole excitation

[c] There are two exceptions to this naming scheme. The pseudoscalar mesons with $J^P = 0^-$, which would be called K_0, are actually called K. The vector mesons with $J^P = 1^-$, which would be called K_1^*, are actually called K^*.

[d] These final-state particles are stable with respect to the strong and electromagnetic interaction, but can decay via the weak interaction. However, weak decays proceed more slowly. Thus, these final-state particles are considered as stable. The only exception is the π^0, which can electromagnetically decay, but which has still a comparably long lifetime of $(8.43 \pm 0.13) \times 10^{-17}$ s [9] and hence can also be considered as stable.

[e] Because of equation (1.5), $J + L_{q\bar{q}'}$ has to be even for a negative naturality state. This is possible only for $L_{q\bar{q}'} = J$ as $S_{q\bar{q}'} \leq 1$ [see equation (1.3)].

spectrum of states with increasing masses.[f] While K_J^* states have always $S_{q\bar{q}'} = 1$,[g] K_J states can have $S_{q\bar{q}'} = 0$ or $S_{q\bar{q}'} = 1$. Thus, for a given J^P, $L_{q\bar{q}'}$, and radial excitation there are two states $K_{J,a}$ and $K_{J,b}$ with different $S_{q\bar{q}'}$, which cannot be distinguished by their J^P quantum numbers and which are close in mass. These two states can mix. Thus, the two physical states, for example the $K_1(1270)$ and the $K_1(1400)$, are actually a mixture of $K_{J,a}$ and $K_{J,b}$.

So far, we mainly discussed strange mesons in the context of the quark-model. However, QCD in principle allows for more than just constituent quark-model states, which are build up from a $q\bar{q}'$ pair. For example, there could be states with four constituent quarks called molecules or tetraquarks. Also, so-called hybrids could exist, which have an excited gluon-field that contributes to their quantum numbers. Historically, states beyond the constituent quark-model are called exotics. In the non-strange light-meson sector, a candidate for such an exotic state is the $\pi_1(1600)$ [11], which has quantum numbers that are forbidden for a $q\bar{q}'$ state. In order to establish exotic states, it is important to find their strange partners in the corresponding SU(3) flavor multiplet. In the strange-meson sector, exotic states have the same quantum numbers as ordinary quark-model states. Therefore, such exotic states are also called crypto-exotic. They appear only as supernumerary states in addition to the ordinary states of the quark-model SU(3) flavor nonets. Establishing exotic strange mesons hence requires to completely map out the strange meson spectrum and to compare it to quark-model predictions in order to identify supernumerary states.

At the low energies of the light-meson masses, QCD cannot be solved perturbatively. The only available first-principles approach is lattice QCD, i.e. the numerical simulation of QCD on a discrete space-time lattice. This approach has recently made significant progress [12, 13]. However, most lattice QCD calculations for hadron spectroscopy still need to be performed at unphysically high quark masses. This makes an extrapolation down to the physical point necessary and introduces additional uncertainties to the lattice QCD predictions. Nevertheless, lattice QCD provides important insight into the spectrum of mesons including the existence of potential exotic states. With improved methods and computing power, lattice QCD also started to study the strong decays of meson resonances, such as the $K^*(892)$ [14–16]. This opens the possibility to compare first-principle QCD predictions for hadron resonances with experimental observations. However, such a comparison requires a complete and precise picture of the strange-meson spectrum from experiments.

Strange mesons also appear as resonances in multi-body decays of heavy mesons or τ leptons with kaons in the final state. Hence, a complete understanding of such decays typically requires incorporating all appearing strange mesons in an amplitude analysis. This is a challenge especially in rare decays, because even with the largest data sets currently available, the precision is typically not high enough to determine all appearing mesons from the data set itself. Thus, also for these analyses a precise knowledge of the complete strange meson spectrum is mandatory as an input. Such rare decays of B and D mesons are studied, e.g., in searches for CP violation and in

[f] Side note: According to the quark model calculation in ref. [10], the first radial excitation of a K_J^* ground state, which has $L_{q\bar{q}'} = J - 1$, is close in mass to the angular excitation, which has $L_{q\bar{q}'} = J + 1$.

[g] Because of equation (1.5), a positive naturality state must have $L_{q\bar{q}'} \neq J$, which can only be satisfied for $S_{q\bar{q}'} = 1$ [see equation (1.3)].

the measurements of the angles of the unitarity triangle of the CKM matrix performed at the Belle [17], LHCb [18], and BaBar [19] experiments. Strange mesons also play a role in the search for new physics, e.g. in the decay $B^0 \to K^+\pi^-l^+l^-$,[h] where a complete understanding of all strange-meson contributions to the $K^+\pi^-$ system is mandatory [20, 21]. These requirements on a precise and complete picture of the strange meson spectrum will become even more demanding with upcoming high-precision data from experiments such as Belle II and LHCb. Therefore, strange-meson spectroscopy not only allows us to study QCD, but gives also important input to other fields of fundamental physics.

At experiments, strange mesons can be produced in various ways in order to study them. At fixed-target experiments such as LASS at SLAC [22], and WA3 [23] and the Ω spectrometer [24] at CERN, strange mesons were produced in the scattering of high-energy kaon beams off stationary targets. In this process, the beam kaon is excited to K_J^* and K_J states. The produced excited strange mesons were then observed in their decays to various final states such as $K\pi$ or $K\pi\pi$. Strange mesons can also be produced in the scattering of high-energy photon beams. Such photoproduction reactions are currently studied at the GlueX experiment at Jefferson Lab [25]. Yet another way to access the strange meson spectrum is in multi-body decays of heavy mesons such as $D^0 \to K^\mp\pi^\pm\pi^\pm\pi^\mp$ [26], $B^+ \to J/\psi K^+\pi^+\pi^-$ [27], or $J/\psi \to K^+K^-\pi^0$ [28]; or in τ decays such as $\tau^- \to K^-\pi^+\pi^-\nu_\tau$ [29]. Here, the strange mesons appear in subsystems of the multi-body final states such as the $K\pi$ and $K\pi\pi$ subsystems. These studies of strange mesons were performed or are still ongoing at experiments such as LHCb, Belle (II), BESIII, and CLEO.

Figure 1.1 shows the current status of our knowledge about the strange-meson spectrum. At the moment, the PDG [9] lists 25 strange mesons. Only 16 of them are considered as established states (blue data points). The remaining 9 states still need further confirmation (orange data points). The black horizontal lines in figure 1.1 represent the result of the quark-model calculation from ref. [10]. Many of the predicted states were not yet observed experimentally. Especially, in the high-mass region above about $1.8\,\mathrm{GeV}/c^2$, many of the predicted states still lack experimental evidence and most of the states listed in the PDG, e.g. the $K_3(2320)$ [30, 31] and the $K_4(2500)$ [31], were seen by only a few or even only a single experiment. A reason for this is that it is experimentally more challenging to find resonances in the high-mass region, due to the large overlap between the states given by the high density of states (see figure 1.1) and their typically large widths. Not only are many parts of the strange meson sector still unexplored after more than 70 years of experimental searches [32], but also most of the experimental studies of the strange-meson spectrum were performed more than 30 years ago. Only four additional strange mesons have been included in the PDG listening since 1990 [33]. Most of the more recent studies were performed based on large data samples of heavy-meson or τ decays from experiments such as Belle [27], BESIII [28], and LHCb [34]. However, even with these large data samples they could often study only a limited set of J^P sectors and only limited mass ranges. In general, most of the previous measurements of strange mesons were focused only on limited mass ranges and only on limited sets of J^P sectors, thereby neglecting the contributions of states outside these limits. For example, the two ground state $K_2(1770)$ and $K_2(1820)$ [34, 35] and the excited $K_2(2250)$ [31, 36, 37] were studied so far in completely separate sets of analyses,

[h] l stands for lepton.

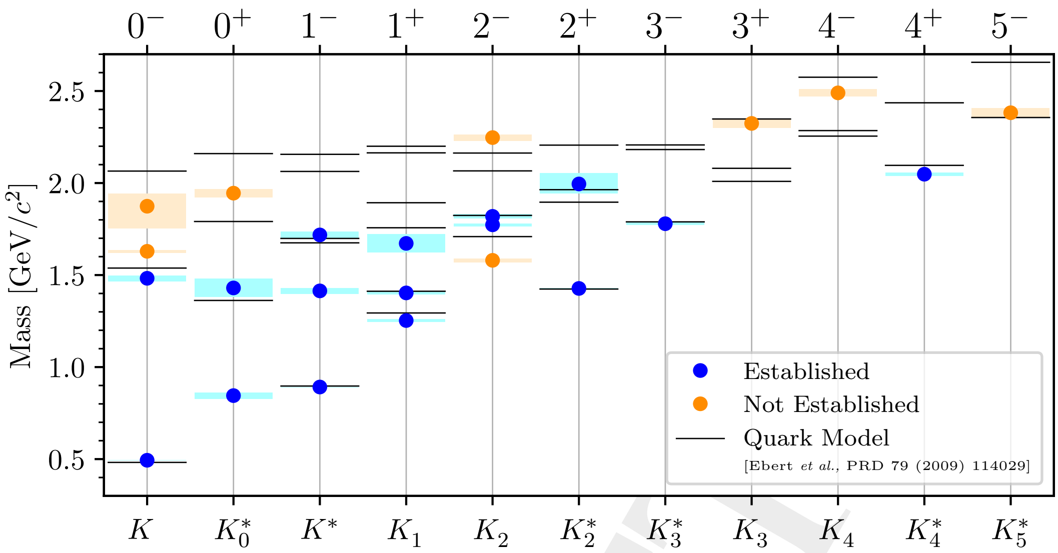

Figure 1.1: Spectrum of strange mesons, i.e. nominal masses of strange mesons grouped by their J^P quantum numbers. The blue data points show the masses of established states, the orange data points those of not established states as listed by the PDG [9]. The similarly colored boxes represent the corresponding uncertainties. The black horizontal lines show the masses of states as predicted by the quark-model calculation in ref. [10]. As we show only masses below 2.7 GeV$/c^2$ for a better visualization, the not-established $K(3100)$ is omitted here.

although the $K_2(2250)$ partly overlaps with the ground states. A more complete analysis covering a wide mass range and considering many J^P sectors simultaneously is still missing and would give a more complete and realistic picture of the strange-meson spectrum.

The main goal of the spectroscopy program at the COMPASS experiment at CERN is to obtain a more complete picture of the non-strange and strange light-meson spectrum. Using the dominant π^- contribution in the beam, COMPASS performed a detailed high-precision measurement of the isovector light-meson spectrum. COMPASS measured the largest data sample for the decay to the $\pi^-\pi^-\pi^+$ final state in the reaction $\pi^- + p \to \pi^-\pi^-\pi^+ + p$. The COMPASS $\pi^-\pi^-\pi^+$ analysis is the so-far most comprehensive analysis of this reaction, where novel analysis techniques were applied [11, 38–42]. An even more detailed analysis of the $\pi^-\pi^-\pi^+$ final state at COMPASS is currently ongoing [43].

The goal of this thesis is to obtain a more complete picture of the strange-meson spectrum by mapping out the spectrum of strange mesons similarly to the measurement of the isovector light-meson spectrum by COMPASS. Therefore, we used the K^- contribution in the high-energy hadron beam at COMPASS and studied strange mesons in their decay to the $K^-\pi^-\pi^+$ final state in the diffractive scattering reaction $K^- + p \to K^-\pi^-\pi^+ + p$, which is similar to the reaction $\pi^- + p \to \pi^-\pi^-\pi^+ + p$ used for isovector-meson spectroscopy. Based on a first analysis of only a subset of the COMPASS data [44], we aimed to extend and improve the event selection in order to obtain a large data sample of the reaction $K^- + p \to K^-\pi^-\pi^+ + p$. In order to search for strange mesons in this data sample, our goal was to perform the so far most comprehensive partial-wave analysis (PWA) of the $K^-\pi^-\pi^+$ final state, which is split into two stages. In the first stage called partial-wave decomposition (PWD), the data are decomposed into contributions from various J^P sectors. We aimed to develop and apply models and analyses techniques that go beyond what was used in previous analyses of the $K^-\pi^-\pi^+$ final state. To this end, much of the experience gained in the COMPASS $\pi^-\pi^-\pi^+$ analysis entered our analysis and was developed further, and some methods applied in our analysis were developed in close collaboration with the currently ongoing COMPASS $\pi^-\pi^-\pi^+$ analysis. In the second stage of our analysis called resonance-model fit (RMF), strange-meson resonances are extracted and their masses and widths are measured. Here, our goal was to study a large variety for strange mesons from many J^P sectors and from a wide mass range simultaneously in a single analysis. Finally, we intended to scrutinize our analysis methods and results in extensive systematic studies and Monte Carlo input-output studies.

In chapter 2, we discuss the reaction $K^- + p \to K^-\pi^-\pi^+ + p$ and briefly introduce the COMPASS experimental setup. In chapter 3, we discuss improvements in the identification of beam kaons at COMPASS and the performance of the final-state particle identification, which were major challenges of our analysis. In chapter 4, we describe the event selection and present kinematic distributions of the $K^-\pi^-\pi^+$ final state. In chapter 5, we describe the partial-wave decomposition. We also provide a first glimpse on the results of the PWD, and we discuss extensive studies to scrutinize the PWD. In chapter 6, we describe the resonance-model fit. We also provide a first glimpse on the results of the RMF, and we discuss extensive studies to scrutinize the RMF. In chapter 7, we discuss the major physics results of our analysis and compare them to previous measurements and to theory predictions. In chapter 8, we present a first attempt to also study mesons appearing in the $K^-\pi^+$ and $\pi^-\pi^+$ subsystems of the $K^-\pi^-\pi^+$ final state using the so-called freed-isobar approach. Finally, in chapter 9, we conclude our results and present further prospects for strange-meson spectroscopy at COMPASS and at other experiments. Technical details of our analysis and additional results are given in appendices A to H. Important expressions and terminology specific to this analysis are underlined in the text and summarized in the glossary.

2 Strange-Meson Spectroscopy at the COMPASS Experiment

2.1 The Studied Process: Diffractive Production of $K^-\pi^-\pi^+$

Our goal is to explore the strange meson-spectrum with COMPASS by studying the diffractive[a] scattering of a K^- beam off a liquid-hydrogen target. At high center-of-momentum energies of the $K^-_{\text{beam}}p_{\text{target}}$ system, like at COMPASS, the scattering process is dominated by the t-channel exchange of a Pomeron $\mathbb{P}$. Pomeron exchange is an effective description of the underlying strong-interaction processes using Regge theory [45, 46]. In the reaction of interest, the target proton remains intact, whereas the beam K^- gets excited into an intermediate state X^- with mass m_X.[b] Here, X^- represents the excited strange mesons that we aim to study. In this way, we can produce all K^*_J and K_J states, except for K^*_0 states.[c] Finally, we observe these strange mesons in their decays to final state particles. In this work, we focus on the decay to the $K^-\pi^-\pi^+$ final state. The reaction is depicted in figure 2.1.

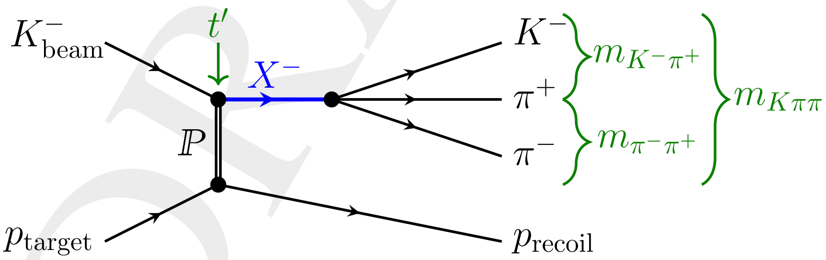

Figure 2.1: Schematic view of the reaction $K^- + p \to K^-\pi^-\pi^+ + p$.

[a] Diffractive scattering reactions are inelastic scattering reactions, where the energy transfer between the two hadrons is comparably small and where one or both hadrons dissociate into a multi-particle final state. Diffractive scattering reactions are analogous to scattering off a gray disk in optics.

[b] In principle, there can be also excitations of the target proton. However, in our analysis excitations of the target proton are experimentally suppressed by the event selection section 4.1.

[c] As the beam K^- is a $J^P = 0^-$ state, the relative orbital angular momentum $L_{K\mathbb{P}}$ of the $K^-_{\text{beam}}\mathbb{P}$ system has to be equal to the spin $J_{\mathbb{P}}$ of the exchange particle in order to produce a $J = 0$ system. The $\mathbb{P}$ has positive naturality, which means that it has a parity of $(-1)^{J_{\mathbb{P}}}$. Hence, the parity of the $K^-_{\text{beam}}\mathbb{P}$ system with $J = 0$, i.e. the parity of X^- with $J = 0$, is $(-1)^{1+J_{\mathbb{P}}+L_{K\mathbb{P}}} = (-1)^{1+2J_{\mathbb{P}}} = -1$. Thus, only K states with $J^P = 0^-$ can be produced in diffractive kaon scattering, but no K^*_0 states with $J^P = 0^+$.

In addition to the center-of-momentum energy, the invariant mass $m_{K\pi\pi}$ of the $K^-\pi^-\pi^+$ system, and the invariant masses $m_{K^-\pi^+}$ and $m_{\pi^-\pi^+}$ of the $K^-\pi^+$ and $\pi^-\pi^+$ subsystems, respectively, the reaction is characterized by the Mandelstam variable t, which is the squared four-momentum transfer between the beam K^- and the target proton. It is always negative and given by

$$t = (p_{\text{beam}} - p_X)^2 = m_{\text{beam}}^2 + m_X^2 - 2\left(E_{\text{beam}}E_X - |\vec{p}_{\text{beam}}|\,|\vec{p}_X|\cos\theta\right). \tag{2.1}$$

Here, p_{beam} is the four-momentum of the beam particle, p_X is the four-momentum of the X^-, E_i are the corresponding energies, $|\vec{p}_i|$ are the corresponding magnitudes of the three-momenta, and θ is the scattering angle, i.e. the angle between the X^- and the beam K^- momenta. It is more convenient to use the reduced squared four-momentum transfer

$$t' \equiv |t| - |t|_{\text{min}}, \tag{2.2}$$

which takes into account the minimal squared four-momentum transfer,

$$|t|_{\text{min}} = -m_{\text{beam}}^2 - m_X^2 + 2\left(E_{\text{beam}}^{\text{CoM}}E_X^{\text{CoM}} - |\vec{p}_{\text{beam}}^{\text{ CoM}}|\,|\vec{p}_X^{\text{ CoM}}|\right), \tag{2.3}$$

necessary to produce an excited state with mass m_X. Here, the energies E_i^{CoM} and momenta $|\vec{p}_i^{\text{ CoM}}|$ are given in the overall center-of-momentum frame of the $K_{\text{beam}}^- p_{\text{target}}$ system.[d] For the kinematic region analyzed in this work, $|t|_{\text{min}} \ll |t|$ and hence $t' \approx |t|$.

2.1.1 Non-Resonant Production of the $K^-\pi^-\pi^+$ Final State

In addition to the reaction depicted in figure 2.1, there can be other processes that also end up in the $K^-\pi^-\pi^+$ final state. However, these reactions do not proceed via intermediate resonances X^- in the $K^-\pi^-\pi^+$ system. Hence, they are called non-resonant processes.

One class of such non-resonant processes are the so-called Deck-like reactions [47] depicted in figure 2.2. The dominant graph, where a virtual pion is exchanged and rescatters off the target proton, is shown in figure 2.2a. In forward direction in the laboratory frame, a fast intermediate resonance ξ is produced, which then decay into $K^-\pi^+$. Figure 2.2b shows another possible graph, where a virtual kaon is exchanged and a forward going $\pi^-\pi^+$ system is produced. Due to the higher mass of the kaon, this process is suppressed with respect to the pion-exchange process.

Further possible non-resonant processes are central-production reactions shown in figure 2.3. In the dominant graph shown in figure 2.3a, both the target proton and the beam K^- emit a Pomeron. The two Pomerons fuse and centrally[e] produce an intermediate resonance ξ, which then decays

[d] In general, E_i and $|\vec{p}_i|$ depend on θ. However, in the overall center-of-momentum frame, the energies E_i^{CoM} equal to the two-body breakup energies and the momenta $|\vec{p}_i^{\text{ CoM}}|$ equal to the two-body breakup momenta. This means E_i^{CoM} and $|\vec{p}_i^{\text{ CoM}}|$ are independent of θ. Hence, in this frame, equation (2.1) has a maximum for $\cos\theta = 1$, which is a minimum of $|t|$.

[e] Here, "centrally" means that the intermediate $\pi\pi$ resonance ξ is approximately at rest in the overall $K_{\text{beam}}^- p_{\text{target}}$ center-of-momentum frame.

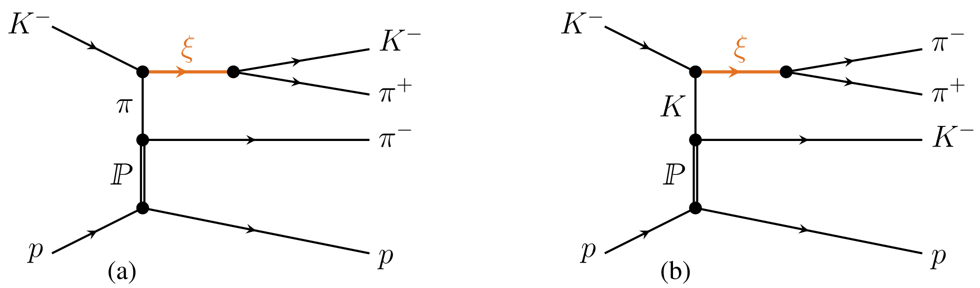

Figure 2.2: Schematic view of Deck-like reactions with (a) pion exchange and (b) kaon exchange.

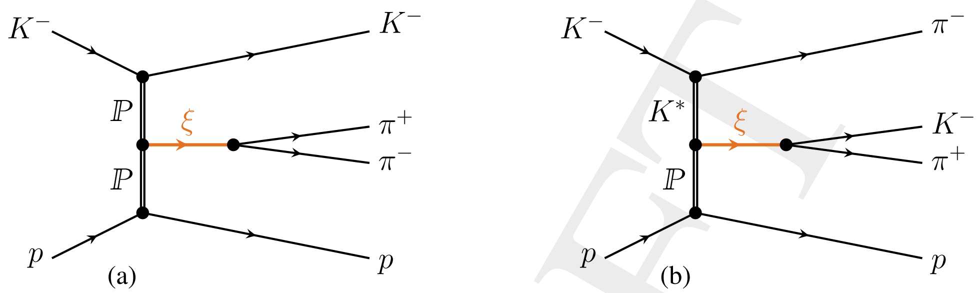

Figure 2.3: Schematic view of central-production reactions for a centrally produced $\pi^-\pi^+$ (a) or $K^-\pi^+$ (b) subsystem.

into $\pi^-\pi^+$. Alternatively, a virtual K^* can be exchanged at the top vertex in order to centrally produce an intermediate resonance ξ, which decays into $K^-\pi^+$ as shown in figure 2.3b. Further exchanges in addition to $\mathbb{P}$ and K^* are in principle also possible.

The main goal of this thesis is to study strange-meson resonances in the $K^-\pi^-\pi^+$ system. Here, non-resonant processes are considered as background. We discuss the treatment of these backgrounds in section 6.1.2. However, studies of non-resonant processes, as done by JPAC based on COMPASS data on the $\eta\pi$ and $\eta'\pi$ final states [48], are an interesting topic for themselves.

2.2 The COMPASS Experiment at CERN

COMPASS (COmmon Muon Proton Apparatus for Structure and Spectroscopy) is a very versatile experiment designed to study QCD in the low-energy regime. It was used to study the internal structure of hadrons by measuring, for example, the polarizability of pions [50] or the contribution of the transverse quark spins to the nucleon spin [51]. The 2008 and 2009 diffraction data-taking campaigns at COMPASS were mainly devoted to light-meson spectroscopy. In the following, we briefly introduce the COMPASS experimental setup as it was used during 2008 and 2009. A detailed description can be found in refs. [49, 52].

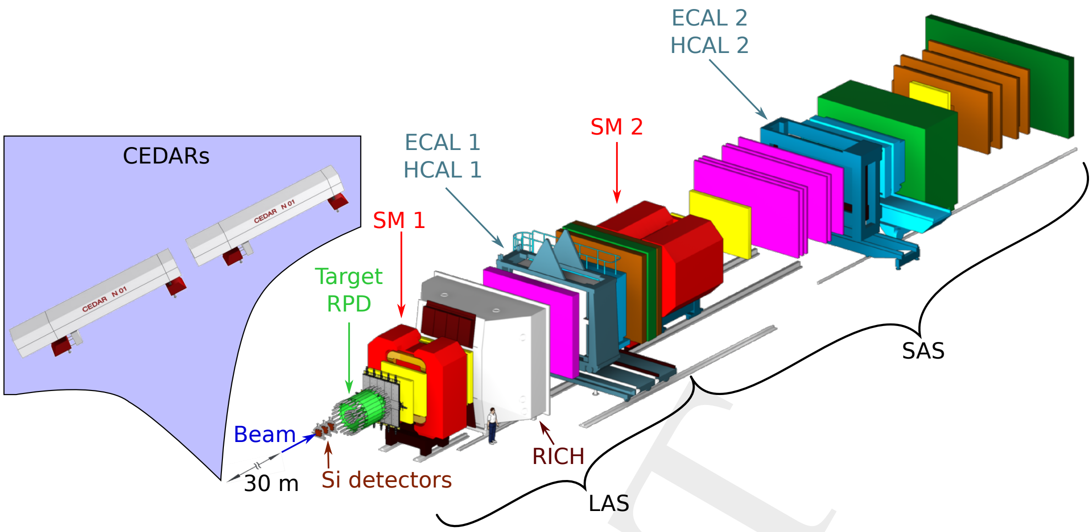

Figure 2.4: Schematic view of the COMPASS setup for measurements with hadron beams. The beam (blue arrow) is entering the target region surrounded by the RPD (green) from the left side. The final-state particles are measured with the COMPASS Large-Angle (LAS) and Small-Angle (SAS) magnetic Spectrometer. Different detector types are represented by different colors. The CEDAR detectors placed upstream of the COMPASS target are shown as an inset. The figure was taken from ref. [49] and adjusted.

COMPASS is a fixed-target experiment located at the M2 beam line at the CERN accelerator laboratory. The setup is shown in figure 2.4. Protons from the Super Proton Synchrotron (SPS) accelerator with a momentum of about 400 GeV/c impinge on a Beryllium production target (not shown), where showers of secondary hadrons; mainly pions, kaons, and protons; are produced with a large momentum spread. Then, particles in the desired momentum range are selected by a series of magnets and collimators along the about 1 km long beam line. For the diffraction data taking, we used a 190 GeV/c negative hadron beam, which corresponds to a center-of-momentum energy of about 19 GeV/c^2 for the reaction shown in figure 2.1. This beam has a high nominal intensity of $5 \times 10^6\,\mathrm{s}^{-1}$ with a low momentum spread of about 1 % [49]. It is mainly composed out of π^- (96.8 %), with smaller contributions from K^- (2.4 %) and $\bar{p}$ (0.8 %) [49]. To distinguish the beam-particle species, two alike CEDAR detectors (ChErenkov Differential counters with Achromatic Ring focus) are positioned approximately 30 m upstream of the COMPASS target.

The negative hadron beam impinges on a cylindrical liquid-hydrogen target with a diameter of 35 mm and a length of 400 mm. The latter corresponds to about 5.5 % of the nuclear interaction length [49]. Silicon microstrip detectors are placed upstream and downstream of the target to measure the tracks of charged beam and final-state particles with high precision. This allows us to reliably find and precisely reconstruct the interaction point of the beam particle with the target proton. Furthermore, the target is surrounded by a barrel-shaped recoil-proton detector (RPD), which measures the track of the recoiling proton. Detecting the recoil protons requires them to have a minimal kinetic energy, which imposes a lower limit on t' of about 0.1 GeV/c^2.[f]

[f] For $t' < 0.1\,\mathrm{GeV}/c^2$, the RPD acceptance quickly drops and becomes practically zero for $t' < 0.07\,\mathrm{GeV}/c^2$.

The momenta of the forward-going charged final-state particles are measured by a two-stage magnetic spectrometer. The first stage called Large-Angle Spectrometer (LAS) covers polar angles of the final-state particles of up to 180 mrad [49]. It is followed by the Small-Angle Spectrometer (SAS), which extends the experimental acceptance to particles going in very forward direction with small polar angles in the range ±30 mrad [52]. Each of the two stages consists of a bending magnet (SM 1/2) surrounded by multiple layers of tracking detectors. For a high-precision measurement of tracks close to the beam axis micropattern gaseous detectors are used namely Gas Electron Multipliers (GEM) and micromesh gaseous structure detectors (micromegas), as well as Scintillating Fibre counter (SciFi). To cover larger areas up to 12 m^2 further away from the beam axis, wire-based gas detectors are used such as Drift Champers (DC), Multi-Wire Proportional Chambers (MWPC), and straw-tube chambers. Final-state particle identification is performed by the Ring-Imaging CHerenkov detector (RICH), which distinguishes pions, kaons and (anti)protons. Furthermore, each spectrometer stage is equipped with an Electromagnetic CALorimeter (ECAL) used to measure high-energy photons and electrons and a Hadronic CALorimeter (HCAL). The calorimeters were not used in our analysis.

Events are recorded only if they fulfill certain trigger criteria. The so-called Diffractive Trigger (DT0) was designed to perselect diffractive scattering events studied in this analysis. It requires coincidence of three signals: (i) an incoming beam particle is measured by two scintillator-based beam-trigger detectors placed upstream of the COMPASS target; (ii) a recoil proton is measured by the RPD; (iii) there is no signal from the veto system, which rejects events with beam particles that enter the setup outside the target region, events with final-state particles outside the LAS acceptance, or events with non-interacting beam particles. The DT0 trigger was designed to have a minimal bias on the selected events. For data management, the recorded data were grouped into up to approximately 2 hour long periods in time, the so-called runs. Finally, the recorded data were processed by the COMPASS reconstruction and analysis software CORAL [53].

The setups for 2008 and 2009 were nearby identical, with only minor changes. For example, between 2008 and 2009 one additional tracking detector was installed for detector testing and during 2009 the position of one of the beam trigger detectors was shifted, because a small part of the sensitive area of this detector was not working anymore. These effects had only a minor influence on the detector performance. Nonetheless, we take into account these changes in the partial-wave decomposition discussed in chapter 5 by splitting the total data set into three subsets labeled by: (i) 2008, (ii) 2009 W2X, (iii) 2009 W35.

Due to its two-stage layout, COMPASS has a large experimental acceptance for charged particles, which uniformly covers a wide kinematic range. Furthermore, COMPASS has a high resolution for the measurement of the momenta of charged particles. The CEDAR and RICH detectors allow us to identify events with kaons in the initial and final state, which is important for the studied reaction $K^- + p \to K^-\pi^-\pi^+ + p$ studied. Hence, COMPASS is perfectly suited for strange-meson spectroscopy, which requires applying partial-wave analysis techniques that rely on a precise knowledge of the involved particles and their momenta.

3 Particle Identification

One of the main experimental challenges in analyzing the reaction $K^- + p \to K^-\pi^-\pi^+ + p$ is the identification of the particle species of the beam and final-state particles. Beam kaons have to be separated from the about 36 times larger pion content of the beam. In order to achieve a high efficiency of beam-kaon identification, while maintaining a sufficiently low pion contamination of the kaon-beam sample, we developed a novel likelihood approach using the information from two Cherenkov differential counters (CEDARs) [54], which is presented in section 3.1. Applying this method, we gained a factor two in beam-particle identification efficiency over a previously used method. The main task of the final-state particle identification is to distinguish the K^- from the π^- in the $K^-\pi^-\pi^+$ final state. In section 3.2 we briefly introduce the method used to identify charged particles in the final state using information from the ring-imagine Cherenkov detector (RICH). In addition, we present in sections 3.1 and 3.2 performance studies of the applied methods, which were performed separately for the 2008 and 2009 diffraction data set. The results of the performance studies are discussed exemplary for the 2008 diffraction data set. The 2009 diffraction data set shows similar results.

3.1 Beam-Particle Identification

3.1.1 The CEDAR Detectors

The negatively charged hadron beam at COMPASS is mainly composed out of pions (96.8 %), with smaller contributions from kaons (2.4 %) and antiprotons (0.8 %) [49]. To distinguish these particle species, two alike CEDAR detectors [55, 56] are positioned 30 m upstream of the COMPASS target. The central part of each CEDAR is a 6 m long vessel containing pressurized helium gas. Beam particles traverse the CEDAR approximately parallel to its optical axis, which is represented by the dashed line in figure 3.1. Since they move faster than the speed of light in the helium gas, they emit Cherenkov light, which is focused by a concave mirror and a system of lenses. Using a diaphragm, Cherenkov light that is emitted in a narrow angular range with respect to the optical axis is selected. Finally, the Cherenkov photons are detected by eight photomultipliers (PMTs) arranged on a ring around the optical axis. The momentum as defined by the beam optics is approximately the same for all beam particles. Therefore, the angle under which the Cherenkov light is emitted is the same for beam particles of the same species, but different for beam pions, kaons, or antiprotons. Each CEDAR detector can be tuned to identify a certain particle species, by selecting the pressure of the helium gas and the opening of the

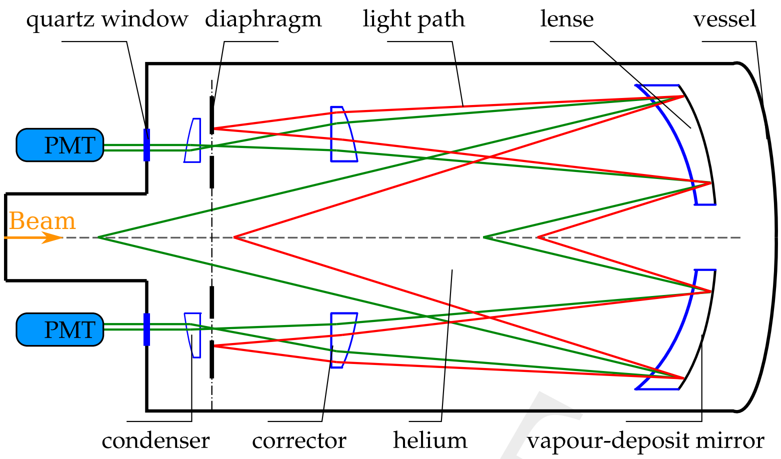

Figure 3.1: Basic operation principle of a CEDAR detector. The dashed line represents the optical axis of the detector, which coincides with the direction of the beam. The green and red lines represent the paths of Cherenkov light, which is emitted under different angles. Taken from ref. [49] and modified.

diaphragm, such that the Cherenkov ring of the selected species is focused on the PMTs (green lines in figure 3.1), while the Cherenkov rings of the other species are shielded by the diaphragm (red lines in figure 3.1).

For the diffraction data taking, both CEDARs were tuned to identify kaons. This means that the kaon Cherenkov ring was focused on the PMTs. Thus, a beam kaon should generate signals in the PMTs, while a beam pion or antiproton should not.

3.1.2 Challenges of the CEDAR Beam-Particle Identification

In previous analyses [44, 57], beam kaons were identified by requiring signals in the PMTs in coincidence with the incoming beam particle. Taking into account the imperfect efficiency of the PMTs, a signal in at least six out of the eight PMTs of one of the two CEDARs was required.

Unfortunately, this so-called majority method has a low efficiency of only 40 to 50 % [44]. The main reason is the finite spread in the inclination of the beam particles with respect to the optical axis of the CEDAR detectors. This beam divergence is about 200 µrad and thus of the same order of magnitude as the difference between the kaon and pion Cherenkov angles, which is around 130 µrad for the CEDAR parameters used in the diffraction data taking. For particles traversing the CEDAR parallel to its optical axis (figure 3.2a), the Cherenkov ring of a kaon (green ring) is in the sensitive area covered by the PMTs (gray circular area) and the Cherenkov ring of a pion (red ring) is outside of the PMTs' acceptance. However, if the beam particle has some finite inclination with respect to the optical axis its Cherenkov ring is shifted with respect to the diaphragm aperture. In the example shown in figure 3.2b, the Cherenkov light of a kaon would no longer hit the topmost three and bottommost three PMTs and only the leftmost and rightmost PMT would have a signal, while for a pion with the same inclination the topmost

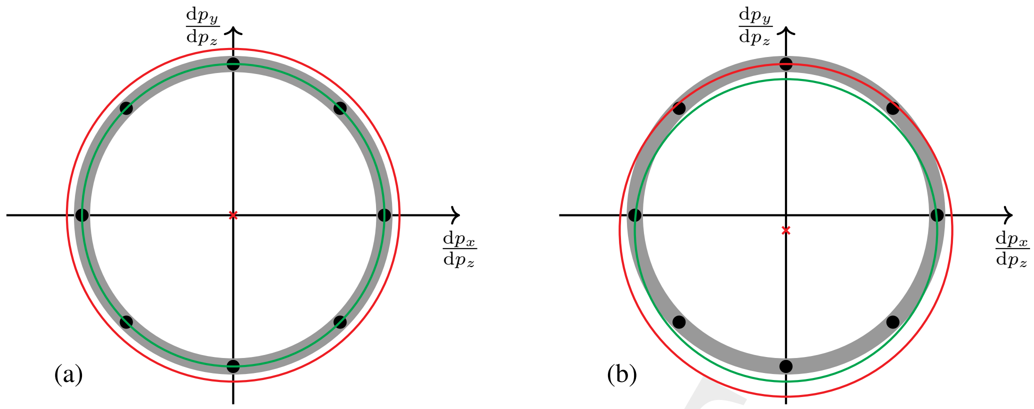

Figure 3.2: Illustration of the Cherenkov rings in the inclination space of beam particles represented by the red crosses. The green ring represents a beam-kaon Cherenkov ring. The red ring represents a beam-pion Cherenkov ring. The gray band represents the acceptance for Cherenkov photons defined by the diaphragm of the CEDAR. The black dots represent the position of the eight PMTs. (a) illustrates kaons and pions that traverse the CEDAR parallel to its optical axis. (b) illustrates kaons and pions that have some finite inclination in y-direction with respect to the optical axis.

PMTs would now give a signal. Therefore, for larger beam-kaon inclinations, fewer PMTs give a signal leading to the low efficiency of the majority method. However, figure 3.2 also shows that a certain hit pattern in the eight PMTs (i.e. which of the PMTs give a signal) is characteristic for a certain particle species at a given inclination. We exploit this to formulate a likelihood ansatz in section 3.1.3.

In a previous analysis of the Primakoff reactions measured in a different COMPASS data-taking campaign; Friedrich J., et al. developed in ref. [58] already a likelihood-based approach for the beam-particle identification. In ref. [59], a first attempt to formulate another likelihood-based approach for the 2008 diffraction data set was developed. Both approaches have in common, that they use independent parameterizations for the likelihood of beam kaons and pions with independent sets of parameters. Therefore, both methods rely on large calibration samples of pure beam kaons and pure beam pions.

In addition, the CEDAR parameters exhibit large modulations with time. For example, the helium gas density varied (see figure 3.5), caused by small gas leaks, which made a daily refilling of the gas vessel necessary. Also, the temperature of the CEDARs was not stable enough. These variations considerably effected the position of the Cherenkov rings making a time-dependent calibration mandatory. This exacerbates the requirement on the size of the calibration samples.

For the diffraction data set, the size of such beam samples, especially of a pure kaon-beam sample, is very limited, as shown in section 3.1.6. Therefore, pure kaon-beam and pure pion-beam samples that are sufficiently large to perform a time-dependent calibration of the CEDARs could not be obtained from the diffraction data sets. The goal of the likelihood ansatz developed in the following section is to not rely on pure kaon and pion-beam samples, but to extract the calibration from a mixed sample of beam kaons and pions.

3.1.3 Likelihood Method

The main difference between particle species S, e.g. kaons or pions, traversing the CEDAR detectors is their different Cherenkov angle[a]

$$\cos\theta_{\mathrm{Ch}}^{S} = \frac{1}{n\beta} = \frac{1}{n}\sqrt{1 + \left(\frac{m_S}{|\vec{p}|}\right)^2}. \tag{3.1}$$

The known beam momentum $|\vec{p}|$[b] and the refraction index of the helium gas n are the same for all particle species. The only particle-species specific quantity is the particle mass m_S, which is known [9]. The CEDARs are designed to accept light emitted in a certain angular range with respect to their optical axis. The emission angle is determined by the value of the Cherenkov angle and by the inclination of the beam-particle's trajectory with respect to the optical axis of CEDAR k. The inclination is defined by the beam particle momentum[c] in the small-angle approximation[d] as

$$^{k}\!\left(\frac{\mathrm{d}p_x}{\mathrm{d}p_z}\right)_{\mathrm{Beam}} \equiv {}^{k}\vartheta_x \qquad \text{and} \qquad ^{k}\!\left(\frac{\mathrm{d}p_y}{\mathrm{d}p_z}\right)_{\mathrm{Beam}} \equiv {}^{k}\vartheta_y. \tag{3.2}$$

Coordinate System

The CEDAR response on a Cherenkov photon only depends on its emission angle with respect to the CEDARs optical axis. For a given emission angle, the response is independent of the particle species. Thus, the response of the individual PMTs can be parameterized uniformly for all particle species. As we did not measure the emission angle of individual photons, we first had to define a suitable coordinate system to parameterize the response of a PMT. Therefore, we find for a certain particle species all possible beam particle inclinations (red/orange points in figure 3.3a), where the corresponding Cherenkov rings (red/orange rings in figure 3.3a) hit the PMT centrally. In the inclination space, these beam particles lie on a circle around the PMT with radius given by the Cherenkov angle (dashed green circle in figures 3.3a and 3.3b). For a beam particle of species S with an arbitrary inclination, e.g. the magenta point in figure 3.3b, the probability for a signal in PMT j[e] mainly depends on the distance, to the ideal inclination that

[a] The difference in the number of emitted Cherenkov photons (see equation 34.43 in ref. [9]) is about 1 % and hence negligible.
[b] The beam-momentum spread is less than 1 % [49] and hence has a negligible effect on the Cherenkov angle compared to the difference in m_S.
[c] The beam particle inclination was measured by the silicon beam telescope near the target position with high precision. From this, the inclination at the CEDAR position was calculated using a transport matrix determined from the known beam optics [60]. The inclinations of the beam particle with respect to optical axes were calculated, taking into account the CEDARs' tildes with respect to the laboratory frame.
[d] The small beam inclinations of about 200 µrad allows to use the small-angle approximation, i.e. $\sin\vartheta \approx \vartheta$
[e] The index, j, uniquely identifies each PMT in the two CEDARs. Therefore, $j = 0, \ldots, 15$.

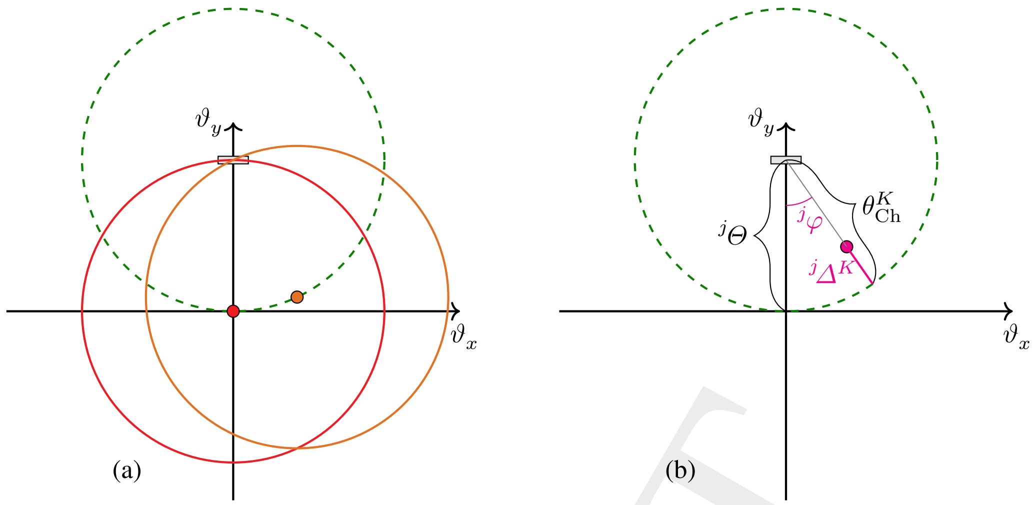

Figure 3.3: Two-dimensional inclination space of a beam particle with respect to the CEDARs optical axis. The gray box represents the center of the sensitive region of a PMT defined by the diaphragm. For illustration, the coordinate system was rotated such that the center of the PMT is on the vertical axis. (a) shows two exemplary beam inclinations (red/orange points), where the corresponding Cherenkov rings for kaons (red/orange circles) and the PMTs sensitive region intersect. The green dash circle shows all inclinations that fulfill this constraint. (b) shows a beam particle with arbitrary inclination (magenta point).

yields a signal in the PMT:

$$ {}^j\Delta^S\left({}^k\vartheta_x, {}^k\vartheta_y\right) = \theta^S_{\mathrm{Ch}} - \left\| \begin{pmatrix} {}^k\vartheta_x \\ {}^k\vartheta_y \end{pmatrix} - \begin{pmatrix} {}^j\Theta \cos {}^j\Phi \\ {}^j\Theta \sin {}^j\Phi \end{pmatrix} \right\| . \tag{3.3} $$

Here, ${}^j\Theta$ and ${}^j\Phi$ are the PMT's "position" in the inclination space, i.e. the direction in which a photon has to be emitted in order to hit the PMT centrally. As the CEDARs were tuned to beam-kaon identification, ${}^j\Theta \approx \theta^K_{\mathrm{Ch}}$.

The PMT response depends also on the angle ${}^j\varphi$, which corresponds to the tilt of the Cherenkov ring with respect to the sensitive area of the PMT defined by the diaphragm. It is calculated from the measured inclination and the PMT position as

$$ \sin\left[{}^j\varphi({}^k\vartheta_x, {}^k\vartheta_y)\right] = \frac{{}^k\vartheta_x\, {}^j\Theta \sin {}^j\Phi - {}^k\vartheta_y\, {}^j\Theta \cos {}^j\Phi}{\sqrt{\left({}^k\vartheta_x\right)^2 + \left({}^k\vartheta_y\right)^2 + \left({}^j\Theta\right)^2 - 2\left({}^k\vartheta_x\, {}^j\Theta \cos {}^j\Phi - {}^k\vartheta_y\, {}^j\Theta \sin {}^j\Phi\right) {}^j\Theta}} . \tag{3.4} $$

Equations (3.3) and (3.4) define the coordinate transformation from $({}^k\vartheta_x, {}^k\vartheta_y)$ to $({}^j\Delta^S, {}^j\varphi)$, which is different for each PMT j and each particle species S.

Parameterization of the Likelihood

The probability of a signal in PMT j, called hit probability ${}^{j}P_{\mathrm{PMT}}(\mathrm{Hit}\,|\,{}^{j}\!\Delta^{S}, {}^{j}\varphi)$, is a detector property given by the PMT response to a Cherenkov photon. Its functional dependence on ${}^{j}\!\Delta^{S}$ and ${}^{j}\varphi$ is the same for all particle species. Thus, we could model it with one uniform parameterization using the same parameters for all particle species. The hit probability consist of a signal part and background part that accounts for hits, uncorrelated to the incoming beam particle. The ${}^{j}\!\Delta^{S}$ dependence of the signal, which we discuss first, is dominated by the diaphragm, which selects a range in ${}^{j}\!\Delta^{S}$. We modeled this range by a rectangular function with a width of $2\,{}^{j}\Gamma$. This rectangular function was smeared out e.g. by the uncertainty of the measured beam inclination or by chromatic aberration of the CEDAR optics. We took this into account by convoluting the rectangular function with a Gaussian function of width ${}^{j}\sigma$. This equals to a difference of two error functions

$$\mathrm{Signal}({}^{j}\!\Delta^{S}, {}^{j}\varphi) = \mathrm{Erf}\left(\frac{{}^{j}\!\Delta^{S} + {}^{j}\Gamma({}^{j}\varphi)}{{}^{j}\sigma({}^{j}\varphi)}\right) - \mathrm{Erf}\left(\frac{{}^{j}\!\Delta^{S} - {}^{j}\Gamma({}^{j}\varphi)}{{}^{j}\sigma({}^{j}\varphi)}\right). \tag{3.5}$$

To obtain the total hit probability, we added a constant background term ${}^{j}\mathrm{Bkg}$ to this signal. The sum was normalized to its maximum at ${}^{j}\!\Delta^{S} = 0$ and multiplied by an amplitude parameter ${}^{j}\mathcal{A}$, which takes into account the efficiency of the PMT. The final parameterization for a hit and for no hit in the PMT reads

$$\begin{aligned} {}^{j}P_{\mathrm{PMT}}(\mathrm{Hit}\,|\,{}^{j}\!\Delta^{S}, {}^{j}\varphi) &= {}^{j}\mathcal{A}({}^{j}\varphi)\frac{\mathrm{Signal}({}^{j}\!\Delta^{S}, {}^{j}\varphi) + {}^{j}\mathrm{Bkg}}{\mathrm{Signal}(0\,\mathrm{rad}, {}^{j}\varphi) + {}^{j}\mathrm{Bkg}}, \text{ and} &(3.6)\\ {}^{j}P_{\mathrm{PMT}}(\overline{\mathrm{Hit}}\,|\,{}^{j}\!\Delta^{S}, {}^{j}\varphi) &= 1 - {}^{j}P_{\mathrm{PMT}}(\mathrm{Hit}\,|\,{}^{j}\!\Delta^{S}, {}^{j}\varphi), &(3.7)\end{aligned}$$

respectively. We expected the hit probability to be only weakly modulated within the small range in ${}^{j}\varphi$ of about 10 mrad covered by the beam divergence.[f] This modulation was modeled by a quadratic dependence of the ${}^{j}\mathcal{A}$, ${}^{j}\Gamma$, and ${}^{j}\sigma$ parameters on ${}^{j}\varphi$:

$$\begin{aligned} {}^{j}\mathcal{A}({}^{j}\varphi) &= {}^{j}c_0^{\mathcal{A}} + {}^{j}c_2^{\mathcal{A}} \cdot ({}^{j}\varphi)^2 &(3.8)\\ {}^{j}\Gamma({}^{j}\varphi) &= {}^{j}c_0^{\Gamma} + {}^{j}c_2^{\Gamma} \cdot ({}^{j}\varphi)^2 &(3.9)\\ {}^{j}\sigma({}^{j}\varphi) &= {}^{j}c_0^{\sigma} + {}^{j}c_2^{\sigma} \cdot ({}^{j}\varphi)^2 &(3.10)\end{aligned}$$

In total, the parameterization in equation (3.6) contains seven free parameters.

Assuming, that the hit probabilities for the eight PMTs are independent, the total probability to see a certain hit pattern in CEDAR k for a given particle species and particle inclination is

$${}^{k}P_{\mathrm{C}}(\text{Hit pattern}\,|\,S\,;\,{}^{k}\vartheta_x, {}^{k}\vartheta_y) = \prod_{j \in \text{CEDAR } k} {}^{j}P_{\mathrm{PMT}}(\text{Hit pattern}\,|\,S\,;\,{}^{k}\vartheta_x, {}^{k}\vartheta_y), \tag{3.11}$$

[f] The beam divergence of about 200 µrad translates to a range in ${}^{j}\varphi$ of ±10 mrad in the inclination space.

where

$$ {}^{j}P_{\mathrm{PMT}}(\text{Hit pattern}\,|\,S\,;\,{}^{k}\vartheta_x,{}^{k}\vartheta_y) = \begin{cases} {}^{j}P_{\mathrm{PMT}}(\text{Hit}\,|\,{}^{j}\Delta^S\,,{}^{j}\varphi) \text{ if PMT } j \text{ is hit} \\ {}^{j}P_{\mathrm{PMT}}(\overline{\text{Hit}}\,|\,{}^{j}\Delta^S\,,{}^{j}\varphi) \text{ if PMT } j \text{ is not hit} \end{cases} . \tag{3.12} $$

Equation (3.11) is the likelihood function that the beam particle is of species S using the information from CEDAR k

$$ {}^{k}\mathcal{L}_{\mathrm{C}}(S\,;\,\text{Hit pattern},{}^{k}\vartheta_x,{}^{k}\vartheta_y) = {}^{k}P_{\mathrm{C}}(\text{Hit pattern}\,|\,S\,;\,{}^{k}\vartheta_x,{}^{k}\vartheta_y). \tag{3.13} $$

For the coordinate transformations $({}^{k}\vartheta_x,{}^{k}\vartheta_y) \to ({}^{j}\Delta^S\,,{}^{j}\varphi)$, the positions of PMTs in the inclination space has to be known, which gives two additional free parameters per PMT. We used the difference, ${}^{j}\Delta\Theta = {}^{j}\Theta - \theta^{K}_{\mathrm{Ch}}$, of the PMT positions, ${}^{j}\Theta$, to the expected position of the kaon Cherenkov ring at θ^{K}_{Ch} as free parameter in the fit, which reduced the correlation among the fit parameters and therefore lead to a more robust fit. Also, the refraction index of the helium gas has to be known, which is one further parameter common for all PMTs of one CEDAR. Therefore, the employed likelihood parameterization for a single CEDAR detector has in total $8(7+2)+1 = 73$ free parameters to be determined by from data. All of them are detector specific parameters, which are independent of the particle species.

Finally, the information of both CEDARs was combined in a single likelihood

$$ \mathcal{L}(S\,;\,\text{Hit pattern},\vartheta_x,\vartheta_y) = {}^{1}\mathcal{L}_{\mathrm{C}}(S\,;\,\text{Hit pattern},{}^{1}\vartheta_x,{}^{1}\vartheta_y)\cdot{}^{2}\mathcal{L}_{\mathrm{C}}(S\,;\,\text{Hit pattern},{}^{2}\vartheta_x,{}^{2}\vartheta_y). \tag{3.14} $$

Based on this likelihood, two particle hypotheses can be compared by calculating the log-likelihood difference of hypotheses S and S':

$$ \mathcal{D}_{\mathrm{C}}(S,S') = \log_{10}\left[\mathcal{L}(S\,;\,\text{Hit pattern},\vartheta_x,\vartheta_y)\right] - \log_{10}\left[\mathcal{L}(S'\,;\,\text{Hit pattern},\vartheta_x,\vartheta_y)\right], \tag{3.15} $$

which is the same as the $\log_{10}$ of the likelihood-ratio. We assumed a beam particle to be of species S if $\mathcal{D}_{\mathrm{C}}(S,S')$ was above a chosen threshold $\mathcal{T}_{\mathrm{C}}(S)$ using the information of the CEDARs.[g]

3.1.4 Likelihood Calibration

In the section above, we formulated in equation (3.13) a likelihood for each CEDAR detector. Therefore, we could calibrate the two detectors separately. In order to account for the time dependence of the CEDAR parameters, we performed the calibration independently in up to 2 hour long periods in time, the so-called runs.[h]

[g] We used the $\log_{10}$ as the likelihoods cover a wide dynamic range.

[h] In studies, we performed calibrations in time periods shorter than a run and compared the resulting likelihood parameters. From these studies we concluded, that a run-by-run calibration is sufficient to resolve the time evolution of the CEDAR parameters.

Before calibrating the likelihood parameters, we determined the tilt of the CEDAR detectors with respect to the nominal beam axis in the laboratory frame and the time resolution of the PMTs, which determines when a signal in a PMT is associated to the event and considered to be a hit. The time resolution of the PMTs is about 0.13 ns and the tilt of the CEDARs is about 70 µrad. Details can be found in ref. [54].

All 73 free parameters of the likelihood function in equation (3.13) are detector specific parameters that are independent of the particle species hypothesis. Therefore, any sufficiently large data sample with a mixture of particle species can be used to calibrate the likelihood. The precision of the measured beam-particle inclination is higher for a larger number of final-state particles.[i] In order to obtain a calibration sample that has a similar beam-inclination precision as the $K^-\pi^-\pi^+$ sample analyzed in this work, but is much larger than the $K^-\pi^-\pi^+$ sample, we used events with three charged hadrons in the final state for calibration. The applied event selection is explained in detail in appendix A.1.1. The number of calibration events per run is in the range of 1×10^4 to 7×10^5 events, which is sufficient to perform an independent calibration in each run. In total, the calibration sample consists of 1.5×10^8 events for the 2008 and 1.3×10^8 events for the 2009 diffraction data set.

For calibrating the likelihood, we take into account only the pion and kaon hypothesis. Muons and electrons in the beam have almost the same Cherenkov angle as pions,[j] and thus cannot be separated from pions. Antiprotons in the beam have a Cherenkov angle much smaller than that of kaons.[k] Therefore, the vast majority of antiprotons will not produce a hit in any of the PMTs, similar to the majority of pions. This means, also antiprotons are indistinguishable from pions. Given the much larger pion fraction in the beam; electrons, muons, and antiprotons do not bias the result of the likelihood calibration.[l]

The admixture of beam pions and kaons in the calibration sample is taken into account in the formulation of the probability for seeing a certain hit pattern in CEDAR detector k:

$$\begin{aligned} {}^k\mathcal{P}_\mathrm{C}(\text{Hit pattern}\,|\,{}^k\vartheta_x, {}^k\vartheta_y,) = {}&{}^k\mathcal{P}_\mathrm{C}(\text{Hit pattern}\,|\,\pi;\, {}^k\vartheta_x, {}^k\vartheta_y)\,[1 - P(K)] \\ &+ {}^k\mathcal{P}_\mathrm{C}(\text{Hit pattern}\,|\,K;\, {}^k\vartheta_x, {}^k\vartheta_y)\, P(K). \end{aligned} \tag{3.16}$$

This approach adds only one additional free parameter, which is the probability $P(K)$ to find a kaon in the beam. The probabilities ${}^k\mathcal{P}_\mathrm{C}(\text{Hit pattern}\,|\,\pi;\, {}^k\vartheta_x, {}^k\vartheta_y)$ and ${}^k\mathcal{P}_\mathrm{C}(\text{Hit pattern}\,|\,K;\, {}^k\vartheta_x, {}^k\vartheta_y)$ share the same set of 73 likelihood parameters used to parameterize the CEDAR response. Their

[i] The precision of the measured position of the beam particle in the target is given by the precision of the interaction-vertex reconstruction. It is higher for a larger number of final-state particles, because more information entered the vertex reconstruction. As the beam-particle inclination at the CEDAR position is related to its position in the target region by the beam optics, the vertex reconstruction also determines the precision of the beam-particle inclination.

[j] Muons have almost the same mass as pions. The Chrerenkov angle of electrons is only 10 µrad larger than the one of pions for the helium pressure of the CEDARs.

[k] For the CEDAR parameters during the diffraction data taking, the Cherenkov angle of antiprotons is approximately 350 µrad smaller than the Cherenkov angle of kaons, which is a large difference compared to the beam divergence of about 200 µrad.

[l] In a study, we tried to include the antiproton hypothesis in the likelihood calibration. This lead to very unstable and partly unrealistic results.

only difference is the different transformation $({}^{k}\vartheta_x, {}^{k}\vartheta_y) \to ({}^{j}\Delta^S, {}^{j}\varphi)$, which requires only the known particle masses. Finally, the likelihood function that is maximized in an unbinned maximum-likelihood fit to determine the 74 free parameters, $\{p_C\}$, reads

$$\mathcal{L}_{\text{Fit}}(\{p_C\}) = \prod_{\zeta=1}^{N_{\text{Events}}} {}^{k}P_C(\text{Hit pattern}^{(\zeta)} \,|\, {}^{k}\vartheta_x^{(\zeta)}, {}^{k}\vartheta_y^{(\zeta)}, \{p_C\}). \tag{3.17}$$

3.1.5 Agreement of the Likelihood Parameterization with the Calibration Sample

To illustrate the results of the likelihood calibration, a single run[m] is used as an example. The hit probability for PMT0 of CEDAR1, i.e. the ratio of events with a PMT hit to the total number of events (data points in figure 3.4), is reproduced well by the result of the calibration fit (red dashed curves). In the central ${}^{0}\varphi$ region shown in figure 3.4a, the hit probability distribution exhibits a clear peak at ${}^{0}\Delta^K \approx -130\,\mu\text{rad}$, which is dominantly described by the pion contribution (orange curve below the red curve). Furthermore, the data show a slight shoulder around ${}^{0}\Delta^K = 0\,\mu\text{rad}$, which is described by the kaon contribution (green curve). As we chose to use the coordinate transformation for the kaon hypothesis (${}^{0}\Delta^K$) to show the data, it is expected that the kaon peak is at ${}^{0}\Delta^K = 0\,\mu\text{rad}$ and that the distance between the kaon and the pion peak corresponds to the difference between their Cherenkov angle, which is about $130\,\mu\text{rad}$. Also, the ${}^{0}\varphi$ dependence of the hit probability is described well by the calibrated likelihood, as shown by the hit probability distribution in the outer ${}^{0}\varphi$ region in figures 3.4a and 3.4b. Due to the limited beam spread, only half of the pion peak can be accessed in the outer ${}^{0}\varphi$ region. Overall, the agreement of the calibrated likelihood function with the calibration sample is similarly good for all PMTs and runs of the diffraction data taking. Therefore, we can conclude, that the employed likelihood parameterization of equation (3.13) is able to describe the CEDAR response and that we are able to reliably determine its parameters from data.

Time Evolution of the Likelihood Parameters

In the following, the time dependence of the CEDAR likelihood parameters is discussed based on selected examples of the parameters of PMT0 in CEDAR1 during the 2008 diffraction data taking. The time evolution of the refraction index parameter is stable within small fluctuations on the 10^{-5} level, except for the last few days of the data taking (see black line with blue band in figure 3.5). However, it is not proportional to the measured density of the helium gas (red dots) as it would be expected. Despite, the positions ${}^{j}\Theta$ of the PMTs in the inclination space, which are also free parameters, exhibit a clear correlation with the helium density, as shown exemplarily for PMT0 in CEDAR1 by the black line with blue band in figure 3.6. The reason is an approximate ambiguity in the likelihood function between the refraction-index parameter

[m] We use the data from run number 70450.

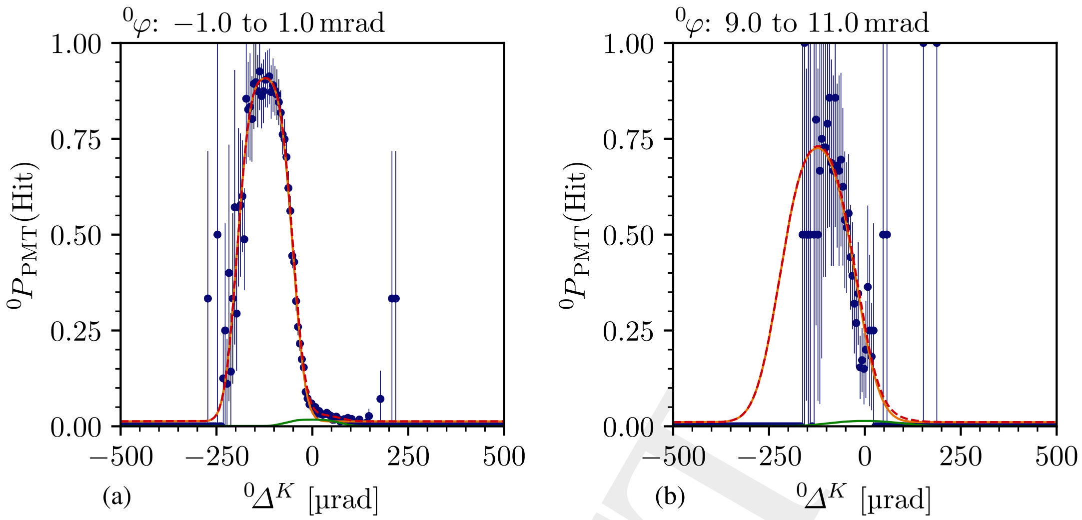

Figure 3.4: Hit probability distribution for PMT0 of CEDAR1 as a function of the distance ${}^{0}\varDelta^{K}$ to the nominal kaon ring for (a) the central and (b) an outer ${}^{j}\varphi$ region. The points represent the data. The red dashed curve is the result of the maximum-likelihood fit. The orange curve represents the pion and the green curve the kaon contribution according to equation (3.6).[m]

and the PMT-position parameters.[n] As the refraction-index parameter cannot be determined precisely in the likelihood calibration, we obtained a roughly constant refraction-index parameter. The true variation of the refraction index of the helium gas is effectively accounted for by the PMT-position parameters.[o]

The time evolution of the width parameter ${}^{j}c_{0}^{\varGamma}$ of the rectangular function of the hit-probability parameterization in equation (3.6) exhibits two clear steps as shown in figure 3.7. These steps coincide with the narrowing and widening of the diaphragm aperture during data taking. The determined value of ${}^{j}c_{0}^{\varGamma}$ is approximately directly proportional to the measured aperture, as expected. Except for these steps, the parameter is stable. The width ${}^{j}c_{0}^{\sigma}$ of the Gaussian smearing of the rectangular function is also stable with time (not shown) and is not affected by the changes of the diaphragm aperture.

[n] The reason for this ambiguity is, that the position of the peaks in the hit probability distribution in ${}^{j}\varDelta^{S}$ (see figure 3.4) is given by two parameters [see equation (3.3)]. First, the peak positions depend on the predicted Cherenkov angle, θ^{S}_{Ch}, and thereby on the refraction-index parameter. Second, the peak positions can be shifted by adjusting the PMT-position parameters ${}^{j}\varTheta$. The PMT-position parameters cannot be determined from other constraints. The refraction-index parameter could in principle be determined from two other constraints. Either from the radius of the Cherenkov ring, i.e. the green dashed line in figure 3.3b. However, the beam illuminates only a very small segment of this circle, which is insufficient to determine the refraction index. Or by the difference between the pion and the kaon Cherenkov angle, given by the difference of the peak positions. However, this difference is less sensitive on the refraction index than the absolute Cherenkov angle. Therefore, it is also insufficient to determine the refraction index.

[o] The refraction index could not be calculated from the measured helium density, because it was not measured for the full diffraction data taking.

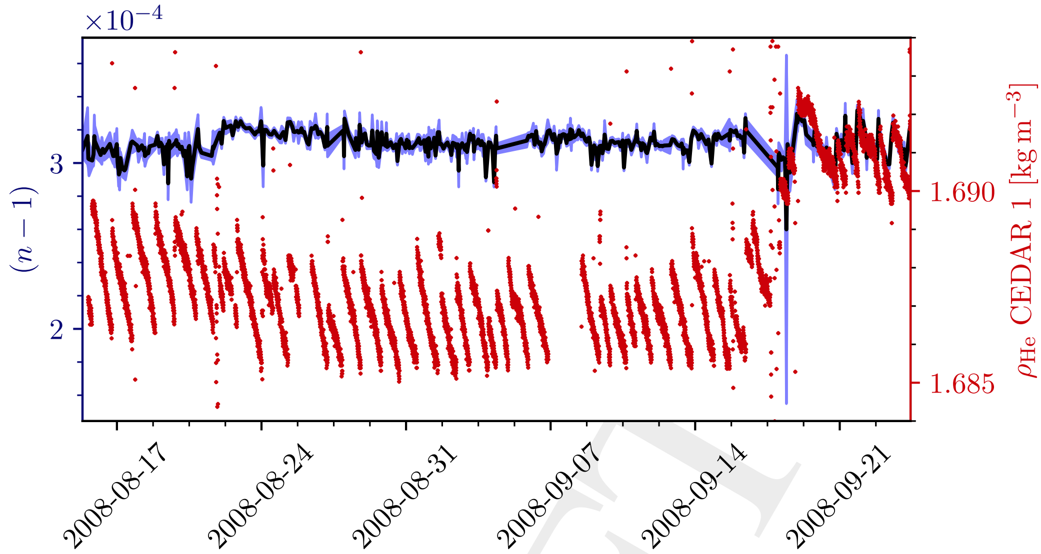

Figure 3.5: Time evolution of the refraction index n of the He gas in CEDAR1. The black line represents the central values and the blue band the statistical uncertainties of the refraction index as determined by the likelihood calibration fit. The red dots represent the density ρ_{He} in CEDAR1 as measured during the data taking. The CEDAR1 density was not measured continuously.

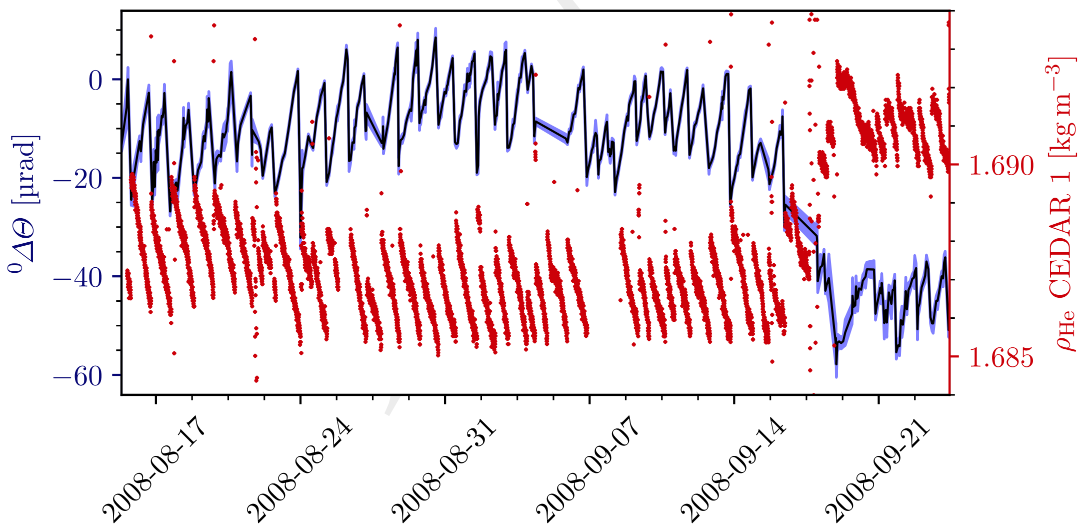

Figure 3.6: Time evolution of the ${}^{j}\Theta$-position of PMT0 in CEDAR1. The black line represents the central value and the blue band the statistical uncertainty of the difference between the PMT ${}^{j}\Theta$-position with respect to the kaon Cherenkov ring as determined by the likelihood calibration fit. The red dots represent the density in CEDAR1 as recorded during the data taking. The CEDAR1 density was not measured continuously.

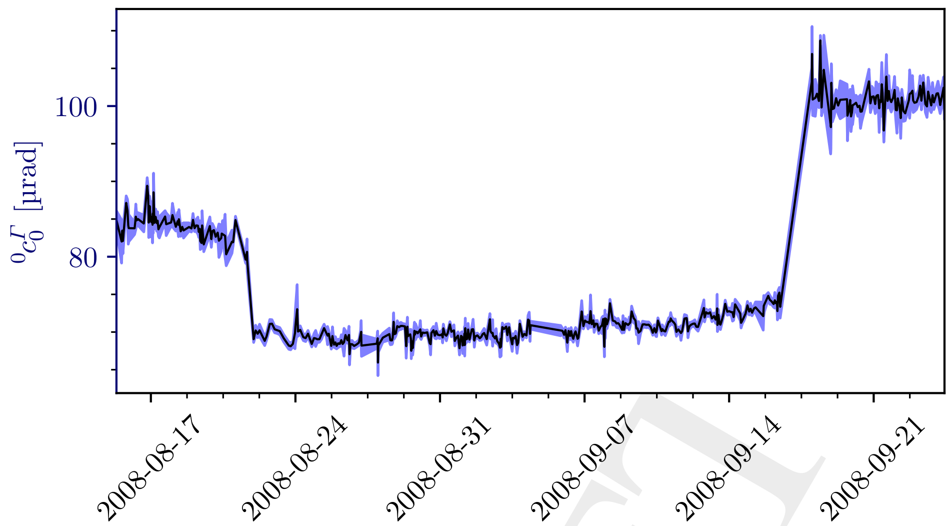

Figure 3.7: Time evolution of the width parameter ${}^0c_0^\sigma$ of PMT0 in CEDAR1. The black line represents the central values and the blue band the statistical uncertainties of the width parameter as determined by the likelihood calibration fit.

Overall, we were able to determine all likelihood parameters reliably. Some parameters such as ${}^jc_0^\Gamma$ follow the physical quantities their represent. Other parameters such as the refraction index and the PMT positions act as an effective parameterization of the corresponding physical quantities. This shows, that the likelihood parameterization is able to reproduce the physical properties of the CEDARs.

3.1.6 Estimation of Particle Identification Performance

As was shown in section 3.1.5, the likelihood parameterization in equation (3.17) is able to reproduce the calibration sample and the obtained parameters correlate with the physical quantities of the CEDAR detectors, as expected. However, we still have to verify, that the likelihood-based beam-particle identification is able to separate kaons from pions. The efficiency of the particle identification, i.e. the fraction beam particles of species S that are identified as S, and its impurity, i.e. the fraction of beam particles of another species contained in a data set where the beam particle species was identified as S, has to be determined. This requires pure pion-beam and kaon-beam validation samples. In contrast to the calibration sample, the size of the validation samples may be significantly smaller. However, it must still be sufficiently large in order to be able to study the CEDAR performance for the 2008 and 2009 diffraction data set separately.

To obtain a clean pion-beam sample, we selected events of the reaction $\pi^- + p \to \pi^-\pi^0\pi^0 + p$, where we identified all final-state particles. Thereby, we ensure that the beam particle is a pion without using the CEDAR information.[p] The pion-beam sample consist of about 10^6 events each for the 2008 and 2009 diffraction data set. In order to obtain a pure kaon-beam sample, we selected decays of beam kaons into different final states: $K^- \to \mu^- \bar{\nu}_\mu$, $K^- \to \pi^-\pi^-\pi^+$, and $K^- \to \pi^-\pi^0$; with about 80×10^3, 15×10^3, and 7×10^3 events; respectively; each for the 2008 and 2009 diffraction data set. The $K^- \to \pi^-\pi^-\pi^+$ and $K^- \to \pi^-\pi^0$ samples show non-negligible background, which is accounted for by performing a statistical background subtraction. The event selections for the calibration samples are explained in detail in appendix A.1.2.

Likelihood Distributions and Particle Identification Cuts

We verified the calibrated likelihood in equation (3.13) by identifying beam particles in the pion- and kaon-beam[q] samples selected from the 2008 diffraction data set using the information of only CEDAR1. The distribution of the log-likelihood difference is shown in figure 3.8a as a function of the beam-particle inclination,[r]

$$ {}^{1}\vartheta = \sqrt{\left({}^{1}\vartheta_x\right)^2 + \left({}^{1}\vartheta_y\right)^2}, \tag{3.18} $$

for the pion-beam sample. As expected, the distribution concentrates mainly in the region where the log-likelihood difference is below 1, i.e. where the pion hypothesis is the more likely one. Likewise, the log-likelihood difference distribution for the kaon-beam sample (see figure 3.8b) is concentrated in the region where the log-likelihood difference is above 1, i.e. where the kaon hypothesis is the more likely one. With increasing beam-particle inclination, both distributions approach the central region where pion and kaon hypothesis become similar and therefore harder to distinguish (dashed line).

Both distributions in figures 3.8a and 3.8b show clear bands. To understand their origin, we study the log-likelihood difference distribution of events with a certain number of hits in the PMTs of CEDAR1. Requiring hits in all eight PMTs projects out the topmost band of the log-likelihood difference distribution in the kaon-beam sample (see figure 3.8d), while the pion-beam sample contains practically no events with eight PMT hits (see figure 3.8c). Here, the discrimination between kaons and pions works best, which is exploited in the majority method (see section 3.1.2). However, figure 3.8d also shows, that the inclination for beam particles with eight PMT hits is limited to be below about 100 µrad. For larger inclinations, the kaon Cherenkov ring moves out of the PMTs' acceptance defined by the diaphragm aperture. The validation data show similar limitations of the ${}^{1}\vartheta$ range for events with seven or six PMT hits. Therefore, the majority method is able to distinguish beam pions from kaons only in a limited inclination range, which explains its low efficiency. Beam pions and kaons with hits in only four

[p] By ensuring that the final state consists only of pions, we ensured that the beam particle was also a pion and not a kaon or antiproton, because of strangeness and baryon number conservation in diffractive scattering reactions.

[q] Here, we use only the $K^- \to \mu^- \bar{\nu}_\mu$ sample. It is the only one that is nearly background free and sufficiently large.

[r] The beam-particle inclination with respect to the optical axis of CEDAR k, ${}^{k}\vartheta$, is different from the beam inclination in the laboratory frame due to the finite tilt of the CEDAR detectors of about 70 µrad, which is similar for both CEDAR detectors. We chose to use ${}^{1}\vartheta$ to show the data.

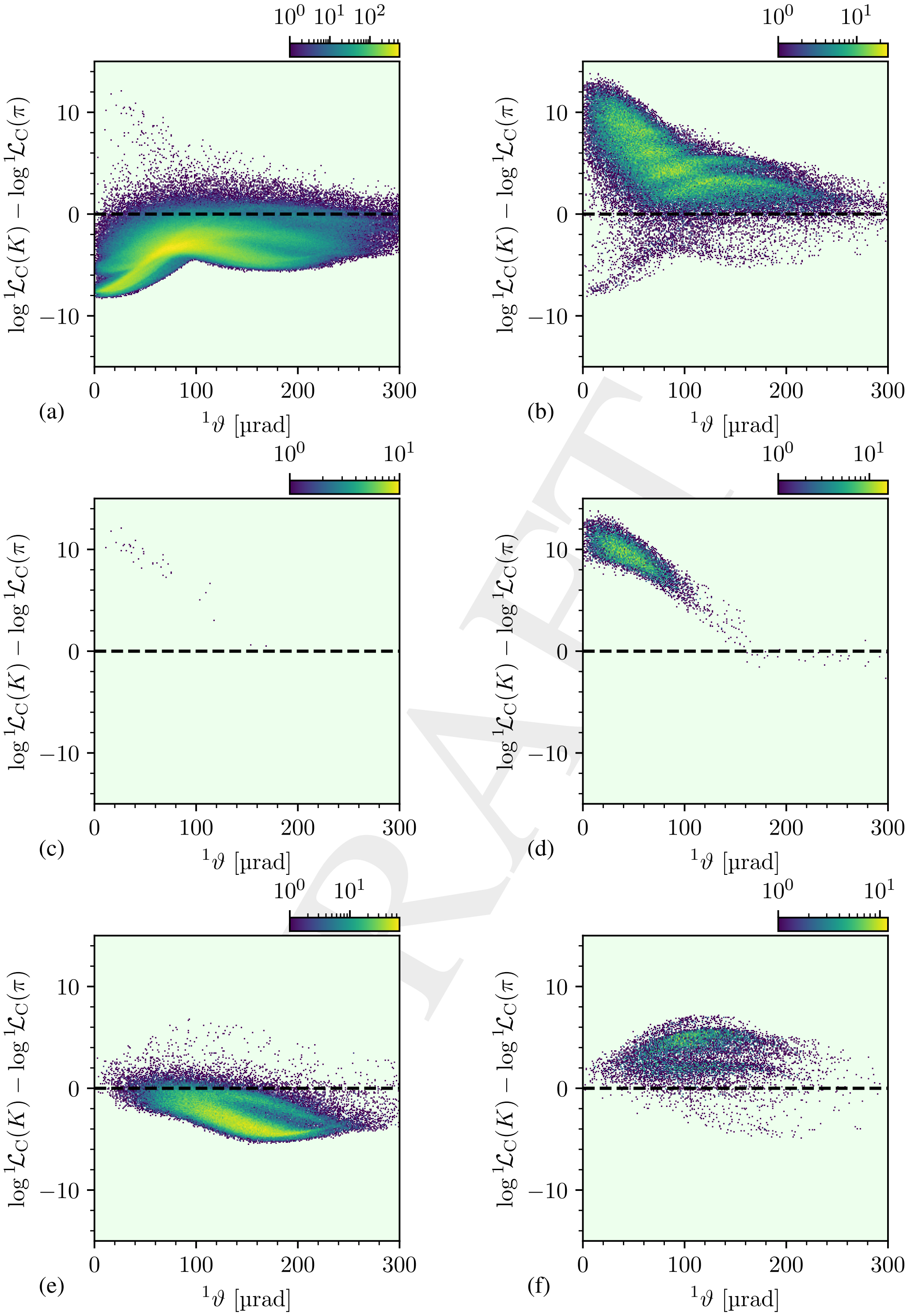

Figure 3.8: Difference of the kaon and pion log-likelihood for CEDAR1 as a function of the beam inclination angle ${}^{1}\vartheta$ defined in equation (3.18). The left column shows the pion-beam sample, the right column shows the kaon-beam sample. The first row shows all events, the second row shows events with hits in all eight PMTs, and the last row shows events with hits in four PMTs. Histogram cells with zero events are shown in light green.

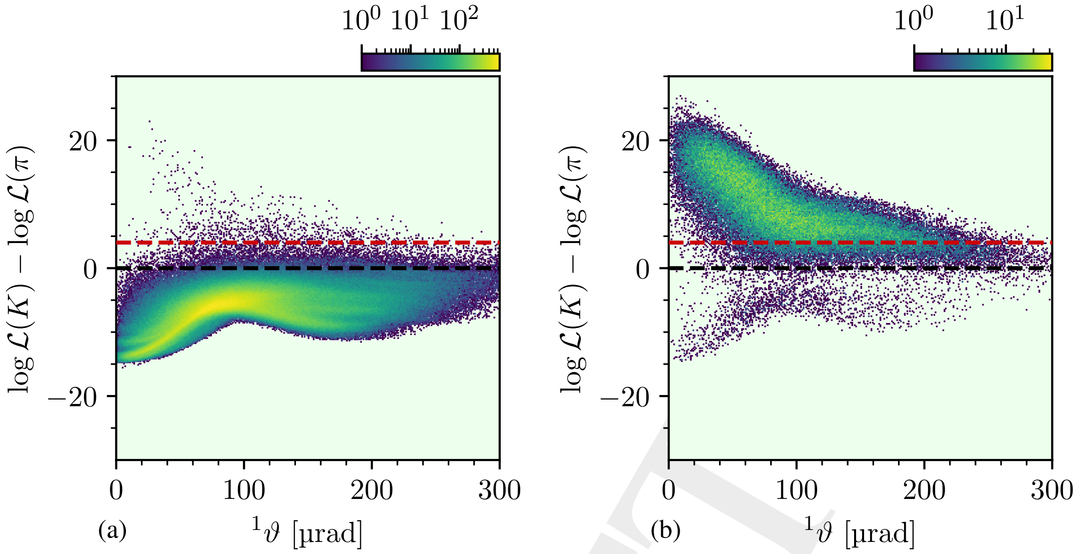

Figure 3.9: Difference of the kaon and pion log-likelihood for both CEDARs as defined in equation (3.15). We chose the beam inclination angle, $^1\vartheta$, with respect to the optical axis of CEDAR1 as coordinate system. The left column shows the pion-beam sample, the right column shows the kaon-beam sample. The dashed red line represents the threshold, $\mathcal{T}_\mathrm{C}(K) = 4.0$, in log-likelihood difference for kaon identification. Histogram cells with zero events are shown in light green.

PMTs cannot be discriminated using the majority method. However, the log-likelihood difference discrimination clearly favors the pion hypothesis for the pion-beam sample (see figure 3.8e) and the kaon hypotheses for the kaon-beam sample (see figure 3.8f). This improved discrimination power of the likelihood-based method compared to the multiplicity method arises from taking into account the difference in the hit patterns for pions and kaons, even for a small number of PMT hits. Hence, the likelihood-based method allows separating beam kaons from pions also for larger inclinations beyond 100 µrad.

For the final decision about the beam-particle species, the likelihood of both CEDARs was combined into a single likelihood for a given particle-species hypothesis according to equation (3.14). The distribution of the combined log-likelihood difference again exhibits bands as shown in figure 3.9. Due to the combination of the information from both CEDARs, the bands are smeared out compared to the log-likelihood difference distribution of a single CEDAR discussed above. Comparing the log-likelihood difference distribution for the kaon- and pion-beam samples, a clear separation between kaons and pions in the likelihood space is observed. To identify a beam particle as a kaon, we required the log-likelihood difference in equation (3.15) to be above a certain threshold $\mathcal{T}_\mathrm{C}(K)$ (red dashed lines in figure 3.9). To identify a beam particle as a pion, we required the log-likelihood difference to be below another threshold $\mathcal{T}_\mathrm{C}(\pi)$.

Efficiency and Purity

Efficiency and impurity of this method depend on the choice of the thresholds $\mathcal{T}_\mathrm{C}(\pi)$ and $\mathcal{T}_\mathrm{C}(K)$ in log-likelihood difference. For an optimum choice of these thresholds we determined estimates for efficiency and impurity as a function of the threshold. Therefore, we compared the number of pions or kaons before and after applying the CEDAR likelihood method to the pion or kaon beam validation samples, respectively. Details can be found in appendix A.1.3. As determining a single number for the efficiency or impurity implies averaging over the beam-particle inclinations, the distribution of the beam particles in the validation samples should be similar to the one in the $K^-\pi^-\pi^+$ sample analyzed in this work. This holds approximately for the pion-beam sample. The inclination distributions of the three kaon-beam samples however differ slightly from the ones in the $K^-\pi^-\pi^+$ sample (see figure A.1). To estimate the corresponding systematic effect, we determined efficiency and impurity from all three samples. $\mathcal{T}_\mathrm{C}(K)$ and $\mathcal{T}_\mathrm{C}(\pi)$ were optimized using the kaon-beam sample from $K^- \to \pi^-\pi^-\pi^+$ decays of the 2008 diffraction data set.

For the beam kaon identification, the dependence of efficiency and impurity on $\mathcal{T}_\mathrm{C}(K)$ is shown in figure 3.10a. To achieve a small impurity, but still maintain a high efficiency, we have chosen a threshold for the kaon identification of $\mathcal{T}_\mathrm{C}(K) = 4.0$. Table 3.1 summarizes the results for all three kaon-beam samples and for the 2008 and 2009 diffraction data. The various kaon-beam samples give slightly different results, which provides a measure the systematic uncertainty on the measured efficiency and impurity. Overall, we obtained a kaon-identification efficiency of about 85 % at an impurity of about 3 %. The impurity of the identified-kaon sample due to the antiprotons in the beam is expected to be negligible.[s]

For the beam pion identification, which is important in other analyses[43, 61, 62], the dependence of efficiency and impurity on $\mathcal{T}_\mathrm{C}(\pi)$ is shown in figure 3.10b. As the impurity is already very small for all considered thresholds, we chose a pion identification threshold of $\mathcal{T}_\mathrm{C}(\pi) = 0$ to achieve a high efficiency of about 98 % with a low impurity of about 0.05 % as listed in table 3.2.[t] The impurity of the identified-pion due to the antiproton fraction in the beam cannot be larger than the overall antiproton fraction in the beam of about 1 % [63].

In summary, the likelihood-based method developed in this work identifies the species of beam particles with high efficiency, while maintaining a low impurity from other species. The method provides a similar performance as the likelihood method developed in ref. [58] for the COMPASS Primakoff data set.[u] Using the fact, that the CEDAR response on Cherenkov photons emitted under a certain angle with respect to the CEDAR's optical axis is independent of the particle

[s] With the approach used here, we cannot make quantitative statements on the impurity of an identified-kaon sample due to the antiprotons in the beam. However, as the antiprotons should mainly be tagged as pions (see section 3.1.4), we expect a similar suppression for antiprotons and pions of about 10^{-3}. Since the antiproton fraction in the beam is small, the antiproton impurity of a kaon-identified sample is a negligible effect.

[t] We suspect, that the reason for the large impurity value from $K^- \to \pi^-\pi^0$ kaon-beam sample is that it is not clean enough to obtain a reasonable value for the misidentification probability $P(K \to \pi)$ from it. The two other validation samples give consistent results for the impurity value.

[u] To directly compare the results of both methods, we applied our method and the method from ref. [58] to a small fraction of the Primakoff data. Both methods yielded similar results.

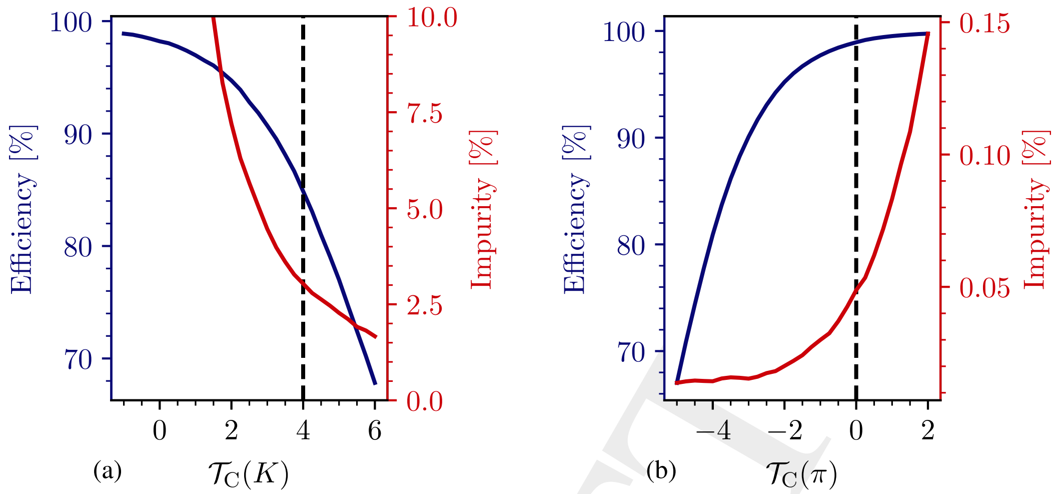

Figure 3.10: Efficiency (blue) and impurity (red) for (a) kaon and (b) pion particle identification as a function of the thresholds $\mathcal{T}_{\mathrm{C}}(K)$ and $\mathcal{T}_{\mathrm{C}}(\pi)$, respectively, applied to the log-likelihood difference. The black dashed lines shows the chosen threshold values. The pion-beam sample is used to determine the efficiency of the pion identification and the impurity an identified-kaon sample. The $K^- \to \pi^-\pi^-\pi^+$ sample is used to determine the efficiency of the kaon identification and the impurity of an identified-pion sample.

Table 3.1: Efficiency and impurity of the beam-kaon identification. The efficiency was obtained either from the $K^- \to \pi^-\pi^-\pi^+$, the $K^- \to \pi^-\pi^0$, or from the $K^- \to \mu^-\bar{\nu}_\mu$ sample. The misidentification probability was obtained from the pion-beam sample. The table lists the central values and statistical uncertainties.

		$K^- \to \pi^-\pi^-\pi^+$	$K^- \to \pi^-\pi^0$	$K^- \to \mu^-\bar{\nu}_\mu$
Efficiency ($K \to K$)	2008 [%]	84.9 ± 1.0	88.9 ± 2.0	89.2 ± 0.5
	2009 [%]	83.2 ± 1.0	84.4 ± 2.0	86.3 ± 0.6
Impurity ($\pi \to K$)	2008 [%]	3.04 ± 0.13	2.90 ± 0.14	2.89 ± 0.12
	2009 [%]	2.89 ± 0.13	2.85 ± 0.14	2.79 ± 0.12

Table 3.2: Efficiency and impurity of the beam-pion identification. The efficiency was obtained from the pion-beam sample. The misidentification probability was obtained either from the $K^- \to \pi^-\pi^-\pi^+$, the $K^- \to \pi^-\pi^0$, or from the $K^- \to \mu^-\bar{\nu}_\mu$ sample. The table lists the central values and statistical uncertainties. The value of the efficiency is independent of the used kaon-beam sample and therefore given only once.

Efficiency ($\pi \to \pi$)	2008 [%]	98.94 ± 0.13		
	2009 [%]	97.56 ± 0.13		
		$K^- \to \pi^-\pi^-\pi^+$	$K^- \to \pi^-\pi^0$	$K^- \to \mu^-\bar{\nu}_\mu$
Impurity ($K \to \pi$)	2008 [%]	0.049 ± 0.003	0.18 ± 0.05	0.038 ± 0.003
	2009 [%]	0.050 ± 0.003	0.14 ± 0.05	0.044 ± 0.003

species, the calibration of the likelihood method developed here does not require pure kaon-beam and pion-beam samples. This is a major advantage over the methods developed in refs. [58, 59] and allowed us to perform a time-dependent calibration. Compared to the majority method used in previous analyses [44, 57], our method achieves a two times larger kaon-identification efficiency, mainly by being able to identity beam kaons also at larger inclinations.

3.2 Final-State Particle Identification

Final-state particles of various species are produced in the interaction of the high-energy hadron beam with the liquid-hydrogen target. In the analysis presented here, we are interested only in charged final-state particles. The charged final-state particles that are measured with the COMPASS spectrometer are electrons, muons, pions, kaons, or protons. These particle species are distinguished by employing the information from Cherenkov photons measured in the ring-imaging Cherenkov detector (RICH).

3.2.1 Particle Identification using the RICH Detector

High-energy final-state particles produce Cherenkov photons while traversing the 3 m long RICH vessel, which is filled with C_4F_{10} as a radiator gas [49]. The Cherenkov photons are focused by a system of mirrors onto two arrays of position-sensitive photon detectors, [v] where they from rings. Measuring the radius of these rings allows to determine the Cherenkov angle defined in equation (3.1) under which the Cherenkov photons were emitted.

The Cherenkov angle is directly related to the particle species by its mass, its measured momentum, and the known refraction index of the gas in the RICH volume. In contrast to beam particles, which have approximately the same momentum, final-state particles have a broad momentum distribution leading to a broad distribution of their Cherenkov angles. Therefore, the value of the Cherenkov angle is measured for each final-state particle and is compared to predictions for the various particle-species hypotheses to identify the particle.

Figure 3.11 shows the distribution of the measured Cherenkov angles as a function of the particle momentum. This distribution exhibits clear bands from pions, kaons, and protons for momenta above about 2.5, 9, and 17 GeV/c, respectively. These lower limits are determined by the corresponding Cherenkov threshold,[w] which is given by the particle mass. Above about 50 GeV/c, the Cherenkov angles of kaons and pions become similar, which limits the kaon-pion separation to lower momenta. Similarly, proton identification is limited to momenta below about

[v] In the peripheral regions, multiwire proportional chambers with solid-state CsI photocathodes are used. In the central region with higher background, multi-anode photomultiplier tubes are used.

[w] In order to reconstruct the Cherenkov ring and determine the Cherenkov angle, a minimum of four measured Cherenkov photons is required. This translates so a minimal Cherenkov angle of about 20 mrad.

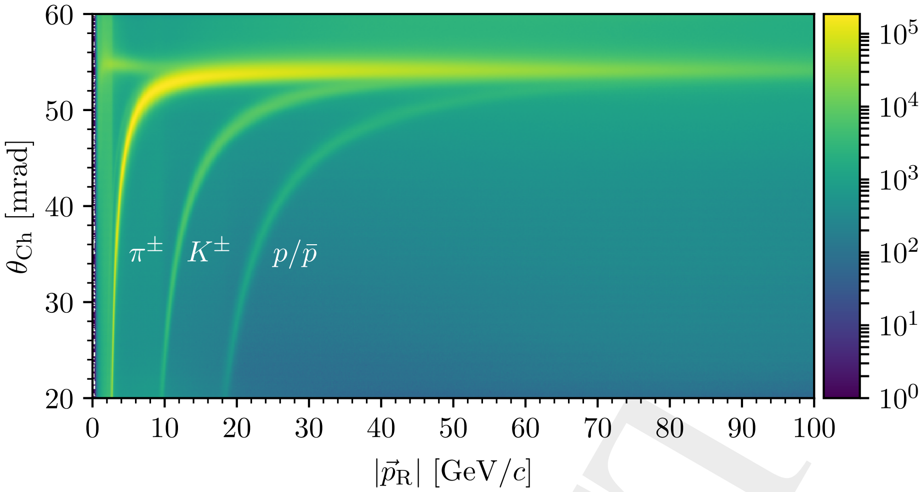

Figure 3.11: Distribution of the measured Cherenkov angles as a function of the final-state particle momentum, $|\vec{p}_{\mathrm{R}}|$, at the RICH position. We show the data sample with three charged particles per event obtained by applying the preselection criteria (see section 4.1) to the 2008 diffraction data set.

80 GeV/c, because for higher momenta the Cherenkov angle of protons becomes similar to the angles of kaons and pions. Muons cannot be separated well from pions for most of the momentum range, due to their similar mass. Electrons have $\beta \approx 1$ for most of the momentum range and therefore end up in the upper horizontal band at about 55 mrad. As we study hadronic reactions in this work, there is only a small contribution of electrons and muons in the final state from background reactions. Therefore, they play only a minor role in the final-state particle identification.

The likelihood for a given final-state particle hypothesis S is formulated in terms of the probability of the measured hit pattern of individual Cherenkov photons in the RICH detector. Details can be found in appendix A.2.1 and in ref. [64]. Using this approach, we obtained for each final-state particle a likelihood $\mathcal{L}(S)$ for each particle-species hypothesis S. In order to compare several hypotheses we calculated the likelihood ratio

$$\mathcal{R}_{\mathrm{R}}(S) = \frac{\mathcal{L}(S)}{\max\limits_{S' \neq S} \mathcal{L}(S')}, \tag{3.19}$$

where $\max\limits_{S' \neq S} \mathcal{L}(S')$ is the largest likelihood of all other particle hypothesis S' different from S. In order to assign a particle hypothesis S to a final-state particle, we required the likelihood ratio for S to be above a certain threshold,[x] i.e. $\mathcal{R}_{\mathrm{R}}(S) > \mathcal{T}_{\mathrm{R}}$, where $\mathcal{T}_{\mathrm{R}}$ is the so-called RICH threshold. Thereby, we implicitly required, that we can distinguish hypothesis S from all other hypotheses that were taken into account in order to assign S to a final-state particle. We took into account

[x] We used the same threshold for all particle-species hypotheses, which was optimized for a high efficiency and a low misidentification probability.

the hypotheses pion, kaon, proton, and background.[y] The background hypothesis represents Cherenkov photons that are uncorrelated to the final-state particle. If the background hypothesis was assigned to a particle, we treated this as if no hypothesis could have been assigned to it.

A steel pipe of 5 cm radius around the nominal beam axis separates non-interacting beam particles from the RICH gas vessel, in order to avoid background. However, also final-state particles can traverse the RICH detector within this steel pipe volume. Such particles do not produce Cherenkov light within the RICH gas volume. Therefore, we did not assign a particle hypothesis to final-state particles that traverse the RICH within this steel pipe, i.e. if the distance of the particle position from the nominal beam axis at the RICH entrance window is smaller than 5 cm.

3.2.2 Final-State Particle Identification Performance

In order to estimate the performance of the RICH particle identification; i.e. the efficiency to identify a particle, $P(S \to S)$, and the misidentification probability, $P(S \to S')$, to assign the wrong particle hypothesis S', validation samples of final-state particles are required. These samples need to contain particles that were identified without using the RICH information. Such samples were obtained by selecting decays of known particles into daughter particles of a specific species. Following ref. [64], we used the decay $K^0_S \to \pi^-\pi^+$ as a source of pions, the decay $\phi(1020) \to K^-K^+$ as a source of kaons, and the decay $\overset{(-)}{\Lambda} \to \pi^\pm \overset{(-)}{p}$ as a source of (anti)protons.[z] Details can be found in appendix A.2.2.

The efficiency and misidentification probability can depend on the particles charge on its kinematics at the position of the RICH detector, especially on its momentum $|\vec{p}_\mathrm{R}|$ and on the angle θ_R of its trajectory with respect to the beam axis.[aa] We took this into account by determining the efficiency and misidentification probability independently in cells of $(|\vec{p}_\mathrm{R}|, \sqrt{\theta_\mathrm{R}})$[ab] and separately for positive and negative particles.

Negative pions are identified efficiently for momenta above about 3 GeV/c (see figure 3.12a). Most of the pions below this limit are attributed to the background hypothesis or are unidentified. The maximum momentum for which pions can be identified efficiently is about 40 GeV/c. Above this limit, most of the pions are not identified, because they cannot be separated from kaons. The pion identification efficiency shows only a weak dependence on the angle of the particle track. In the center of the distribution, it is about 95 %.

[y] We did not consider the muon and electron particle hypotheses, because they cannot be distinguished from pions for momenta above about 10 GeV/c.

[z] Instead of $\overset{(-)}{\Lambda}$ decays, we used K^0_S decays as a pion source, because they cover a broader kinematic range. This is important, because this data sample is also used to model the RICH acceptance (see appendix C.2.3).

[aa] The particle kinematics $(|\vec{p}_\mathrm{R}|, \theta_\mathrm{R})$ at the position of the RICH detector are in general different from its kinematics at the interaction vertex in the target region. We used the kinematics at the RICH entrance window for the characterization of the RICH performance.

[ab] We use $\sqrt{\theta_\mathrm{R}}$ instead of θ_R, because the former better maps out the region in which the efficiency changes (see figure 3.12b).

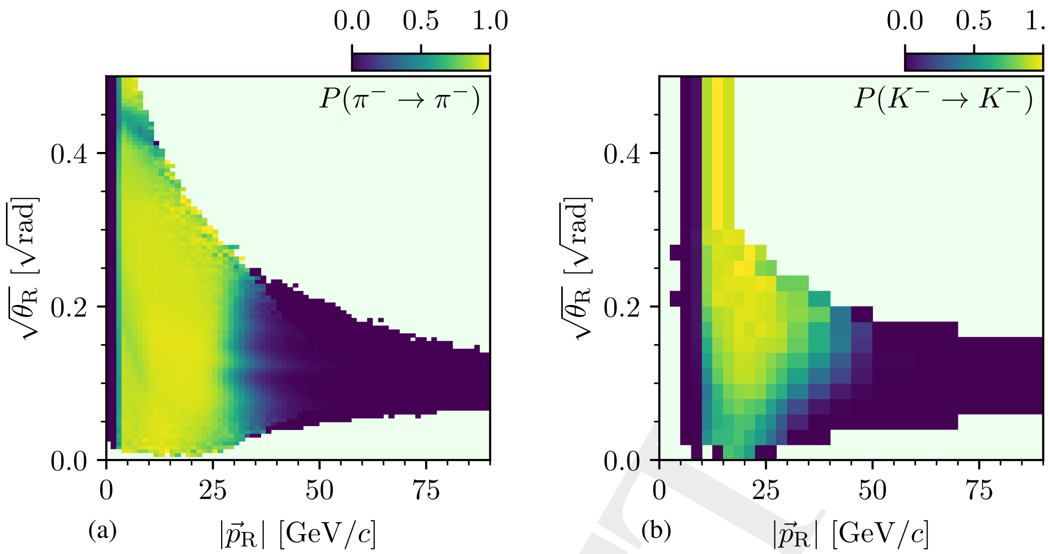

Figure 3.12: RICH efficiency for the identification of (a) negative pions and (b) negative kaons in cells of the particle momentum $|\vec{p}_R|$ and the square-root of the track angle θ_R at the position of the RICH detector. The plots show the 2008 diffraction data set for a likelihood-ratio threshold value of $\mathcal{T}_R = 1.15$. Regions without calibration data are drawn in light green.

Due to the larger kaon mass, the minimum momentum necessary to identify a negative kaon of about 10 GeV/c is larger than for the identification of pions (see figure 3.12b). The maximum momentum for which kaons can be identified efficiently, depends on the angle of the particle track. For small angles, we can identify kaons only up to about 30 GeV/c, while for larger angles, kaon identification is possible up to about 50 GeV/c.[ac] In the central kinematic region we achieve a high efficiency of about 90 %.

Figure 3.13 shows that the efficiencies and misidentification probabilities for the RICH final-state particle identification depend strongly on the choice of the likelihood-ratio threshold $\mathcal{T}_R$. The maximum efficiency for pion identification does not strongly depend on the choice of $\mathcal{T}_R$ (see figure 3.13a). The lower momentum limit is not sensitive to $\mathcal{T}_R$, because it is given by the Cherenkov threshold. As expected, the drop in efficiency for high momenta strongly depends on $\mathcal{T}_R$. While for $\mathcal{T}_R = 1.00$, the efficiency to identify a pion is above 20 % also for momenta above 50 GeV/c, it drops quickly in the region around 30 GeV/c when applying larger likelihood-ratio thresholds. However, for $\mathcal{T}_R = 1.00$, the misidentification probability increases drastically above 30 GeV/c (see figure 3.13b), while for $\mathcal{T}_R = 1.15$, it stays below 2 %. A likelihood-ratio threshold of $\mathcal{T}_R = 1.00$ means that we always assign the hypothesis with the largest likelihood. At high momenta, kaons cannot be separated from pions. Therefore, their likelihoods become similar and, for $\mathcal{T}_R = 1.00$, we almost randomly assign the pion or kaon hypothesis. This explains the comparably high misidentification probability and also the high efficiency above 20 %. For a

[ac] The maximum momentum up to which the particle species can be identified is higher for kaons than for pions. The reason for this is, that the Cherenkov angle of identified pions has an upper limit for $\beta \to 1$ and a lower limit given by the kaon hypothesis, while the Cherenkov angle of identified kaons has only an upper limit given by the pion hypotheses (see figure 3.11).

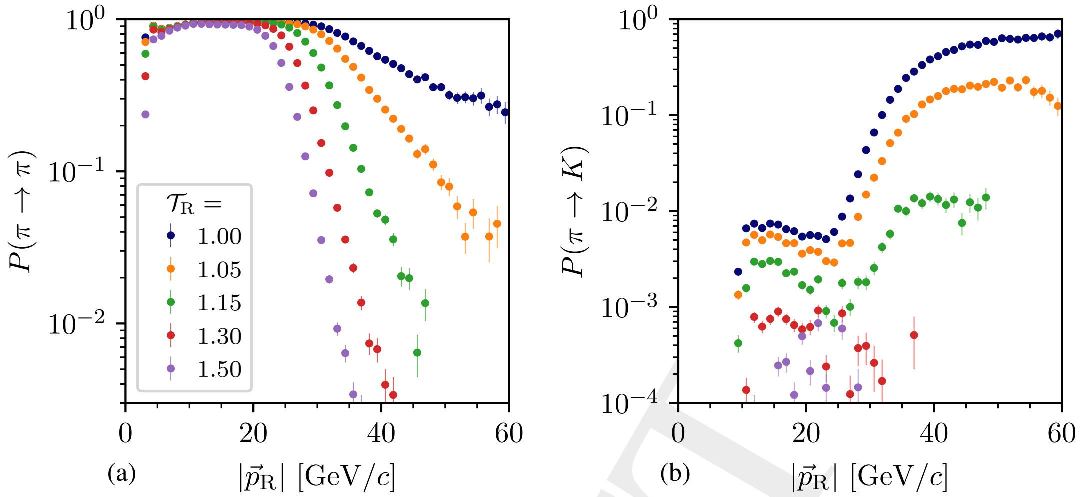

Figure 3.13: (a) RICH efficiency to identify a negative pion and (b) probability to misidentify a negative pion as a kaon as a function of the particle momentum at a track angle of about $\sqrt{\theta_\mathrm{R}} = 0.15\ \sqrt{rad}$ for the 2008 diffraction data set. The different colors represent different RICH likelihood-ratio thresholds.

reliable identification of final-state particles of species S it is important to require a significantly larger likelihood for the hypothesis S, i.e. it is important to use a likelihood-ratio threshold greater than one. More details on the RICH performance can be found in appendix A.2.3.

3.2.3 RICH Threshold Optimization for the $K^-\pi^-\pi^+$ Final State

As discussed in the previous section, the performance of the final-state particle identification depends on the kinematic distribution of the final-state particles. Therefore, the final choice of $\mathcal{T}_\mathrm{R}$ depends on the analyzed final state, which is $K^-\pi^-\pi^+$ in this work, and must be optimized to achieve high efficiency purity. Here, the purity is the fraction of events where the K^- and π^- hypothesis were assigned correctly. Figure 3.14 shows how both quantities depend on the likelihood-ratio threshold. Details on how we estimated these numbers can be found in appendix A.2.4.

As expected, the efficiency continuously decreases with increasing $\mathcal{T}_\mathrm{R}$. In contrast, the purity rises steeply with increasing $\mathcal{T}_\mathrm{R}$ and saturates at about $\mathcal{T}_\mathrm{R} = 1.2$. In order to achieve a high purity, while maintaining a high efficiency, we chose a likelihood-ratio threshold of $\mathcal{T}_\mathrm{R} = 1.15$. Using this threshold, the K^- and π^- were identified correctly by the RICH for 98.1 % of the selected $K^-\pi^-\pi^+$ events, while efficiency remains sufficiently high as the relative efficiency is 67.3 %.

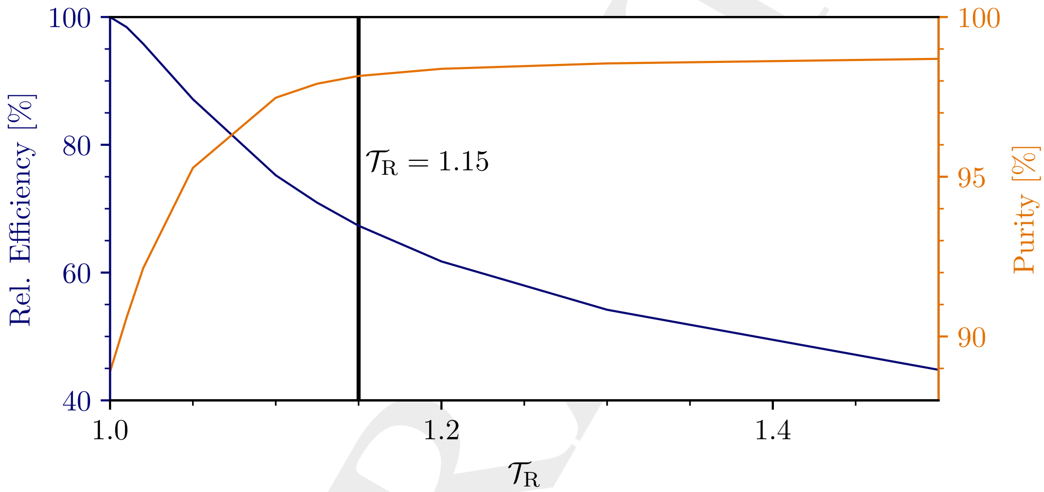

Figure 3.14: Efficiency to identify the $K^{-}\pi^{-}\pi^{+}$ final state relative to the efficiency for a likelihood-ratio threshold of $\mathcal{T}_{\mathrm{R}} = 1.0$ (blue curve). The orange curve represents the purity, i.e. fraction of events where the K^{-} and π^{-} were correctly identified. Details on how we estimated these numbers can be found in appendix A.2.4.

4 Event Selection

COMPASS collected data of various reactions during the data taking campaign in the years 2008 and 2009. The main task of the event selection discussed in section 4.1 is to extract a clean sample of the diffractive dissociation reaction $K^- + p \to K^-\pi^-\pi^+ + p$ from the total data set. An additional challenge of the event selection of this reaction is to determine which of the three final-state particles belongs to which species.

Unless stated differently, all plots in this section show the final $K^-\pi^-\pi^+$ sample of the combined 2008 and 2009 diffraction data set. The probability to measure a produced event, the so-called acceptance, is non-uniform in the kinematic variables of the $K^-\pi^-\pi^+$ final state. Thus, the shapes of the measured kinematic distributions shown in this chapter are distorted with respect to the physical distributions. However, the measured distributions still exhibit qualitatively the main features of the physical distributions. Due to the high dimensionality of the kinematic distributions of the $K^-\pi^-\pi^+$ final state and the complex dependence of the acceptance on these distributions, a correction of these acceptance effects is feasible only at the level of the partial-wave decomposition discussed in chapter 5.

4.1 Selection of the $K^-\pi^-\pi^+$ Final State

In order to select the reaction $K^- + p \to K^-\pi^-\pi^+ + p$, we applied a series of selection criteria, called cuts, to the diffraction data set. They can be grouped into six stages: (i) preselection cuts to select events with three charged final-state particles, (ii) cuts on the event topology, (iii) cuts on the initial- and final-state particle species, (iv) cuts to ensure energy and momentum conservation, (v) cuts to suppress non-diffractive reactions that lead to the same final state, and (vi) cuts that limit the data sample to the kinematic region of interest. Figure 4.1 gives an overview over the number of events after the cuts for the 2008 and 2009 diffraction data set.

The event selection was inspired by previous analyses of the reaction $K^- + p \to K^-\pi^-\pi^+ + p$ [44] and other reactions [39] that were performed on a subset of the COMPASS diffraction data set. We improved and extended them, and we optimized their parameters in order to increase the size of the data sample and to improve the quality of the data.

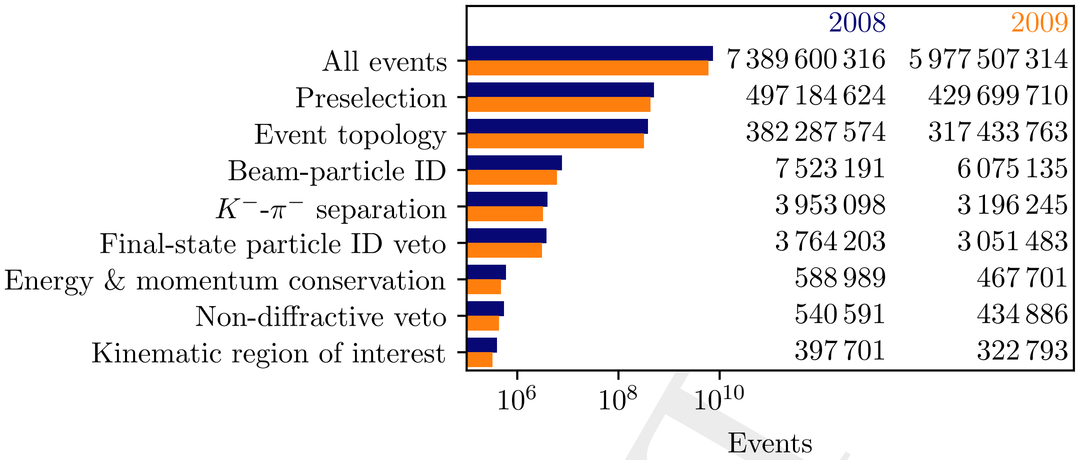

Figure 4.1: Number of selected events after applying the six stages of selection cuts for the reaction $K^- + p \to K^-\pi^-\pi^+ + p$. The cuts on the initial- and final-state particle identification [stage (iii)] are listed separately. The blue bars and the numbers in the first column show the results for the 2008 diffraction data set. The orange bars and the numbers in the second column show the results for the 2009 diffraction data set. The cuts are explained in the text.

Preselection Cuts

Diffractive scattering of pion or kaon beams can produce a whole family of final states that consists of three charged particles. The first stage of the event selection aims to select a sample of event candidates of this generic type. This sample is used also in the analyses of other diffractive reactions such as $\pi^- + p \to \pi^-\pi^-\pi^+ + p$ [43], $\pi^- + p \to \pi^-K^-K^+ + p$ [65], $\pi^- + p \to \pi^-\pi^0\omega + p$ with $\omega \to \pi^-\pi^+\pi^0$ [62], $\pi^- + p \to \pi^-\eta + p$ with $\eta \to \pi^-\pi^+\pi^0$ [66], and $\pi^- + p \to \pi^-\eta' + p$ with $\eta' \to \pi^-\pi^+\eta$ [66].

First, we required that at least one interaction point of a beam particle with a target proton, a so-called interaction vertex, was reconstructed in the target area.[a] Next, we required that three charged particles leave the interaction vertex.[b] As the beam particle is negatively charged, we required the charge sum of these three final-state particles to be minus one. Finally, we checked the stability of the data taking by studying the time evolution of various kinematic distributions of the reactions $K^- + p \to K^-\pi^-\pi^+ + p$ and $\pi^- + p \to \pi^-\pi^-\pi^+ + p$ (see appendix B.4). We removed data that show clear outliers in one of the studied kinematic variables.[c]

[a] We required the interaction-vertex position Z_{vtx} along the beam direction to be within $-200 \leq Z_{\text{Vtx}} < 160\,\text{cm}$, which includes the liquid-hydrogen target cell and additionally about 130 cm before and after the target.

[b] If more than one interaction vertex was reconstructed in the event, we chose the “best” vertex candidate, which is the one with most associated particles and with the smallest χ^2 value from the vertex reconstruction fit.

[c] First, we studied the time evolution of kinematic distributions after applying all event-selection cuts, except for this cut on the time stability. Then, in a second iteration of the event-selection, we removed data that show clear outliers.

From the 13.4 billion events in the diffraction data set, we pre-selected 931 million event candidates of the generic type with three charged final-state particles. Roughly 54 % of the events were collected in 2008, the remaining 46 % were collected in 2009.

Cuts on Event Topology

The so-called DT0 trigger was designed to include diffractive scattering reactions with minimal bias as described in section 2.2. Therefore, we selected only events that were triggered by a DT0 signal.

Due to the high intensity of the hadron beam, it infrequently happened that two or more beam particles enter the experimental setup during the time window that defines an event. In cases where two or more beam particles interact with the target, we reconstruct multiple interaction vertices. To remove such events, we rejected events with more than one interaction vertex. In cases where we reconstruct only one interaction vertex, e.g. if only one of the beam particles interacts with the target, we ensured that we associated the correct beam particle with the interaction vertex. This is done by requiring a coincidence in time between the trigger signal and the measurement of the beam particle,[d] in addition to the spatial constraints, imposed by the interaction vertex reconstruction.

Beam particles do not only interact with the protons in the liquid-hydrogen target, but may interact with any material on their path. This can be seen in figure 4.2a, which shows the distribution of interaction vertices along the direction of the beam. In addition to the plateau from about -65 to -25 cm, which corresponds to interactions within the 40 cm long target cell, the distribution exhibits a peak at about -68 cm. This peak arises from beam particles interacting with the cooling pipe of the target [57]. In the plane transverse to the beam axis, the hadron beam is well focused on the liquid-hydrogen target as shown in figure 4.2b. Still, some vertices lie outside the target cylinder indicated by the gray circle. To select only events where the beam particle interacts with a proton of the target, we required the interaction vertex position to be within $-65 \leq Z_{\text{Vtx}} < -30$ cm along the beam axis and within a radial distance of $R_{\text{Vtx}} < 1.5$ cm in the plane transversal to the nominal beam axis.

Cuts on Particle Species

In order to separate the kaon component in the beam from the about 36 times larger pion component, we applied a novel likelihood approach, which employs the full information provided by both CEDAR detectors (see section 3.1 for details). Using a log-likelihood difference threshold

[d] Coincidence in time of the trigger signal and the beam particle was enforced by selecting events only if the time of the beam particle was within $\pm 3\sigma_t$ around the trigger signal, where σ_t is the time resolution. The time of the beam particle was calculated from the measured hit times in the tracking detectors.

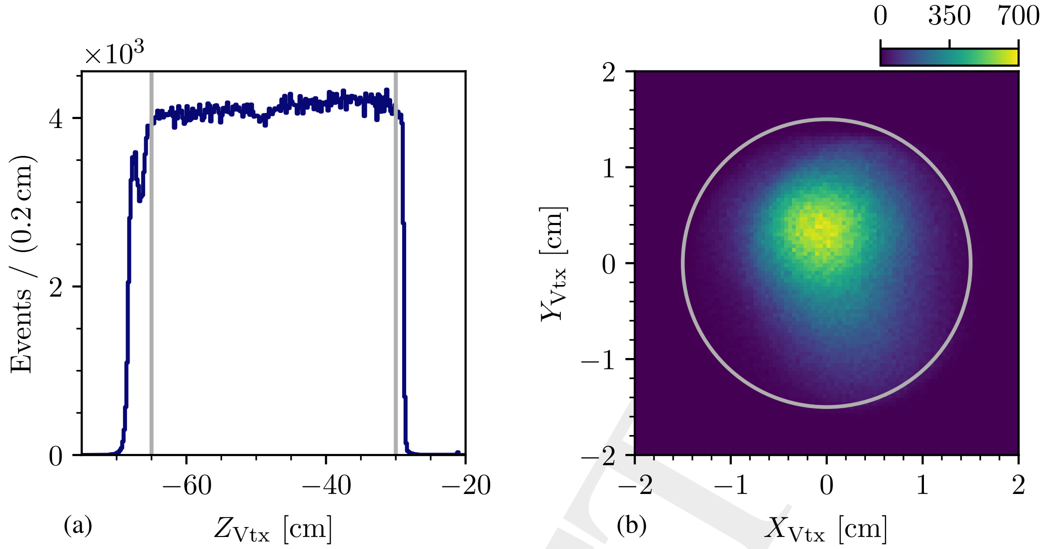

Figure 4.2: Spatial distribution of the interaction-vertex position. (a) shows the position along the beam axis, without the cut on the vertex Z-position. (b) shows the position in the plane transverse to the beam axis, without the cut on the vertex R-position. The gray lines represent the cuts on Z- and R-position, respectively.

of $\mathcal{T}_\mathrm{C}(K) = 4.0$ for the selection, we achieved a high kaon-identification efficiency of about 85 %.

The $K^-\pi^-\pi^+$ final state has two negative particles of different species. To distinguish them, we employed the information from the RICH detector (see section 3.2.3). Particles can be identified as pions, kaons, protons, muons, electrons; or they can be not identified. We identified all three final-state particles separately, using a likelihood-ratio threshold of $\mathcal{T}_\mathrm{R} = 1.15$ and limiting the particle identification to the momentum range where the RICH identification works with a high purity, and where we can describe the effects imposed by the RICH particle identification in the detector Monte Carlo simulation discussed in appendix C.2.3.[e]

As discussed in section 3.2.2, the final-state particle identification works efficiently only up to about 50 GeV/c. However, the final-state particles have momenta up to the beam momentum of about 190 GeV/c. Therefore, we cannot identify all three particles in the final state using the RICH detector. Therefore, we assumed that the data set contains only events of the $K^-\pi^-\pi^+$ final state, because were able to select beam kaons with high purity using the CEDARs and the $K^-\pi^-\pi^+$ final state it is the dominant final state for kaon diffraction into three charged particles. Under this assumption, the positive particle was assumed to be a pion and the main task of the final-state particle identifications is to separate the K^- from the π^-. We either identified both negative particles accordingly or we identified only one of the negative particles as a kaon or a pion and assumed for the not-identified particle the other particle species, respectively. If none of

[e] The momentum ranges for particle identification are $3 \leq |\vec{p_\pi}| < 60$ GeV/c for pions, $10 \leq |\vec{p_K}| < 60$ GeV/c for kaons and $18 \leq |\vec{p_p}| < 100$ GeV/c for protons.

the negative particles was identified or if the negative particles were identified to be both pions or both kaons, the event was rejected.

To suppress events where the three reconstructed particles do not belong to the $K^-\pi^-\pi^+$ final state, e.g. decays to $K^-K^-K^+$, we rejected events where the assigned particle species hypothesis conflicts the $K^-\pi^-\pi^+$ assumption, i.e. if the positive particle was identified as a kaon or if one of the three final-state particles was identified as a (anti)proton. However, this suppresses only a small fraction of the background, as the identification of the $K^-\ \pi^-$ system requires one of the negative particles to have a momentum below about $50\,\text{GeV}/c$, which is the region where the RICH is efficient. Given the total beam momentum of about $190\,\text{GeV}/c$, the two remaining final-state particles therefore typically have momenta above $50\,\text{GeV}/c$, which is too large for the particles to be identified by the RICH. Thus, the final-sate particle ID veto rejects only a small number of events (see figure 4.1).

The limited momentum range of the final-state particle identification introduces large acceptance effects. They can be best seen in the momentum distribution of the final-state particles that have to be identified, i.e. the π^- and the K^-, shown in figure 4.3. We observe a horizontal and a vertical band. For events in the horizontal band, the K^- have momenta in the range of about $10 \leq |\vec{p}_{K^-}| < 50\,\text{GeV}/c$, in which they are identified by the RICH. For events in the vertical band, the π^- have momenta in the range of about $3 \leq |\vec{p}_{\pi^-}| < 50\,\text{GeV}/c$, in which they are identified. We find more events in the vertical band where the π^- was identified. For events where both negative particles have momenta above about $50\,\text{GeV}/c$, we could not decide which of the two negative particles is which species. Therefore, we rejected those events. However, this leads to a region with zero experimental acceptance in the triangular region of the momentum distribution where both negative particles have momenta above about $50\,\text{GeV}/c$. This hole in the momentum distribution introduces a non-uniform acceptance also in many other kinematic variables, in particular in the mass spectra and angular distributions used in the partial-wave analysis. The treatment of this acceptance effect and its consequences are one of the major challenges of this analysis and will be a topic throughout this work.

Cuts on Energy and Momentum Conservation

The data set contains contamination from background events with more than three final-state particles, but where some of these final-state particles were not detected. For example, reactions of the type $K^- + p \to K^-\pi^-\pi^+\pi^0 + p$, where the neutral π^0 was not detected.[f] Such, so-called non-exclusive events can be suppressed in the event selection by requiring energy and momentum conservation of the measured energies and momenta of the initial- and final-state particles in the scattering process.

[f] In the event selection presented here, we did not use the information from the electromagnetic calorimeters to detect π^0 and suppress events with π^0 in the final state, as the electromagnetic calorimeters would require a computationally expensive and complicated treatment in the detector Monte Carlo simulation. However, we performed a study where we applied such a cut to suppress π^0. This cut had a negligible effect on the final event sample.

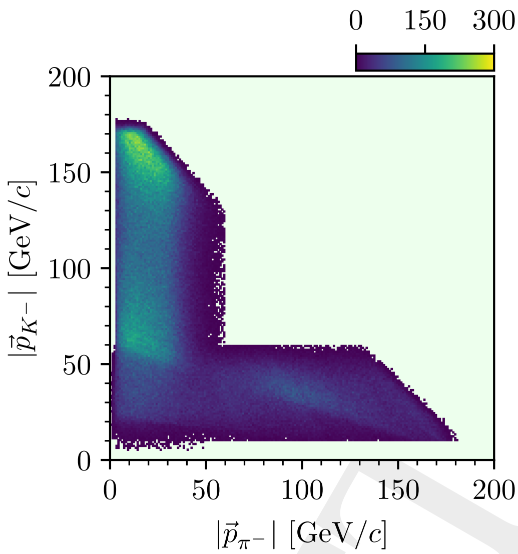

Figure 4.3: Distributions of the magnitudes of the reconstructed momenta of the identified $K^-\pi^-$ subsystem in the $K^-\pi^-\pi^+$ final state.

Unfortunately, the energy of the individual beam particle was not measured by the experimental setup. However, the energy spread of the beam is only about 1 % [49]. In addition, we can calculate the beam particle energy from the measured three-momenta of the $K^-\pi^-\pi^+$ final-state particles and the measured inclination of the beam particle, which were both measured with high precision (see section 2.2), by applying energy conservation. The calculation can be found in appendix B.1. The distribution of the reconstructed beam-particle energy is shown in figure 4.4a and exhibits a clear exclusivity peak at 191.29 GeV, which corresponds to the nominal beam energy. We selected events if the reconstructed beam energy was within $\pm 3\sigma_\mathrm{E}$ around the peak center, where σ_E is the Gaussian width of the peak of about $\sigma_\mathrm{E} = 1.71\,\mathrm{GeV}/c$.[g]

Due to momentum conservation, the projections of the total momentum of the $K^-\pi^-\pi^+$ system and the momentum of the recoil proton in the plane perpendicular to the beam-particle track must be back-to-back for exclusive events. This means that the azimuthal angle between these two projections must be 180°. We employed this constraint to suppress non-exclusive events in our data by requiring that

$$\Delta\phi_\mathrm{recoil} = 180° - \measuredangle(\vec{p}^{\,\perp}_{K^-\pi^-\pi^+}, \vec{p}^{\,\perp}_\mathrm{recoil}) \tag{4.1}$$

is compatible with zero within one standard deviation of the angular resolution of the RPD detector, with which the recoil proton was measured.[h]

[g] We fitted a single Gaussian function plus a third-order background polynomial to the peak region of $182 \leq E_\mathrm{beam} < 200\,\mathrm{GeV}$ to determine the Gaussian width of the peak, i.e. the width of the Gaussian function.

[h] The angular resolution of the RPD detector depends on the hit pattern in the scintillator segments and can be either ±8.432° or ±5.377°. We applied cuts on $\Delta\phi_\mathrm{recoil}$ accordingly. See ref. [67] for details.

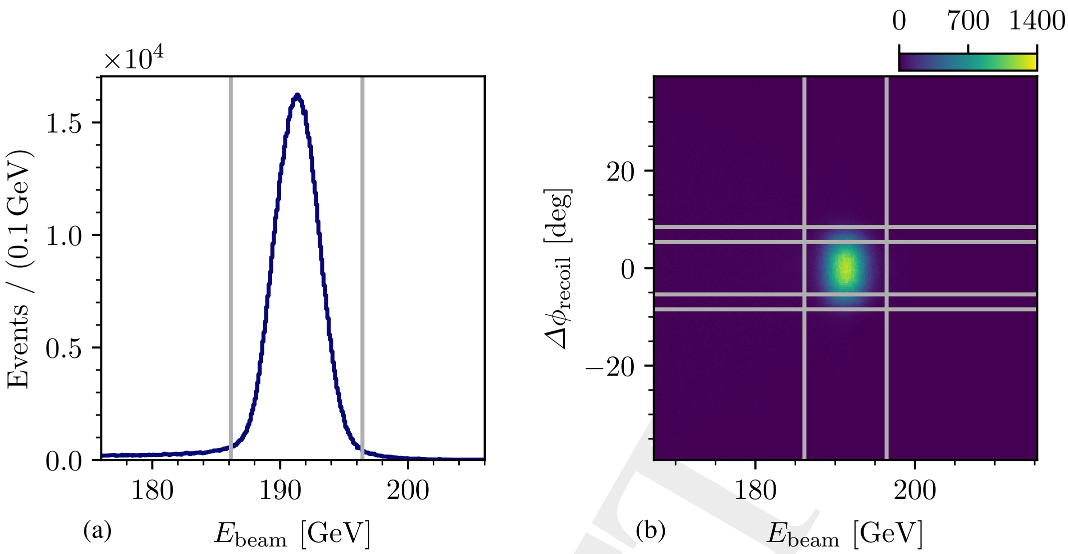

Figure 4.4: Distribution of the kinematic variables used to select exclusive events. (a) shows the distribution of the reconstructed beam energy after all cuts except for the cut on E_{beam}. (b) shows the distribution of $\Delta\phi_{\mathrm{recoil}}$, which is a measure of momentum conservation (see text), versus the beam energy after all cuts, except for the cuts on $\Delta\phi_{\mathrm{recoil}}$ and E_{beam}. The gray lines represent the applied cuts.[h]

We do not observe correlations between $\Delta\phi_{\mathrm{recoil}}$ and the beam energy (see figure 4.4b). This indicates, that both variables give independent information and applying both cuts helps to better separate exclusive from non-exclusive events. The non-exclusive background in the final $K^-\pi^-\pi^+$ sample was estimated to be only about $(2 \pm 1\,(\mathrm{sys.}))\,\%$.[i]

Cuts to suppress Non-Diffractive Reactions

In addition to diffractive scattering, there are other exclusive processes that lead also to the $K^-\pi^-\pi^+$ final state (see section 2.1.1). Thus, these processes cannot be separated from diffractive scattering in terms of their event topology, the particle species, or energy and momentum conservation. A special role play central-production reactions. The kinematic characteristic of central production is different from the one of diffractive scattering. In central production, the kaon scatters elastically of the centrally produced $\pi^-\,\pi^+$ system. The scattered kaon goes mostly in very forward direction. To characterize this, the Feynman-x variable of the final-state kaon is used, which can be approximated by [9]

$$x_{\mathrm{F}}^{K} \approx \frac{2p_{\parallel}^{\mathrm{cm}}}{\sqrt{s}}. \tag{4.2}$$

[i] As there is no model for the distribution of the reconstructed beam energy for non-exclusive contributions, this is only a rough estimate. See appendix B.2 for details.

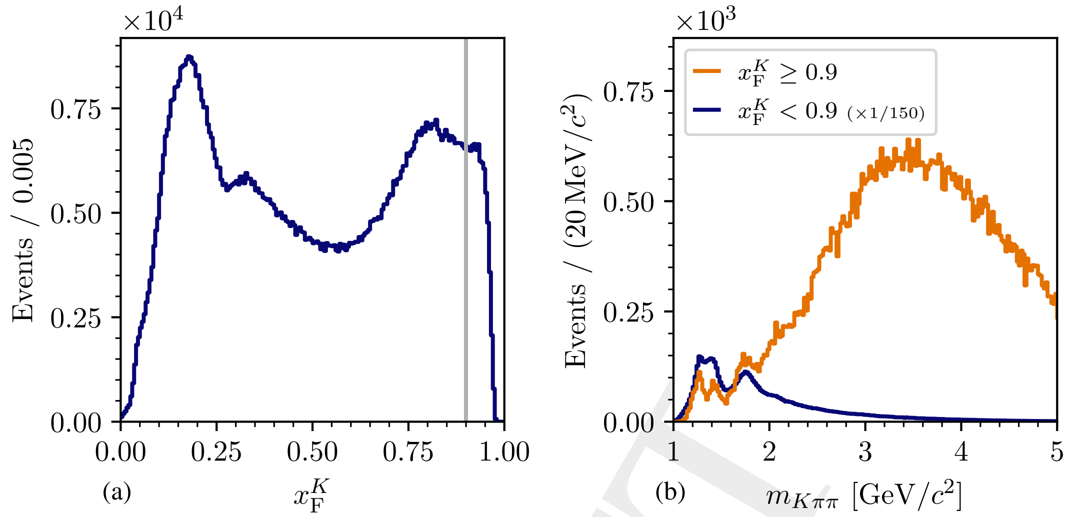

Figure 4.5: Kinematic distributions to study central-production reactions. (a) shows the distribution in x_F^K. The orange histogram in (b) shows the invariant mass spectrum of the $K^-\pi^-\pi^+$ system for the subset of data with $x_F^K \geq 0.9$. The blue histogram in (b) shows the corresponding distribution for the complementary data set with $x_F^K < 0.9$ scaled by a factor of 1/150. For all distributions, the cuts on the t' and $m_{K\pi\pi}$ region were not applied.

Here, $p_{\parallel}^{\mathrm{cm}}$ is the momentum component of the final-state kaon in the direction of the incoming beam kaon in the $K^-\pi^-\pi^+ + p$ center-of-momentum frame and $\sqrt{s}$ is the center-of-momentum energy. We expect $x_F^K \approx 1$ for the forward-scattered kaon of central-production reactions. Figure 4.5a shows the x_F^K distribution. As x_F^K is directly correlated with the momentum of the scattered kaon, most of the structures observed in this distribution arise from acceptance effects of the final-state particle identification shown in figure 4.3. In addition, a small peak at $x_F^K \approx 0.92$ is observed, which might be caused by central-production reactions. To suppress these events, we required $x_F^K < 0.9$. The $m_{K\pi\pi}$ distribution of the central-production sample with $x_F^K \geq 0.9$ (orange histogram in figure 4.5b) exhibits a broad bump at about 3.5 GeV/c^2, with a small low-mass tail leaking into the $m_{K\pi\pi}$ region of interest below 3 GeV/c^2. A comparison with the selected $K^-\pi^-\pi^+$ sample (blue histogram in figure 4.5b) shows, that the central-production sample does not contribute dominantly to the $m_{K\pi\pi}$ region of interest. In this low-mass tail, we observe structures on top of the continuous tail, similar to those of the selected $K^-\pi^-\pi^+$ sample. This indicates, that by applying this cut, we also rejected a small fraction below 1 % of diffractive scattering reactions.

It should be noted, that first Monte Carlo studies based on simple models for central-production reactions [68, 69] also yielded a peak at large x_F^K, but with a dominant tail towards smaller values down to $x_F^K \approx 0.5$ for $m_{K\pi\pi} < 3$ GeV/c^2. This suggests, that the cut $x_F^K < 0.9$ suppress only part of the central-production contribution to the $K^-\pi^-\pi^+$ sample, which, however, is in general small for $m_{K\pi\pi} < 3$ GeV/c^2.

Cuts on the Kinematic Region of Interest

As a last step, we defined the kinematic region of interest in t' and $m_{K\pi\pi}$. The lower limit of $t' = 0.1\,(\text{GeV}/c)^2$ is given by the minimal energy necessary for the recoil proton to produce a signal in the recoil-proton detector (see section 2.2). For $t' > 1.0\,(\text{GeV}/c)^2$ or for $K^-\pi^-\pi^+ < 1.0\,\text{GeV}/c^2$, an insufficient amount of data is available to perform a partial-wave analysis. Up to now, there are no well-known strange-meson resonances in the range $m_{K\pi\pi} \gtrsim 2.5\,\text{GeV}/c^2$ [9]. Therefore, we limited ourselves to the t' range of $0.1 \le t' < 1.0\,(\text{GeV}/c)^2$ and the $m_{K\pi\pi}$ range of $1.0 \le m_{K\pi\pi} < 3.0\,\text{GeV}/c^2$.

Applying all cuts defined in this section, we obtained a final $K^-\pi^-\pi^+$ sample of 307 701 events for the 2008 and 322 793 events for the 2009 diffraction data set, in the kinematic region of interest. In total, the COMPASS data sample for diffractive $K^-\pi^-\pi^+$ production contains 720 494 events, which is about 2.7 times larger than the sample from a previous unpublished COMPASS analysis [44]. It is the so-far world's largest sample of this reaction and is 3.6 times larger compared to the previously world's largest sample measured by the WA3 experiment [23].

4.2 Kinematic Distributions of the $K^-\pi^-\pi^+$ Sample

In order to search for strange-meson resonances decaying into $K^-\pi^-\pi^+$, the most interesting kinematic variable to look at is the invariant mass spectrum of the $K^-\pi^-\pi^+$ system shown in figure 4.6a. In the simplest case we expect resonances to appear as peaks in this spectrum. We observe clear peaks in the mass regions of the well-known $K_1(1270)$, $K_1(1400)$, and $K_2(1770)$ resonances. These peaks sit on top of a broad spectrum starting at about $1\,\text{GeV}/c^2$ and having a long tail beyond $3\,\text{GeV}/c^2$. In order to separate these signals and to also study weaker signals hidden in the broad spectrum, a comprehensive partial-wave analysis is mandatory. This will be discussed in chapters 5 to 8.

An important property of the diffractive scattering process is its dependence on the squared four-momentum transfer t'. The t' spectrum shown in figure 4.6b falls approximately exponentially with t'. The slope becomes smaller for larger values of t'. In addition, the slope also changes with $m_{K\pi\pi}$. The extraction of the slope of the t' spectrum as a function of $m_{K\pi\pi}$ is discussed in appendix B.3. The measured slope parameters are similar to those found in the COMPASS $\pi^-\pi^-\pi^+$ analysis [39]. Since both final states were produced in diffractive scattering reactions, this similarity demonstrates that the t' dependence is a property of the production mechanism. The observed approximately exponential t' dependence is also expected from Regge theory [46]. However, the slope may be different for different $K^-\pi^-\pi^+$ resonances. As the observed spectrum arises from various resonances and non-resonant contributions, its shape is the result of a superposition of many exponential shapes, which can only be separated by a partial-wave analysis. The different t' dependencies of the resonances also lead to a t'-dependent shape of the $m_{K\pi\pi}$ spectrum. For example, the relative strengths of the peaks in the low-t' (figure 4.6c) and the high-t' (figure 4.6d) region.

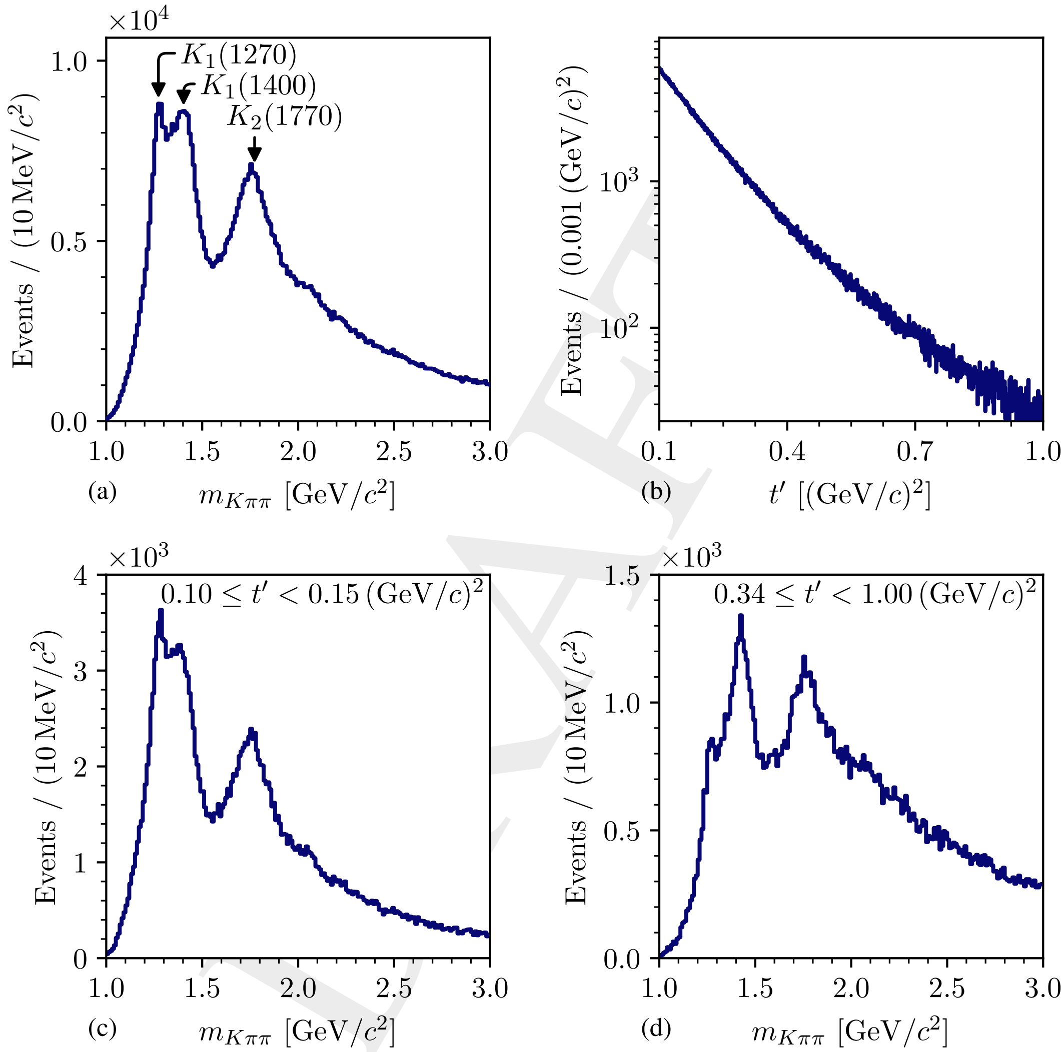

Figure 4.6: Invariant mass spectrum of the diffractively produced $K^{-}\pi^{-}\pi^{+}$ system (a) for the full analyzed t' range and in (c) and (d) for the low- and high-t' region, respectively. In (b) we show the corresponding t' spectrum. The arrows in (a) indicate well-known kaon resonances decaying into $K^{-}\pi^{-}\pi^{+}$ according to the PDG [9].

Also the invariant mass spectra of the $K^-\pi^+$ and $\pi^-\pi^+$ subsystems show clear peaks at the position of well-known resonances. The $K^-\pi^+$-mass spectrum shown in figure 4.7a is dominated by the $K^*(892)$ resonance. A second peak appears at about $1.4\,\mathrm{GeV}/c^2$ where two kaon resonances exist, the $K_2^*(1430)$ and the $K_0^*(1430)$. Both resonances have a similar mass but a different spin. They can be separated only by a partial-wave analysis.

The $\pi^-\pi^+$ mass spectrum shown in figure 4.7b is dominated by the well-known $\rho(770)$ resonances, sitting on a broad distribution. The shoulder in the high-mass tail of the $\rho(770)$ at about $1\,\mathrm{GeV}/c^2$ can be associated with the $f_0(980)$ resonance. The higher-lying peak corresponds to the $f_2(1270)$. Similar structures are observed in the $\pi^-\pi^+$ subsystem of the $\pi^-\pi^-\pi^+$ final state [39]. The narrow peak at $m_{\pi^-\pi^+} \approx 0.38\,\mathrm{GeV}/c^2$ is due to a small contamination of the $K^-\pi^-\pi^+$ sample from events of the reaction $K^- + p \to K^-\phi(1020) + p$, with $\phi(1020) \to K^-K^+$, where the RICH erroneously identified the second K^- and the K^+.[j] The wrong mass assumption for the final-state particles shifts the narrow $\phi(1020)$ peak to about $0.38\,\mathrm{GeV}/c^2$. From a coarse event selection of the $K^-K^-K^+$ final state using COMPASS data, we estimated the $K^-K^-K^+$ background to the $K^-\pi^-\pi^+$ sample to be below $4\,\%$.[k]

The $K^-\pi^-$ spectrum exhibits a broad continuous distribution with a maximum at about $1\,\mathrm{GeV}/c^2$. No peaking or other resonant-like structures are observed, as expected as there are no known doubly-negatively charged light mesons.

Finally, we compare our results to those from the ACCMOR collaboration [23] shown in figure 4.8. In their data, the peak in the $K_2(1770)$ region of the $m_{K\pi\pi}$ spectrum (see figure 4.8a) is less pronounced with respect to the double-peak in the K_1 region (cf. figure 4.6a). This has two reasons. First, ACCMOR analyzed a lower t' region, which can have a different composition of resonances. Second, the experimental acceptance of our measurement drops with lower $m_{K\pi\pi}$ (see figure D.35a). This suppresses the double-peak in the K_1 region with respect to the peak in the $K_2(1770)$ region. The $m_{K^-\pi^+}$ spectrum from ACCMOR shown in figure 4.8b exhibits clear peaks from the $K^*(892)$ and the $K_2^*(1430)$, in agreement with our observations (cf. figure 4.7a). Also, their $m_{\pi^-\pi^+}$ spectrum shown in figure 4.8c exhibits similar structures (cf. figure 4.7b). Changes in the relative strength of the observed structures might be caused by the different t' range and our experimental acceptance. Overall, at this level of the analysis the kinematic distributions from ACCMOR are consistent with our observations, while the smoothness of our distributions demonstrates the improved statistical precision due to our 3.6 times larger sample.

[j] Requiring the RICH to always identify the positive particle as a pion strongly suppresses the peak at about $0.38\,\mathrm{GeV}/c^2$ with respect to the rest of the spectrum. However, this requirement would also reduce the efficiency of the $K^-\pi^-\pi^+$ selection by about $30\,\%$. Therefore, this cut was not applied in the $K^-\pi^-\pi^+$ event selection.

[k] From the peak at about $0.38\,\mathrm{GeV}/c^2$ we estimated the $\phi(1020)$ contamination of the $K^-\pi^-\pi^+$ sample to be about $0.26\,\%$. From the $m_{K^-K^+}$ spectrum of the COMPASS $K^-K^-K^+$ sample, we estimated the fraction of $\phi(1020)$ production in the $K^-K^-K^+$ sample to be about $6.6\,\%$. We assumed, that the fraction of $\phi(1020)$ in the $K^-K^-K^+$ contamination of the $K^-\pi^-\pi^+$ sample is the same as in the selected $K^-K^-K^+$ sample.

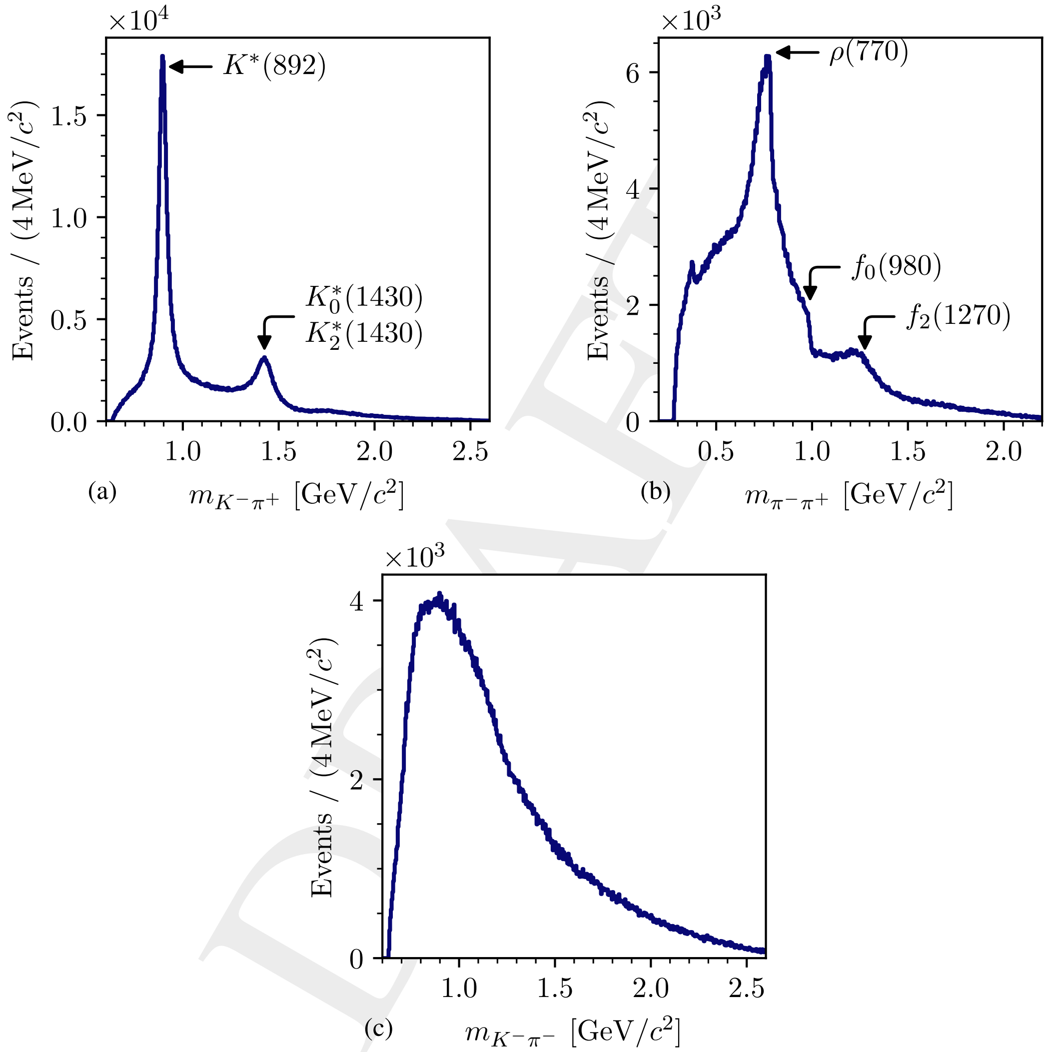

Figure 4.7: Invariant mass spectra of the two-body subsystems of the $K^-\pi^-\pi^+$ final state: (a) $K^-\pi^+$, (b) $\pi^-\pi^+$, and (c) $K^-\pi^-$. The arrows indicate well-known resonances appearing in these two-body systems according to the PDG [9].

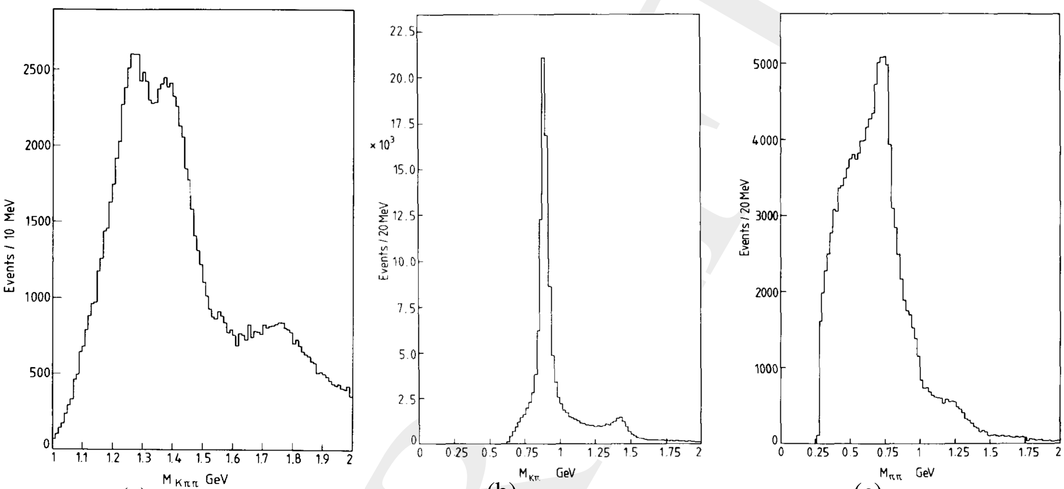

(a) (b) (c)

Figure 4.8: Kinematic distributions of the $K^-\pi^-\pi^+$ final state in the range $0 \leq t' \leq 0.7\,(\mathrm{GeV}/c)^2$ as measured by the WA3 experiment and analyzed by ACCMOR [23]. (a) shows the $m_{K\pi\pi}$ distribution. (b) and (c) show the invariant mass distribution of the $K^-\pi^+$ and $\pi^-\pi^+$ subsystem, respectively.

5 The Partial-Wave Decomposition

In order to separate the strange-meson resonances X^- appearing in the $K^-\pi^-\pi^+$ system, which is produced in the reaction $K^- + p \to K^-\pi^-\pi^+ + p$ (see figure 4.6a), and to identify their J^P quantum numbers, we performed a comprehensive partial-wave analysis (PWA) based on the $K^-\pi^-\pi^+$ sample described in the previous chapter 4. We performed the partial-wave analysis in two stages. In the first stage called partial-wave decomposition (PWD), the data are decomposed into amplitudes coming from intermediate states X^- with various J^P quantum numbers and various decay paths. In the PWD, the $m_{K\pi\pi}$ dependence of the reaction is not modeled explicitly, but our data are subdivided into narrow $m_{K\pi\pi}$ bins, and the PWD is performed independently in these $m_{K\pi\pi}$ bins. In this way, we determined the $m_{K\pi\pi}$ dependence of the amplitudes from data. In the same spirit, we subdivided each $m_{K\pi\pi}$ bin in four t' bins to also determine the t' dependence of the amplitudes. In the second analysis stage called resonance-model fit, the $m_{K\pi\pi}$ dependence of the amplitudes is then modeled explicitly, which allows us to identify strange-meson resonances appearing in the $K^-\pi^-\pi^+$ system and to measure their masses and widths.

An upper limit for the $m_{K\pi\pi}$ bin widths are mainly given by the widths of the appearing strange-meson resonances, which are in the range of about $100\,\text{MeV}/c^2$ or larger. Hence, we used for $m_{K\pi\pi} < 2\,\text{GeV}/c^2$ a bin width of $20\,\text{MeV}/c^2$. For $m_{K\pi\pi} > 2\,\text{GeV}/c^2$ we used a bin width of $40\,\text{MeV}/c^2$, because the $K^-\pi^-\pi^+$ sample size quickly shrinks towards high $m_{K\pi\pi}$, while at the same time strange-meson resonances typically become wider at higher masses. Given the approximately exponential shape of the t' spectrum, we subdivided our data into four t' bins, which we chose such that the number of events in the first bin, the second bin, and the last two bins combined is approximately the same.[a] The t'-bin borders are listed in table 5.1. In total, we split the analyzed kinematic range of $1.0 \leq m_{K\pi\pi} < 3.0\,\text{GeV}/c^2$ and $0.1 \leq t' < 1.0\,(\text{GeV}/c)^2$ into 300 $(m_{K\pi\pi}, t')$ cells, in which the PWD was performed independently.

In this chapter, we first describe in section 5.1 the PWD formalism. In sections 5.2 to 5.4, we present extensions of this general approach that were developed for our analysis. In sections 5.5 and 5.6, we give a first glimpse on the results of the PWD. In sections 5.7 to 5.10, we present systematic and pseudodata studies of the PWD. The resonance-model fit, which used the results of the PWD as input, is presented in chapter 6. The physics results are discussed in chapter 7.

Table 5.1: Borders of the four t' bins as used for the partial-wave decomposition.

$[(\text{GeV}/c)^2]$	0.10	0.15	0.24	0.34	1.00

[a] We rounded the t' bin borders to two significant digits in our analysis.

5.1 Method

5.1.1 Isobar Model and Coordinate System

The $m_{K^-\pi^+}$ and $m_{\pi^-\pi^+}$ distributions shown in figures 4.7a and 4.7b, respectively, are dominated by various two-body resonances. This indicates that the intermediate state X^- does not directly decay to $K^-\pi^-\pi^+$, but dominantly decays first into a two-body resonance ξ^0 called isobar and the third remaining particle b^- called bachelor particle, and then the isobar decays into the two-body subsystem. This is schematically shown in figure 5.1. Figure 5.1a shows the graph if the isobar resonance is in the $K^-\pi^+$ subsystem and hence the π^- is the bachelor particle. Figure 5.1b shows the graph if an isobar resonance is in the $\pi^-\pi^+$ subsystem and hence the K^- is the bachelor particle. As the $K^-\pi^-$ subsystem does not exhibit resonance signals (see figure 4.7c) and as there are no known resonances that decay to $K^-\pi^-$, we considered isobars only in the $K^-\pi^+$ and $\pi^-\pi^+$ subsystems in the PWD. In summary, we employ the isobar model [70, 71], i.e. we split the reaction $K^- + p \to K^-\pi^-\pi^+ + p$ into the inelastic two-body scattering process $K^- + p \to X^- + p$ and a series of two successive two-body decays: (i) $X^- \to \xi^0 b^-$, (ii) $\xi^0 \to K^-\pi^+$ or $\xi^0 \to \pi^-\pi^+$

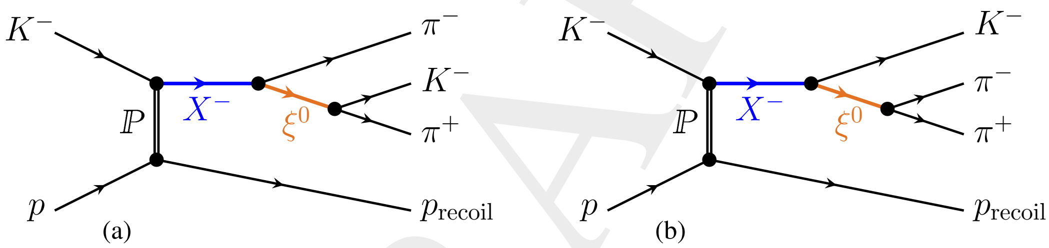

Figure 5.1: Schematic view of the reaction $K^- + p \to K^-\pi^-\pi^+ + p$ in the isobar model, where the intermediate state X^- successively decays to the $K^-\pi^-\pi^+$ system via a two-body resonance ξ^0 called isobar. (a) shows the reaction if the isobar resonance is in the $K^-\pi^+$ subsystem. (b) show the reaction if the isobar resonance is in the $\pi^-\pi^+$ subsystem. The third remaining particle b^- is called bachelor particle, which in (a) is the π^- and in (b) is the K^-.

In order to disentangle the various contributions from the different intermediate states X^-, the PWD employs the full information from the measured kinematic distributions of the final-state particles. The choice of the kinematic variables that describe the reaction $K^- + p \to K^-\pi^-\pi^+ + p$ is not unique. A convenient definition is motivated by the isobar-model picture. The inelastic scattering reaction $K^- + p \to X^- + p$ is described by the center-of-momentum energy s, which is constant due to the fixed beam momentum; the reduced squared four-momentum transfer t'; and the invariant mass $m_{K\pi\pi}$ of the $K^-\pi^-\pi^+$ system. For fixed s, $m_{K\pi\pi}$ and t', the X^- decay is described by five phase-space variables summarized by τ. The decay $X^- \to \xi^0 b^-$ is described in the X^- rest frame using the Gottfried-Jackson (GJ) frame shown in figure 5.2. This reference frame is a right-handed coordinate system, where the $\vec{z}_{\text{GJ}}$ axis is given by the direction of the beam K^- and the $\vec{y}_{\text{GJ}}$ axis is given by the normal of the X^- production plane. The X^- production plane (orange plane in figure 5.2) is given by the momenta of the recoil proton and the beam K^-. Since in the X^- rest frame the momenta of the ξ^0 and the bachelor particle are back to back, the X^-

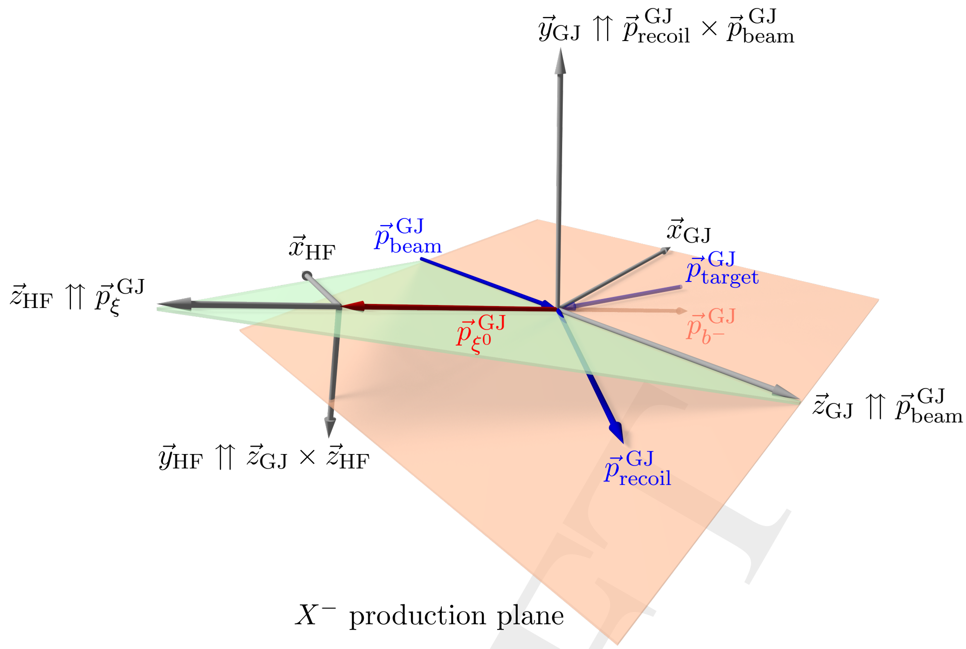

Figure 5.2: Definition of the Gottfried-Jackson (GJ) and helicity (HF) frames used to describe the reaction $K^- + p \to K^-\pi^-\pi^+ + p$ with an intermediate state X^- in the $K^-\pi^-\pi^+$ system decaying to a two-body isobar ξ^0 and the bachelor particle b^-. The Gottfried-Jackson frame is defined in the X^- rest frame. The helicity frame is defined in the ξ^0 rest frame. The momenta of the beam K^-, the target proton, and the recoiling proton in the Gottfried-Jackson frame are $\vec{p}^{\,\mathrm{GJ}}_{\mathrm{beam}}$, $\vec{p}^{\,\mathrm{GJ}}_{\mathrm{target}}$, and $\vec{p}^{\,\mathrm{GJ}}_{\mathrm{recoil}}$, respectively. The unit vectors of the coordinate axes are labeled $\vec{x}_i$, $\vec{y}_i$, $\vec{z}_i$. In this work, we consider two cases, which yield different coordinate systems, one if the ξ^0 is in the $K^-\pi^+$ subsystem and one if the ξ^0 is in the $\pi^-\pi^+$ subsystem. Taken from ref. [67] and adjusted.

decay is described by two decay angles of one of the daughter particles. We chose the polar angle θ_{GJ} and the azimuthal angle ϕ_{GJ} of the isobar. The decay of the isobar ξ^0 is described in its rest frame using the helicity frame (HF). The helicity frame is constructed by boosting from the X^- rest frame to the ξ^0 rest frame. The $\vec{z}_{\mathrm{HF}}$ axis is given by the momentum of ξ^0 in the Gottfried-Jackson frame. The $\vec{y}_{\mathrm{HF}}$ axis is given by the normal of the plane (green plane in figure 5.2) that is defined by $\vec{z}_{\mathrm{GJ}}$ and the momentum of ξ^0. Since in the ξ^0 rest frame the momenta of the two decay products are back to back, the ξ^0 decay is described by two decay angles of one of the daughter particles. We chose the polar angle θ_{HF} and the azimuthal angle ϕ_{HF} of the negative decay product, which is either the K^- or the π^-. In addition to the four angles, the invariant mass of the two-body isobar subsystem completes the set of variables that span the $K^-\pi^-\pi^+$ phase space.

Given that we consider isobars in the $K^-\pi^+$ and $\pi^-\pi^+$ subsystems, there are two different definitions of these phase-space variables that are used in the following: (i) if the isobar is in the $K^-\pi^+$ subsystem, the phase-space variables are $m_{K\pi\pi}$, t', and $\tau^{K\pi} = (\theta^{K\pi}_{\mathrm{GJ}}, \phi^{K\pi}_{\mathrm{GJ}}, m_{K^-\pi^+}, \theta^{K^-}_{\mathrm{HF}}, \phi^{K^-}_{\mathrm{HF}})$; (ii) if the isobar is in the $\pi^-\pi^+$ subsystem, the phase-space variables are $m_{K\pi\pi}$, t', and $\tau^{\pi\pi} = (\theta^{\pi\pi}_{\mathrm{GJ}}, \phi^{\pi\pi}_{\mathrm{GJ}}, m_{\pi^-\pi^+}, \theta^{\pi^-}_{\mathrm{HF}}, \phi^{\pi^-}_{\mathrm{HF}})$.

5.1.2 Partial-Wave Decomposition Formalism

In the following, we give a brief introduction into the PWD formalism. A detailed and general description of the PWD formalism used in our work can be found in ref. [72]. We mainly follow the derivations, notation, and conventions given in ref. [72]. All formulas, except explicitly stated otherwise are taken from ref. [72] or from references therein. The PWD formalism for the special case of the COMPASS $\pi^-\pi^-\pi^+$ analysis, which is similar to our analysis, can be found in ref. [39].

Cross Section

The differential cross section for the reaction $K^- + p \to K^-\pi^-\pi^+ + p$ is given by

$$\frac{\mathrm{d}\sigma}{\mathrm{d}\Phi_4} = \frac{|\mathcal{M}|^2}{\mathfrak{F}}. \tag{5.1}$$

Here, the flux factor,

$$\mathfrak{F} = 4\sqrt{(p_{\text{beam}}\, p_{\text{target}})^2 - m^2_{\text{beam}} m^2_{\text{target}}}, \tag{5.2}$$

is approximately a constant given by the fixed beam momentum. $\mathcal{M}$ is the Lorentz-invariant matrix element that encodes the whole dynamics of the reaction $K^- + p \to K^-\pi^-\pi^+ + p$.[b] The differential phase-space element $\mathrm{d}\Phi_4$ of the $K^-\pi^-\pi^+ p$ final state can be split into the two-body phase-space $\mathrm{d}\Phi_2$ of the $X^- p$ system and the three-body phase-space $\mathrm{d}\Phi_3$ of the $K^-\pi^-\pi^+$ final state, i.e.

$$\mathrm{d}\Phi_4 = \mathrm{d}\Phi_2 \mathrm{d}\Phi_3 \frac{2m_{K\pi\pi}}{2\pi} \mathrm{d}m_{K\pi\pi}. \tag{5.3}$$

Expressing the two-body phase-space in terms of t' and the azimuthal angle ϕ of the production plan around the beam-particle direction yields:

$$\mathrm{d}\Phi_4 = \frac{1}{2(2\pi)^2}\frac{1}{\mathfrak{F}} \mathrm{d}\phi\, \mathrm{d}t' \mathrm{d}\Phi_3 \frac{2m_{K\pi\pi}}{2\pi} \mathrm{d}m_{K\pi\pi}, \tag{5.4}$$

where the flux factor is appearing again (see ref. [72]). Since we consider unpolarized reactions, the matrix element does not depend on ϕ. Hence, integration over ϕ is trivial and yields for the differential cross section in equation (5.1):

$$\frac{\mathrm{d}\sigma(\tau, m_{K\pi\pi}, t')}{\mathrm{d}\Phi_3\, \mathrm{d}m_{K\pi\pi}\, \mathrm{d}t'} = \frac{1}{\mathfrak{F}^2}\frac{1}{4\pi}\frac{2m_{K\pi\pi}}{2\pi} |\mathcal{M}(\tau, m_{K\pi\pi}, t')|^2. \tag{5.5}$$

Finally, the number density; i.e. the distribution of the number N_{ev} of produced events, which is the number of events that were actually produced in the experiment, differential in $m_{K\pi\pi}$, t', and

[b] Amplitudes from various incoherent contributions may contribute to the reaction. At this point, we absorb these incoherent contributions in $|\mathcal{M}|^2$ before we explicitly formulate them in equation (5.14).

the 5-dimensional $K^-\pi^-\pi^+$ phase-space $\mathrm{d}\Phi_3$; reads

$$\frac{\mathrm{d}N_{\mathrm{ev}}(\tau, m_{K\pi\pi}, t')}{\mathrm{d}\Phi_3\,\mathrm{d}m_{K\pi\pi}\,\mathrm{d}t'} = \mathscr{L}\frac{\mathrm{d}\sigma(\tau, m_{K\pi\pi}, t')}{\mathrm{d}\Phi_3\,\mathrm{d}m_{K\pi\pi}\,\mathrm{d}t'} = \frac{\mathscr{L}}{(2\pi\mathfrak{F})^2} m_{K\pi\pi} |\mathcal{M}(\tau, m_{K\pi\pi}, t')|^2, \tag{5.6}$$

where $\mathscr{L}$ is the integrated luminosity. We chose the distribution of the number of events to be differential in the Lorentz-invariant $K^-\pi^-\pi^+$ phase-space element $\mathrm{d}\Phi_3(\tau; m_{K\pi\pi})$, which contains the respective Jacobian that may appear from the explicit choice of the phase-space variables as discussed in section 5.1.3.

Matrix Element for a Single Intermediate State

We first formulate a model for $|\mathcal{M}(\tau, m_{K\pi\pi}, t')|^2$ that considers only a single intermediate state X^- and a single decay chain of X^-. The production, the propagation, and the decay of X^- are assumed to be independent of each other. Hence, the amplitude,

$$\mathcal{M}_{Kp\to Xp\to K\pi\pi p}(\tau, m_{K\pi\pi}, t') = \mathcal{P}_{Kp\to Xp}(m_{K\pi\pi}, t')\,\mathcal{D}_X(m_{K\pi\pi})\tilde{\Psi}_{X\to K\pi\pi}(\tau, m_{K\pi\pi}) \tag{5.7}$$

factorizes into three parts: (i) an amplitude $\mathcal{P}_{Kp\to Xp}(m_{K\pi\pi}, t')$ that models the production of X^-, (ii) an amplitude $\mathcal{D}_X(m_{K\pi\pi})$ that models the propagation of X^-, and (iii) an amplitude $\tilde{\Psi}_{X\to K\pi\pi}(\tau, m_{K\pi\pi})$ that models the decay of X^- via a particular decay chain.

Decay Amplitudes

The amplitude for the X^- decay shown in figure 5.3 can be calculated in the isobar model. It describes the decay of a certain intermediate state X^- with spin J, parity P, and spin projection M^ε,[c],[d] into the bachelor particle and a certain isobar with spin J_ξ and helicity λ_ξ. In addition, the bachelor particle and the isobar have a relative orbital angular momentum L. We call the combination,

$$a = J^P\, M^\varepsilon\, \xi\, b\, L, \tag{5.8}$$

of these quantum number a partial wave label.[e]

It is a well-established experimental fact that the strong interaction conserves parity. Parity conservation can be implemented in the PWD formalism by using the so-called reflectivity basis [73] for the subprocess $K^- + p \to X^- + p$. The reflectivity operation is a space inversion followed by an 180° rotation about the production plane normal. This corresponds to a reflection through the production plane. As all momenta of the four particles of the subprocess $K^- + p \to X^- + p$

[c] We define the reflectivity quantum number ε below.
[d] The $\vec{z}_{\mathrm{GJ}}$ axis in the Gottfried-Jackson frame is the quantization axis and defines the spin projection.
[e] For simplicity, the charge of the isobar and of the bachelor particle are dropped in the partial-wave labels. The spin J_ξ of the isobar does not explicitly appear in a as it is implicitly given by ξ, e.g. $\xi = \rho(770)$ implies $J_\xi = 1$. The helicity λ_ξ of the isobar is also not given as it is an internal quantum number and summed over in equation (5.9).

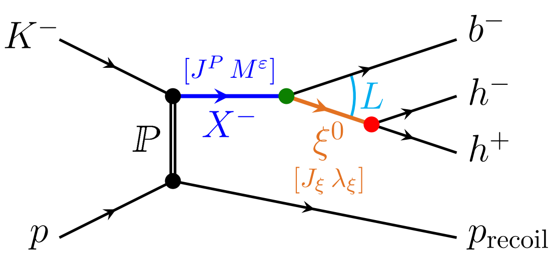

Figure 5.3: Schematic view of the reaction $K^- + p \to K^-\pi^-\pi^+ + p$ in the isobar model, where the intermediate state X^- with spin J, parity P, and spin projection M^ε successively decays to the $K^-\pi^-\pi^+$ final state via a two-body resonance ξ^0 called isobar with spin J_ξ and helicity λ_ξ. L is the relative orbital angular momentum between the bachelor particle b^- and the isobar. $h^\pm$ are the two final-state particles of the ξ^0 decay. The colors correspond to the colors of the terms in equation (5.9).

lie in the production plane by construction (see figure 5.2), the reflection operation leaves those momenta unchanged. In the following, we construct decay amplitudes that are eigenfunctions of the reflectivity operator with eigenvalues ε called reflectivity. For mesons, the reflectivity can be $\varepsilon = \pm 1$.[f] Partial waves with different ε do not interfere due to parity conservation [73].

In the reflectivity basis, M is defined to be $M \geq 0$. For each M in the range $0 < M \leq J$, there is one state with $\varepsilon = +1$ and one with $\varepsilon = -1$. In addition, there is one state with $M = 0$ and $\varepsilon = P(-1)^J$.[g] Hence, also in the reflectivity basis there are in total $2J + 1$ states, as expected for the total multiplicity of a state with spin J.

The main advantage of using the reflectivity basis is that in the limit of a high center-of-momentum energy, the reflectivity is approximately identical to the naturality of the exchange particle in the scattering process [74–76]. Since at COMPASS energies the scattering process is dominated by Pomeron exchange, which has positive naturality, dominantly positive reflectivity states are produced.[h] Hence, we may neglect negative-reflectivity states, which drastically reduces the amount of states, i.e. partial waves, that need to be considered in the PWD by about a factor two.[i]

[f] In general, the reflectivity of bosons is $\varepsilon = \pm 1$.

[g] A detailed explanation can be found in section 5.2.3 of ref. [72].

[h] It was shown in ref. [48] that even at the high center-of-momentum energy at COMPASS, f_2 exchange also has some contribution to the scattering process. As the f_2 exchange has also positive naturality, we still expect the reaction to be dominated by positive-reflectivity states. Ref. [48] did not find significant contributions from exchanges with negative naturality.

[i] For the wave-set selection discussed in section 5.2, we performed a study were we also considered partial waves with negative reflectivity. However, none of the negative-reflectivity waves picked up significant intensity.

Following the derivation in ref. [72], the total decay amplitude for a partial wave a reads

$$\begin{aligned}\tilde{\Psi}_a(\tau, m_{K\pi\pi}) = \sum_{\lambda_\xi} & \alpha_{X\to\xi bL}\sqrt{\frac{2L+1}{4\pi}}\left[{}^{\varepsilon}D^{J}_{M\lambda_\xi}(\phi_{\mathrm{GJ}},\theta_{\mathrm{GJ}},0)\right]^{*} F_L(m_{K\pi\pi})\left(L,0;J_\xi,\lambda_\xi\middle|J,\lambda_\xi\right) \\ & \times\ \mathcal{D}_\xi(m_{h^-h^+}) \\ & \times\ \alpha_\xi\sqrt{\frac{2J_\xi+1}{4\pi}}\left[D^{J_\xi}_{\lambda_\xi 0}(\phi_{\mathrm{HF}},\theta_{\mathrm{HF}},0)\right]^{*} F_{J_\xi}(m_{h^-h^+}),\end{aligned} \tag{5.9}$$

i.e. factorizes into three parts represented by the three lines in equation (5.9). The colors match the respective parts in figure 5.3.

The first line shown in green represents the amplitude of the two-body decay $X^- \to \xi^0 b^-$. Here, the complex-valued coupling $\alpha_{X\to\xi bL}$ encodes the strength and relative phase of the X^- decay into $\xi^0 b^-$ with a given L. The Wigner D-function in the reflectivity basis, ${}^{\varepsilon}D^{J}_{M\lambda_\xi}(\phi_{\mathrm{GJ}},\theta_{\mathrm{GJ}},0)$, describes the dependence of the decay amplitude on the angles in the X^- decay (see equation (177) in ref. [72]). The centrifugal-barrier factor $F_L(m_{K\pi\pi})$ accounts for the additional energy needed to produce an orbital angular momentum of L. It is a model-dependent term, which modifies the coupling at the X^- decay vertex. We used the parameterization from von Hippel and Quigg [77].[j] Finally, the Clebsch-Gordan coefficient $\left(L,0;J_\xi,\lambda_\xi\middle|J,\lambda_\xi\right)$ describes the coupling of the orbital-angular momentum L and the isobar spin J_ξ to the X^- spin J in the L-S coupling scheme used here.[k]

The second line shown in orange represents the propagation amplitude of the isobar. It is given by the dynamic amplitude $\mathcal{D}_\xi(m_{h^-h^+})$ of the isobar resonance as a function of the invariant mass $m_{h^-h^+}$ of the two-body subsystem, i.e. as a function of $m_{K^-\pi^+}$ or $m_{\pi^-\pi^+}$. For most of the considered isobar resonances, we used a relativistic Breit-Wigner amplitude. The various dynamic amplitudes are separately discussed in section 5.1.4.

The third line shown in red represents the amplitude of the two-body decay of the isobar. Here, the complex-valued coupling α_ξ encodes the strength and relative phase of the decay to $K^-\pi^+$ or $\pi^-\pi^+$. The Wigner D-function $D^{J_\xi}_{\lambda_\xi 0}(\phi_{\mathrm{HF}},\theta_{\mathrm{HF}},0)$ [78, 79] describes the dependence of the total decay amplitude on the angles in the ξ^0 decay. $F_{J_\xi}(m_{h^-h^+})$ is the centrifugal-barrier factor in the ξ^0 decay. As the two final-state particles are spin-less, the orbital angular momentum between them equals to J_ξ. The same parameterization is used as for $F_L(m_{K\pi\pi})$.

The helicity λ_ξ of the intermediate isobar is an intermediate quantum number. The corresponding decay amplitudes are constraint by the other quantum numbers and the Clebsch-Gordan coefficient. Hence, equation (5.9) contains a coherent sum over all allowed helicities, such that decay amplitudes with different helicities interfere.

[j] See appendix D in ref. [72] for the definition of the centrifugal-barrier factors using $z = [q(m_{K\pi\pi}, m_{h^-h^+}, m_{b^-})/q_{\mathrm{R}}]^2$, where q is the two-body break-up momentum of the $X^- \to \xi^0 b^-$ decay [see equation (5.41)] and $q_{\mathrm{R}} = 197.3\,\mathrm{MeV}/c$.

[k] Other Clebsch-Gordan coefficients that appear according to the general formula in equation (152) of ref. [72] are one in our case of three spin-less final-state particles.

One should note that the isobar model is only an approximation for the actual physical process. For example, it neglects all kinds of rescattering effects among all three final-state particles, and it neglects a direct three-body decay of X^-. However, such effects are expected to be small, except for very special cases, e.g. if triangle singularities appear in the rescattering amplitudes [80].

The total decay amplitude as given by equation (5.9) can be calculated up to the in general unknown couplings $\alpha_{X\to\xi bL}$ and α_ξ. To remove these unknowns, we define the normalized decay amplitudes Ψ_a, also simply called decay amplitudes, in the following way:

$$\Psi_a(\tau, m_{K\pi\pi}) \equiv \frac{\tilde{\Psi}_a(\tau, m_{K\pi\pi})}{\alpha_{X\to\xi bL}\,\alpha_\xi\,\sqrt{\mathfrak{N}_a(m_{K\pi\pi})}}. \tag{5.10}$$

Here, we additionally divide by the square root of the wave-normalization integral,[l] which is given by the integral of the absolute-squared of the total decay amplitude without couplings over the $(m_{K\pi\pi}, t')$ kinematic cell and over the $K^-\pi^-\pi^+$ phase space, i.e.[m]

$$\mathfrak{N}_a(m_{K\pi\pi}) = \int\limits_{(m_{K\pi\pi},t')} \mathrm{d}\tilde{m}_{K\pi\pi}\mathrm{d}\tilde{t}' \int \mathrm{d}\Phi_3(\tau) \left|\frac{\tilde{\Psi}_b(\tau, \tilde{m}_{K\pi\pi})}{\alpha_{X\to\xi bL}\,\alpha_\xi}\right|^2. \tag{5.11}$$

$\mathfrak{N}_a$ incorporates the $K^-\pi^-\pi^+$ phase-space volume accessible at $m_{K\pi\pi}$ and can be interpreted as the phase-space volume filled by partial wave a.

Multiple Intermediate States and Incoherent Contributions

The amplitude in equation (5.7) describes the production and propagation of a single intermediate state X^- and its decay via a single decay path. However, a state can decay into the $K^-\pi^-\pi^+$ final state via various decay chains, i.e. via various isobars and various values for the orbital angular momentum L. Also, as already seen in the $m_{K\pi\pi}$ distribution in figure 4.6a, various states X^- appear in our data. As these are all intermediate states, they interfere and thus have to be added up coherently to obtain the total amplitude. Hence, equation (5.7) needs to be extended:

$$\mathcal{M}(\tau, m_{K\pi\pi}, t') = \sum_{a\in\mathbb{W}} \left\{ \sum_{k\in\mathbb{S}_a} \mathcal{P}_{k,a}(m_{K\pi\pi}, t')\,\mathcal{D}_k(m_{K\pi\pi})\alpha_{k\to\xi bL} \right\} \alpha_\xi \sqrt{\mathfrak{N}_a(m_{K\pi\pi})}\,\Psi_a(\tau, m_{K\pi\pi}). \tag{5.12}$$

Here, we use the normalized decay amplitudes given in equation (5.10). The outer sum runs over the set $\mathbb{W}$ of all considered partial waves, i.e. over all considered $J^P M^\varepsilon$ quantum number combinations of X^- and over all considered decay paths. We discuss in section 5.2 how we chose $\mathbb{W}$. The inner sum runs over all intermediate states X^- labeled by k that may appear in partial

[l] Dividing by the wave-normalization integral yields the convenient property that the diagonal elements of the integral matrix defined in equation (5.22) are one.

[m] The wave-normalization integral is proportional to the t'-bin width. As we used different t'-bin widths in our analysis (see table 5.1), $\mathfrak{N}_a(m_{K\pi\pi})$ in principle also depends on t'. We omit this t' dependence in the formulas for simplicity.

wave a, e.g. it runs over ground and excited states with the same J^P quantum numbers. Since the production amplitude not only depends on which state k is produced, but also depends on the spin-projection M^ε with which this state is produced, $\mathcal{P}_{k,a}(m_{K\pi\pi}, t')$ has an additional wave label a, which includes M^ε.

The PWD model for the distribution of the number N_{ev} of produced events differential in $m_{K\pi\pi}$, t', and the 5-dimensional $K^-\pi^-\pi^+$ phase-space $\mathrm{d}\Phi_3$ is obtained by inserting equation (5.12) in equation (5.6):

$$\frac{\mathrm{d}\widehat{N}_{\mathrm{ev}}^{\mathrm{coh}}(\tau, m_{K\pi\pi}, t')}{\mathrm{d}\Phi_3\,\mathrm{d}m_{K\pi\pi}\,\mathrm{d}t'} = \left|\sum_{a\in\mathbb{W}} \sqrt{\frac{\mathscr{L}}{(2\pi\mathfrak{F})^2}}\,\sqrt{m_{K\pi\pi}} \left\{\sum_{k\in\mathbb{S}_a} \mathcal{P}_{k,a}(m_{K\pi\pi}, t')\,\mathcal{D}_k(m_{K\pi\pi})\alpha_{k\to\xi bL}\right\} \alpha_\xi\,\sqrt{\mathfrak{N}_a(m_{K\pi\pi})}\,\Psi_a(\tau, m_{K\pi\pi})\right|^2 . \tag{5.13}$$

We use a hat to indicate that $\widehat{N}_{\mathrm{ev}}$ is the PWD model prediction for the actual quantity N_{ev}.

Up to now, we considered perfect coherence of the partial-wave amplitudes. However, there are also reactions where the corresponding amplitudes do not interfere and hence have to be summed incoherently in the total cross section. For example, scattering reactions with spin flip and spin non-flip of the target proton have to be summed at the cross-section level as the proton spin was not measured. Another example are background processes, which are discussed in section 5.3. Generally, incoherent contributions are implemented in our formalism by an incoherent sum over various <u>coherent sectors</u> labeled by z that may contribute to our data sample. Hence, the PWD model for the distribution of the number of produced events reads

$$\mathcal{I}(\tau, m_{K\pi\pi}, t') \equiv \frac{\mathrm{d}\widehat{N}_{\mathrm{ev}}(\tau, m_{K\pi\pi}, t')}{\mathrm{d}\Phi_3\,\mathrm{d}m_{K\pi\pi}\,\mathrm{d}t'} = \sum_z \left|\sum_{a\in\mathbb{W}_z} \sqrt{\frac{\mathscr{L}}{(2\pi\mathfrak{F})^2}}\,\sqrt{m_{K\pi\pi}} \left\{\sum_{k\in\mathbb{S}_a} \mathcal{P}^z_{k,a}(m_{K\pi\pi}, t')\,\mathcal{D}_k(m_{K\pi\pi})\alpha_{k\to\xi bL}\right\} \alpha_\xi\,\sqrt{\mathfrak{N}_a(m_{K\pi\pi})}\,\Psi_a(\tau, m_{K\pi\pi})\right|^2 . \tag{5.14}$$

The quantity $\mathcal{I}$ is also called the <u>model intensity</u>. In general, the sets $\mathbb{W}_z$ of partial waves may be different in the coherent sectors. Also, the production amplitudes may be different for different production processes. Hence, $\mathcal{P}^z_{k,a}(m_{K\pi\pi}, t')$ has an additional z label. The propagation depends only on the intermediate state k and the decay amplitude is completely determined by the partial-wave label a. Hence, both amplitudes do not have a z label.

In addition to the partial waves defined in equation (5.8), we included a single so-called <u>flat wave</u> in our model, which has a flat decay amplitude, i.e. $\Psi_{\mathrm{flat}}(\tau, m_{K\pi\pi}) = \mathrm{const}$. It is added incoherently to the other partial waves, i.e. there is an own coherent sector containing only the flat wave. This flat wave effectively models incoherent background in our data that has an isotropic phase-space distribution.

Transition Amplitudes

Within the isobar model, the decay amplitudes are known and can be calculated without free parameters. We combine all other terms in equation (5.14), which are partly unknown, to the so-called transition amplitudes

$$\mathcal{T}_a^z(m_{K\pi\pi}, t') \equiv \sqrt{\frac{\mathscr{L}}{(2\pi\mathfrak{F})^2}}\,\sqrt{m_{K\pi\pi}}\left\{\sum_{k\in\mathbb{S}_a}\mathcal{P}_{k,a}^z(m_{K\pi\pi}, t')\,\mathcal{D}_k(m_{K\pi\pi})\alpha_{k\to\xi bL}\right\}\alpha_\xi\,\sqrt{\mathfrak{N}_a(m_{K\pi\pi})}. \quad (5.15)$$

The transition amplitudes of a partial wave a incorporate the production and propagation of all intermediate states that may appear in wave a. As the transition amplitudes contain the couplings $\alpha_{k\to\xi bL}$ and α_ξ, they incorporate also the strengths and phases of the decays of the intermediate and isobar states. Using the transition amplitudes simplifies equation (5.14) to

$$\mathcal{I}(\tau, m_{K\pi\pi}, t') = \sum_z\left|\sum_{a\in\mathbb{W}_z(m_{K\pi\pi},t')}\mathcal{T}_a^z(m_{K\pi\pi}, t')\,\Psi_a(\tau, m_{K\pi\pi})\right|^2. \quad (5.16)$$

It is important to note, that the transition amplitudes depend only on $m_{K\pi\pi}$ and t'. The known decay amplitudes are the only terms that depend on the $K^-\pi^-\pi^+$ phase-space variables τ. As mentioned at the beginning of this section, we performed the PWD independently in narrow $(m_{K\pi\pi}, t')$ cells. We chose these cells to be sufficiently narrow so that we can assume the transition amplitudes to be approximately constant within each cell. Hence, the $m_{K\pi\pi}$ and t' dependencies of the transition amplitudes are not explicitly modeled in the PWD, but complex-valued piecewise constant functions are used instead to approximate these dependencies in a model-independent way. For a given $(m_{K\pi\pi}, t')$ cell, the constant transition amplitudes are the free parameters that are determined in the PWD fits described in section 5.1.3. Using this binned approach, the $m_{K\pi\pi}$ and t' dependence of the transition amplitudes are measured in the PWD. As indicated in equation (5.16), also the set $\mathbb{W}_z(m_{K\pi\pi}, t')$ of partial waves may depend on $m_{K\pi\pi}$ and t', which is discussed in section 5.2.

Spin-Density Matrix

Expanding the absolute-value-squared term in equation (5.16) yields

$$\mathcal{I}(\tau, m_{K\pi\pi}, t') = \sum_z\sum_{a,b\in\mathbb{W}_z(m_{K\pi\pi},t')}\mathcal{T}_a^z(m_{K\pi\pi}, t')\left[\mathcal{T}_b^z(m_{K\pi\pi}, t')\right]^*\Psi_a(\tau, m_{K\pi\pi})\left[\Psi_b(\tau, m_{K\pi\pi})\right]^*, \quad (5.17)$$

where the transition amplitudes appear in pairs. Exchanging the two sums in equation (5.17), the model intensity can be expressed in terms of the so-called spin-density matrix

$$\rho_{ab}(m_{K\pi\pi}, t') = \sum_z\mathcal{T}_a^z(m_{K\pi\pi}, t')\left[\mathcal{T}_b^z(m_{K\pi\pi}, t')\right]^*. \quad (5.18)$$

If a wave a does not appear in coherent sector z, the corresponding transition amplitude is zero. This means, if waves a and b appear only in different coherent sectors, the corresponding spin-density matrix element is zero.[n] Using the spin-density matrix, the model intensity in equation (5.17) reads[o]

$$\mathcal{I}(\tau, m_{K\pi\pi}, t') = \sum_{a,b \in \mathbb{W}(m_{K\pi\pi}, t')} \Psi_a(\tau, m_{K\pi\pi})\, \rho_{ab}(m_{K\pi\pi}, t') \left[\Psi_b(\tau, m_{K\pi\pi})\right]^* . \tag{5.19}$$

It is important to note that the transition amplitudes cannot be uniquely determined, because any unitary transformation $\mathcal{U}_{z'z}$ of the transition amplitudes,

$$\mathcal{T}'^{z'}_a(m_{K\pi\pi}, t') = \sum_z \mathcal{U}_{z'z}\, \mathcal{T}^z_a(m_{K\pi\pi}, t'), \tag{5.20}$$

results in the same model intensity [81]. The reason is, that the transition amplitudes always appear in pairs in equation (5.17). Also, the spin-density matrix is invariant under such a unitary transformation. Hence, the measured transition amplitudes $\mathcal{T}^z_a(m_{K\pi\pi}, t')$ are in general different from the transition amplitudes $\mathcal{T}^{\mathfrak{p}}_a(m_{K\pi\pi}, t')$ of individual physics processes $\mathfrak{p}$, e.g. spin flip and spin non-flip, because $\mathfrak{p} = z' \neq z$.

The measured transition amplitudes $\mathcal{T}^z_a(m_{K\pi\pi}, t')$ that appear in equation (5.16) are only an effective parameterization of the spin-density matrix. Different parameterizations of the spin-density matrix are possible in order to fix the arbitrary unitary transformation. We used the so-called Chung-Trueman parameterization [73], which is explained in Appendix E of ref. [72].

A model parameter that needs to be chosen is the rank of the spin-density matrix, which corresponds to the number of incoherent sectors in the sum over z in equation (5.16).[p] Our choice for the rank of the spin-density matrix is discussed in section 5.3.

Observables

The most important observable is the model intensity given in equation (5.19) as it is related to the distribution of the measured $K^-\pi^-\pi^+$ sample.

[n] For example, if z labels the two coherent sectors with positive and negative reflectivity, which do not interfere, the wave set of the coherent sector with positive reflectivity and the wave set of the coherent sector with negative reflectivity are disjoint. Hence, the corresponding spin-density matrix has block-diagonal form, where one block corresponds to positive-reflectivity waves and the other block corresponds to negative-reflectivity waves.

[o] In equation (5.19), the sum goes over the full set $\mathbb{W}(m_{K\pi\pi}, t')$ of all partial waves from all coherent sectors, i.e. $\mathbb{W}(m_{K\pi\pi}, t') = \bigcup_z \mathbb{W}_z(m_{K\pi\pi}, t')$.

[p] As discussed above, we included an incoherent flat wave in our model. However, we do not count the flat wave for what we call the rank of the PWD model or the rank of the spin-density matrix, because the main analysis yields practically zero intensity for the flat wave as discussed in section 5.3. This means, e.g., that a spin-density matrix of a rank=3 PWD model, i.e. a PWD model with a rank=3 spin-density matrix, technically has a rank of 4.

The estimate for the total number of produced events in a $(m_{K\pi\pi}, t')$ cell can be calculated by integrating equation (5.19) over the ranges of the kinematic $(m_{K\pi\pi}, t')$ cell and over all five $K^-\pi^-\pi^+$ phase-space variables τ, i.e.[q]

$$\begin{aligned}\widehat{N}_{\text{ev}}(m_{K\pi\pi}, t') &= \int\limits_{(m_{K\pi\pi}, t')} \mathrm{d}\tilde{m}_{K\pi\pi}\,\mathrm{d}\tilde{t}' \int \mathrm{d}\Phi_3(\tau)\, \mathcal{I}(\tau, \tilde{m}_{K\pi\pi}, \tilde{t}') \\ &= \sum_{a,b\in\mathbb{W}(m_{K\pi\pi},t')} \rho_{ab}(m_{K\pi\pi}, t') \int\limits_{(m_{K\pi\pi}, t')} \mathrm{d}\tilde{m}_{K\pi\pi}\,\mathrm{d}\tilde{t}' \int \mathrm{d}\Phi_3(\tau)\, \Psi_a(\tau, \tilde{m}_{K\pi\pi}) \left[\Psi_b(\tau, \tilde{m}_{K\pi\pi})\right]^* \\ &= \sum_{a,b\in\mathbb{W}(m_{K\pi\pi},t')} \rho_{ab}(m_{K\pi\pi}, t')\, I_{ab}(m_{K\pi\pi}, t'). \end{aligned} \tag{5.21}$$

In the last line, we introduce the so-called phase-space integral matrix

$$I_{ab}(m_{K\pi\pi}, t') \equiv \int\limits_{(m_{K\pi\pi}, t')} \mathrm{d}\tilde{m}_{K\pi\pi}\,\mathrm{d}\tilde{t}' \int \mathrm{d}\Phi_3(\tau)\, \Psi_a(\tau, \tilde{m}_{K\pi\pi}) \left[\Psi_b(\tau, \tilde{m}_{K\pi\pi})\right]^* . \tag{5.22}$$

Limiting the sum in equation (5.17) to only a single partial wave a yields the expected number of produced events for this wave, i.e.

$$\widehat{N}_a(m_{K\pi\pi}, t') \equiv \rho_{aa}(m_{K\pi\pi}, t')\, I_{aa}(m_{K\pi\pi}, t') = \rho_{aa}(m_{K\pi\pi}, t'). \tag{5.23}$$

Here, we use that $I_{aa}(m_{K\pi\pi}, t') = 1$, due to the normalization of the decay amplitudes in equation (5.10). $\widehat{N}_a(m_{K\pi\pi}, t')$ is also called the intensity of a partial wave and equals to the corresponding diagonal element of the spin-density matrix. Accordingly, we call $\widehat{N}_{\text{ev}}(m_{K\pi\pi}, t')$ defined in equation (5.21) also the total model intensity.

As explained in section 2.2, we split our total data set into three subsets (i) with slightly different experimental acceptances $\eta^{(i)}(\tau, m_{K\pi\pi}, t')$. The PWD model for the distribution of the number $N_{\text{ev}}^{(i)}$ of produced events in data set (i) reads

$$\frac{\mathrm{d}\widehat{N}_{\text{ev}}^{(i)}(\tau, m_{K\pi\pi}, t')}{\mathrm{d}\Phi_3\, \mathrm{d}m_{K\pi\pi}\, \mathrm{d}t'} = \hat{r}^{(i)}(m_{K\pi\pi}, t')\, \frac{\mathrm{d}\widehat{N}_{\text{ev}}(\tau, m_{K\pi\pi}, t')}{\mathrm{d}\Phi_3\, \mathrm{d}m_{K\pi\pi}\, \mathrm{d}t'} = \hat{r}^{(i)}(m_{K\pi\pi}, t')\, \mathcal{I}(\tau, m_{K\pi\pi}, t'). \tag{5.24}$$

The so-called data-set fraction, i.e. the fraction of produced events in data set (i), are given by

$$\hat{r}^{(i)}(m_{K\pi\pi}, t') = \frac{\mathrm{d}\widehat{N}_{\text{ev}}^{(i)}(\tau, m_{K\pi\pi}, t')}{\mathrm{d}\Phi_3\, \mathrm{d}m_{K\pi\pi}\, \mathrm{d}t'} \Bigg/ \frac{\mathrm{d}\widehat{N}_{\text{ev}}(\tau, m_{K\pi\pi}, t')}{\mathrm{d}\Phi_3\, \mathrm{d}m_{K\pi\pi}\, \mathrm{d}t'} = \widehat{N}_{\text{ev}}^{(i)}(m_{K\pi\pi}, t') \Big/ \widehat{N}_{\text{ev}}(m_{K\pi\pi}, t'). \tag{5.25}$$

[q] In the second line, the fact that our piecewise parameterization for the transition amplitudes and hence the spin-density matrix is constant within a $(m_{K\pi\pi}, t')$ cell is used.

The data-set fractions fulfill the condition

$$\sum_{(i)} \hat{r}^{(i)}(m_{K\pi\pi}, t') = 1. \tag{5.26}$$

As the data-set fractions correspond to the number of produced events and not to the number of measured events, they cannot be directly calculated from the fractions of measured events in the $K^-\pi^-\pi^+$ sample. Therefore, the $\hat{r}^{(i)}(m_{K\pi\pi}, t')$ are free real-valued parameters in the PWD fits and their values are determined from data. The actual data-set fractions are global constants, i.e. independent of $(m_{K\pi\pi}, t')$. However, as the PWD fits are performed independently in $(m_{K\pi\pi}, t')$ cells, independent parameters for the data-set fraction are used in each $(m_{K\pi\pi}, t')$ cell. The consistency of the extracted the data-set fractions is discussed in section 5.5.

In order to compare the model intensity to the measured distributions, the experimental acceptance has to be taken into account. The acceptance distorts the measured distribution of events with respect to the model intensity, i.e. with respect to the distribution of produced events. The PWD model for the distribution of the number $\overline{N}_{\text{ev}}^{(i)}$ of measured events in data set (i) differential in $m_{K\pi\pi}$, in t', and in the 5-dimensional $K^-\pi^-\pi^+$ phase-space $\mathrm{d}\Phi_3$ reads[r]

$$\frac{\mathrm{d}\widehat{\overline{N}}_{\text{ev}}^{(i)}(\tau, m_{K\pi\pi}, t')}{\mathrm{d}\Phi_3\,\mathrm{d}m_{K\pi\pi}\,\mathrm{d}t'} = \eta^{(i)}(\tau, m_{K\pi\pi}, t')\,\hat{r}^{(i)}(m_{K\pi\pi}, t')\,\mathcal{I}(\tau, m_{K\pi\pi}, t'). \tag{5.27}$$

The <u>acceptance models</u> $\eta^{(i)}(\tau, m_{K\pi\pi}, t')$; i.e. the models for the probability to measure an event that was produced with $m_{K\pi\pi}$, t', and τ; are obtained by Monte Carlo simulations of the detector as described in appendix C.2.

Analogously to equation (5.21), the expected total number of measured events in data set (i) in a $(m_{K\pi\pi}, t')$ cell is calculated as

$$\begin{aligned}\widehat{\overline{N}}_{\text{ev}}^{(i)}(m_{K\pi\pi}, t') &= \int\limits_{(m_{K\pi\pi},t')}\mathrm{d}\tilde{m}_{K\pi\pi}\mathrm{d}\tilde{t}'\int\mathrm{d}\Phi_3(\tau)\,\eta^{(i)}(\tau, \tilde{m}_{K\pi\pi}, \tilde{t}')\,\hat{r}^{(i)}(\tilde{m}_{K\pi\pi}, \tilde{t}')\,\mathcal{I}(\tau, \tilde{m}_{K\pi\pi}, \tilde{t}') \\ &= \sum_{a,b\in\mathbb{W}(m_{K\pi\pi},t')} \rho_{ab}(m_{K\pi\pi}, t')\,\hat{r}^{(i)}(m_{K\pi\pi}, t')\,\bar{I}_{ab}^{(i)}(m_{K\pi\pi}, t').\end{aligned} \tag{5.28}$$

Here, the so-called <u>acceptance-integral matrix</u>,

$$\bar{I}_{ab}^{(i)}(m_{K\pi\pi}, t') \equiv \int\limits_{(m_{K\pi\pi},t')}\mathrm{d}\tilde{m}_{K\pi\pi}\mathrm{d}\tilde{t}'\int\mathrm{d}\Phi_3(\tau)\,\eta^{(i)}(\tau, \tilde{m}_{K\pi\pi}, \tilde{t}')\,\Psi_a(\tau, \tilde{m}_{K\pi\pi})\left[\Psi_b(\tau, \tilde{m}_{K\pi\pi})\right]^*, \tag{5.29}$$

appears, which takes into account the experimental acceptance of data set (i).

[r] In equation (5.27), we neglect detector resolution effects that may lead to a smearing of the variables $(\tau, m_{K\pi\pi}, t')$, because of the good detector resolution of COMPASS (see appendix C.4). Incorporating these effects would require a convolution of equation (5.27) with the detector resolution function. The calculation of such high-dimensional convolution integrals is computationally prohibitively expensive.

Finally, the PWD model for the distribution of the number $\overline{N}_{\text{ev}}$ of measured events in all data sets reads

$$\frac{\mathrm{d}\widehat{\widehat{N}}_{\text{ev}}(\tau, m_{K\pi\pi}, t')}{\mathrm{d}\Phi_3\,\mathrm{d}m_{K\pi\pi}\,\mathrm{d}t'} = \sum_{(i)} \frac{\mathrm{d}\widehat{\widehat{N}}^{(i)}_{\text{ev}}(\tau, m_{K\pi\pi}, t')}{\mathrm{d}\Phi_3\,\mathrm{d}m_{K\pi\pi}\,\mathrm{d}t'} = \left\{\sum_{(i)} \eta^{(i)}(\tau, m_{K\pi\pi}, t')\,\hat{r}^{(i)}(m_{K\pi\pi}, t')\right\} \mathcal{I}(\tau, m_{K\pi\pi}, t'), \tag{5.30}$$

and the estimated total number of measured events in all data sets in a $(m_{K\pi\pi}, t')$ cell is

$$\widehat{\widehat{N}}_{\text{ev}}(m_{K\pi\pi}, t') = \sum_{(i)} \widehat{\widehat{N}}^{(i)}_{\text{ev}}(m_{K\pi\pi}, t') = \sum_{a,b\in\mathbb{W}(m_{K\pi\pi},t')} \rho_{ab}(m_{K\pi\pi}, t') \left\{\sum_{(i)} \hat{r}^{(i)}(m_{K\pi\pi}, t')\,\overline{\mathcal{I}}^{(i)}_{ab}(m_{K\pi\pi}, t')\right\}. \tag{5.31}$$

5.1.3 Maximum-Likelihood Fit

In order to measure the $m_{K\pi\pi}$ and t' dependence of the spin-density matrix elements, we subdivided our data into narrows bins in $m_{K\pi\pi}$ and in t'. The number of events per $(m_{K\pi\pi}, t')$ cell is between 10 and 7000 events with about 2400 events on average. We fitted the PWD model in equation (5.16) independently in each of the 300 $(m_{K\pi\pi}, t')$ cells to data. The free parameters in these fits are the transition amplitudes $\{\mathcal{T}^{z}_{a}\}$, which are complex-valued constants within each $(m_{K\pi\pi}, t')$ cell,[s] and the data-set fractions $\{\hat{r}^{(i)}\}$, which are real-valued constants within one $(m_{K\pi\pi}, t')$ cell. We performed an unbinned extended maximum-likelihood fit in each $(m_{K\pi\pi}, t')$ cell, where we maximized the likelihood function $\mathcal{L}_{\text{PWD}}$ with respect to the free fit parameters.

Likelihood Function

First, we formulate the likelihood function $\mathcal{L}^{(i)}_{\text{PWD}}$ for a single data set. This likelihood function is the joint probability density function of the measured events in the given $(m_{K\pi\pi}, t')$ cell, which is the product of the probability density functions of the single events. The probability density function of a single event is proportional to the density of the measured number of events in the kinematic variables τ, $m_{K\pi\pi}$, t' as given in equation (5.27) and reads

$$\begin{aligned} p^{(i)}(\tau; m_{K\pi\pi}, t') &= \frac{\Phi_3(\tau; m_{K\pi\pi})\,\eta^{(i)}(\tau, m_{K\pi\pi}, t')\,\hat{r}^{(i)}(m_{K\pi\pi}, t')\,\mathcal{I}(\tau, m_{K\pi\pi}, t')}{\int\limits_{(m_{K\pi\pi},t')} \mathrm{d}\tilde{m}_{K\pi\pi}\mathrm{d}\tilde{t}' \int \mathrm{d}\tau\, \Phi_3(\tau; m_{K\pi\pi})\,\eta^{(i)}(\tau, m_{K\pi\pi}, t')\,\hat{r}^{(i)}(m_{K\pi\pi}, t')\,\mathcal{I}(\tau, m_{K\pi\pi}, t')} \\ &= \frac{\Phi_3(\tau; m_{K\pi\pi})\,\eta^{(i)}(\tau, m_{K\pi\pi}, t')\,\hat{r}^{(i)}(m_{K\pi\pi}, t')\,\mathcal{I}(\tau, m_{K\pi\pi}, t')}{\widehat{\widehat{N}}^{(i)}_{\text{ev}}(m_{K\pi\pi}, t')}. \end{aligned} \tag{5.32}$$

[s] In the Chung-Trueman parameterization of the spin-density matrix, some transition amplitudes are zero and some are real-valued by construction.

Here, we express the probability density for an explicit choice for the phase-space variables τ using $\mathrm{d}\Phi_3 = \mathrm{d}\tau\Phi_3(\tau; m_{K\pi\pi})$, where $\Phi_3(\tau; m_{K\pi\pi})$ is the density of states in the phase-space, which includes the Jacobian term that arises from the choice of variables. Interestingly, the normalization integral, which appears in the denominator in equation (5.32), equals to the predicted number of measured events for the given $(m_{K\pi\pi}, t')$ cell in equation (5.28).

The intensity model enters linear in the numerator and the denominator of equation (5.32) and the transition amplitudes appear quadratic in the intensity model in equation (5.16). Hence, $p^{(i)}(\tau; m_{K\pi\pi}, t')$ is invariant under a multiplication of all transition amplitudes by a common constant, i.e. $\mathcal{T}_a^z(m_{K\pi\pi}, t') \to c\mathcal{T}_a^z(m_{K\pi\pi}, t')$. The same holds for the data-set fraction $\hat{r}^{(i)}(m_{K\pi\pi}, t')$.

To fix the scale of the transition amplitudes and the data-set fraction,[t] the extended maximum-likelihood formalism is used. The corresponding extended likelihood function reads

$$\mathcal{L}_{\mathrm{PWD}}^{(i)}(m_{K\pi\pi}, t') = \frac{\left[\widehat{\overline{N}}_{\mathrm{ev}}^{(i)}(m_{K\pi\pi}, t')\right]^{\overline{N}_{\mathrm{ev}}^{(i)}(m_{K\pi\pi}, t')} e^{-\widehat{\overline{N}}_{\mathrm{ev}}^{(i)}(m_{K\pi\pi}, t')}}{\overline{N}_{\mathrm{ev}}^{(i)}(m_{K\pi\pi}, t')!} \prod_{k=1}^{\overline{N}_{\mathrm{ev}}^{(i)}(m_{K\pi\pi}, t')} p^{(i)}(\tau^k; m_{K\pi\pi}^k, t'^k). \tag{5.33}$$

The fraction in equation (5.33) is the Poisson probability to actually measure $\overline{N}_{\mathrm{ev}}^{(i)}(m_{K\pi\pi}, t')$ events given that we expect $\widehat{\overline{N}}_{\mathrm{ev}}^{(i)}(m_{K\pi\pi}, t')$ events according to equation (5.28).

Inserting equation (5.32) in equation (5.33) yields

$$\begin{aligned} \mathcal{L}_{\mathrm{PWD}}^{(i)}(m_{K\pi\pi}, t') = &\frac{e^{-\widehat{\overline{N}}_{\mathrm{ev}}^{(i)}(m_{K\pi\pi}, t')}}{\overline{N}_{\mathrm{ev}}^{(i)}(m_{K\pi\pi}, t')!} \left[\hat{r}^{(i)}(m_{K\pi\pi}, t')\right]^{\overline{N}_{\mathrm{ev}}^{(i)}(m_{K\pi\pi}, t')} \\ &\times \prod_{k=1}^{\overline{N}_{\mathrm{ev}}^{(i)}(m_{K\pi\pi}, t')} \Phi_3(\tau^k; m_{K\pi\pi}^k)\, \eta^{(i)}(\tau^k, m_{K\pi\pi}^k, t'^k)\, \mathcal{I}(\tau^k, m_{K\pi\pi}^k, t'^k). \end{aligned} \tag{5.34}$$

Here, the facts are used that the denominator of the probability density in equation (5.32) cancels with the $\left[\widehat{\overline{N}}_{\mathrm{ev}}^{(i)}\right]^{\overline{N}_{\mathrm{ev}}^{(i)}}$ term of the Poisson probability and that the data-set fraction is the same for all events within one $(m_{K\pi\pi}, t')$ cell.

As the data sets are independent, the total likelihood is the product of the likelihoods of the individual data sets, i.e.

$$\mathcal{L}_{\mathrm{PWD}}(m_{K\pi\pi}, t') = \prod_{(i)} \mathcal{L}_{\mathrm{PWD}}^{(i)}(m_{K\pi\pi}, t'). \tag{5.35}$$

[t] The transition amplitudes and the data-set fraction have two independent scales to be fixed, while the extended maximum-likelihood formalism gives only one constraint. The other constraint is given by the normalization condition of the data-set fraction parameters according to equation (5.26). This is discussed below in detail for multiple data sets.

Instead of maximizing $\mathcal{L}_{\mathrm{PWD}}$, it is numerically more stable to minimize the negative log-likelihood

$$-\ln \mathcal{L}_{\mathrm{PWD}}(m_{K\pi\pi}, t') = -\sum_{(i)} \ln \mathcal{L}^{(i)}_{\mathrm{PWD}}(m_{K\pi\pi}, t'). \tag{5.36}$$

Inserting equation (5.34) into equation (5.36) yields

$$\begin{aligned}-\ln \mathcal{L}_{\mathrm{PWD}}(m_{K\pi\pi}, t') = -\sum_{(i)} \Bigg\{ & -\widehat{\overline{N}}{}^{(i)}_{\mathrm{ev}}(m_{K\pi\pi}, t') - \ln\left[\overline{N}^{(i)}_{\mathrm{ev}}(m_{K\pi\pi}, t')!\right] \\ & + \overline{N}^{(i)}_{\mathrm{ev}}(m_{K\pi\pi}, t') \ln\left[\hat{r}^{(i)}(m_{K\pi\pi}, t')\right] \\ & + \sum_{k=1}^{\overline{N}^{(i)}_{\mathrm{ev}}(m_{K\pi\pi}, t')} \ln\left[\Phi_3(\tau^k; m^k_{K\pi\pi})\, \eta^{(i)}(\tau^k, m^k_{K\pi\pi}, t'^k)\, \mathcal{I}(\tau^k, m^k_{K\pi\pi}, t'^k)\right] \Bigg\}.\end{aligned} \tag{5.37}$$

We can split this into multiple sub-terms

$$\begin{aligned}-\ln \mathcal{L}_{\mathrm{PWD}}(m_{K\pi\pi}, t') = & -\sum_{(i)} \left\{\overline{N}^{(i)}_{\mathrm{ev}}(m_{K\pi\pi}, t') \ln\left[\hat{r}^{(i)}(m_{K\pi\pi}, t')\right] - \widehat{\overline{N}}{}^{(i)}_{\mathrm{ev}}(m_{K\pi\pi}, t')\right\} \\ & - \sum_{(i)} \sum_{k=1}^{\overline{N}^{(i)}_{\mathrm{ev}}(m_{K\pi\pi}, t')} \ln\left[\mathcal{I}(\tau^k, m^k_{K\pi\pi}, t'^k)\right] \\ & + \sum_{(i)} \ln\left[\overline{N}^{(i)}_{\mathrm{ev}}(m_{K\pi\pi}, t')!\right] \\ & - \sum_{(i)} \sum_{k=1}^{\overline{N}^{(i)}_{\mathrm{ev}}(m_{K\pi\pi}, t')} \ln\left[\Phi_3(\tau^k; m^k_{K\pi\pi})\, \eta^{(i)}(\tau^k, m^k_{K\pi\pi}, t'^k)\right].\end{aligned} \tag{5.38}$$

The first line (blue) in equation (5.38) represents the N_{dataset} conditions arising from the Poisson terms of the extended maximum-likelihood ansatz. Together with the normalization condition for the data-set fraction in equation (5.26),[u] they constrain the N_{dataset} data-set fraction parameters and the absolute common scale of the transition amplitudes.

The second line (orange) in equation (5.38) takes into account the distribution of the data in the $K^-\pi^-\pi^+$ phase space. It constrains the transition amplitudes.

The last two lines (green) do not contain any free fit parameters. Hence, they are constant in the likelihood maximization and can be dropped. Especially noteworthy, the experimental acceptance for each of the measured events $\eta^{(i)}(\tau^k, m^k_{K\pi\pi})$, which is computationally very expensive to calculate, can be dropped. The experimental acceptance enters only via the calculation of

[u] We implemented the normalization condition for the data-set fraction parameters by allowing for only $(N_{\mathrm{dataset}} - 1)$ free data-set fraction parameters, while one data-set fraction parameter is calculated for each iteration from the $(N_{\mathrm{dataset}} - 1)$ free data-set fraction parameters using equation (5.26).

$\widehat{N}_{\text{ev}}^{(i)}(m_{K\pi\pi}, t')$ via the acceptance-integral matrices in equation (5.29). Thus, the acceptance does not need to be calculated for each measured event in the PWD fit, but only the acceptance-integral matrix has to be calculated using Monte Carlo integration techniques. Furthermore, the acceptance-integral matrix does not contain any free fit parameters and can thus be calculated before the PWD fit. This drastically reduces the computational costs of evaluating the negative log-likelihood. Still, the computational costs for all PWD fits performed in this analysis are of the order of a million CPUh. Also, the $K^-\pi^-\pi^+$ phase-space $\Phi_3(\tau; m_{K\pi\pi})$, which incorporates the Jacobian from the explicit choice of the set of phase-space variables, can be dropped.

PWD Fit Procedure

In order to obtain the maximum-likelihood estimates for the transition amplitudes and data-set fractions, the negative log-likelihood function in equation (5.38) is minimized dropping the constant terms shown in green.[v]

The start-parameter values for the transition amplitudes and data-set fraction are generated in two steps. In the first step, values for the real and imaginary parts of the transition amplitudes are randomly drawn from a uniform distribution in the range from $-\sqrt{\overline{N}_{\text{ev}}(m_{K\pi\pi}, t')}$ to $\sqrt{\overline{N}_{\text{ev}}(m_{K\pi\pi}, t')}$. In the second step, the data-set fractions and the absolute scale of the transition amplitudes are calculated such that $\widehat{N}_{\text{ev}}^{(i)}(m_{K\pi\pi}, t') = \overline{N}_{\text{ev}}^{(i)}(m_{K\pi\pi}, t')$ based on the transition amplitudes that were obtained in the first step. This second step turned out to be mandatory in the case of fitting multiple data sets in order to achieve a stable fit that reliably finds the parameter values that correspond to the smallest negative log-likelihood value. Fits without this second step get easily trapped in local minima of the likelihood function far away from the physical solution.

5.1.4 Dynamic Amplitudes of the Isobars

So far, we introduced in sections 5.1.1 to 5.1.3 the well-established PWD formalism. Before being able to perform a PWD fit to our $K^-\pi^-\pi^+$ sample, an explicit PWD model has to be constructed. We discuss the construction of the wave set and extensions of the PWD formalism that are special to this analysis in sections 5.2 to 5.4. Important choices when formulating an explicit PWD model are the employed parameterizations for the dynamic amplitudes of the isobar resonances. For most of the isobar resonances considered in this analysis, we used a relativistic Breit-Wigner amplitude [see equation (5.39) below]. However, the $K\pi$ and $\pi\pi$ S-wave amplitudes are not approximated well by Breit-Wigner amplitudes.

For the $\pi\pi$ S-wave amplitude, we used the same approach as in the COMPASS $\pi^-\pi^-\pi^+$ analysis [39]. The $\pi\pi$ S-wave amplitude contains dominantly three poles: the $f_0(500)$, the $f_0(980)$,

[v] As minimizer, we used the low-memory BFGS (LBFGS) [82–84] implementation of the NLopt package [85]. This algorithm approximates the Broyden-Fletcher-Goldfarb-Shanno (BFGS) algorithm [86–89] and is a quasi-Newton method that was designed to have a low memory requirement.

and the $f_0(1500)$. The couplings of each of these three poles to the total amplitude are different for different intermediate states X^- that decay to the $\pi\pi$ S-wave system. Therefore, we separated the total $\pi\pi$ S-wave amplitude into three independent partial waves, each with its own transition amplitude: (i) The $f_0(1500)$ is parameterized by a relativistic Breit-Wigner amplitude [see equation (5.39) below], (ii) the $f_0(980)$ is parameterized by the so-called Flatté parameterization [see equation (5.43) below], (iii) the "remaining" broad $\pi\pi$ S-wave component [see equation (5.44) below], which contains the $f_0(500)$.

Analogously to the $\pi\pi$ S-wave amplitude, the $K\pi$ S-wave amplitude contains dominantly three poles: the $K_0^*(700)$, the $K_0^*(1430)$, and the $K_0^*(1950)$. However, in contrast to the $\pi\pi$ S-wave amplitude, where the small width of the $f_0(980)$ allows us to separate it from the broad $\pi\pi$ S-wave component, the larger width of the $K_0^*(1430)$ prohibits such an approach for the $K\pi$ S-wave amplitude. Therefore, we present below an alternative approach to simultaneously take into account all three poles [see equations (5.50) and (5.51) below].

Relativistic Breit-Wigner Amplitude

In this analysis, we used a relativistic Breit-Wigner amplitude [46, 90] of the form

$$\mathcal{D}_{\mathrm{BW}}(m; m_0, \Gamma_0) = \frac{m_0 \Gamma_0}{m_0^2 - m^2 - i\, m_0\, \Gamma(m)}, \tag{5.39}$$

where m_0 and Γ_0 are the nominal mass and width of the resonance, respectively. The mass-dependent width is modeled by the sum over the decay channels i

$$\Gamma(m) = \sum_i \Gamma_i(m) = \sum_i \Gamma_i \frac{q_i(m)}{m} \frac{m_0}{q_i(m_0)} \frac{F_{L_0}^2(m)}{F_{L_0}^2(m_0)}, \tag{5.40}$$

which takes into account the opening of the phase-space for the decay channel i in the two-body approximation. The two-body break-up momentum,

$$q_i(m) = q(m, m_1, m_2) = \frac{\sqrt{\left[m^2 - (m_1 + m_2)^2\right]\left[m^2 - (m_1 - m_2)^2\right]}}{2m}, \tag{5.41}$$

is given by the masses m_1 and m_2 of the daughter particles. $F_{L_0}(m)$ is the centrifugal barrier factor as used in the decay amplitudes, where L_0 is the orbital angular momentum between the daughter particles. The partial decay widths Γ_i sum up to the total decay width, i.e. $\Gamma_0 = \sum_i \Gamma_i$.

For the parameterizations of the dynamic amplitudes of isobars, we included in the sum in equation (5.40) only the $K^-\pi^+$ or the $\pi^-\pi^+$ decay channel, depending on the isobar, such that

$$\Gamma(m) = \Gamma_0 \frac{q(m)}{m} \frac{m_0}{q(m_0)} \frac{F_{J_\xi}^2(m)}{F_{J_\xi}^2(m_0)}. \tag{5.42}$$

As the final-state particles are spin less, the orbital angular momentum between them equals to the isobar spin, i.e. $L_0 = J_\xi$. The mass m_0 and width Γ_0 of the isobar resonances are taken from the PDG [91].[w]

Flatté Parameterization for the $f_0(980)$

The $f_0(980)$ is very close in mass to the $K\bar{K}$ threshold, which leads to strong deviations of the amplitude from a Breit-Wigner shape. To take this into account, we employed the Flatté parameterization [93] for the $f_0(980)$ isobar using the formula and the parameters determined by BESIII [94]

$$\mathcal{D}_{\text{Flatté}}(m) = \frac{1}{m_0^2 - m^2 - i\left(g_{\pi\pi}\,\varphi_2^{\pi\pi}(m) + g_{K\bar{K}}\,\varphi_2^{K\bar{K}}(m)\right)}. \tag{5.43}$$

Here, the $\varphi_2^i(m)$ are the two-body phase spaces terms for the two decay channels $i = \pi\pi$ and $i = K\bar{K}$ that are analytically continued below the threshold where they become complex-valued, and the g_i are the couplings.

AMPK Parameterization for the Broad $\pi\pi$ S-Wave Component

The broad $\pi\pi$ S-wave component, which contains the $f_0(500)$ is parameterized following the ansatz suggested by the VES collaboration [95]. The so-called M solution obtained from analyzing $\pi\pi \to \pi\pi$ scattering and defined by equations (3.15) and (3.20) in ref. [96] provides a parameterization of the $\pi\pi$ S-wave amplitude, which also includes the $f_0(980)$ pole. In order to remove the $f_0(980)$ from this amplitude, the parameters f_1^1, f_2^1, f_1^3, c_{11}^4, and c_{22}^4 and all diagonal elements of the M matrix were set to zero. Finally, we used the $\pi\pi \to \pi\pi$ element of the T-matrix (T_{11}) defined in equation (3.15) in ref. [96] as the amplitude for the broad $\pi\pi$ S-wave component called $[\pi\pi]_S^{\text{AMPK}}$:

$$\mathcal{D}_{\text{AMPK}}(m) = T_{11}(m). \tag{5.44}$$

Figure 5.4 illustrates the intensity and the real and imaginary parts of this amplitude.

Palano-Pennington Parameterization for the $K\pi$ S-Wave

A variety of elaborate models for the $K\pi$ S-wave amplitude are on the market [97–101]. However, many of them suffer from covering only a limited mass range, typically up to at most $1.5\,\text{GeV}/c^2$. However, analyzing an $m_{K\pi\pi}$ range up to $3\,\text{GeV}/c^2$ demands a $K\pi$ S-wave amplitude that is valid up to $m_{K^-\pi^+} \approx 2.9\,\text{GeV}/c^2$. We tried different parameterizations such as the classic LASS

[w] For some resonances, the PDG lists more than one average value. The masses and widths that were used in these cases are listed in ref. [92].

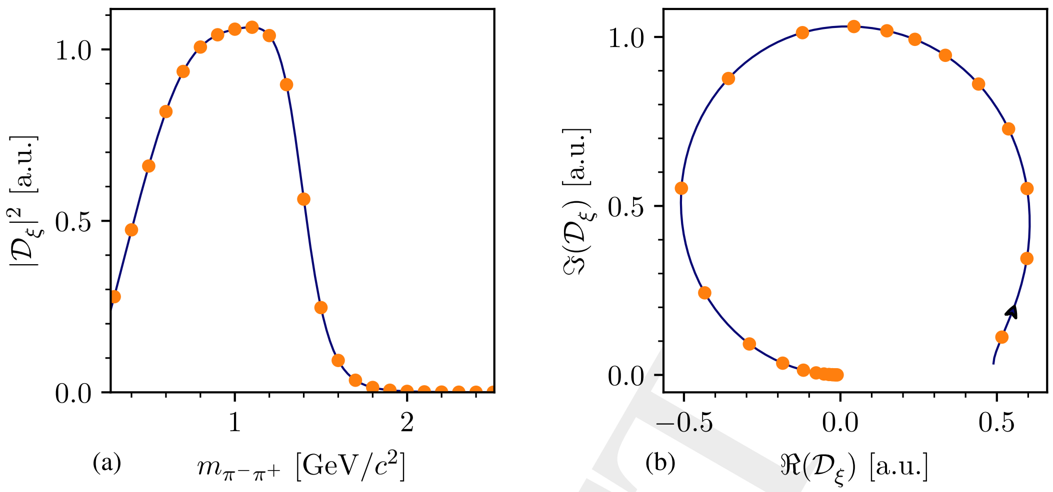

Figure 5.4: Dynamic amplitude of the $[\pi\pi]_S^{\mathrm{AMPK}}$ isobar. (a) shows the intensity as a function of $m_{\pi^-\pi^+}$, (b) shows the Argand diagram, i.e. real vs. imaginary part of the dynamic amplitude of the $[\pi\pi]_S^{\mathrm{AMPK}}$ isobar. The orange dots in the Argand diagram are drawn at the same $m_{\pi^-\pi^+}$ values as the corresponding orange dots in the intensity spectrum. The black arrow indicates the direction of increasing $m_{\pi^-\pi^+}$. Figure 10 in ref. [39], which also shows the dynamic amplitude of the $[\pi\pi]_S^{\mathrm{AMPK}}$ isobar, is wrong due to a mistake. Here, we show the correct amplitude.

parameterization [97] with parameters taken from ref. [102] and the generalized LASS (GLASS) parameterization [99] with parameters taken from ref. [103]. At the end we obtained the best results in terms of likelihood and in terms of fit stability using an approach that simultaneously takes into account all three K_0^* poles as explained in detail in the following.

The scattering amplitude for the process $i \to f$, e.g. $K\pi \to K\pi$ or $K\eta \to K\pi$, can be described in terms of the T matrix. If the final state f is not produced in a scattering process, but in the decay of a heavier state, as in our case, the decay amplitude F_f can be written in terms of the Q vector equation

$$F_f(m) = \sum_i T_{if}(m) Q_i(m), \tag{5.45}$$

where m is the invariant mass of the initial and final state. Q_i represents the production of the intermediate state i in the decay, which then rescatters to the final state f. The rescattering is expressed by the T-matrix element T_{if}. The T matrix is independent of the process. Thus, it can be determined from other experiments, e.g. from $K\pi \to K\pi$ scattering experiments, and used as input here. Typically, the elements $Q_i(m)$ are parameterized by polynomials in m^2, with the leading term being constant. Using equation (5.45) as isobar parameterizations in equation (5.9) and taking into account only the leading term $Q_i(m) \approx$ const, allows us to merge the sum $\sum_i$ in equation (5.45) and the sum $\sum_a$ over different waves in equation (5.16). Hence, the different states i can be interpreted as independent partial waves. The constants Q_i can be absorbed into the transition amplitudes of the waves with the dynamic isobar amplitudes given by the corresponding T-matrix element T_{if}.

We took the T-matrix elements from a two-channel K-matrix parameterization in ref. [100], with the two channels $1 = K\pi$ and $2 = K\eta$. One should note that despite $K\eta$ is in principle the first inelastic channel, it is well known from measurements that the inelasticity actually starts at the higher-lying threshold of the $K\eta'$ channel. Therefore, the second channel should be interpreted as an effective inelastic channel, in addition to $K\pi$.

We shortly recapitulate the most important formulas here.[x] The T-matrix elements relevant for the $K\pi$ final state read in terms of the K-matrix elements K_{ij}:

$$T_{11} = \frac{K_{11} - i\varphi_2^2 \mathrm{det}K}{\delta}, \qquad \text{and} \qquad T_{21} = T_{12} = \frac{K_{12}}{\delta}. \tag{5.46}$$

Here, $\mathrm{det}K = K_{11}K_{22} - K_{12}^2$, φ_2^i is the two-body phase space for the channel i, analytically continued for energies below the corresponding threshold, and[y]

$$\delta = 1 - i\varphi_2^1 K_{11} - i\varphi_2^2 K_{22} - \varphi_2^1\varphi_2^2 \mathrm{det}K. \tag{5.47}$$

The K-matrix elements are parameterized by a sum of two poles at s_a and s_b and a third-order polynomial:

$$K_{ij} = \frac{(s - s_\mathrm{A})}{s_{K\pi}} \left[\sum_{\alpha=a,b} \frac{g_i^\alpha g_j^\alpha}{s_\alpha - s} + \sum_{n=0}^{3} C_{ij,n} X^n \right], \tag{5.48}$$

where

$$X = \frac{2s - (s_\mathrm{top} + s_\mathrm{bot})}{s_\mathrm{top} - s_\mathrm{bot}} \tag{5.49}$$

depends on $s = m^2$. The parameters $s_{K\pi} = m_K^2 + m_\pi^2$, $s_\mathrm{A} = 0.87753 s_{K\pi}$, $s_\mathrm{top} = 5.832\,\mathrm{GeV}^2$, and $s_\mathrm{bot} = 0.36\,\mathrm{GeV}^2$ are fixed. The remaining parameters were determined in ref. [100] by a fit to scattering data from LASS [97] and Estabrooks et. al. [104] and to BaBar data on the decay $\eta_c \to \bar{K}K\pi$ [105] (see TABLE I in ref. [100]).

Finally, the two dynamic functions included in the PWD are

$$\mathcal{D}_{[K\pi]_S^{K\pi}}(m) = T_{11}(s = m^2) \tag{5.50}$$

$$\mathcal{D}_{[K\pi]_S^{K\eta}}(m) = T_{12}(s = m^2). \tag{5.51}$$

Figures 5.5 and 5.6 show the isobar dynamic amplitudes in the $m_{K^-\pi^+}$ range relevant for this analysis.

The T_{11} element as determined in ref. [100] exhibits an unphysical behavior in the mass region above $2.5\,\mathrm{GeV}/c^2$ as there are no experimental data to constrain the amplitude in this region. Thus, we set both amplitudes $\mathcal{D}_{[K\pi]_S^{K\pi}}(m) = 0$ and $\mathcal{D}_{[K\pi]_S^{K\eta}}(m) = 0$ above $m = 2.4\,\mathrm{GeV}/c^2$.

[x] There are some known typos in the formulas of ref. [100], which are corrected here.
[y] In ref. [100], Δ was used instead of δ.

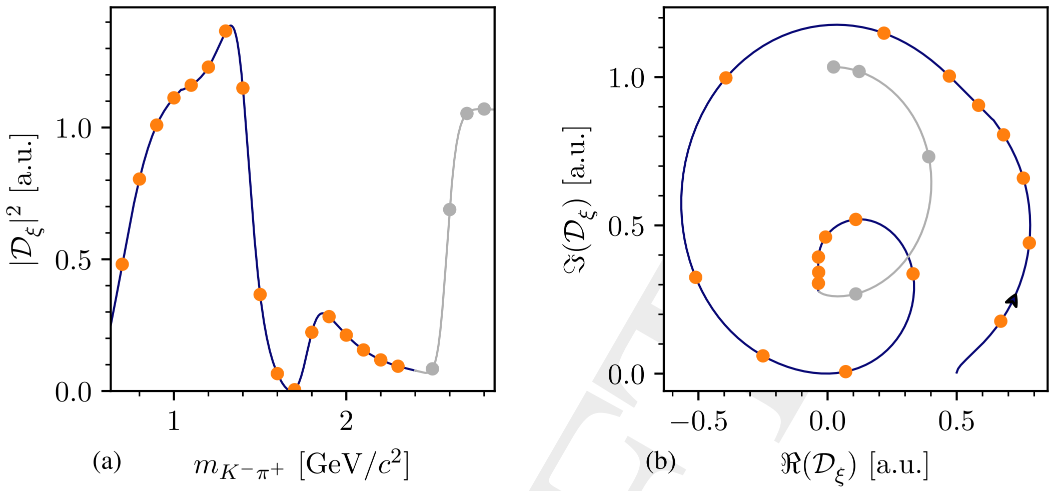

Figure 5.5: Same as figure 5.4, but showing the dynamic amplitude of the $[K\pi]_S^{K\pi}$ isobar. The gray lines and points are the extrapolation beyond the region where we set the amplitude to zero.

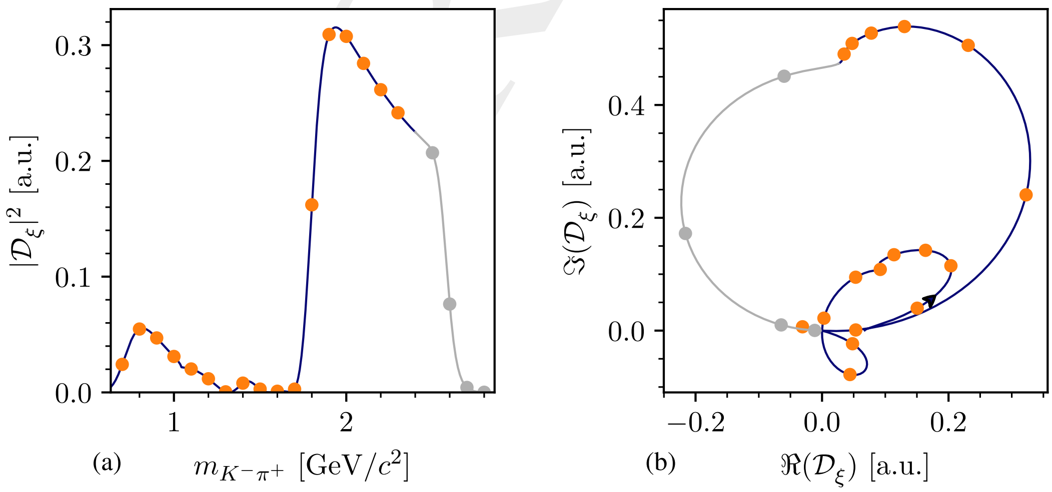

Figure 5.6: Same as figure 5.4, but showing the dynamic amplitude of the $[K\pi]_S^{K\eta}$ isobar. The gray lines and points are the extrapolation beyond the region where we set the amplitude to zero.

5.2 Wave-Set Selection

In principle there is an infinite number of possible partial waves that may contribute to the data, e.g. as the spins and orbital angular momenta can take any integer number. Not all of these partial waves might be realized in reality and not all of the realized partial waves might contribute significantly to the $K^-\pi^-\pi^+$ sample such that they can be resolved with the given precision of the measured data.[z] As we measured only a finite amount of data and only a finite amount of computing resources is available, we have to truncate the sum over partial waves in the intensity model in equation (5.16) by selecting a certain set of partial waves, the so-called wave set, that we include in the model. On the one hand, a too large wave set causes overfitting in the PWD fit, because the number of fit parameters is approximately proportional to the number of partial waves included in the wave set. Overfitting can lead to findings in the PWD that arise from noise in the data [106]. This is an issue especially in amplitude analysis like the PWD, because the coherent sum squared over complex-valued amplitudes like in equation (5.16) introduces non-linear effects in the model. For example, two or more amplitudes may destructively interfere with each other. Such a destructive interference may lead to large artificial enhancements of the interfering amplitudes, while it leads to only a small change in the total model intensity and thus to only a small change in description of the data, which may be misused to describe noise in the data. In addition, an overfitted model is less robust against systematic effects, e.g. from background processes like $K^- + p \to K^-K^-K^+ + p$ that also entered the $K^-\pi^-\pi^+$ sample (see section 4.2). On the other hand, a too small wave set, i.e. a wave set that is missing waves that significantly contribute to the data, may lead to artifacts in the results of the PWD, because it leaves structures in the data that arise from the missed waves undescribed. These structures might be partly accounted for in the PWD fit by the waves that are included in the wave set. This might lead to artificial structures in these waves. Additionally, the missed waves may contain interesting physics signals that we would miss. As we present in this work the so-far world's largest sample of the reaction $K^- + p \to K^-\pi^-\pi^+ + p$, we are especially interested in such weak signal that were not seen before. Therefore, the goal of the wave-set selection is to find a minimal wave set that is sufficient to describe all significant structures in the $K^-\pi^-\pi^+$ sample.

Traditionally, these wave sets had been constructed by hand in the following iterative process. Starting from a wave set constructed based on previous knowledge, partial waves are manually added or removed. Then, the result of a PWD of these modified wave sets is studied. Based on pre-defined criteria the modified wave set is accepted or rejected. Such a criterion can be whether a newly added wave shows "significant intensity". Also, likelihood-ratio tests are used to decide whether removing a wave leads to a similar good description of the data such that the wave set without the corresponding wave can be accepted. This procedure of adding and removing waves is repeated until a "good enough" wave set is found. Following this approach potentially introduces observer bias. The selection of waves that are added or removed is a personal choice,

[z] In addition to the diffractive scattering reaction $K^- + p \to K^-\pi^-\pi^+ + p$, for which the partial waves were constructed in section 5.1.2, there are other processes, e.g. Deck-like reactions (see section 2.1.1) or incoherent background from reactions like $K^- + p \to K^-K^-K^+ + p$, that also contribute to the $K^-\pi^-\pi^+$ sample. As the partial waves were not constructed to describe these processes, their contribution in the $K^-\pi^-\pi^+$ sample projects in principle to all partial waves, but not all of these projections contribute significantly to the data.

because not all possible combinations of adding and removing waves can be tested. This holds especially for partial-wave analyses, where the contribution of a partial wave to the data is caused not only by its own intensity, but also by its interference with other partial waves [107]. A partial wave may become significant only when it is added together with other waves. Also, often the decisions when to accept or reject a wave and when to stop the procedure is taken based on subjective criteria, which are hard to quantify and thus hard to reproduce.

In this work, we minimized this potential observer bias by inferring the wave set from data. Various techniques exist for construction optimal models that consist of sets of individual components, e.g. in our case partial-waves. These model-selection techniques have applications also in other fields, e.g. in machine learning. They all have in common that they select an optimal subset of model components that is sufficient to describe the data from a large pool of potentially possible components. Such a method was first applied to partial-wave analyses in ref. [107]. At COMPASS, such methods were applied in the analysis of the reaction $\pi^- + p \to \pi^-\pi^-\pi^-\pi^+\pi^+ + p$ [67] and $\pi^- + p \to \pi^-\pi^-\pi^+ + p$ [43, 108]. They all share the same idea. First, a large set of waves, the so-called <u>wave pool</u>, is systematically constructed by including all waves that are expected to potentially contribute to the data (see section 5.2.1). In the second step, the so-called <u>wave-set selection fit</u>, the data are fitted using the whole wave pool. However, using the likelihood in equation (5.38) would lead to massive overfitting, as the wave pool is typically much lager than the wave set needed to describe the data. In order to circumvent overfitting, regularization techniques are applied to the wave-set selection fit, with the goal to suppress insignificant waves (see section 5.2.2). In the third step, the waves that acquire significant intensity in the wave-set selection fit are selected for the wave set (see section 5.2.5). In the final step, the set of selected waves is fitted to the data, without regularization. This fit yields the final results for the PWD (see section 5.5). Applying this approach to each $(m_{K\pi\pi}, t')$ cell yields an individual wave set for each cell. Due to the finite amount of measured data, there are fluctuations of the wave set between neighboring $(m_{K\pi\pi}, t')$ cells. Such fluctuations can be suppressed by impose a continuity criterion in the wave-set selection (see section 5.2.3).

5.2.1 Construction of the Wave Pool

As a starting point for the wave-set selection, we had to construct a pool of partial waves that on the one hand contains all waves that potentially contribute significantly to our data, but that on the other hand is still manageable in size. In order to avoid bias from the construction of the wave pool, we considered large ranges of the partial-wave quantum numbers. We included partial-waves with spin $J \leq 7$ and orbital angular-momentum $L \leq 7$. We considered only waves with positive reflectivity[aa] and with spin projections $M = 0, 1, 2$. Finally, we considered twelve isobars that are known to decay to the $\pi^-\pi^+$ and $K^-\pi^+$ final state [91], six in the $\pi^-\pi^+$ subsystem and six in the $K^-\pi^+$ subsystem. They are listed in table 5.2.

[aa] Due to the high beam momentum, we assumed that production via Pomeron exchange dominates our data, which produces only positive-reflectivity waves (see section 5.1). Also, in a wave-set selection study including negative-reflectivity waves, none of the negative-reflectivity waves picked up significant intensity.

Table 5.2: Two-body isobars included in the systematic construction of the wave pool. The first row shows the quantum numbers. The second row gives the name of the isobar resonance. The third row gives the parametrization used in the PWD model.

J_ξ^{PC}	0^{++}			1^{--}	2^{++}	3^{--}
$\pi^-\pi^+$ isobars	$[\pi\pi]_S^{\text{AMPK}}$	$f_0(980)$	$f_0(1500)$	$\rho(770)$	$f_2(1270)$	$\rho_3(1690)$
Amplitude	section 5.1.4	(5.43)	(5.39)	(5.39)	(5.39)	(5.39)

J_ξ^{P}	0^{+}		1^{-}		2^{+}	3^{-}
$K^-\pi^+$ isobars	$[K\pi]_S^{K\pi}$	$[K\pi]_S^{K\eta}$	$K^*(892)$	$K^*(1680)$	$K_2^*(1430)$	$K_3^*(1780)$
Amplitude	(5.50)	(5.51)	(5.39)	(5.39)	(5.39)	(5.39)

Within these weak limitations, we included all combinations of quantum numbers and isobars that are allows by the conservation laws of strong interaction. This resulted in a large wave pool of 596 partial waves plus the incoherent flat wave to be fitted to the data. The pool of considered partial waves is much larger than the wave set constructed by hand in the ACCMOR analysis [23], which consisted of only 21 waves with $J \leq 2$ and $L \leq 2$. Compared to other analyses that applied wave-set selection techniques, the challenge in the analysis presented here is to determine the wave set from a large wave pool with only a limited amount of data. The wave pool in ref. [107] consisted of only 40 waves. In the COMPASS $\pi^-\pi^-\pi^+$ analysis we used a wave-pool of similar size, but the $\pi^-\pi^-\pi^+$ sample is about 100 times larger than the $K^-\pi^-\pi^+$ sample analyzed in this work.[ab]

Assuming that the $K^-\pi^-\pi^+$ sample is dominated by high-energy diffractive scattering, which is a coherent process,[ac] we used a rank=1 model for the wave-selection fit, i.e. we use a PWD model with a rank=1 spin-density matrix as discussed in section 5.1.2. The number of 1194 free parameters[ad] of the PWD model is small enough to be determined by the limited amount of data and also technically manageable.[ae]

[ab] In addition to the minimization of bias from the wave pool, another argument for constructing a larger wave pool is that we require the PWD model to be flexible enough to describe also background contributions to the $K^-\pi^-\pi^+$ sample as discussed in section 5.3. This is a challenge especially in this work, where the expected background from other processes of about 10 % is large compared to, e.g., the COMPASS $\pi^-\pi^-\pi^+$ analysis.

[ac] As discussed in section 5.1, spin flip of the target proton is suppressed at COMPASS energies.

[ad] The real and imaginary parts of the transition amplitudes of the 596 waves, with one of them being real-valued to account for the unknown global phase, plus a real-valued amplitude for the flat wave, plus two data-set fraction parameters, i.e. $2 \cdot 596 - 1 + 1 + 2 = 1194$

[ae] A rank=3 model would have nearly three times the number of parameters as the rank=1 model.

5.2.2 Regularization of the Likelihood Function

Using the wave pool in a fit of equation (5.38) to the data would lead to massive overfitting, as the number of free parameters is larger than the number of events in some $(m_{K\pi\pi}, t')$ cells. In order to avoid this, we used regularization methods. There are different approaches to implement regularization. Here, we added for each coherent sector[af] z and each partial wave a in the wave pool a so-called <u>regularization term</u> $\ln \mathcal{L}_{\text{Reg}}$ to the log-likelihood that imposes a penalty on $|\mathcal{T}_a^z| \neq 0$, i.e.[ag]

$$\ln \mathcal{L}'_{\text{WSS}} = \ln \mathcal{L}_{\text{PWD}} + \sum_{z,a} \ln \mathcal{L}_{\text{Reg}} \left[|\mathcal{T}_a^z|; \{p_{\text{Reg}}\} \right]. \tag{5.52}$$

Here, $\ln \mathcal{L}_{\text{PWD}}$ is the log-likelihood function of the PWD as defined in equation (5.38), which contains the information from the data sample and $\{p_{\text{Reg}}\}$ represents the set of additional parameters of the regularization term, which must be tuned. A wave that does not significantly contribute to the data has no support from $\mathcal{L}_{\text{PWD}}$ and is therefore driven by the regularization term, which is designed to suppress this wave such that $|\mathcal{T}_a^z| \to 0$.

Different forms for the regularization term are possible. We used the <u>Cauchy regularization</u>:

$$\ln \mathcal{L}_{\text{Reg}} \left[|\mathcal{T}_a^z|; \Gamma_a^z \right] = -\ln \left[1 + \frac{|\mathcal{T}_a^z|^2}{(\Gamma_a^z)^2} \right], \tag{5.53}$$

which had been already applied successfully in the COMPASS analysis of the reaction $\pi^- + p \to \pi^-\pi^-\pi^-\pi^+\pi^+ + p$ [67]. Its free parameter Γ_a^z sets the scale for the magnitude of the transition amplitude and thereby the strength of the regularization. Figure 5.7a shows the shape of the Cauchy regularization term in the complex plane of a transition amplitude. The term has a maximum at $|\mathcal{T}_a^z| = 0$, as required to suppress insignificant waves.

We also performed tests using a LASSO regularization[ah], a ridge regression,[ai] or a combination of both. None gave satisfactory results. Either the intensities even of large and significant waves were heavily suppressed or the intensities of insignificant waves were not suppressed enough to perform a selection. We obtained similar results in the wave-set selection performed in the COMPASS $\pi^-\pi^-\pi^+$ analysis [43]. We concluded, that LASSO regularization or ridge regression cannot handle well the large dynamic range of the partial-wave intensities of up to five orders of magnitude. However, in the Cauchy regularization the logarithm brings the intensities to a common scale on, which the regularization was performed. Furthermore, to study the systematic effects of the wave set on the results of the PWD we constructed another wave set using principles of information field theory as discussed in section 5.7.2.

[af] We used a rank=1 model with only one coherent sector for the 596 partial waves of the wave pool plus one sector containing the incoherent flat wave.

[ag] Here, we drop the $m_{K\pi\pi}$ and t' dependence for simplicity.

[ah] LASSO regularization uses the following regularization term [109]: $\ln \mathcal{L}_{\text{Reg}} \left[|\mathcal{T}_a^z|; \lambda \right] = -\lambda |\mathcal{T}_a^z|$.

[ai] Ridge regression uses the following regularization term [110]: $\ln \mathcal{L}_{\text{Reg}} \left[|\mathcal{T}_a^z|; \lambda \right] = -\lambda |\mathcal{T}_a^z|^2$.

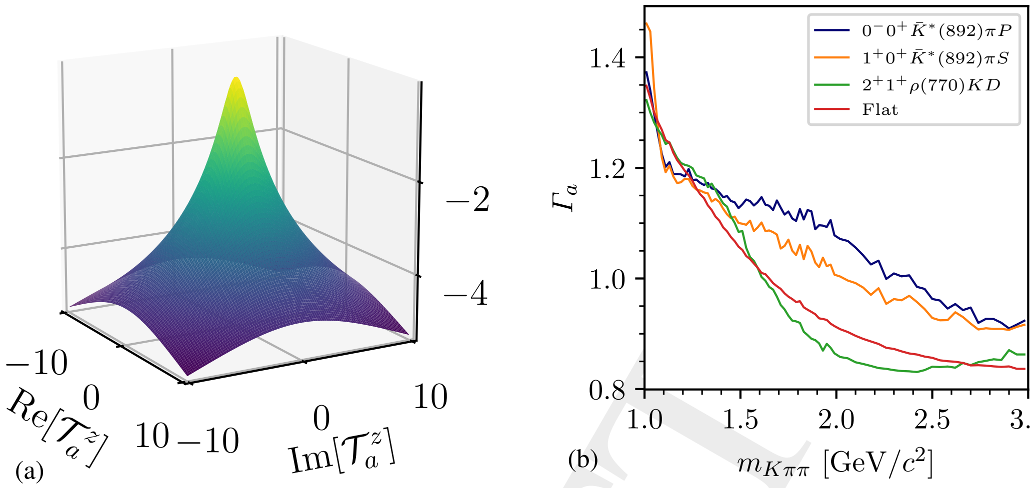

Figure 5.7: Properties of the Cauchy regularization term. (a) shows $\ln \mathcal{L}_{\mathrm{Reg}}$ in the complex plane of a transition amplitude $\mathcal{T}_a^z$. (b) shows the dependence of Γ_a on $m_{K\pi\pi}$ defined in equation (5.56) for four selected partial waves in the lowest t' bin.

Whether a wave is significant and hence should be included in the wave set depends on whether its intensity is large enough to be resolved with the given precision of our data. However, the partial-wave intensities corresponds to the produced number of events if the data would contain only the given wave, while the precision of the data depends on the total number of measured events. Therefore, the partial-wave intensity cannot be compared directly to the precision of the data, but acceptance effects have to be taken into account. As the acceptance is different for different partial waves,[aj] this requires a different scale parameter Γ_a^z in the Cauchy regularization term for each of the waves in the wave pool, which needs to be tuned. The same scale parameter can be used if the same wave appears in different coherent sectors z, i.e. $\Gamma_a^z = \Gamma_a$. In order to reduce this task to one common scale parameter for all waves, we applied the regularization penalty to the number,[ak]

$$\widehat{\overline{N}}{}_a^z = |\mathcal{T}_a^z|^2 \, \bar{I}_{aa}, \tag{5.54}$$

of measured events predicted for wave a by the model, i.e. the expected number of measured events if the data would contain only wave a. As $\overline{N}_a^z$ incorporates the acceptance effects it allowed us to use a common scale parameter Γ in the regularization, i.e.

$$\ln \mathcal{L}_{\mathrm{Reg}}\left[|\mathcal{T}_a^z|; \Gamma\right] = -\ln\left[1 + \frac{\widehat{\overline{N}}{}_a^z}{\Gamma^2}\right]. \tag{5.55}$$

[aj] As the acceptance is strongly modulated in the phase-space variables (see section 5.6), the average acceptance of a partial wave depends on the phase-space distribution of the given wave.

[ak] Here, the diagonal element of the acceptance-integral matrix $\bar{I}_{aa}^{2008}(m_{K\pi\pi}, t')$ enters, which is the average acceptance of wave a [see equation (5.29)]. As the experimental acceptance of the three different data sets considered in this analysis are very similar, we used for simplicity only the acceptance-integral matrix of the 2008 data set in the regularization term.

We implemented this in equation (5.53) by using a different parameter Γ_a for each wave in each $(m_{K\pi\pi}, t')$ cell[al] given by

$$\Gamma_a(m_{K\pi\pi}, t') \equiv \frac{\Gamma}{\sqrt{\bar{I}_{aa}(m_{K\pi\pi}, t')}}. \tag{5.56}$$

This is shown for four exemplary selected waves in figure 5.7b. The overall drop of Γ_a for all partial waves is caused by the rise of the acceptance towards higher masses (see figure C.4b). Also, the different acceptances of the waves due to their different kinematic distributions of the final-state particles is taken into account here. This means that a wave with larger intensity can be less significant than a wave with smaller intensity if the former has a lower acceptance and thereby effectively contributes less to the measured data.

In this analysis, we chose $\Gamma = 0.36$. This value was tuned such that the effect from the Cauchy regularization is as weak as possible in order to not strongly bias the results of significant waves with large intensities, while still being strong enough to suppress insignificant waves, which is necessary to perform the wave-set selection. Using equation (5.56), the choice of Γ becomes independent of the acceptance of the analyzed channel. A similar value for Γ was found in the COMPASS $\pi^-\pi^-\pi^+$ analysis, where a different final state with a completely different acceptance was studied [43].

5.2.3 Imposing Continuity of the Wave Set in $m_{K\pi\pi}$

As the wave sets for each $(m_{K\pi\pi}, t')$ cell were inferred from data, they exhibit statistical fluctuations. For example, almost every of the considered 596 waves appeared in at least one $(m_{K\pi\pi}, t')$ cell when we fitted equation (5.52) to the data. To suppress these fluctuations, we imposed continuity of the wave sets in $m_{K\pi\pi}$. This was done by fitting multiple neighboring $m_{K\pi\pi}$ bins simultaneously in one fit and by adding another penalty term for each wave that favors the corresponding transition amplitudes to be continuous in $m_{K\pi\pi}$. We do not impose a continuity condition in t'.

As a measure of discontinuity, we used the sum of the squared deviations of the transition amplitudes of one $m_{K\pi\pi}$ bin to the neighboring bin at $m_{K\pi\pi} + \Delta m_{K\pi\pi}$ in a limited $m_{K\pi\pi}$ range $(m_{K\pi\pi}^{\text{Start}}, m_{K\pi\pi}^{\text{End}})$:[am]

$$\ln \mathcal{L}_{\text{Cont}}\left[\mathcal{T}_a^z(m_{K\pi\pi}^{\text{Start}}, t'), \ldots, \mathcal{T}_a^z(m_{K\pi\pi}^{\text{End}}, t'); \lambda\right] = -\sum_{m_{K\pi\pi}=m_{K\pi\pi}^{\text{Start}}}^{m_{K\pi\pi}^{\text{End}}-\Delta m_{K\pi\pi}} \lambda \left|\mathcal{T}_a^z(m_{K\pi\pi}, t') - \mathcal{T}_a^z(m_{K\pi\pi} + \Delta m_{K\pi\pi}, t')\right|^2. \tag{5.57}$$

[al] The acceptance and thereby $\bar{I}_{aa}(m_{K\pi\pi}, t')$ depends on $m_{K\pi\pi}$ and t'.

[am] We used $\lambda = 0.8$, which was tuned in a similar way as the Γ parameter of the Cauchy regularization (see section 5.2.2).

The total log-likelihood function of the wave-set selection fit across multiple $m_{K\pi\pi}$ bins reads

$$\ln \mathcal{L}_{\mathrm{WSS}} = \sum_{m_{K\pi\pi}=m_{K\pi\pi}^{\mathrm{Start}}}^{m_{K\pi\pi}^{\mathrm{End}}} \ln \mathcal{L}'_{\mathrm{WSS}}(m_{K\pi\pi};t') + \sum_{z,a} \ln \mathcal{L}_{\mathrm{Cont}} \left[\mathcal{T}_a^z(m_{K\pi\pi}^{\mathrm{Start}}, t'), \ldots, \mathcal{T}_a^z(m_{K\pi\pi}^{\mathrm{End}}, t'); \lambda\right]. \quad (5.58)$$

Maximizing $\ln \mathcal{L}_{\mathrm{WSS}}$, large fluctuations among neighboring bins are suppressed.

Since different $m_{K\pi\pi}$ regions are dominated by different resonances, the wave set is necessarily a function of $m_{K\pi\pi}$. Therefore, we included only a limited range of 15 consecutive $m_{K\pi\pi}$ bins that are fitted simultaneously in the wave-set selection fit. Still, the wave-set selection was carried out for each $(m_{K\pi\pi}, t')$ cell individually using seven $m_{K\pi\pi}$ bins above and seven $m_{K\pi\pi}$ bins below the $(m_{K\pi\pi}, t')$ cell for which the wave-set selection was performed.[an], [ao]

5.2.4 Sub-Threshold Decays of Isobar Resonances

The invariant mass of a two-body subsystem at a given three-body mass $m_{K\pi\pi}$ is kinematically limited to be below $m_{K\pi\pi} - m_b$, where m_b is the mass of the bachelor particle. If this limit is smaller than the nominal mass $m_{\xi,0}$ of an isobar resonance in the corresponding two-body subsystem we can only observe the low-mass tail of the resonance. Waves in $m_{K\pi\pi}$ regions, where $m_{K\pi\pi} - m_b$ is much smaller than $m_{\xi,0}$, the so-called sub-threshold waves, are not expected to contribute significantly to the data, because the low-mass tail of the isobar resonances results in a small decay amplitude of the corresponding wave. In addition, the low-mass tail of the isobar amplitude of a sub-threshold wave has no clear signature, which would allow to unambiguously distinguish this wave from other waves with the same quantum numbers but with a different isobar resonance. For example, the phase of the isobar amplitude is approximately constant. This lack of a clear signature of sub-threshold waves leads to ambiguities that are known, e.g. from the COMPASS $\pi^-\pi^-\pi^+$ analysis [43], to cause artifacts in the PWD.

Therefore, we fixed the amplitude of partial waves with heavy isobars[ap] to be zero below a certain threshold $m_{K\pi\pi}^{\xi,\mathrm{thr}}$ in the wave-set selection fits. We chose this threshold such that above $m_{K\pi\pi}^{\xi,\mathrm{thr}}$, we are able to observe a significant part of the phase motion of the amplitude of the isobar. Therefore, the threshold is defined by the two-body mass, where the phase motion of the amplitude of the isobar is $1/8$ of the total phase motion.

[an] At the borders of the $m_{K\pi\pi}$ spectrum, we still included 15 $m_{K\pi\pi}$ bins, but the $m_{K\pi\pi}$ cell for which the wave-set selection fit was performed was no longer in the center of this range.

[ao] To avoid effects due to the change in the chosen $m_{K\pi\pi}$ binning, we used for all 15 bins the same bin width in $m_{K\pi\pi}$ as in the $(m_{K\pi\pi}, t')$ cell, for which the wave-selection fit was performed. For example, for $(m_{K\pi\pi}, t')$ cells around $m_{K\pi\pi} = 2\,\mathrm{GeV}/c^2$, where the bin width changes from $20\,\mathrm{MeV}/c^2$ to $40\,\mathrm{MeV}/c^2$, we used in the wave-set selection fits for wave sets at $m_{K\pi\pi} < 2\,\mathrm{GeV}/c^2$ bins of $20\,\mathrm{MeV}/c^2$ width, also for those of the 15 bins with $m_{K\pi\pi} > 2\,\mathrm{GeV}/c^2$; and vice versa for wave sets at $m_{K\pi\pi} > 2\,\mathrm{GeV}/c^2$.

[ap] We applied these thresholds to waves with $K^*(1680)$, $K_3^*(1780)$, $f_0(980)$, $f_0(1500)$, and $f_2(1270)$ isobars.

This translates into an $m_{K\pi\pi}$ threshold of[aq]

$$m_{K\pi\pi}^{\xi,\text{thr}} = m_b + m_{\xi,0} - 1.5\,\Gamma_{\xi,0}, \tag{5.59}$$

below which the respective partial wave amplitude was fixed to be zero in the wave-set selection fit. Here, $\Gamma_{\xi,0}$ is the nominal width of the isobar.

This approach has two effects. First, for $(m_{K\pi\pi}, t')$ cells below $m_{K\pi\pi}^{\xi,\text{thr}}$ a wave with isobar resonance ξ was not included in the selected wave sets. Second, as we fitted 15 consecutive cells in $m_{K\pi\pi}$ to impose continuity (see section 5.2.3), the wave-set selection fits for $(m_{K\pi\pi}, t')$ cells just above $m_{K\pi\pi}^{\xi,\text{thr}}$ also included $(m_{K\pi\pi}, t')$ cells below $m_{K\pi\pi}^{\xi,\text{thr}}$. For those cells below $m_{K\pi\pi}^{\xi,\text{th.}}$, we also fixed the amplitude of the sub-threshold waves to zero. Due to the zero amplitude of sub-threshold waves in $(m_{K\pi\pi}, t')$ cells below $m_{K\pi\pi}^{\xi,\text{th.}}$, the continuity criterion in equation (5.57) leads to an additional regularization of the corresponding waves in $(m_{K\pi\pi}, t')$ cells above $m_{K\pi\pi}^{\xi,\text{thr}}$. Consequently, $m_{K\pi\pi}^{\xi,\text{thr}}$ is not a hard threshold, but a constraint that smoothly becomes weaker for higher $m_{K\pi\pi}$, similar to how we expect such a wave to contribute to the data.

5.2.5 Results of the Wave-Set Selection Fit

Following the procedure described in sections 5.2.1 to 5.2.4, we fitted the likelihood in equation (5.58) to the data to obtain a wave set for each $(m_{K\pi\pi}, t')$ cell. We performed 700 attempts with random start paramter values for each cell in order to account for possible multimodality of $\ln \mathcal{L}_\text{WSS}$. From these 700 fit attempts, the best fit result, i.e. the result with the largest log-likelihood value, is used to determine the wave set. As shown in figure 5.8a, for many $(m_{K\pi\pi}, t')$ cells, the best result was found multiple times, but there are some cells where the best result was found only once. These bins suffer from multimodality of $\ln \mathcal{L}_\text{WSS}$, which seems to be more pronounced in the high-$m_{K\pi\pi}$ region. As an example, figure 5.8b show the likelihood distribution of a $(m_{K\pi\pi}, t')$ cell where the best solution was found only once. This distribution exhibits a 500 units wide continuous peak[ar] from which we conclude, that $\ln \mathcal{L}_\text{WSS}$ has a very large number of local minima, which, however, yield similar description of the data. Similar results were observed in other applications of the Cauchy regularization [43, 67]. A possible explanation for this multimodality is the non-convex shape of the Cauchy regularization in equation (5.53), which is known to induce multimodality [43, 111, 112].

In order to decide which waves enter the wave set, we ordered the waves by intensity in each $(m_{K\pi\pi}, t')$ cell as shown in figure 5.9. Figure 5.9b shows the typical behavior in an $(m_{K\pi\pi}, t')$ cell in the high-mass region. The intensities obtained from the best result (orange points) fall

[aq] Here, we used a relativistic Breit-Wigner amplitude and the nominal isobar mass and width from ref. [91] to determine this threshold.

[ar] The first bin of the histogram shown in figure 5.8b has more than 300 entries and not 1 entry as it would be expected for the likelihood distribution of a $(m_{K\pi\pi}, t')$ cell where the best solution was found only once. The reason is that in order to show the spread in $\ln \mathcal{L}$, the bin width of this histogram was chosen much wider than the 0.1 units in $\ln \mathcal{L}_\text{WSS}$ different, which define two solutions to be the same. Therefore, the fist bin contains multiple different solutions.

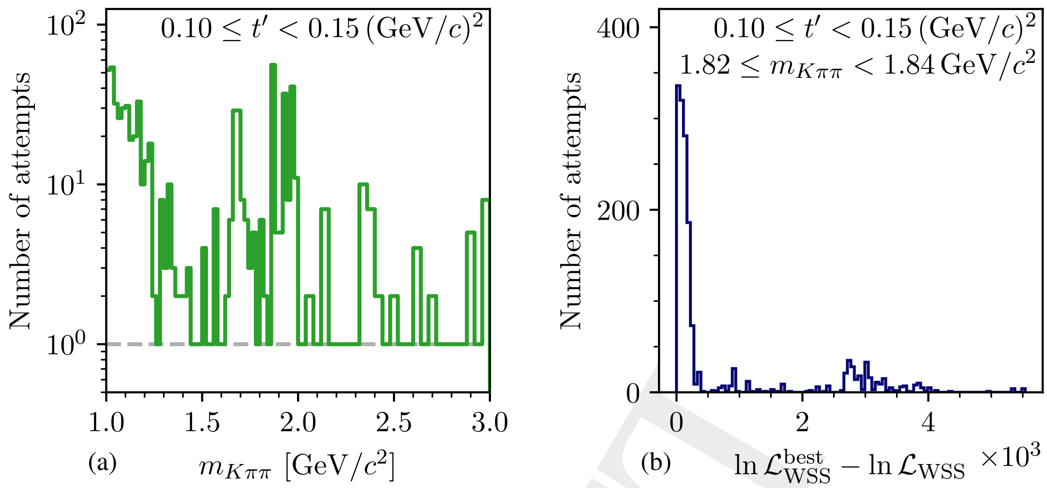

Figure 5.8: Stability of the wave-set selection fits. (a) shows the number of fit results that yielded the best solution, i.e. an $\ln \mathcal{L}_{\mathrm{WSS}}$ value at most 0.1 units smaller than the overall largest $\ln \mathcal{L}_{\mathrm{WSS}}$ value found in all 700 fit attempts, as a function of $m_{K\pi\pi}$ in the lowest t' bin. (b) shows the distribution of the $\ln \mathcal{L}_{\mathrm{WSS}}$ values obtained by minimizing equation (5.58) relative to the overall largest $\ln \mathcal{L}_{\mathrm{WSS}}$ value of the best fit result from the wave-set selection fit in one $(m_{K\pi\pi}, t')$ cell.

continuously until they reach a value of $|\mathcal{T}_a^z|^2 \approx 5$, where the intensity distribution has a jump discontinuity. The jump is followed by a long tail of about 550 waves nearly all of them with $|\mathcal{T}_a^z|^2 << 1$. The waves in this tail do not significantly contribute to the data. Therefore, we selected all waves with an intensity above a threshold given by the jump (black horizontal line in figure 5.9). The sub-optimal solutions with lower $\ln \mathcal{L}_{\mathrm{WSS}}$ are shown by the other colored points. They exhibit a significant spread around the best solution, especially for the deselected waves. The reason for this is, that insignificant waves are not pulled to exactly zero intensity by the Cauchy regularization.[as] This leaves some freedom to the fit to distribute intensity among the waves in the deselected tail without having a large influence on $\ln \mathcal{L}_{\mathrm{WSS}}$. As these fluctuations mainly affects the deselected waves that have an intensity well below the threshold, it does not strongly influence the selection of the wave set.

Figure 5.9a shows the typical behavior in the low-mass region. Also here, we observe a clear jump at a similar intensity of $|\mathcal{T}_a^z|^2 \approx 5$. In addition, we observe small jumps at higher intensities, i.e. in the region of the selected waves. They seem to be driven by correlations among neighboring $m_{K\pi\pi}$ bins, because if we did not use equation (5.57), those small jumps were much less pronounced.

Overall, the jumps always appear at a similar intensity of the order of 1, which means that a wave has to contribute with a common minimum intensity to the data in order to be resolved. Still, we determined the thresholds individually for each $(m_{K\pi\pi}, t')$ cell using the method discussed in appendix D.1.1. All waves that in the wave-set selection fit have an intensity above the respective

[as] This is because the gradient of $\ln \mathcal{L}_{\mathrm{Reg}}$ is zero at $|\mathcal{T}_a^z| = 0$. Other regularization approaches, e.g. LASSO, do not have this drawback, but require special minimization techniques.

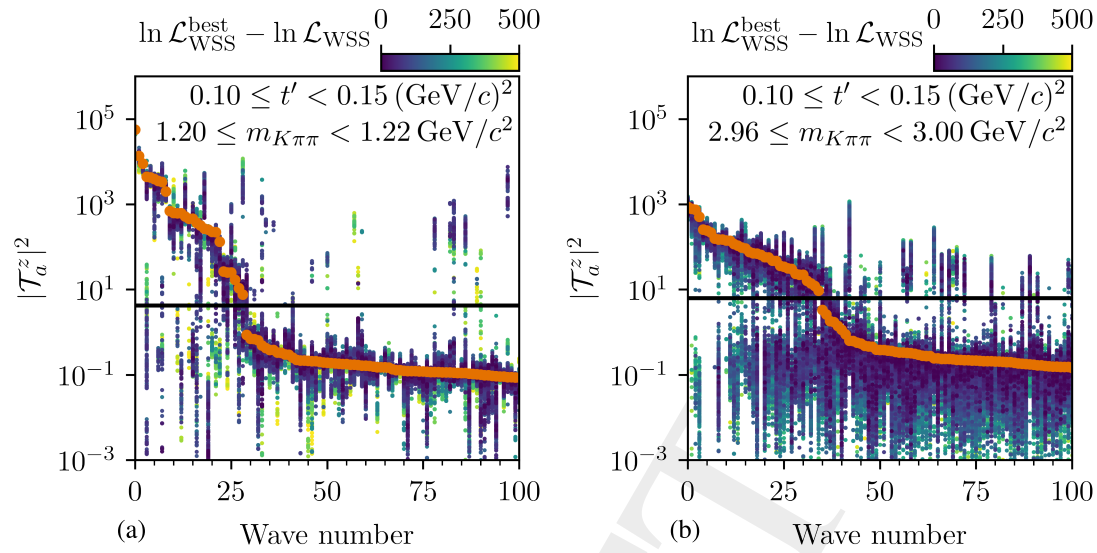

Figure 5.9: Partial waves ordered by their intensity in two neighboring $m_{K\pi\pi}$ bins in the lowest t' bin. The waves are ordered by intensity as obtained from the best result in each cell and numbered accordingly. The orange points show the best result out of 700 fit attempts. The other colored points show the results from the other fit attempts. Their color represents $\ln \mathcal{L}_{\mathrm{WSS}}^{\mathrm{best}} - \ln \mathcal{L}_{\mathrm{WSS}}$. Only results where this difference is smaller than 500 units are plotted. Only the 100 waves with the largest intensity are shown. The black horizontal line marks the threshold, above which waves were selected for the wave set.

threshold entered the wave set of the given $(m_{K\pi\pi}, t')$ cell. The incoherent flat wave was always included in the selected wave set, independent of the result of the wave-set selection.

5.2.6 The Selected Wave-Set

As discussed above, we determined the wave set individually for each $(m_{K\pi\pi}, t')$ cell. Hence, a wave might be deselected in individual cells, while it is selected in the neighboring cells. This is observed, e.g., in the tails of $K^-\pi^-\pi^+$ resonances where the intensity becomes small and fluctuates around the threshold above which the wave is selected. However, this leads to a bias towards larger intensities when studying such waves in the resonance-model fit discussed in chapter 6. This is because statistical fluctuations towards smaller intensities favor the wave to be deselected and thus are not considered in the χ^2 statistics used in the RMF, while fluctuations towards larger intensities favor the wave to be selected and thus are considered in the RMF. To circumvent this effect, we manually included waves that show interesting signals into the wave sets of all $(m_{K\pi\pi}, t')$ cells considered by the resonance-model fit, independent of the result of the wave-set selection fit. The list of those waves is given in table D.1 in the appendix. As this procedure adds only a few waves in a few $(m_{K\pi\pi}, t')$ cells, it only weakly affects other waves in the PWD. We verified this by comparing the results of two PWD fits. One using the wave set directly obtained from the wave-set selection fits and one using the modified wave set.

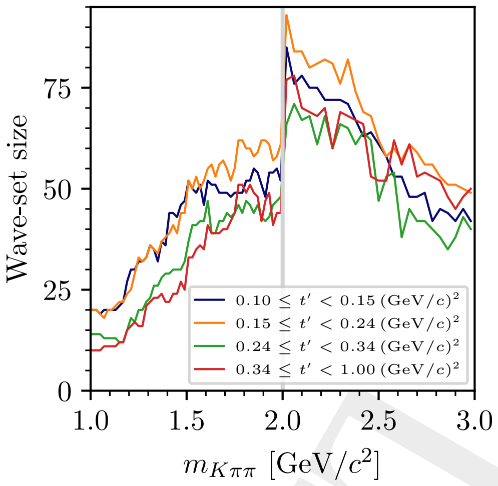

Figure 5.10: Number of waves in the selected wave sets of the individual $(m_{K\pi\pi}, t')$ cells as a function of $m_{K\pi\pi}$. The different line colors represent the four t' bins. The gray line indicates the $m_{K\pi\pi}$ value where we changed from $20\,\text{MeV}/c^2$ to $40\,\text{MeV}/c^2$ wide bins in $m_{K\pi\pi}$.

The size of the selected wave sets exhibits a pronounced $m_{K\pi\pi}$ dependence as shown in figure 5.10. The wave-set size ranges from about 15 waves in the lowest $m_{K\pi\pi}$ bins that contain only a few events up to about 80 waves in the $2\,\text{GeV}/c^2$ region. The wave-set size rises with increasing $m_{K\pi\pi}$ up to about $2\,\text{GeV}/c^2$ because at higher masses more decay channels and higher spins contribute. As expected, doubling the $m_{K\pi\pi}$ bin width at $2\,\text{GeV}/c^2$ leads to a jump of the wave-set size, because more waves can be resolved due to the larges number of events. No significant discontinuity at $2\,\text{GeV}/c^2$ is observed in the results for the transition amplitudes (see section 5.5). Above about $2\,\text{GeV}/c^2$, the wave-set size decreases again, because the number of events becomes smaller. Similarly, the selected wave set is smaller in the two highest t' bins (green and red lines in figure 5.10), which have about half the number of events compared to the two lowest t' bins (blue and orange lines in figure 5.10).

Overall, 238 partial waves[at] were selected in at least one $(m_{K\pi\pi}, t')$ cell. Most of them were selected over wide continuous $m_{K\pi\pi}$ ranges such as the $0^- 0^+ [K\pi]^{K\pi}_S \pi S$ wave shown in figure 5.11. This proves that the continuity condition in equation (5.57) works. About 90 of 238 waves appear only in a few individual $(m_{K\pi\pi}, t')$ cells such as the $0^- 0^+ \rho_3(1690)\, K\, F$ wave shown in figure 5.11. This represents the statistical uncertainty of the wave set.[au] The complete list of selected partial waves can be found in appendix D.1.3 in figures D.3 to D.34. As expected from the observed structures in the $m_{K^-\pi^+}$ and $m_{\pi^-\pi^+}$ distribution shown in figures 4.7a and 4.7b, respectively, a large fraction of the selected partial waves represent decays to ground-state isobar resonances like the $K^*(892)$, $K_2^*(1430)$, $\rho(770)$, or the $f_2(1270)$. Furthermore, the selected partial

[at] This does not include the incoherent flat wave.

[au] We studied the influence of these about 90 noisy waves on the other waves, by performing a PWD using a wave set without these noisy waves. The results are consistent with those from the PWD using the complete 238-wave set.

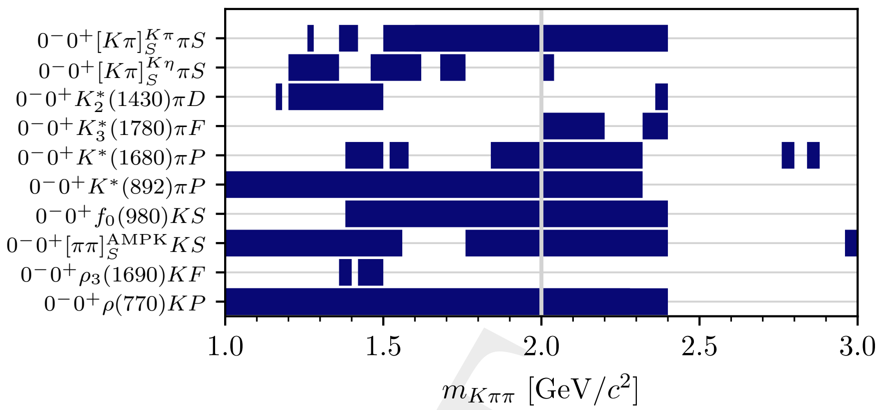

Figure 5.11: Mass ranges of selected waves with $J^P = 0^-$ in the lowest t' bin. The gray vertical line indicates the mass where the $m_{K\pi\pi}$ binning changes from 20 MeV/c^2 to 40 MeV/c^2 wide bins.

waves are dominated by waves with $J \lesssim 5$, which is consistent with previous observations as there is no known or expected strange-meson resonance with $J > 5$ (see figure 1.1). Therefore, we conclude that the wave-set selection yielded reasonable results. We substantiate this statement when studying the agreement between the PWD model and data in section 5.6.

Finally, the so-called 238-wave set that we inferred from data using the wave-set selection approach as discussed in this section was used in equation (5.16) as the model for the PWD of the measured $K^-\pi^-\pi^+$ data. In addition, it was also used for many pseudodata studies discussed in sections 5.8, 5.10, and 6.4.

5.3 Modeling Incoherent Background Processes

As discussed in section 5.1, the reaction $K^- + p \to K^-\pi^-\pi^+ + p$ is dominantly a coherent process. In the PWD, it can be modeled therefore by a rank=1 spin-density matrix in equation (5.18). However, also events from other processes passed the event selection discussed in section 4.1 and thereby entered the $K^-\pi^-\pi^+$ sample. For example, there is contamination of beam pions in the $K^-\pi^-\pi^+$ sample (see section 3.1.6). These beam pions may also undergo diffractive scattering reactions leading to a final state with three charged particles, i.e. the reaction $\pi^- + p \to \pi^-\pi^-\pi^+ + p$. We expect this $\pi^-\pi^-\pi^+$ background to be the largest background component in the $K^-\pi^-\pi^+$ sample as discussed in detail in section 5.10. Another source of background are reactions with three kaons in the final state, i.e. $K^- + p \to K^-K^-K^+ + p$. Such events entered the $K^-\pi^-\pi^+$ sample due to limitations of the final-state particle identification. We estimated the $K^-K^-K^+$ background to be about 4 % as discussed in section 4.2. All these background processes include different, i.e. distinguishable final-state particles. Therefore, these processes cannot be modeled as a sum of coherent amplitudes, but the corresponding amplitudes have to be summed incoherently.

In order to treat these incoherent background processes using the formalism developed in section 5.1, we formulated a spin-density matrix of the 238-wave set with rank > 1. This allows for incoherence in the PWD model and thereby takes into account the incoherent background components in an effective way. In section 5.3.1, we give a detailed motivation for this approximation. We know of at least three processes contributing to the $K^-\pi^-\pi^+$ sample: the signal reaction $K^- + p \to K^-\pi^-\pi^+ + p$, and the background reactions $\pi^- + p \to \pi^-\pi^-\pi^+ + p$ and $K^- + p \to K^-K^-K^+ + p$. Consequently, we formulated the PWD model in equation (5.19) using a rank=3 spin-density matrix. In order to study whether a PWD model using a rank=3 spin-density matrix is sufficient to take into account all incoherent background processes, we performed a study in which we used a much larger rank. i.e. a rank=6 spin-density matrix. This study yielded results consistent with those from the rank=3 PWD fits, which suggests that the additional freedom in the rank=6 PWD fits from the almost two times larger number of free parameters is not needed to describe the data. Thus, we conclude that the PWD model using a rank=3 spin-density matrix, which is called rank=3 model in the following, is sufficient to effectively take into account the incoherent background processes.

As discussed in section 5.2, the 238-wave set was constructed based on a rank = 1 model. Historically, we initially had used a rank=1 model not only for the wave-set selection fits, but also for the final PWD, analogously to the COMPASS $\pi^-\pi^-\pi^+$ analysis [39]. Unfortunately, it turned out that a later state of the analysis the incoherent background processes play a significant role, i.e. when describing the results of the PWD in terms of a resonance model as done in the RMF described in chapter 6. Hence, we had to take into account the incoherent background processes in the RMF by incoherently adding background components to the coherent resonance model for the process $K^- + p \to K^-\pi^-\pi^+ + p$. However, describing the results of the PWD that were based on the coherent rank=1 model by an incoherent resonance model would have been inconsistent. Thus, we had to treat the incoherent background processes also at the level of the PWD by using a rank=3 model. Performing the wave-set selection again would have been very time-consuming and computationally very expensive. Hence, we used the 238-wave set, which is based on a rank=1 model, for the PWD using the rank=3 model, because by switching to a rank=3 model we only added more freedom to the fit as the rank=1 model is a subset of the rank=3 model. Furthermore, we observe overall the same structures in the partial waves when comparing the results using the rank=3 and the rank=1 models. When introducing the higher rank, we observe the largest change in the incoherent flat wave. While the flat wave contributed about 2 % to the total intensity when using the rank=1 model, it became practically zero when using the rank=3 model. As the flat wave models background from events where the three final state particles are uncorrelated, the zero intensity of the flat wave indicates that there is a negligible fraction of such events in the $K^-\pi^-\pi^+$ sample. This underlines the selectivity of the event selection presented in section 4.1. The non-vanishing flat wave when using the rank=1 model accounted for part of the incoherent background processes, as it was the only incoherent model component in the rank=1 model. However, as final-state particles from incoherent background processes are correlated, the flat wave is only a rough approximation for these contributions only for data samples where these incoherent backgrounds are small, e.g. in the COMPASS $\pi^-\pi^-\pi^+$ analysis [39].

5.3.1 Effective Background Description using a Higher Rank

In order to include the incoherent background processes in the PWD model, one would need to write the total probability $P\left(\tau^{K\pi\pi}\right)$ to measure an event as a sum of probabilities of the $K^-\pi^-\pi^+$ and the background processes, bkg, i.e.[av]

$$P\left(\tau^{K\pi\pi}\right) = P^{K\pi\pi}\left(\tau^{K\pi\pi}\right) + \sum_{\text{bkg}} P^{\text{bkg}}\left(\tau^{\text{bkg}}\right) \cdot J\left(\text{bkg} \to K\pi\pi\right). \tag{5.60}$$

Here, the phase-space variables $\tau^{K\pi\pi}$ (see section 5.1.1) are used to formulate the total probability. Depending on which process $\mathfrak{p}$ we are assuming for the event, its probability to be measured is described by a different set of phase-space variables $\tau^{\mathfrak{p}}$. This introduces additional Jacobian terms J that arise due to the transformation from the set $\tau^{\mathfrak{p}}$ of variables to $\tau^{K\pi\pi}$. Modeling the individual probabilities analogously to equation (5.32), yields:[aw]

$$P\left(\tau^{K\pi\pi}\right) \propto \eta^{K\pi\pi}\left(\tau^{K\pi\pi}\right) \cdot \mathcal{I}^{K\pi\pi}_{K\pi\pi}\left(\tau^{K\pi\pi}\right) + \sum_{\text{bkg}} \eta^{\text{bkg}}\left(\tau^{\text{bkg}}\right) \cdot \mathcal{I}^{\text{bkg}}_{\text{bkg}}\left(\tau^{\text{bkg}}\right) \cdot J\left(\text{bkg} \to K\pi\pi\right). \tag{5.61}$$

Here, $\eta^{\mathfrak{p}}$ is the experimental acceptance of the event assuming that it is of process $\mathfrak{p}$, and $\mathcal{I}^{\mathfrak{p}}_{\mathfrak{q}}$ is the model intensity formulated according to equation (5.16) for events produced by process $\mathfrak{q}$ but modeled in terms of partial waves assuming the process $\mathfrak{p}$. For example, $\mathcal{I}^{K\pi\pi}_{K\pi\pi}$ is the intensity model for the $K^-\pi^-\pi^+$ component in the data formulated in terms of partial waves of the reaction $K^- + p \to K^-\pi^-\pi^+ + p$ as given in equation (5.10).

Including the incoherent background processes according to equation (5.61) is impossible mainly due to two reasons. First, this would require a model for $\mathcal{I}^{\text{bkg}}_{\text{bkg}}$ as input. However, for most background processes such as $K^- + p \to K^-K^-K^+ + p$, such a model is unknown.[ax] Second, the calculation of the difference acceptances $\eta^{\mathfrak{p}}(\tau^{\mathfrak{p}})$ of the various processes is not feasible here. As shown in section 5.1.3, for a single process, the acceptance of each event can be combined from all events to one summand, $\sum_k \eta^{K\pi\pi}(\tau_k^{K\pi\pi})$, in the $\ln \mathcal{L}_{\text{PWD}}$ in equation (5.38). This summand is independent of the fit parameters. Thus, this term can be dropped from the likelihood function, i.e. it can be ignored in the maximum-likelihood fits.[ay] However, for multiple processes we would have to use equation (5.61), where the acceptance is not a global coefficient, but the various processes contribute with different acceptances. Therefore, for multiple processes the acceptance of each event cannot be combined to one summand in $\ln \mathcal{L}_{\text{PWD}}$ and thus cannot be dropped. Hence, we would need to determine the acceptance individually for each measured event and for each considered process. In practice, it is not feasible to determine these acceptances in a reasonable amount of time.[az] This prevents us from using equation (5.61).

[av] For simplicity, we drop the dependencies on $m_{K\pi\pi}$ and t' here.
[aw] For simplicity, we omit the constant normalization factor.
[ax] The only exception is for the $\pi^-\pi^-\pi^+$ background, for which we determined such a model in the COMPASS $\pi^-\pi^-\pi^+$ analysis [39].
[ay] The acceptance is still correctly considered in the maximum-likelihood fits. It enters via the acceptance-integral matrix given in equation (5.29).
[az] As described in section 5.1, we implemented acceptance effects in the PWD in the acceptance-integral matrix

We circumvented these limitations and took into account the incoherent background processes by effectively modeling the background contributions and their acceptances in terms of an intensity model consisting of partial waves of the reaction $K^- + p \to K^-\pi^-\pi^+ + p$, i.e. we used

$$\mathcal{I}^{K\pi\pi}_{\text{bkg}}\left(\tau^{K\pi\pi}\right) \equiv \frac{\eta^{\text{bkg}}\left(\tau^{\text{bkg}}\right)}{\eta^{K\pi\pi}\left(\tau^{K\pi\pi}\right)} \mathcal{I}^{\text{bkg}}_{\text{bkg}}\left(\tau^{\text{bkg}}\right) \cdot J\left(\text{bkg} \to K\pi\pi\right). \tag{5.62}$$

With this, the total probability in equation (5.61) reads

$$P\left(\tau^{K\pi\pi}\right) \propto \eta^{K\pi\pi}\left(\tau^{K\pi\pi}\right) \cdot \mathcal{I}^{K\pi\pi}_{K\pi\pi}\left(\tau^{K\pi\pi}\right) + \sum_{\text{bkg}} \eta^{K\pi\pi}\left(\tau^{K\pi\pi}\right) \cdot \mathcal{I}^{K\pi\pi}_{\text{bkg}}\left(\tau^{K\pi\pi}\right). \tag{5.63}$$

Now, each model intensity is multiplied by the same acceptance $\eta^{K\pi\pi}$. Therefore, the acceptance can be factored out and dropped in the likelihood function, which resolves the issue of determining $\eta^{K\pi\pi}$ on an event-by-event basis.

Still, a model $\mathcal{I}^{K\pi\pi}_{\text{bkg}}$ for the background processes is needed. However, as all terms in equation (5.63) are functions of the same set $\tau^{K\pi\pi}$ of phase-space variables, $\mathcal{I}^{K\pi\pi}_{\text{bkg}}$ can be modeled in terms of partial waves of the reaction $K^- + p \to K^-\pi^-\pi^+ + p$, analogously to equation (5.16). This yields for the probability of an event:[ba]

$$P \propto \eta^{K\pi\pi} \left[\sum_{z_{K\pi\pi}} \left| \sum_{a \in \mathbb{W}_{z_{K\pi\pi}}} \mathcal{T}_a^{z_{K\pi\pi}} \Psi_a^{z_{K\pi\pi}} \right|^2 + \sum_{\text{bkg}} \sum_{z_{\text{bkg}}} \left| \sum_{a \in \mathbb{W}_{z_{\text{bkg}}}} \mathcal{T}_a^{z_{\text{bkg}}} \Psi_a^{z_{\text{bkg}}} \right|^2 \right]. \tag{5.64}$$

Grouping all incoherent sums over the coherent sectors z into a single sum and using the same wave set $\mathbb{W}$ with the same set $\{\Psi_a\}$ of decay amplitudes for all coherent sectors allows us to describe the $K^-\pi^-\pi^+$ signal and the background processes by a single condensed expression:

$$P \propto \eta^{K\pi\pi} \underbrace{\left[\sum_{\mathfrak{p}=\{z_{K\pi\pi},\, z_{\pi\pi\pi},\, z_{KKK},\, \dots\}} \left| \sum_{a \in \mathbb{W}} \mathcal{T}_a^{\mathfrak{p}} \Psi_a \right|^2 \right]}_{\equiv\, \mathcal{I}^{K\pi\pi}_{\text{tot}}}, \tag{5.65}$$

i.e. by a single total model intensity $\mathcal{I}^{K\pi\pi}_{\text{tot}}$. Finally, $\mathcal{I}^{K\pi\pi}_{\text{tot}}$ can be written in terms of a single spin-density matrix [see equation (5.18)]

$$\rho_{ab} = \sum_{\mathfrak{p}=\{z_{K\pi\pi},\, z_{\pi\pi\pi},\, z_{KKK},\, \dots\}} \mathcal{T}_a^{\mathfrak{p}} \left[\mathcal{T}_b^{\mathfrak{p}}\right]^*. \tag{5.66}$$

defined in equation (5.29). We calculated the elements of this matrix by a Monte Carlo integration based on one reconstructed pseudodata sample. Here, we would need to determine the acceptance individually for each measured event and for each considered process. This would require generating more and orders of magnitude larger pseudodata samples and is thus computationally extremely expensive.

[ba] For simplicity, we drop the dependence on $\tau^{K\pi\pi}$ here as it is the same for all functions.

The rank of this matrix and thereby the rank of the PWD model is given by the incoherent processes, i.e. by the sum over $\mathfrak{p}$. Equation (5.65) has the same form as equation (5.32) with coherent sectors now representing the $K^-\pi^-\pi^+$ signal and the various background processes. Therefore, when taking into account the incoherent background by using a rank > 1 PWD model, we can use the same PWD formalism described in section 5.1, e.g. the same decay amplitudes and the same likelihood function. Just the number of free parameters increases when using a model with a higher rank.

As explained in section 5.1, in the PWD fits the measurable quantities are the spin-density matrix elements. The transition amplitudes $\mathcal{T}_a^z$ in equation (5.18) are an effective parameterization of the spin-density matrix. In general, they are different from the transition amplitudes $\mathcal{T}_a^{\mathfrak{p}}$ of the various physics processes $\mathfrak{p}$ in equation (5.66) by an unknown unitary transformation. Thus, we cannot determine the transition amplitudes of the individual processes uniquely. Therefore, we cannot separate the $K^-\pi^-\pi^+$ signal from the background processes at the stage of the PWD. This is only possible at the level of the RMF as discussed in chapter 6.

In summary, using a PWD model with rank = 3 allows us to take into account incoherent background processes in an effective way, while still employing the formalism presented in section 5.1. This, however, requires the $K^-\pi^-\pi^+$ PWD model to be flexible enough to approximate the phase-space distribution of the background processes according to equation (5.62). We studied this approximation for the dominant $\pi^-\pi^-\pi^+$ background as discussed in section 5.10.2. Overall, the PWD model using the 238-wave set is able to approximate the $\pi^-\pi^-\pi^+$ background in the $K^-\pi^-\pi^+$ sample. Also in the resonance-model fit, we find consistent results for the background contributions in the $K^-\pi^-\pi^+$ sample as presented in section 6.2, which was the initial motivation to formulate a rank=3 PWD model.

5.4 Improving Estimates of Partial-Wave Decomposition Results

The physics quantities that we determine in the PWD fits are the real and imaginary parts of the spin-density matrix elements defined in equation (5.18). Our estimates for the values of these quantities, together with the corresponding statistical uncertainties and correlations, enter the RMFs as discussed in section 6.1.5. Hence, in addition to a precise and accurate estimation of the values of the spin-density matrix elements, we aim for an accurate estimate of their statistical uncertainties and correlations.[bb] The latter are represented by the entries of the covariance matrix of the spin-density matrix elements.

Performing a maximum-likelihood fit of equation (5.38) to the measured $K^-\pi^-\pi^+$ sample yields the optimal parameter values for the fit parameters, i.e. the real and imaginary parts of the transition amplitudes ${}^{\text{MLE}}\mathcal{T}_a^z$ and the data-set fraction parameters. These optimal values are called maximum-likelihood estimates. The covariance matrix of the fit parameters is estimated

[bb] Systematic uncertainties are discussed in section 5.7.

by evaluating the inverse of the Hessian matrix of the log-likelihood function at its maximum (see equation (40.12) in ref. [9]). The observables we are actually interested in are the spin-density matrix elements that are calculated from the transition amplitudes according to equation (5.18). The maximum-likelihood estimates of the spin-density matrix elements are calculated by inserting ${}^{\mathrm{MLE}}\mathcal{T}_a^z$ into equation (5.18). The corresponding covariance matrix is calculated using linear uncertainty propagation, i.e. by a linear approximation of equation (5.18), (see equation (40.42) in ref. [9]).

This maximum-likelihood approach was used in previous partial-wave analyses [39, 113, 114] to obtain the estimates of the values and covariance matrix of the spin-density matrix elements. However, this approach has limitations. First, the uncertainty estimation of the fit parameters assumes that the log-likelihood function is approximated well a multivariate Gaussian function in the fit parameters, which is true only for large data samples. For finite sample sizes as in this analysis, this approximation may lead to biased uncertainties as discussed in ref. [108]. Second, the linear uncertainty propagation is only an approximation when calculating the uncertainties of observables that depend in a non-linear way on the fit parameters. For example, the real and imaginary parts of the spin-density matrix elements depend on the products of real and imaginary parts of the transition amplitudes:

$$\Re\left(\rho_{ab}\right) = \sum_z \left[\Re\left(\mathcal{T}_a^z\right)\Re\left(\mathcal{T}_b^z\right) + \Im\left(\mathcal{T}_a^z\right)\Im\left(\mathcal{T}_b^z\right)\right] \tag{5.67}$$

$$\Im\left(\rho_{ab}\right) = \sum_z \left[\Im\left(\mathcal{T}_a^z\right)\Re\left(\mathcal{T}_b^z\right) - \Re\left(\mathcal{T}_a^z\right)\Im\left(\mathcal{T}_b^z\right)\right]. \tag{5.68}$$

The linear uncertainty propagation is a sufficient approximation only if the relative uncertainties on the transition amplitudes are small. To overcome these approximations, we applied the method of Bootstrapping [115] in order to obtain better estimates for the values and the covariance matrix of the observables, e.g. of spin-density matrix elements. This is discussed in the following section 5.4.1.

5.4.1 The Bootstrapping Method

In this section, we explain the Bootstrapping method on the example of spin-density matrix elements. The same method can be applied for any other observable, e.g. for the data-set ratio parameters. For the purpose of notation, we collect all real and imaginary parts of the spin-density matrix elements in one real-valued vector $\vec{\lambda}$. λ_i is the i^{th} entry of $\vec{\lambda}$ as defined in equation (6.20), i.e. the real or imaginary part of one spin-density matrix element. The maximum-likelihood estimates λ_i^{MLE} of the spin-density matrix elements depend on the data sample from which they were determined. The data sample is subject to statistical fluctuations. These fluctuations propagate to λ_i^{MLE}, which means that they are also statistically distributed quantities. The uncertainties of λ_i^{MLE} and the correlations between them are given by the covariance matrix $\mathrm{Cov}\left[\lambda_i^{\mathrm{MLE}}, \lambda_j^{\mathrm{MLE}}\right]$ of this distribution.

We approximated the underlying distribution of λ_i^{MLE} by a finite set $\{\lambda_i^{(h)}\}$ that is distributed accordingly. Obtaining such a set requires a set of data samples indexed by h, where each of these samples is distributed in the same way as the measured $K^-\pi^-\pi^+$ sample. Since we cannot remeasure the $K^-\pi^-\pi^+$ sample multiple times, we employed an approximation method that belongs to the class of so-called resampling methods [115, 116], to construct random data samples from the measured $K^-\pi^-\pi^+$ sample. The size of these data samples must be the identical to the size of the measured $K^-\pi^-\pi^+$ sample, because the precision of the data determines the number of waves that can be resolved in the partial-wave decomposition (see section 5.2). Applying the 238-wave set, which was optimized for the measured $K^-\pi^-\pi^+$ sample, to a smaller data sample may lead to overfitting and thereby bias the distribution of λ_i^{MLE}. This constrains the choice of applicable resampling methods.

Due to the limitations discussed above, we used the Bootstrapping method [115]. Based on this method we generated N_{BS} Bootstrapping samples indexed by h by randomly drawing $\overline{N}_{\text{ev}}$ events from the $\overline{N}_{\text{ev}}$ measured events of the $K^-\pi^-\pi^+$ sample. This means that in a Bootstrapping sample h some of the measured events are used more than once.[bc] The distribution of the Bootstrapping samples approximates the underlying distribution of the $K^-\pi^-\pi^+$ sample.[bd] Thus, they allow us to approximate the distribution of any observable obtained from the $K^-\pi^-\pi^+$ sample. For example, to study the distribution of the spin-density matrix elements, we determined their maximum-likelihood estimates $\lambda_i^{(h)}$ for each Bootstrapping sample h. To this end, we first performed a maximum-likelihood fit of equation (5.38) to each Bootstrapping sample, which yielded the maximum-likelihood estimates of the transition amplitudes. Then, we calculated for each Bootstrapping sample the spin-density matrix elements $\lambda_i^{(h)}$ from the maximum-likelihood estimates of the transition amplitudes.

This procedure yielded for each spin-density matrix element i a set $\{\lambda_i^{(h)}\}$ of N_{BS} estimates, one from each Bootstrapping sample h. These sets approximate the underlying physical distribution of the spin-density matrix elements. Thus, they allow us to estimate the covariance matrix of the spin-density matrix elements

$$\text{Cov}\left[\lambda_i^{\text{MLE}}, \lambda_j^{\text{MLE}}\right] = \frac{1}{N_{\text{BS}} - 1} \sum_{h=1}^{N_{\text{BS}}} \left(\lambda_i^{(h)} - \langle\lambda_i\rangle\right)\left(\lambda_j^{(h)} - \langle\lambda_j\rangle\right). \tag{5.69}$$

The mean value of the spin-density matrix elements, called Bootstrapping mean value, reads

$$\langle\lambda_i\rangle = \frac{1}{N_{\text{BS}}} \sum_{h=1}^{N_{\text{BS}}} \lambda_i^{(h)}. \tag{5.70}$$

[bc] When adding an event to the Bootstrapping sample, we randomly selected it from the full sample of measured events.

[bd] Formally, we approximated the underlying distribution of the $K^-\pi^-\pi^+$ sample by the empirical distribution that is based on the measured $K^-\pi^-\pi^+$ sample [see equation (1.6) in ref. [117]]. Then we drew a set of samples from this empirical distribution, which are the Bootstrapping samples.

It is also used to approximate the bias on λ_i^{MLE} [117]:

$$\mathrm{bias}\left[\lambda_i^{\mathrm{MLE}}\right] \approx \langle \lambda_i \rangle - \lambda_i^{\mathrm{MLE}}. \tag{5.71}$$

For each $(m_{K\pi\pi}, t')$ cell we generated $N_{\mathrm{BS}} = 2000$ Bootstrapping samples. For each Bootstrapping sample indexed by h in each $(m_{K\pi\pi}, t')$ cell we performed 50 maximum-likelihood fit attempts of equation (5.38) with randomly chosen start-parameter values. The fit with the largest likelihood value determined the maximum-likelihood estimate $\lambda_i^{(h)}$ for Bootstrapping sample h. In total, we performed 30×10^6 single PWD fits to obtain the Bootstrapping results discussed in the following section 5.4.2.

5.4.2 Comparison of Bootstrapping and Maximum-Likelihood Estimates

First, we compare the Bootstrapping and maximum-likelihood estimates of the intensities, i.e. the diagonal spin-density matrix elements. From each of the $N_{\mathrm{BS}} = 2000$ Bootstrapping samples for each $(m_{K\pi\pi}, t')$ cell we obtained an estimate for the partial-wave intensities. As an example, the distributions of the Bootstrapping estimates of the intensity of the $1^+\,0^+\,\rho(770)\,K\,S$ wave are shown by the histograms in figures 5.12a and 5.12b for two neighboring $m_{K\pi\pi}$ bins. Both distributions are approximated well by a Gaussian (orange curve) with expectation value and width given by the mean and standard deviation of the Bootstrapping distribution according to equations (5.69) and (5.70), respectively:

$$\mu_i = \langle \lambda_i \rangle \qquad \text{and} \qquad \sigma_i = \sqrt{\mathrm{Cov}\left[\lambda_i^{\mathrm{MLE}}, \lambda_i^{\mathrm{MLE}}\right]}. \tag{5.72}$$

In general, using the mean and the standard deviation of the distribution as the expectation value and width of a Gaussian yield the best possible Gaussian approximation of this distribution independent of the actual shape of the distribution.[be] We find similar agreement with a Gaussian for most partial-waves that have an intensity value that is large compared to the uncertainty.

The red curves in figure 5.12 represent Gaussian distributions with expectation value and width given by the maximum-likelihood estimates of the intensity value and its uncertainty from the $K^-\pi^-\pi^+$ sample. In figure 5.12a, the maximum-likelihood estimate yielded a slightly smaller intensity and a slightly larger uncertainty compared to the estimates from Bootstrapping. Also in figure 5.12b, the maximum-likelihood estimate of the intensity is only slightly smaller, but the uncertainty estimate is unreasonably larger. We observe similarly large uncertainties from the maximum-likelihood estimate in a few other $(m_{K\pi\pi}, t')$ cells. We suspect these unreasonably large uncertainties to arises from numerical instabilities due to the large number of free parameters in the rank = 3 PWD model, which lead to an approximately singular Hessian matrix of the likelihood function. We did not observe such unreasonably large uncertainties when using a

[be] Using the mean and standard deviation of the distribution as expectation value and width of the Gaussian approximation minimizes the Kullback-Leibler divergence [118], which is a measure how different the Gaussian approximation is with respect to the true distribution.

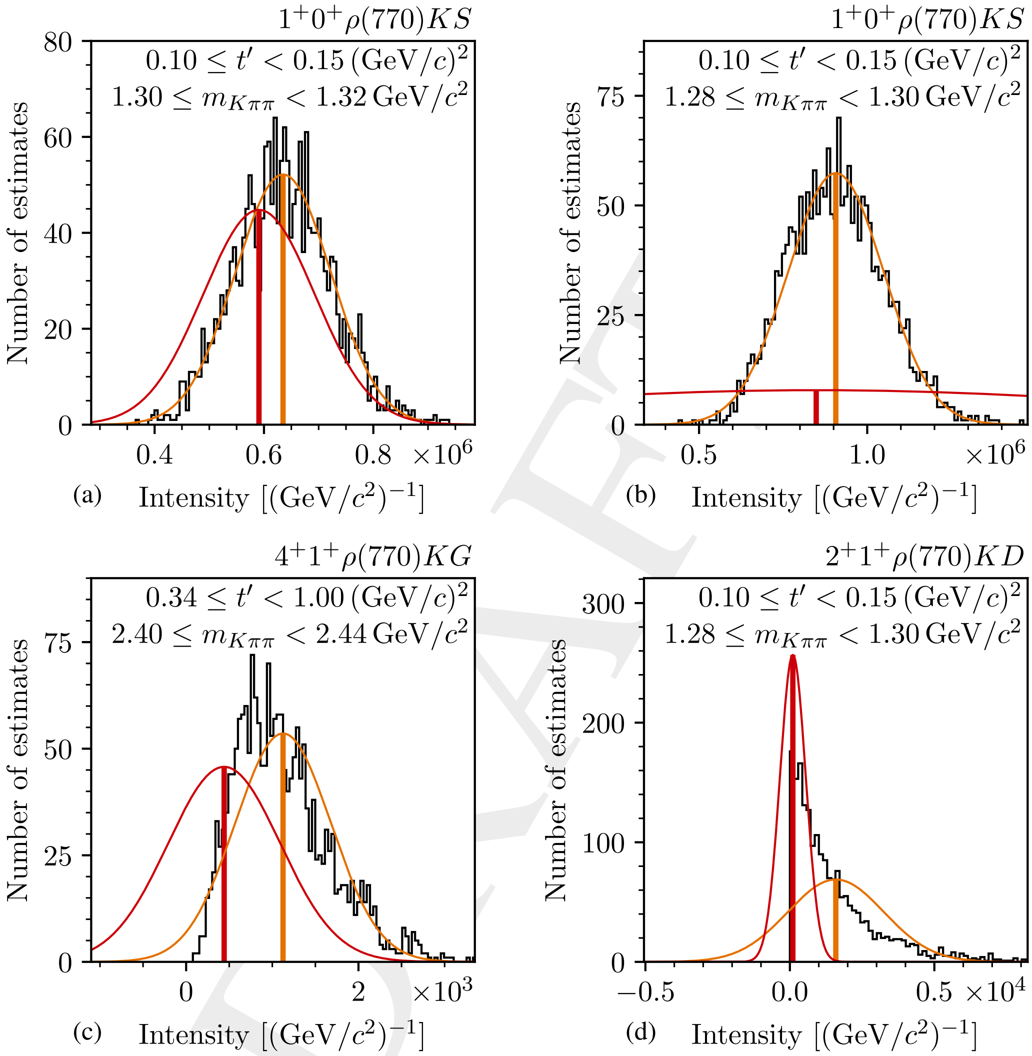

Figure 5.12: Distribution of the intensity estimates for selected partial-waves in the given $(m_{K\pi\pi}, t')$ cells as obtained from the Bootstrapping samples (histograms). The orange curves are Gaussian distributions with expectation values and widths given by the mean values (vertical orange lines) and standard deviations of the distributions. The red curves are Gaussian distributions with expectation values and widths given by the maximum-likelihood estimates of the intensity value (vertical red lines) and its uncertainty, respectively. (a) and (b) show the intensity of the $1^+\,0^+\,\rho(770)\,K\,S$ wave in two neighboring $m_{K\pi\pi}$ bins. (c) shows the intensity of the $4^+\,1^+\,\rho(770)\,K\,G$ wave. (d) shows the intensity of the $2^+\,1^+\,\rho(770)\,K\,D$ wave from a PWD using a rank=1 PWD model. (a) to (c) were obtained using a rank=3 PWD model.

rank=1 PWD model. As we did not use the maximum-likelihood estimates of the uncertainties in this analysis, we did not study this effect further.

For partial-waves in $(m_{K\pi\pi}, t')$ cells that have intensity values that are small compared to their uncertainties, the distributions of the intensity estimates deviate from a Gaussian. This is shown, e.g., in figure 5.12c. As the intensity cannot be negative, the distribution is asymmetric with a tail towards larger intensities. The maximum-likelihood estimate yielded a larger uncertainty than the corresponding Bootstrapping estimate. The intensity value from the maximum-likelihood estimate is close to zero and much smaller than the Bootstrapping mean value. A partial-wave intensity, i.e. a diagonal element of the spin-density matrix, is the sum of the squared real and imaginary parts of the transition amplitude [see equation (5.67) for $a = b$]. This means, that the intensity depends quadratically on the individual fit parameters. Therefore, we expect its distribution to be approximated well by a Gaussian only if its uncertainty is small compared to its value. The deviation of the intensity distribution from a Gaussian is even more pronounced for many waves when using a rank=1 PWD model. An extreme example is shown in figure 5.12d. For a rank=3 model the sum in equation (5.67) has three times more terms than for a rank=1 model. Due to the central-limit theorem, we expect the intensity distribution of a rank=3 model to be more similar to a Gaussian.

On average, the maximum-likelihood estimates of the uncertainties are about twice as large as the corresponding Bootstrapping estimates,[bf] with a large spread across the $(m_{K\pi\pi}, t')$ cells. This spread is independent of the $(m_{K\pi\pi}, t')$ region as shown, for example, in figure 5.13a for the uncertainty on the intensity of the $1^+\,0^+\,\rho(770)\,K\,S$ wave in the lowest t' bin. The bias of the maximum-likelihood estimates of the intensities as defined in equation (5.71) is spread across the $(m_{K\pi\pi}, t')$ cells as exemplarily shown in figure 5.13b for the intensity of the $1^+\,0^+\,\rho(770)\,K\,S$ wave in the lowest t' bin. Typically, this spread is smaller than the intensity's uncertainty. On average, the Bootstrapping means are similar to the maximum-likelihood estimates.

The distributions of the real and imaginary parts of the off-diagonal elements of the spin-density matrix obtained from Bootstrapping are in good agreement with a Gaussian even in cases where the values of the real and imaginary parts are small compared to their uncertainties as shown in figure 5.14. Also, the maximum-likelihood estimate yielded similar results for the values and the uncertainties of the off-diagonal elements. In contrast to the intensities, the real and imaginary parts of the off-diagonal elements of the spin-density matrix are sums of products of real and imaginary parts of different transition amplitudes [see equations (5.67) and (5.68) for $a \neq b$]. Hence, the off-diagonal spin-density matrix elements depend linearly on the individual fit parameters, i.e. they depend linearly on individual fit parameters if keeping the other fit parameters fixed. If the correlations between the fit parameters are weak, this means that the functional dependence of the off-diagonal spin-density matrix elements on all fit parameters is better approximated by a linear function compared to the functional dependence of the intensities. Therefore, the distribution of the off-diagonal spin-density matrix elements is better approximated by a Gaussian. Also, the maximum-likelihood estimates agree better

[bf] This is in contrast to rank=1 PWD models, for which the maximum-likelihood estimates of the uncertainties are typically slightly smaller than the corresponding Bootstrapping estimates.

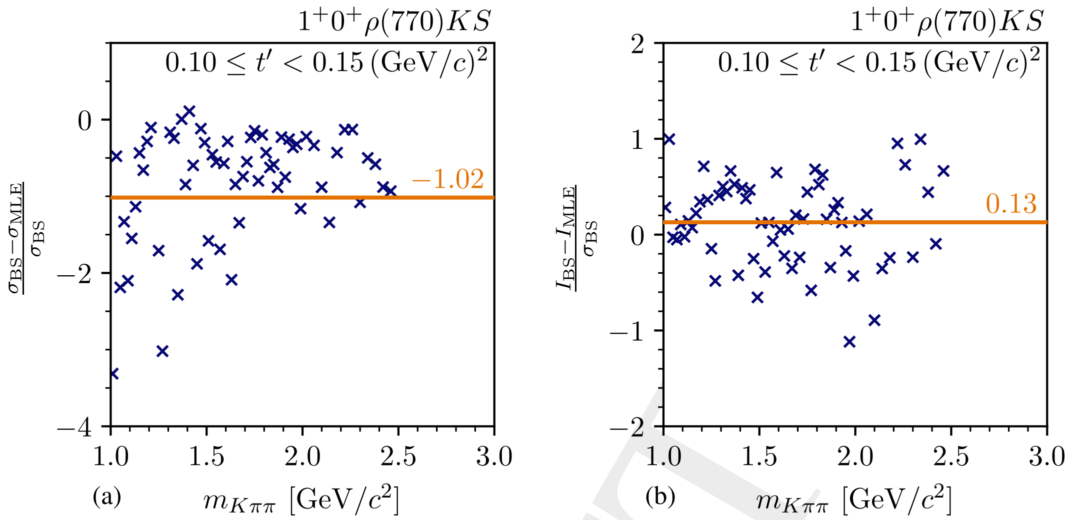

Figure 5.13: Difference between the estimates from Bootstrapping (BS) and the maximum-likelihood estimates (MLE) for the $1^+\,0^+\,\rho(770)\,K\,S$ wave as a function of $m_{K\pi\pi}$ in the lowest t' bin. (a) shows the relative difference between the uncertainty estimates. (b) shows the bias on the maximum-likelihood estimate of the intensity as defined in equation (5.71) relative to the uncertainty as obtained from Bootstrapping. The orange numbers and horizontal lines represent the corresponding average over all $m_{K\pi\pi}$ bins.

with the results from Bootstrapping as calculating the maximum-likelihood estimates of the spin-density matrix elements involves linear uncertainty propagation.

According to equation (5.69), Bootstrapping allows us to study the covariance matrix of the spin-density matrix elements, including their linear correlations. Typically, the intensity values exhibit small correlations. For example, the Pearson correlation coefficient [119]

$$\mathrm{Cov}\left[\lambda_i^{\mathrm{MLE}}, \lambda_j^{\mathrm{MLE}}\right] \Big/ \sqrt{\mathrm{Cov}\left[\lambda_i^{\mathrm{MLE}}, \lambda_i^{\mathrm{MLE}}\right] \mathrm{Cov}\left[\lambda_j^{\mathrm{MLE}}, \lambda_j^{\mathrm{MLE}}\right]} \tag{5.73}$$

of the intensities of the $1^+\,0^+\,\rho(770)\,K\,S$ and the $2^+\,1^+\,\rho(770)\,K\,D$ waves obtained from Bootstrapping is only 0.04 for the $(m_{K\pi\pi}, t')$ cell shown in figure 5.15a. Also, the real and imaginary parts of the spin-density matrix elements show only small correlations, which are, however, typically larger than the correlations between intensities. Figure 5.15b shows as an example the distribution of the real and imaginary parts of a selected spin-density matrix element, which yields a Pearson correlation coefficient of −0.13. Consistent with our findings for the uncertainties, the maximum-likelihood estimate of the covariance matrix of real and imaginary parts, represented by the red uncertainty ellipse in figure 5.15b, agrees well with the corresponding Bootstrapping estimate (orange uncertainty ellipse), while the maximum-likelihood estimate of the full covariance of the intensities in figure 5.15a yielded a larger uncertainty ellipse compared the Bootstrapping estimate.[bg]

[bg] The difference in the positions of the ellipses arises for the same reason as difference between the maximum-likelihood estimates of the intensity values and the Bootstrapping means, also seen in figure 5.12.

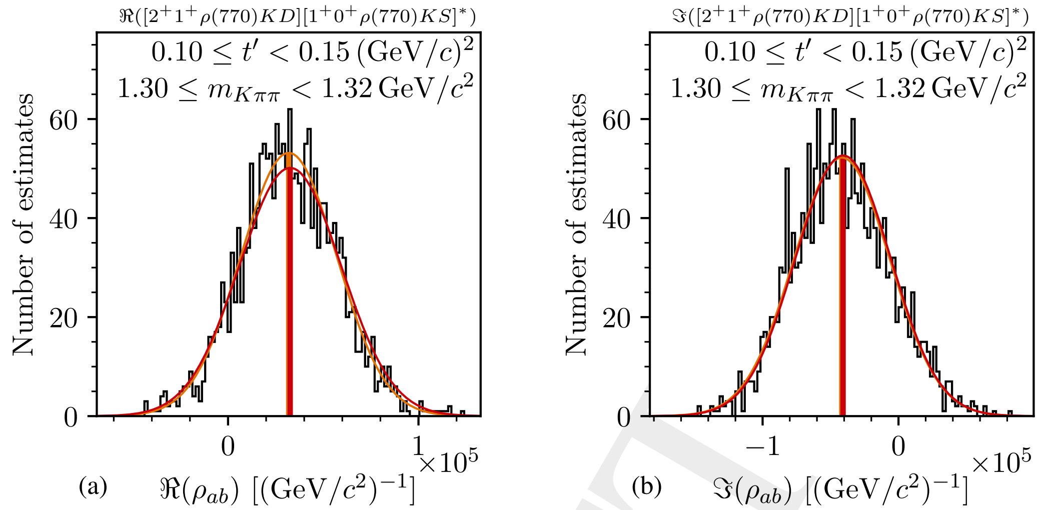

Figure 5.14: Distribution of (a) the real part $\Re(\rho_{ab})$ and (b) the imaginary part $\Im(\rho_{ab})$ of the spin-density matrix element for a selected pair of waves as obtained from the Bootstrapping samples (histograms). The orange curves are Gaussian distributions with expectation value and width given by the mean value (vertical orange lines) and the standard deviation of the distributions. The red curves are Gaussian distributions with expectation value and width given by the maximum-likelihood estimate of the intensity value (vertical red lines) and its uncertainty, respectively.

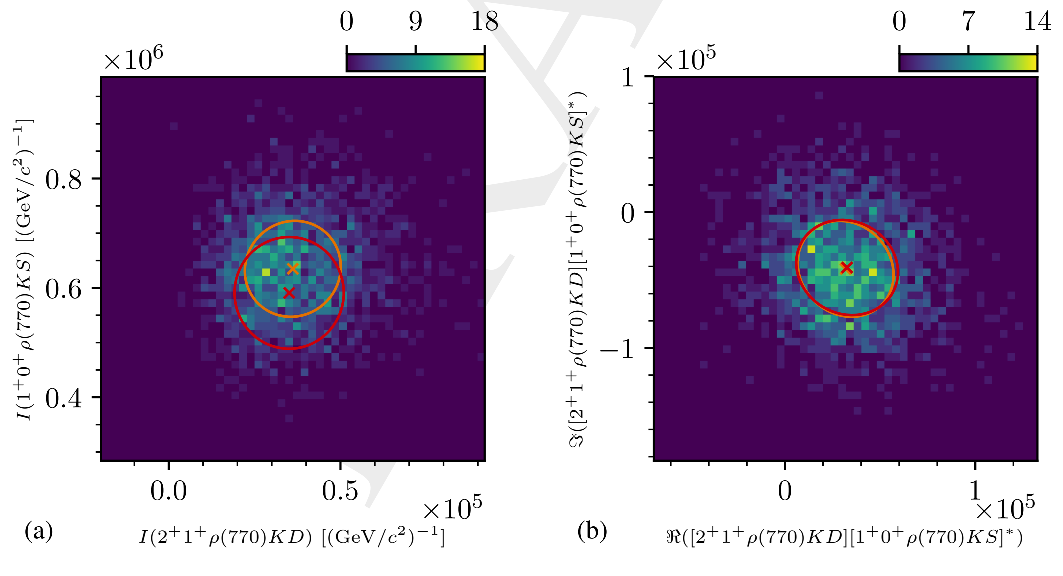

Figure 5.15: Correlations between spin-density matrix elements for the $(m_{K\pi\pi}, t')$ cells with $1.30 \le m_{K\pi\pi} < 1.32\,\mathrm{GeV}/c^2$ and $0.10 \le t' < 0.15\,(\mathrm{GeV}/c)^2$ as obtained from the Bootstrapping samples. (a) shows the correlation between the intensities of the $1^+\,0^+\,\rho(770)\,K\,S$ and the $2^+\,1^+\,\rho(770)\,K\,D$ waves. (b) shows the correlation between the real and imaginary part of the off-diagonal spin-density matrix element of the same two waves. The orange crosses indicate the mean values from Bootstrapping. The orange uncertainty ellipses represent the covariances. The red crosses indicate the maximum-likelihood estimates of the spin-density matrix elements. The red uncertainty ellipses represent the covariances as obtained from the maximum-likelihood estimates.

Using the Bootstrapping method, we were able to estimate the uncertainties and correlations of observables, e.g. spin-density matrix element or data-set fraction parameters, determined from the results of the PWD in a reliable way. Thereby, we took into account non-linearities in the calculation of the observables and we approximated their true distribution with a Gaussian in the best possible way. Thus, we used the Bootstrapping estimates for the uncertainties and correlations in all further analysis steps. Unless stated differently, we show in all figures that present results of a PWD the uncertainties from Bootstrapping. As discussed above, we observe a non-vanishing bias of the maximum-likelihood estimates for the values of observables, e.g. the intensity values. This bias is spread across the $(m_{K\pi\pi}, t')$ cells as exemplarily shown in figure 5.13b. In order to reduce this bias, we used also the mean values from Bootstrapping defined in equation (5.70) as central values for all data points. Unless state differently, we do this when showing the results of a PWD. Furthermore, we used the Bootstrapping mean values as data points in the RMFs. Although the covariance matrix obtained from Bootstrapping is the covariance of the maximum-likelihood estimates, we used it as an approximation for the covariance of the Bootstrapping mean values.[bh] We tested the effect of this approximation in a systematic study that is discussed in section 6.3. For simplicity, we refer to the Bootstrapping mean values of the spin-density matrix elements $\langle\lambda_i\rangle$ obtained from measured data as measured values and use the symbol λ_i in the rest of the text. We do the same also for other observables, e.g. for the data-set fraction parameters.

5.5 A First Glimpse on the Partial-Wave Decomposition Results

Using the formalism described in section 5.1, we performed a PWD of the COMPASS $K^-\pi^-\pi^+$ data sample. As a model, we used the 238-wave set, which was inferred from data in the wave-set selection procedure described in section 5.2. At the level of the PWD we cannot separate the reaction $K^- + p \to K^-\pi^-\pi^+ + p$ from incoherent backgrounds that are present in the $K^-\pi^-\pi^+$ sample. Therefore, we effectively modeled these incoherent contributions by using a rank=3 model in the PWD as discussed in section 5.3. Finally, we obtained more accurate estimates for the observables and their uncertainties from the PWD using the Bootstrapping method, which is presented in section 5.4. In this section, we give a general overview over the results of the PWD fit to the $K^-\pi^-\pi^+$ sample, which is called the 238-wave PWD in the rest of the text. Especially, we focus on the quality of the fit. The physics signals that we observe in the various partial waves are discussed in chapter 7.

For each of the 2000 Bootstrapping samples in each $(m_{K\pi\pi}, t')$ cell we performed 50 fit attempts with random start-parameter values for the transition amplitudes and data-set fractions. Figure 5.16 shows the result of the 50 fit attempts of one exemplary Bootstrapping sample for each

[bh] As the Bootstrapping mean values are estimators of observables, they fluctuate statistically. To obtain an estimate for the covariance matrix of the Bootstrapping mean values, we would need to perform a Bootstrapping of the Bootstrapping. This is computationally prohibitively expensive.

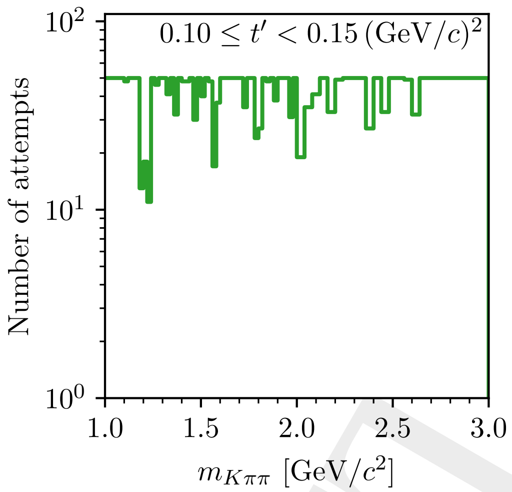

Figure 5.16: Stability of the 50 PWD fit attempts per $(m_{K\pi\pi}, t')$ cell for an exemplarily selected Bootstrapping sample as a function of $m_{K\pi\pi}$ in the lowest t' bin. The green line shows the number of fit attempts that found the best result, i.e. that found a value of $\ln \mathcal{L}_{\mathrm{PWD}}$ that is at most 0.1 units worse than the largest $\ln \mathcal{L}_{\mathrm{PWD}}$ value.

$m_{K\pi\pi}$ bin in the lowest t' bin. In all $m_{K\pi\pi}$ bins, all of the 50 fit attempts converged[bi] and hence yielded a fit result. The best result, i.e. the one with the largest likelihood, was found in more than 10 of the 50 fit attempts in all $m_{K\pi\pi}$ bins as shown by the green histogram in figure 5.16. For most of the $m_{K\pi\pi}$ bins, it was even found in more than 30 fit attempts. The $m_{K\pi\pi}$ regions that yielded the best result less than about 20 times, e.g. at about $1.2\,\mathrm{GeV}/c^2$, correspond to the $m_{K\pi\pi}$ regions with a large amount of events (see figure 4.6a). In these regions the higher precision of the data leads to more distinct local minima. The other three t' bins and all Bootstrapping samples behave similarly. Only in a few Bootstrapping samples the result with the largest value of $\ln \mathcal{L}_{\mathrm{PWD}}$ was found only once. Hence, we may not have found the best result for these samples. However, these rare occurrences do not influence our final estimates in equations (5.69) and (5.70) from the averages over the Bootstrapping samples.[bj] Overall, the large number of fit attempts that found the best solution shows that the PWD fit of the rank=3 model using the 238-wave set is stable. In particular, the fit is much more stable than the wave-set selection fits shown in figure 5.8a. This proves that the fit can reliably find the fit-parameter values that describe the data best.

The fraction of produced events in each of three data sets of the $K^-\pi^-\pi^+$ sample are represented by the data-set fraction parameters $\hat{r}^{(i)}(m_{K\pi\pi}, t')$, which are independent free parameters in each $(m_{K\pi\pi}, t')$ cell as defined in equation (5.25). The estimates for $\hat{r}^{(i)}(m_{K\pi\pi}, t')$ from the PWD are shown in figure 5.17 for the lowest and highest t' bins. We expect the data-set fractions to be

[bi] We used the low-memory BFGS (LBFGS) [82–84] implementation of the NLopt package [85] as minimizer, which determines the convergence criteria.

[bj] We did two studies in a selected $(m_{K\pi\pi}, t')$ cell where we performed only one random fit attempt and where we used 500 random fit attempts. Both studies yielded results that are consistent with the main analysis where we used 50 random fit attempts.

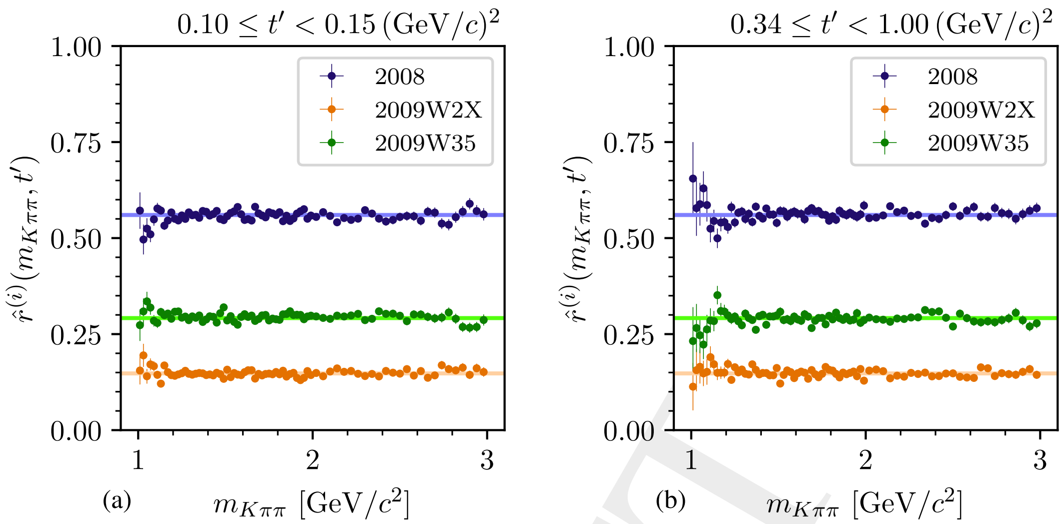

Figure 5.17: Data-set fractions, i.e. the fraction of produced events in each of the three data sets of the $K^-\pi^-\pi^+$ sample defined in equation (5.25), as a function of $m_{K\pi\pi}$ (a) in the lowest t' bin and (b) in the highest t' bin. The colored horizontal lines show the corresponding average values .[bk]

the same in all $(m_{K\pi\pi}, t')$ cell. This is because the physical distribution of events is the same in each data set and because the data-set fractions represent the fraction of produced events, which are not affected by acceptance effects that depend on $(m_{K\pi\pi}, t')$. The data-set fractions in the $(m_{K\pi\pi}, t')$ cells show no systematic deviation from their corresponding average values,[bk] which are represented by the colored horizontal lines in figure 5.17. The average values are 0.56, 0.15, and 0.29 for the 2008, 2009W2X, and 2009W35 data sets, respectively. They agree with the fractions of measured events of 0.55, 0.14, and 0.31 as expected, because the experimental acceptance, which may bias the fraction of measured events with respect to fraction of produced events, is similar for the three data sets. This agreement demonstrates, that our estimates of the data-set fraction parameters reliably reproduce the physical quantities they represent. It is a first successful test of the quality of the PWD fit.

A χ^2 test using the average values as constant hypothesis yielded p-values of 0.003, 0.080, and 0.016 for the 2008, 2009W2X, and 2009W35 data sets, respectively.[bl] These p-values mean that the deviations of the data points from the average are somewhat larger than expected by the statistical uncertainties. As we assume that our estimates of the statistical uncertainties obtained from Bootstrapping are realistic, these deviations indicate systematic effects in the estimates for $\hat{r}^{(i)}(m_{K\pi\pi}, t')$. However, the obtained p-values are still reasonably large. Hence, these systematic effects are small. Furthermore, we do not observer an overall systematic deviation from a constant. Thus, we conclude that we obtained realistic estimates for the data-set fractions in each

[bk] We determined the average of each data-set fraction over all $(m_{K\pi\pi}, t')$ cells by calculating the variance-weighted mean (see equation (7.26) in ref. [119]), which uses the uncertainty of the data-set fraction parameter as determined from Bootstrapping. Doing so, we neglected correlations between the data-set fraction parameters.

[bl] See sections 4.5 and 4.7 in ref. [119] for details on the p-value calculation. As for the average, we neglected the correlations between the data-set fractions for the p-value calculation.

$(m_{K\pi\pi}, t')$ cell. The imperfect statistical consistency that fluctuates from bin to bin indicates that the data-set fractions are affected by systematic effects that are different from bin to bin. For example, such small systematic effects may arise from the wave set. As we individually inferred the wave set from data for each $(m_{K\pi\pi}, t')$ cell as explained in section 5.2, also the wave set is affected by fluctuations from cell to cell. These fluctuations may lead to small systematic effects when using the wave sets in the PWD that is presented here. This is a first indication that the statistical and systematic uncertainties of this analysis are of similar orders of magnitude.

We are mainly interested in the $m_{K\pi\pi}$ dependencies of the spin-density matrix elements of the partial waves as they provide information about the resonances that decay to the $K^-\pi^-\pi^+$ final state. Before discussing the individual partial waves, we discuss the $m_{K\pi\pi}$ dependence of the total model intensity, i.e. the distribution of the predicted number $\widehat{N}_{\text{ev}}$ of produced events in $m_{K\pi\pi}$ according to equation (5.21). However, as we used a non-equidistant binning in $m_{K\pi\pi}$, $\widehat{N}_{\text{ev}}$ has a jump discontinuity at the $m_{K\pi\pi}$ position were the bin width changes. In order take this into account, we show in the following the so-called intensity spectra, which represent the number density in $m_{K\pi\pi}$, i.e. the intensity divided by the $m_{K\pi\pi}$-bin width as a function of $m_{K\pi\pi}$. The intensity spectra are continuous functions in $m_{K\pi\pi}$. The blue points in figure 5.18 show the intensity spectrum of the total model intensity summed over the analyzed t' bins, which is so-called t'-summed total intensity spectrum. As expected, it exhibits similar features as the measured $m_{K\pi\pi}$ distribution shown in figure 4.6a,[bm] i.e. a double-peak in the mass region of the $K_1(1270)$ and the $K_1(1400)$ and a second peak at about $1.8\,\text{GeV}/c^2$ in the mass region of the $K_2^*(1430)$.

The PWD enables us to study the contributions from partial waves with given J^P quantum numbers to the total intensity spectrum. Figure 5.18 gives an overview over these contributions. The orange, green, red, and purple data points show for each J^P included in the 238-wave set the total intensity of all waves with the given J^P quantum numbers, i.e. the predicted number of produced events if only these waves are considered in the corresponding calculation in equation (5.21). As expected, the 1^+ waves represented by the green points in figure 5.18a dominantly contribute to the double-peak structure at about $1.4\,\text{GeV}/c^2$. Also, the 0^- waves (green points in figure 5.18a) strongly contribute to the mass region of the double-peak. Above about $1.5\,\text{GeV}/c^2$ they have a similar intensity as the 1^+ waves. The 2^- waves (green points in figure 5.18b) strongly contribute to the second peak in the total intensity spectrum at about $1.8\,\text{GeV}/c^2$. This supports our assumption that this peak arises from K_2 resonances in the spectrum. The 2^+ waves (orange points in figure 5.18b) show a clear peak in the mass range of the $K_2^*(1430)$. Except for this peak, the 2^+ waves pick up only little intensity. Similarly, the 4^+ waves (orange points in figure 5.18c) contribute only little to the data, but they show a clear peak at about $2\,\text{GeV}/c^2$, i.e. in the mass region of the $K_4^*(2045)$ resonance.

The total intensities for waves with 3^+, 4^-, 4^+, or 5^+ quantum numbers (red points in figure 5.18b and green, orange, and red points in figure 5.18c, respectively) show peaking structures in the

[bm] The total intensity spectrum represents the acceptance-corrected $m_{K\pi\pi}$ distribution, i.e. the underlying physical $m_{K\pi\pi}$ distribution, according to the PWD results. The measured $m_{K\pi\pi}$ spectrum is distorted with respect to the physical distribution due to the experimental acceptance.

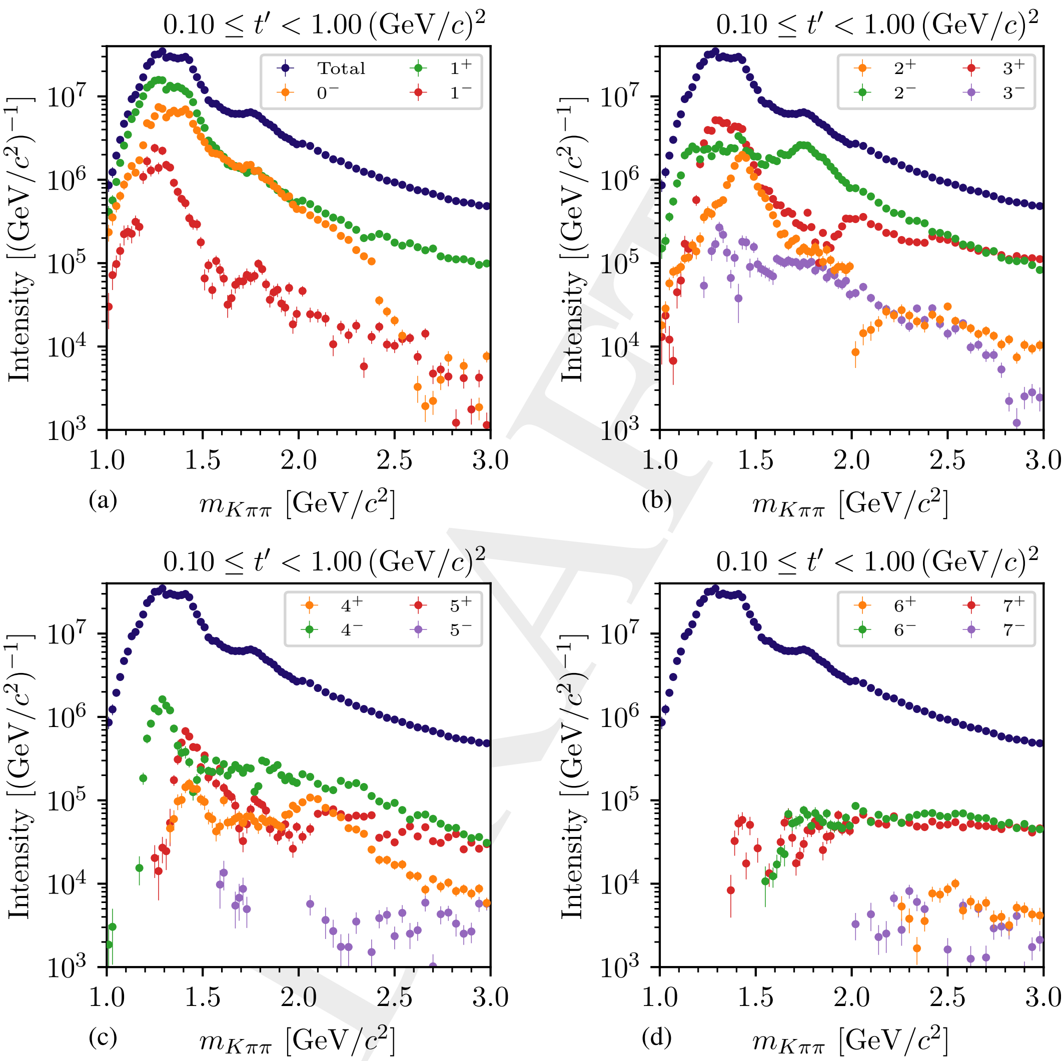

Figure 5.18: t'-summed spectrum of the total intensity according to equation (5.21) [blue data points in (a) to (d)]. The differently colored data points show for each J^P included in the 238-wave set the t'-summed total intensity spectra of all waves with given J^P.

low-mass region of 1.2 to 1.6 GeV/c^2. Also, the 2^- waves (green points in figure 5.18b) show intensity in this $m_{K\pi\pi}$ region. As there are no known or expected resonances with these quantum numbers below about 1.6 GeV/c^2 (see figure 1.1), these structures require a detailed investigation in systematic and pseudodata studies. The conclusions on this so-called low-mass structures are discussed in section 5.9.

The intensities of partial waves with high spin shown in figure 5.18d exhibit no resonance-like structures. The waves with 6^+ (orange points) and 7^- (purple points) quantum numbers do not pick up significant intensity. The 6^- (green points) and 7^+ (red points) waves pick up significant intensity only above about 1.6 GeV/c^2. Their intensity spectrum is flat. As there are no known or expected strange-meson resonances with such high spins, we suspect the $J = 6$ and 7 waves to be dominated by contributions from non-resonant processes. Especially, Deck-like reactions introduced in section 2.1.1 are known to contribute to partial waves with high spin [11].

Overall, we observe that among waves with odd J, those with positive parity are enhanced with respect to those with negative parity. For example, the total intensity of $J^P = 1^+$ waves (green data points in figure 5.18a) is larger than the total intensity of 1^- waves (red data points). For waves with even J it is vice versa. The waves with enhanced intensity corresponds to K_J states, while those with suppressed intensity correspond to K_J^* states (see chapter 1). Hence, this observation means that K_J states contribute more strongly to the $K^-\pi^-\pi^+$ final state. This can be explained with the fact that many K_J^* stats dominantly decay to the $K\pi$ final state, while K_J states cannot decay to the $K\pi$ final state. Hence, assuming that K_J^* and K_J states are produced with a similar strength in diffractive scattering, we expect a smaller contribution from K_J^* states to the $K^-\pi^-\pi^+$ final state as some of them decay to the $K\pi$ final state.[bn]

We separate in the PWD not only the contributions of intermediate states with given J^P, but we also distinguish various spin projections M^ε and decay modes when defining the partial waves in equation (5.8). The intensity spectrum of a partial wave is the $m_{K\pi\pi}$ dependence of its intensity defined equation (5.23). Figures 5.19a, d, and f show the intensity spectra of three selected partial waves. Figure 5.19f shows the intensity spectrum of the $1^+\,0^+\,\rho(770)\,K\,S$ partial wave. This wave represents states with $J^P\,M^\varepsilon = 1^+0^+$ quantum numbers that decay to the $\rho(770)$ isobar and the bachelor K with both in an S-wave, i.e. with relative orbital angular momentum $L = 0$. As the wave-set selection yielded a minimal wave set for each $(m_{K\pi\pi}, t')$ cell, some waves were selected only in certain $m_{K\pi\pi}$ regions. For example, the $1^+\,0^+\,\rho(770)\,K\,S$ wave was selected only for $m_{K\pi\pi} \leq 2.5$ GeV/c^2 in the second highest t' bin as shown in figure 5.19f. Furthermore, we do not observe any discontinuity at $m_{K\pi\pi} = 2$ GeV/c^2, where we doubled the $m_{K\pi\pi}$ bin width.

The intensity spectrum of the $1^+\,0^+\,\rho(770)\,K\,S$ wave exhibits a clear peak at about 1.3 GeV/c^2. The PDG lists the well established $K_1(1270)$ resonance in this mass region. As we expect Breit-Wigner-like resonances to appear as peaks in the intensity spectra (see section 5.1.4), the peak at 1.3 GeV/c^2 is consistent with a $K_1(1270)$ decaying to $\rho(770)\,K$. In section 7.1 we discuss this signal in detail. Compared to the total intensity spectrum of all 1^+ waves shown by the green data

[bn] K_J^* and K_J states can also decay to other final states, e.g. the $K\omega$ final state. However, the possibility to decay to the $K\pi$ final state is the major difference between K_J^* and K_J states.

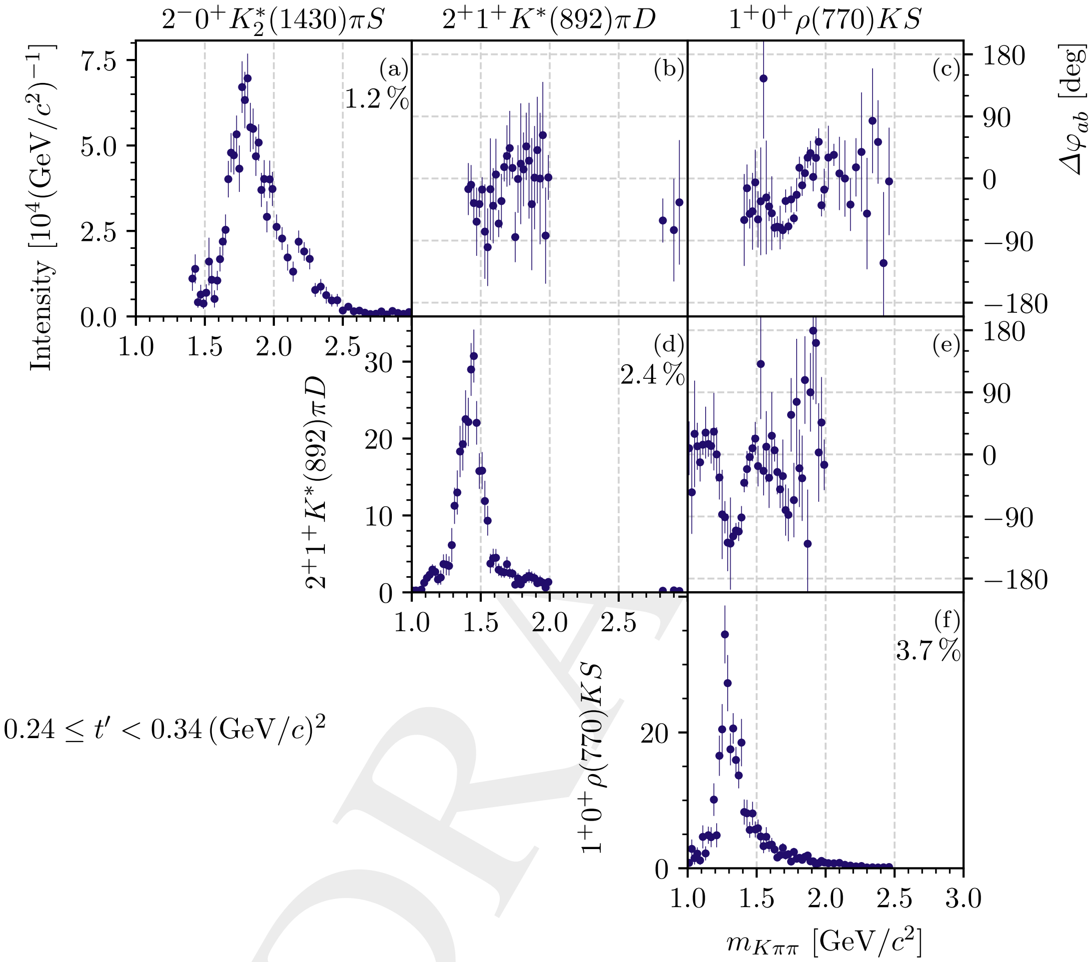

Figure 5.19: Representation of the spin-density matrix for the $2^-\,0^+\,K_2^*(1430)\,\pi\,S$, $2^+\,1^+\,K^*(892)\,\pi\,D$, and $1^+\,0^+\,\rho(770)\,K\,S$ waves in the second highest t' bin. The diagonal elements show the partial-wave intensities as defined in equation (5.23). To account for the different $m_{K\pi\pi}$ bin widths below and above $2\,\mathrm{GeV}/c^2$, the intensities are shown in units of number of events per $1\,\mathrm{GeV}/c^2$ interval. The off-diagonal elements show the relative phases $\Delta\varphi_{ab}(m_{K\pi\pi}, t')$ between wave a (given by the row) and wave b (given by the column) as defined in equation (5.74). The relative phases represent the interference between partial waves. The percentage number in the upper-right corner of each intensity spectrum is the relative intensity of the corresponding wave as defined in equation (5.76).

points in figure 5.18a, the peak in the $1^+\,0^+\,\rho(770)\,K\,S$ wave is more clear. This demonstrates the power of the PWD when studying individual partial waves. The intensity spectrum of the $2^+\,1^+\,K^*(892)\,\pi\,D$ wave shown in figure 5.19d exhibits a clear narrow peak at about $1.4\,\mathrm{GeV}/c^2$, i.e. in the mass region of the well-established $K_2^*(1430)$ resonance. Although the 2^+ peak corresponds to only a small fraction of the total intensity (see figure 5.18b), we presumably were able to extract a clean $K_2^*(1430)$ signal. In section 7.2 we discuss the 2^+ waves in detail. The intensity spectrum of the $2^-\,0^+\,K_2^*(1430)\,\pi\,S$ wave shown in figure 5.19a exhibits a broad peak at about $1.8\,\mathrm{GeV}/c^2$ with a tail towards higher masses. The PDG lists two established resonances with $J^P = 2^-$ in this mass region, the $K_2(1770)$ and the $K_2(1820)$. The high-mass tail might arises from the $K_2(2250)$ resonance, which is a state that needs further confirmation. The contributions of these resonances can be separated only by modeling the partial-wave amplitudes in the RMF. The results are discussed in section 7.4.

We observe a small backgrounds in the intensity spectra of the partial waves, e.g. below the peak in the intensity spectrum of the $2^+\,1^+\,K^*(892)\,\pi\,D$ wave shown in figure 5.19d. These background might arise from background processes that also contribute to the $K^-\pi^-\pi^+$ sample (see sections 2.1.1 and 5.3). We account of these contributions in the resonance-model fit described in chapter 6. Also, imperfections in the PWD model can bias the estimates, e.g., of the intensity spectra, which might lead to the observed background. We tested such imperfections in the systematic studies presented in section 5.7.

The PWD allows us to study not only the intensity spectra of partial waves but also the interference between them, which is represented by the complex-valued off-diagonal elements of the spin-density matrix. To more clearly see interference effects it is often more instructive to study the <u>phase of a wave</u> a relative to a reference wave b, i.e. the <u>relative phase</u> of two partial-waves, which is the phase of the corresponding off-diagonal element of the spin-density matrix:

$$\varDelta\varphi_{ab}(m_{K\pi\pi}, t') \equiv \arg\left[\rho_{ab}(m_{K\pi\pi}, t')\right]. \tag{5.74}$$

The relative phases as a function of $m_{K\pi\pi}$, the so-called <u>phase motion</u>, for the selected pairs of waves are shown in figures 5.19b, c, and e. For the rank=3 model employed in this analysis, the relative phases are in general different from the phases of the transition amplitudes of the individual physics processes. In order to interpret the observed relative phases on a qualitative level, we assume that the $K^-\pi^-\pi^+$ sample is dominated by diffractive scattering into the $K^-\pi^-\pi^+$ final state,[bo] which is a coherent process. Inserting equation (5.18) in equation (5.74) yields

$$\begin{aligned}\varDelta\varphi_{ab}(m_{K\pi\pi}, t') &= \arg\left[\sum_z \mathcal{T}_a^z(m_{K\pi\pi}, t')\left[\mathcal{T}_b^z(m_{K\pi\pi}, t')\right]^*\right] \\ &\approx \arg\left[\mathcal{T}_a^{z=K\pi\pi}(m_{K\pi\pi}, t')\left[\mathcal{T}_b^{z=K\pi\pi}(m_{K\pi\pi}, t')\right]^*\right] \\ &= \arg\left[\mathcal{T}_a^{z=K\pi\pi}(m_{K\pi\pi}, t')\right] - \arg\left[\mathcal{T}_b^{z=K\pi\pi}(m_{K\pi\pi}, t')\right].\end{aligned} \tag{5.75}$$

[bo] We estimated the incoherent background contributions to be about 10 % (see sections 4.2 and 5.10).

Therefore, the relative phases obtained from the rank=3 PWD can be interpreted in terms of the transition amplitudes of the process $K^- + p \to K^-\pi^-\pi^+ + p$ on a qualitative level, especially in terms of the amplitudes of resonances decaying to the $K^-\pi^-\pi^+$ final state.[bp]

Figure 5.19e shows the relative phase between the $a = 2^+\,1^+\,K^*(892)\,\pi\,D$ wave and the $b = 1^+\,0^+\,\rho(770)\,K\,S$ wave. This phase drops sharply by about 120° around 1.3 GeV/c^2 and then rises again by about 120° around 1.4 GeV/c^2. For Breit-Wigner-like resonances, we expect a rise of the phase of the corresponding amplitude by 180° around the nominal resonance position (see section 5.1.4). The rise around 1.4 GeV/c^2 is consistent with a dominant contribution of the $K_2^*(1430)$ resonance to the $2^+\,1^+\,K^*(892)\,\pi\,D$ wave. As the 1^+ wave enters with a minus sign in equation (5.75), the drop of the phase around 1.3 GeV/c^2 is consistent with the $K_1(1270)$ resonance dominating the $1^+\,0^+\,\rho(770)\,K\,S$ wave. We do not observe full 180° phase motion, because the decreasing phase from the $K_1(1270)$ is partly compensated by the rising phase of the $K_2^*(1430)$ in the intermediate 1.35 GeV/c^2 mass region. In addition, non-resonant contributions and incoherent background in the rank=3 PWD model can reduce the height of the phase motion, i.e. can make the relative phases more shallow. The relative phase between the $2^-\,0^+\,K_2^*(1430)\,\pi\,S$ and the $1^+\,0^+\,\rho(770)\,K\,S$ wave shown in figure 5.19c rises in the mass region around 1.8 GeV/c^2, where we also observe the peak in the intensity spectrum of the 2^- wave. However, this rise in the relative phase is slower compared to the one in figure 5.19e, which indicates that the K_2 states in this mass region have a larger width compared to the $K_1(1270)$ and the $K_2^*(1430)$. This would be consistent with previous observations [9]. As the $2^-\,0^+\,K_2^*(1430)\,\pi\,S$ wave shows no significant structures below about 1.6 GeV/c^2 and the $2^+\,1^+\,K^*(892)\,\pi\,S$ wave shows no significant structures above about 1.6 GeV/c^2, the two waves do not share a mass region where both have large intensities. Therefore, their relative phase shown in figure 5.19b has a large uncertainty. This means, in order to obtain phase information from the PWD, we have to study at least two waves simultaneously. In addition, these waves must have significant intensities in overlapping $m_{K\pi\pi}$ regions in order to reliably determine their relative phase.

As shown by the red data points in figure 5.18, the 1^+ waves contribute most to the total intensity. The $1^+\,0^+\,\rho(770)\,K\,S$ wave is one of the largest waves in the 238-wave set. It contributes about 4 % to the total intensity. This so-called relative intensity,

$$\frac{\sum\limits_{t',\,m_{K\pi\pi}} \rho_{aa}(m_{K\pi\pi}, t')}{\sum\limits_{t',\,m_{K\pi\pi}} \sum\limits_{a,b} \rho_{ab}(m_{K\pi\pi}, t') I_{ab}(m_{K\pi\pi}, t')} = \frac{\sum\limits_{t',\,m_{K\pi\pi}} \widehat{N}_a(m_{K\pi\pi}, t')}{\sum\limits_{t',\,m_{K\pi\pi}} \widehat{N}_{\mathrm{ev}}(m_{K\pi\pi}, t')}, \tag{5.76}$$

is the ratio of the intensity of the wave summed over all $(m_{K\pi\pi}, t')$ cells and the total intensity defined in equation (5.21) summed over all $(m_{K\pi\pi}, t')$ cells. The latter one takes into account the interference between partial waves. This equals to the ratio of predicted number $\widehat{N}_a$ of produced

[bp] For the expert: We calculated the degree of coherence as defined in equation (H.1) of ref. [72]. For example, in the second highest t' bin the degree of coherence between the $2^+\,1^+\,K^*(892)\,\pi\,D$ and $1^+\,0^+\,\rho(770)\,K\,S$ waves shown in figure 5.19 is mainly above 0.6 for $m_{K\pi\pi} < 1.6$ GeV/c^2, i.e. in the $m_{K\pi\pi}$ region of the peaks in both waves. This value is sufficiently large to interpret the relative phase between both waves in the $m_{K\pi\pi}$ region of the peaks in terms of the transition amplitudes of the process $K^- + p \to K^-\pi^-\pi^+ + p$ on a qualitative level.

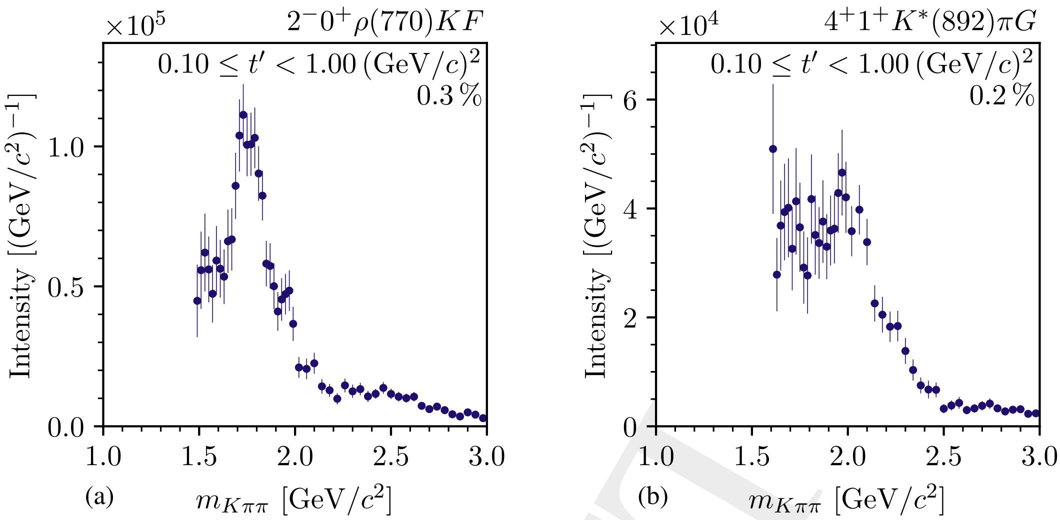

Figure 5.20: t'-summed intensity spectra, i.e. the partial-wave intensities in each $m_{K\pi\pi}$ bin summed over the analyzed t' bins, of (a) the $2^-\,0^+\,\rho(770)\,K\,F$ wave and (b) the $4^+\,1^+\,K^*(892)\,\pi\,G$ wave. To account for the different $m_{K\pi\pi}$ bin widths below and above $2\,\text{GeV}/c^2$, the intensities are shown in units of number of events per $1\,\text{GeV}/c^2$ interval. The percentage number in the upper-right corner of each intensity spectrum is the relative intensity of the corresponding wave as defined in equation (5.76).

events in all cells if there would be only wave a and the total predicted number $\widehat{N}_{\text{ev}}$ of produced events in all cells. [bq]

We observe signals not only in comparably large waves at the percent level, e.g. the waves that are shown in figure 5.19, but also in waves at the per-mill level. In figure 5.20 we show the t'-summed intensity spectra, i.e. the intensity of the partial waves according to equation (5.23) summed over the analyzed t' bins, of two small waves. The $2^-\,0^+\,\rho(770)\,K\,F$ wave shown in figure 5.20a exhibits a narrow peak at about $1.8\,\text{GeV}/c^2$. The peak is in the same mass region as the peak in the $2^-\,0^+\,K_2^*(1430)\,\pi\,S$ wave shown in figure 5.19a. This is expected, because both waves have the same J^P quantum numbers and hence the same K_2 states should appear in both waves. However, the two 2^- waves represent different decay modes, i.e. the $\rho(770)\,K\,F$-wave and the $K_2^*(1430)\,\pi\,S$-wave decays. The various K_2 states may couple to these two decay modes with different strengths, which can explain the different shapes of the intensity spectra, e.g. the narrower peak in the $2^-\,0^+\,\rho(770)\,K\,F$ wave compared to the $2^-\,0^+\,K_2^*(1430)\,\pi\,S$ wave. It is one of the advantages of the $K^-\pi^-\pi^+$ final state, that we can study the same states in different decay modes in a single consistent analysis.

In contrast to the high-mass tail, the low-mass tail of the intensity spectrum of the $2^-\,0^+$ $\rho(770)\,K\,F$ wave does become small, as it would be expected, but instead levels out at an intensity of about $0.5 \times 10^5\,/(\text{GeV}/c^2)$ for masses down to about $1.5\,\text{GeV}/c^2$. Below $1.5\,\text{GeV}/c^2$ the wave-set selection did not include this wave in the PWD model. We observe similar

[bq] Unfortunately, the relative intensities are biased by the so-called leakage effect. The relative intensities can still be used as measure of whether a wave is large or small as discussed in section 5.9.1.

enhanced low-mass tails also for other small partial waves at the per-mill level, e.g. for the $4^+\,1^+$ $K^*(892)\,\pi\,G$ wave shown in figure 5.20b. The high-mass tail of a potential signal from the well-known $K_4^*(2045)$ resonance above $2\,\mathrm{GeV}/c^2$ is clearly visible, but below $2\,\mathrm{GeV}/c^2$ the intensity is almost constant down to a mass of about $1.6\,\mathrm{GeV}/c^2$, below which the wave-set selection did not select this wave. As the $K_4^*(2045)$ is the lightest known 4^+ state, we would expect the intensity of the $4^+\,1^+\,K^*(892)\,\pi\,G$ wave to become small below the nominal $K_4^*(2045)$ mass of about $2\,\mathrm{GeV}/c^2$. Furthermore, the amplitude of this wave is suppressed at low masses, because of the additional energy needed to produced its high spin of $J = 4$ and its large orbital angular momentum of $L = 4$.[br] Similar arguments hold for the enhanced low-mass tail in the $2^-\,0^+\,\rho(770)\,K\,F$ wave. Therefore, we suspect these enhanced low-mass tails to be artifacts of our analyses. They may arise from the incoherent background in our data, which is studied in section 5.10 or from imperfections in the analysis model, which are tested in various systematic studies discussed in section 5.7. Furthermore, the enhanced low-mass tails are less pronounced when using a rank=1 PWD model of the 238-wave set, which has about three times fewer free fit parameters than the used rank=3 model. As the 238-wave set was constructed using a rank=1 model (see section 5.2), the rank=3 model may contain more parameters than can be reliably determined from data. This additional freedom of the rank=3 model might be misused by the fit to account for imperfections of the PWD model, e.g. by leading to destructive interference, and thereby causing such enhanced low-mass tails. Apart from the enhanced low-mass tails, we do not observe any signs that would indicate a too large PWD model. For example, too large models typically suffer from multimodality, but we reliably found the best fit result as discussed at the beginning of this section. In contrast to the low-mass structures observed e.g. in the 3^+ waves as discussed above, the enhanced low-mass tails do not show any peaking resonance-like signals. In addition, the enhanced low-mass tails are only a small effect. They only affect small partial waves at the per-mill level. In this analysis, we focus mostly on large partial waves.

In our data, the $K_4^*(2045)$ is only a small signal at the per-mill level that is potentially affected by model imperfection as discussed above. However, in general it is a well-established resonance observed by various previous experiments and its mass and width are known [28, 120–122]. Therefore, we use the $K_4^*(2045)$ as a kind of standard candle in our analysis. It allows to test the reliability of our results. Our results for the $K_4^*(2045)$ resonance are discussed in section 7.3.

From this first glimpse of the results of the PWD we conclude that the fits yielded stable and consistent results. We observe resonance-like signals in various partial waves in $m_{K\pi\pi}$ regions of well known strange-meson resonances. We also observe potential signals of excited states that need further confirmation such as the $K_2(2250)$. Before modeling these signals in the resonance-model fit presented in chapter 6 and interpreting them in chapter 7, we further study the reliability of the results of the PWD. To do so, we compare in section 5.6 the predictions of the PWD model with optimized parameters for kinematic distributions to the corresponding measured distributions. In section 5.7 we study the influence of systematic effects from the event selection and the PWD. In section 5.8 we study the consistency of the PWD based on a pseudodata sample for the reaction $K^- + p \to K^-\pi^-\pi^+ + p$. Finally, in section 5.10, we study the influence of incoherent background from the reaction $\pi^- + p \to \pi^-\pi^-\pi^+ + p$ on our results.

[br] In the PWD model described in section 5.1, this effect is modeled by the angular-momentum barrier factors.

5.6 Agreement between Partial-Wave Model and Data

The goal of the construction of the 238-wave set presented in section 5.2 was to find a minimal set of waves that is sufficient to describe the data. In this section, we study how well the result of the PWD fit using the 238-wave set describes the $K^-\pi^-\pi^+$ sample. The maximum-likelihood formalism presented in section 5.1.3 does not directly yield a goodness-of-fit criterion. Therefore, we compare the predictions of the PWD model for the kinematic distributions of the measured final-state particles according to equation (5.30) using the parameter estimates from the 238-wave PWD,[bs] the so-called PWD predictions, to the corresponding measured distributions.

The five-dimensional phase space of the $K^-\pi^-\pi^+$ final state can be represented by four angles and the invariant mass of one of the three two-body subsystems as discussed in section 5.1.1. Hence, different representations of the same $K^-\pi^-\pi^+$ kinematics are possible, depending on which two final-state particles are in the two-body isobar system. We consider here the $K^-\pi^+$ and $\pi^-\pi^+$ isobar systems. The five phase-space variables are the decay angles $\cos\theta_{\mathrm{GJ}}$ and ϕ_{GJ} of the isobar in the decay $X^- \to \xi^0 b^-$ defined in the Gottfried-Jackson rest frame of X^-; the decay angles $\cos\theta_{\mathrm{HF}}$ and ϕ_{HF} of the K^- or π^- in the decay $\xi^0 \to K^-\pi^+$ or $\xi^0 \to \pi^-\pi^+$, respectively, defined in the helicity rest frame of the ξ^0; and the invariant mass $m_{K^-\pi^+}$ or $m_{\pi^-\pi^+}$, respectively, of the two-body isobar system.

In order to visualize the five-dimensional phase-space distribution, we show one- and two-dimensional projection in the following. Figure 5.21 shows exemplarily the measured $K^-\pi^-\pi^+$ distribution (blue data points) and the corresponding PWD predictions (orange histograms), in the $m_{K\pi\pi}$ region of the K_1 double-peak in the five phase-space variables defined for the $\pi^-\pi^+$ isobar system. The distributions of all analyzed $m_{K\pi\pi}$ regions and for both, the $\pi^-\pi^+$ and the $K^-\pi^+$ isobar systems can be found in appendix D.2 in figures D.36 to D.47. Overall, the PWD predictions agree well with the corresponding measured distributions. The PWD model reproduces the features of the angular distributions of the X^- decay, exemplarily shown in figures 5.21a and 5.21b, and of the isobar decay, exemplarily shown in figures 5.21c and 5.21d. As the angular distributions represent the spin and orbital angular momentum of the contributing partial waves, this agreement suggests that we do not miss important waves with certain J and L in the wave set, i.e. limiting ourselves to $J \leq 7$ and $L \leq 7$ when constructing the wave pool was sufficient; and that the wave-set selection selected the significant waves. The structures observed in the angular distributions in figures 5.21a to 5.21d are hard to interpret directly, because they arise not only from waves with $\pi^-\pi^+$ isobars, but also from waves with $K^-\pi^+$ isobars. The latter ones have a complicated distribution in the phase-space variables defined for the $\pi^-\pi^+$ isobar system. Figure 5.21e shows the $m_{\pi^-\pi^+}$ spectrum, which exhibits a clear peak from the $\rho(770)$ resonances at about $0.8\,\mathrm{GeV}/c^2$ and two shoulders: one in the mass region of the $f_0(980)$ at about $1\,\mathrm{GeV}/c^2$ and one in the mass region of the $f_2(1270)$ at about $1.3\,\mathrm{GeV}/c^2$. The $m_{K^-\pi^+}$ spectrum shown in figure 5.22a exhibits a clear $K^*(892)$ signal at about $0.9\,\mathrm{GeV}/c^2$ and a second peak in the mass region of the $K_0^*(1430)$ and $K_2^*(1430)$ resonances. All these structures are reproduced

[bs] We determined the histograms that show the PWD predictions by weighting a reconstructed phase-space pseudodata sample using weights that are proportional to the model intensity in equation (5.16) using the parameter estimates from the 238-wave PWD. See appendix C.3 for details.

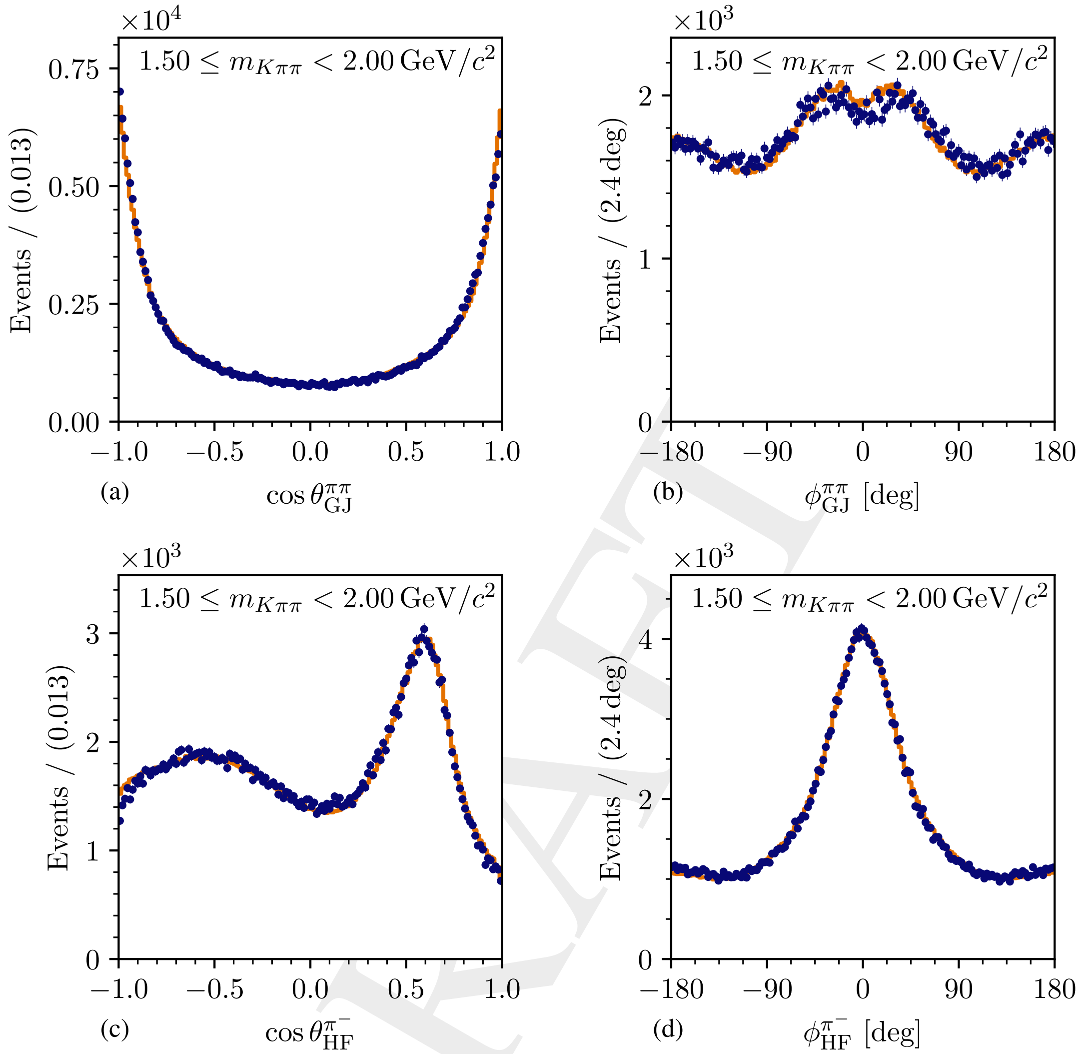

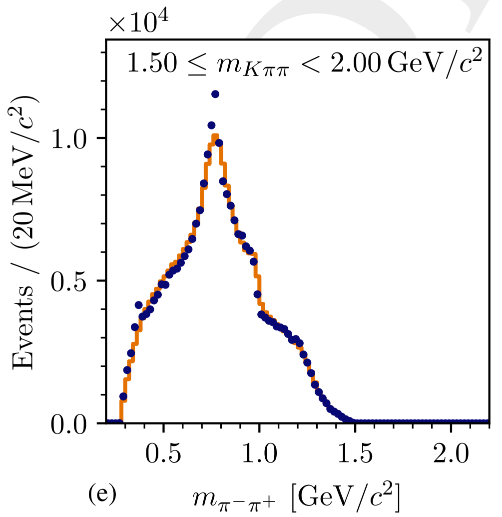

Figure 5.21: Distributions of the five phase-space variables defined for the $\pi^-\pi^+$ isobar system in the mass range $1.5 \leq m_{K\pi\pi} < 2.0\,\mathrm{GeV}/c^2$ integrated over the analyzed t' range. The blue points show the measured distributions. Their uncertainties are calculated assuming a Poisson distribution in each bin. The orange histograms show the corresponding PWD predictions.[bs]

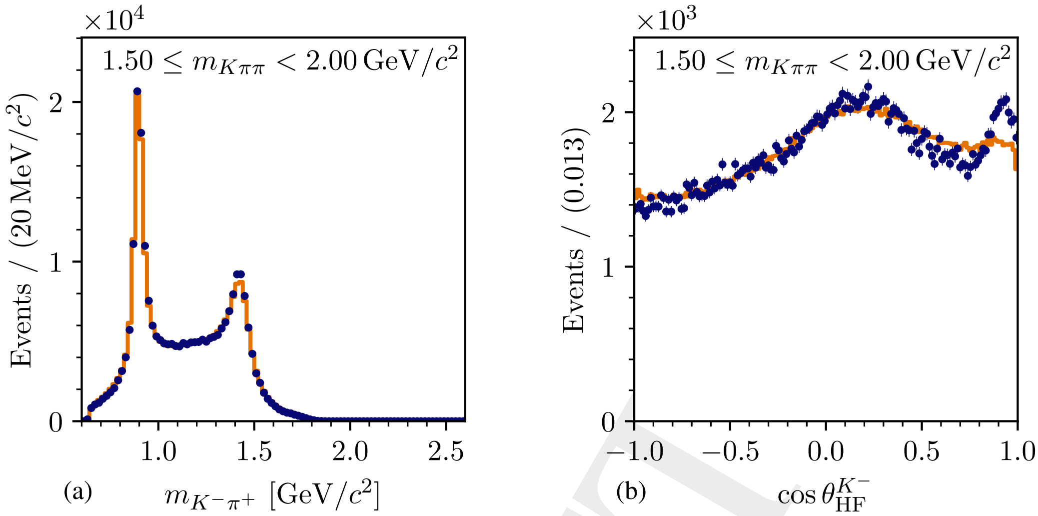

Figure 5.22: Distributions of two phase-space variables defined for the $K^-\pi^+$ isobar system in the mass range $1.5 \leq m_{K\pi\pi} < 2.0\,\mathrm{GeV}/c^2$ integrated over the analyzed t' range. The blue points show the measured distributions. The uncertainties are calculated assuming a Poisson distribution in each bin. The orange histograms show the corresponding PWD predictions. (a) shows the distribution in $m_{K^-\pi^+}$. (b) shows the distribution in $\cos\theta_{\mathrm{HF}}^{K^-}$ of the decay $\xi^0_{K^-\pi^+} \to K^-\pi^+$.

well by the PWD model; which suggest that we do not miss isobar resonances that contribute significantly to the data, i.e. that the list of isobar resonances considered when constructing the wave pool was sufficient (see table 5.2).

However, we also observe regions where the PWD model does not perfectly reproduce the measured distributions. The angular distributions of the X^- decay are not perfectly described as shown, e.g. in figure 5.21b. This imperfection becomes more apparent in the 2D distribution of the Gottfried-Jackson angles, i.e. when not marginalizing over $\cos\theta_{\mathrm{GJ}}^{\pi\pi}$ or $\phi_{\mathrm{GJ}}^{\pi\pi}$. The difference between the measured distribution in the Gottfried-Jackson angles and the corresponding PWD prediction is shown in figure 5.23a relative to the expected standard deviation in each $(\cos\theta_{\mathrm{GJ}}^{\pi\pi}, \phi_{\mathrm{GJ}}^{\pi\pi})$ cell according to a Poisson distribution. We observe a band (blue region) where the PWD model underestimates the measured number of events. This band coincides with the kinematic region where the acceptance changes most and practically vanishes as shown by the dark blue region in figure 5.23b. This strong modulation of the acceptance is caused by the limited momentum range of the final-state particle identification by the RICH detector (see section 3.2.2). The imperfection in the description of the measured distributions by the PWD model may indicate that the treatment of acceptance effects caused by the RICH is not complete (see appendix C.2.3 for details on how we modeled the RICH acceptance). We studied the robustness of the PWD results against incompleteness in the treatment of the RICH acceptance in the systematic studies described in section 5.7. The acceptance for the reaction $K^- + p \to K^-\pi^-\pi^+ + p$ is discussed in appendix D.2.

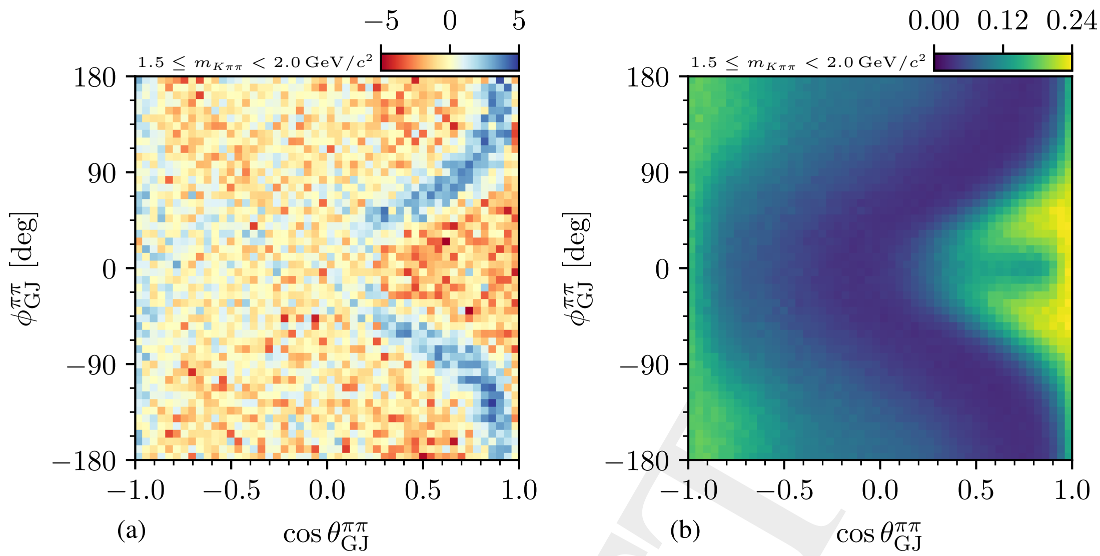

Figure 5.23: Distribution of the two two-body decay angles for the decay $X^- \to \xi^0_{\pi^-\pi^+} K^-$ in the mass range $1.5 \leq m_{K\pi\pi} < 2.0\,\mathrm{GeV}/c^2$ integrated over the analyzed t' range. (a) shows the difference between the measured number of events and the corresponding PWD prediction[bs] divided by the square root of the PWD prediction. (b) shows the acceptance.

As discussed in section 4.2, we expect about 4 % background from events of the reaction $K^- + p \to K^-K^-K^+ + p$ in the $K^-\pi^-\pi^+$ sample. A part of these background events, where the $K^-\ K^+$ subsystem arises from a $\phi(1020)$ decay, manifests itself in a narrow peak at about $0.38\,\mathrm{GeV}/c^2$ in the $m_{\pi^-\pi^+}$ spectrum observed in the measured data (blue data points in figure 5.21e). As expected, this $\phi(1020)$ peak is not reproduced by the PWD model as the 238-wave set is not able to effectively describe such a narrow signal. Furthermore, the background from $\phi(1020)$ decays is more pronounced at $m_{K\pi\pi}$ above $2\,\mathrm{GeV}/c^2$ than in the low-$m_{K\pi\pi}$ region (compare figures D.36e and D.40e). The $K^-K^-K^+$ background should be also visible in the phase-space variables defined for the $K^-\pi^+$ isobar system. For example, we observe an enhancement at $\cos\theta_{HF}^{K^-} \approx 0.9$ as shown in figure 5.22b, which is not reproduced by the PWD model, similar to the $\phi(1020)$ peak in the $m_{\pi^-\pi^+}$ spectrum. This enhancement accounts for about 2 % of the total distribution. We expect this enhancement to mainly arise from part of the about 4 % $K^-K^-K^+$ background, because the angular distribution as predicted from a simplified model for the reaction $K^- + p \to K^-\phi(1020) + p$ with $\phi(1020) \to K^-K^+$ strongly peaks at $\cos\theta_{HF}^{K^-} \approx 0.95$, similar to the enhancement observed in our data.[bt] Hence, the discrepancies between the measured distribution and the PWD prediction discussed in this paragraph are mainly due to the non-description of part of the $K^-K^-K^+$ background. The other part of the $K^-K^-K^+$ background is effectively taken into account by using a rank = 3 PWD model as discussed in section 5.3. We do not expect that this small non-description biases significantly the physics results of this analysis, i.e. the measurement of the resonance parameters discussed in chapter 6. The $K^-K^-K^+$ background belongs to a different coherent sector than the $K^-\pi^-\pi^+$ resonance contribution that we

[bt] We generated a pseudodata sample of the reaction $K^- + p \to K^-\phi(1020) + p$ with $\phi(1020) \to K^-K^+$, because the events from $\phi(1020)$ decays are a significant contribution to the total $K^-K^-K^+$ background. We used a simplified model based on the findings in ref. [37] and analyzed this pseudodata sample applying the $K^-\pi^-\pi^+$ hypothesis.

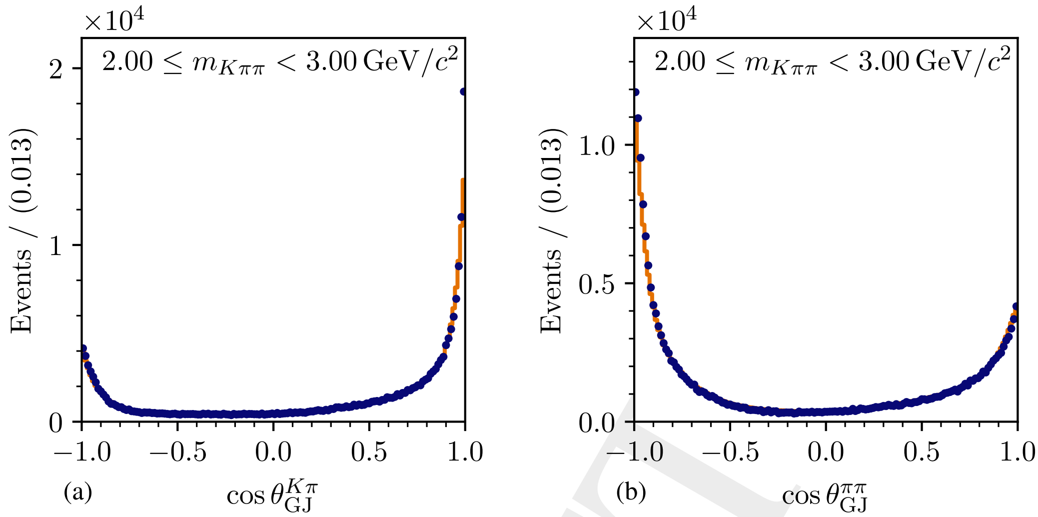

Figure 5.24: Agreement between PWD model and data in the mass range $2.0 \leq m_{K\pi\pi} < 3.0\,\mathrm{GeV}/c^2$ integrated over the analyzed t' range. The blue points show the measured distributions. The uncertainties are calculated assuming a Poisson distribution in each bin. The orange histograms show the corresponding PWD predictions. (a) shows the distribution in $\cos\theta_{\mathrm{GJ}}^{K\pi}$ of the decay $X^- \to \xi^0_{K^-\pi^+}\pi^-$. (b) shows the distribution in $\cos\theta_{\mathrm{GJ}}^{\pi\pi}$ of the decay $X^- \to \xi^0_{\pi^-\pi^+}K^-$.

are interested in. Furthermore, we tested the robustness of the PWD results against the influence of the $K^-K^-K^+$ background contributions in the systematic studies of the final-state particle identification discussed in section 5.7.1, because weaker or more restrictive particle-identification cuts change the fraction of the $K^-K^-K^+$ background in the $K^-\pi^-\pi^+$ sample.

Figure 5.24 shows the $\cos\theta_{\mathrm{GJ}}$ distributions for the X^- decay in the $m_{K\pi\pi}$ region above $2\,\mathrm{GeV}/c^2$. The distribution for the decay to the $K^-\pi^+$ isobar system shown in figure 5.24a peaks strongly towards $\cos\theta_{\mathrm{GJ}}^{K\pi} = +1$, i.e. we observe an enhancement of events where the $K^-\pi^+$ system goes in forward direction with respect to the direction of the beam K^- in the $K^-\pi^-\pi^+$ center-of-momentum frame. The distribution for the decay to the $\pi^-\pi^+$ isobar system shown in figure 5.24b peaks strongly towards $\cos\theta_{\mathrm{GJ}}^{\pi\pi} = -1$, i.e. we observe an enhancement of events where the $\pi^-\pi^+$ system goes backwards in the $K^-\pi^-\pi^+$ center-of-momentum frame. This behavior is consistent with models for non-resonant production. In Deck-like reactions, the $K^-\pi^+$ system is produced at the upper vertex by exchanging a virtual pion (see figure 2.2a), so that the $K^-\pi^+$ system goes mainly in the direction of the beam K^- leading to a peak at $\cos\theta_{\mathrm{GJ}}^{K\pi} = +1$. Kinematically, this peak becomes sharper at higher $m_{K\pi\pi}$ [123]. In central-production reactions (see figure 2.3a), the beam K^- scatters elastically and a $\pi^-\pi^+$ system is produced approximately at rest in the overall $K^-_{\mathrm{beam}}p_{\mathrm{target}}$ center-of-momentum frame. In the Gottfried-Jackson angles defined in the $K^-\pi^-\pi^+$ center-of-momentum frame, this translates to $\cos\theta_{\mathrm{GJ}}^{\pi\pi} \approx -1$. At high $m_{K\pi\pi}$, $\cos\theta_{\mathrm{GJ}}^{\pi\pi}$ is kinematically anti-correlated with $\cos\theta_{\mathrm{GJ}}^{K\pi}$. Therefore, we attribute both peaks at $\cos\theta_{\mathrm{GJ}}^{K\pi} = +1$ and $\cos\theta_{\mathrm{GJ}}^{\pi\pi} = -1$ in our data to both, Deck-like and central-production reactions. Based only on the angular distributions we cannot separate the two processes.[bu] The narrow peaks in the

[bu] Deck-like reactions with pion exchange exhibit structures from $K^-\pi^+$ resonances in the $m_{K^-\pi^+}$ distribution and

measured angular distributions can be described fairly well by the PWD model mainly by using partial waves with high spin $J \gtrsim 5$ shown in figures 5.18c and 5.18d. The description of the non-resonant processes in terms of partial waves requires in principle infinitely high spins [124], but including waves with $J \gg 7$ in the wave pool would significantly increase its size. Thus, we decided to consider only waves with $J \leq 7$ when constructing the wave pool in section 5.2.1, at the expense of small imperfections in the description of the $\cos\theta_{\text{GJ}}$ distribution for $\cos\theta_{\text{GJ}}^{K\pi} \approx +1$ and accordingly $\cos\theta_{\text{GJ}}^{\pi\pi} \approx -1$ at high $m_{K\pi\pi}$.[bv]

Overall, the PWD model describes the kinematic distributions of the $K^-\pi^-\pi^+$ sample well. Therefore, we conclude that the PWD fit yielded reliable results that can be interpreted in terms of physics signals. The small remaining imperfections can be attributed to non-resonant and incoherent background contributions, for which the $K^-\pi^-\pi^+$ partial waves were not constructed, or to potential imperfections of the detector model used to estimate the acceptance. We test the influence of these imperfections in the systematic studies discussed in the following section 5.7.

5.7 Systematic Studies

Given the increasing size of data samples from high-precision experiments, the statistical uncertainties become smaller and uncertainties imposed by systematic effects play a more important role. This underlines the importance of performing detailed systematic studies to test the influence of systematic effects on the analysis results. For example, the systematic uncertainties of measured masses and widths of isovector light-meson resonances observed in the COMPASS $\pi^-\pi^-\pi^+$ analysis are more than a factor 10 larger compared to the corresponding statistical uncertainties [41].

Acceptance effects were taken into account in the PWD fits as explained in section 5.1.3. Nonetheless, the model for the acceptance may be imperfect, which may introduce systematic effects in the results of the PWD. This holds especially for analyses where the acceptance is strongly modulated in the kinematic variables in which the analysis is performed, as it is the case in this work (see figure 5.23b and appendix D.2). The strongest acceptance effect in the $K^-\pi^-\pi^+$ sample arises from the limited kinematic range of the final-state particle identification by the RICH detector. Also, the misidentification of final-state particles by the RICH is the largest source of background events in the $K^-\pi^-\pi^+$ sample. Therefore, we present in section 5.7.1 three systematic studies that test the influence of the final-state particle identification on the results of the PWD.

a continuous spectrum in the $m_{\pi^-\pi^+}$ distribution, while central-production reactions with a centrally produced $\pi^-\pi^+$ system exhibit structures from $\pi^-\pi^+$ resonances in the $m_{\pi^-\pi^+}$ distribution and a continuous spectrum in the $m_{K^-\pi^+}$ distribution. Still, based only on kinematics the two processes cannot be separated completely, because their kinematic distributions overlap.

[bv] In the COMPASS $\pi^-\pi^-\pi^+$ analysis, first studies were performed of including models for Deck and central-production amplitudes into the PWD model to account for non-resonant contributions [43, 125]. In these studies, the description of the data by the model improved. However, these studies did not yield a convincing description of all non-resonant contributions yet [125].

Another important source of systematic effects are assumptions entering the PWD model. The most critical of these assumptions is the used wave set. In order to minimize systematic effects caused by the chosen wave set, we inferred the wave set from data using the model-selection techniques discussed in section 5.2. Nonetheless, the employed wave-set selection method may induce systematic effects in the selected wave set and thereby in the PWD results. To test for such effects, we present in section 5.7.2 an alternative approach for the wave-set selection.

In order to estimate the systematic effects, we compare in the following the results from the studies to those from the 238-wave PWD of the main analysis shown in section 5.5. In particular, we compare intensity spectra of partial waves, representative for the results of the PWD. However, performing a Bootstrapping of the PWD fit as done in the main analysis (see section 5.4) is computationally too expensive and cannot be done for the systematic studies. Thus, we show in sections 5.7.1 and 5.7.2 the maximum-likelihood estimates of the partial-wave intensities. As for the main analysis, we expect the bias from using the maximum-likelihood estimates to be small on average (see figure 5.13b). As the maximum-likelihood estimates of the uncertainties are strongly biased towards larger values (see section 5.4), we do not show error bars for the results of the systematic studies. For the results of the main analysis, we show the estimates from Bootstrapping for the values and uncertainties as in the rest of the text.

5.7.1 Final-State Particle Identification

In order to test for systematic effects introduced by the final-state particle identification, we performed three systematic studies where we changed the acceptance and the misidentification probability of the final-state particle identification in three different ways. We accounted for the different acceptances by adjusting our acceptance model accordingly in the PWD fits. We used the 238-wave set for the PWD, which is also used in the main analysis. In these RICH studies we tested three aspects: (i) can the acceptance model reproduce the corresponding change in the RICH acceptance; (ii) are the results of the PWD sensitive to the shape of the acceptance; and (iii) is the PWD result robust with respect to bias caused by misidentified final-state particles?

The probabilities to identify and misidentify a final-state particle are functions of the particle momentum that change when changing the RICH likelihood-ratio threshold $\mathcal{T}_\mathrm{R}$ as shown in figure 3.13. Especially, the region between 30 and 60 GeV/c, where the efficiency drops, is sensitive to the choice of $\mathcal{T}_\mathrm{R}$. We performed two systematic studies in which we changed $\mathcal{T}_\mathrm{R}$.

In one study, we used a weaker RICH threshold of $\mathcal{T}_\mathrm{R} = 1.05$ instead of 1.15, which is used in the main analysis. Using a lower RICH threshold increases the fraction of misidentified K^- and π^- in the final state to about 8 %, which is a factor of 4 larger than in the main analysis (see figure 3.14). In addition, the size of the data sample in this study is about 17 % larger than in the main analysis. Also, the momentum range, in which the RICH identifies a particle efficiently, is slightly enlarged when using the weaker RICH threshold (see figure 3.13a). Thus, we have access to a larger fraction of the $K^-\pi^-\pi^+$ phase-space in this study, which adds more information to the PWD fit, at the expense of a reduced purity of the sample.

In the second study, we used a more restrictive RICH threshold of $\mathcal{T}_\mathrm{R} = 1.30$ instead of 1.15. This reduces the misidentification probability only marginally, while it introduces much stronger acceptance effects. In this study, the size of the data sample is about 30 % smaller than in the main analysis. One should note, that for such a significantly reduced data sample the 238-wave set, which was selected based on the larger $K^-\pi^-\pi^+$ sample of the main analysis, might be too large. This might introduce artifacts from overfitting in the PWD.

As presented in section 5.6, we observe imperfections in the description of the data by the PWD model in kinematic regions where the acceptance decreases rapidly. These imperfections may be caused by imperfections of the employed acceptance model in these regions. Therefore, we excluded in the third RICH study the region in the final-state particle momenta, in which the identification probability decreases most rapidly, i.e. we limited the RICH particle identification to momenta below 40 GeV/c instead of 60 GeV/c, which was used in the main analysis. This hard cut in the particle momenta can be perfectly reproduced by the acceptance model in this study, while modeling the momentum dependence of the particle-identification probability as done in the main analysis (see appendix C.2.3) implicates some approximations. For example, the dependence of the particle-identification probability on other kinematic variables, such as the position at which the particle traverses the RICH detector, is neglected.[bw] Applying the more restrictive RICH momentum cut reduces the sample size by about 10 % compared to the main analysis.

Figure 5.25 compares the results of the PWD from the three RICH studies to those from the main analysis for four exemplary selected partial waves. Overall, we find good agreement of the results from the three RICH studies and from the main analysis for most partial waves. For example, the intensity spectrum of the $1^+\,0^+\,\rho(770)\,K\,S$ wave shown in figure 5.25a exhibits the same peak at about 1.3 GeV/c^2 in all studies and in main analysis. Also, the shoulder at about 1.5 GeV/c^2 and the high-mas tail of the intensity spectrum agrees among all results. Only for the small plateau between about 1.0 and 1.2 GeV/c^2, the study with a more restrictive RICH threshold (red data points) yielded slightly higher intensities compared to the main analysis, while the studies with a weaker RICH threshold (green data points) and with a more restrictive momentum limit (orange data points) yielded a slightly lower intensity. Therefore, we conclude, that this small plateau is an artifact from imperfections in our analysis.

Such artifacts may arise from overfitting or from destructive interferences, because both are sensitive also to small systematic effects. Such artifacts are visible especially in small partial waves at the per-mill level, e.g. in the $4^+\,1^+\,K^*(892)\,\pi\,G$ wave shown in figure 5.25b. In the $m_{K\pi\pi}$ region above 2 GeV/c^2, where we expected the high-mass tail of the $K_4^*(2045)$ resonance, the RICH studies yielded results that are similar to those from the main analysis, except for the study with a more restrictive RICH threshold, which yielded slightly different results. However, this difference can be explained by the 30 % smaller amount of data in this study, which may

[bw] The dependence of the particle-identification probability on other kinematic variables, except for the momentum and the track angle of the particle, is assumed to be small. This assumption is supported by a first study of the $\pi^\pm$ identification probability as a function of the position at which the particle traverses the RICH. This study revealed only a weak dependence of the particle-identification probability on the position at which the particle traverses the RICH.

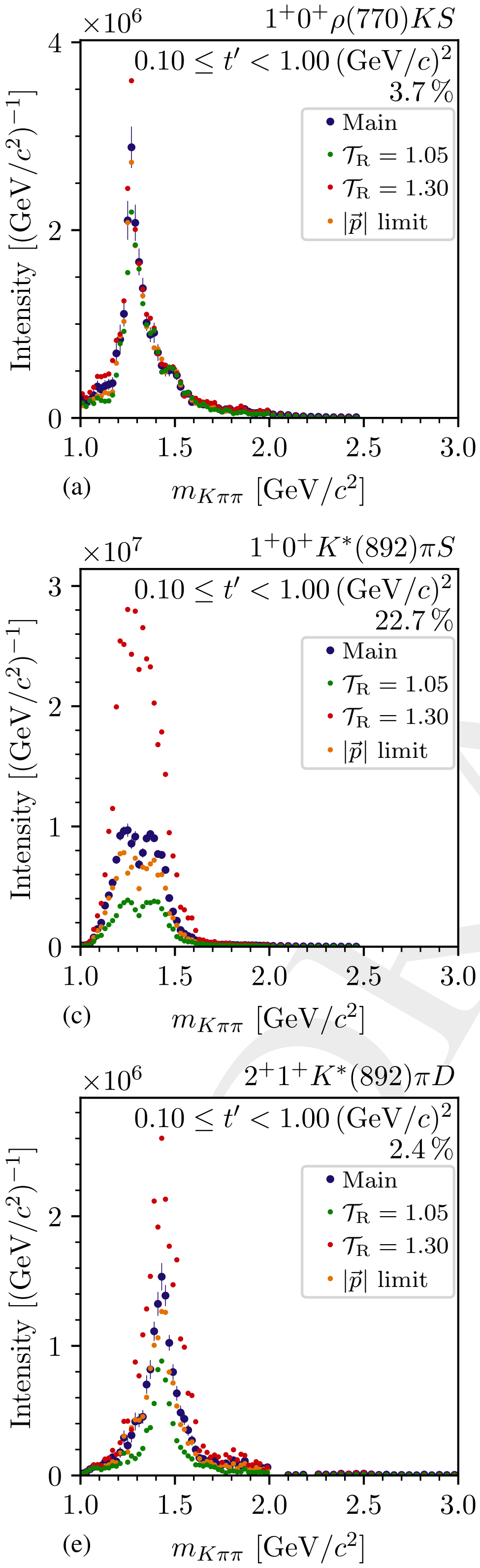

Figure 5.25: Comparison between the PWD results from the three RICH studies and from the main analysis. (a) to (e) show the t'-summed intensity spectra of four selected partial waves. The blue data points show the Bootstrapping estimates from the main analysis. The green, red, and orange data points show the maximum-likelihood estimates from the studies with a weaker RICH threshold of $\mathcal{T}_\mathrm{R} = 1.05$, with a more restrictive RICH threshold of $\mathcal{T}_\mathrm{R} = 1.30$, and with a more restrictive momentum limit of $40\,\mathrm{GeV}/c$ for final-state particle identification, respectively. We do not show uncertainties for the maximum-likelihood estimates from the systematic studies (see text).

lead to artifacts from overfitting in addition to the statistical fluctuations. The enhancement in the intensity below about $2\,\mathrm{GeV}/c^2$ is sensitive to systematic effects. Especially, the study with weaker RICH threshold yields a smaller enhancement. We observe similar results for other partial waves that exhibit such enhanced low-mass tails such as the $2^-\,0^+\,\rho(770)\,K\,F$ wave shown in figure 5.20a. These observations support our assumption that these enhanced low-mass tails are mainly analysis artifacts. They become smaller when adding information to the PWD fit as done in the study with weaker RICH threshold.

Given the good agreement between the various systematic RICH studies and the main analysis for most partial waves, we observe surprisingly large effects in some other waves. Two of these waves are shown as an example in figures 5.25c and 5.25d. As expected, we observe in the main analysis a double-peak structure in the intensity spectrum of the $1^+\,0^+\,K^*(892)\,\pi\,S$ wave, which presumably originates from the known $K_1(1270)$ and $K_1(1400)$ resonances. The RICH studies yielded similar shapes, but with intensities that are different by a factor more than 2. Especially the study with a more restrictive RICH threshold yielded an about 2.6 times larger intensity and the study with a weaker RICH threshold yielded an about 2.5 times smaller intensity. Above about $1.6\,\mathrm{GeV}/c^2$, we find again good agreement of the results from the RICH studies with the main analysis. As already discussed for the total intensity distribution of waves with $J^P = 3^+$ in section 5.5, we observe a peak-like structure in the intensity spectrum of the $3^+\,1^+\,K^*(892)\,\pi\,D$ wave in the mass range between about 1.2 and $1.6\,\mathrm{GeV}/c^2$ (see figure 5.25d). However, there is no known or expected K_3 state in this mass region (see figure 1.1). Furthermore, this low-mass structure is very sensitive to systematic effects, similar to the double-peak in the $1^+\,0^+\,K^*(892)\,\pi\,S$ wave. The structure in the $3^+\,1^+\,K^*(892)\,\pi\,D$ wave nearly vanishes in the study with a weaker RICH threshold, while it becomes almost a factor 3 larger in the study with a more restrictive RICH threshold. Interestingly, the mass range of about 1.0 to $1.6\,\mathrm{GeV}/c^2$, in which we observe the large systematic effects described above, coincided with the mass range of the low-mass structure seen in the $3^+\,1^+\,K^*(892)\,\pi\,D$ wave. Also, the $2^+\,1^+\,K^*(892)\,\pi\,D$ wave shown in figure 5.25e is sensitive to systematic effects. While the shape of its intensity spectrum is similar in the RICH studies and in the main analysis, its intensity becomes larger in the study with a more restrictive RICH threshold and smaller in the study with a weaker RICH threshold, analogously to the two waves discussed above. However, in the $2^+\,1^+\,K^*(892)\,\pi\,D$ wave these systematic effects are much weaker compared to the $1^+\,0^+\,K^*(892)\,\pi\,S$ and $3^+\,1^+\,K^*(892)\,\pi\,D$ waves. Before being able to conclude on the origin of this effect in section 5.9, we add another piece of information obtained from the pseudodata studies presented in section 5.8.

5.7.2 Alternative Approach for Wave-Set Selection

The potentially largest sources of systematic effects in the wave-set selection are the regularization term used to suppress insignificant waves in equation (5.53) and the term in equation (5.57) designed to impose continuity. In the main analysis, we chose a certain form for these terms based on experience from previous analyses and based on tests using other forms (see sections 5.2.2 and 5.2.3). Also, the choice of the parameter values for Γ and λ appearing in the regularization and continuity terms may introduce systematic effects.

Therefore, we used in this study an alternative approach for the wave-set selection fit based on information field theory (IFT) [126]. IFT is a Bayesian probability theory. It allows us to apply regularization and to impose continuity as a function of $m_{K\pi\pi}$ consistently using a common formalism. The regularization and continuity conditions are formulated in terms of the prior probability. The so-called hyperparameters of the prior probability are inferred from data by formulating hyperpriors for these parameters. Thereby, this approach potentially reduces the bias in the wave-set selection that originates from the choice of these parameters. We present in appendix G.1.1 the IFT model used in this study, which was developed in close collaboration with the information field theory group at the Max Planck institute for Astrophysics [127, 128]. In the IFT model, we formulated a prior probability that favors small partial-wave intensities and thus suppresses insignificant waves. Continuity of the transition amplitudes in $m_{K\pi\pi}$ is represented in terms of the correlations between the transition amplitudes at different $m_{K\pi\pi}$ locations. Continuity is imposed by requiring a strong correlation between nearby $m_{K\pi\pi}$ locations in the prior term, while allowing for weaker correlations between $m_{K\pi\pi}$ locations that are far apart. A detailed introduction to IFT is given in ref. [126].

In the IFT study, we follow the same strategy as outlined in section 5.2: Based on the same wave pool as used in the main analysis (see section 5.2.1) and applying the same thresholds for sub-threshold decays of heavy isobar resonances (see section 5.2.4), we performed wave-set selection fits that use the IFT approach to suppress insignificant waves and to impose continuity in the wave set. As in the main analysis, we used a rank=1 model for the wave-set selection fits. Based on the results of these wave-set selection fits, we constructed a wave set in each $(m_{K\pi\pi}, t')$ cell by requiring a minimal intensity for a partial wave to be selected, similar as in the main analysis discussed in section 5.2.5.[bx] Finally, we performed a PWD fit using equation (5.38) with these selected wave sets, which yielded the final results of the IFT study.

We used the Python framework NIFTy [129] to implement the IFT model in equation (G.15), together with the likelihood of the PWD for a single data set given in equation (5.33). Fitting of multiple data sets is not yet developed for this framework. Hence, we used only the $K^-\pi^-\pi^+$ sample from the 2008 diffraction data set for the wave-set selection fits in this study, which corresponds to about 56 % of the full $K^-\pi^-\pi^+$ sample. The reduced amount of data in this study might lead to smaller wave sets, because small signals may become insignificant with respect to the reduced precision. Employing the continuity condition as imposed by the IFT approach required us to include the full analyzed $m_{K\pi\pi}$ range in a single IFT wave-set selection fit, while in the main analysis we considered only small $m_{K\pi\pi}$ ranges of 15 bins in one fit. This prohibits using an $m_{K\pi\pi}$-dependent binning in $m_{K\pi\pi}$. Hence, we used 20 MeV/c^2 wide $m_{K\pi\pi}$ bins over the full analyzed $m_{K\pi\pi}$ range. For the final PWD with the selected wave set we used the 2008 and 2009 sample, and we used 40 MeV/c^2 wide bins for $m_{K\pi\pi} > 2$ GeV/c^2 as in the main analysis.

Figure 5.26 shows selected results from the IFT study. The size of the wave sets from the IFT wave-set selection fits as a function of behaves similar $m_{K\pi\pi}$ as in the main analysis (cf.

[bx] The IFT method does not produce jump discontinuities in the ordered partial-wave intensities. Thus, we used a constant intensity threshold of 3, which is the same value as used in the main analysis for $(m_{K\pi\pi}, t')$ cells where the automatic threshold detection failed (see appendix D.1.1).

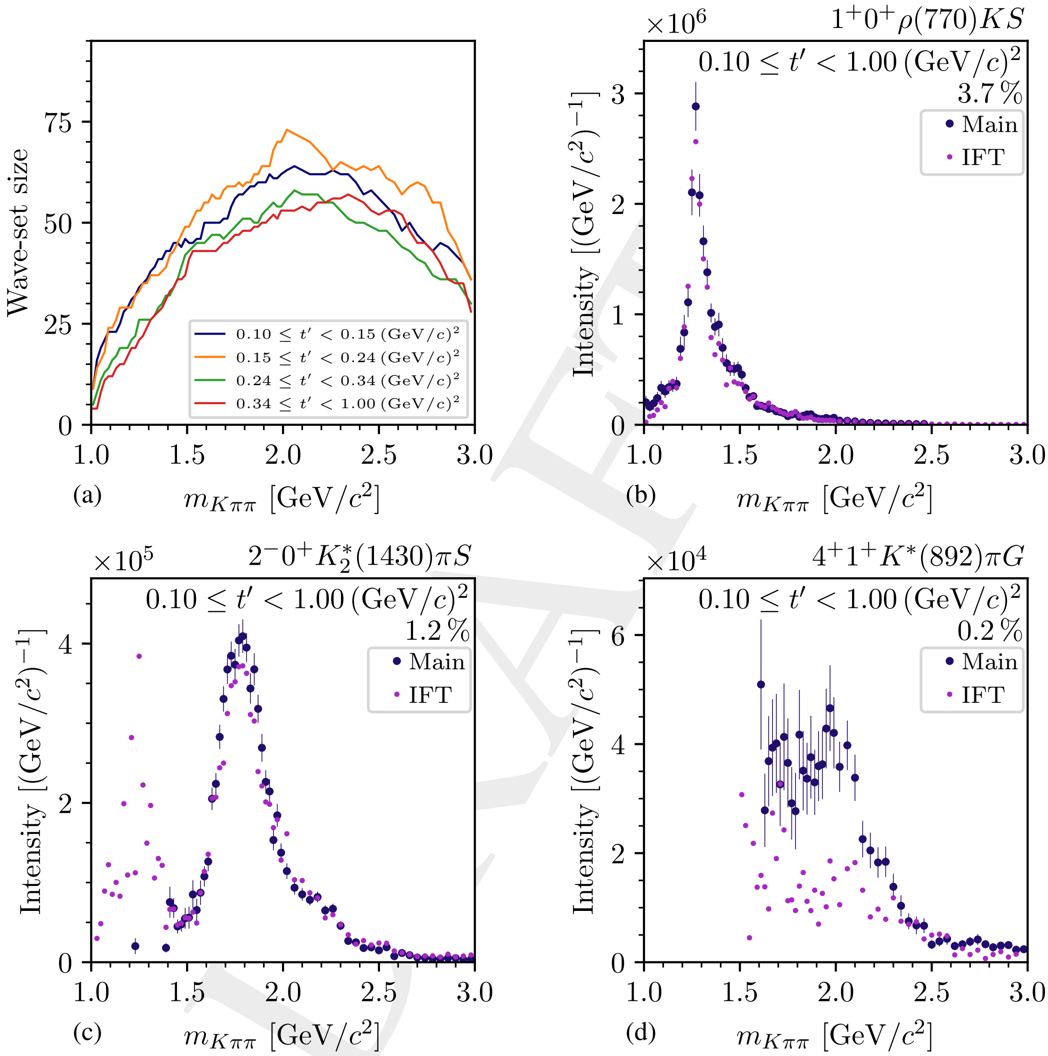

Figure 5.26: Results from the study using a wave set that was selected using IFT. (a) shows the size of the wave sets obtained in the IFT study as a function of $m_{K\pi\pi}$ in the four t' bins. (b) to (d) show the t'-summed intensity spectra of three selected partial waves. The blue data points show the Bootstrapping estimates from the main analysis. The violet data points show the maximum-likelihood estimates from the study using the wave set constructed from the IFT wave-set selection fits. We do not show uncertainties for the maximum-likelihood estimates form the systematic study (see text).

figures 5.10 and 5.26a). Only the jump of the wave-set size at $2\,\mathrm{GeV}/c^2$ is not visible in the IFT study as we did not change the $m_{K\pi\pi}$ binning here. The t' dependence of the wave-set size is also consistent with the main analysis. Given the potentially reduced bias in the IFT study by inferring the prior hyperparameters from data, this good agreement between the IFT study and the main analysis suggests that our choice for the regularization parameters was appropriate. This means that the regularization in the main analysis was strong enough to suppress insignificant waves so that the wave sets did not become too large and this means also the regularization in the main analysis was not too strong so that significant waves were not suppressed.

Considering all $(m_{K\pi\pi}, t')$ cells, the wave set from the IFT study consists of 104 partial waves.[by] This is significantly smaller than the 238-wave set selected in the main analysis. However, about 90 of the 238 partial waves contain only noise as discussed in section 5.2.6, while we find only six noisy waves in the IFT wave set. That these noisy waves were not included in the IFT wave-set demonstrates that IFT is a superior approach to impose continuity. One reason for this is that the whole analyzed $m_{K\pi\pi}$ range could be considered in a single IFT wave-set selection fit.

Figures 5.26b to 5.26d compare the result of the PWD using the IFT wave set (violet data points) to those from the main analysis (blue data points). For most partial waves, we find good agreement between the IFT study and the main analysis, exemplarily shown in figure 5.26b for the t'-summed intensity spectrum of the $1^+\,0^+\,\rho(770)\,K\,S$ wave. Thus, we expect no large systematic effects from the wave-set selection in the main analysis.

For some partial waves, we find low-mass enhancements in the IFT study. For example, the $2^-\,0^+\,K_2^*(1430)\,\pi\,S$ wave shown in figure 5.26c is practically not selected in the main analysis in $m_{K\pi\pi}$ bins below about $1.4\,\mathrm{GeV}/c^2$, while it was selected in the IFT study also below $1.4\,\mathrm{GeV}/c^2$ resulting in a low-mass enhancement that peaks about $1.3\,\mathrm{GeV}/c^2$. As there are no known or expected K_2 states in this mass region, we assume this low-mass enhancement to be a model artifact. The continuity of the wave set imposed by the IFT wave-set selection extends over the full analyzed $m_{K\pi\pi}$ range. This leads to a wider $m_{K\pi\pi}$ range in which the $2^-\,0^+\,K_2^*(1430)\,\pi\,S$ wave was selected. However, in the $m_{K\pi\pi}$ region below about $1.4\,\mathrm{GeV}/c^2$, the $2^-\,0^+\,K_2^*(1430)\,\pi\,S$ wave may destructively interference with other waves, which can case such low-mass enhancements as discussed for sub-threshold waves in section 5.2.4. For $m_{K\pi\pi} > 1.4\,\mathrm{GeV}/c^2$, the results from the IFT study agree well with those from the main analysis.

For some partial waves at the per-mill level such as the $4^+\,1^+\,K^*(892)\,\pi\,G$ wave shown in figure 5.26d, the IFT study disagrees with the main analysis. In contrast to the main analysis, the result of the IFT study does not exhibit a potential intensity peak from the $K_4^*(2045)$ resonance, which is expected to be observed in this partial wave at about $2\,\mathrm{GeV}/c^2$. Partial waves with such small intensities are most sensitive to bias from the selected wave set. Also the IFT method has some parameters that must be chosen a priori, e.g. the parameters of the hyper-priors in equations (G.13) and (G.14). As those parameters were not yet fine-tuned in the IFT study, their choice might lead to some bias in small waves from the IFT wave-set selection.

[by] In addition to the 104 partial waves, we also included the incoherent flat wave in the PWD fits.

Finally, we observe large systematic effects in those waves that exhibit low-mass structures and that already showed large systematic effects in the RICH studies discussed in section 5.7.1. Such a wave is, for example the $3^+\,1^+\,K^*(892)\,\pi\,D$ partial wave shown in figure G.3g.

Overall, the wave-set selection using IFT yielded very promising results. However, there are some caveats such as the missing $K_4^*(2045)$ signal, which have to be resolved before the IFT wave-set selection can be used in the main analysis.

Reviewing all studies presented in this section 5.7, the systematic studies and the main analysis agree well for most partial waves. From this we conclude that we expect no large systematic effects on the results of the PWD for these waves. appendix G.1, we present an overview over all systematic studies for those partial waves that are discussed in this work. However, for some partial waves, we observe large systematic effects in the mass region below $1.6\,\mathrm{GeV}/c^2$ together with unexpected low-mass structures in this mass region. These effects demand further clarification, and we will conclude on them in section 5.9.

5.8 Pseudodata Studies using the $K^-\pi^-\pi^+$ PWD Model

To further test the consistency of our PWD results, we studied our analysis in an environment where we controlled the input, i.e. where we knew the distribution from which the events were produced, how the measurement process distorted these distributions, and what values of the spin-density matrix elements we expect. These input-output studies were carried out by generating pseudodata samples. Hence, we call them pseudodata studies. What we will call produced pseudodata samples are simulated samples of events that are distributed according to a given physics model. In this section, we discuss samples that were generated according to a PWD model as given in equation (5.16). In order to study apparatus effects, i.e. resolution and acceptance effects, the produced pseudodata events are processed through the COMPASS detector Monte Carlo simulation and the event reconstruction algorithm.[bz] Then we applied the same event selection criteria as for the measured data. This procedure yields so-called reconstructed pseudodata samples, which resemble the distribution of measured events. A detailed description of how we generated these samples is given in appendix C.

In this section, we discuss pseudodata samples for the reaction $K^- + p \to K^-\pi^-\pi^+ + p$, which were generated according to three different PWD models. All three models are based on the results of a PWD fit of the 238-wave set to the measured $K^-\pi^-\pi^+$ sample, which is called the 238-wave pseudodata model in the text below.[ca] We applied the same procedure to the

[bz] We used the Monte Carlo simulation of the experimental setup of the 2008 diffraction data taking for all pseudodata studies. The 2009 setup is nearly identical to the 2008 setup. Thus, the conclusions drawn from the pseudodata studies using the 2008 setup can be applied to the main analysis of the measured $K^-\pi^-\pi^+$ sample from 2008 and 2009.

[ca] We generated the pseudodata samples by applying equation (5.16) with the maximum-likelihood estimates of the parameters from a PWD fit using a rank=1 model and the 238-wave set without applying table D.1. This model is called the 238-wave pseudodata model. This was done, because historically, we generated the pseudodata samples

pseudodata samples as in the main analysis; i.e. we applied the same event selection, which is discussed in section 4.1, and we performed a PWD using a rank=3 model and the 238-wave set.[cb] As for the systematic studies presented in section 5.7, performing a Bootstrapping of the PWD for all pseudodata studies was computationally too expensive. Thus, we present in this section the maximum-likelihood estimates from the PWD of the pseudodata samples, and we do not show the corresponding uncertainties. In section 6.4, we present pseudodata studies where we also performed a Bootstrapping.

5.8.1 Pseudodata Sample based on the 238-Wave Pseudodata Model

We generated a pseudodata sample of the reaction $K^- + p \to K^-\pi^-\pi^+ + p$ that is as similar as possible to the measured $K^-\pi^-\pi^+$ sample. To this end, we used the 238-wave pseudodata model. In total, we generated 50×10^6 produced events in the analyzed $m_{K\pi\pi}$ and t' range. About 3.18×10^6 events of all produced events were reconstructed, i.e. passed all event-selection criteria.[cc]

Figure 5.27 shows the t'-summed intensity spectra of four exemplary selected partial waves from the PWD of this pseudodata sample. The results of the PWD of the produced pseudodata sample (cyan data points), i.e. the pseudodata sample without acceptance and resolution effects,[cd] agree well with the reference model (blue crosses), i.e. the expectation from the 238-wave pseudodata model. This demonstrates that the PWD formalism presented in section 5.1 works in the ideal case with perfect acceptance and with a perfect PWD model, which by construction is able to describe the data.

The results of the PWD of the reconstructed pseudodata sample are shown by the green data points. The reconstructed pseudodata sample is afflicted with the same acceptance affects, resolution effects, and misidentification of the final-state particles as the measured data. Thus, we test in this pseudodata study whether our analysis is robust with respect to these apparatus effects. The results of this study agree with the reference model for most partial waves. We find good agreement for relatively large partial waves such as the $1^+\,0^+\,\rho(770)\,K\,S$ wave shown in figure 5.27a as well as for small waves at the per-mill level such as the $4^+\,1^+\,K^*(892)\,\pi\,G$ wave shown in figure 5.27b. In figure 5.25e we show that the intensity of the $2^+\,1^+\,K^*(892)\,\pi\,D$

before deciding to switch to a rank=3 spin-density matrix in the PWD, before extending the wave set from the wave-set selection fits according to table D.1, and before using Bootstrapping. As all three changes in the PWD resulted in a similar agreement between the PWD model and the measured data, the pseudodata samples based on the 238-wave pseudodata model reproduce the measured $K^-\pi^-\pi^+$ sample. As generating these pseudodata samples is computationally very expensive, we did not regenerate the pseudodata samples after changing the analysis.

[cb] We used the 238-wave set without applying table D.1 to be consistent with the 238-wave pseudodata model.

[cc] The fraction of reconstructed events corresponds to an average acceptance of 6.44 %. However, this estimate is strongly biased by the leakage effect as discussed in section 5.9.1. Based on the findings shown there, we estimated an actual average acceptance of about 12 %. This comparably low acceptance is mainly due to the limited kinematic range of the final-state particle identification.

[cd] As the produced pseudodata sample is not affected by acceptance effects, we used a perfect-acceptance model in the corresponding PWD fit, i.e. we used $\eta^{(i)}(\tau, m_{K\pi\pi}, t') = 1$ in equation (5.27).

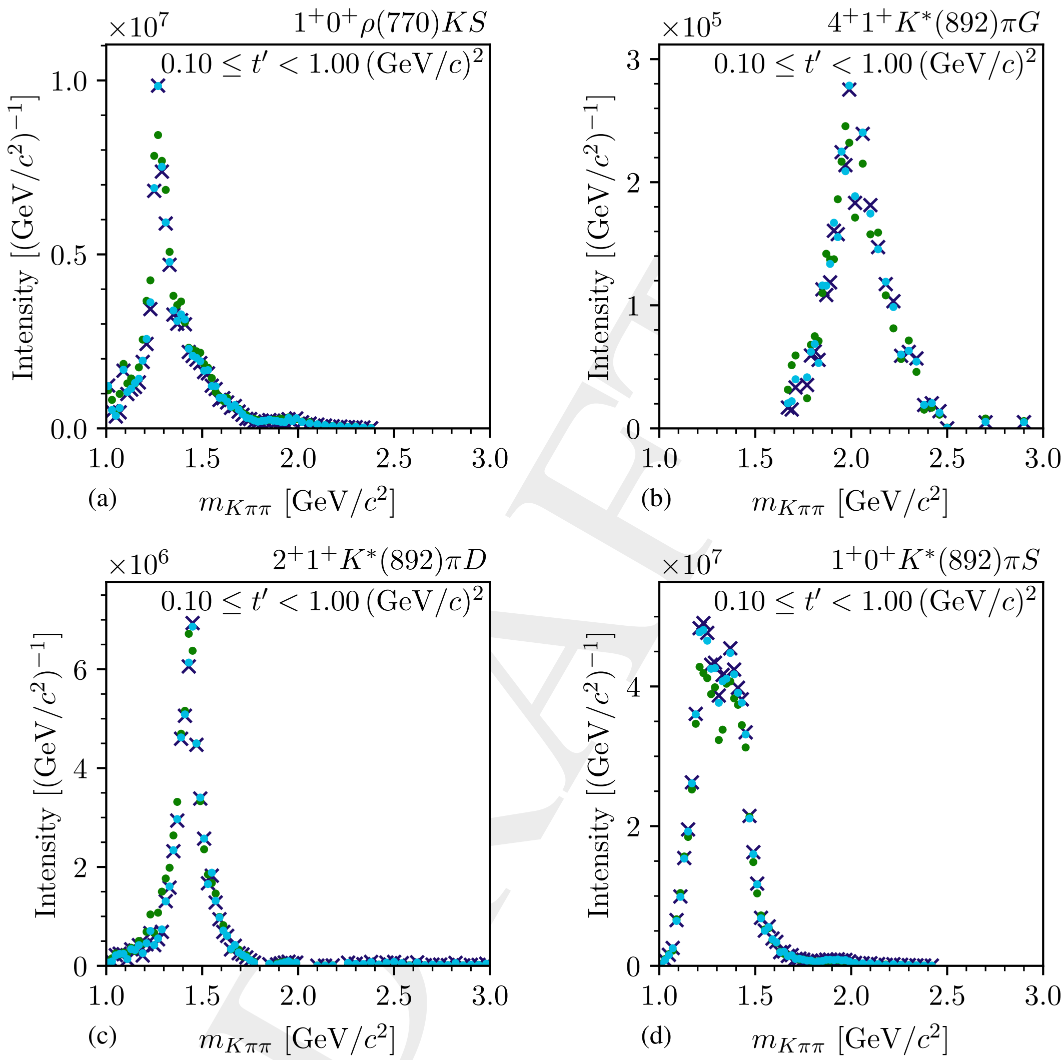

Figure 5.27: t'-summed intensity spectra of four selected partial waves as obtained from the PWD of the pseudodata sample that was generated using the full 238-wave pseudodata model. The cyan data points represent the PWD of the produced pseudodata sample. The green data points represent the PWD of the reconstructed pseudodata sample. The blue crosses represent the expected values, i.e. the values from the 238-wave pseudodata model scaled such that its prediction for the total number of produced events is equal to the number of produced pseudodata events. We show the maximum-likelihood estimates of the intensities obtained from the pseudodata. The corresponding maximum-likelihood estimates of the uncertainties are not shown (see text).

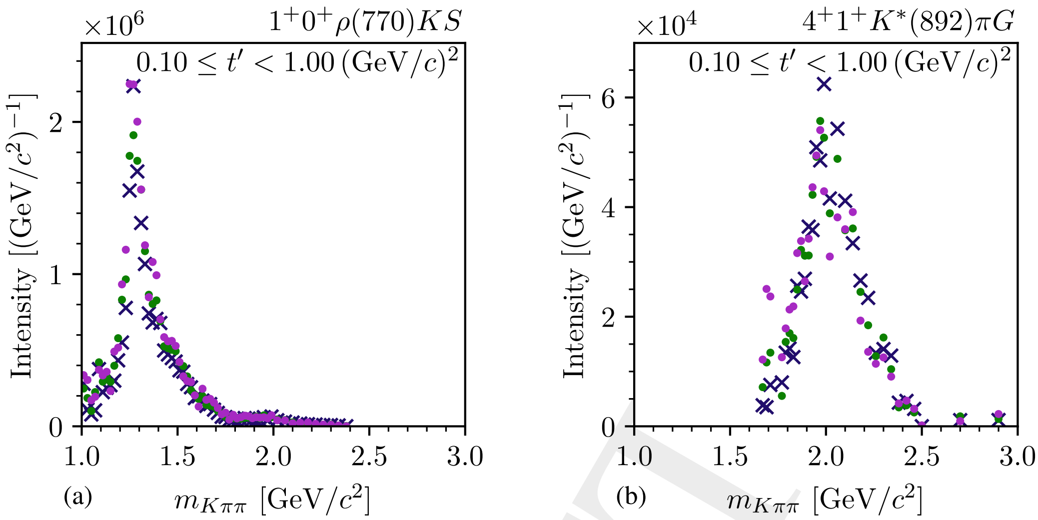

Figure 5.28: Same as figure 5.27, but showing in addition to the results of the PWD of a subset of 720×10^3 events of the reconstructed pseudodata sample (violet data points).

wave exhibits a modest sensitivity to systematic effects. In contrast, we find here consistent results for the intensity spectrum of the $2^+\,1^+\,K^*(892)\,\pi\,D$ wave in figure 5.27c. Hence, the $2^+\,1^+\,K^*(892)\,\pi\,D$ wave is interpreted in terms of physics signals as discussed in section 7.2. From the findings discussed in this paragraph we conclude that the signals in most of the partial waves are robust with respect to these apparatus effects.

As expected, we observe larger fluctuations of the results from the reconstructed pseudodata sample compared to those from the produced pseudo data samples because the size of the reconstructed pseudodata sample is about 20 times smaller. Still, the reconstructed pseudodata sample is about 4.3 times larger than the measured $K^-\pi^-\pi^+$ sample and thus more precise. To test whether the sample size biases the results of the PWD, we performed a PWD where we used only a sub-sample of 720×10^3 events of the reconstructed pseudodata sample, which hence has the same size as the measured $K^-\pi^-\pi^+$ sample. The violet data points in figure 5.28 show the results of this study for two exemplary selected waves. The results are similar to those using the full reconstructed pseudodata sample (green data points) and to the 238-wave pseudodata reference model (blue crosses), even for waves at the per-mill level such as the $4^+\,1^+\,K^*(892)\,\pi\,G$ wave shown in figure 5.28b. Thus, we conclude, that our analysis is robust with respect to statistical fluctuations, e.g. that we do not expect large artifacts from overfitting in most partial waves.

However, there is a certain set of partial waves for which the results from the reconstructed pseudodata sample do not agree well with the 238-wave pseudodata reference model. For example, the intensity spectrum of the $1^+\,0^+\,K^*(892)\,\pi\,S$ wave obtained from the reconstructed pseudodata sample (green points in figure 5.27d) is slightly but systematically smaller compared to the reference model in the $m_{K\pi\pi}$ region below about $1.6\,\mathrm{GeV}/c^2$. Interestingly, we observe these discrepancies only in the PWD of the reconstructed pseudodata sample, while the results obtained from the produced pseudodata sample agree with the reference. As the difference between both pseudodata samples are acceptance effects, this suggests that this discrepancy is related to effects from the experimental acceptance.[ce] Understanding these discrepancies requires further investigations, which will be summarized in section 5.9.

5.8.2 Introducing Imperfections into the Pseudodata

In this section we test the robustness of our PWD with respect to imperfections in the analysis model. To this end, we used the reconstructed pseudodata sample based on the 238-wave pseudodata model, but performed a PWD fit using a detuned acceptance model. Instead of using the acceptance model of the main analysis, which would be the correct one, we used the acceptance model from the systematic study with a more restrictive momentum limit for the RICH final-state particle identification (see section 5.7.1). This means we identified final-state pions and kaons up to 60 GeV/c in the reconstructed pseudodata sample, but when fitting the PWD model to this pseudodata sample, we wrongly set the probability to identify final-state particles to zero in the range $40 \leq |\vec{p}| < 60\,\mathrm{GeV}/c$ in the acceptance model. This introduced a modest but not negligible imperfection in the PWD fit. In particular, the introduced imperfection is located in a kinematic region where the acceptance in the main analysis strongly changes and where we observe some deviations between the PWD model predictions and the measured data in this kinematic region as discussed in section 5.6. Thus, we expect the PWD fit to be sensitive to imperfections especially in this kinematic region. As we modeled the acceptance in this kinematic region in the acceptance model used in the main analysis, we assume that the imperfections in the measured data are not larger than the imperfections introduced in this study. Hence, the study using the detuned acceptance model is suited well to test the robustness of the PWD.

The orange data points in figure 5.29 represent the results of the PWD using the detuned acceptance model. Given the introduced imperfection, we still find good agreement between the results of this study and the 238-wave pseudodata reference model (blue crosses) for most of the waves as exemplarily shown in figures 5.29a and 5.29b. Only in the low-mass tail of the $1^+\,0^+\,\rho(770)\,K\,S$ wave shown in figure 5.29a, i.e. in the $m_{K\pi\pi}$ region below about $1.3\,\mathrm{GeV}/c^2$, this study yielded intensities slightly larger than the reference model. This might indicate that the imperfections due to the detuned acceptance model lead to small artifacts in the low-mass region, similar to the low-mass enhancements discussed in section 5.5. Nonetheless, from the good agreement found in most of the partial waves we conclude that our analysis model and analysis procedure is robust with respect to such modest imperfections in the description of the acceptance.

[ce] In addition to acceptance effects, the reconstructed pseudodata sample is also affected by resolution effects. We excluded that the observed discrepancies are caused by resolution effects in a study, where we used the true physical values of the kinematic variables, i.e. the values with which the event was produced, in the PWD of the reconstructed pseudodata sample instead of using the reconstructed values. Hence, in this study the PWD fit is free of resolution effects. The results of this study show similar discrepancies as those observed when using the reconstructed quantities.

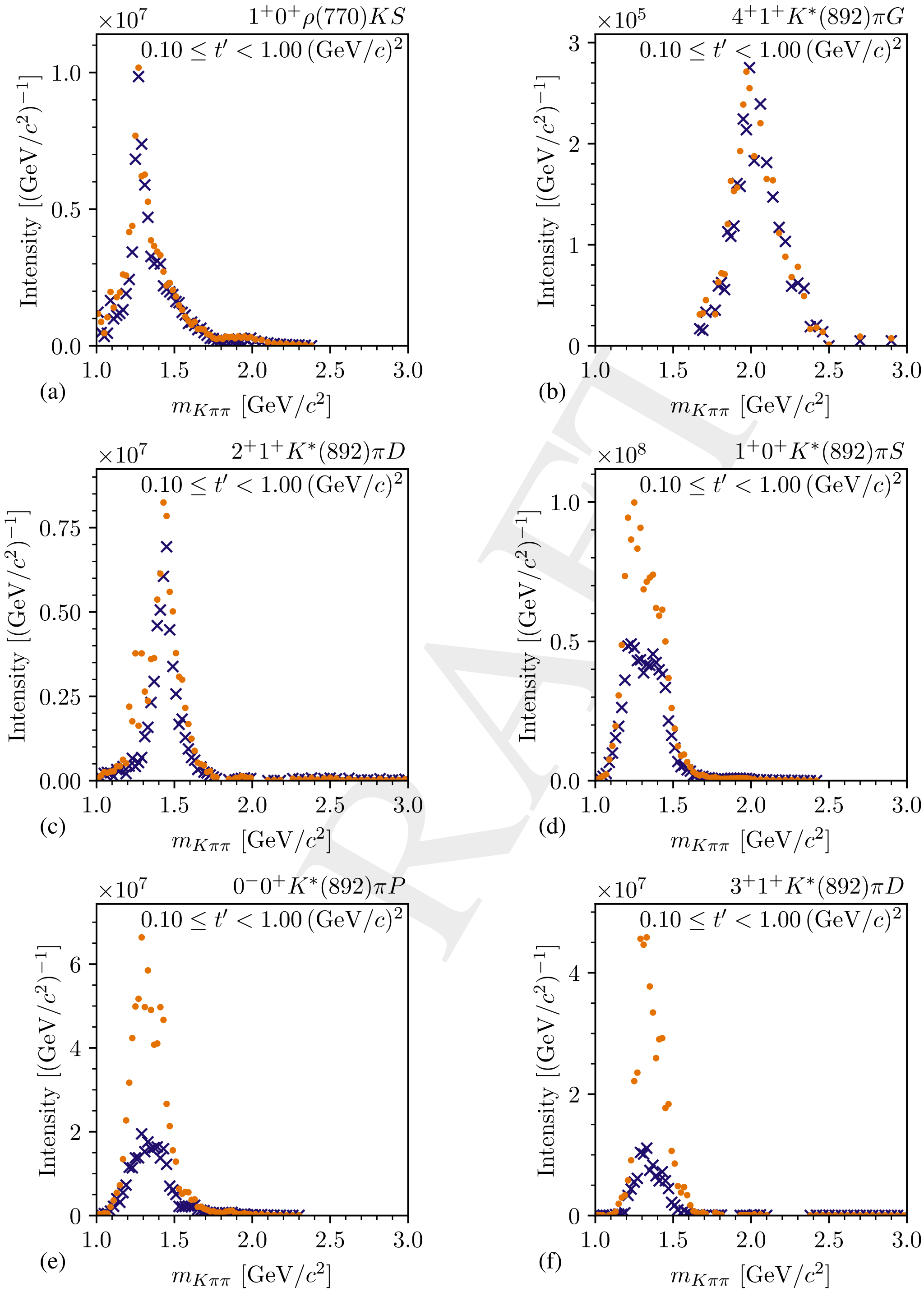

Figure 5.29: Same as figure 5.27, but showing the result of the PWD of the reconstructed pseudodata using the detuned acceptance model (orange data points).

Using the detuned acceptance model yielded a slightly larger intensity of the $2^+\,1^+\,K^*(892)\,\pi\,D$ wave compared to the 238-wave pseudodata reference model as shown in figure 5.29c, while the shape remains similar. This is consistent with our finding that the $2^+\,1^+\,K^*(892)\,\pi\,D$ wave from the measured $K^-\pi^-\pi^+$ sample is only modestly sensitive to systematic effects as discussed in section 5.7.1. Only in about four $m_{K\pi\pi}$ bins at about $1.3\,\mathrm{GeV}/c^2$, the intensity is much larger than in the reference model. We do not observe such a deviation if we use the correct model for the acceptance. Thus, the discrepancy may arise due to destructive interference of the $2^+\,1^+$ $K^*(892)\,\pi\,D$ wave with other partial waves that were selected only in those $m_{K\pi\pi}$ bins. The resulting, typically small, effect on the total model intensity from such a destructive interference may be misused by the fit to partly account for the introduced imperfection.

Finally, we find large deviations for a certain set of partial waves when using the detuned acceptance model. Among these waves are the $1^+\,0^+\,K^*(892)\,\pi\,S$, the $0^-\,0^+\,K^*(892)\,\pi\,P$, and the $3^+\,1^+\,K^*(892)\,\pi\,D$ waves shown in figures 5.29d, 5.29e, and 5.29f; respectively. In all waves, the intensity obtained using the detuned acceptance model is much larger than the reference model. However, this discrepancy is limited to the $m_{K\pi\pi}$ region below about $1.6\,\mathrm{GeV}/c^2$. Most of these waves have the $K^*(892)$ isobar. As shown e.g. in figure 5.27d, we find discrepancies in a similar set of waves also when using the correct model for the acceptance. However, these discrepancies are much smaller. Interestingly, we find these small deviations in the same partial waves for which we observe large systematic effects (see section 5.7) and in many of these waves we observe unexpected low-mass structures (see section 5.5). In section 5.9, we will conclude on this effect.

5.8.3 Pseudodata without the $1^+\,0^+\,\rho(770)\,K\,S$ or $2^+\,1^+\,K^*(892)\,\pi\,D$ Waves

In order to study artifacts due to wrongly assigned intensity in individual partial waves in more detail, we generated pseudodata samples based on the 238-wave pseudodata model, but we omitted in each study a single wave, i.e. we set the amplitude of this wave to zero. Thus, the PWD of such a pseudodata sample should yield zero intensity for the omitted wave. Any significant deviation from zero intensity would indicate artifacts in the omitted wave.

We generated a pseudodata sample where we omitted the $1^+\,0^+\,\rho(770)\,K\,S$ wave.[cf] Figure 5.30a shows the t'-summed intensity spectrum of the $1^+\,0^+\,\rho(770)\,K\,S$ wave as obtained from this pseudodata sample using the correct model for the acceptance (green data points) or using the detuned acceptance model (orange data points). We used the same detuned acceptance model as in section 5.8.2. Overall, the intensity of the $1^+\,0^+\,\rho(770)\,K\,S$ wave obtained in this study is small compared to the intensity observed in the measured $K^-\pi^-\pi^+$ sample (blue crosses).[cg] We obtained similar results when using the correct and the detuned acceptance

[cf] We generated 40×10^6 pseudodata events.

[cg] We determined the scale factor for the full 238-wave pseudodata model, such that the prediction for the number of produced events from the 238-wave pseudodata model without the $1^+\,0^+\,\rho(770)\,K\,S$ wave is equal to the number of produced pseudodata events in this study. The scaled 238-wave pseudodata model gives the expected spin-density matrix elements for all waves except for the $1^+\,0^+\,\rho(770)\,K\,S$ wave, for which the expectation is zero.

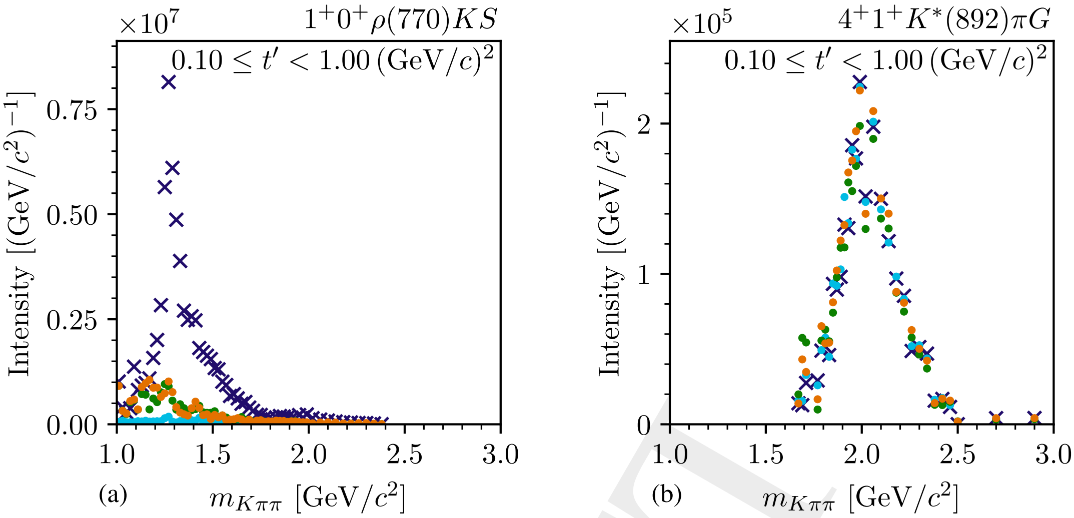

Figure 5.30: Results from the PWD of the pseudodata sample that was generated from the 238-wave pseudodata model, but with the $1^+\,0^+\,\rho(770)\,K\,S$ amplitudes set to zero. The t'-summed intensity spectra of two selected partial waves are shown. The cyan data points represent the PWD of the produced pseudodata. The green data points represent the PWD of the reconstructed pseudodata using the correct model for the acceptance. The orange data points represent the PWD of the reconstructed pseudodata using the detuned acceptance model. The blue crosses represent the full 238-wave pseudodata model scaled accordingly.[cg] We show the maximum-likelihood estimates of the intensities obtained from the pseudodata. The corresponding maximum-likelihood estimates of the uncertainties are not shown.

model. However, the intensity is not zero as expected. Especially, in the $m_{K\pi\pi}$ region below about $1.3\,\mathrm{GeV}/c^2$ we observe small artificial intensities in this partial wave. The PWD of the produced pseudodata sample (cyan data points) yielded practically zero intensity in the $1^+\,0^+\,\rho(770)\,K\,S$ wave. Thus, we conclude that the small artifacts observed in the $1^+\,0^+\,\rho(770)\,K\,S$ wave arise from the limited acceptance, which is mainly caused by the limited range of the RICH final-state particle identification. These artifacts are not sensitive to imperfections in the analysis model. As discussed in section 5.7.1, we also observe small systematic effects in this $m_{K\pi\pi}$ region in the $1^+\,0^+\,\rho(770)\,K\,S$ wave obtained from the PWD of the measured $K^-\pi^-\pi^+$ sample. The other partial waves are not affected when omitting the $1^+\,0^+\,\rho(770)\,K\,S$ wave as exemplarily shown in figure 5.30b. In all pseudodata and systematic studies discussed so far, most of the partial waves behave similar to the $1^+\,0^+\,\rho(770)\,K\,S$ wave. Thus, we expect the conclusions drawn here for the $1^+\,0^+\,\rho(770)\,K\,S$ wave to hold also for most of the other waves.

One of the exceptions is the $2^+\,1^+\,K^*(892)\,\pi\,D$ wave, which is affected by small systematic effects (see figure 5.25e). Thus, we performed another pseudodata study using a pseudodata sample where we omitted the $2^+\,1^+\,K^*(892)\,\pi\,D$ wave.[ch] In the highest t' bin shown in figure 5.31b, we observe only little intensity in the $2^+\,1^+\,K^*(892)\,\pi\,D$ wave, as expected. Only in two $m_{K\pi\pi}$ bins at about $1.3\,\mathrm{GeV}/c^2$ and only when we used the detuned acceptance model (orange data points), the $2^+\,1^+\,K^*(892)\,\pi\,D$ wave picked up some intensity. We observe larger intensities in

[ch] We generated again 40×10^6 pseudodata events.

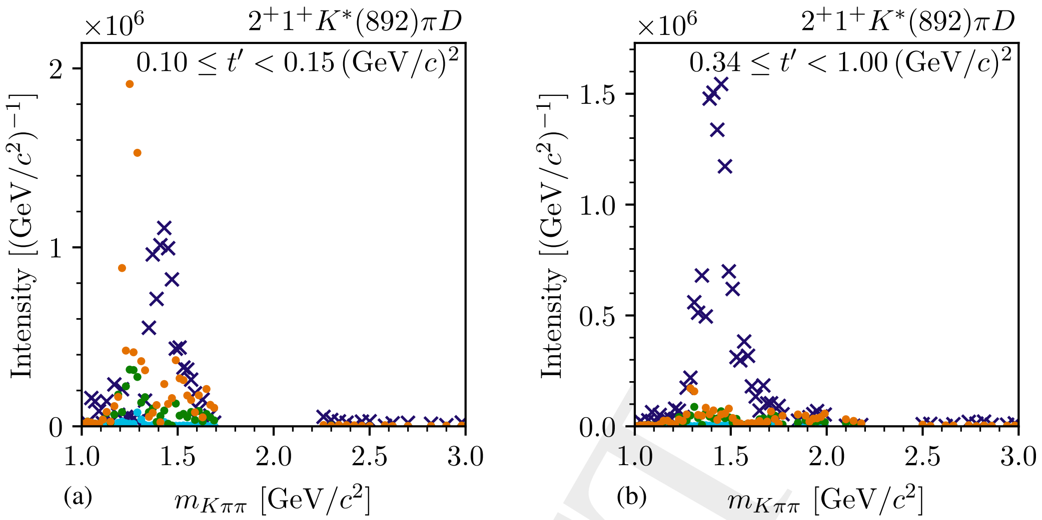

Figure 5.31: Same as figure 5.30 but for the pseudodata study based on the 238-wave pseudodata model without the $2^+\,1^+\,K^*(892)\,\pi\,D$ wave component.

the lowest t' bin shown in figure 5.31a. The intensity obtained using the correct model for the acceptance (green data points) peaks at about $1.3\,\text{GeV}/c^2$. This peak becomes larger when using the detuned acceptance model (orange data points). It is even larger than the intensity obtained from the measured $K^-\pi^-\pi^+$ sample (blue crosses). Such a large artificial intensity is typical for destructive interferences, which become enhanced when introducing imperfections, because they are misused by the fit to account for the imperfections. The intensity obtained from the PWD of the produced pseudodata sample (cyan data points) is practically zero, in agreement with the reference model. From this pseudodata study, we expect modest artifacts in the $2^+\,1^+$ $K^*(892)\,\pi\,D$ wave obtained from the PWD of the measured $K^-\pi^-\pi^+$ sample mainly in the low-t' and low-$m_{K\pi\pi}$ region, which is consistent with the findings in the systematic studies. The results for the other waves (not shown) are not biased when omitting the $2^+\,1^+\,K^*(892)\,\pi\,D$ wave.

Reviewing all studies presented in this section 5.8 we conclude that for most of the partial waves we expect no considerable artifacts in our analysis caused by e.g. an imperfect acceptance model. We find indications for modest artificial intensities in the $2^+\,1^+\,K^*(892)\,\pi\,D$ wave mainly in the low-t' and low-$m_{K\pi\pi}$ region. However, there is a certain set of partial waves, e.g. the $1^+\,0^+$ $K^*(892)\,\pi\,S$ wave, whose results are very sensitive to imperfections in the analysis model, e.g. to a detuned acceptance model. We discuss this set of waves in the following section 5.9.

5.9 The Leakage Effect

As discussed in section 5.7, there is a certain set of partial waves, for which we observe large systematic effects, e.g. for which the various systematic studies yielded different intensity spectra. In the PWD pseudodata studies discussed in section 5.8, we find a similar set of partial waves, for which we obtained results that differ from the reference model, especially when using the detuned acceptance model. Among these waves are the $1^+\,0^+\,K^*(892)\,\pi\,S$, $0^-\,0^+\,K^*(892)\,\pi\,P$, and $3^+\,1^+\,K^*(892)\,\pi\,D$ waves, for which the discrepancies are largest. The deviations are limited to the region $m_{K\pi\pi} \lesssim 1.6\,\mathrm{GeV}/c^2$. In the same $m_{K\pi\pi}$ region, we observe in the measured data an unexpected peaking structure in the $3^+\,1^+\,K^*(892)\,\pi\,D$ wave (see blue data points in figure 5.25d), while there is no known or expected K_3 state in this mass region. The peaking structure dominates this wave, which contributes a surprisingly large fraction of 6.4 % to the total intensity. Also, the $1^+\,0^+\,K^*(892)\,\pi\,S$ and $0^-\,0^+\,K^*(892)\,\pi\,P$ waves exhibit peaking structures in the low-mass region, which depend strongly on the details of the analysis procedure, e.g. on the RICH threshold as shown in figure 5.25c. In contrast to the $3^+\,1^+\,K^*(892)\,\pi\,D$ wave, there are known resonances, which may contribute to these structures, i.e. the $K_1(1270)$, the $K_1(1400)$, and the $K(1460)$. In the rest of the text, we denote such unexpected low-mass structures that have large systematic uncertainties and correspond to deviations in the PWD pseudodata studies by the term <u>leakage artifacts</u>.

We observe leakage artifacts only in a limited set of partial waves, the so-called <u>leakage waves</u>. The other partial waves are called <u>non-leakage waves</u>. Thus, the leakage artifacts must be linked to the distributions of events in the phase-space variables as predicted for the leakage waves. The distribution in the phase-space variables of a wave is characteristic for this wave and is given by the corresponding decay amplitude defined in equation (5.10). In order to study the properties of the decay amplitudes we study the phase-space integral matrix defined in equation (5.22). Figure 5.32a shows the magnitude of the elements of this matrix. The phase-space integral matrix can be interpreted as the Gram matrix [130] of the decay amplitudes. It is also similar to the matrix of overlap integrals used in quantum chemistry [131]. The diagonal elements have a value of one by construction. The off-diagonal elements called <u>overlaps</u> in this work are a measure for the orthogonality of the decay amplitudes as a function of the phase-space variables. If $|I_{ab}| = 0$, the decay amplitudes of waves a and b are orthogonal. If $|I_{ab}| = 1$, the decay amplitudes of waves a and b are linearly dependent, i.e. the distribution of events in the phase-space variables is identical for both waves. Overall, we observe very small overlaps (dark blue off-diagonal cells in figure 5.32a). For example, the overlaps between waves with different J^P are practically zero as expected, because the Wigner D-functions are orthogonal. There are a few exceptions of waves with larger overlaps (green and yellow off-diagonal cells in figure 5.32a), which are understood as discussed in appendix D.3. They do not cause issues in the main analysis and are not related to the leakage waves. In summary, the phase-space integral matrices do not give a hint to understand the leakage artifacts.

However, we observe the leakage artifacts only in data affected by detector acceptance effects. The phase-space integral matrix provides a measure of the orthogonality of waves in the full phase space. However, the phase-space is non-uniformly covered by the detector acceptance. In

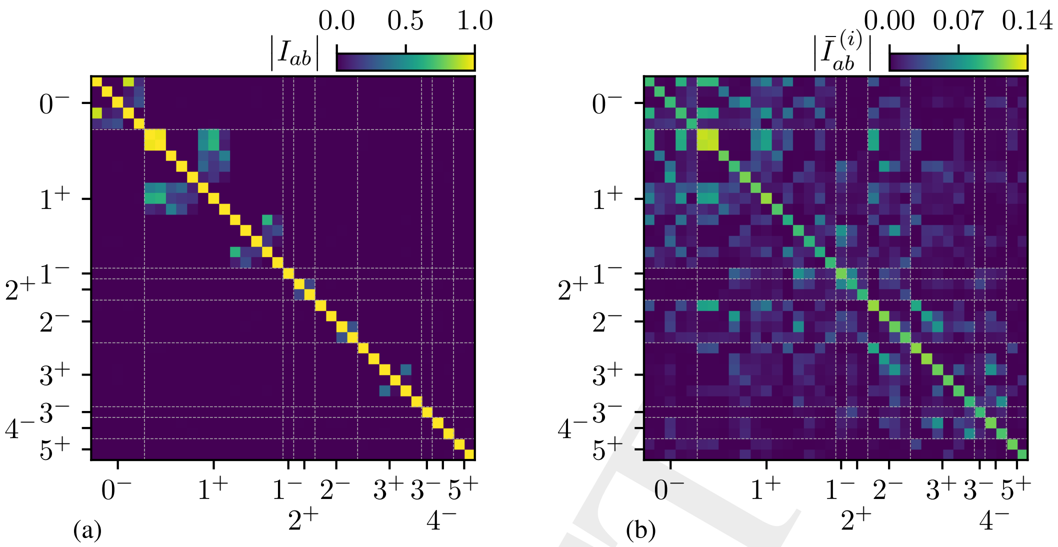

Figure 5.32: Magnitude of the integral-matrix elements for the waves that were selected in the kinematic cell at $m_{K\pi\pi} = 1.31\,\mathrm{GeV}/c^2$ in the lowest t' bin. (a) shows the phase-space integral matrix given in equation (5.22). (b) shows the acceptance-integral matrix given in equation (5.29) for the acceptance of the $i = 2008$ setup. The incoherent flat wave is not shown.

particular, there are parts of the phase-space that are experimentally not accessible in measured data, which is mainly caused by the limited kinematic range of the RICH final-state particle identification (see figure 5.23b). This leads to a loss of information, i.e. there is no information about a part of the phase-space distribution in the measured data. These acceptance effects are taken into account in the acceptance-integral matrix defined in equation (5.29), which can be interpreted as the Gram matrix of the decay amplitudes in the experimentally accessible part of the phase space.[ci] Figure 5.32b shows the magnitude of the acceptance-integral matrix elements in the $m_{K\pi\pi}$ region of the leakage artifacts. The acceptance-integral matrix exhibits completely different features compared to the phase-space integral matrix in figure 5.32a. The diagonal elements are smaller than one, because they represent the average acceptance of the corresponding wave, i.e. the average acceptance if the data would contain only this wave. Particularly noteworthy are the large overlaps with respect to the diagonal elements between almost all waves in the wave set,[cj] also between waves with different J^P. These large overlaps show a none-orthogonality of the decay amplitudes that is caused by the loss of information due to the limited acceptance. However, this does not mean that the partial waves cannot be distinguished at all in the PWD, but the large overlaps indicate that the decay amplitudes are more similar in the experimentally accessible region of the phase space. Thus, they are harder to distinguish and more sensitive to systematic effects.

[ci] To be precise, the acceptance does not just select certain regions of the phase space, i.e. is not just zero or one, but is a continuous function in the phase-space variables with values between zero and one (neglecting resolution effects). When interpreting the acceptance-integral matrix as the Gram matrix of the decay amplitudes, we take into account the limitation and distortion of the phase-space by the acceptance.

[cj] The magnitudes of the off-diagonal elements of $\bar{I}_{ab}^{(i)}$ are not limited to the range $0 \leq \bar{I}_{ab}^{(i)} \leq 1$. Still, the color scale allows us to interpret off-diagonal elements that are green or yellow as large and those that are dark blue as small.

In order to identify waves with large overlaps, we performed an eigenvalue decomposition of the acceptance-integral matrix, i.e.[ck]

$$\bar{I}_{ab} = \sum_{h} \mathfrak{e}^h \mathfrak{v}_a^h \left[\mathfrak{v}_b^h\right]^* . \tag{5.77}$$

Here, $\mathfrak{e}^h$ are the eigenvalues of the acceptance-integral matrix labeled by h and $\mathfrak{v}_a^h$ is the element of the eigenvector of $\mathfrak{e}^h$ that belongs to the partial wave a. In the eigenvalue basis, the PWD prediction for the total number of measured events in a given $(m_{K\pi\pi}, t')$ cell as defined in equation (5.28) reads[ck]

$$\widehat{\widehat{N}}_{\text{ev}} = \sum_{a,b\in\mathbb{W}} \rho_{ab} \bar{I}_{ab} = \sum_{h} \mathfrak{e}^h \sum_{a,b\in\mathbb{W}} \rho_{ab} \mathfrak{v}_a^h \left[\mathfrak{v}_b^h\right]^* . \tag{5.78}$$

As the contribution of each eigenvector to $\widehat{\widehat{N}}_{\text{ev}}$ is multiplied by the corresponding eigenvalue, eigenvectors of vanishing eigenvalues, i.e. eigenvalues close to zero, do not strongly influence $\widehat{\widehat{N}}_{\text{ev}}$. This means that the corresponding partial waves, i.e. partial waves with large corresponding $\mathfrak{v}_a^h$, may destructively interfere such that even large intensities in the individual partial waves lead to only a small change in the description of the measured sample by the PWD model.[cl] Hence, these waves are only loosely constrained by the data. This may be an explanation for the leakage effect. We therefore searched for vanishing eigenvalues and studied which partial waves contribute to the eigenvectors that correspond to vanishing eigenvalues, i.e. we searched for waves with large $\mathfrak{v}_a^h$, while the corresponding $\mathfrak{e}^h$ is vanishing.

We find vanishing eigenvalues of the acceptance-integral matrix shown in figure 5.32b. The smallest eigenvalue, which has a value of 0.0010, mainly arises from waves with $[K\pi]_S^{K\pi}$, $[K\pi]_S^{K\eta}$, and $[\pi\pi]_S^{\text{AMPK}}$ isobars as discussed in appendix D.3. Those waves exhibit similarly large overlaps already in the phase-space integral matrix in figure 5.32a. Hence, the smallest eigenvalue is not driven by acceptance effects. Since the leakage artifacts only appear in data affected by acceptance effects, this smallest eigenvalue is not related to the leakage artifacts. The second smallest eigenvalue, which has a value of 0.0021, arises from large contributions of the $0^- 0^+ K^*(892)\,\pi\,S$, $3^+ 1^+ K^*(892)\,\pi\,D$, $2^- 0^+ K^*(892)\,\pi\,P$, $1^- 1^+ K^*(892)\,\pi\,P$, $1^+ 1^+ K^*(892)\,S$, and $1^+ 0^+ K^*(892)\,\pi\,S$ waves; ordered by the corresponding $|\mathfrak{v}_a^h|$ value; and other waves with smaller $|\mathfrak{v}_a^h|$. We find large contributions of similar partial waves to the two next largest eigenvalues with values of 0.0027 and 0.0032. The fifth smallest eigenvalues becomes quickly larger with a value of about 0.0068. Hence, the fifth and all other remaining eigenvalues are not further interest here. With increasing $m_{K\pi\pi}$, the smallest eigenvalues become significantly larger. For example at $m_{K\pi\pi} \approx 1.6\,\text{GeV}/c^2$, the smallest eigenvalue has a value of 0.16. Thus, at higher masses even the smallest eigenvalues do not vanish and contribute to the total model intensity.

[ck] Here, we drop the data-set label (i) for simplicity, because we want to demonstrate a general feature of the acceptance-integral matrix.

[cl] The PWD model describes the distribution in the phase-space variables and not only $\overline{N}_{\text{ev}}$. Nonetheless, combinations of waves that correspond to vanishing eigenvalues do not strongly contribute to the model predictions for the phase-space distributions in equation (5.28). For example, if an eigenvalue is exactly zero, the corresponding linear combination of decay amplitudes is exactly zero everywhere in phase space.

This set of waves that mainly contributes to vanishing eigenvalues of the acceptance-integral matrix agrees with the leakage waves observed in the systematic and pseudodata studies. Furthermore, the vanishing eigenvalues become larger and the leakage artifacts become smaller at a similar $m_{K\pi\pi}$ of about $1.6\,\mathrm{GeV}/c^2$. Thus, we conclude that the leakage artifacts are related to the vanishing eigenvalues, i.e. they are related by the loss of information due to the limited acceptance. This acceptance-induced effect is called leakage effect in the rest of the text. However, the eigenvalues that correspond to the leakage effect are not exactly zero, which means that the leakage waves can be distinguished in principle. This is supported by our finding that the leakage artifacts are small in the PWD pseudodata studies in section 5.8 where we used the correct model for the acceptance and where we fitted a pseudodata sample that is much larger than the measured $K^-\pi^-\pi^+$ sample. However, in the measured $K^-\pi^-\pi^+$ sample, where we have only a limited amount of data available and where the analysis model is not perfect, e.g. due to background in the sample, the leakage waves may easily be misused by the PWD fit to account for imperfections in the model. This is strongly supported by our finding that the leakage artifacts are much more pronounced in the pseudodata study where we used a detuned acceptance model (see section 5.8.2).

5.9.1 Reproducing the Leakage Effect in Pseudodata

Having identified the cause of the leakage effect, we further studied it using additional pseudodata samples. As the $1^+\,0^+\,K^*(892)\,\pi\,S$ wave is the largest wave in our analysis with an intensity of about 23 % of the total intensity and as this wave contributes strongly to the leakage effect, we generated a pseudodata sample of 50×10^6 events according to only the $1^+\,0^+\,K^*(892)\,\pi\,S$ wave from the 238-wave pseudodata model.

The results of the PWDs of the produced pseudodata sample and of the reconstructed pseudodata sample using the correct model for the acceptance (not shown) do not exhibit artifacts from the leakage effect in any of the waves in the produced pseudodata and in any of the non-leakage waves in the reconstructed pseudodata. They are consistent with the findings in the previous pseudodata studies discussed in section 5.8. In the leakage waves we observe only small artifacts from the leakage effect in the reconstructed pseudodata when using the correct model for the acceptance.

The results of the PWD of the reconstructed pseudodata using the detuned acceptance model are shown by the orange data points in figure 5.33. The intensity of the $1^+\,0^+\,K^*(892)\,\pi\,S$ wave is larger than the reference model, which is expected from the previous studies due to the leakage effect. However, we observe surprising results for some of the leakage waves. For example, although the reference model is zero for the $3^+\,1^+\,K^*(892)\,\pi\,D$ wave, we find a peaking structure in the corresponding intensity spectrum at about $1.3\,\mathrm{GeV}/c^2$ (orange data points in figure 5.33b), which is similar to the 238-wave pseudodata model (blue crosses), which was obtained from the measured $K^-\pi^-\pi^+$ sample. Also, the intensity spectrum of the $0^-\,0^+\,K^*(892)\,\pi\,P$ wave (orange data points figure 5.33c) is surprisingly similar to the one obtained from measured data in the mass region below about $1.6\,\mathrm{GeV}/c^2$, although it is expected to vanish.

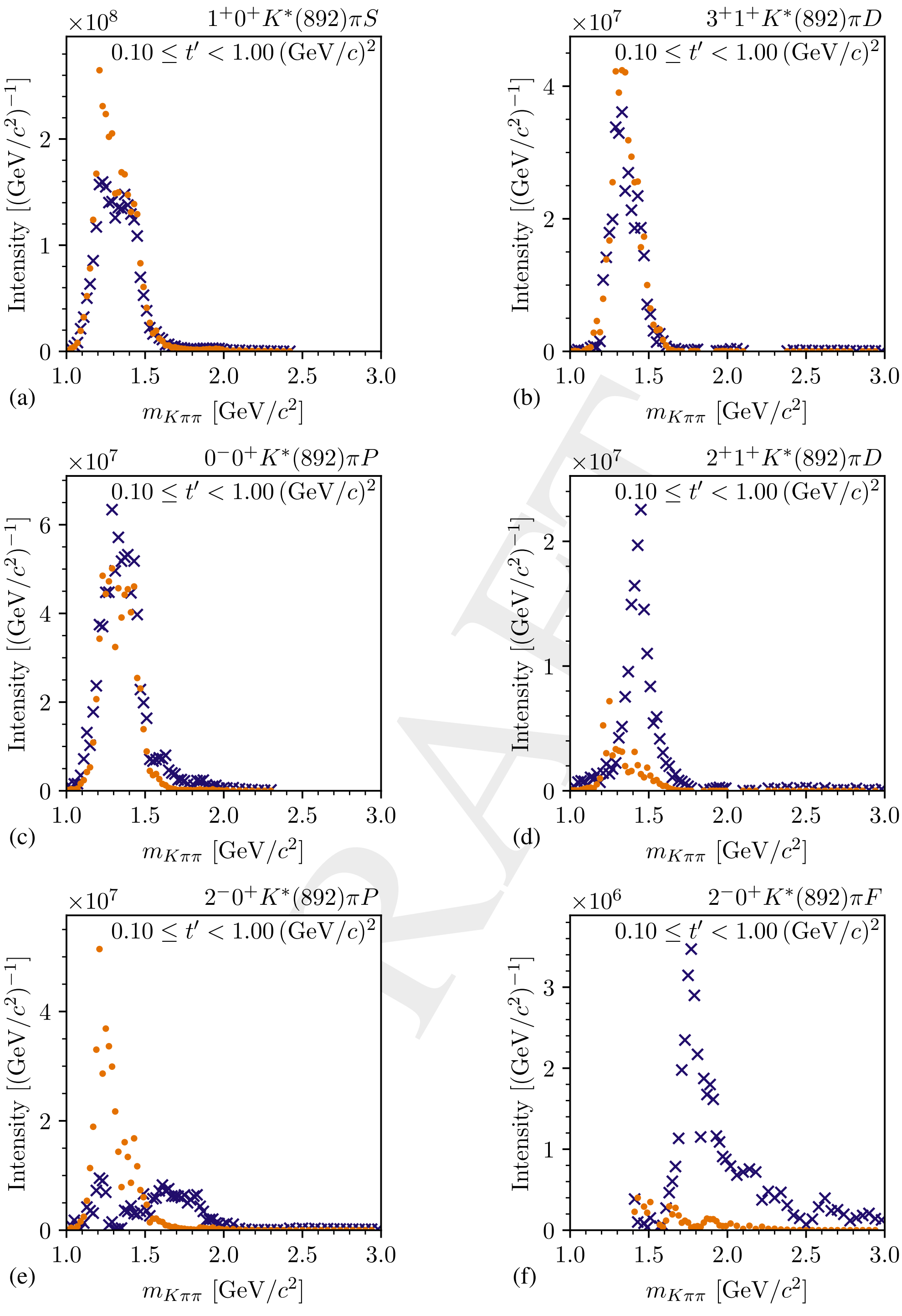

Figure 5.33: Results from the PWD using the detuned acceptance model of the reconstructed pseudodata sample that was generated using only the $1^+\,0^+\,K^*(892)\,\pi\,S$ wave from the 238-wave pseudodata model (orange data points). The blue crosses represent the full 238-wave pseudodata model scaled accordingly (see figure 5.30). We show the maximum-likelihood estimates of the intensities obtained from the pseudodata. The corresponding maximum-likelihood estimates of the uncertainties are not shown (see section 5.8).

As the intensity of the reference model of those 3^+ and 0^- waves is zero, the low-mass structures in this pseudodata study are artifacts that are generated by our analysis procedure. As these artifacts appear only in the PWD of the reconstructed pseudodata and only when using the detuned acceptance model; and as these artifacts appear only in leakage waves, we conclude that these artifacts arise from the leakage effect. This supports our conclusion, that the leakage artifacts observed in the measured $K^-\pi^-\pi^+$ sample are an acceptance-induced effect.

The low-mass structures observed e.g. in the 3^+ and 0^- waves in this pseudodata study are similar to the low-mass structures observed in the measured $K^-\pi^-\pi^+$ sample in the same waves. Hence, we conclude that these low-mass structures observed in the measured $K^-\pi^-\pi^+$ sample are dominantly caused by the leakage effect. For example, for the $3^+\,1^+\,K^*(892)\,\pi\,D$ wave this is also consistent with the fact that there is no known or expected K_3 state in this $m_{K\pi\pi}$ region. Furthermore, when adding information to the PWD fit and thereby potentially weakening the leakage effect, as done in the systematic study with a less restrictive RICH threshold, the low-mass structure in the $3^+\,1^+\,K^*(892)\,\pi\,D$ wave becomes much smaller (green data points in figure 5.25d).[cm] When removing information and thereby potentially enhancing the leakage effect, as done in the systematic study with more restrictive RICH threshold, the low-mass structure in the $3^+\,1^+\,K^*(892)\,\pi\,D$ wave becomes even larger (red data points in figure 5.25d). Both observations are consistent with the assumption that the low-mass structure in the $3^+\,1^+$ $K^*(892)\,\pi\,D$ wave arises mainly from the leakage effect. We find similar effects also in other leakage waves, e.g. in the $0^-\,0^+\,K^*(892)\,\pi\,P$ wave.

Fortunately, the leakage effect affects only a limited and identifiable subset of the partial waves. Most of them have a $K^*(892)$ isobar. In general, waves with $\pi^-\pi^+$ isobar are not affected by the leakage effect.[cn] In some cases, a different orbital angular momentum is already sufficient to suppress artifacts from the leakage effect. For example, we observe large artifacts in the $2^-\,0^+$ $K^*(892)\,\pi\,P$ wave shown in figure 5.33e, which are even larger than the 238-wave pseudodata model representing the measured data;[co] while the artifacts in the $2^-\,0^+\,K^*(892)\,\pi\,F$ wave shown in figure 5.33f are negligibly small, i.e. they are two orders of magnitude smaller than in the $2^-\,0^+\,K^*(892)\,\pi\,P$ wave. The $2^+\,1^+\,K^*(892)\,\pi\,D$ wave shown in figure 5.33d exhibits modest artifacts from the leakage effect. They are mainly focused in the low-mass tail of the peak. This is consistent with the modest systematic effects observed in this wave (see section 5.7). Hence, an interpretation of the $2^+\,1^+\,K^*(892)\,\pi\,D$ wave in terms of physics signals is possible.

[cm] In the study with a less restrictive RICH threshold, the intensity in the low-mass region of the $3^+\,1^+\,K^*(892)\,\pi\,D$ wave is drastically reduced, but there is a non-negligible remaining low-mass intensity, which indicates a remaining bias from the leakage effect. As this study uses already a very low RICH threshold, we conclude that we cannot circumvent the leakage effect. As such a very low RICH threshold leads to larger misidentification, it may cause other systematic effects in our analysis. Thus, we kept the RICH threshold of the main analysis.

[cn] Only the $1^+\,0^+\,[\pi\pi]_S^{\mathrm{AMPK}}\,K\,P$ wave shows artifacts for $m_{K\pi\pi} < 1.6\,\mathrm{GeV}/c^2$. However, this wave is not discussed in this work as it shows no physics signals. Furthermore, these artifacts may also arise from other effects than from the leakage effect, e.g. from destructive interference with the $1^+\,0^+\,f_0(980)\,K\,P$ wave.

[co] The fact that the pseudodata study yielded even larger artifacts in the $2^-\,0^+\,K^*(892)\,\pi\,P$ wave than the leakage artifacts observed in measured data indicates that we do not exactly reproduce the leakage artifacts in this pseudodata study, especially in small waves such as the $2^-\,0^+\,K^*(892)\,\pi\,P$ wave. This is expected, because the imperfection that we introduced in this pseudodata study by using the detuned acceptance model is different and probably larger than the imperfections in the analysis of the measured data and because the leakage artifacts are triggered by imperfections in our analysis.

The appearance of the leakage effect in this pseudodata study allows us to also investigate its footprint in the kinematic distributions. Figure 5.34 shows the distribution in the two-body decay angles of the decay $X^- \to \xi^0_{K^-\pi^+}\pi^-$ in the Gottfried-Jackson frame (GJ). As expected, the prediction of the reconstructed distribution from the PWD fit to the reconstructed pseudodata using the detuned acceptance model (see figure 5.34b) agrees with the actual reconstructed distribution of the pseudodata sample (see figure 5.34a).[cp] Figure 5.34c shows the distribution of the produced pseudodata sample, i.e. without acceptance effects. The distribution is flat in the Gottfried-Jackson angles as expected.[cq] However, the PWD prediction for the produced distribution shown in figure 5.34d drastically deviates from the actual distribution in figure 5.34c. The PWD model overestimates the distribution by more than a factor of six in the region where the acceptance is practically zero (see dark blue regions in figure 5.34e). This large deviation is caused by the leakage effect, which artificially predicts produced events in the region of practically zero acceptance, i.e. in the region where we are blind experimentally. Hence, the leakage effect has only little influence on the prediction for the reconstructed distributions, which in the PWD fit is compared to the measured distribution (cf. figures 5.34a and 5.34b). Thus, the leakage waves are only weakly constrained by the data.

The leakage effect biases not only the PWD prediction of the distribution of produced events, but the PWD model also overestimates the total number of produced events $\widehat{N}_{\mathrm{ev}}$. In the pseudodata study that is based on the full 238-wave pseudodata model in section 5.8.1, which is most similar to the measured $K^-\pi^-\pi^+$ sample, the PWD model overestimates the total number of produced events by about a factor two. This also leads to a bias of the relative intensities defined in equation (5.76), because $\widehat{N}_{\mathrm{ev}}$ enters the denominator. Especially the relative intensities of non-leakage waves are affected as the nominator in equation (5.76) is not biased by the leakage effect. Assuming that the leakage effect appears with a similar strength also in the PWD of the measured $K^-\pi^-\pi^+$ sample, the relative intensities of non-leakage waves are underestimated by about a factor 2 in the 238-wave PWD. Hence, the relative intensities cannot directly be interpreted in terms of how much a wave contributes to the measured data. Nonetheless, the relative intensities can be compared among non-leakage waves as the bias from the leakage effect is the same for all of them. Thus, the relative intensities can sill be used as a measure of whether a wave is large or small.

In the pseudodata study discussed above, we showed that if the pseudodata contain only the $1^+\,0^+\,K^*(892)\,\pi\,S$ wave with an amplitude that is similar to the one obtained from the measured $K^-\pi^-\pi^+$ sample, we reproduce the leakage effect with a similar shape and strength as in the measured $K^-\pi^-\pi^+$ sample for most of the leakage waves. To study whether this is also the case for other partial waves, we produced a pseudodata sample containing only the $3^+\,1^+\,K^*(892)\,\pi\,D$

[cp] The pseudodata distribution is less noisy than the corresponding distribution from the PWD prediction. The samples to generate both distributions contain a similar number of events. While the events in the reconstructed pseudodata sample are already distributed accordingly, we used reconstructed events that are phase-space distributed and weighted them to obtain the PWD prediction for the reconstructed distribution (see appendix C.3). Given the same number of events, the first sample contains more information. Therefore, the distribution of the pseudodata sample is less noisy.

[cq] The pseudodata sample was generated based on the decay amplitude of the $1^+\,0^+\,K^*(892)\,\pi\,S$ wave. We expect a flat distribution in the Gottfried-Jackson angles as this wave has $M = 0$ and $L = 0$ [132].

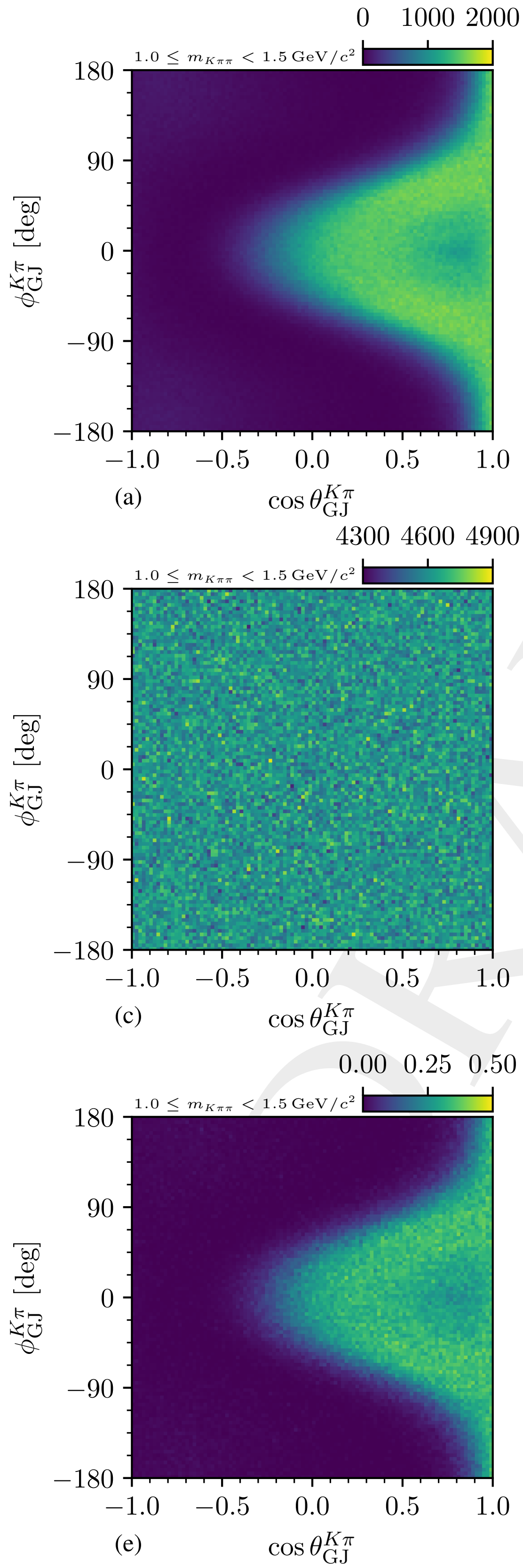

Figure 5.34: Distribution in the two-body decay angles of the decay $X^- \to \xi^0_{K^-\pi^+}\pi^-$ from the pseudodata containing only the $1^+\,0^+\,K^*(892)\,\pi\,S$ wave. (a) and (c) show the distribution of the reconstructed and produced pseudodata sample, respectively. (b) and (d) show the corresponding predictions based on a PWD fit to the reconstructed pseudodata using the detuned acceptance model. (e) shows the acceptance. It is different from figure D.43e as the marginalization over the not-shown phase-space variables is based on a model that contains only the $1^+\,0^+\,K^*(892)\,\pi\,S$ wave, while figure D.43e is based on the full PWD model obtained in the main analysis. The distributions are integrated over the mass range $1.0 \leq m_{K\pi\pi} < 1.5\,\mathrm{GeV}/c^2$ and over the full analyzed t' range.

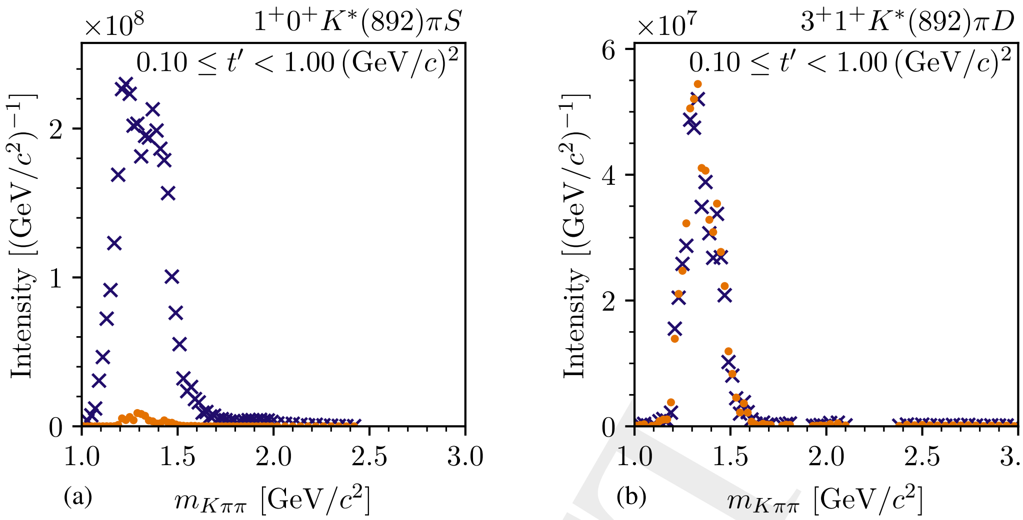

Figure 5.35: Same as figure 5.33, but showing the PWD using the detuned acceptance model of the reconstructed pseudodata sample that was generated using only the $3^+\,1^+\,K^*(892)\,\pi\,D$ wave from the 238-wave pseudodata model.

wave from the 238-wave pseudodata model. Figure 5.35 shows the results of a PWD of these pseudodata. The intensity spectrum of the $3^+\,1^+\,K^*(892)\,\pi\,D$ wave obtained using the detuned acceptance model (orange data points) agrees with the reference model (blue crosses). The other partial waves exhibit only negligibly small artifacts from the leakage effect as exemplarily shown for the $1^+\,0^+\,K^*(892)\,\pi\,S$ wave in figure 5.35a. Thus, the $3^+\,1^+\,K^*(892)\,\pi\,D$ wave alone does not lead to a leakage effect similar to the one observed in the measured $K^-\pi^-\pi^+$ sample.

In another pseudodata study, we tested whether the combination of all waves except for the $1^+\,0^+$ $K^*(892)\,\pi\,S$ wave can reproduce the leakage artifacts. Therefore, we generated a pseudodata sample using the 238-wave pseudodata model without the $1^+\,0^+\,K^*(892)\,\pi\,S$ wave. Figure 5.36 shows the results from this study. Using the detuned acceptance model causes artifacts in the leakage waves exemplarily shown in figures 5.36a and 5.36b. As we expect the low-mass structure in the $3^+\,1^+\,K^*(892)\,\pi\,D$ wave in the reference model obtained from the measured $K^-\pi^-\pi^+$ sample (blue crosses) to be dominantly produced by the leakage effect and as we obtained in this study a low-mass structure (orange data points), which is about twice as large as the reference model, we conclude that the leakage artifacts in this study are of similar strength as in the measured $K^-\pi^-\pi^+$ sample.

From these pseudodata studies we conclude that the strength of the artifacts caused by the leakage effect depends on the data. The leakage effect itself is given by the decay amplitudes of the leakage waves and the acceptance and corresponds to an approximate ambiguity in the PWD model. The amount by which this ambiguity creates artifacts in the partial waves is given by how much the leakage waves actually contribute to the data sample. The $1^+\,0^+\,K^*(892)\,\pi\,S$ wave is the dominant contribution.

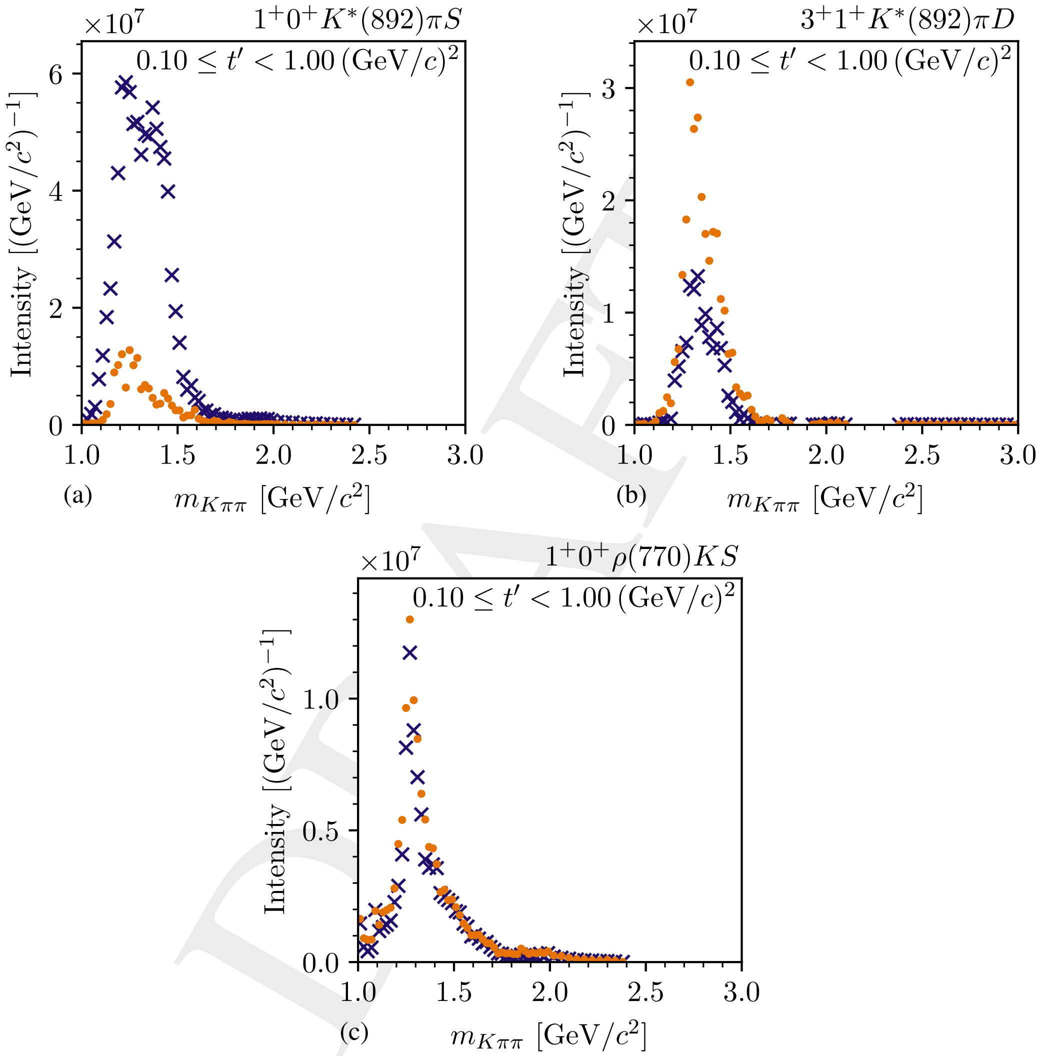

Figure 5.36: Same as figure 5.33, but showing the PWD using the detuned acceptance model of the reconstructed pseudodata sample that was generated using the 238-wave pseudodata model without the $1^+\,0^+\,K^*(892)\,\pi\,S$ wave.

5.9.2 Robustness of Non-Leakage Waves with respect to the Leakage Effect

As discussed in sections 5.7 and 5.8, the non-leakage waves are in general robust with respect to systematic effects and imperfections in the analysis model. Having identified the cause of the leakage effect, we performed further studies to explicitly test for a potential influence of the leakage effect on the non-leakage waves. In the pseudodata studies discussed in section 5.9.1, in which we reproduced the leakage effect, the non-leakage waves exhibited only small artifacts, which are negligible compared to the physics signals in these waves, as shown e.g. in figures 5.33f and 5.36c.

As the $3^+\,1^+\,K^*(892)\,\pi\,D$ wave is one of the major waves affected the leakage effect and as we assume the low-mass structure in this wave to be predominantly a leakage artifact, we performed a PWD of the measured $K^-\pi^-\pi^+$ sample using the 238-wave set but omitting the $3^+\,1^+\,K^*(892)\,\pi\,D$ wave for $m_{K\pi\pi} < 1.6\,\mathrm{GeV}/c^2$. Figure 5.37 shows the results from this systematic study (light red data points) compared to the main analysis (blue data points). The intensity spectra of the leakage waves obtained from this study deviate from the main analysis as shown in figures 5.37a and 5.37b. This is expected, because by omitting the $3^+\,1^+\,K^*(892)\,\pi\,D$ wave from the wave set, we changed the eigenvalue decomposition of the acceptance-integral matrix and thereby altered the leakage effect.[cr] The results of the non-leakage waves agree with the main analysis as exemplarily shown in figure 5.37c. Even the $2^+\,1^+\,K^*(892)\,\pi\,D$ wave shown in figure 5.37d, which exhibits modest systematic effects and modest artifacts from the leakage effect in the previous studies, is robust when omitting the $3^+\,1^+\,K^*(892)\,\pi\,D$ wave. This is another indication for the robustness of the non-leakage waves with respect to the leakage effect.

Reviewing our findings presented in this section 5.9, we can explain the large systematic effects observed for some partial waves in section 5.7 and the deviations observe in the same waves in the PWD pseudodata studies in section 5.8 in terms of the leakage effect. The leakage effect is caused by the loss of information due to the limited detector acceptance, which is dominated by the limited kinematic range of the RICH final-state particle identification. This effect is visible in the acceptance-integral matrix. We identified those waves that are affected by the leakage effect using three different approaches: (i) waves that exhibit unstable intensities in the systematic studies, (ii) waves with deviations from the corresponding reference model in the PWD pseudodata studies, and (iii) waves with large overlaps in the acceptance-integral matrix. All three approaches yield a consistent set of leakage waves. Figure G.3 shows the intensity distribution of all leakage waves that are discussed in this work. Furthermore, we identified the $m_{K\pi\pi}$ range that is affected by the leakage effect to be $m_{K\pi\pi} \lesssim 1.6\,\mathrm{GeV}/c^2$. An interpretation of the leakage waves in this $m_{K\pi\pi}$ region in terms of physics signals is possible only to a very limited extend and only on a qualitative level. The leakage effect also strongly biases the PWD model predictions for the distribution of produced events. The non-leakage waves are robust with respect to the leakage effect. Thus, they can be interpreted in terms of physics signals as done in the RMF introduced in chapter 6. The physics signals in the individual partial waves are discussed in chapter 7.

[cr] However, as the leakage effect is caused by several leakage waves, we still expect the results from this study to be biased by the leakage effect.

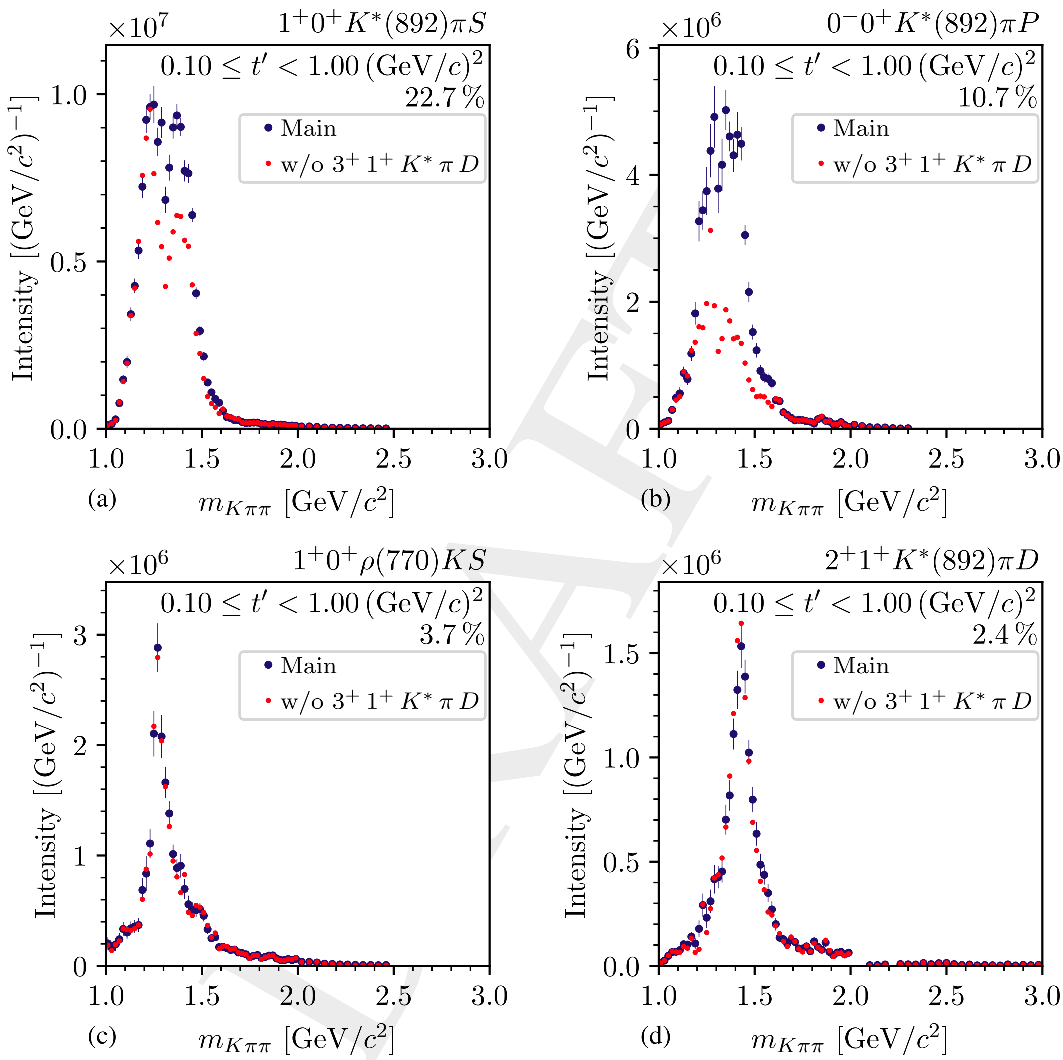

Figure 5.37: Comparison between the results of the PWD of the measured $K^-\pi^-\pi^+$ sample omitting the $3^+\,1^+\,K^*(892)\,\pi\,D$ wave for $m_{K\pi\pi} < 1.6\,\mathrm{GeV}/c^2$ (maximum-likelihood estimates; light red data points) and the main analysis (Bootstrapping estimates; blue data points). We do not show uncertainties for the maximum-likelihood estimates (see section 5.7).

5.10 $\pi^-\pi^-\pi^+$ Pseudodata Studies

The treatment of incoherent background processes is an important task in the analysis of the reaction $K^- + p \to K^-\pi^-\pi^+ + p$, as discussed in section 5.3. We expect the largest background from events of the reaction $\pi^- + p \to \pi^-\pi^-\pi^+ + p$, where the beam pion that was erroneously identified as a kaon and where one of the final-state pions was wrongly assumed to be a kaon. This background is called $\pi^-\pi^-\pi^+$ background. Since the pion component in the beam is 36 times larger than the kaon component, this leads to a non-negligible $\pi^-\pi^-\pi^+$ background in the $K^-\pi^-\pi^+$ sample, even considering the excellent misidentification probability for beam particle identification of only 1 ‰. The final-state particle identification can suppress this background only to a very limited extend, because we required only one of the two negative final-state particle to be identified either as a K^- or a π^- and the $K^-\pi^-\pi^+$ and the $\pi^-\pi^-\pi^+$ final state both contain a π^-.

In order to study the $\pi^-\pi^-\pi^+$ background in the $K^-\pi^-\pi^+$ sample, we generated a pseudodata sample for the reaction $\pi^- + p \to \pi^-\pi^-\pi^+ + p$, which is called $\pi^-\pi^-\pi^+$ pseudodata sample. In order to follow the same approach as in the $K^-\pi^-\pi^+$ pseudodata studies in section 5.8 requires a PWD model of this reaction. Fortunately, COMPASS collected the so-far world's largest sample of the reaction $\pi^- + p \to \pi^-\pi^-\pi^+ + p$ using the dominant π^- component in our beam. Based on this sample, an extensive PWD was performed using the so-far world's largest PWD model in this channel [39]. The results of the COMPASS $\pi^-\pi^-\pi^+$ analysis were studied in detail and are well understood [38–41, 72, 80, 133]. Based on these results, an improved re-analysis of this reaction based on the 2008 diffraction data set was performed and will be presented in ref. [43].[cs] The COMPASS results hence provide a reliable and realistic model for the reaction $\pi^- + p \to \pi^-\pi^-\pi^+ + p$. We used the PWD model obtained in the analysis in ref. [43] and summarized in appendix D.4.1 to generate a pseudodata sample for the reaction $\pi^- + p \to \pi^-\pi^-\pi^+ + p$. We generated 47 405 138 pseudodata events, which corresponds to exactly 1/3 of the number of produced events that we expect in the 2008 diffraction data set as predicted by the PWD model.

To determine the amount and the kinematic distribution of the $\pi^-\pi^-\pi^+$ background in the measured $K^-\pi^-\pi^+$ sample, we processed the produced $\pi^-\pi^-\pi^+$ pseudodata events through the COMPASS detector Monte Carlo simulation. Then, we misinterpreted them as $K^-\pi^-\pi^+$ events, i.e. we applied the CEDAR and RICH misidentification probabilities as described in appendices C.2.2 and C.2.3, respectively. Finally, we applied the same event selection criteria to the $\pi^-\pi^-\pi^+$ pseudodata sample as applied to the measured $K^-\pi^-\pi^+$ sample (see section 4.1). This procedure yielded the reconstructed $\pi^-\pi^-\pi^+$ pseudodata sample.

[cs] The 2009 diffraction data set was not used in the $\pi^-\pi^-\pi^+$ analysis when obtaining the model for the $\pi^-\pi^-\pi^+$ pseudodata, yet.

5.10.1 The Reconstructed $\pi^-\pi^-\pi^+$ Pseudodata Sample

The amount of $\pi^-\pi^-\pi^+$ background in the measured $K^-\pi^-\pi^+$ sample can be predicted from the amount of reconstructed $\pi^-\pi^-\pi^+$ pseudodata events. Analogously to the effective intensity model for the background contributions in equation (5.62), the absolute detector acceptance in the COMPASS $\pi^-\pi^-\pi^+$ analysis and in this analysis enter the prediction for the amount of $\pi^-\pi^-\pi^+$ background. For the PWD only the modulation of the acceptance in the phase-space variables is important. Imperfections in modeling the absolute acceptance do not bias the results of the PWD.[ct] Therefore, the acceptance model was not fine-tuned for the determination the absolute acceptance in either of the two analysis. However, the same approach to determine the experimental acceptance as used in this analysis and described in appendix C.2 was also used in the $\pi^-\pi^-\pi^+$ analysis in ref. [43], from which we took the model for the $\pi^-\pi^-\pi^+$ pseudodata sample. Thus, potential systematic effects from imperfect estimates of the absolute acceptances should cancel out to first order [see equation (5.62)]. Hence, we expect the $\pi^-\pi^-\pi^+$ pseudodata sample to yield a rough but realistic estimate for the predicted amount of $\pi^-\pi^-\pi^+$ background.

From the 47 405 138 produced $\pi^-\pi^-\pi^+$ pseudodata events 8934 events were reconstructed as $K^-\pi^-\pi^+$ events. Taking into account that the size of the produced pseudodata sample is only $1/3$ of the predicted number of produced $\pi^-\pi^-\pi^+$ events in the measured data, we expect a $\pi^-\pi^-\pi^+$ background of 26 802 events in the measured $K^-\pi^-\pi^+$ sample of the 2008 diffraction data set. This corresponds to a $\pi^-\pi^-\pi^+$ contamination of 6.7 %. Given the similar acceptance for the 2008 and 2009 diffraction data sets, we expect the same $\pi^-\pi^-\pi^+$ contamination in the combined 2008 and 2009 $K^-\pi^-\pi^+$ sample. Compared to other backgrounds, e.g. the background from $K^- + p \to K^-K^-K^+ + p$ events of about 4 %, we expect the $\pi^-\pi^-\pi^+$ background to be the largest background in the $K^-\pi^-\pi^+$ sample. A detailed reasoning for the amount of $\pi^-\pi^-\pi^+$ background is given in appendix D.4.2.

In figure 5.38, we compare the $\pi^-\pi^-\pi^+$ pseudodata sample reconstructed as $K^-\pi^-\pi^+$ events (red histograms) to the measured $K^-\pi^-\pi^+$ sample (blue histograms). The $\pi^-\pi^-\pi^+$ pseudodata exhibit a broad distribution in $m_{K\pi\pi}$ shown in figure 5.38a. No clear peaks from $\pi^-\pi^-\pi^+$ resonances are observed. Thus, the peaks observed in the $m_{3\pi}$ spectrum in figure 5 of ref. [39] are smeared out by the wrong final-state particle mass assumption and none of the peaks observed in the measured $m_{K\pi\pi}$ spectrum is caused by the $\pi^-\pi^-\pi^+$ background.

The $m_{\pi^-\pi^+}$ spectrum obtained from the reconstructed $\pi^-\pi^-\pi^+$ pseudodata sample shows similar structures as the one from the $K^-\pi^-\pi^+$ sample (see figure 5.38b). Both show clear signals from

[ct] For example, the energies E_{beam}, with which the beam particles in the pseudodata sample were produced, were taken from a sample of measured beam energies in a chosen E_{beam} range (see appendix C.2.1). This range is wider than the E_{beam} range, in which those pseudodata events were accepted in the $K^-\pi^-\pi^+$ event selection, as described in section 4.1. The choice of this E_{beam} range, in which the pseudodata samples were generated, does not affect the PWD. This is so because only the reconstructed pseudodata events that survived the $K^-\pi^-\pi^+$ event selection, i.e. that lied within the narrower E_{beam} range of the event selection, affect the modulation of the acceptance in the phase-space variables in the acceptance model. However, the choice of this E_{beam} range, in which the pseudodata samples were generated, affects the estimate for the absolute acceptance as it affects the fraction of produce pseudodata events that were reconstructed.

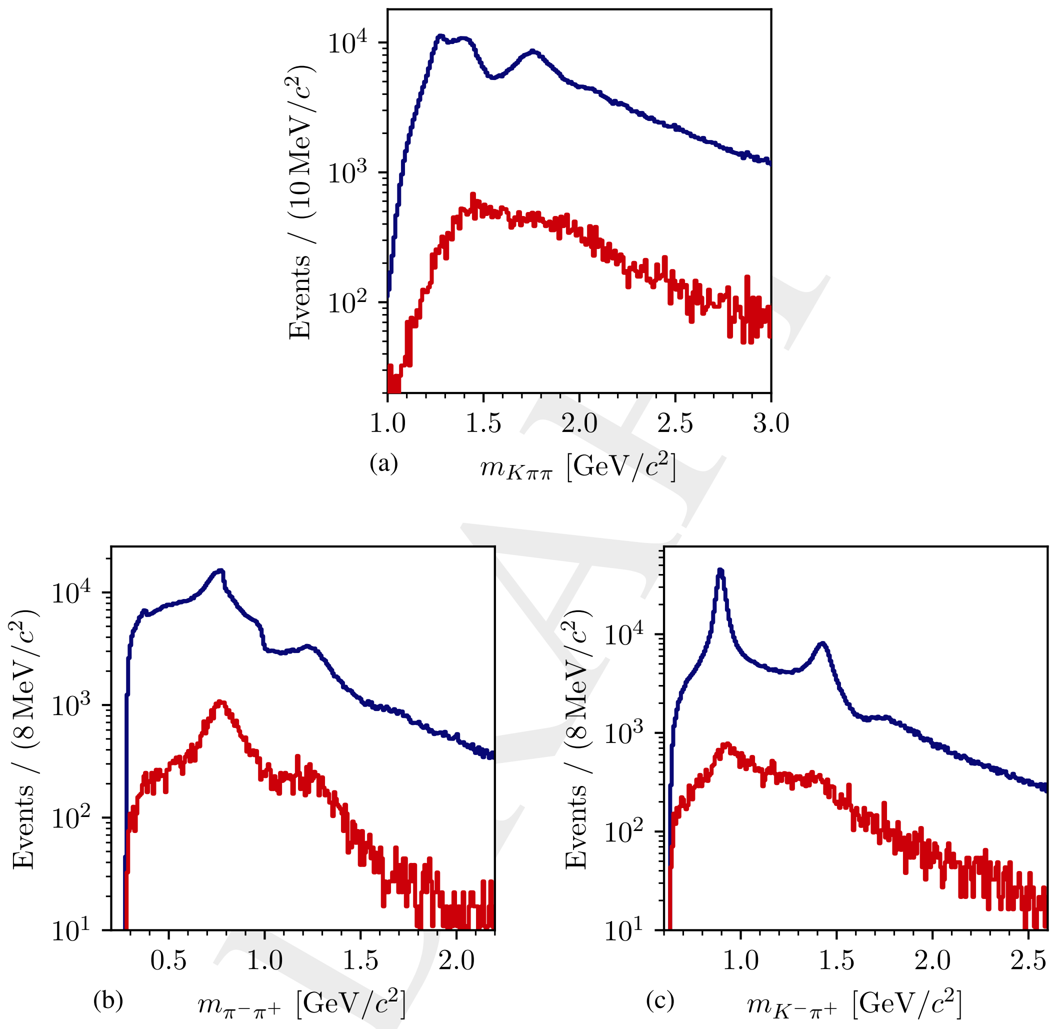

Figure 5.38: Distributions in the invariant masses of (a) the $K^-\pi^-\pi^+$ system, (b) the $\pi^-\pi^+$ subsystem, and (c) the $K^-\pi^+$ subsystem. The red histograms show the $\pi^-\pi^-\pi^+$ pseudodata sample reconstructed as $K^-\pi^-\pi^+$ events (see text) and scaled such that the total number of reconstructed $\pi^-\pi^-\pi^+$ pseudodata events corresponds to the predicted amount of $\pi^-\pi^-\pi^+$ background in the $K^-\pi^-\pi^+$ sample. The blue histograms show the measured $K^-\pi^-\pi^+$ sample (same as figures 4.6a, 4.7a, and 4.7b, respectively).

$\pi^-\pi^+$ resonances such as the $\rho(770)$ and $f_2(1270)$, and a shoulder from the $f_0(980)$. This is expected, because both reactions, i.e. $\pi^- + p \to \pi^-\pi^-\pi^+ + p$ and $K^- + p \to K^-\pi^-\pi^+ + p$, contain the $\pi^-\pi^+$ subsystem in the final states.

The $m_{K^-\pi^+}$ spectrum from the reconstructed $\pi^-\pi^-\pi^+$ pseudodata exhibits a broad distribution shown by the red histogram in figure 5.38c. On top of this distribution we find a peak at about $0.94\,\text{GeV}/c^2$. This peak corresponds to the $\rho(770)$ resonance in the $\pi^-\pi^+$ subsystem of the $\pi^-\pi^-\pi^+$ final state. Compared to the nominal $\rho(770)$ mass, it is shifted towards higher masses, i.e. when erroneously identifying the π^- as K^-. Interestingly, this "$\rho(770)$ peak" is at a similar $m_{K^-\pi^+}$ position as the narrow peak in the measured $K^-\pi^-\pi^+$ sample, which arises from the $K^*(892)$ resonance in the $K^-\pi^+$ subsystem. However, the "$\rho(770)$ peak" is about 4 times broader than the $K^*(892)$ resonance. Furthermore, the $m_{K^-\pi^+}$ spectrum from the reconstructed $\pi^-\pi^-\pi^+$ pseudodata sample exhibits a shoulder at about $1.4\,\text{GeV}/c^2$, which corresponds to the $f_2(1270)$ resonance in the $\pi^-\pi^+$ subsystem. Interestingly, this "$f_2(1270)$ peak" is at a similar $m_{K^-\pi^+}$ position as and has an about 1.3 times larger width than the higher-lying peak in the measured $K^-\pi^-\pi^+$ sample, which partly arises from the $K_2^*(1430)$ resonance in the $K^-\pi^+$ subsystem. Despite the similar resonance position, the signals in the measured $K^-\pi^-\pi^+$ sample and in the reconstructed $\pi^-\pi^-\pi^+$ pseudodata sample arise from different resonances. Hence, they are in detail different and a model for the reaction $K^- + p \to K^-\pi^-\pi^+ + p$ may not be able to perfectly describe the $\pi^-\pi^-\pi^+$ background. This is discussed in the following section 5.10.2.

5.10.2 Partial-Wave Decomposition of $\pi^-\pi^-\pi^+$ Pseudodata

In order to study the influence of the $\pi^-\pi^-\pi^+$ background on the PWD of the measured $K^-\pi^-\pi^+$ sample, we performed a PWD of the $\pi^-\pi^-\pi^+$ pseudodata sample that was reconstructed as $K^-\pi^-\pi^+$ events. In the rest of the text it is called the $\pi^-\pi^-\pi^+$ background PWD.[cu]

To compare the results of the $\pi^-\pi^-\pi^+$ background PWD to those from the measured $K^-\pi^-\pi^+$ sample, we used the same 238-wave set. In the COMPASS $\pi^-\pi^-\pi^+$ analysis, the measured $\pi^-\pi^-\pi^+$ sample is described well by a PWD model with a rank = 1 spin-density matrix.[cv] However, in the $\pi^-\pi^-\pi^+$ background PWD performed here, we misinterpreted the pseudodata events as $K^-\pi^-\pi^+$ events, and we effectively modeled their distribution using partial waves of the reaction $K^- + p \to K^-\pi^-\pi^+ + p$. This means, e.g., that events from different $m_{3\pi}$ bins, which

[cu] The reconstructed $\pi^-\pi^-\pi^+$ pseudodata sample contains only 8934 events and is thus insufficient to perform a PWD. Since, in the $K^-\pi^-\pi^+$ event selection, it is mainly the beam-particle identification that suppresses the $\pi^-\pi^-\pi^+$ events, we omitted the beam-particle identification cut (BPID cut) when selecting the sample that was used for the PWD. The BPID cut affects only the number of accepted events and their distribution in the inclination space of the beam particle (see section 3.2 and figure C.3b). The distribution of the beam particle has a negligible influence on the phase-space distribution of the final-state particles, which was verified. Omitting the BPID cut yielded a reconstructed $\pi^-\pi^-\pi^+$ pseudodata sample of about 8.37×10^6 events, which is well suited to perform a PWD.

[cv] The positive-reflectivity waves are modeled by a rank=1 spin-density matrix, the negative-reflectivity waves by a rank=2 spin-density matrix. Also, an incoherent flat wave was added to the model. The latter two account for only 2.2 % and 3.1 % of the total intensity, respectively [39]. Hence, the $\pi^-\pi^-\pi^+$ background PWD model is dominantly a coherent rank=1 model.

need to be treated incoherently, enter the same $m_{K\pi\pi}$ bin, which is described by one PWD model. Therefore, the $\pi^-\pi^-\pi^+$ background PWD requires a model with rank >1. This was confirmed by tests using a rank=1 PWD model to describe the reconstructed $\pi^-\pi^-\pi^+$ pseudodata sample, which yielded unsatisfactory results for the $\pi^-\pi^-\pi^+$ pseudodata sample based on the measured $\pi^-\pi^-\pi^+$ sample as well as for the measured $K^-\pi^-\pi^+$ sample. For $\pi^-\pi^-\pi^+$ pseudodata sample for example, the description phase-space distribution of the $\pi^-\pi^-\pi^+$ pseudodata by the rank=1 PWD model was insufficient. Also, the obtained intensity spectra of the partial waves were strongly fluctuating from $m_{K\pi\pi}$ bin to $m_{K\pi\pi}$ bin. For the measured $K^-\pi^-\pi^+$ sample, taking into account the $\pi^-\pi^-\pi^+$ background in an RMF to the $K^-\pi^-\pi^+$ PWD (see chapter 6) using a rank=1 model for the $\pi^-\pi^-\pi^+$ background PWD, the RMF was not able to describe the partial-waves. Thus, we finally used a rank=2 PWD model in the $\pi^-\pi^-\pi^+$ background PWD, which turned out to be sufficient to remedy these imperfections as discussed in the following.

Performing a Bootstrapping of the $\pi^-\pi^-\pi^+$ background PWD was computationally too expensive.[cw] Thus, we give in the following the maximum-likelihood estimates from the $\pi^-\pi^-\pi^+$ background PWD and we do not give the corresponding uncertainty estimates for the same reason as given in section 5.7.

Figure 5.39 shows the results of the $\pi^-\pi^-\pi^+$ background PWD (orange data points), i.e. the $\pi^-\pi^-\pi^+$ background predicted in the various partial waves. We find large intensities in partial waves with a $\rho(770)$ isobar. Figure 5.39a shows exemplarily the intensity spectrum of the $2^+\,1^+\,\rho(770)\,K\,D$ wave, which is the wave with the largest $\pi^-\pi^-\pi^+$ background relative the intensity spectrum obtained from the measured $K^-\pi^-\pi^+$ sample (blue data points). These large backgrounds in waves with a $\rho(770)$ isobar are expected, as the $\pi^-\pi^-\pi^+$ pseudodata contain a large contribution from the $\rho(770)$ isobar in the $\pi^-\pi^+$ subsystem as shown in figure 5.38b. Interestingly, in the $2^+\,1^+\,\rho(770)\,K\,D$ wave the $\pi^-\pi^-\pi^+$ background PWD yielded a peaking structure at about $1.5\,\text{GeV}/c^2$, i.e. at a similar mass as the peak in the measured $K^-\pi^-\pi^+$ sample, which arises from the $K_2^*(1430)$ resonance. This similarity of physics and background signals stresses the importance of a proper treatment of the $\pi^-\pi^-\pi^+$ background contributions in the PWD (see section 5.3) and in the RMF (see chapter 6).

Similarly, the intensity spectra of waves with an $f_2(1270)$ isobar show small but non-negligible structures in the $\pi^-\pi^-\pi^+$ background PWD, exemplarily shown for the intensity spectrum of the $2^-\,0^+\,f_2(1270)\,K\,S$ wave in figure 5.39b. In this wave, the $\pi^-\pi^-\pi^+$ background peaks at $m_{K\pi\pi} \approx 1.9\,\text{GeV}/c^2$, similar to the peak observed in the measured $K^-\pi^-\pi^+$ sample.

The $\pi^-\pi^-\pi^+$ background PWD exhibits negligible intensity in partial waves with a $K^*(892)$ isobar exemplarily shown in figure 5.39c. This is expected, because there is no $K^*(892)$ resonance in the $\pi^-\pi^-\pi^+$ pseudodata and the structures in the $m_{K^-\pi^+}$ spectrum of the reconstructed $\pi^-\pi^-\pi^+$ pseudodata sample, especially the peak at about $0.94\,\text{GeV}/c^2$, which is caused by the $\rho(770)$ resonance (see figure 5.38c), differ from the shape of the $K^*(892)$ isobar resonance.

[cw] Furthermore, given the much larger size of the $\pi^-\pi^-\pi^+$ pseudodata sample as compared to the measured $K^-\pi^-\pi^+$ sample and thus the higher precision, we expect the maximum-likelihood estimates from the $\pi^-\pi^-\pi^+$ background PWD to be not strongly biased by non-linearities, which are discussed in section 5.4.

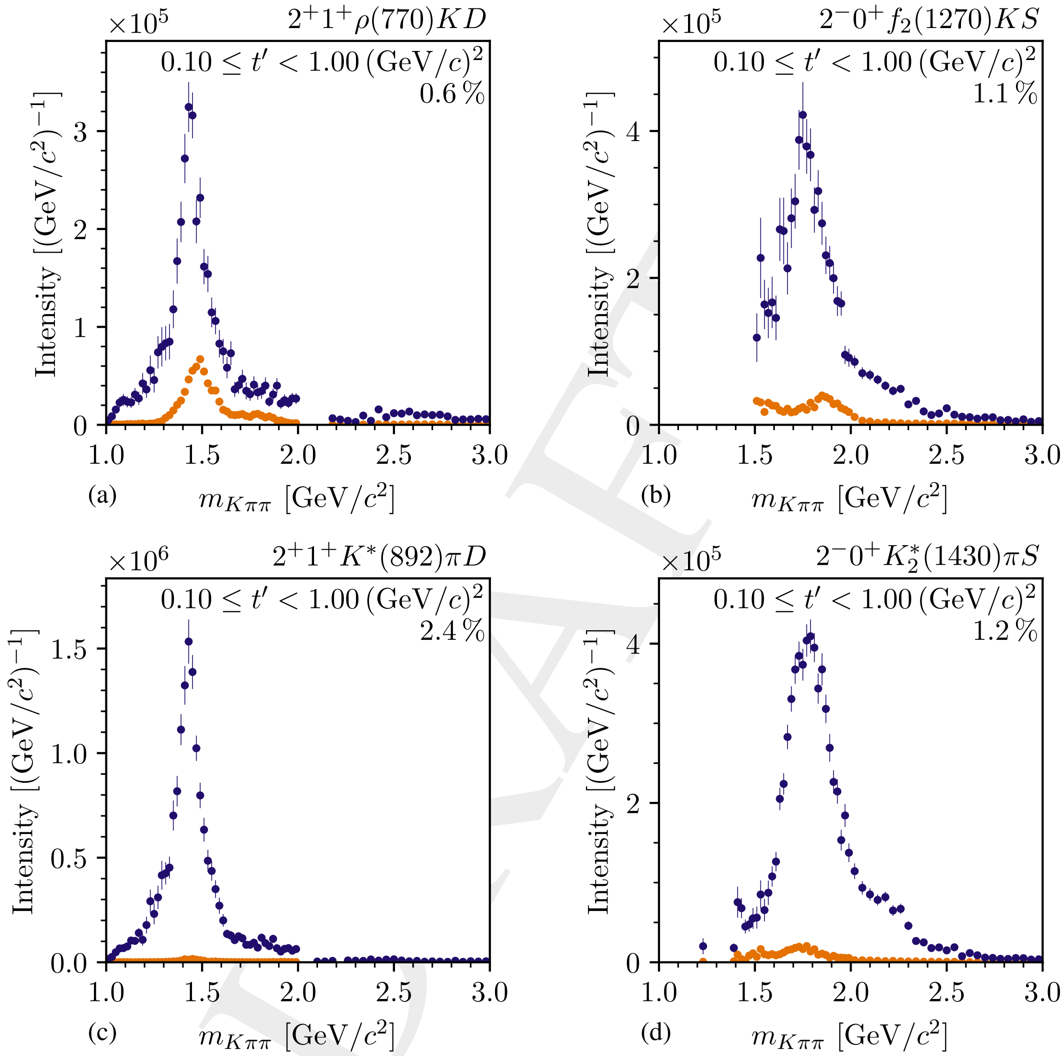

Figure 5.39: t'-summed intensity spectra of four selected partial waves as obtained from the $\pi^-\pi^-\pi^+$ background PWD (orange data points). The blue data points show the corresponding results from the PWD of the measured $K^-\pi^-\pi^+$ sample. The percentages give the contribution of each wave to the total intensity as obtained from the measured $K^-\pi^-\pi^+$ sample. The results of the $\pi^-\pi^-\pi^+$ background PWD are scaled such that the total number of reconstructed $\pi^-\pi^-\pi^+$ pseudodata events corresponds to the predicted amount of $\pi^-\pi^-\pi^+$ background in the $K^-\pi^-\pi^+$ sample. We give the maximum-likelihood estimates from the $\pi^-\pi^-\pi^+$ background PWD. The corresponding uncertainties are not shown (see text).

In contrast to waves with a $K^*(892)$ isobar, the intensity spectra of waves with $K_2^*(1430)$ isobar show small but non-negligible structures in the $\pi^-\pi^-\pi^+$ background PWD (see for example figure 5.39d). Due to the larger width of the $K_2^*(1430)$ resonance compared to the $K^*(892)$, waves with $K_2^*(1430)$ isobar are used by the PWD more easily to effectively describe the distribution of the $\pi^-\pi^-\pi^+$ pseudodata. Furthermore, the shoulder at about $1.4\,\text{GeV}/c^2$ in the $m_{K^-\pi^+}$ distribution of the reconstructed $\pi^-\pi^-\pi^+$ pseudodata (see figure 5.38c) is similar to the shape of the $K_2^*(1430)$ isobar. Hence, we expect a non-negligible intensity from the $\pi^-\pi^-\pi^+$ background PWD in waves with $K_2^*(1430)$ isobar.

As discussed in section 5.3, we effectively take into account incoherent background processes, such as the $\pi^-\pi^-\pi^+$ background, in the PWD of the measured $K^-\pi^-\pi^+$ sample by using a rank=3 PWD model. This requires the phase-space distribution of the background events to be sufficiently well modeled by the $K^-\pi^-\pi^+$ PWD model, i.e. by the partial waves of the reaction $K^- + p \to K^-\pi^-\pi^+ + p$ that were selected in the 238-wave set. We tested this assumption for the $\pi^-\pi^-\pi^+$ background by comparing the prediction of the phase-space distribution from the $\pi^-\pi^-\pi^+$ background PWD to the actual distribution of the reconstructed $\pi^-\pi^-\pi^+$ pseudodata sample as shown in figure 5.40. Hence, we perform a similar comparison as for the measured $K^-\pi^-\pi^+$ sample in section 5.6.

The $K^-\pi^-\pi^+$ PWD model (orange histogram) describes the $m_{\pi^-\pi^+}$ distribution of the reconstructed $\pi^-\pi^-\pi^+$ pseudodata sample (blue data points) well as show in figure 5.40a. This is expected, because the $K^-\pi^-\pi^+$ model contains waves with $\pi^-\pi^+$ isobars, which were designed to model this distribution. Accordingly, the $\cos\theta_{\text{GJ}}^{\pi\pi}$ distribution for the decay $X^- \to \xi^0_{\pi^-\pi^+}K^-$ shown in figure 5.40b is also reproduced well by the $K^-\pi^-\pi^+$ PWD model.

In the low-$m_{K\pi\pi}$ region shown in figure 5.40c, the $m_{K^-\pi^+}$ distribution of the reconstructed $\pi^-\pi^-\pi^+$ pseudodata sample shows a narrow peak on top of a bump at about $0.9\,\text{GeV}/c^2$. This shape arises from a complicated interplay of $\pi^-\pi^-\pi^+$ events where one of the π^- was erroneously identified as a K^-. As the waves in the $K^-\pi^-\pi^+$ PWD model are not explicitly designed to describe this shape, it is effectively described by a combination of various partial waves. The $K^-\pi^-\pi^+$ model approximates well the $m_{K^-\pi^+}$ distribution of the reconstructed $\pi^-\pi^-\pi^+$ pseudodata sample. In the high-$m_{K\pi\pi}$ region, the $K^-\pi^-\pi^+$ PWD model only roughly reproduces the very broad bump in the $m_{K^-\pi^+}$ distribution of the reconstructed $\pi^-\pi^-\pi^+$ pseudodata sample as shown in figure 5.40d.

Reviewing our findings presented in this section, the $K^-\pi^-\pi^+$ partial wave model is able to sufficiently well reproduce the distribution of the reconstructed $\pi^-\pi^-\pi^+$ pseudodata sample. Thus, our approach to treat the incoherent $\pi^-\pi^-\pi^+$ background described in section 5.3 is applicable. We expect waves with $K^*(892)$ isobar to be mainly free of $\pi^-\pi^-\pi^+$ background, while we expect significant $\pi^-\pi^-\pi^+$ background in waves with $\rho(770)$ isobar. In waves with other isobars, such as the $K_2^*(1430)$ or the $f_2(1270)$ isobar, we expect modest $\pi^-\pi^-\pi^+$ background. As the $\pi^-\pi^-\pi^+$ background is expected to be the dominant background in the $K^-\pi^-\pi^+$ sample and hence demands the most accurate treatment, we assume that also other incoherent background processes are treated sufficiently well by using a rank=3 PWD model. However, it is important to note that this treatment does not separate physics signals from background at the stage of the PWD. This separation is done at the stage of the resonance-model fits discussed in chapter 6.

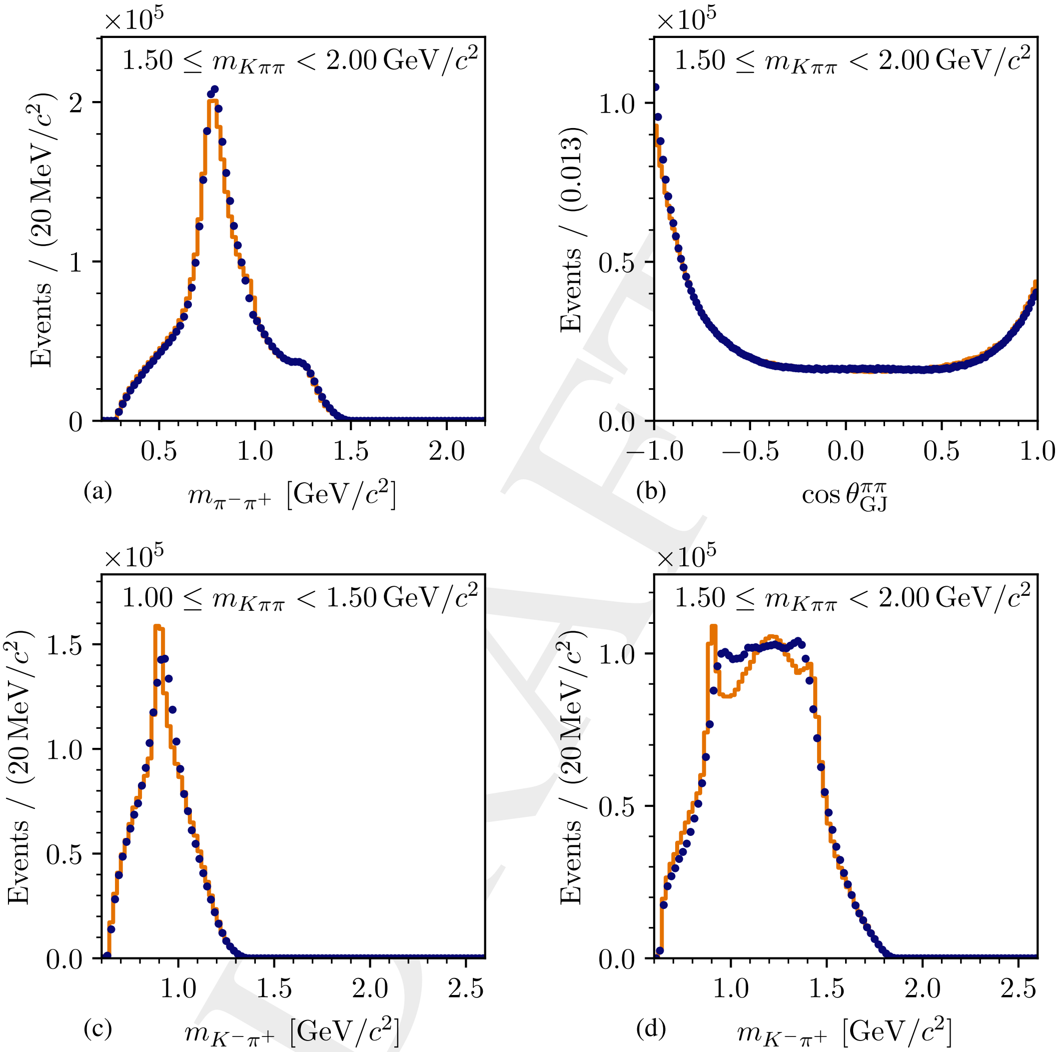

Figure 5.40: Distribution of selected phase-space variables in the mass range $1.5 \leq m_{K\pi\pi} < 2.0\,\mathrm{GeV}/c^2$ ((a), (b), and (d)) and in the mass range $1.0 \leq m_{K\pi\pi} < 1.5\,\mathrm{GeV}/c^2$ (c), all integrated over the analyzed t' range. The blue data points show the distribution of the reconstructed $\pi^-\pi^-\pi^+$ pseudodata sample. The orange histograms show the corresponding predictions from the $\pi^-\pi^-\pi^+$ background PWD (see appendix C.3 for details on how these histograms were obtained). (a) shows the distribution in $m_{\pi^-\pi^+}$. (b) shows the distribution in $\cos\theta_{\mathrm{GJ}}^{\pi\pi}$ of the decay $X^- \to \xi^0_{\pi^-\pi^+} K^-$. (c) and (d) show the distribution in $m_{K^-\pi^+}$ in the low- and high-$m_{K\pi\pi}$ region, respectively.

6 The Resonance-Model Fit

The so-called resonance-model fit (RMF), which is the second stage of our analysis, aims to identify strange-meson resonances that appear in the various partial waves and to measure their masses and widths. To this end, the $m_{K\pi\pi}$ dependence of the spin-density matrix elements, which was measured in the PWD, is modeled in the RMF. In order to employ all the available information in a coherent way, all four t' bins are fit simultaneously in one RMF. While in the PWD, the full $K^-\pi^-\pi^+$ sample must be modeled, in the RMF we can select a suitable subset of partial waves that we want to study. This is a big advantage of our two-stage analysis approach, as we can select partial waves with clear resonance-like signals, and we can avoid modeling the leakage waves.

We first introduce in section 6.1 the RMF formalism. Then, in section 6.2 we give a first glimpse on the results of the 10-wave RMF, which represents the main results of this analysis. Finally, we discuss in sections 6.3 and 6.4 various systematic and pseudodata studies that we performed in order to scrutinize our results.

6.1 Method

6.1.1 Modeling the Spin-Density Matrix

Our $K^-\pi^-\pi^+$ sample does not only contain events of the signal reaction $K^- + p \to K^-\pi^-\pi^+ + p$, but has also contributions from background reactions such as $\pi^- + p \to \pi^-\pi^-\pi^+ + p$. At the stage of the PWD, we took these background contributions into account in an effective way by formulating a PWD model with a rank=3 spin-density matrix. However, in this approach we did not yet separate the signal from the background contributions. As indicated by equation (5.66), the spin-density matrix that was measured in the PWD is an incoherent sum over the $K^-\pi^-\pi^+$ signal and the various backgrounds. Hence, the measured spin-density matrix $\rho_{ab}(m_{K\pi\pi}, t')$ is modeled by a sum of spin-density matrices, one for each contribution, i.e.

$$\hat{\rho}_{ab}(m_{K\pi\pi}, t') = \hat{\rho}_{ab}^{K\pi\pi}(m_{K\pi\pi}, t') + \hat{\rho}_{ab}^{3\pi}(m_{K\pi\pi}, t') + \hat{\rho}_{ab}^{\mathrm{eBKG}}(m_{K\pi\pi}, t'). \tag{6.1}$$

$\hat{\rho}_{ab}^{K\pi\pi}(m_{K\pi\pi}, t')$ represents the RMF model for the $K^-\pi^-\pi^+$ spin-density matrix of the signal reaction $K^- + p \to K^-\pi^-\pi^+ + p$, which is discussed in section 6.1.2. $\hat{\rho}_{ab}^{3\pi}(m_{K\pi\pi}, t')$ represents the RMF model for the $\pi^-\pi^-\pi^+$ background, which is explicitly modeled as discussed in section 6.1.3.

$\hat{\rho}^{\text{eBKG}}_{ab}(m_{K\pi\pi}, t')$ represents the effective background component (eBKG), which effectively takes into account all other background contributions. It is explained in section 6.1.4.

6.1.2 Modeling the $K^-\pi^-\pi^+$ Signal

We used a naïve model of the reaction $K^- + p \to K^-\pi^-\pi^+ + p$, which is based on a sum of Breit-Wigner amplitudes for the resonances. In principle, there are more elaborate models to parameterize resonance amplitudes such as K-matrix models [23] or N-over-D models [134]. However, they typically require to simultaneously model all decay channels of a studied resonance, while we have access to only a limited set of decay channels, i.e. those that finally lead to the $K^-\pi^-\pi^+$ final state. Also, these more elaborate approaches are theoretically and computationally more demanding, and it turned out that in many cases they yield results similar to those from simpler Breit-Wigner models (compare ref. [41] and ref. [135]). Hence, we used sum-of-Breit-Wigner models in our analysis.

Modeling the Transition Amplitudes

Our model $\hat{\rho}^{K\pi\pi}_{ab}(m_{K\pi\pi}, t')$ for the spin-density matrix of the reaction $K^- + p \to K^-\pi^-\pi^+ + p$ is formulated in terms of a model $\hat{\mathcal{T}}^{K\pi\pi}_a(m_{K\pi\pi}, t')$ for the corresponding transition amplitudes. In this model, multiple resonance components are included for the various strange-meson resonances that appear in the partial waves. In addition, a single so-called non-resonant component is added for each partial wave, which models the coherent non-resonant contributions from processes such as Deck-like reactions discussed in section 2.1.1. The wave components are labeled by k.

Following equation (5.15), the transition amplitude of component k in wave a reads

$$ {}^{k}\hat{\mathcal{T}}^{K\pi\pi}_a(m_{K\pi\pi}, t') = \sqrt{\frac{\mathscr{L}}{(2\pi\mathfrak{F})^2}}\ \sqrt{m_{K\pi\pi}}\mathcal{P}^{K\pi\pi}_{k,a}(m_{K\pi\pi}, t')\, \mathcal{D}_k(m_{K\pi\pi}; \zeta_k)\, \alpha_{k\to\xi bL}\, \alpha_\xi \sqrt{\mathfrak{N}_a(m_{K\pi\pi})}, \quad (6.2) $$

where ζ_k are the shape parameters of our parameterization $\mathcal{D}_k(m_{K\pi\pi}; \zeta_k)$ for the dynamic amplitude of component k, e.g. in the case of a resonance components the mass and width of that resonance. The shape parameters are determined in the RMFs.

The production amplitude $\mathcal{P}^{K\pi\pi}_{k,a}(m_{K\pi\pi}, t')$ can be split into three parts. First, a complex-valued coupling $\alpha^{M^\varepsilon}_{K\mathbb{P}\to k}(t')$, which represents the strength and phase with which each component k in partial wave a is produced at the $K\mathbb{P} \to k$ vertex (see X^- production vertex in figure 5.3). Second, a complex-valued coupling $\alpha^{a}_{p\mathbb{P}\to p}(t')$, which represents the bottom vertex in figure 5.3. Both couplings depend in general on t'. Third, the production factor $\mathcal{P}_{\mathbb{P}}(m_{K\pi\pi}, t')$. This factor models the scattering process via t-channel Pomeron exchange, which we assume to dominate at the high center-of-momentum energy at COMPASS. The production factor is the same for all partial waves and for all components. It is given in equation (6.12) below.

With the factorization of the production amplitude discussed above and after re-ordering the terms, equation (6.2) reads

$$
\begin{aligned}
&{}^{k}\hat{\mathcal{T}}_a^{K\pi\pi}(m_{K\pi\pi}, t') = \\
&\sqrt{\mathfrak{N}_a(m_{K\pi\pi}) m_{K\pi\pi}}\, \mathcal{P}_{\mathbb{P}}(m_{K\pi\pi}, t') \sqrt{\frac{\mathscr{L}}{(2\pi\mathfrak{F})^2}}\, \alpha^{M^\varepsilon}_{K\mathbb{P}\to k}(t')\, \alpha^{a}_{p\mathbb{P}\to p}(t')\, \alpha_{k\to\xi bL}\, \alpha_\xi\, \mathcal{D}_k(m_{K\pi\pi}; \zeta_k).
\end{aligned} \tag{6.3}
$$

As only the $m_{K\pi\pi}$ dependence is explicitly modeled in the RMF, we collect all terms that do not depend on $m_{K\pi\pi}$ in the so-called <u>coupling amplitudes</u>

$$
{}^{k}\mathcal{C}_a^{K\pi\pi}(t') \equiv \sqrt{\frac{\mathscr{L}}{(2\pi\mathfrak{F})^2}}\, \alpha^{M^\varepsilon}_{K\mathbb{P}\to k}(t')\, \alpha^{a}_{p\mathbb{P}\to p}(t')\, \alpha_{k\to\xi bL}\, \alpha_\xi. \tag{6.4}
$$

The coupling amplitudes encode the overall strength and phase with which component k appears in partial-wave a and are in general unknown. The t' dependence of the coupling amplitudes is parameterized by piecewise constant functions in t', i.e. there is an independent complex-valued parameter for each t' bin for each coupling amplitude.[a] These parameters are determined in the RMF. In this way, the t' dependence of each model component in each partial wave in which it appears is determined from the data in a model-independent way.

Finally, our model for the transition amplitude of a single component k in a wave a reads

$$
{}^{k}\hat{\mathcal{T}}_a^{K\pi\pi}(m_{K\pi\pi}, t') = \sqrt{\mathfrak{N}_a(m_{K\pi\pi}) m_{K\pi\pi}}\, \mathcal{P}_{\mathbb{P}}(m_{K\pi\pi}, t')\; {}^{k}\mathcal{C}_a^{K\pi\pi}(t')\, \mathcal{D}_k(m_{K\pi\pi}; \zeta_k). \tag{6.5}
$$

The RMF model for the total transition amplitude of wave a hence reads

$$
\begin{aligned}
\hat{\mathcal{T}}_a^{K\pi\pi}(m_{K\pi\pi}, t') &= \sum_{k\in\mathbb{S}_a} {}^{k}\hat{\mathcal{T}}_a^{K\pi\pi}(m_{K\pi\pi}, t') \\
&= \sqrt{\mathfrak{N}_a(m_{K\pi\pi}) m_{K\pi\pi}}\, \mathcal{P}_{\mathbb{P}}(m_{K\pi\pi}, t') \sum_{k\in\mathbb{S}_a} {}^{k}\mathcal{C}_a^{K\pi\pi}(t')\, \mathcal{D}_k(m_{K\pi\pi}; \zeta_k).
\end{aligned} \tag{6.6}
$$

The sum in equation (6.6) runs over the set $\mathbb{S}_a$ of all components that we assume to contribute to partial wave a.

Modeling the Spin-Density Matrix

In the RMF, the signal reaction $K^- + p \to K^-\pi^-\pi^+ + p$ is modeled as a fully coherent process. Hence, $\hat{\rho}_{ab}^{K\pi\pi}(m_{K\pi\pi}, t')$ has rank $= 1$. It is constructed from the transition amplitudes in equation (6.6) in the following way

$$
\hat{\rho}_{ab}^{K\pi\pi}(m_{K\pi\pi}, t') = \hat{\mathcal{T}}_a^{K\pi\pi}(m_{K\pi\pi}, t') \left[\hat{\mathcal{T}}_b^{K\pi\pi}(m_{K\pi\pi}, t')\right]^*. \tag{6.7}
$$

[a] One coupling amplitude has to be chosen real-valued and positive in order to fix the indeterminable global phase.

Parameterization of the Resonance Components

We parameterized the dynamic amplitudes $\mathcal{D}_k(m_{K\pi\pi};\zeta_k)$ of resonance appearing in the $K^-\pi^-\pi^+$ system by relativistic Breit-Wigner amplitudes according to equation (5.39). The dynamic width of these Breit-Wigner amplitudes takes into account only the dominant decay channel of the corresponding resonance as listed in tables E.1 and E.5. The shape parameters of the resonance components are the nominal masses and widths of the resonances, i.e. $\zeta_k = (m_0^k, \Gamma_0^k)$. In this way, the masses and widths of the strange-meson resonances are measured in the RMF.

Parameterization of the Non-Resonant Components

As discussed in section 2.1.1, there are additional processes that also lead to the $K^-\pi^-\pi^+$ final state, but do not proceed via an intermediate strange-meson resonance in the $K^-\pi^-\pi^+$ system. Similar to the background contributions, they are effectively decomposed into partial waves in the PWD, and they need to be explicitly treated at the stage of the RMF. In contrast to the background contributions, the non-resonant contributions must be added coherently to the amplitudes for the $K^-\pi^-\pi^+$ resonances.

As there are various non-resonant processes that may contribute and as there are no generally accepted theory models available for them, we parameterized the dynamic amplitudes of the non-resonant components by a phenomenological parameterization with a flexible shape that is adjusted to the data in the RMF. The employed parameterization is inspired by ref. [136] and was used in previous analyses, such as the COMPASS $\pi^-\pi^-\pi^+$ analysis [40, 41]. It reads

$$\mathcal{D}_k^{\mathrm{NR}}(m_{K\pi\pi}; a_k, c_k) = (m_{K\pi\pi} - m_{\mathrm{thr}})^{a_k} e^{-b(c_k)\,\tilde{q}_k^2(m_{K\pi\pi})}. \tag{6.8}$$

Here, a_k and c_k are the free shape parameters that are determined by the RMF. One should note, that each partial wave has its own non-resonant component with its own set of shape parameters. The pre-factor $(m_{K\pi\pi} - m_{\mathrm{thr}})^{a_k}$ allows the fit to adjust the low-$m_{K\pi\pi}$ behavior with respect to the $\sqrt{\Re_a(m_{K\pi\pi})m_{K\pi\pi}}\,\mathcal{P}_{\mathbb{P}}(m_{K\pi\pi}, t')$ term in equation (6.6). Here, $m_{\mathrm{thr}} = m_K + 2m_\pi$ is the kinematic threshold for $m_{K\pi\pi}$. The exponential function in equation (6.8) damps the non-resonant amplitude at large masses, i.e. large two-body break-up momenta $q(m_{K\pi\pi})$ of the isobar-bachelor system, as expected e.g. from models for Deck-like reactions [11, 41, 124].

The slop parameter $b(c_k)$ of the exponential function in equation (6.8) has to be greater than zero such that the exponential function damps the non-resonant amplitude at large masses. As $b(c_k)$ turned out to be close to zero for the non-resonant component in few partial waves, we limited $b(c_k)$ to be in the range $b > -1\,(\mathrm{GeV}/c)^{-2}$ by using the following parameter mapping of $b(c_k)$ in terms of c_k:

$$b(c_k) = -1\,(\mathrm{GeV}/c)^{-2} + 1\,(\mathrm{GeV}/c)^{-2} \cdot \exp\left[c_k\right]. \tag{6.9}$$

$q(m_{K\pi\pi}) = q(m_{K\pi\pi}, m_\xi, m_b)$ is the two-body break-up momentum of the isobar-bachelor system using the nominal mass m_ξ of the isobar resonance and the mass m_b of the bachelor particle. According to equation (5.41), it is not defined for $m_{K\pi\pi} < m_\xi + m_b$. However, there can be events below this limit due to the finite width of the isobar resonance and equation (6.8) still needs to be valid in these cases. Therefore, in equation (6.8), an extension of the two-body break-up momentum is used, which takes into account the finite width of the isobar and is thus valid also below this limit. It is given by

$$\tilde{q}_k(m_{K\pi\pi}) = q(m_{\text{norm}}, m_\xi, m_b)\frac{m_{K\pi\pi}\mathfrak{N}_{a_k}(m_{K\pi\pi})}{m_{\text{norm}}\mathfrak{N}_{a_k}^{m_{\text{norm}}}(m_{K\pi\pi})}, \tag{6.10}$$

where a_k is the partial wave that belongs to the non-resonant component k. This approximation is motivated by the facts that $\mathfrak{N}_a(m_{K\pi\pi})$ can be interpreted as the phase-space volume occupied by wave a and that the two-body phase space of the isobar-bachelor system is proportional to $q(m_{K\pi\pi})/m_{K\pi\pi}$. By equalizing $\mathfrak{N}_a(m_{K\pi\pi})$ to the quasi-two-body phase space and requiring $\tilde{q}_k(m_{\text{norm}}) = q(m_{\text{norm}})$ at $m_{\text{norm}} = 3\,\text{GeV}/c^2$ one obtains equation (6.10), which is valid over the full analyzed $m_{K\pi\pi}$ range.

For most of the studied partial waves, a simplified version of equation (6.8) with $a_k = 0$ and $b(c_k) = b_k$, i.e.

$$\mathcal{D}_k^{\text{NR}}(m_{K\pi\pi}; b_k) = e^{-b_k\,\tilde{q}_k^2(m_{K\pi\pi})}, \tag{6.11}$$

turned out to be sufficient to describe the non-resonant components.

Parameterization of the Production Factor

For the production factor, the same parameterization as in the COMPASS $\pi^-\pi^-\pi^+$ analysis [41, 72] is used. It is based on a phenomenological Regge approach to describe central-production reactions by double-Pomeron exchange [69], analogously to those shown in figure 2.3a. It reads[b]

$$\left|\mathcal{P}_{\mathbb{P}}(m_{K\pi\pi}, t')\right|^2 = \left(\frac{s}{m_{K\pi\pi}^2}\right)^{2\alpha_{\mathbb{P}}(t')-1}. \tag{6.12}$$

Here, s is the overall center-of-momentum energy of the K^-p system, which is fixed by the beam momentum. For the Regge trajectory of the Pomeron,[c]

$$\alpha_{\mathbb{P}}(t') = \alpha_0 - \alpha' t', \tag{6.13}$$

we used $\alpha_0 = 1.2$ as measured in ref. [137] and $\alpha' = 0.26\,(\text{GeV}/c)^{-2}$ as measured in ref. [138].

[b] For each of the four t' bins, $\alpha_{\mathbb{P}}(t')$ is evaluated at the bin center.
[c] Here, we use $\alpha(t) = \alpha_0 + \alpha' t \approx \alpha_0 - \alpha' t'$, because $t' \approx -t$ as $|t|_{\text{min}}$ is negligibly small in our kinematic range.

Branching Amplitudes

The t' dependence of the coupling amplitudes ${}^{k}\mathcal{C}_{a}^{K\pi\pi}(t')$ defined in equation (6.4) only depends on the production of the resonance, not on its decay. The same resonance may appear in different partial waves with the same $J^P\, M^\varepsilon$ quantum numbers, but with different decay modes. The coupling amplitudes that correspond to the different decay modes are hence expected to be proportional to each other. The complex-valued proportionality constant is called branching amplitude. For a given component k, this constraint is implemented in the RMF by replacing the coupling amplitudes ${}^{k}\mathcal{C}_{b}^{K\pi\pi}$ of all partial waves b that have the same $J^P\, M^\varepsilon$ quantum numbers, except for one selected wave a, by the coupling amplitudes ${}^{k}\mathcal{C}_{a}^{K\pi\pi}$ of wave a and one branching amplitude ${}^{k}_{b}\mathcal{B}_{a}^{K\pi\pi}$ for each partial wave b, which is independent of t', i.e.

$$ {}^{k}\mathcal{C}_{b}^{K\pi\pi}(t') = {}^{k}_{b}\mathcal{B}_{a}^{K\pi\pi}\; {}^{k}\mathcal{C}_{a}^{K\pi\pi}(t'). \tag{6.14} $$

This drastically reduces the number of coupling amplitudes, which are free parameters in the RMF, and thereby improves the fit stability.

6.1.3 Modeling the $\pi^-\pi^-\pi^+$ Background

We modeled the $\pi^-\pi^-\pi^+$ background by the results of the PWD of the $\pi^-\pi^-\pi^+$ pseudodata sample that was obtained from the $\pi^-\pi^-\pi^+$ COMPASS analysis as discussed in section 5.10.2. This means that the background is modeled based on data that where obtained in the same data taking campaigns at the same experiment as our $K^-\pi^-\pi^+$ sample. The $\pi^-\pi^-\pi^+$ background component in equation (6.1) is parameterized by

$$ \hat{\rho}_{ab}^{\pi\pi\pi}(m_{K\pi\pi}, t') = \left|\mathcal{C}^{\pi\pi\pi}\right|^2 \rho_{ab}^{\pi\pi\pi}(m_{K\pi\pi}, t'). \tag{6.15} $$

Here, $\rho_{ab}^{\pi\pi\pi}(m_{K\pi\pi}, t')$ is the spin-density matrix of $K^-\pi^-\pi^+$ partial waves as obtained from the PWD of the $\pi^-\pi^-\pi^+$ pseudodata sample using the $K^-\pi^-\pi^+$ 238-wave set, and the $\pi^-\pi^-\pi^+$ pseudodata sample is based on the $\pi^-\pi^-\pi^+$ sample measured at COMPASS. It is important to note that $\rho_{ab}^{\pi\pi\pi}(m_{K\pi\pi}, t')$ is fully determined by the pseudodata sample, i.e. it has no free parameters. This means that at the stage of the RMF, a fixed parameterization for the $\pi^-\pi^-\pi^+$ background in our $K^-\pi^-\pi^+$ sample is used. The absolute amount of $\pi^-\pi^-\pi^+$ background in our sample is given by the free parameter $|\mathcal{C}^{\pi\pi\pi}|^2$. This means $|\mathcal{C}^{\pi\pi\pi}|^2$ is determined from the measured $K^-\pi^-\pi^+$ sample, while $\rho_{ab}^{\pi\pi\pi}(m_{K\pi\pi}, t')$ is completely determined by the measured $\pi^-\pi^-\pi^+$ sample.

6.1.4 Modeling the Effective Background

Other incoherent background processes, such as $K^- + p \to K^-K^-K^+ + p$, also contribute to the $K^-\pi^-\pi^+$ sample. As there are no explicit models available for these processes, we parameterized them in an effective way by using the same approach as used for the non-resonant components.

Following equation (6.5), the RMF model for the effective background components reads[d]

$$\hat{\mathcal{T}}_a^{\text{eBKG}}(m_{K\pi\pi}, t') = \sqrt{\Re_a(m_{K\pi\pi}) m_{K\pi\pi}}\, \mathcal{P}_{\mathbb{P}}(m_{K\pi\pi}, t')\; C_a^{\text{eBKG}}(t')\, \mathcal{D}_{k_a}^{\text{eBKG}}(m_{K\pi\pi}; a_{k_a}, c_{k_a}). \tag{6.16}$$

For the dynamic amplitudes of the effective background components, the same parameterizations as for the non-resonant components are used, but with independent shape parameters. For most of the partial waves, we used the simplified parameterization [same as equation (6.11)]:

$$\mathcal{D}_k^{\text{eBKG}}(m_{K\pi\pi}; b_k) = e^{-b_k\, \tilde{q}_k^2(m_{K\pi\pi})}. \tag{6.17}$$

For some partial waves we used the full parameterization [same as equation (6.8)]:

$$\mathcal{D}_k^{\text{eBKG}}(m_{K\pi\pi}; a_k, c_k) = (m_{K\pi\pi} - m_{\text{thr}})^{a_k} e^{-b(c_k)\, \tilde{q}_k^2(m_{K\pi\pi})}. \tag{6.18}$$

6.1.5 χ^2 Formalism

In order to estimate the free parameters of the RMF model, we performed a χ^2 fit. In order to measure the deviation between the RMF Model $\hat{\rho}_{ab}(m_{K\pi\pi}, t')$ and the measured spin-density matrix elements $\rho_{ab}(m_{K\pi\pi}, t')$, the real-valued spin-density matrix,[e]

$$\Lambda_{ab}(m_{K\pi\pi}, t') = \begin{cases} \Re\left(\rho_{ab}(m_{K\pi\pi}, t')\right) & \text{, if } a \leq b \\ \Im\left(\rho_{ba}(m_{K\pi\pi}, t')\right) & \text{, if } a > b \end{cases}, \tag{6.19}$$

is constructed. The diagonal elements of $\Lambda_{ab}(m_{K\pi\pi}, t')$ are the partial-wave intensities. The upper-right triangular part of $\Lambda_{ab}(m_{K\pi\pi}, t')$ contains the real parts of the spin-density matrix elements, whereas the lower-left triangular part of $\Lambda_{ab}(m_{K\pi\pi}, t')$ contains the imaginary parts of the spin-density matrix elements. As the spin-density matrix is Hermitian, $\Lambda_{ab}(m_{K\pi\pi}, t')$ contains the full information of $\rho_{ab}(m_{K\pi\pi}, t')$. The vector $\vec{\lambda}(m_{K\pi\pi}, t')$ is the vectorization of $\Lambda_{ab}(m_{K\pi\pi}, t')$, whose elements read

$$\lambda_i(m_{K\pi\pi}, t') = \Lambda_{ab}(m_{K\pi\pi}, t'), \qquad \text{where} \quad i = a \cdot n_{\text{waves}} + b \tag{6.20}$$

and where n_{waves} is the number of waves in the spin-density matrix.

Analogously, the equivalent quantities of the RMF model read

$$\hat{\Lambda}_{ab}(m_{K\pi\pi}, t') = \begin{cases} \Re\left(\hat{\rho}_{ab}(m_{K\pi\pi}, t')\right) & \text{, if } a \leq b \\ \Im\left(\hat{\rho}_{ba}(m_{K\pi\pi}, t')\right) & \text{, if } a > b \end{cases}, \tag{6.21}$$

[d] As the transition amplitude for the effective background of each wave contains only one component, the coupling amplitude $C_a^{\text{eBKG}}(t')$ has no additional component label and the component label k_a of the dynamic amplitude is fixed by the wave label a.

[e] Here and in equations (6.20) to (6.22) we use the wave labels a and b as indices that run from 1 to n_{waves}, where n_{waves} is the number of partial waves in the spin-density matrix.

and

$$\hat{\lambda}_i(m_{K\pi\pi}, t') = \hat{\Lambda}_{ab}(m_{K\pi\pi}, t'), \qquad \text{where} \quad i = a \cdot n_{\text{waves}} + b. \tag{6.22}$$

Using the data and model vectors given in equations (6.20) and (6.22), respectively, the χ^2 function that is minimized in the RMF reads

$$\chi^2_{\text{RMF}} = \sum_{t', m_{K\pi\pi}} \sum_{i,j=1}^{n_{\text{waves}}} \Delta\lambda_i(m_{K\pi\pi}, t')\, \text{Prec}\left[\lambda_i(m_{K\pi\pi}, t'), \lambda_j(m_{K\pi\pi}, t')\right] \Delta\lambda_j(m_{K\pi\pi}, t'). \tag{6.23}$$

The residuals $\Delta\lambda_i$, which represent the difference between measured spin-density matrix elements and the RMF model, are given by

$$\Delta\lambda_i(m_{K\pi\pi}, t') = \lambda_i(m_{K\pi\pi}, t') - \hat{\lambda}_i(m_{K\pi\pi}, t'). \tag{6.24}$$

The outer sum in equation (6.23) runs over all $(m_{K\pi\pi}, t')$ cells, which are independent.

The precision matrix $\text{Prec}[\lambda_i, \lambda_j]$ is the inverse of the covariance matrix $\text{Cov}[\lambda_i, \lambda_j]$ of the measured spin-density matrix elements λ_i. $\text{Cov}[\lambda_i, \lambda_j]$ is determined by our Bootstrapping approach of the PWD that is discussed in section 5.4.

The maximal possible rank of $\text{Cov}[\lambda_i, \lambda_j]$ is n^2_{waves} with n_{waves} being the number of considered partial waves, because there are n^2_{waves} real-valued spin-density matrix elements. However, we limited the rank r of the spin-density matrix to be $r = 3$ when formulating the PWD model (see sections 5.1.2 and 5.3.1). Consequently, the number of free parameters of the spin-density matrix is given by

$$n^{\rho}_{\text{para}} = r(2n_{\text{waves}} - r). \tag{6.25}$$

This means that the n^2_{waves} real-valued spin-density matrix elements are build up from n^{ρ}_{para} free parameters. In our case, n^{ρ}_{para} is much smaller than n^2_{waves}. Hence, there are functional dependencies among the spin-density matrix elements. As a consequence, ${}^{\text{MLE}}\text{Cov}[\lambda_i, \lambda_j]$ as obtained from the covariance matrix of the maximum-likelihood estimates of the transition amplitudes via linear error propagation, is singular and cannot be directly inverted.

However, we determined $\text{Cov}[\lambda_i, \lambda_j]$ using the Bootstrapping approach, which does not determine the covariance matrix at a fixed point in the $\vec{\lambda}$ space, but determines the covariance matrix from the spread in the distribution of $\vec{\lambda}$. This distribution also includes non-linear effects from the calculation of the spin-density matrix elements [see equations (5.67) and (5.68)]. Hence, the functional dependencies among the spin-density matrix elements are not exactly implemented in $\text{Cov}[\lambda_i, \lambda_j]$ from Bootstrapping, so that $\text{Cov}[\lambda_i, \lambda_j]$ is not exactly singular anymore. In fact, it has full rank and can be inverted. In order to make the inversion procedure of $\text{Prec}[\lambda_i, \lambda_j]$ used in equation (6.23) numerically more stable[f] and to implement the mass ranges as described below, we employed the Moore-Penrose pseudo-inverse [139–142][g] when

[f] Although, $\text{Cov}[\lambda_i, \lambda_j]$ is not exactly singular anymore, some eigenvalues of $\text{Cov}[\lambda_i, \lambda_j]$ are still numerically close to zero. This leads to numerical instabilities when using the conventional matrix inverse.

[g] See equations (27) and (28) on page 207 of ref. [139].

calculating $\text{Prec}[\lambda_i, \lambda_j]$.[h] A systematic study investigating effects from the rank of $\text{Cov}[\lambda_i, \lambda_j]$ can be found in section 6.3.2.

Some $m_{K\pi\pi}$ ranges of partial waves that are studied in the RMF are excluded from χ^2_{RMF}. An elegant way of implementing these mass ranges in the RMF is to take advantage of the pseudo inverse that is used to calculate $\text{Prec}[\lambda_i, \lambda_j]$. To this end, for each $(m_{K\pi\pi}, t')$ cell the elements of $\text{Cov}[\lambda_i, \lambda_j]$ that belong to waves outside their mass ranges are set to zero before calculating $\text{Prec}[\lambda_i, \lambda_j]$.

6.1.6 Fit Procedure

In an RMF, the χ^2 function in equation (6.23) is minimized with respect to the free parameters of the RMF model, which are shape parameters, e.g. the masses and widths of the resonance components, and the coupling and branching amplitudes.[i] In general, the χ^2 function is multi-modal in the parameter space. In order to map out the parameter space, to avoid bias induced by the choice of the start-parameter values, and to reliably find the parameter values that yield the minimal χ^2 value, multiple minimizations are performed for the same RMF model using different start-parameter values.

While we have some prior knowledge about the shape parameters, e.g. from previous measurements of the studied resonances, we have only poor prior knowledge about the coupling and branching amplitudes. For the shape parameters of the resonance components, the non-resonant components, and the effective background components, the start-parameter values are randomly drawn from uniform distributions with ranges that we chose individually for each component based on prior knowledge. These start-parameter ranges are listed and discussed in section 6.2 and appendices E.1.1 and E.2. For the real and imaginary parts of the coupling amplitudes and the branching amplitudes, the start-parameter values are randomly drawn from a uniform distribution in the wide range $(-1, 1)$.[j]

Optimizing all parameters at once frequently leads to artificial solutions far away from the physics parameters, because some parameters of the RMF model are highly correlated.[k] Therefore, the fit procedure is performed in two steps. In the first step, the parameters for the coupling

[h] In order to calculate the Moore-Penrose pseudo-inverse a singular-value decomposition is used, where numerically small singular values $\mathfrak{s}_j$ are set to zero in the inverse, i.e. a singular value is set to zero if $\mathfrak{s}_j < \max_k[\mathfrak{s}_k] \cdot 10^{-14}$. Here, j and k label the various singular values determined in the singular-value decomposition.

[i] We used the `iminuit` package [143] for minimization, which is a Python module that implements the MINUIT minimizer.

[j] In the "sfitter" fitting software (see table H.1), the coupling and branching amplitudes defined in equations (6.4) and (6.14) to (6.16) are normalized by introducing normalization constants, such that the magnitudes of the real and imaginary parts of the coupling amplitudes are of the order of 1, i.e. of the same order as the shape parameters. This was mandatory to improve the stability of the MINUIT minimization.

[k] We performed studies where the optimization was performed by freeing all parameter simultaneously in a single step. This approach yielded the same best χ^2 value as the two-step approach. However, it required much more minimization attempts with different start-parameter values as the best solution was found less frequently. See section 6.2.2 for a discussion on the stability of the RMF.

and branching amplitudes are optimized, while keeping the shape parameters fixed to their start-parameter values, which are based on prior knowledge. In the second step, the results from the first step are used as start-parameters values and also the shape parameters are freed such that all parameters are optimized simultaneously.

In summary, the RMF formalism described in this section 6.1 allowed us to identify strange-meson resonances and to measure their masses and widths. In contrast to the PWD, the resonance, non-resonant, and background contributions are explicitly modeled in the RMF. This allowed us to separate the resonance signals from the non-resonant and background contributions.

6.2 The 10-Wave RMF

6.2.1 The 10-Wave RMF Model

In order to study resonances appearing in the $K^-\pi^-\pi^+$ final state and to measure their masses and widths, we used the formalism developed in section 6.1 to fit RMF models to the results of the PWD of the measured $K^-\pi^-\pi^+$ sample. We selected ten partial waves with $J^P = 1^+, 2^+, 2^-$, and 4^+ to be included into the RMF. We chose waves that show interesting signals, e.g. from excited states such as the $K_2(2250)$ that needs further clarification. We also chose waves that show clear signals from well-known resonances such as the $K_2^*(1430)$. These clear signals can be reliably modeled and act as reference amplitudes for weaker signals to interfere with, which makes the fit more robust. In addition, comparing our measurements of the resonance parameters of these well-known states to previous ones allows us to identify potential bias in the analysis. The so-called 10-wave RMF is defined in the remaining of this section. Its results are discussed in sections 6.2.2 and 7.1 to 7.4. When developing the so-called 10-wave RMF model employed in the 10-wave RMF, we started with RMFs of individual waves, and then successively added partial waves and model components, and tuned the parameters of the model. In total, we performed more than 200 individual RMFs during this procedure. We studied further partial waves from other J^P sectors using the 10-wave RMF model as a starting point for extended RMFs. These studies are discussed in sections 7.5 to 7.8.

Table 6.1 lists the waves included in the 10-wave RMF. In the following, we give a short reasoning for how we constructed this model. A detailed discussion about the signals in the individual waves can be found in chapter 7. The 2^+ and 4^+ waves exhibit resonance-like signals of the corresponding ground-state resonances (see figures 5.19d and 5.20b). We modeled them accordingly by including the $K_2^*(1430)$ and $K_4^*(2045)$ resonance components. Apart from these dominant signals, the waves exhibit no further resonance-like structures. The 1^+ and 2^- waves exhibit dominant signals in the $m_{K\pi\pi}$ region of the known ground-state resonances; which are the $K_1(1270)$ and $K_1(1400)$ resonances, and the $K_2(1780)$ and $K_2(1820)$ resonances, respectively (see figures 5.19f and 5.19a). Hence, we added the corresponding resonance components to our model. In addition, some 1^+ and 2^- waves exhibit high-mass tails, which may arise from excited states. We modeled them by including resonance components for the K_1' and $K_2(2250)$ states. As

Table 6.1: List of partial waves and model components included in the 10-wave RMF. The second column lists the resonance components included in $\mathbb{S}_a$ in equation (6.6). They are specified in table E.1. The third column lists the parameterization used for the dynamic amplitudes of the non-resonant components (NR). The fourth column lists the model used for the $\pi^-\pi^-\pi^+$ background components. The fifth column lists the parameterizations used for the dynamic amplitudes of the effective background components (eBKG) in equation (6.16).[1] The last two columns list the $m_{K\pi\pi}$ range in which data from this partial wave are considered in the RMF. A detailed discussion of the individual components is given in appendix E.1.1.

Partial Wave	Resonances	NR	$\pi^-\pi^-\pi^+$	eBKG	$m_{K\pi\pi}$ Range GeV/c^2	
$1^+\,0^+\,\rho(770)\,K\,S$	$\{K_1(1270), K_1(1400), K_1'\}$	(6.11)	(6.15)	(6.17)	1.10	2.50
$1^+\,1^+\,\rho(770)\,K\,S$		(6.11)	(6.15)	(6.17)	1.10	2.50
$2^+\,1^+\,K^*(892)\,\pi\,D$	$\{K_2^*(1430)\}$	(6.11)	(6.15)	(6.17)	1.20	1.70
$2^+\,1^+\,\rho(770)\,K\,D$		(6.11)	(6.15)	(6.17)	1.30	1.70
$2^-\,0^+\,K^*(892)\,\pi\,F$	$\{K_2(1770), K_2(1820), K_2(2250)\}$	(6.11)	(6.15)	(6.17)	1.60	2.00
$2^-\,0^+\,K_2^*(1430)\,\pi\,S$		(6.8)	(6.15)	(6.18)	1.50	2.80
$2^-\,0^+\,\rho(770)\,K\,F$		(6.11)	(6.15)	(6.17)	1.60	2.00
$2^-\,0^+\,f_2(1270)\,K\,S$		(6.11)	(6.15)	(6.17)	1.60	2.80
$4^+\,1^+\,K^*(892)\,\pi\,G$	$\{K_4^*(2045)\}$	(6.11)	(6.15)	(E.1)	1.80	2.50
$4^+\,1^+\,\rho(770)\,K\,G$		(6.11)	(6.15)	(6.17)	1.80	2.50

our estimate for the mass of the K_1' component is significantly higher than the nominal mass of the $K_1(1650)$ state, which is listed by the PDG, we call this component K_1' instead of $K_1(1650)$ in our model (see discussion in section 7.1.1).

We chose the $m_{K\pi\pi}$ range in which we considered data points of the spin-density matrix elements that correspond to a wave individually for each wave. The selected $m_{K\pi\pi}$ ranges cover the resonances we want to study and a sufficiently large region around these resonances that allows us to reliably determine not only the parameters of the resonances but also those of the non-resonant and background components. With the given model we were not able to describe the region $m_{K\pi\pi} \geq 2\,\mathrm{GeV}/c^2$ of the $2^-\,0^+\,K^*(892)\,\pi\,F$ and $2^-\,0^+\,\rho(770)\,K\,F$ waves (see section 7.4). Thus, we excluded this mass region from the RMF for these to waves. Also, we excluded the region $m_{K^-\pi^+} \geq 1.7\,\mathrm{GeV}/c^2$ from the RMF for the two 2^+ waves, because both waves exhibit no resonance-like signal in this mass region.

We use the same set of resonance components for partial waves with the same J^P quantum numbers. Except for the 1^+ waves, all waves with the same J^P have also the same M^ε. Hence, we required that a resonance component has the same t' dependence in all partial waves in which it is included by applying equation (6.14). This leaves us with one set of t'-dependent coupling amplitudes for each resonance component and one t'-independent branching amplitude for each additional wave in which this resonance component appears. As the two included 1^+ waves have different M^ε, we do not expect the t' dependence of resonances appearing in both waves to be the same. Thus, we did not apply equation (6.14) for the $K_1(1270)$ and K_1' resonance components. As discussed in section 7.1, the $K_1(1400)$ is only a weak signal in the included 1^+ waves. In order to reduce the number of free parameters and thereby stabilize the fit, we applied a modified version of equation (6.14), where the expected change of the t' shape due to the different spin projections, which will be given in equation (6.29), is taken into account, i.e. we applied

$$ {}^{K_1(1400)}\mathcal{C}^{K\pi\pi}_{1^+\,1^+\,\rho(770)\,K\,S}(t') = \sqrt{t'} \cdot {}^{K_1(1400)}_{1^+\,1^+\,\rho(770)\,K\,S}\mathcal{B}^{K\pi\pi}_{1^+\,0^+\,\rho(770)\,K\,S} \cdot {}^{K_1(1400)}\mathcal{C}^{K\pi\pi}_{1^+\,0^+\,\rho(770)\,K\,S}(t'). \quad (6.26) $$

For all eight resonance components we used a relativistic Breit-Wigner amplitude given in section 5.1.4 with a dynamic width that takes into account a single decay channel. In order to measure the Breit-Wigner mass m_0 and width Γ_0, we optimized the corresponding fit parameters in the RMF (see section 6.1.6 for details on the fitting procedure). We chose the parameter limits for the m_0 and Γ_0 parameters to be as little restrictive as possible in order to not bias our results. Furthermore, we selected the start-parameter ranges for m_0 and Γ_0 such that their cover a reasonable range including previous measurements [91] plus a safety margin. The resonance components, their parameter limits, and the start-parameter ranges are listed in table E.1. In appendix E.1.1 we discuss their choice in more detail. As the $K_1(1400)$ is only a weak signal in the two considered 1^+ waves, we could not reliably determine its mass and width in the 10-wave RMF. Thus, we fixed the mass and width parameters of the $K_1(1400)$ component to the corresponding PDG average values [91] as listed in table E.1.

Using the simplified shape for the non-resonant and effective background components given in equations (6.11) and (6.17) turned out to be sufficient in most of the 10 waves (see table 6.1). Only for the $2^-\,0^+\,K_2^*(1430)\,\pi\,S$ and $4^+\,1^+\,K^*(892)\,\pi\,G$[I] waves, which exhibit larger non-resonant and background contributions, we used the extended non-resonant and effective background shapes in equations (6.8) and (6.18). We chose the parameter limits of the non-resonant and effective background components in all 10 waves to be much larger than expected, i.e. larger than observed in the first RMFs and larger than the typical values observed in the COMPASS $\pi^-\pi^-\pi^+$ analysis [41] where a similar non-resonant parameterization was used. Similarly, we chose the start-parameter ranges to cover typical values for the non-resonant and effective background parameters. The final choice of the parameter limits and start-parameter ranges is listed in appendix E.1.1.

Finally, we modeled the $\pi^-\pi^-\pi^+$ background using the results of the $\pi^-\pi^-\pi^+$ partial-wave decomposition as discussed in section 6.1.3. This model has only one free fit parameter, which is the overall amount of $\pi^-\pi^-\pi^+$ background in the $K^-\pi^-\pi^+$ sample. We estimated this parameter in the RMF.

[I] For the effective background component in the $4^+\,1^+\,K^*(892)\,\pi\,G$ wave we used a modified version of equation (6.18) as discussed in appendix E.1.1.

In total, the 10-wave RMF model has 291 free fit parameters: 7 m_0 and 7 Γ_0 parameters of 7 resonance components,[m] 8 shape parameters of the non-resonant components,[n] 12 shape parameters of the effective background components, and 257 parameters for the coupling and branching amplitudes. These 291 free parameters are constrained by 7816 data points, i.e. the real and imaginary parts of the spin-density matrix elements obtained from the PWD of the $K^-\pi^-\pi^+$ sample.

6.2.2 A First Glimpse on the Results of the 10-Wave RMF

We fitted the 10-wave RMF model defined in section 6.2.1 to the PWD results of the $K^-\pi^-\pi^+$ sample presented in section 5.5. In order to explore the parameter space of the RMF sufficiently well we performed a large number of 2000 fit attempts with random start-parameter values. Figure 6.1a shows the χ^2 distribution obtained from these 2000 attempts. The best fit result yielded a χ^2 value of 6215.61, i.e. this is the smallest χ^2 value found in all attempts. Taking into account the number of degrees of freedom, this corresponds to a reduced χ^2 of $\chi^2_{\text{red}} = 0.826$. The interpretation of this value is discussed further in section 6.3.1. In total, 121 of the 2000 fit attempts found this best result,[o] which represents the final result of this RMF, i.e. which yielded the final parameter estimates. There are further results that were found frequently. However, they all have a χ^2 value that is at least 12 units larger, i.e. significantly worse, than the best fit result. Hence, they are not of interest here. Finally, there are rarely found fit results with $\chi^2 < \chi^2_{\text{best}} + 12$ as shown in figure 6.1b. These rare fit results have resonance parameters that agree with those from the best fit result. Thus, they are also not of further interest. The large number of fit attempts that found the best fit result, the consistency of the parameter values for fit results with similar χ^2, and the significantly larger χ^2 of other fit results demonstrates that we reliably found the minimal χ^2, i.e. the set of parameters that describes the data best.

Figure 6.2 shows for illustration purposes the real and imaginary parts of the spin-density matrix elements of the 10 waves included in the 10-wave RMF in the lowest t' bin. The data points represent the spin-density matrix elements obtained from the PWD of the measured $K^-\pi^-\pi^+$ sample. We refer to the corresponding intensities as measured intensities and to the off-diagonal spin-density matrix elements as measured spin-density matrix elements in the following. The 1954 data points from the first t' bin shown in blue are those that entered the RMF. In total, we included all four spin-density matrices from the four analyzed t' bins simultaneously in one RMF. This results in a total amount for 7816 data points that entered the RMF. All four spin-density matrices are shown in appendix E.1.2. These data points were calculated from the transition amplitudes, i.e. from a smaller number of fit parameters compared to the number of real and imaginary parts of the spin-density matrix elements. Hence, spin-density matrix elements from

[m] The mass and width of the $K_1(1400)$ component were fixed.

[n] The shape parameters of the non-resonant terms in the 2^+ waves and in the $2^-\,0^+\,K^*(892)\,\pi\,F$ wave were fixed (see appendix E.1.1).

[o] We consider two fit results to be the same if their χ^2 values differ by less than 10^{-2} units, if for each parameter the difference of the estimates is less than 10 % of the corresponding uncertainty from the best fit result, and if each for each parameter the difference of the uncertainty estimates is less than 50 % of the uncertainty estimate from the best result. The latter criterion was chosen to identify unrealistic uncertainty estimates appearing in unstable fits.

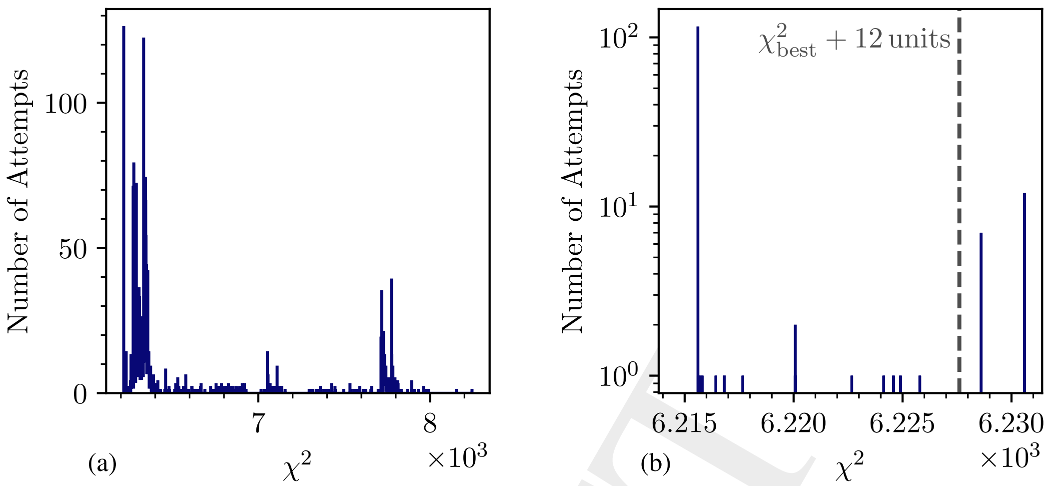

Figure 6.1: χ^2 distribution obtained from the 2000 attempts of the 10-wave RMF. (a) shows the full χ^2 range of all 2000 attempts. (b) shows in log-scale only those attempts that yielded a χ^2 that is at most 15 units worse than the smallest found χ^2. The dashed dark-gray vertical line indicates $\chi^2 = \chi^2_{\text{best}} + 12$ units.

the same $(m_{K\pi\pi}, t')$ cell are strongly correlated. Spin-density matrix elements from different $(m_{K\pi\pi}, t')$ cells are independent. The red curves in figure 6.2 represent the result of the 10-wave RMF. We discuss in the following the fit quality. Detailed discussions and interpretations of the results for the individual waves are given in chapter 7.

Overall, the RMF is able to reproduce the measured intensities and the off-diagonal spin-density matrix elements sufficiently well. Figure 6.3a shows exemplarily the t'-summed intensity spectrum of the $1^+\,0^+\,\rho(770)\,K\,S$ wave. The total RMF model (red curve) reproduces well the features of the measured intensity spectrum (blue data points). As expected, the peak at about $1.3\,\text{GeV}/c^2$ is dominantly described by the $K_1(1270)$ component of the RMF (blue curve). We find small contributions to the total model intensity from the non-resonant component (green curve), the $\pi^-\pi^-\pi^+$ background component (orange curve), and the effective background component (brown curve). The RMF underestimates the measured intensity in the low-mass tail of the peak, especially in the extrapolation below the fitted $m_{K\pi\pi}$ region shown by the gray data points and lighter curves. We expect artifacts in form of these low-mass enhancements in our analysis (see section 5.5). Thus, we excluded this low-mass region from the $m_{K\pi\pi}$ fit range.

Similarly, the peak at about $1.4\,\text{GeV}/c^2$ in the $2^+\,1^+\,\rho(770)\,K\,D$ wave shown in figure 6.3b is reproduced well by the RMF, while it underestimates the measured intensity in the tails of the peak. We find a large contribution of the $\pi^-\pi^-\pi^+$ background component (orange curve) to this wave, while the total RMF model curve seems to be completely saturated by the K_2^* component. The reason is, that the K_2^* component destructively interferes with the non-resonant component in this wave (green curve) such that the intensity $\hat{\rho}^{K\pi\pi}_{aa}(m_{K\pi\pi}, t')$ of the RMF model for the $K^-\pi^-\pi^+$ spin-density matrix is smaller than the measured intensity. Adding the $\pi^-\pi^-\pi^+$ background component, the total RMF model reproduced well the peak region.

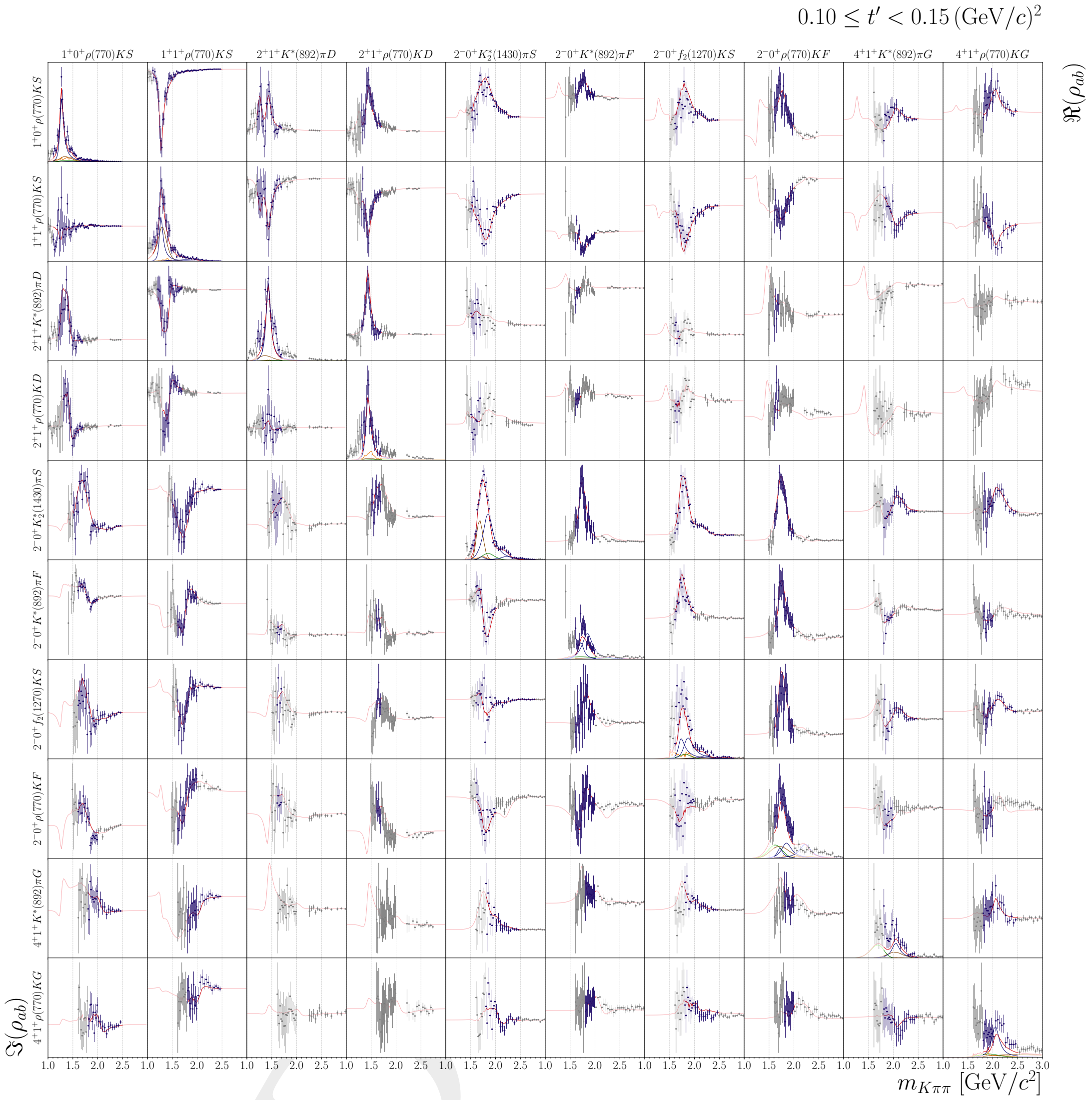

Figure 6.2: Real and imaginary parts of the spin-density matrix elements, i.e. $\Lambda_{ab}(m_{K\pi\pi}, t')$ in equation (6.19), as a function of $m_{K\pi\pi}$ in the lowest of the four t' bins for the 10 partial waves that were included in the 10-wave RMF. The figures on the diagonal show the intensity spectra. The upper-right and lower-left off-diagonal figures show the real and imaginary parts of the off-diagonal elements of the spin-density matrix, respectively. The blue data points represent the measured spin-density matrix elements. The curves represent the result of the 10-wave RMF to these data points. The red curves represent the total RMF model. The blue curves represent the individual resonance components, the green curves the non-resonant components, the orange curves the $\pi^-\pi^-\pi^+$ background components, and the brown curves the effective background components. The extrapolations beyond the $m_{K\pi\pi}$ fit ranges are shown in lighter colors. The corresponding data points are shown in gray. The ranges of the vertical axes are different for each subplot. They are adjusted to the data shown in each subplot. Hence, we do not show tick marks for the vertical axes.

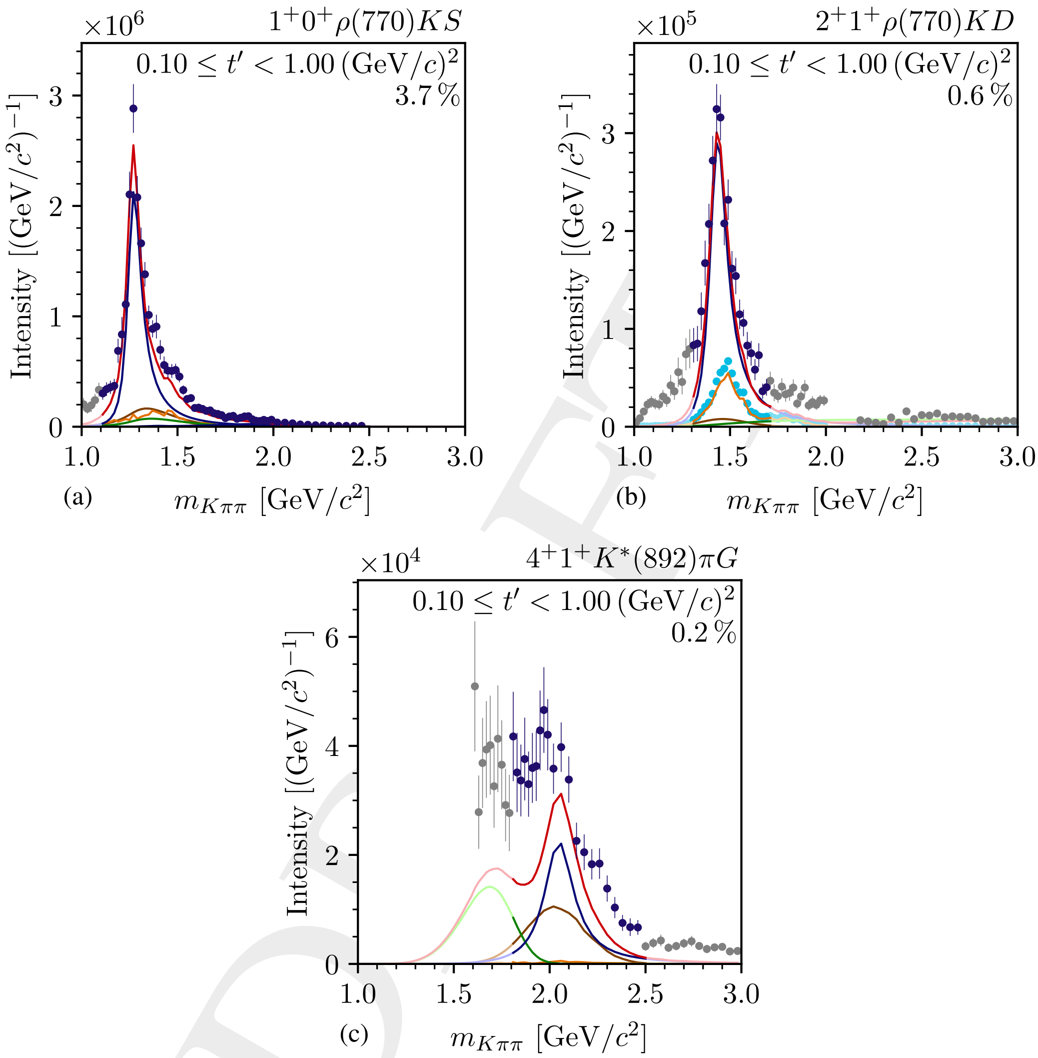

Figure 6.3: 10-wave RMF result for the t'-summed intensity spectra of three selected partial waves. The blue data points represent the measured spin-density matrix elements. The curves represent the result of the 10-wave RMF. The red curves represent the total RMF model. The blue curves represent the individual resonance components, the green curves the non-resonant components, the orange curves the $\pi^-\pi^-\pi^+$ background components, and the brown curves the effective background components. The extrapolations beyond the $m_{K\pi\pi}$ fit ranges are shown in lighter colors. The corresponding data points are shown in gray. The cyan data points in (b) show the result of the $\pi^-\pi^-\pi^+$ background PWD scaled such that the total number of reconstructed $\pi^-\pi^-\pi^+$ pseudodata events corresponds to the predicted amount of $\pi^-\pi^-\pi^+$ background in the $K^-\pi^-\pi^+$ sample (same as orange data points in figure 5.39a).

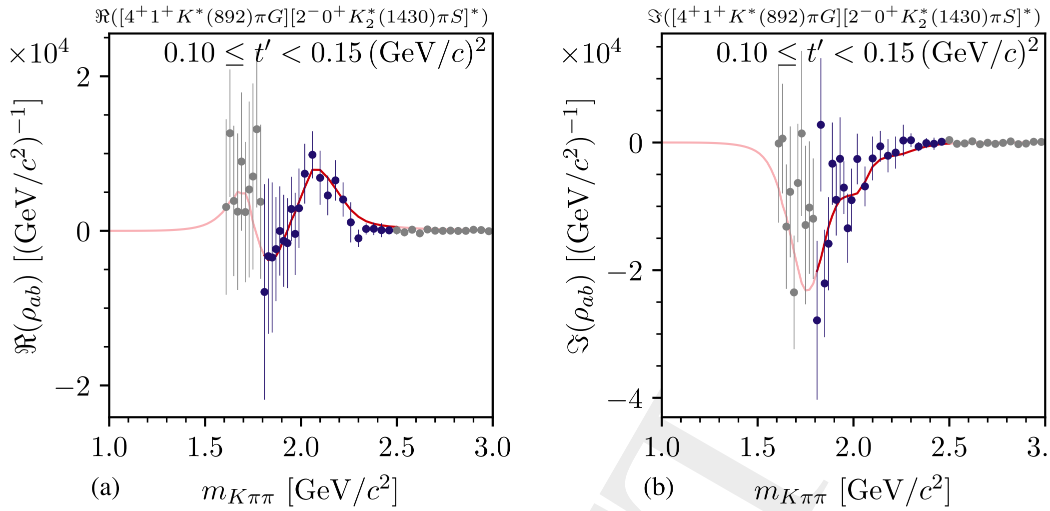

Figure 6.4: Same as figure 6.3, but for (a) the real part and (b) the imaginary part of the off-diagonal spin-density matrix element of the 4^+ 1^+ $K^*(892)\,\pi\,G$ and 2^- 0^+ $K_2^*(1430)\,\pi\,S$ waves in the lowest t' bin.

The shape of the $\pi^-\pi^-\pi^+$ background component is the same as the shape from the $\pi^-\pi^-\pi^+$ background PWD by construction (see section 6.1.3), while the amount of $\pi^-\pi^-\pi^+$ background is a free parameter in the RMF. Remarkably, the amount of $\pi^-\pi^-\pi^+$ background as estimated by the RMF based on the measured $K^-\pi^-\pi^+$ sample agrees well with the expected amount of $\pi^-\pi^-\pi^+$ background (cf. orange curve and cyan data points in figure 6.3b, respectively). The estimate of the $\pi^-\pi^-\pi^+$ background from the RMF was obtained from the measured $K^-\pi^-\pi^+$ sample. The expected amount of $\pi^-\pi^-\pi^+$ background is based on the $\pi^-\pi^-\pi^+$ pseudodata, which were obtained from the measured $\pi^-\pi^-\pi^+$ sample, i.e. from an independent data sample. This good agreement strongly supports our approach to effectively model the incoherent background contributions by a rank=3 spin-density matrix in the PWD and explicitly model them at the level of the RMF. As the strength parameter of the $\pi^-\pi^-\pi^+$ background component is independent of the partial wave by construction, we find the same good agreement in all 10 partial waves.

We observe discrepancies between the RMF curve and the measured intensity spectra of the 4^+ waves, exemplarily shown for the t'-summed intensity spectrum of the 4^+ 1^+ $K^*(892)\,\pi\,G$ wave in figure 6.3c. While the RMF roughly reproduces the shape of the spectrum, it underestimates the overall intensity by about 20 %. However, the RMF reproduces well the measured off-diagonal spin-density matrix elements of the 4^+ 1^+ $K^*(892)\,\pi\,G$ wave with respect to all other partial waves. Figure 6.4 exemplarily shows the real and imaginary parts of one of these off-diagonal elements. Especially noteworthy is that the magnitudes of the measured off-diagonal elements are not underestimated, which would naïvely be expected from the discrepancy observed in the intensity spectrum. This suggests that there are contributions to the measured intensity spectrum of this wave that do not enter the off-diagonal spin-density matrix elements and that are not reproduced by the RMF.

The spin-density matrix element for a given $(m_{K\pi\pi}, t')$ cell is the sum over all physics processes $\mathfrak{p}$ that contribute to wave a or b:[p]

$$\rho_{ab} = \sum_{\mathfrak{p}} \mathcal{T}_a^{\mathfrak{p}} \left[\mathcal{T}_b^{\mathfrak{p}}\right]^* . \tag{6.27}$$

Assume, a process $\mathfrak{p}_1$ contributes only to wave a but not to wave b, i.e. $\mathcal{T}_b^{\mathfrak{p}_1} = 0$. This process affects the intensity of wave a, because $\mathcal{T}_a^{\mathfrak{p}_1} \left[\mathcal{T}_a^{\mathfrak{p}_1}\right]^*$ appears in equation (6.27) for $a = b$. However, $\mathfrak{p}_1$ does not affect the off-diagonal spin-density matrix element of waves a and b, because $\mathcal{T}_a^{\mathfrak{p}_1} \left[\mathcal{T}_b^{\mathfrak{p}_1}\right]^*$ appears in equation (6.27) for $a \neq b$ and $\mathcal{T}_b^{\mathfrak{p}_1} = 0$. Hence, the off-diagonal spin-density matrix elements are less affected by processes that dominantly contribute to only a subset of waves.

We expect the process under study in this work, i.e. $K^- + p \to K^-\pi^-\pi^+ + p$, to contribute to all partial waves as the wave set was designed for this process. However, background processes may significantly contribute to only a subset of partial waves. For example, we know from the $\pi^-\pi^-\pi^+$ background PWD that this background does practically not contribute to waves with $K^*(892)$ isobar (see section 5.10.2). Therefore, we expect not only the intensities of waves with $K^*(892)$ isobar to be practically free of $\pi^-\pi^-\pi^+$ background, but also the off-diagonal spin-density matrix elements of all waves with respect to waves with $K^*(892)$ isobar. Thus, in general the intensities may be most affected by backgrounds. In addition, the model for the effective background components is only an approximation, which may be imperfect (see section 6.1.4). This may explain the discrepancy between the RMF curve and the measured intensity spectra of the 4^+ waves, while the off-diagonal elements of those waves are reproduced well. Furthermore, one should note that 6504 of the 7816 data points that entered the RMF represent off-diagonal spin-density matrix elements, while only 1312 represent intensities.[q] Hence, the off-diagonal elements influence the results of the RMF more strongly such that imperfections in the description of the intensities may not strongly pull the results.

We performed the PWD independently in four bins in t'. This allowed us to determine not only the $m_{K\pi\pi}$ dependence, but also the t' dependence of the spin-density matrix elements. We employed this t' resolved information in the RMF, where we separate resonances from non-resonant and background contributions. Hence, we studied the t' dependence of the amplitudes of the individual model components. However, given the low number of t' bins, we could determine only the coarse features of their t' dependence. Due to the normalization of the measured spin-density matrix elements, $\left|{}^k\hat{\mathcal{T}}_a^z(m_{K\pi\pi}, t')\right|^2$ from equation (6.5) represents the predicted number of produced events in each $(m_{K\pi\pi}, t')$ cell for a single wave a and the coherent sector z and if there would be only component k in wave a. The corresponding intensity as a function of t', i.e. the

[p] As discussed in section 5.1, we cannot disentangle the transition amplitudes $\mathcal{T}_a^{\mathfrak{p}}$ of the physics processes. The transition amplitudes $\mathcal{T}_a^z$ that appear in the PWD model are only an effective parameterization of the spin-density matrix.

[q] The number of off-diagonal elements and intensities must be calculated for each $(m_{K\pi\pi}, t')$ cell individually and summed up. This is because not all the 10 waves were considered in the RMF in all $(m_{K\pi\pi}, t')$ cells (see table 6.1). The number of considered waves ranges from one to eight. There are no $(m_{K\pi\pi}, t')$ cells where all the 10 waves are considered, because the 2^+ and 4^+ waves have non-overlapping fit ranges. On average, about five waves are considered in each $(m_{K\pi\pi}, t')$ cell.

number density in t' summed over the analyzed $m_{K\pi\pi}$ region, reads

$$^{k}\mathfrak{I}_a(t') = \frac{1}{\Delta t'_{\text{bin}}} \sum_{m_{K\pi\pi}} \left| {}^{k}\hat{\mathcal{T}}_a(m_{K\pi\pi}, t') \right|^2 , \tag{6.28}$$

where $\Delta t'_{\text{bin}}$ is the width of the considered t' bin. As each model component appears only in one coherent sector, we dropped the sector label. In general, the t' dependence of the intensity of a model component may be different in different partial waves. However, for most of these resonance components we applied equation (6.14). Hence, the t' dependence of the intensities of a such component in the various waves is the same by construction and only the total intensities differ by mainly $|{}^{k}_{b}\mathcal{B}^{z}_{a}|^2$.[r] As ${}^{k}\mathfrak{I}_a(t')$ depends in a complicated, non-linear way on the fit parameters, determining its uncertainties requires elaborate and computationally expensive Monte Carlo uncertainty propagation. As we discuss ${}^{k}\mathfrak{I}_a(t')$ only on a quantitative level in this work, we show the central values without uncertainties in the following.

Figure 6.5 shows the t'-dependence of the intensity of the $K_1(1270)$ component in the $1^+\,0^+$ $\rho(770)\,K\,S$ wave, i.e. the so-called t' spectrum. It exhibits an approximately exponentially falling shape. This is expected for resonances in waves with $M = 0$ from Regge theory, assuming single Pomeron exchange in the scattering process [46]. For partial waves with $M \neq 0$, the exponentially falling shape is modified by an additional factor $(t')^{|M|}$ such that the expected shape for the t' spectra reads[s]

$$^{k}\hat{\mathfrak{I}}_a(t') = {}^{k}\mathfrak{A}_a \cdot \left(t'\right)^{|M|} \cdot e^{-{}^{k}\mathfrak{b}_a t'} . \tag{6.29}$$

Here, ${}^{k}\mathfrak{A}_a$ is the parameter for magnitude of ${}^{k}\hat{\mathfrak{I}}_a(t')$ and ${}^{k}\mathfrak{b}_a$ the slope of the exponential function. Figure 6.6 illustrates the effect of the additional factor $(t')^{|M|}$ on the t' spectra for a wave with $M = 0$ and a wave with $M = 1$, where both t' spectra have a similar slope and magnitude in the high-t' region.

Finally, the quantities we are mainly interested in are the resonance parameters, i.e. the masses and widths of the appearing strange-meson resonances. Table 6.2 lists our estimates for m_0 and Γ_0 of the seven resonance components that were freely fitted in the 10-wave RMF. These values are discussed in the corresponding sections of chapter 7. We give the χ^2 estimates for the statistical uncertainties of the resonance parameters (symmetric uncertainties in table 6.2).[t] Realistic estimates for systematic uncertainties of the resonance parameters require a comprehensive set

[r] Due to the different wave-normalization integrals in equation (6.5) for different partial waves, the total value and the convolution of the production factor with the other functions in equation (6.5) is different for different partial waves. As the production factor depends on t', the t' dependence of a component in various waves is slightly different, even if equation (6.14) is applied. However, this effect is small.

[s] For $M \neq 0$, the intensity is suppressed when the X^- goes in forward direction in the reaction $K^- + p \to X^- + p$. This suppression is purely of kinematic origin and is given by the forward-limit of the Wigner D-functions, which yields the $(t')^{|M|}$ factor in the intensity [46, 72].

[t] We determined the χ^2 estimates for the uncertainties from the inverse of the Hessian matrix in the minimum of the χ^2 function in equation (6.23) (see equation (40.24) in ref. [9]). In principle, those uncertainty estimates may be improved using the same Bootstrapping approach as discussed in section 5.4 for the PWD. However, this requires a very robust RMF model. Bootstrapping of the RMF was beyond the scope of this work. As the systematic effects on the resonance parameters are typically larger than the statistical uncertainties, we expect the χ^2 estimates for the statistical uncertainties to be sufficiently accurate.

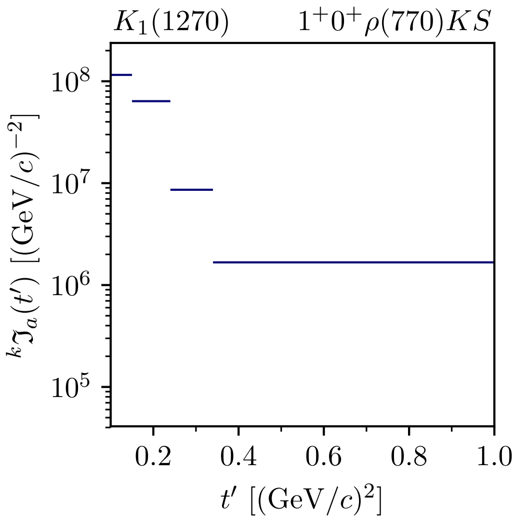

Figure 6.5: The t' spectrum of the $K_1(1270)$ component in the $1^+\,0^+\,\rho(770)\,K\,S$ wave as obtained from the 10-wave RMF. The horizontal blue bars represent the intensity in each t' bin according to equation (6.28).

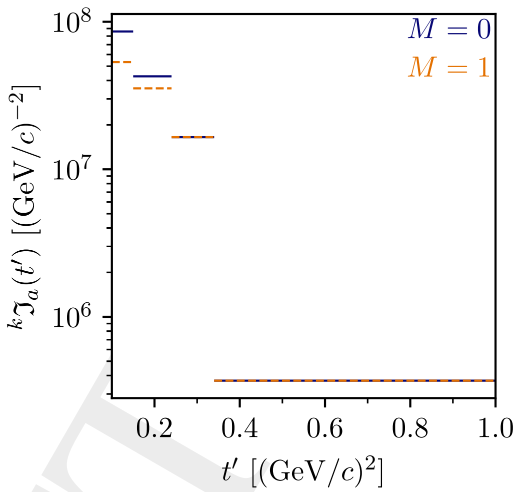

Figure 6.6: Two exemplary t' spectra following the theory model in equation (6.29) for $M = 0$ in blue and $M = 1$ in orange. We chose ${}^k\mathfrak{b}_{M=0} = 10\,(\text{GeV}/c)^{-2}$ for the spectrum in blue, and we chose ${}^k\mathfrak{b}_{M=1} = 12.2\,(\text{GeV}/c)^{-2}$ and ${}^k\mathfrak{A}_{M=1} = 6.53\,{}^k\mathfrak{A}_{M=0}$ for the spectrum in orange such that both spectra agree in the two highest t' bins.

of studies of all relevant systematic effects that may bias the results of the RMF as has been done for the COMPASS $\pi^-\pi^-\pi^+$ analysis in ref. [40]. We present in sections 5.7 and 6.3 several systematic studies of the PWD and the RMF, respectively. However, a complete set of studies was beyond the scope of this work. Hence, our estimates for the asymmetric uncertainties in table 6.2 should be considered as are lower limits on the actual systematic uncertainties. Based on the studies presented in section 6.3 the systematic effects are at least as large as the statistical uncertainties. The parameter estimates for the shape parameters of the non-resonant and effective background components are listed in tables E.2 and E.3, respectively.

6.3 Systematic Studies

In addition to the various systematic effects discussed in section 5.7, also the formalism of the RMF and the employed model may introduce systematic effects. During the development of the 10-wave RMF, we already performed many studies with different RMF models, which gave us a first impression on systematic effects. Once we finished the 10-wave RMF, we performed six dedicated systematic studies described in the following sections 6.3.1 to 6.3.3 and labeled by

Table 6.2: Resonance parameters as obtained from the 10-wave RMF. The first quoted uncertainties are statistical, the second systematic uncertainties. The quoted systematic uncertainties determined from a limited set of performed systematic studies represent only a lower limit on the actual systematic uncertainties (see section 6.3). The parameters of the $K_1(1400)$ component were fixed to the corresponding PDG average values. The values and uncertainties are rounded to the same precision according to the PDG rounding [9]. The number of significant digits is given by the total uncertainty. For the total uncertainty, we quadratically add the statistical uncertainty to the upper and lower systematic uncertainties. For comparison, the PDG averages from ref. [9] are listed. The PDG lists more than one average value for the $K_2^*(1430)$ resonance. We list here the PDG average values for the charged $K_2^*(1430)$ from measurements of only the $K\pi$ final state.

(a) K_1-like resonances

		$K_1(1270)$	K_1'
Discussed in section		7.1	7.1
COMPASS	m_0 [MeV/c^2]	$1267.7 \pm 1.9^{+1.6}_{-4.5}$	$1940 \pm 10^{+90}_{-70}$
	Γ_0 [MeV/c^2]	$83 \pm 4^{+15}_{-4}$	$462 \pm 22^{+27}_{-119}$
PDG	m_0 [MeV/c^2]	1253 ± 7	1672 ± 50
	Γ_0 [MeV/c^2]	90 ± 20	158 ± 50

(b) K_2-like resonances

		$K_2(1770)$	$K_2(1820)$	$K_2(2250)$
Discussed in section		7.4	7.4	7.4
COMPASS	m_0 [MeV/c^2]	$1715 \pm 4^{+1}_{-6}$	$1848 \pm 5^{+6}_{-20}$	$2230 \pm 11^{+7}_{-61}$
	Γ_0 [MeV/c^2]	$139 \pm 7^{+14}_{-7}$	$250 \pm 10^{+17}_{-23}$	$266 \pm 29^{+225}_{-16}$
PDG	m_0 [MeV/c^2]	1773 ± 8	1819 ± 12	2247 ± 17
	Γ_0 [MeV/c^2]	186 ± 14	264 ± 34	180 ± 30

(c) K_J^*-like resonances

		$K_2^*(1430)$	$K_4^*(2045)$
Discussed in section		7.2	7.3
COMPASS	m_0 [MeV/c^2]	$1430.1 \pm 1.5^{+1.3}_{-2.0}$	$2059 \pm 6^{+9}_{-1}$
	Γ_0 [MeV/c^2]	$109 \pm 3^{+6}_{-2}$	$188 \pm 11^{+27}_{-18}$
PDG	m_0 [MeV/c^2]	1427.3 ± 1.5	2048^{+8}_{-9}
	Γ_0 [MeV/c^2]	100.0 ± 2.1	199^{+27}_{-19}

A to ***F*** to investigate systematic effects.[u] We selected studies to investigate the potentially largest systematic effects on the RMF. Performing a complete set of systematic studies was beyond the scope of this analysis. We studied whether the assumptions and approximations that entered the χ^2 function in equation (6.23), which is minimized in the RMFs, may introduce systematic effects. Such effects are discussed in sections 6.3.1 and 6.3.2. We also studied potential systematic effects introduced by the $K_1(1400)$ and $K_2(1820)$ components that are discussed in section 6.3.3. In the same section also the influence of our choice for the rank of the $K^-\pi^-\pi^+$ spin-density matrix is discussed. The resonance parameters obtained in the six systematic studies are listed in table 6.4. Findings that are specific to individual waves are discussed in chapter 7 and only general findings are discussed in the following subsections.

6.3.1 Effects from Using Bootstrapping vs. Maximum-Likelihood Estimates

As discussed in sections 5.4.2 and 6.1.5, we not only used the Bootstrapping estimates for the covariance matrix of the measured spin-density matrix elements, but also for the measured values of the spin-density matrix elements, i.e. the central values of the data points that entered the RMF. To study the effect of this approach, we performed an RMF in study ***A*** where we used the maximum-likelihood estimates[v] as data points, i.e. we used $\lambda_i(m_{K\pi\pi}, t') = \lambda_i^{\text{MLE}}(m_{K\pi\pi}, t')$ in equation (6.23). For the covariance matrix of the spin-density matrix elements, we still used the Bootstrapping estimates as done in the main analysis.

Compared to the main analysis, study ***A*** yielded slightly different resonance parameters. These differences have a similar size as other systematic effects (see table 6.4). Hence, we consider the results of this study to be consistent with the results of the main analysis within the expected uncertainties.

The main analysis, which used the Bootstrapping means as data points, yielded and χ^2_{red} value of 0.826. This χ^2_{red} value corresponds to an unexpectedly large p-value of practically one. Such a low χ^2_{red} may arise for two reasons. First, the RMF has too much freedom and overfits the data. However, this would disagree with the statistically large deviations between some measured spin-density matrix elements and the corresponding RMF result in the main analysis. Such deviations are discussed for example for the intensity spectrum of the $4^+\,1^+\,K^*(892)\,\pi\,G$ wave in section 6.2.2. Hence, we expect the χ^2_{red} value to be even larger than one. i.e. $\chi^2_{\text{red}} \gtrsim 1.0$. Second, the uncertainty estimates of the measured spin-density matrix elements are too large.

[u] Except for the changes explicitly mentioned in the systematic studies discussed in the following; the RMF model, the χ^2 definition, and the fitting procedure remain the same as in the main analysis discussed in sections 6.1 and 6.2. To reduce the computational costs of the systematic studies, we performed about 200 fit attempts with random start-parameter values for each study. This turned out to be sufficient to reliably find the best result, i.e. to find the result with the lowest χ^2 value in more than 10 of the 200 fit attempts.

[v] As defined in section 5.4, the maximum-likelihood estimates are the results of the maximum-likelihood fit of equation (5.38) to the measured $K^-\pi^-\pi^+$ sample.

Table 6.4: Resonance parameters of the eight resonance components included in the 10-wave RMF as obtained in the main analysis (Main) and in the systematic studies ***A*** to ***F***. The last column shows the largest positive and negative deviation from the values obtained in the main analysis that were observed across all systematic studies. As the set of systematic studies is not complete, these deviations give only a lower limit for the full systematic uncertainties. Parameters of resonance components that were not included in the model in a study are indicated by "—". The estimates for the mass and width of the $K_2(1770)$ from study ***E*** (shown in gray) are not included in the corresponding deviations (see text). The resonance parameters of the $K_1(1400)$ component that are marked by $^{(*)}$ were fixed to the corresponding PDG average values. We do not give statistical uncertainties here. The values are rounded according to the corresponding statistical uncertainty from the main analysis following the PDG rounding rules [9].

Resonance	Parameter	Main	***A***	***B***	***C***	***D***	***E***	***F***	Extremes
$K_1(1270)$	m_0 [MeV/c^2]	1267.7	1264.6	1269.2	1265.2	1264.0	1266.5	1263.2	$^{+1.6}_{-4.5}$
	Γ_0 [MeV/c^2]	83	79	98	83	82	82	86	$^{+15}_{-4}$
$K_1(1400)$	m_0 [MeV/c^2]	$^{(*)}$1403	$^{(*)}$1403	$^{(*)}$1403	1514	—	$^{(*)}$1403	$^{(*)}$1403	$^{+111}_{-0}$
	Γ_0 [MeV/c^2]	$^{(*)}$174	$^{(*)}$174	$^{(*)}$174	178	—	$^{(*)}$174	$^{(*)}$174	$^{+4}_{-0}$
K_1'	m_0 [MeV/c^2]	1938	1978	1929	1907	1930	2031	1866	$^{+93}_{-71}$
	Γ_0 [MeV/c^2]	462	457	489	455	428	448	343	$^{+27}_{-119}$
$K_2^*(1430)$	m_0 [MeV/c^2]	1430.1	1431.4	1428.0	1430.7	1430.0	1429.9	1430.0	$^{+1.3}_{-2.0}$
	Γ_0 [MeV/c^2]	108.9	107.3	113.3	109.9	114.5	110.4	112.5	$^{+5.7}_{-1.6}$
$K_2(1770)$	m_0 [MeV/c^2]	1714.6	1716.0	1714.8	1715.4	1715.8	1740.1	1708.7	$^{+25.5}_{-6.0}$
	Γ_0 [MeV/c^2]	139	151	146	131	144	210	153	$^{+71}_{-7}$
$K_2(1820)$	m_0 [MeV/c^2]	1848	1854	1840	1842	1849	—	1827	$^{+6}_{-20}$
	Γ_0 [MeV/c^2]	250	267	262	236	237	—	227	$^{+17}_{-23}$
$K_2(2250)$	m_0 [MeV/c^2]	2230	2237	2222	2232	2222	2170	2232	$^{+7}_{-61}$
	Γ_0 [MeV/c^2]	266	283	303	250	298	491	274	$^{+225}_{-16}$
$K_4^*(2045)$	m_0 [MeV/c^2]	2059	2062	2067	2058	2060	2068	2060	$^{+9}_{-1}$
	Γ_0 [MeV/c^2]	188	177	189	195	185	170	214	$^{+27}_{-18}$

Study $\boldsymbol{A}$, which used the maximum-likelihood estimates as data points, yielded an increased χ^2_{red} value of 1.071, which is in agreement with our expectation of $\chi^2_{\text{red}} \gtrsim 1.0$.[w] This χ^2_{red} value corresponds to a low p-value of about 10^{-5}.

The uncertainties of the spin-density matrix elements from Bootstrapping were determined from the distribution of the maximum-likelihood estimates that were obtained from each of the Bootstrapping samples. Hence, the uncertainties estimate the uncertainty of the maximum-likelihood estimates. Using in study $\boldsymbol{A}$ the maximum-likelihood estimates as data points yielded an χ^2_{red} value in the expected range. Thus, we conclude that the Bootstrapping yielded realistic estimates for the uncertainties of the maximum-likelihood estimates. However, using these uncertainty estimates in the main analysis together with the Bootstrapping means as data points yielded an unexpectedly small χ^2_{red}. This indicates that the uncertainty estimates for the maximum-likelihood estimates overestimate the uncertainties of the Bootstrapping means. This can be directly observed in some spin-density matrix elements. For example; in figure 6.4 the scatter of the data points, which are the Bootstrapping means, is smaller than expected from the shown uncertainties.[x]

A possible explanation for the larger uncertainties, i.e. larger spread, of the maximum-likelihood estimates compared to the Bootstrapping means is the leakage effect discussed in section 5.9. It leads not only to large artifacts in the leakage waves. As it is approximately an ambiguity in the partial-wave model, whose magnitude is given by the specifics of the data sample, e.g. by fluctuation, the leakage effect may also introduce an additional spread in the distributions of the spin-density matrix elements from the different Bootstrapping samples, thereby yielding larger the uncertainty estimates. Even non-leakage waves may be influenced by this spread to a small degree. Also, the maximum-likelihood estimates from the measured $K^-\pi^-\pi^+$ sample are affected by the leakage effect, i.e. by one realization of this ambiguity with a certain magnitude given by the specifics of the measured $K^-\pi^-\pi^+$ sample. Thus, we expect the uncertainties from Bootstrapping to yield a realistic estimate for the actual uncertainties of the maximum-likelihood estimates by including the leakage effect. In contrast, when calculating the Bootstrapping means, the additional spread introduced by the leakage effect may average out to some extent, because we average over different data samples, which potentially have a different magnitude of the leakage effect. Thus, the Bootstrapping means should be less biased by the spread introduced by the leakage effect and should have smaller uncertainties.[y] This would be consistent with the observation that our estimates of the uncertainties overestimate the actual uncertainties of the Bootstrapping means.

We used the Bootstrapping means in the main analysis as data points in order to potentially reduce the bias, e.g. from the leakage effect, on the measured spin-density matrix elements. We

[w] We used the same 10-wave RMF model for the main analysis and for study $\boldsymbol{A}$. Similar to the main analysis, the RMF could not describe some measured spin-density matrix elements.

[x] One should note that considering individual spin-density matrix elements gives an incomplete picture as the spin-density matrix elements from the same $(m_{K\pi\pi}, t')$ cell are strongly correlated.

[y] While calculating the Bootstrapping means may reduce the spread introduced by the leakage effect, it cannot purge the leakage effect. This means in particular that we still expect the leakage waves to be biased by the leakage effect.

did this at the expense of using potentially overestimated uncertainties.[z] This also means, that the χ^2 value of the RMF in equation (6.23) is systematically too small. However, it is still a valid measure for the deviation of the RMF from the measured spin-density matrix elements and can thus be used to estimate the parameter values of the RMF model. Only its interpretation in terms of a χ^2 distributed test statistic is limited. For example, this means that χ^2_{red} values from fits with different numbers of degrees of freedom are hard to compare.

6.3.2 Effects from the Eigenvalue Spectrum of the Precision Matrix

As discussed in section 6.1.5, for a single PWD fit the rank of the covariance matrix of the real-valued elements of the spin-density matrix is the number of free parameters n^{ρ}_{para} of that spin-density matrix. However, we estimated the covariance matrix of the spin-density matrix elements from Bootstrapping, i.e. from the distribution of 2000 independent PWD fits. The rank of this covariance matrix does not correspond to n^{ρ}_{para} of a rank=3 spin-density matrix. In fact, the covariance matrix has full rank. Hence, also the precision matrix, which is the inverse of the covariance matrix, that appears in the χ^2 formulation of the RMF in equation (6.23) has full rank. To test for potential systematic effects from the higher rank of the precision matrix, we performed an RMF in study ***B*** where we constructed a precision matrix with rank n^{ρ}_{para}. To this end, we considered only the n^{ρ}_{para} largest eigenvalues of the covariance matrix when constructing the precision matrix in each $(m_{K\pi\pi}, t')$ cell, i.e.

$$\mathrm{Prec}'[\lambda_i, \lambda_j] = \sum_{h=1}^{n^{\rho}_{\text{para}}} \frac{1}{\mathfrak{e}^h} \mathfrak{v}^h_i \left[\mathfrak{v}^h_j\right]^* . \tag{6.30}$$

Here, $\mathfrak{e}^h$ is the h'th largest eigenvalue of the covariance matrix of the spin-density matrix elements and $\mathfrak{v}^h_i$ is the i'th entry of the corresponding eigenvector. The precision matrix as given in equation (6.30) is similar to the Moore-Penrose pseudo-inverse as used in the main analysis. However, here we did not only set the inverse of zero eigenvalues to zero, but we also set the inverse of all but the n^{ρ}_{para} largest eigenvalues to zero, and we used the eigenvalue decomposition[aa] instead of the singular-value decomposition.

This means that there are some directions in the $\vec{\lambda}(m_{K\pi\pi}, t')$ space in which deviations between the measured spin-density matrix elements and the RMF are not considered in χ^2_{RMF}. These directions are given by the eigenvectors belonging to eigenvalues whose inverse is set to zero according to equation (6.30). In principle, the elements of a rank = 3 spin-density matrix are already constrained in these directions by the limited rank. However, the Bootstrapping means of the spin-density matrix elements, which are used as data points in the RMF, do not exactly fulfill this constraints due to the averaging in the mean calculation. Also, the RMF model for the spin-density matrix in equation (6.1) has rank = [4], which is larger than the rank of the measured spin-density matrix, and hence is less constrained. Thus, neglecting in χ^2_{RMF} all

[z] Explicitly determining Bootstrapping estimates for the uncertainties of the Bootstrapping means would be computationally prohibitively expensive (see section 5.4.2).

[aa] See equation (8) on page 43 and equation (19) on page 156 of ref. [139].

directions belonging to eigenvalues whose inverse is set to zero according to equation (6.30) removes constraints from the RMF and is hence not exactly correct. Furthermore, we determined these directions only with a finite precision given by the precision with which we measured the covariance matrix of the spin-density matrix elements in the Bootstrapping. Hence, study $\boldsymbol{B}$ is an extreme test for effects from the eigenvalue spectrum of the precision matrix.

Using the precision matrix given in equation (6.30) in the RMF in study $\boldsymbol{B}$ yielded $\chi^2_{\text{red}} = 0.899$, which is slightly worse than $\chi^2_{\text{red}} = 0.826$ from the main analysis.[ab] A reason for this may be, that the eigenvectors of the n^{ρ}_{para} largest eigenvalues only approximately span the space of the degrees of freedom of a rank=3 spin-density matrix. This is mainly because of two effects: (i) the finite precision of the eigenvectors given by the finite precision, with which the covariance matrix was determined from the finite set of Bootstrapping samples; (ii) the non-linear effects in the calculation of the spin-density matrix elements, which are discussed in section 5.4. For some resonance parameters, the parameter estimates from study $\boldsymbol{B}$ define the extreme deviations with respect to the estimates from the main analysis. Hence, systematic effects from the eigenvalue spectrum of the precision matrix are part of our systematic uncertainties. However, in general the systematic effects observed in study $\boldsymbol{B}$, which can be considered as an extreme test for the effects from the eigenvalue spectrum of the precision matrix, are of similar size as other systematic effects (see table 6.4). Therefore, we expect no artifacts from the eigenvalue spectrum of the precision matrix on the results of the RMF.

6.3.3 Effects from the Formulation of the $K^-\pi^-\pi^+$ RMF Model

Effects from the $K_1(1400)$ Component

As the $K_1(1400)$ is only a weak signal in the 1^+ waves included in the 10-wave RMF, we fixed its resonance parameters to the corresponding PDG average values in the main analysis. Although the $K_1(1400)$ is one of the best known strange mesons, previous measurements of its resonance parameters exhibit a considerable spread (see section 7.1). To test whether the PDG average values for the $K_1(1400)$ are consistent with our data, we performed an RMF in study $\boldsymbol{C}$ where we left the mass and width parameters of the $K_1(1400)$ component as free fit parameters.

To study the influence of the $K_1(1400)$ component on the measurement of the other resonance parameters, we performed an RMF in study $\boldsymbol{D}$ where we omitted the $K_1(1400)$ component from the RMF model, i.e. where we modeled the 1^+ waves by only two resonances.[ac] The results of these studies are discussed in section 7.1.

[ab] Using equation (6.30) reduces the number of degrees of freedom in the RMF; because by setting the inverse of certain eigenvalues to zero, we ignore certain direction in the $\vec{\lambda}$ space. This means we effectively remove some data from the χ^2 term. The number of degrees of freedom in the RMF $\boldsymbol{B}$ is the sum over the rank of $\text{Prec}'[\lambda_i, \lambda_j]$ from all $(m_{K\pi\pi}, t')$ cells minus the number of free parameters in the fit.

[ac] The model for the 1^+ waves still included the non-resonant components, the $\pi^-\pi^-\pi^+$ background components, and the effective background components as in the 10-wave RMF model in table 6.1.

Effects from the $K_2(1820)$ Component

As discussed in section 7.4, many previous measurements of the K_2 resonances considered only one K_2 state in the region $1.7 \leq m_{K\pi\pi} < 2.0\,\text{GeV}/c^2$, while we included the $K_2(1780)$ and $K_2(1820)$ components in the 10-wave RMF. To obtain resonance parameter estimates that are directly comparable with these previous measurements, we performed an RMF in study $\boldsymbol{E}$ where we omitted the $K_2(1820)$ component, i.e. where we modeled the low-$m_{K\pi\pi}$ region of the 2^- waves by only the $K_2(1780)$ component.[ad] As the model without the $K_2(1820)$ component represents a fundamentally different interpretation of the 2^- waves for $m_{K\pi\pi} \lesssim 2\,\text{GeV}/c^2$, we did not consider the results of this study in our estimates for the systematic uncertainties of the resonance parameters of the $K_2(1770)$ in table 6.2. The results of this study are discussed in section 7.4.

Effects from the Chosen Rank of the Model for the $K^-\pi^-\pi^+$ Spin-Density Matrix

When constructing the RMF model for the $K^-\pi^-\pi^+$ spin-density matrix in section 6.1.2, we assumed that the reaction $K^- + p \to K^-\pi^-\pi^+ + p$ is dominated by Pomeron exchange. Accordingly, we modeled the $K^-\pi^-\pi^+$ spin-density matrix $\hat{\rho}_{ab}^{K\pi\pi}$ in equation (6.7) as a rank$=1$ matrix. To study this choice we performed an RMF in study $\boldsymbol{F}$ where we constructed a rank=2 spin-density matrix,

$$\rho_{ab}^{K\pi\pi}(m_{K\pi\pi}, t') = \sum_{z=1}^{2} \mathcal{T}_a^{K\pi\pi,z}(m_{K\pi\pi}, t') \left[\mathcal{T}_b^{K\pi\pi,z}(m_{K\pi\pi}, t')\right]^*, \tag{6.31}$$

to model the reaction $K^- + p \to K^-\pi^-\pi^+ + p$. Therefore, we defined two sets of transition amplitudes analogously to equation (6.6),

$$\hat{\mathcal{T}}_a^{K\pi\pi,z}(m_{K\pi\pi}, t') = \sqrt{\mathfrak{R}_a(m_{K\pi\pi}) m_{K\pi\pi}} \mathcal{P}_{\mathbb{P}}(m_{K\pi\pi}, t') \sum_{k\in\mathbb{S}_a} {}^{k}\mathcal{C}_a^{K\pi\pi,z}(t')\, \mathcal{D}_k(m_{K\pi\pi}; \zeta_k) \tag{6.32}$$

one for each of the two coherent sectors z, including the same resonance components with the same mass and width parameters in both sectors, but with independent coupling amplitudes ${}^{k}\mathcal{C}_a^{K\pi\pi,z}(t')$.[ae] The non-resonant components were included only in the first set of transition amplitudes with $z = 1$. In this study $\boldsymbol{F}$, we significantly increased the number of free fit parameters from 291 parameters in the main analysis to 391 parameters.

The reduced χ^2 decreased in this study from $\chi^2_{\text{red}} = 0.826$ as obtained in the main analysis to $\chi^2_{\text{red}} = 0.738$. This means that the measured spin-density matrix elements are better described by the RMF model using a $K^-\pi^-\pi^+$ spin-density matrix of rank=2. However, as discussed in

[ad] The model for the 2^- waves still included the $K_2(2250)$ component for the high-$m_{K\pi\pi}$ region and the non-resonant components, the $\pi^-\pi^-\pi^+$ background components, and the effective background components as in the 10-wave RMF model in table 6.1.

[ae] As in the main analysis, we also enforced the t' dependence of a resonance component that appears in multiple waves with the same $J^P M^\varepsilon$ to be the same by applying equation (6.14). We introduced an independent set of branching amplitudes ${}^{k}_{b}\mathcal{B}_a^{K\pi\pi,2}$ for the additional set of transition amplitudes.

section 6.3.1, the χ^2 defined in equation (6.23) can be interpreted in terms of a χ^2 distribution only to a limited extend. Furthermore, the shape parameters b_k of the effective background components of the $2^- 0^+ K^*(892)\,\pi\,F$ and $4^+ 1^+ \rho(770)\,K\,G$ waves end up at the lower parameter-limit of $-0.1\,(\mathrm{GeV}/c)^{-2}$. This indicates that for these waves the result of this study is biased towards an unphysical solution.[af] For some resonance parameters, e.g. for the mass and width of the K_1', this study yielded the largest deviation from the results of the main analysis. These deviations are discussed in chapter 7.

6.4 Pseudodata Studies using the $K^-\pi^-\pi^+$ RMF Model

In this section, we discuss input-output studies based on pseudodata samples to investigate the consistency of the full analysis chain up to the measurement of resonance parameters in the RMF, similar to section 5.8, where we used pseudodata samples to investigate effects on the results of the PWD. To this end, we generated pseudodata samples based on the results of the 10-wave RMF. Hence, we know a priori which resonances appear in the pseudodata with which strength and, most notably, which resonance parameters they have. As we explicitly modeled the background contributions and hence separated the backgrounds from the signals in the RMF, we also control the background contributions in these pseudodata samples. This is in contrast to the $K^-\pi^-\pi^+$ PWD pseudodata studies presented in section 5.8 and allows us to test for systematic effects from our treatment of background contributions (see sections 5.3, 6.1.3, and 6.1.4).

First, we generated a pseudodata sample of 50×10^6 events, whose distribution is given only by the resonances and the non-resonant contributions. To this end, we took from the result the 10-wave RMF discussed in section 6.2.2 only the $K^-\pi^-\pi^+$ signal part given by the $K^-\pi^-\pi^+$ spin-density matrix in equation (6.7).[ag] We used the 10-wave RMF result of $\hat{\rho}_{ab}^{K\pi\pi}(m_{K\pi\pi}, t')$ as input to a PWD model as defined in equation (5.19). Using this PWD model, we produced a pseudodata sample applying the same approach as in section 5.8. We call this sample the <u>10-wave pseudodata sample</u>. It is distributed according to the resonant and non-resonant components of the 10 waves included in the 10-wave RMF. The contributions from the other 228 waves of the 238-wave set are zero. Hence, the 10-wave pseudodata sample does not follow the same distribution as the full $K^-\pi^-\pi^+$ sample. Still, this pseudodata sample allow us to study the consistency of the measurement of resonances parameters. Finally, only both sets of pseudodata studies, those based in the $K^-\pi^-\pi^+$ RMF model discussed here and those based on the 238-wave PWD discussed in section 5.8, yield a complete picture of our analysis.

We applied the complete analysis chain presented in this work to the produced 10-wave pseudodata sample. This means, we processed it through the COMPASS detector Monte Carlo simulation (see appendix C.2) and we applied the same event selection criteria as applied to the

[af] The lower parameter limit of $-0.1\,(\mathrm{GeV}/c)^{-2}$ was chosen such that fit results with this parameter value are not completely unphysical and can still be interpreted in terms of physics signals to some extent. However, we consider such results to be not sufficient for the main analysis.

[ag] Technically we achieved this by setting $C^{\pi\pi\pi}(t') = 0$ in equation (6.15) and ${}^{k}C_a^{\mathrm{eBKG}}(t') = 0$ in equation (6.16).

measured $K^-\pi^-\pi^+$ sample (see section 4.1). Then, we performed a PWD of the reconstructed pseudodata sample using the rank=3 model of the 238-wave set.[ah] In contrast to all previous pseudodata and systematic studies, we performed here a Bootstrapping of the PWD as discussed for the main analysis in section 5.4. This allows us to study the consistency of our Bootstrapping approach. Finally, we performed a fit of the 10-wave RMF model defined in section 6.2.1 to the results from the Bootstrapping of the PWD.

The 10-wave pseudodata sample described above is free of background as we used only the $K^-\pi^-\pi^+$ RMF model part of the 10-wave RMF to generate it. In order to study effects from incoherent background processes, we admixed events from the reconstructed $\pi^-\pi^-\pi^+$ pseudodata sample (see section 5.10) to the reconstructed 10-wave pseudodata sample on an event-by-event basis. Hence, the combined 10-wave pseudodata sample with admixed $\pi^-\pi^-\pi^+$ background mimics the situation in the measured $K^-\pi^-\pi^+$ sample as realistically as possible. We chose the amount of admixed $\pi^-\pi^-\pi^+$ events such that it corresponds to the amount of $\pi^-\pi^-\pi^+$ background in the measured $K^-\pi^-\pi^+$ sample as predicted by the $\pi^-\pi^-\pi^+$ pseudodata.[ai] Analogously to the 10-wave pseudodata sample without admixed $\pi^-\pi^-\pi^+$ background, we performed a PWD with Bootstrapping,[aj]and we performed an RMF to the results of this PWD. As the $\pi^-\pi^-\pi^+$ background is the only background in the 10-wave pseudodata sample with admixed $\pi^-\pi^-\pi^+$ background, we expect the effective background components as obtained from this RMF to be small. Furthermore, we performed an additional RMF omitting the effective background components from the model.

Table 6.5 lists the resonance-parameter estimates from the RMFs to the 10-wave pseudodata sample with and without admixed $\pi^-\pi^-\pi^+$ background.For some resonance parameter, e.g. the m_0 parameter of the $K_1(1270)$ component, the estimates deviate from the reference value, i.e. the result of the 10-wave RMF from the measured $K^-\pi^-\pi^+$ sample, by more than their statistical uncertainty. However, all deviations are smaller than the systematic effects discussed in section 6.3, except for the m_0 parameter of the $K_2(2250)$ component, whose deviation is, however, still of similar size as the systematic effects.[ak] This means that the bias on our resonance-parameter estimates as determined in this pseudodata study is small. This also indicates that our first estimates for systematic uncertainties have a realistic size (see section 6.3).

[ah] We used the correct acceptance model in the PWD fits, in contrast to the previous studies where we used the detuned acceptance model as discussed e.g. in section 5.8.2.

[ai] As the 10-wave RMF model represents only part of the $K^-\pi^-\pi^+$ sample, while the $\pi^-\pi^-\pi^+$ background distributes to all 238 $K^-\pi^-\pi^+$ partial waves, the fraction of $\pi^-\pi^-\pi^+$ background events in the 10-wave pseudodata sample with admixed $\pi^-\pi^-\pi^+$ background is not 6.7 % as predicted for the total measured $K^-\pi^-\pi^+$ sample (see section 5.10.1). The reconstructed 10-wave pseudodata sample with admixed $\pi^-\pi^-\pi^+$ background contains about 28 % $\pi^-\pi^-\pi^+$ background events.

[aj] As the $\pi^-\pi^-\pi^+$ background distributes to all 238 $K^-\pi^-\pi^+$ partial waves, we used a rank=3 model of the 238-wave set as in the main analysis. Therefore, we expect the same projections of the $\pi^-\pi^-\pi^+$ background into the individual partial waves as predicted by the $\pi^-\pi^-\pi^+$ background PWD.

[ak] The largest positive deviation for the m_0 parameter of the $K_2(2250)$ component observed in the systematic studies is $7\,\mathrm{MeV}/c^2$, i.e. smaller than the deviation of $26\,\mathrm{MeV}/c^2$ found in the pseudodata studies. However, the largest negative deviation observed in the systematic studies is $-61\,\mathrm{MeV}/c^2$, i.e. larger in magnitude than the deviation found here.

Table 6.5: Resonance parameters of seven resonance components obtained from fits of the 10-wave RMF model to the 10-wave pseudodata sample with and without admixed $\pi^-\pi^-\pi^+$ background. For the pseudodata sample with admixed $\pi^-\pi^-\pi^+$ background, we performed two RMFs, one with the full 10-wave RMF model and one omitting the effective background (eBKG) components from the 10-wave RMF model. The "Reference" column lists the resonance parameters used to generate these pseudodata samples, which are the resonance parameters obtained in the 10-wave RMF to the measured $K^-\pi^-\pi^+$ sample (see table 6.2). The last column shows the largest positive and negative deviation from the reference values observed in all three studies. We do not list the resonance parameters of the $K_1(1400)$ component as they were fixed in all three studies. We do not give uncertainties. The values are rounded according to the corresponding statistical uncertainty from the main analysis following the PDG rounding rules [9].

		Reference	10-wave pseudodata			Extremes
$\pi^-\pi^-\pi^+$ admixed			✓	✓	✘	
eBKG component			✓	✘	✓	
$K_1(1270)$	m_0 [MeV/c^2]	1267.7	1267.4	1264.1	1263.5	$^{+0.0}_{-4.2}$
	Γ_0 [MeV/c^2]	83	88	88	88	$^{+5}_{-0}$
K_1'	m_0 [MeV/c^2]	1938	1940	1945	1944	$^{+7}_{-0}$
	Γ_0 [MeV/c^2]	462	433	453	454	$^{+0}_{-29}$
$K_2^*(1430)$	m_0 [MeV/c^2]	1430.1	1431.4	1431.9	1431.8	$^{+1.8}_{-0.0}$
	Γ_0 [MeV/c^2]	108.9	111.4	110.2	111.6	$^{+2.7}_{-0.0}$
$K_2(1770)$	m_0 [MeV/c^2]	1714.6	1714.5	1713.3	1713.5	$^{+0.0}_{-1.3}$
	Γ_0 [MeV/c^2]	139	144	143	142	$^{+5}_{-0}$
$K_2(1820)$	m_0 [MeV/c^2]	1848	1853	1850	1849	$^{+5}_{-0}$
	Γ_0 [MeV/c^2]	250	249	247	245	$^{+0}_{-5}$
$K_2(2250)$	m_0 [MeV/c^2]	2230	2240	2256	2253	$^{+26}_{-0}$
	Γ_0 [MeV/c^2]	266	267	248	255	$^{+1}_{-17}$
$K_4^*(2048)$	m_0 [MeV/c^2]	2059	2057	2058	2060	$^{+1}_{-2}$
	Γ_0 [MeV/c^2]	188	179	196	200	$^{+13}_{-8}$

Figure 6.7 shows the results of the RMF to the 10-wave pseudodata sample with admixed $\pi^-\pi^-\pi^+$ background as solid curves exemplarily for the t'-summed intensity spectrum of the $2^+\,1^+\,\rho(770)\,K\,D$ wave. The result for the $K_2^*(1430)$ component (solid blue curve) agrees well with the $K_2^*(1430)$ component in the reference (dash-dotted blue curve), i.e. with the result of the 10-wave RMF from the measured $K^-\pi^-\pi^+$ sample. We find similar agreement for all resonance components included in the 10-wave RMF. This means that we were able to reproduce not only the resonance parameters but also the coupling and branching amplitudes of the resonances components in this pseudodata study. Also, the shape of the non-resonant component obtained from the pseudodata sample (solid green curve) agrees well with the reference (dash-dotted green curve). The RMF slightly overestimates the amount of the non-resonant contribution in this wave. This overestimation is small compared to typical systematic effects on the yield of the model components. We find similar agreement for the non-resonant components also in the nine other partial waves. Hence, we conclude that we are able to consistently extract also the non-resonant contributions and separate them from resonance signals in the RMFs. The non-resonant contributions are typically harder to determine, because they have less distinctive features compared to resonances, e.g. we assume that their amplitudes have a constant phase independent of $m_{K\pi\pi}$. Thus, a consistent separation of resonant and non-resonant contributions is a strong indication for the reliability and robustness of our results.

The $\pi^-\pi^-\pi^+$ background component as obtained from the RMF to the pseudodata (solid orange curve) underestimates the actual amount of $\pi^-\pi^-\pi^+$ background, shown by cyan data points, by about a factor of 0.4.[al] We also find a significant contribution of the effective background component (solid brown curve), while there is no such background contribution in the pseudodata. We observe a similar behavior also in other waves. Hence, the RMF describes the $\pi^-\pi^-\pi^+$ background by a combination of the $\pi^-\pi^-\pi^+$ and the effective background components. To further study this behavior, we performed an RMF where we omitted the effective background components from the model. Figure 6.8a shows the result of this study. Again, the resonant and non-resonant components agree well with the reference (cf. solid and dash-dotted curves). The $\pi^-\pi^-\pi^+$ component is larger compared to the previous RMF, because it is the only incoherent component in the model that can be used to account for the $\pi^-\pi^-\pi^+$ background. However, the $\pi^-\pi^-\pi^+$ component still underestimates the amount of $\pi^-\pi^-\pi^+$ background by about a factor of 0.5. In a further study, we admixed three times more $\pi^-\pi^-\pi^+$ background events to the 10-wave pseudodata sample. This yielded an underestimation of the $\pi^-\pi^-\pi^+$ background by about the same factor. Hence, we conclude that the RMF systematically underestimates the amount of $\pi^-\pi^-\pi^+$ background by about a factor of 0.5 in the pseudodata studies.

Also, the 10-wave RMF to the measured $K^-\pi^-\pi^+$ sample yielded an amount of $\pi^-\pi^-\pi^+$ background that is smaller than predicted by the $\pi^-\pi^-\pi^+$ pseudodata sample (see figure 6.3b). However, it is smaller by a factor of only about 0.8. A possible explanation is that the amount of $\pi^-\pi^-\pi^+$ background predicted by the $\pi^-\pi^-\pi^+$ pseudodata sample is too small, assuming that the RMF underestimated the amount of $\pi^-\pi^-\pi^+$ background in the measured $K^-\pi^-\pi^+$ sample by the same factor as in the pseudodata studies. This explanation may be the case, because the prediction

[al] The shape of the $\pi^-\pi^-\pi^+$ component and of the $\pi^-\pi^-\pi^+$ background PWD are the same by construction (see section 6.1.3).

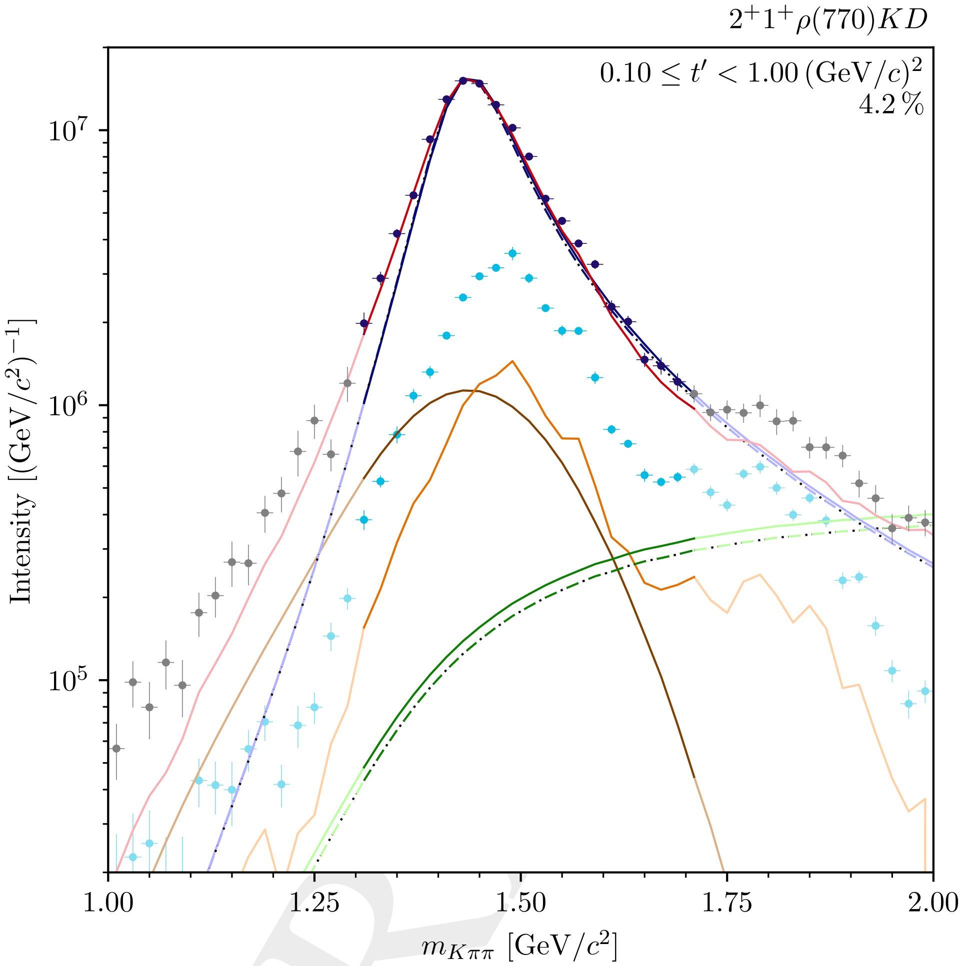

Figure 6.7: Results from fitting the 10-wave RMF model to the PWD of the 10-wave pseudodata sample with admixed $\pi^{-}\pi^{-}\pi^{+}$ background (solid curves) for the t'-summed intensity spectrum of the 2^{+} 1^{+} $\rho(770)\,K\,D$ wave. The blue data points represent the PWD of the 10-wave pseudodata sample with admixed $\pi^{-}\pi^{-}\pi^{+}$ background. The dash-dotted curves represent the model reference, i.e. the results of the 10-wave RMF to the measured data (same as solid curves in section 6.2.2), scaled according to the number of produced pseudodata events. The cyan data points show the results of the $\pi^{-}\pi^{-}\pi^{+}$ background PWD, scaled such that it corresponds to the amount of $\pi^{-}\pi^{-}\pi^{+}$ background in the pseudodata sample. The effective background component was not included in the pseudodata model. Also, the $\pi^{-}\pi^{-}\pi^{+}$ component was not included in the pseudodata model, but $\pi^{-}\pi^{-}\pi^{+}$ events from the $\pi^{-}\pi^{-}\pi^{+}$ pseudodata sample were admixed to the 10-wave pseudodata sample. Hence, we do not show the background component, the $\pi^{-}\pi^{-}\pi^{+}$ component, and the total model curve for the model reference. The red curve represents the total RMF model. The blue curves represent the resonance component. The green curves represent the non-resonant component. The orange curve represents the $\pi^{-}\pi^{-}\pi^{+}$ background component. The brown curve represents the effective background component. The extrapolation to the $m_{K\pi\pi}$ region that was not included in the RMF is shown in brightened colors. The corresponding data points are shown in gray. Only the range $1.0 \leq m_{K\pi\pi} < 2.0\,\mathrm{GeV}/c^2$ is shown. The percentage gives the relative intensity of this wave in the PWD of the pseudodata sample.

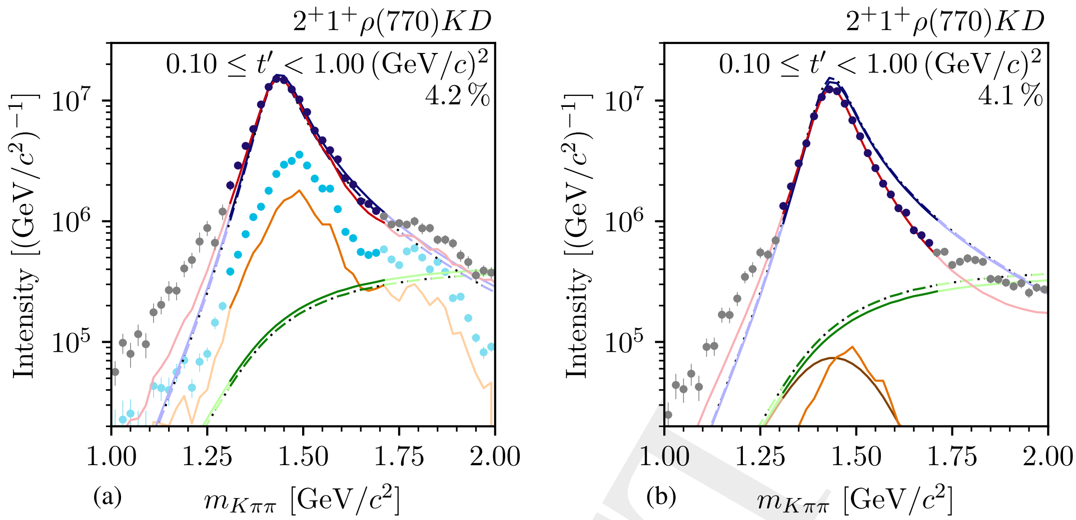

Figure 6.8: Same as figure 6.7, but (a) for the RMF omitting the effective background components in the model, and (b) for the RMF to the 10-wave pseudodata sample without admixed $\pi^-\pi^-\pi^+$ background.

by the $\pi^-\pi^-\pi^+$ pseudodata sample is only a rough estimate, because the absolute acceptance is not accurately known as discussed in section 5.10.1.[am] Another possible explanation is based on the fact that the 10-wave pseudodata sample represents only a part of the measured $K^-\pi^-\pi^+$ sample. Whether the $\pi^-\pi^-\pi^+$ background is admixed to the full $K^-\pi^-\pi^+$ sample as in the measured data, or only to the 10-wave pseudodata sample may affect the result of the PWD of the $\pi^-\pi^-\pi^+$ background. This is because the background contributions are treated only effectively in the PWD (see section 5.3), and imperfections in this description of the $\pi^-\pi^-\pi^+$ background may have different implications depending on the other contributions in the data sample. We also observe that the fit uses a combination of the $\pi^-\pi^-\pi^+$ and the effective background components to describe the actual $\pi^-\pi^-\pi^+$ background when including the effective background component in the RMF model. This indicates that the exact shape of the $\pi^-\pi^-\pi^+$ background in the partial waves slightly differs from the $\pi^-\pi^-\pi^+$ background PWD.[an] Hence, the bias on the RMF estimate of the amount of $\pi^-\pi^-\pi^+$ background may be larger in the pseudodata studies than in the 10-wave RMF to the measured $K^-\pi^-\pi^+$ sample. In the worst case, we expect that the RMF underestimates the actual amount of $\pi^-\pi^-\pi^+$ background in the measured $K^-\pi^-\pi^+$ sample by at most a factor of 0.5.

To further study the separation between signal and background components in the RMF and to test whether the $\pi^-\pi^-\pi^+$ and effective background components can be partly misused by the RMF to account for other effects in the data, we performed an RMF that included both background components to the 10-wave pseudodata sample without admixed $\pi^-\pi^-\pi^+$ background. Figure 6.8b shows the result of this study exemplarily for the intensity spectrum of the $2^+\,1^+$

[am] In contrast to the measured $K^-\pi^-\pi^+$ sample, we know the amount of $\pi^-\pi^-\pi^+$ background in the pseudodata sample exactly.

[an] This difference must be small, because the RMF results for the resonance and non-resonant components are consistent with the reference.

$\rho(770)\,K\,D$ wave. As in the previous studies, the results for the resonant and non-resonant components (solid blue and green curves) agree with the corresponding references (dash-dotted curves). The $\pi^-\pi^-\pi^+$ and effective background components (solid orange and brown curves) practically do not contribute to the total model intensity.[ao] This is expected, because the analyzed pseudodata sample does not contain background events. Hence, we conclude that the RMF does not misuse the $\pi^-\pi^-\pi^+$ and effective background components to describe other effects in the data. This is a strong indication that the RMF is able to reliably separate resonance and non-resonant contributions from background.

The pseudodata studies presented in this section allowed us to test our full analysis chain: starting with the event selection, over the Bootstrapping of the PWD, up to the RMF. Reviewing our findings, the extraction of the resonance parameters, which is the main goal of this analysis, is consistent within the systematic effects discussed in section 6.3 in all performed studies. It is not strongly affected by the estimate for the $\pi^-\pi^-\pi^+$ background. Hence, we conclude that our treatment of the $\pi^-\pi^-\pi^+$ background works sufficiently well. As the $\pi^-\pi^-\pi^+$ background is the largest background contribution to the $K^-\pi^-\pi^+$ sample and as we treat other background contributions similarly (see sections 5.3 and 6.1.4), we expect that the RMF is able to separate resonance and non-resonant contributions from background contributions sufficiently well. As the results from the pseudodata studies for also the non-resonant components agree with the reference, we conclude that the RMF is able to separate well resonances from non-resonant contributions. We hence conclude from our pseudodata studies that our analysis scheme is able to reliably measure the resonance parameters of strange mesons decaying to the $K^-\pi^-\pi^+$ final state.

[ao] Also, the magnitude of the non-resonant component is small for $m_{K\pi\pi} \lesssim 1.6\,\mathrm{GeV}/c^2$. However, the non-resonant component is coherently added to the resonance component (see section 6.1.2), while the $\pi^-\pi^-\pi^+$ and effective background components are added incoherently. Hence, even the small non-resonant component can significantly contribute to the total model intensity via its interference terms with the large resonance components. These contributions of the non-resonant components can be seen by the difference between the total model (red curve) and the resonance components (blue curves).

7 Results for Selected Partial Waves

In the previous chapters, we have discussed the main stages of our analysis starting from the measurement of the data sets (see chapter 2), over the selection of $K^-\pi^-\pi^+$ event candidates (see chapters 3 and 4), and over the partial-wave decomposition using the 238-wave set (see chapter 5), up to the resonance-model fit of 10 selected partial waves (see chapter 6). We performed extensive systematic and pseudodata studies (see sections 5.7, 5.8, 5.10, 6.3, and 6.4) to verify the robustness and reliability of our analysis results. All of this allows us to finally interpret the results in terms of physics signals, i.e. strange-meson resonances appearing in the $K^-\pi^-\pi^+$ final state, to measure their masses and widths, and to compare our results to previous measurements.

In sections 7.1 to 7.4, we discuss the results for partial waves with $J^P = 1^+$, 2^+, 4^+, and 2^-; i.e. with J^P quantum numbers of the waves included in the well-studied 10-wave RMF. If not explicitly stated differently, we show data from the first t' bin or show t'-summed distributions to exemplarily represent our results. Our estimates for the masses and widths of these resonances are summarized in table 6.2. In table 6.2 and in the following, the first quoted uncertainties are statistical, the second systematic uncertainties. The quoted systematic uncertainties determined from a limited set of performed systematic studies represent only a lower limit on the actual systematic uncertainties (see section 6.3). In sections 7.5 to 7.8, we discuss the results for further partial waves with $J^P = 3^-$, 0^-, 3^+, and 4^-. In order to study a possible resonance content of these waves, we performed extended RMFs, where we added selected waves from these J^P sectors to the 10-wave RMF model. However, these extended RMFs are not as well studied as the 10-wave RMF. Hence, their results must be interpreted as a first attempt to also study signals in these waves, and we only quote rough values for our estimates on the corresponding resonance parameters rounded to a precision of $10\,\text{MeV}/c^2$ without giving the uncertainties. The technical details of the extended RMFs are summarized in appendix E.2. In section 7.9, we discuss further interesting results from the PWD.

7.1 $J^P = 1^+$ Partial Waves

The blue data points in figure 7.1a show the measured intensity spectrum of the $1^+\,0^+\,\rho(770)\,K\,S$ wave in the lowest t' bin as obtained from the 238-wave PWD. The spectrum exhibits a clear peak at about $1.3\,\text{GeV}/c^2$. The RMF describes this peak using dominantly the $K_1(1270)$ component (blue curve) with a mass of $(1267.7 \pm 1.9\,^{+1.6}_{-4.5})\,\text{MeV}/c^2$ and a width of $(83 \pm 4\,^{+15}_{-\ 4})\,\text{MeV}/c^2$. The

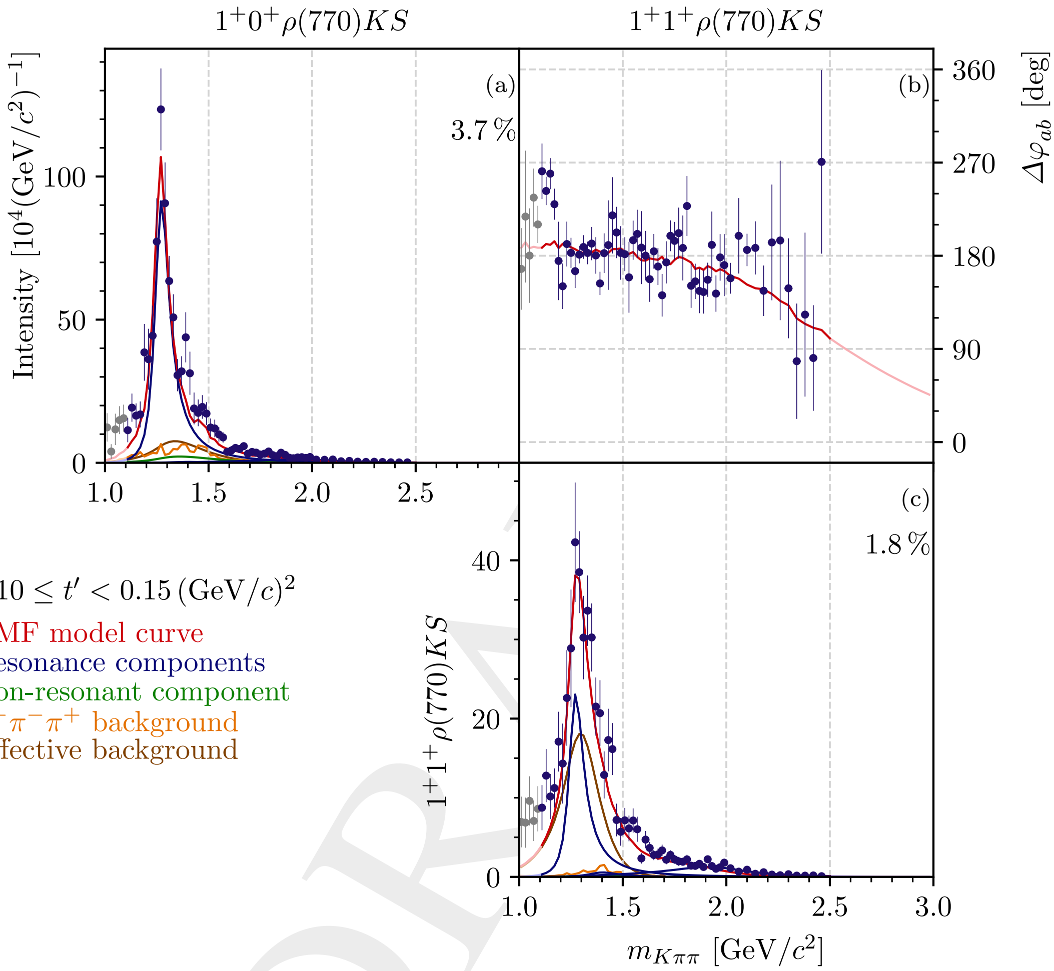

Figure 7.1: Representation of the Spin-density matrix in the lowest t' bin of the two waves with $J^P = 1^+$ that were included in the 10-wave RMF. The figures on the diagonal show the intensity spectra. The off-diagonal figure shows the relative phase as defined in equation (5.74).[c] It represents the off-diagonal element of the spin-density matrix, i.e. the interference term between the two waves. The blue data points represent the measured spin-density matrix elements. The curves represent the result of the 10-wave RMF. The red curves represent the total RMF model. The blue curves represent the individual resonance components, the green curves the non-resonant components, the orange curves the $\pi^-\pi^-\pi^+$ background components, and the brown curves the effective background components. The extrapolations beyond the $m_{K\pi\pi}$ fit ranges are shown in lighter colors. The corresponding data points are shown in gray. The percentages given in the graphics showing intensity spectra give the relative intensity as defined in equation (5.76).

RMF yielded only a small intensity for the $K_1(1400)$ component, with a peak reaching about 10^4 produced events per GeV/c^2as shown in figure 7.2a. Leafing the resonance parameters of the $K_1(1400)$ component free in the RMF as done in systematic study ***C*** or removing the $K_1(1400)$ component from the RMF model as done in systematic study ***D*** has only small effects on the other resonance parameters (see table 6.4).[a] All of these effects are similar in size or smaller than other systematic effects. Hence, using fixed resonance parameters for the $K_1(1400)$ component does not significantly bias the results of our analysis.

The intensity spectrum of the $1^+\,0^+\,\rho(770)\,K\,S$ wave exhibits a shoulder at about $1.5\,\text{GeV}/c^2$, which is clearly seen in the t'-summed intensity spectrum in figure 7.2a. This shoulder is too high in $m_{K\pi\pi}$ in order to arise from the $K_1(1400)$ resonance. Also, the RMF does not use the K_1' component (see table 6.1) to describe it. Even in an additional study where we added another resonance component to the RMF model that was dedicated to describe the $1.5\,\text{GeV}/c^2$ shoulder, it was not described by any resonance component. Hence, this shoulder is not consistent with a Breit-Wigner resonance. Also, we observe no phase motion that would be consistent with a resonance at $1.5\,\text{GeV}/c^2$. Overall, the non-resonant (green curve), the $\pi^-\pi^-\pi^+$ background (orange curve), and the effective background components contribute only little to the total RMF model intensity (red curve). The intensity spectrum of the $1^+\,0^+\,\rho(770)\,K\,S$ wave exhibits a small, broader shoulder at $m_{K\pi\pi} \approx 1.9\,\text{GeV}/c^2$ as shown in figure 7.2a. The RMF describes this shoulder by a dominant contribution of the K_1' component with a mass of $(1940 \pm 10\,^{+90}_{-70})\,\text{MeV}/c^2$ and a width of $(462\,\pm 22\,^{+\,27}_{-119})\,\text{MeV}/c^2$.

We also included the $1^+\,1^+\,\rho(770)\,K\,S$ wave in the 10-wave RMF, i.e. a wave with the same quantum numbers and decay mode, except for the spin-projection which is $M = 1$. The $M = 1$ wave has about half the intensity of the $M = 0$ wave. Figure 7.1c shows the intensity spectrum of this wave in the lowest t' bin. It exhibits the same narrow peak as the intensity spectrum of the $M = 0$ wave. As for the $M = 0$ wave, the peak in the $M = 1$ wave is described by a large contribution of the $K_1(1270)$ component.[b] Figure 7.1b shows the relative phase between the $1^+\,0^+\,\rho(770)\,K\,S$ wave and the $1^+\,1^+\,\rho(770)\,K\,S$ wave.[c] It is practically constant for $m_{K\pi\pi} \gtrsim 1.2\,\text{GeV}/c^2$ with a phase difference of about 180°. Interpreting this relative phase as the phase difference between the corresponding transition amplitudes of the coherent process $K^- + p \to K^-\pi^-\pi^+ + p$ [see equation (5.75)], this means that the amplitudes of both waves have the same phase motion, but opposite sign. It is expected that the amplitudes of both waves have the same phase motion as both waves are dominated by the same $K_1(1270)$ resonance. Below $1.2\,\text{GeV}/c^2$ the relative phase is larger than 180°. This may be caused by the enhanced low-mass tail in both waves, which we assume to be analysis artifacts. Compared to the $1^+\,0^+\,\rho(770)\,K\,S$ wave, the $1^+\,1^+\,\rho(770)\,K\,S$ wave exhibits a more pronounced high-mass tail, which is described in the RMF mainly by the K_1' component.

[a] In study ***C***, the largest effect is that the the K_1' becomes about $30\,\text{MeV}/c^2$ lighter. In study ***D***, the largest effects are that the $K_1(1270)$ becomes about $4\,\text{MeV}/c^2$ lighter and the $K_2^*(1430)$ becomes about $6\,\text{MeV}/c^2$ broader.

[b] We use the same $K_1(1270)$ component in the $M = 0$ and $M = 1$ waves with the same mass and width parameters.

[c] In contrast to other figures of relative phases, which show the phase in the range $-180 \le \Delta\varphi_{ab}(m_{K\pi\pi}, t') < 180°$, we chose in figure 7.1b the range $0 \le \Delta\varphi_{ab}(m_{K\pi\pi}, t') < 360°$ in order to better visualize the phase offset between the two 1^+ waves.

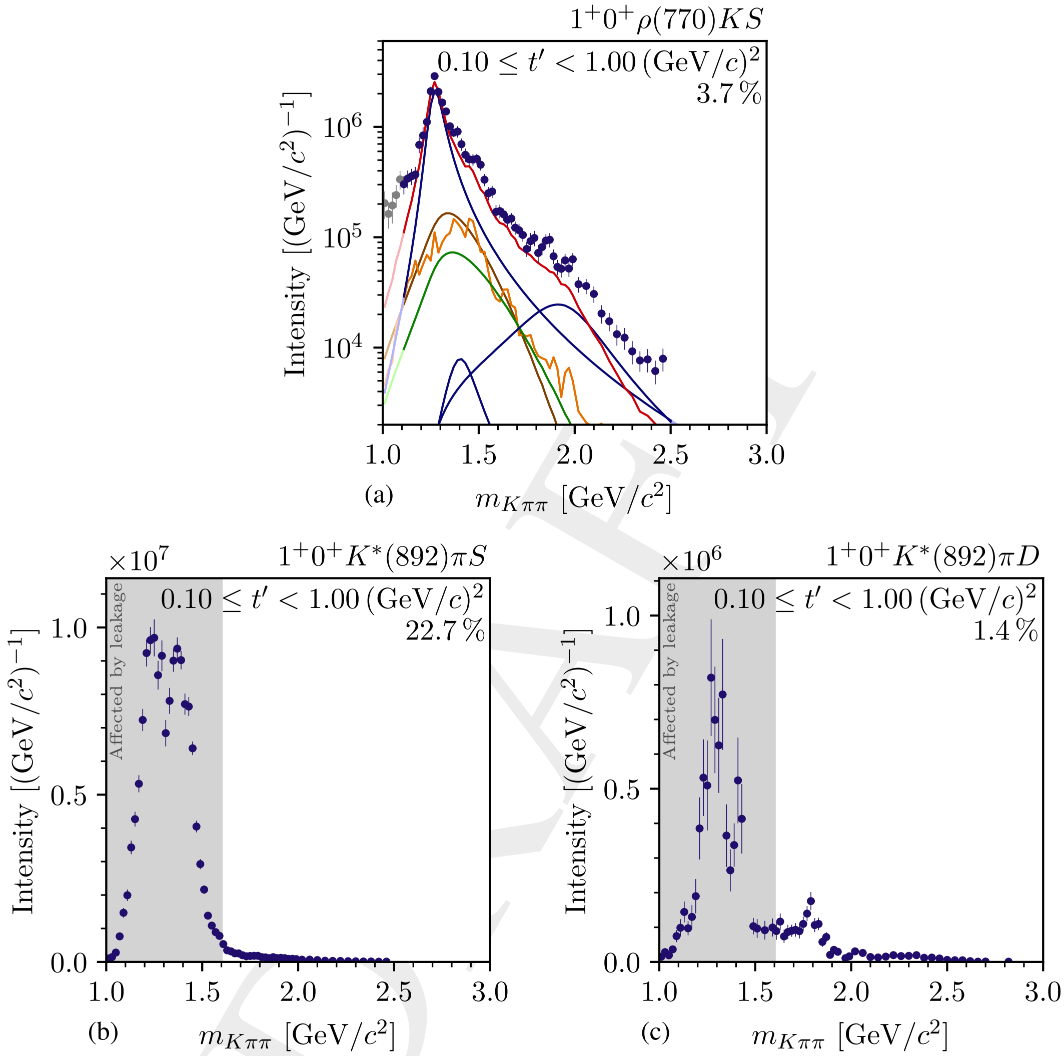

Figure 7.2: t'-summed intensity spectra of (a) the $1^+\,0^+\,\rho(770)\,K\,S$ wave in log-scale, (b) the $1^+\,0^+$ $K^*(892)\,\pi\,S$ wave, and (c) the $1^+\,0^+\,K^*(892)\,\pi\,D$ wave. The blue data points represent the measured intensities. The gray shaded area indicates the $m_{K\pi\pi}$ range affected by the leakage effect (see section 5.9). The percentages give the relative intensity as defined in equation (5.76). The curves in (a) represent the result of the 10-wave RMF. The red curve represents the total RMF model. The blue curves represent the individual resonance components, the green curve the non-resonant component, the orange curve the $\pi^-\pi^-\pi^+$ background component, and the brown curve the effective background component. The extrapolations beyond the $m_{K\pi\pi}$ fit ranges are shown in lighter colors. The corresponding data points are shown in gray.

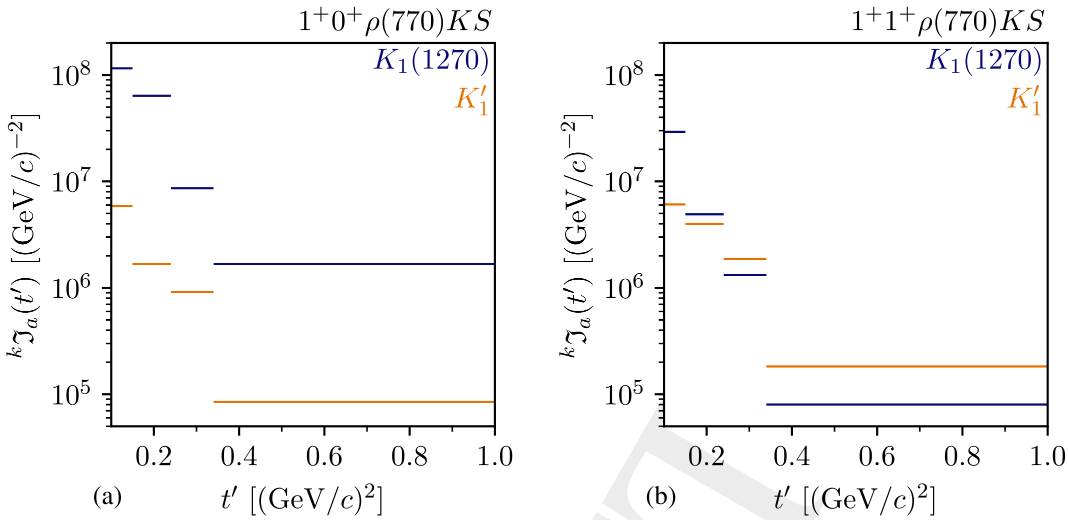

Figure 7.3: t' spectra of the $K_1(1270)$ (blue bars) and the K_1' (orange bars) components (a) in the $1^+\,0^+$ $\rho(770)\,K\,S$ wave and (b) in the $1^+\,1^+\,\rho(770)\,K\,S$ wave as obtained from the 10-wave RMF. The horizontal bars represent the intensity in each t' bin according to equation (6.28). The blue bars in (a) are the same as in figure 6.5.

The RMF yields a large effective background component (brown curve) for the $1^+\,1^+\,\rho(770)\,K\,S$ wave that peaks at a slightly higher mass than the $K_1(1270)$ component. In general, we do not expect such large and peaking background contributions. In a study, where we excluded such a peaking shape for the effective background component by using a more restrictive the parameter limit of the corresponding shape parameter yielded a parameter value at the more restrictive parameter limit. Hence, there is no fit solution without such a peaking effective background component. Furthermore, in this study the RMF was not able to describe the intensity spectrum of the $1^+\,1^+\,\rho(770)\,K\,S$ wave sufficiently well. We studied this peaking effective background component also using the 10-wave pseudodata that do not contain background contributions (see section 6.4).[d] Thus, the effective background component in RMFs to this pseudodata sample is expected to be small. Indeed, we find practically zero contribution from the effective background component to the $1^+\,1^+\,\rho(770)\,K\,S$ wave in all pseudodata studies. In particular, the RMFs did not yield any peaking effective background. Hence, we conclude that the peaking effective background component that we observe in the measured data is driven by the data and not by the construction of the RMF model. Therefore, it is needed in the RMF in order to describe the data. However, the fact that we need such unexpected component in order to describe the data points towards the limitations of the Breit-Wigner RMF model employed in our analysis.

Figure 7.3 shows the t' spectra as defined in equation (6.28) for the $K_1(1270)$ and K_1' components in the two 1^+ waves. In the $1^+\,0^+\,\rho(770)\,K\,S$ wave, both components show an approximately an exponential t' dependence, as expected. The t'-dependencies of the resonance components are independent in the $1^+\,0^+\,\rho(770)\,K\,S$ and $1^+\,1^+\,\rho(770)\,K\,S$ waves. The K_1' component in the

[d] In some studies, we admixed $\pi^-\pi^-\pi^+$ background events to the 10-wave pseudodata sample. However, these contributions should be accounted for by the $\pi^-\pi^-\pi^+$ background component in the RMF.

$1^+\,1^+\,\rho(770)\,K\,S$ wave (orange bars in figure 7.3b) shows an approximately exponential t' shape, which flattens towards $t' = 0.1\,(\mathrm{GeV}/c)^2$ as mainly seen in the lowest t' bin. This flattening is expected for an $M = 1$ wave due to the additional $(t')^{|M|}$ factor as given in equation (6.29). However, the $K_1(1270)$ component in the $M = 1$ wave exhibits no flattening for the approximately exponential t' shape. In particular, in the lowest t' bin, the intensity of the $K_1(1270)$ component is much larger than expected. A reason for this may be that the RMF cannot reliably assign intensity to the $K_1(1270)$ component due to its interplay with the peaking effective background component in this t' bin. In summary, our observation that the t' dependencies of the resonance components, except for the $K_1(1270)$ component in the lowest t' bin of the $M = 1$ wave, follow the expected shape is another indication for a reliable extraction of the $K_1(1270)$ and K_1' contribution to the data in the RMF.

We observe structures also in other waves with $J^P = 1^+$ that were not included in the 10-wave RMF, for example, in the $1^+\,0^+\,K^*(892)\,\pi\,S$ wave, which is the largest wave in our wave set.[e] Its intensity spectrum is shown in figure 7.2b. It exhibits a clear double-peak in the $m_{K\pi\pi}$ region of the $K_1(1270)$ and $K_1(1400)$ resonances, as expected. We observed this double peak already in the measured $m_{K\pi\pi}$ spectrum shown in figure 4.6a. However, the $1^+\,0^+\,K^*(892)\,\pi\,S$ wave is strongly affected by the leakage effect for $m_{K\pi\pi} \lesssim 1.6\,\mathrm{GeV}/c^2$. This prevents us from interpreting the observed structures on a quantitative level.

Figure 7.2c shows the intensity spectrum of the $1^+\,0^+\,K^*(892)\,\pi\,D$ wave. The low-$m_{K\pi\pi}$ region of also this wave is affected by the leakage effect. It exhibits a broad enhancement at about $1.3\,\mathrm{GeV}/c^2$ that is very jumpy and that is strongly biased by the leakage effect. Also, we observe a peak at about $1.8\,\mathrm{GeV}/c^2$ that may arise from the K_1' resonance. As this wave is also affected by the leakage effect, we did not include it in the RMF.

7.1.1 Discussion

The PDG [9] lists three strange mesons with 1^+ quantum numbers; i.e. the well-established $K_1(1270)$ and $K_1(1400)$,[f] and an excited $K_1(1650)$ that was just recently marked as an established state. The PDG averages for their masses and widths are shown by the blue, red, and green stars, respectively, in figure 7.4.

[e] As discussed in section 5.9.1, the intensities of leakage waves are overestimated by potentially more than a factor two due the leakage effect. Hence, the relative intensities of leakage waves cannot be directly compared to those of other waves, especially to those of non-leakage waves. However, the relative intensity of the $1^+\,0^+\,K^*(892)\,\pi\,S$ of about 22.7 % is significantly larger than the 10.7 % of the second-largest leakage wave, which is the $0^-\,0^+\,K^*(892)\,\pi\,P$ wave, and is much larger than the relative intensity of 3.7 % of the largest non-leakage wave, which is the $1^+\,0^+\,\rho(770)\,K\,S$ wave. Hence, we can reliably state that the $1^+\,0^+\,K^*(892)\,\pi\,S$ wave is the largest wave in our wave set.

[f] In the quark-model picture, there is a spin-triplet and a spin-singlet SU(3)-nonet for states with $J^P = 1^+$ and an orbital angular momentum of $L = 1$ in the $q\bar{q}'$ system. The $K_1(1270)$ and $K_1(1400)$ states are assumed to be mixtures of these two SU(3) eigenstates [144].

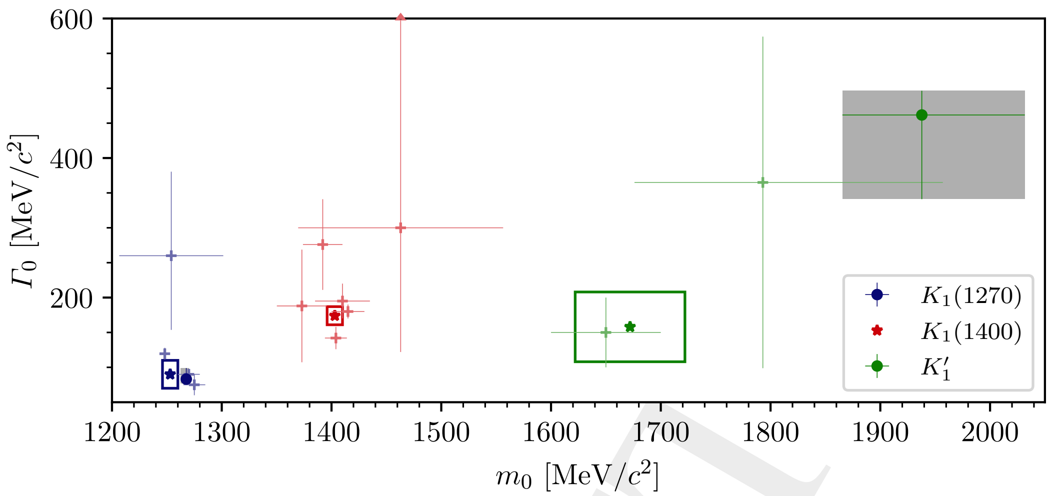

Figure 7.4: Masses m_0 and widths Γ_0 of K_1 resonances. The dots represent the parameter values as obtained from the 10-wave RMF and listed in table 6.2. The thin error bars and gray boxes around the dots indicate our estimates for the total uncertainties, which we calculated by quadratically adding the statistical uncertainties to the corresponding upper and lower systematic uncertainties. One should note that the systematic uncertainties given in this work are only a lower limit on the actual systematic uncertainties (see section 6.3). The stars and colored boxes represent the PDG average values and their uncertainties, respectively [9]. The pluses in lighter color represent the central values of all previous measurements that entered the PDG averages for m_0 and Γ_0. The error bars represent the corresponding total uncertainties calculated by quadratically adding the statistical uncertainties to the corresponding upper and lower systematic uncertainties, if given. Uncertainties that are larger than the shown m_0 and Γ_0 ranges are indicated by an arrowhead at the figure frame. In the 10-wave RMF we fixed the resonance parameters of the $K_1(1400)$ component to the corresponding PDG average values.

The $K_1(1270)$

Our estimate for the width of the $K_1(1270)$ agrees well with the PDG average value, while our estimate for its mass is slightly larger. However, also previous measurements of the $K_1(1270)$ (blue pluses in figure 7.4) cluster mainly around two values for its resonance parameters. There is a high-mass cluster of measurements of a mass above about 1270 MeV/c^2 [23, 26, 145, 146]. Many of these measurements also yielded a small width below 100 MeV/c^2.[g] There is also a low-mass cluster of measurements of a mass below about 1250 MeV/c^2 [27, 29, 147]. All of these measurements of a lower mass also yielded a large width above 100 MeV/c^2.

Among the four previous measurements that entered the PDG average for the $K_1(1270)$ resonance parameters, our estimates for the $K_1(1270)$ parameters agree well with those from ref. [145], who measured the $K_1(1270)$ resonance parameters from its decay to the $\rho(770)\,K$ final state only, as in this analysis, and with those from the ACCMOR analysis [23]. Compared to our

[g] There are several previous measurements that are excluded from the PDG average, which yielded a mass above 1270 MeV/c^2, but a width above 100 MeV/c^2.

analysis, ACCMOR formulated a more elaborate resonance model based on a K-matrix approach including two resonances and six decay channels, which they fitted simultaneously to the partial waves representing the $K^*(892)\,\pi\,S$, $\rho(770)\,K\,S$, $K_0^*\,\pi\,P$, $f_0\,K\,P$, and $K^*(892)\,\pi\,D$ decays.[h] The good agreement between the ACCMOR analysis and our results validates the application of our Breit-Wigner RMF model.

The measurement of the $K_1(1270)$ resonance parameters in the reaction $\tau^- \to K^-\pi^-\pi^+\nu_\tau$ by CLEOII in ref. [29] yielded the largest value of all previous measurements for the width of $\Gamma_0 = (260\,^{+90}_{-70}\,(\text{stat.}) \pm 80\,(\text{sys.}))\,\text{MeV}/c^2$. Even considering its large uncertainty this value is clearly larger than the PDG average and our estimate for the $K_1(1270)$ width. The CLEO value is the result of a limited[i] Dalitz-plot analysis with a series of assumptions. The authors did not allow for a relative phase offset between the different resonance components, i.e. their coupling amplitudes where fixed to be real, which may not be the case. For example, in the COMPASS $\pi^-\pi^-\pi^+$ analysis a phase offset of about 180° was found between many ground and excited states [41]. Furthermore, they fixed the branching fraction ration of $K_1(1270) \to K^*(892)\pi$ and $K_1(1270) \to \rho(770)K$ to the corresponding PDG average value. Finally, contributions from pseudoscalar resonances in the $K^-\pi^-\pi^+$ system were neglected, while the τ^- may also decay to excited pseudoscalar kaons that further decay to $K^-\pi^-\pi^+$ [81]. For example, the τ^- has a similar branching fraction to decay to the pseudo-scalar ground state, i.e. to $K^-\nu_\tau$, (6.96 ‰) and to $K^-\pi^-\pi^+\nu_\tau$ (3.45 ‰) [9]. All these potentially coarse assumptions may bias the resonance parameter estimates of ref. [29].

The Belle collaboration [27] performed a recent analysis of the decay $B^+ \to J/\psi K^+\pi^+\pi^-$, which allowed them to study the $K_1(1270)$ in the $\rho(770)\,K$ and $K^*(892)\,\pi$ decays. They obtained very precise and accurate resonance parameters of $m_0 = (1248.1 \pm 3.3\,(\text{stat.}) \pm 1.4\,(\text{sys.}))\,\text{MeV}/c^2$ and $\Gamma_0 = (119.5 \pm 5.2\,(\text{stat.}) \pm 6.7\,(\text{sys.}))\,\text{MeV}/c^2$. Their estimate for the mass is slightly smaller and their estimate for the width is slightly larger than the PDG average values and then our estimates. However, they fitted the resonance parameters of only the $K_1(1270)$. The resonance parameters of the other states included in the fit were fixed to the corresponding PDG averages, which for some have large uncertainties. Furthermore, they did not include an excited K_1' that may contribute to the 1^+ waves. All of these effects may bias their measurement for the $K_1(1270)$ parameters. However, they did not consider any of these effects when determining the systematic uncertainties. Hence, the uncertainties in ref. [27] may be underestimated. In our analysis, we considered more ground and excited states as in the Belle analysis. As discussed in section 6.3, we also give a first estimate of systematic uncertainties that may arise from excluding certain model components and from fixing resonance parameters to their PDG averages. Considering the good agreement of our measurement with the results from refs. [23, 145] and the caveats of the measurements in refs. [27, 29], the two clusters of measured values of the $K_1(1270)$ resonance parameters may be a pure measurement effect enhanced by underestimated uncertainties.

[h] ACCMOR used an S-wave $\pi\pi$ scattering amplitude to parameterize the f_0 isobar and a Breit-Wigner amplitude with $m_0 = 1250\,\text{MeV}/c^2$ and $\Gamma_0 = 600\,\text{MeV}/c^2$ to parameterize the K_0^* isobar. Both parameterizations approximate the corresponding physical amplitudes only roughly (see section 5.1.4).

[i] In ref. [29], only the $m_{K\pi\pi}$, the $m_{K^-\pi^+}$, and the $m_{\pi^-\pi^+}$ mass spectra were fitted. This was sufficient to determine the $K_1(12700)$ contribution as they assumed that the $K^-\pi^-\pi^+$ system consists only of axial-vector states.

The authors of ref. [144] suggested that the $K_1(1270)$ is not a single state, but arises from two states, i.e. from two poles of the scattering amplitude in the complex plane of the squared energy. From the data of the ACCMOR analysis [23], ref. [144] determines a lighter and broader state at $m_0 \approx 1200\,\mathrm{MeV}/c^2$ and $\Gamma_0 \approx 250\,\mathrm{MeV}/c^2$ that couples stronger to the $K^*(892)\,\pi$ decay; and a heavier and narrower state at $m_0 \approx 1280\,\mathrm{MeV}/c^2$ and $\Gamma_0 \approx 150\,\mathrm{MeV}/c^2$ that couples dominantly to the $\rho(770)\,K$ decay. As different production mechanisms, which may prefer different $K_1(1270)$ poles, were employed and different decay modes where studied in the various previous measurements, the two-pole model suggest in ref. [144] may explain the two clusters of previous measurements of the $K_1(1270)$ resonance parameters. Our estimates for the $K_1(1270)$ resonance parameters are determined from waves with $\rho(770)\,K$ decay mode only and agree with the cluster of heavier and narrow measurements. Hence, our data would fit into this two-pole scenario suggestion in ref. [144].

The $K_1(1400)$

The resonance parameters of the $K_1(1400)$ are determined rather well from previous experiments (red data points in figure 7.4). As for the $K_1(1270)$, the measurement of the $K_1(1400)$ width in the reaction $\tau^- \to K^-\pi^-\pi^+\nu_\tau$ by CLEOII [29] yielded the largest width of all previous measurements of $(300\,^{+370}_{-110}\,(\mathrm{stat.}) \pm 140\,(\mathrm{sys.}))\,\mathrm{MeV}/c^2$. This might indicate a systematic bias towards larger values for the widths in the analysis in ref. [29]. Still, their parameter estimates agree within the large uncertainties with the PDG average values.

In our analysis, the $K_1(1400)$ is only a small contribution in the two considered 1^+ waves. This is consistent with previous observations, e.g. the PDG lists a $\rho(770)\,K$ branching fraction of only $(3.0 \pm 3.0)\,\%$ [9]. In the main analysis, we fixed the resonance parameters of the $K_1(1400)$ to the corresponding PDG average values. In systematic study $\boldsymbol{C}$, we allowed the $K_1(1400)$ resonance parameters to float. Study $\boldsymbol{C}$ yielded a $K_1(1400)$ width of $178\,\mathrm{MeV}/c^2$, which is in good agreement with the PDG average value of $(174 \pm 13)\,\mathrm{MeV}/c^2$, and a $K_1(1400)$ mass of $1514\,\mathrm{MeV}/c^2$, which is about $100\,\mathrm{MeV}/c^2$ larger than the PDG average value of $(1403 \pm 7)\,\mathrm{MeV}/c^2$. The larger mass of may be driven by the high-mass shoulder at about $1.5\,\mathrm{GeV}/c^2$, which we observe on the 1^+ waves. Given the small size of the potential $K_1(1400)$ signal in the two considered 1^+ waves and the potentially large systematic uncertainties on the results of study $\boldsymbol{C}$, we conclude that the PDG average values used in the main analysis for the resonance parameters of the $K_1(1400)$ are consistent with our data. More detailed conclusions on the $K_1(1400)$ could only be drawn by studying the $1^+\,0^+\,K^*(892)\,\pi\,S$ wave, which exhibits a strong potential $K_1(1400)$ signal. Unfortunately, this is not possible with the COMPASS data as the $1^+\,0^+\,K^*(892)\,\pi\,S$ wave is affected by the leakage effect.

Excited K_1 States

The PDG lists a higher-lying K_1 state called $K_1(1650)$ with a mass of $(1672 \pm 50)\,\mathrm{MeV}/c^2$ and a width of $(158 \pm 50)\,\mathrm{MeV}/c^2$ [9]. It is much lighter and narrower than our parameter estimates for a potential excited K_1, which we called K_1'.

The $K_1(1650)$ has been studied in about 10 000 events of the reaction $K^+p \to \phi K^+ p$ at the CERN Omega spectrometer [24]. In their analysis, a model consisting of the sum of a Breit-Wigner amplitude and a non-resonant component was fitted to only the intensity spectrum of the 1^+ wave, which is shown in figure 7.5a.[j] This fit yielded a mass of $(1650 \pm 50)\,\mathrm{MeV}/c^2$ and a width of $(150 \pm 50)\,\mathrm{MeV}/c^2$. It is not clear whether their uncertainty estimates include systematic uncertainties. Given the size of their data sample and the fact that they fitted their model to only one intensity spectrum, a combined statistical and systematic uncertainty of only $\pm 50\,\mathrm{MeV}/c^2$ appears to be rather small, compared to the uncertainties in other [34] and in our analysis.

Ref. [34] presents a recent analysis of 4289 events of the decay $B^+ \to J/\psi\phi K^+$ by LHCb,[k] which allows them studying strange mesons in the ϕK subsystem. They performed a partial-wave analysis including resonances up to $J = 2$ in the ϕK subsystem. In contrast to, e.g., the CLEO analysis [29], the resonance parameters of all considered resonances were free in the fit. Two excited K_1 states, $K(1^+)$ and $K'(1^+)$, were included in the analysis in ref. [34]. Unfortunately, the reaction $B^+ \to J/\psi\phi K^+$ gives access to only a limited mass range of $1.5 \lesssim m_{\phi K} \lesssim 2.2\,\mathrm{GeV}/c^2$. Some strange mesons have nominal masses just outside this mass range, e.g. the $K_2^*(1430)$ or the $K_2(2250)$. The parameters of such strange mesons cannot be determined given the limited $m_{\phi K}$ range. Hence, such states were not included in the analysis in ref. [34]. However, their high- or low-mass tails still may contribute to the analyzed $m_{\phi K}$ range. Thus, omitting strange mesons with nominal masses just outside the accessible mass range may bias the estimates of ref. [34] for the resonance parameters of the included resonances. In ref. [34], these effects were taken into account in the systematic uncertainties. In our analysis, we can access the full $m_{K\pi\pi}$ range, which is one of the major advantages of using diffractive production to study strange mesons. Figure 7.5b shows the $m_{\phi K}$ spectrum (black points) together with the contributions from the two K_1 components. For the lighter state, LHCb measured a mass of $(1739 \pm 59\,(\mathrm{stat.})\,^{+153}_{-101}\,(\mathrm{sys.}))\,\mathrm{MeV}/c^2$ and a width of $(365 \pm 157\,(\mathrm{stat.})\,^{+138}_{-215}\,(\mathrm{sys.}))\,\mathrm{MeV}/c^2$. The PDG included this measurement in the average of the $K_1(1650)$ parameters. However, due to its large uncertainties, it has only a minor influence on the PDG average values. Hence, the PDG average values for the $K_1(1650)$ are mainly driven by the measurement from ref. [24]. For the heavier state, LHCb measured a mass of $(1968 \pm 65\,(\mathrm{stat.})\,^{70}_{-172}\,(\mathrm{sys.}))\,\mathrm{MeV}/c^2$ and a width of $(396 \pm 170\,(\mathrm{stat.})\,^{+174}_{-178}\,(\mathrm{sys.}))\,\mathrm{MeV}/c^2$. This heavier state contributes less strongly to the reaction $B^+ \to J/\psi\phi K^+$ and has a significance of only 1.9σ. Recently, LHCb published an updated analysis of the reaction $B^+ \to J/\psi\phi K^+$ based on a three times larger sample [149]. They obtained consistent parameters for both excited K_1 states. However, owing to the larger sample, they had to include resonances with nominal masses outside their accessible mass range, but where the tails of these states enter their accessible mass range, as discussed above.

[j] Figure 7.5a shows the total $J^P = 1^+$ intensity, i.e. summed over both helicity states of the ϕ decay.
[k] A more detailed discussion and technical aspects of the analysis in ref. [34] can be found in ref. [148].

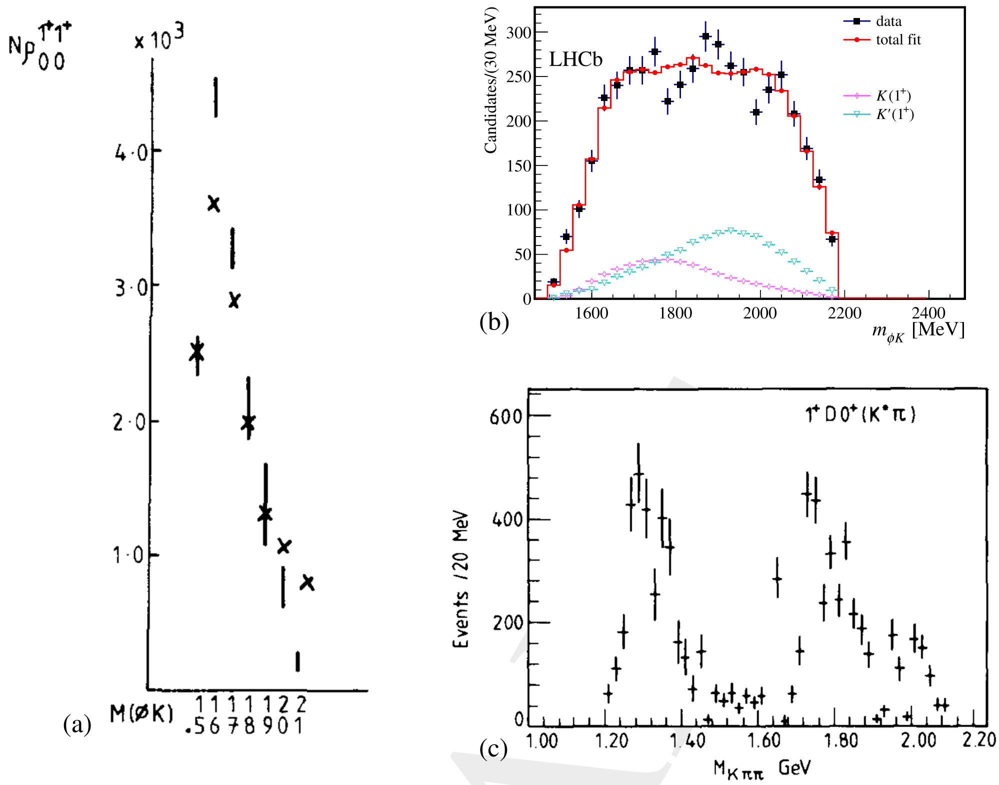

Figure 7.5: Previous studies of excited K_1 states. (a) shows the intensity of the 1^+ partial wave (vertical lines) measured in the reaction $K^+ p \to \phi K^+ p$ at the CERN Omega spectrometer [24]. The crosses represent the prediction of a model for the Deck process. (b) shows the invariant ϕK mass spectrum measured in the reaction $B^+ \to J/\psi \phi K^+$ at LHCb [34]. The black data points represent the measured distribution. The red data points represent the total partial-wave model. The differently colored data points represent the contribution from the two model components representing K_1 states. (c) shows the $1^+\, 0^+\, K^*(892)\, \pi\, D$ wave as obtained in the ACCMOR analysis [23].

Also, ACCMOR observed a potential signal with $J^P = 1^+$ at about $1800\,\text{MeV}/c^2$, e.g. in the $1^+\, 0^+\, K^*(892)\, \pi\, D$ wave shown in figure 7.5c. However, they did not perform an RMF of this signal and hence did not determine its resonance parameters.

Our parameter estimates for the K_1' component are consistent with both states considered by LHCb in ref. [34] and are closer to the central values of the higher-lying state. Our estimate for the K_1' mass is also consistent with the signal observed by ACCMOR in the $1^+\, 0^+\, K^*(892)\, \pi\, D$ wave. Furthermore, we observe a similar peak at about $1.8\,\text{GeV}/c^2$ in this wave (see figure 7.2c). In summary, except for the measurement by the CERN Omega spectrometer in ref. [24], all previous measurements and also our measurement have indications for one or two excited K_1 states with a mass of about $1800\,\text{MeV}/c^2$ or above. Only CERN Omega claims to have observed a much lighter state. As CERN Omega employed the same production mechanism as ACCMOR and as in our analysis, and as CERN Omega studied the same decay mode as the LHCb analysis, there is no clear reason why a different state may appear in the CERN Omega data. Given the limitations of the CERN Omega analysis, the excited $K_1(1650)$ as listed by the PDG may actually be a state at about 1800 MeV/c^2 or above, which would also be in agreement with the quark-model prediction from ref. [10] (see figure 1.1).

7.2 $J^P = 2^+$ Partial Waves

We included two waves with $J^P = 2^+$ quantum numbers in the 10-wave RMF. The intensity spectrum of the first wave, the $2^+\ 1^+\ K^*(892)\,\pi\,D$ wave, in the lowest t' bin is shown in figure 7.6a. It exhibits a clear peak at about 1.4 GeV/c^2. This peak is reproduced well by the RMF using, as expected, mainly the $K_2^*(1430)$ component with a mass of $(1430.1 \pm 1.5\,^{+1.3}_{-2.0})$ MeV/c^2 and a width of $(109 \pm 3\,^{+6}_{-2})$ MeV/c^2. We also find a small contribution of the effective background component in this wave.[I] The $2^+\ 1^+\ K^*(892)\,\pi\,D$ wave also exhibits enhanced low- and high-mass tails, which are not reproduced well by the RMF as they are presumably driven by model artifacts. Hence, we excluded these $m_{K\pi\pi}$ regions from the RMF. We do not find any other clear resonance signals, e.g. from excited K_2^* states, in the $2^+\ 1^+\ K^*(892)\,\pi\,D$ wave.

The second wave with $J^P = 2^+$ that we included in the 10-wave RMF is the $2^+\ 1^+\ \rho(770)\,K\,D$ wave. Its intensity spectrum in the lowest t' bin is shown in figure 7.6d. The relative intensity of the $2^+\ 1^+\ \rho(770)\,K\,D$ wave is about four times smaller than the one of the $2^+\ 1^+\ K^*(892)\,\pi\,D$ wave. Also the $2^+\ 1^+\ \rho(770)\,K\,D$ wave exhibits a clear peak at about 1.4 GeV/c^2, which is reproduced well by the RMF using, as expected, mainly the $K_2^*(1430)$ component. Compared to the $2^+\ 1^+\ K^*(892)\,\pi\,D$ wave, we find more pronounced enhanced low- and high-mass tails. For such a small wave, it is expected that artifacts are relatively large. As discussed in section 6.2.2, the $\pi^-\pi^-\pi^+$ background PWD predicts a large $\pi^-\pi^-\pi^+$ background in the $2^+\ 1^+\ \rho(770)\,K\,D$ wave. Given the consistent results we obtained from the systematic studies discussed in section 6.3 and especially from the pseudodata studies with and without admixed $\pi^-\pi^-\pi^+$ background discussed in section 6.4, we conclude that we can reliably model the $\pi^-\pi^-\pi^+$ background, and that it does not significantly bias our estimates for the resonance parameters. We do not find any other clear resonance signals, e.g. from excited K_2^* states, in the $2^+\ 1^+\ \rho(770)\,K\,D$ wave.

Figure 7.6b shows the relative phase between the $2^+\ 1^+\ K^*(892)\,\pi\,D$ and the $2^+\ 1^+\ \rho(770)\,K\,D$ waves. As expected, it is almost constant, because both waves are dominated by the same $K_2^*(1430)$ resonance. We find a phase offset of about 0° between the two 2^+ waves, as typically observed for the same resonance in two partial waves. The remaining shallow phase motion observed in figure 7.6b may be caused by the different background contributions in both waves.

Figure 7.6c shows the phase of the $2^+\ 1^+\ K^*(892)\,\pi\,D$ wave relative to the $1^+\ 0^+\ \rho(770)\,K\,S$ wave in the lowest t' bin. It exhibits a similar behaviour as in the second highest t' bin shown in

[I] In the $2^+\ 1^+\ K^*(892)\,\pi\,D$ wave in figure 7.6a, the total model intensity (red curve) is similar to only the $K_2^*(1430)$ component (blue curve), while there is also a non-negligible contribution from the effective background component (brown curve) in this wave. In fact, the $K_2^*(1430)$ component and the non-resonant component (too small to be visible in figure 7.6a) interfere destructively in the peak region, such that the intensity $\hat{\rho}_{aa}^{K\pi\pi}(m_{K\pi\pi}, t')$ of only the $K^-\pi^-\pi^+$ part of the RMF model is smaller than the intensity of the total model.

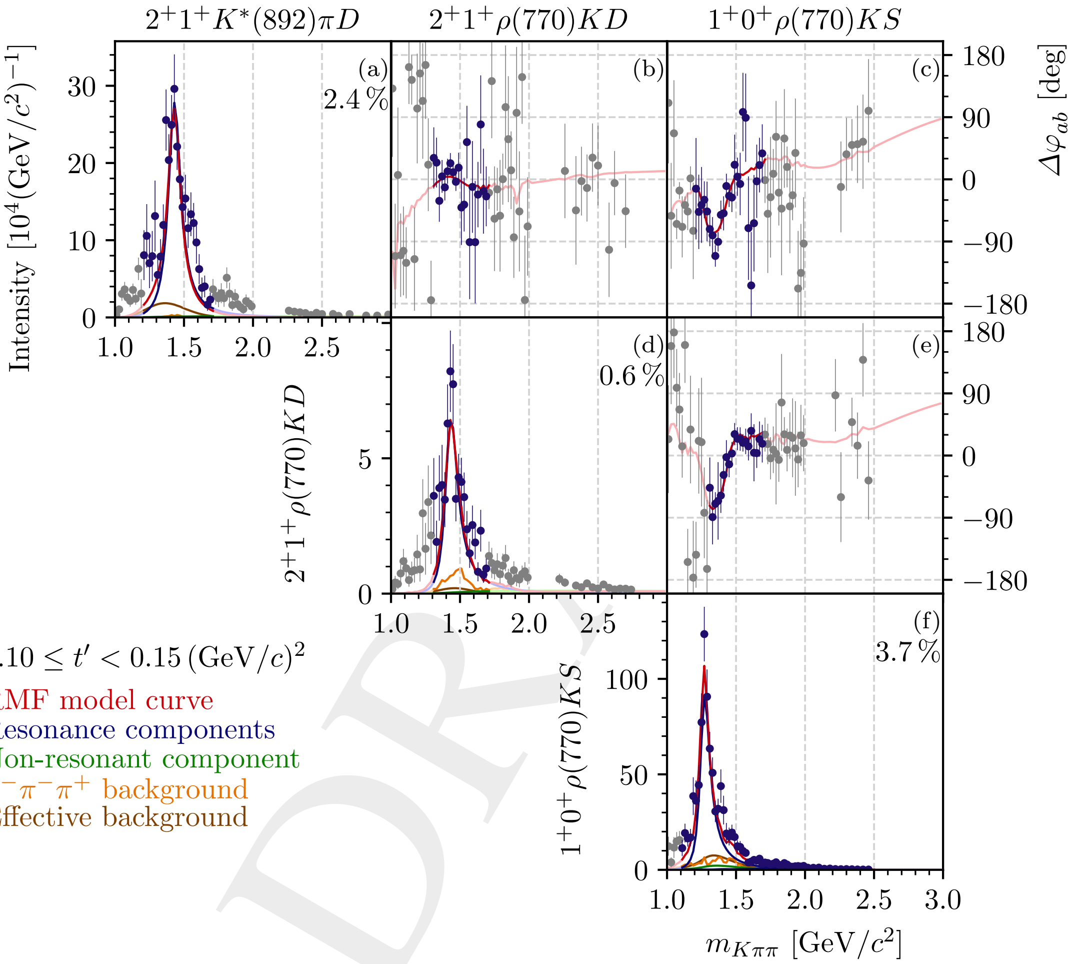

Figure 7.6: Same as figure 7.1, but for the two waves with $J^P = 2^+$ that were included in the 10-wave RMF and the $1^+\,0^+\,\rho(770)\,K\,S$ wave serving as phase reference. The lowest t' bin is shown.

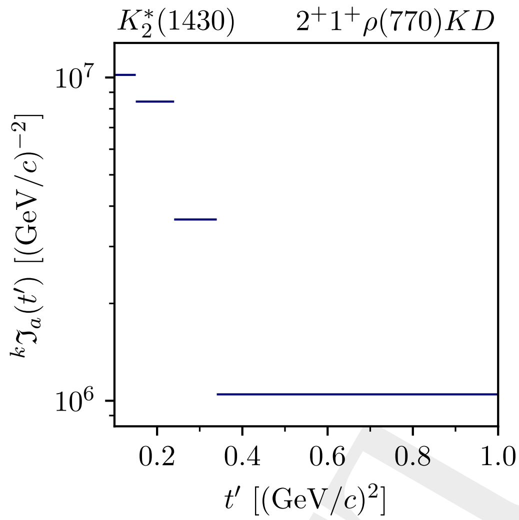

Figure 7.7: Same as figure 7.3, but for the $K_2^*(1430)$ component in the $2^+\,1^+\,\rho(770)\,K\,D$ wave.

figure 5.19: it first drops by about 90° around $1.2\,\mathrm{GeV}/c^2$ and then rises again by about 90° around $1.4\,\mathrm{GeV}/c^2$. Above about $1.5\,\mathrm{GeV}/c^2$ the relative phase is approximately constant. This phase motion is reproduced well by the RMF. The sharp drop of the phase is caused by the $K_1(1270)$ resonance in the $1^+\,0^+\,\rho(770)\,K\,S$ wave, which enters with a minus sign in the relative phase [see equation (5.74)]. The following rise of the phase is caused by the $K_2^*(1430)$ resonance in the $2^+\,1^+\,K^*(892)\,\pi\,D$ wave. This rise is less sharp than the drop caused by the $K_1(1270)$, which reflects the larger width of the $K_2^*(1430)$ compared to the $K_1(1270)$. The phase of the $2^+\,1^+\,\rho(770)\,K\,D$ wave relative to the $1^+\,0^+\,\rho(770)\,K\,S$ waves exhibits similar features as shown in figure 7.6e. In summary, we observe clear signals from the $K_2^*(1430)$ and $K_1(1270)$ not only in the intensity spectra, but also in the interferences terms represented by the relative phases.

Figure 7.7 shows the t' spectrum of the $K_2^*(1430)$ component. By construction, it is the same in both 2^+ waves up to a global factor [see equation (6.14)]. The t' spectrum of the $K_2^*(1430)$ exhibits an approximately exponential shape, which flattens towards $t' = 0.1\,(\mathrm{GeV}/c)^2$. As both 2^+ waves have a spin-projection of $M = 1$, the shape of the t' spectrum qualitatively matches the expected shape for a resonance component as defined in equation (6.29). This is another indication for the reliable extraction of the $K_2^*(1430)$ resonance by the RMF.

Except for the $2^+\,1^+\,K^*(892)\,\pi\,D$ wave and the $2^+\,1^+\,K^*(892)\,\pi\,D$ wave, none of the five other waves with $J^P = 2^+$ exhibit significant structures. They were included into the PWD model by the wave-set selection only in a few scattered $(m_{K\pi\pi}, t')$ cells.

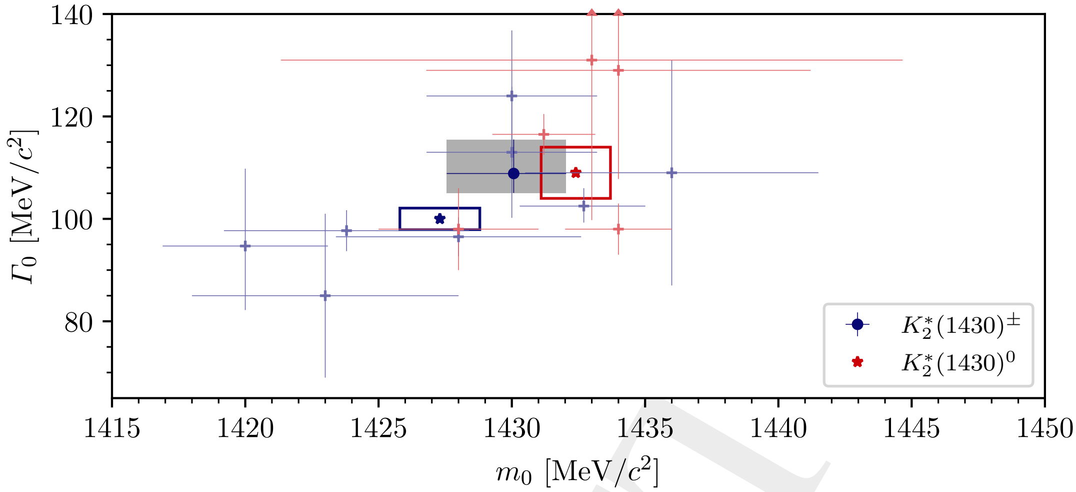

Figure 7.8: Same as figure 7.4, but showing in blue the resonance parameters of the charged $K_2^*(1430)$ and in red the resonance parameters of the neutral $K_2^*(1430)$.[n]

7.2.1 Discussion

The PDG lists the measurements of the charged and of the neutral $K_2^*(1430)$ separately. The blue and red stares with uncertainty boxes in figure 7.8 represent the PDG average values of the resonance parameters of the charged and neutral $K_2^*(1430)$, respectively. The mass and width values of the neutral $K_2^*(1430)$ are slightly larger than those of the charged $K_2^*(1430)$. Our estimate for the mass of the charged $K_2^*(1430)$ agrees with the PDG average value within uncertainties. However, our estimate for the width of the charged $K_2^*(1430)$ is 9 MeV/c^2 larger than the PDG average value, such that the corresponding uncertainty intervals to no overlap.[m] Interestingly, our estimate for the width of the charged $K_2^*(1430)$ is in good agreement with the PDG average width value for the neutral $K_2^*(1430)$. Also, our mass estimate is in good agreement with the PDG average mass value for the neutral $K_2^*(1430)$.

The individual measurements of the $K_2^*(1430)$ parameters that entered the PDG averaging do not clearly group into two clusters of mass and width values, i.e. one for the charged and one for the neutral $K_2^*(1430)$.[n] Not only our measurement, but also other measurements of the charged $K_2^*(1430)$ parameters (blue pluses in figure 7.8) yielded mass and width values that are in good agreement with the PDG average values for the neutral $K_2^*(1430)$. At the same time, the measurement of the neutral $K_2^*(1430)$ in ref. [151] yielded mass and width values that are

[m] Here, we quadratically added our estimated for the statistical uncertainty to the lower systematic uncertainty.

[n] The measurement in ref. [150], which was included in the PDG average values for the neutral $K_2^*(1430)$, is not shown in figure 7.8 as it lies outside of the shown m_0 region. It yielded a mass of (1471 ± 12) MeV/c^2 that is much larger than the mass from any other measurement and a width of (143 ± 34) MeV/c^2 that is among the largest values for the width from all previous measurements. The different values obtained in ref. [150] may be explained by the fact that they fitted their resonance model to only the intensity spectrum of only the $2^+ 1^+ K^*(892) \pi D$ wave.

in good agreement with the PDG average values for the charged $K_2^*(1430)$. However, a later measurement [97] of the same reaction performed by the same experiment as in ref. [151] yielded mass and width values that are in good agreement with the PDG average value for the neutral $K_2^*(1430)$.

Furthermore, the PDG considered for the averaging of the resonance parameters of the charged $K_2^*(1430)$ only measurements of its decay to the $K\pi$ final state. For example, they did not consider the ACCMOR analysis [23], that measured the resonance parameters of the charged $K_2^*(1430)$ in the $K^-\pi^-\pi^+$ final state. Figures 7.9a and 7.9b show the intensity spectra of the $2^+\,1^+\,K^*(892)\,\pi\,D$ and $2^+\,1^+\,\rho(770)\,K\,D$ waves, respectively, as obtained in the ACCMOR analysis in a t' range that is similar to our analyzed t' range. The intensity spectra exhibit the same peak at about $1.4\,\text{GeV}/c^2$ as in our analysis (see figures 7.9c and 7.9d). ACCMOR observed instabilities in the $2^+\,1^+\,K^*(892)\,\pi\,D$ wave for $m_{K\pi\pi} \lesssim 1.3\,\text{GeV}/c^2$ [23], which are not present in our analysis. However, we observe an enhanced low-mass tail in the $2^+\,1^+\,\rho(770)\,K\,D$ wave below about $1.3\,\text{GeV}/c^2$, which is not present in the ACCMOR analysis. Fitting a resonance model to the intensity spectra of both 2^+ waves and to their relative phases, ACCMOR obtained a mass of $1430\,\text{MeV}/c^2$ and a width of $110\,\text{MeV}/c^2$ for the $K_2^*(1430)$. These values are nearly identical to those found by our analysis.

In summary, the resonance parameters of the $K_2^*(1430)$ as obtained in our analysis agree with many previous measurements. The PDG grouping of the measurements by the charge state of the $K_2^*(1430)$ does not necessarily follow the clustering of the measured resonance parameters. The difference between the PDG average values of the resonance parameters of the charged and neutral $K_2^*(1430)$ might have other reasons. A reason may be that for the averaging of the charged $K_2^*(1430)$ only measurements of the $K\pi$ final state were considered, which may introduce a bias as Breit-Wigner parameters are not independent of the reaction.

7.3 $J^P = 4^+$ Partial Waves

Figures 7.10a and d show for the lowest t' bin the intensity spectra of the $4^+\,1^+\,K^*(892)\,\pi\,G$ and $4^+\,1^+\,\rho(770)\,K\,G$ waves, respectively, which were included in the 10-wave RMF. Apart from these two waves, no other 4^+ waves exhibit clear resonance-like signals. The $4^+\,1^+\,K^*(892)\,\pi\,G$ wave exhibits a peak at about $2\,\text{GeV}/c^2$. As discussed in section 6.2.2, the RMF model overall underestimates the intensity of the $4^+\,1^+\,K^*(892)\,\pi\,G$ wave, while the off-diagonal spin-density matrix elements for this wave are reproduced well by the RMF. The $2\,\text{GeV}/c^2$ peak is mainly described by the $K_4^*(2045)$ component with a mass of $(2059 \pm 6\,^{+9}_{-1})\,\text{MeV}/c^2$ and a width of $(188 \pm 11\,^{+27}_{-18})\,\text{MeV}/c^2$. The $K_4^*(2045)$ component sits on top of a broad bump from the effective background component. The non-resonant component is mainly used by the RMF to try to describe the enhanced intensity in the low-mass tail of the $K_4^*(2045)$. The non-resonant component contributes only little to the $K_4^*(2045)$ mass region. The $\pi^-\pi^-\pi^+$ background component does practically not contribute to the $4^+\,1^+\,K^*(892)\,\pi\,G$ wave.

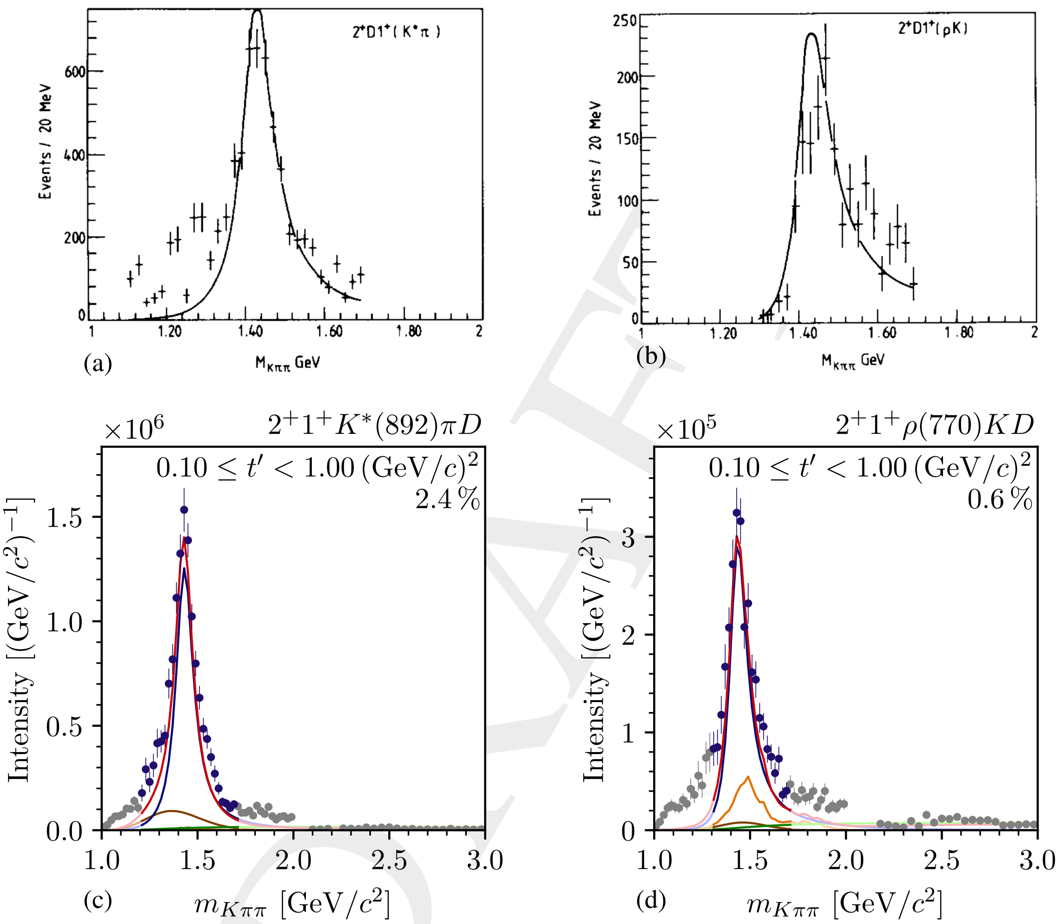

Figure 7.9: Intensity spectra of (left column) the $2^+\ 1^+\ K^*(892)\,\pi\, D$ wave, and (right column) the $2^+\ 1^+$ $\rho(770)\,K\,D$ wave. The top row shows the results as obtained in the ACCMOR analysis in the range $0.05 \le t' \le 0.7\,(\mathrm{GeV}/c)^2$ [23]. The data points represent the results of the PWD. The curves represent the total resonance model from the ACCMOR analysis. The bottom row shows the results obtained in our analysis in the range $0.1 \le t' < 1.0\,(\mathrm{GeV}/c)^2$. Note the different mass scales of the plots. Same color code as in figure 7.2.

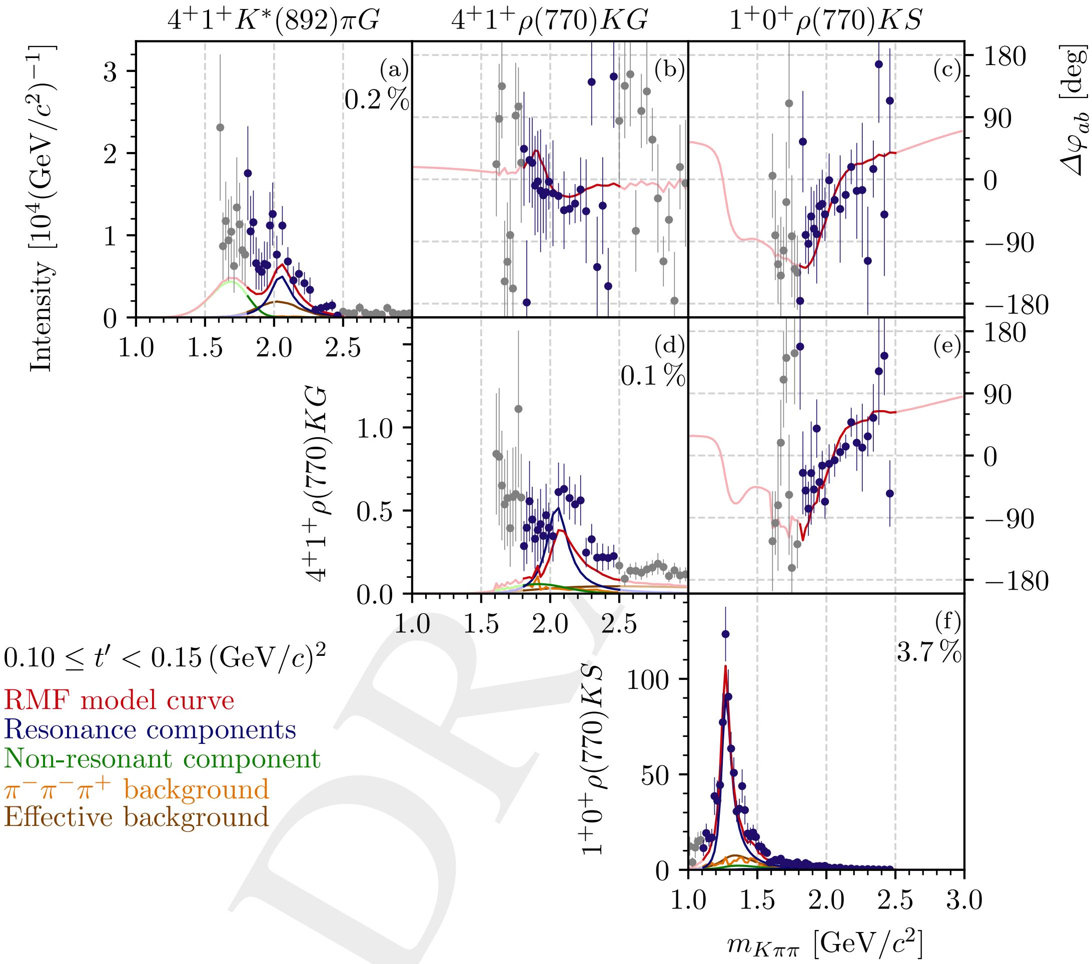

Figure 7.10: Same as figure 7.1, but for the two waves with $J^P = 4^+$ that were included in the 10-wave RMF and the $1^+\,0^+\,\rho(770)\,K\,S$ wave serving as phase reference. The lowest t' bin is shown.

The $4^+\,1^+\,\rho(770)\,K\,G$ wave has about half the relative intensity of the $4^+\,1^+\,K^*(892)\,\pi\,G$ wave. Its intensity spectrum exhibits a peak-like structure in the $K_4^*(2045)$ mass region as shown in figure 7.10d. As for the $4^+\,1^+\,K^*(892)\,\pi\,G$ wave, the RMF overall underestimates intensity of the $4^+\,1^+\,\rho(770)\,K\,G$ wave, while the off-diagonal spin-density matrix elements of this wave are reproduced well by the RMF. The peak is mainly described by the $K_4^*(2045)$ component, which destructively interferes with the small non-resonant component such that the intensity of the total RMF model is actually smaller than the intensity of the $K_4^*(2045)$ component in the peak region. The $\pi^-\pi^-\pi^+$ background component contributes only little to this wave. The effective background component is mainly used by the RMF to account for the enhanced high-mass tail above about $2.2\,\text{GeV}/c^2$.

The relative phase between the $4^+\,1^+\,K^*(892)\,\pi\,G$ and $4^+\,1^+\,\rho(770)\,K\,G$ waves in the lowest t' bin is shown in figure 7.10b. It is centered approximately around zero with a shallow drop of about $50°$ around $1.9\,\text{GeV}/c^2$, which presumably is caused by the different non-resonant and background contributions to these waves. Figure 7.10c shows the phase of the $4^+\,1^+\,K^*(892)\,\pi\,G$ wave relative to the $1^+\,0^+\,\rho(770)\,K\,S$ wave, which rises by about $120°$ in the region around $2\,\text{GeV}/c^2$. We observe a similar rise in the relative phase of the $4^+\,1^+\,\rho(770)\,K\,G$ wave with respect to the $1^+\,0^+\,\rho(770)\,K\,S$ wave as shown in figure 7.10e. All three relative phases are reproduced well by the RMF and are hence consistent with a dominant contribution of the $K_4^*(2045)$ to both 4^+ waves.

Figure 7.11 shows the t' spectrum of the $K_4^*(2045)$ component in the $4^+\,1^+\,\rho(770)\,K\,G$ wave.[o] Except for the lowest t' bin, the spectrum approximately has the expected shape according to equation (6.29). In the lowest t' bin, the expected suppression due to the $(t')^{|M|}$ factor is not observed. This suggests that the intensity of the $K_4^*(2045)$ component is not reliably estimated in the lowest t' bin.

7.3.1 Discussion

Figure 7.12 compares our estimates for the mass and width of the $K_4^*(2045)$ (circle) to the PDG average values (star) and to the previous measurements that entered the PDG averaging (pluses). Our estimate for the width of the $K_4^*(2045)$, which is the so-far most precise measurement of this parameter, agrees well with the PDG average value and accordingly with the values from previous measurements. Our estimate for the mass of the $K_4^*(2045)$ is slightly larger than the corresponding PDG average value. Still, both agree within their uncertainties. Our estimate for the mass agrees particularly well with the measurements in refs. [28, 122]. The PDG average value for the mass is driven by mainly the measurement in ref. [121], which yielded a low mass with small uncertainties of $(2039 \pm 10)\,\text{MeV}/c^2$. However, it is not clear whether their uncertainties include systematic uncertainties.[p] Hence, the uncertainty quoted in ref. [121]

[o] By construction, the t' spectrum of the $K_4^*(2045)$ component is the same in both 4^+ waves up to a global factor [see equation (6.14)].

[p] For example, ref. [122], where a similar reaction was under study as in ref. [121], estimated a statistical uncertainty for the $K_4^*(2045)$ mass of $\pm 14\,\text{MeV}/c^2$ based on a data sample of about 151 000 events; similar to the total

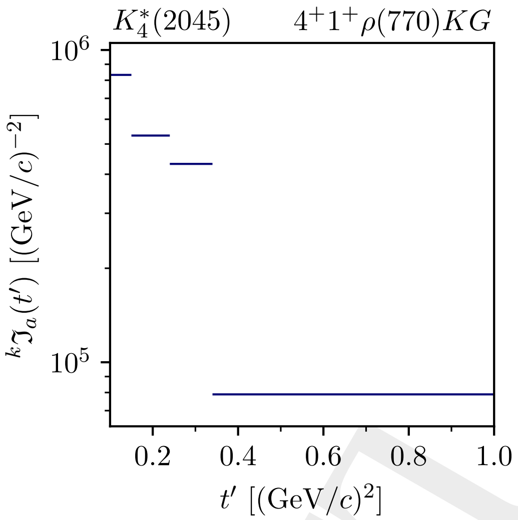

Figure 7.11: Same as figure 7.3, but for the $K_4^*(2045)$ component in the $4^+\,1^+\,\rho(770)\,K\,G$ wave.

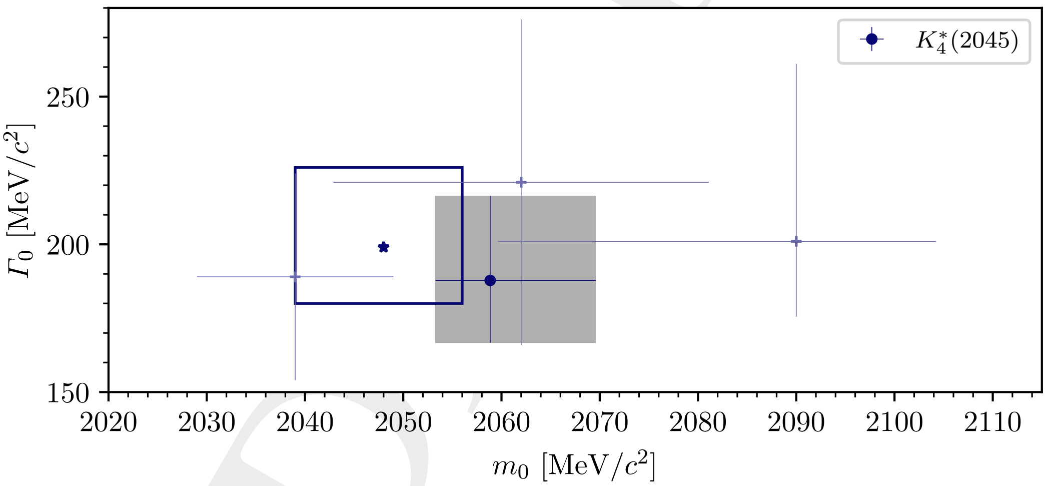

Figure 7.12: Same as figure 7.4, but for the resonance parameters of the $K_4^*(2045)$.

might be underestimated, which would bias the PDG average value towards a smaller $K_4^*(2045)$ mass, i.e. away from our estimate.

Despite the small intensity of the $K_4^*(2045)$ signal at the per-mill level in our data, we were able to reliably extract the $K_4^*(2045)$ component in the 10-wave RMF. This was verified in all

uncertainty given in ref. [121] based on a data sample of only about 35 000 events. Hence, the total uncertainty given in ref. [121] might be purely statistical. Ref. [122] quotes a systematic uncertainty of a similar order of magnitude as their statistical uncertainty.

performed systematic and pseudodata studies, and this is also reflected in the comparably small uncertainties of our estimates for the resonance-parameter of the $K_4^*(2045)$, which are in good agreement with previous measurements. Also, the overall good agreement of the shape of the t' spectrum of the $K_4^*(2045)$ component with the expectation indicates a reliable extraction of the $K_4^*(2045)$. This supports our statement in section 6.2.2, that the imperfections in the description of the intensity spectra of the 4^+ waves by the RMF do not strongly bias the determination of the $K_4^*(2045)$, because the RMF is driven mainly by the off-diagonal spin-density matrix elements. Hence, we are not only able to accurately measure the mass and width of the $K_4^*(2045)$, but the good agreement of our estimates for the parameters of the well-known $K_4^*(2045)$ with previous measurements demonstrates that we are able to determine even signals at the per-mill level and with significant artifacts, e.g. in the corresponding intensity spectra.

7.4 $J^P = 2^-$ Partial Waves

We selected four waves with $J^P = 2^-$ for the 10-wave RMF, which are shown in figures 7.13 and 7.15 in the second-lowest t' bin, where the interesting features are seen clearly. The largest of these four waves is the $2^- 0^+ K_2^*(1430)\,\pi\,S$ wave. Its intensity spectrum is shown in figure 7.13a and exhibits a broad peak at about $1.8\,\mathrm{GeV}/c^2$, with a peak-like high-mass shoulder at about $2.2\,\mathrm{GeV}/c^2$. The peak position moves with t' from about $1.74\,\mathrm{GeV}/c^2$ in the lowest t' bin to about $1.87\,\mathrm{GeV}/c^2$ in the highest t' bin (cf. figures 7.14a and 7.14b). Overall, the RMF reproduces well the intensity spectra of the $2^- 0^+ K_2^*(1430)\,\pi\,S$ wave in all four t' bins. The shift of the position of the $1.8\,\mathrm{GeV}/c^2$ peak with t' is reproduced by the RMF as a complex interplay of the various components, which changes with t'. Overall, the RMF describes the peak by an interference of the $K_2(1770)$ component with a mass of $(1715 \pm 4\,^{+1}_{-6})\,\mathrm{MeV}/c^2$ and a width of $(139 \pm 7\,^{+14}_{-\ 7})\,\mathrm{MeV}/c^2$, the $K_2(1820)$ component with a mass of $(1848 \pm 5\,^{+\ 6}_{-20})\,\mathrm{MeV}/c^2$ and a width of $(250 \pm 10\,^{+17}_{-23})\,\mathrm{MeV}/c^2$, and the non-resonant component. The $K_2(1820)$ component dominates the total intensity of the RMF model. In addition, in the two lowest t' bins shown in figures 7.13a and 7.14a, the low-mass tail of the $1.8\,\mathrm{GeV}/c^2$ peak is mainly described by an unexpectedly strongly peaking effective background component, similar to the one observed in the $1^+ 1^+ \rho(770)\,K\,S$ wave (see figure 7.1c). In the highest t' bin, the effective background component vanishes and the peak is mainly described by the $K_2(1820)$ component (see figure 7.14b). The high-mass shoulder of the $2^- 0^+ K_2^*(1430)\,\pi\,S$ wave is described well by the RMF using the $K_2(2250)$ component with a mass of $(2230 \pm 11\,^{+\ 7}_{-61})\,\mathrm{MeV}/c^2$ and a width of $(266 \pm 29\,^{+225}_{-\ 16})\,\mathrm{MeV}/c^2$. Overall, there is only a small contribution of the $\pi^-\pi^-\pi^+$ background component to the $2^- 0^+ K_2^*(1430)\,\pi\,S$ wave.

The $2^- 0^+ f_2(1270)\,K\,S$ wave has a relative intensity of about 1.1 %, which is similar to the one of the $2^- 0^+ K_2^*(1430)\,\pi\,S$ wave. The intensity spectrum of the $2^- 0^+ f_2(1270)\,K\,S$ wave in the second-lowest t' bin is shown in figure 7.13d and exhibits a clear peak at about $1.7\,\mathrm{GeV}/c^2$, i.e. at slightly lower mass than the peak in the $2^- 0^+ K_2^*(1430)\,\pi\,S$ wave. The peak is reproduced well by the RMF with a dominant contribution of the $K_2(1770)$ component. Also, the $2^- 0^+$ $f_2(1270)\,K\,S$ wave exhibits a high-mass shoulder at about $2.2\,\mathrm{GeV}/c^2$. The RMF is able to

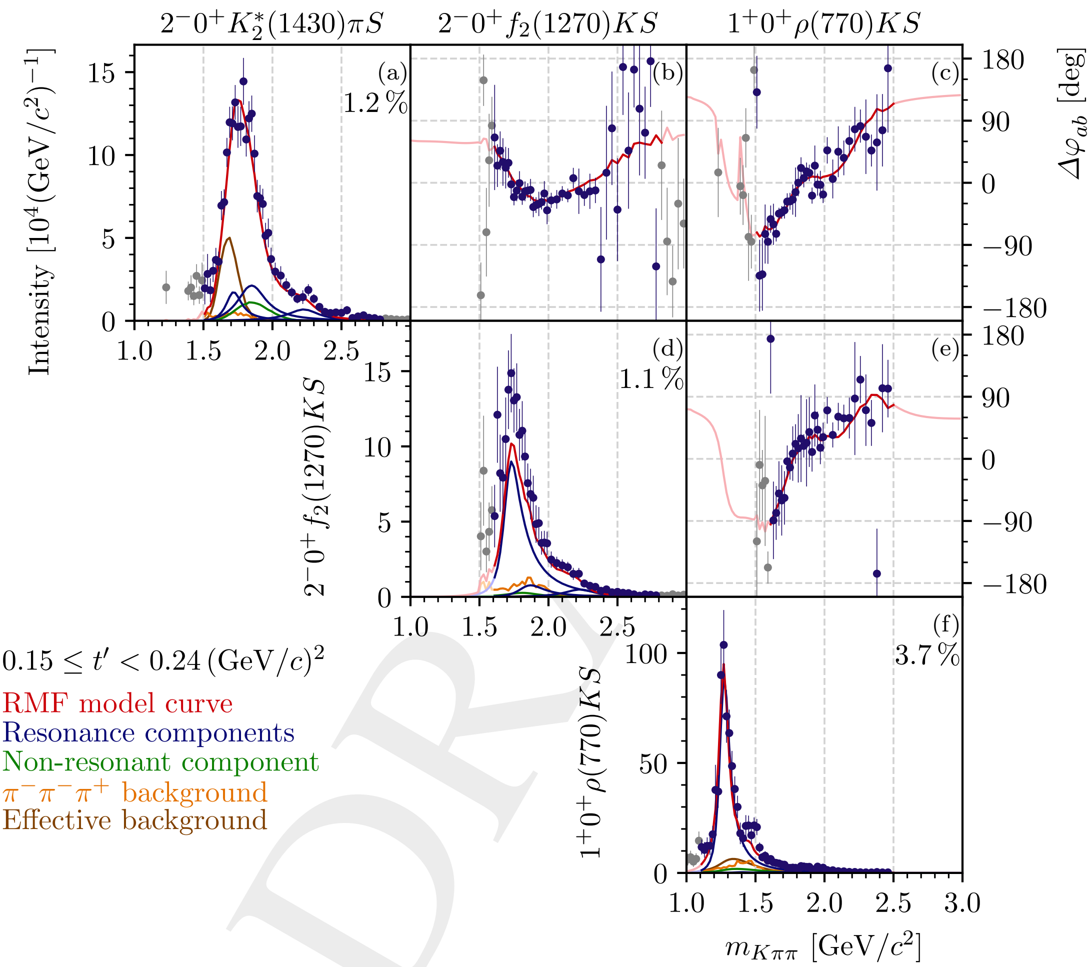

Figure 7.13: Same as figure 7.1, but for the $J^P = 2^-$ waves with $K_2^*(1430)$ or $f_2(1270)$ isobars that were included in the 10-wave RMF and the $1^+\,0^+\,\rho(770)\,K\,S$ wave serving as phase reference. The second-lowest t' bin is shown.

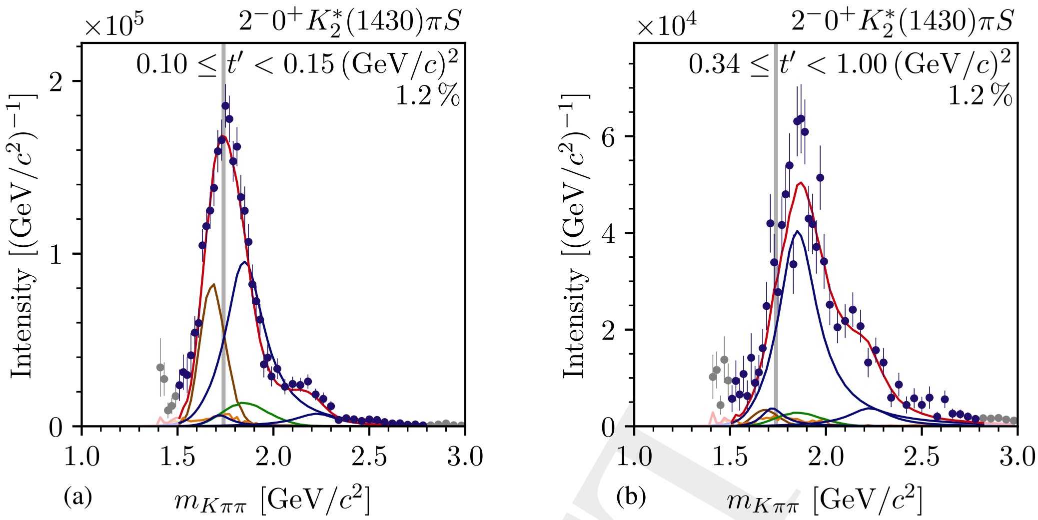

Figure 7.14: Same as figure 7.2, but for the intensity spectra of the $2^-\,0^+\,K_2^*(1430)\,\pi\,S$ wave (a) in the lowest t' bin and (b) in the highest t' bin. The gray vertical lines at $m_{K\pi\pi} = 1.74\,\mathrm{GeV}/c^2$ indicate for comparison the peak position in the lowest t' bin.

reproduce this shoulder using the $K_2(2250)$ component. The non-resonant, $\pi^-\pi^-\pi^+$ background, and effective background components contribute only little to the $2^-\,0^+\,f_2(1270)\,K\,S$ wave.

The phase of the $2^-\,0^+\,K_2^*(1430)\,\pi\,S$ wave relative to the $1^+\,0^+\,\rho(770)\,K\,S$ wave in the second-lowest t' bin is shown in figure 7.13c. It rises by about 90° in the mass region of the $1.8\,\mathrm{GeV}/c^2$ peak. After a short plateau, it rises again in the mass region of the high-mass shoulder. The relative phases of the $2^-\,0^+\,K_2^*(1430)\,\pi\,S$ wave are reproduced well by the RMF, which supports the resonance interpretation of the $1.8\,\mathrm{GeV}/c^2$ peak and the high-mass shoulder. The relative phase of the $2^-\,0^+\,f_2(1270)\,K\,S$ wave with respect to the $1^+\,0^+\,\rho(770)\,K\,S$ wave shows similar features (see figure 7.13e), and is also reproduced well by the RMF. Figure 7.13b shows the relative phase between the $2^-\,0^+\,K_2^*(1430)\,\pi\,S$ wave and the $2^-\,0^+\,f_2(1270)\,K\,S$ wave in the second-lowest t' bin. It drops by about 90° around $1.7\,\mathrm{GeV}/c^2$ and slowly rises again by about 30 °aboveabout1.9 GeV/c^2. The drop of the relative phase can be explained by the $K_2(1770)$ resonance contributing more dominantly to the $2^-\,0^+\,f_2(1270)\,K\,S$ wave, while the following slow rise of the relative phase hints towards more dominant contributions of the $K_2(1820)$ and the $K_2(2250)$ to the $2^-\,0^+\,K_2^*(1430)\,\pi\,S$ wave. Both phase motions are reproduced well by the RMF and are hence consistent with the resonance interpretation of the signals in the $2^-\,0^+\,K_2^*(1430)\,\pi\,S$ and $2^-\,0^+\,f_2(1270)\,K\,S$ waves by the RMF.

The $2^-\,0^+\,K^*(892)\,\pi\,F$ wave has about half the relative intensity of the $2^-\,0^+\,K_2^*(1430)\,\pi\,S$ wave. Its intensity spectrum exhibits a peak at about $1.75\,\mathrm{GeV}/c^2$ as exemplarily shown in figure 7.15a for the second-lowest t' bin. This peak is reproduced by the RMF by an interference between the $K_2(1770)$ and $K_2(1820)$ components and a broad non-resonant component. Here; in contrast to the $K_2^*(1430)$ and $f_2(1270)$ waves, which are dominated either by the $K_2(1820)$ component or by the $K_2(1770)$ component; the t'-summed intensities of both resonance components are of

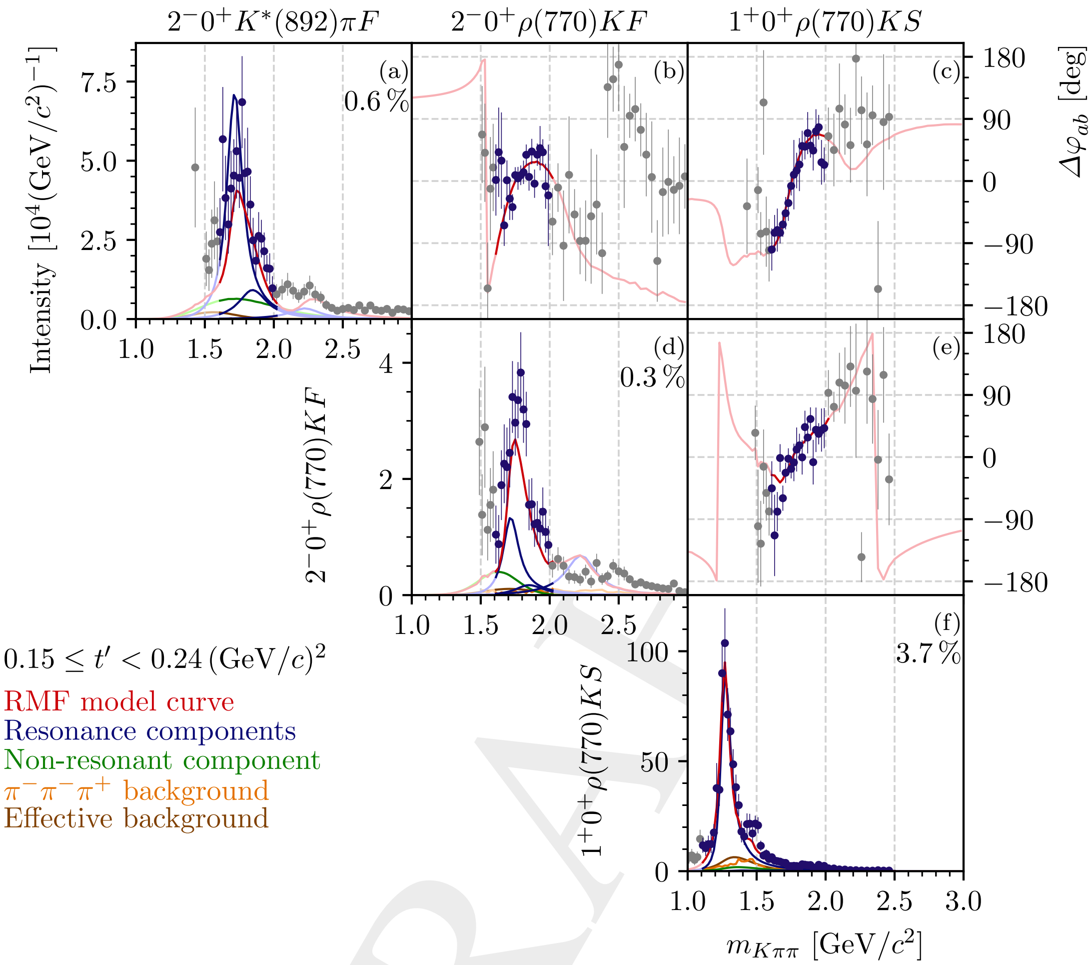

Figure 7.15: Same as figure 7.1, but for the $J^P = 2^-$ waves with $K^*(892)$ or $\rho(770)$ isobars that were included in the 10-wave RMF and the $1^+\,0^+\,\rho(770)\,K\,S$ wave serving as phase reference. The second-lowest t' bin is shown.

a similar order of magnitude. The $\pi^-\pi^-\pi^+$ background and effective background components contribute only little to the $2^-\,0^+\,K^*(892)\,\pi\,F$ wave. The high-mass tail above about $2\,\mathrm{GeV}/c^2$ changes its shape from t'-bin to t'-bin.[q] We were not able to model the high-mass tail in the RMF. Hence, we excluded this wave in the region $m_{K\pi\pi} > 2\,\mathrm{GeV}/c^2$ from the RMF. Below about $1.6\,\mathrm{GeV}/c^2$, the $2^-\,0^+\,K^*(892)\,\pi\,F$ wave exhibits an enhanced low-mass tail as observed also for other small waves and discussed in section 5.5. Hence, we also excluded this wave in the region $m_{K\pi\pi} < 1.6\,\mathrm{GeV}/c^2$ from the RMF.

The $2^-\,0^+\,\rho(770)\,K\,F$ wave is the smallest of the four 2^- waves included in the 10-wave RMF. It has about a quarter of the relative intensity of the $2^-\,0^+\,K_2^*(1430)\,\pi\,S$ wave. Similar to the

[q] For example, while there is almost no enhanced high-mass tail in the lowest t' bin (not shown), the enhanced high-mass tail in the second-lowest t' bin has two peaks at about $2.1\,\mathrm{GeV}/c^2$ and $2.3\,\mathrm{GeV}/c^2$.

$2^- 0^+ K^*(892)\,\pi\,F$ wave, the intensity spectrum of the $2^- 0^+ \rho(770)\,K\,F$ wave exhibits a peak at about $1.75\,\text{GeV}/c^2$ (see figure 7.15d). This peak is described by the RMF by an interference of the $K_2(1770)$ and $K_2(1820)$ components and the high-mass tail of the non-resonant component. Like for the $K^*(892)$ wave, the t'-summed intensities of both resonance components are of a similar order of magnitude. Summed over all t' bins, the RMF yielded a small contribution from the effective background component and a vanishing contribution from the $\pi^-\pi^-\pi^+$ background component to the $2^- 0^+ \rho(770)\,K\,F$ wave. As for the $2^- 0^+ K^*(892)\,\pi\,F$ wave, we observe enhanced low- and high-mass tails in the regions $m_{K\pi\pi} < 1.6\,\text{GeV}/c^2$ and $m_{K\pi\pi} > 2\,\text{GeV}/c^2$, which we could not model in the RMF. Hence, we excluded this wave in these mass regions from the RMF.

The phases of the $2^- 0^+ K^*(892)\,\pi\,F$ and $2^- 0^+ \rho(770)\,K\,F$ waves relative to the $1^+ 0^+ \rho(770)\,K\,S$ wave rise by nearly $180°$ in the mass region of the $K_2(1770)$ and $K_2(1820)$ resonances as shown in figures 7.15c and e, respectively. The RMF is able to reproduce these phase motions well. Above $2\,\text{GeV}/c^2$, we do not observe a rise of the relative phase of the $2^- 0^+ K^*(892)\,\pi\,F$ wave that would indicate a contribution of the $K_2(2250)$ to this wave. Thus, the high-mass tail of the $2^- 0^+ K^*(892)\,\pi\,F$ wave might not arise from the $K_2(2250)$, but might be, for example, a model artifact. The relative phase of the $2^- 0^+ \rho(770)\,K\,F$ wave rises by about $30°$ above $2\,\text{GeV}/c^2$. Still, we were not able to model this wave in the region $m_{K\pi\pi} > 2\,\text{GeV}/c^2$ by the $K_2(2250)$ component. The relative phase between the $2^- 0^+ K^*(892)\,\pi\,F$ wave and the $2^- 0^+ \rho(770)\,K\,F$ wave in the second-lowest t' bin is shown in figure 7.15b. It is centered around approximately zero in the fitted mass region and rises around $1.7\,\text{GeV}/c^2$ by about $60°$. This phase motion is caused by the different strengths with which the various components in the two 2^- waves interfere and is reproduced by the RMF.

Figure 7.16 shows the t' spectra of the three K_2 components included in the 10-wave RMF in the $2^- 0^+ K_2^*(1430)\,\pi\,S$ wave. All four 2^- waves have $M = 0$ quantum number. Therefore, the shape of the t' spectra of each of the three K_2 components by construction is the same in all four 2^- waves because of equation (6.14). In the second-lowest t' bin, the fit assigns less intensity to the $K_2(1820)$ component than expected from the other t' bins, which approximately follow the expected exponential shape (see figure 7.16b). Also, the intensity of the $K_2(1770)$ component does not follow the expected shape in the two lowest t' bins (see figure 7.16a). This is due to a different interference pattern between both components in the two lowest t' bins, which result in a similar description of the data. Hence, the yields of individual components are not determined as reliable as the resonance parameters by the RMF. This holds especially in cases where the resonance components overlap in mass as it is the case for the $K_2(1770)$ and $K_2(1820)$ components. The t' spectrum of the $K_2(2250)$ component exhibits the expected exponential shape as shown in figure 7.16c. This indicates a reliable extraction of the $K_2(2250)$ from our data.

The 2^- waves represent the largest spin-parity sector in the 238-wave set. In the following, we show a selection of further 2^- waves with potentially interesting signals. The t'-summed intensity spectrum of the $2^- 0^+ K^*(892)\,\pi\,P$ wave is shown in figure 7.17a. The $m_{K\pi\pi} \lesssim 1.6\,\text{GeV}/c^2$ region of this wave is strongly affected by the leakage effect. Above this region, the $2^- 0^+$ $K^*(892)\,\pi\,P$ wave exhibits a peak between about $1.7\,\text{GeV}/c^2$ and $1.8\,\text{GeV}/c^2$, similar to the

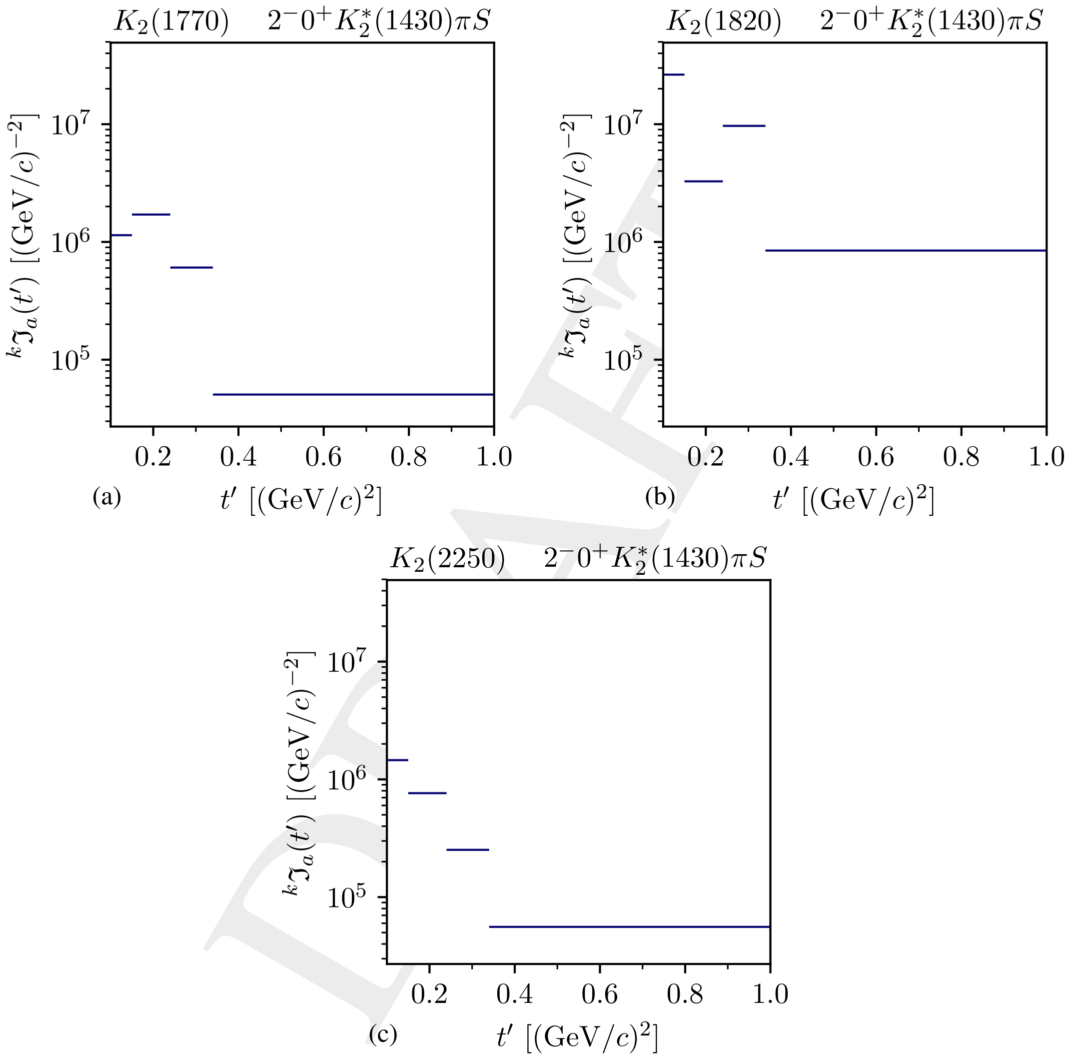

Figure 7.16: Same as figure 7.3 but for (a) the $K_2(1770)$ component, (b) the $K_2(1820)$ component, and (c) the $K_2(2250)$ component in the $2^-0^+K_2^*(1430)\pi S$ wave.

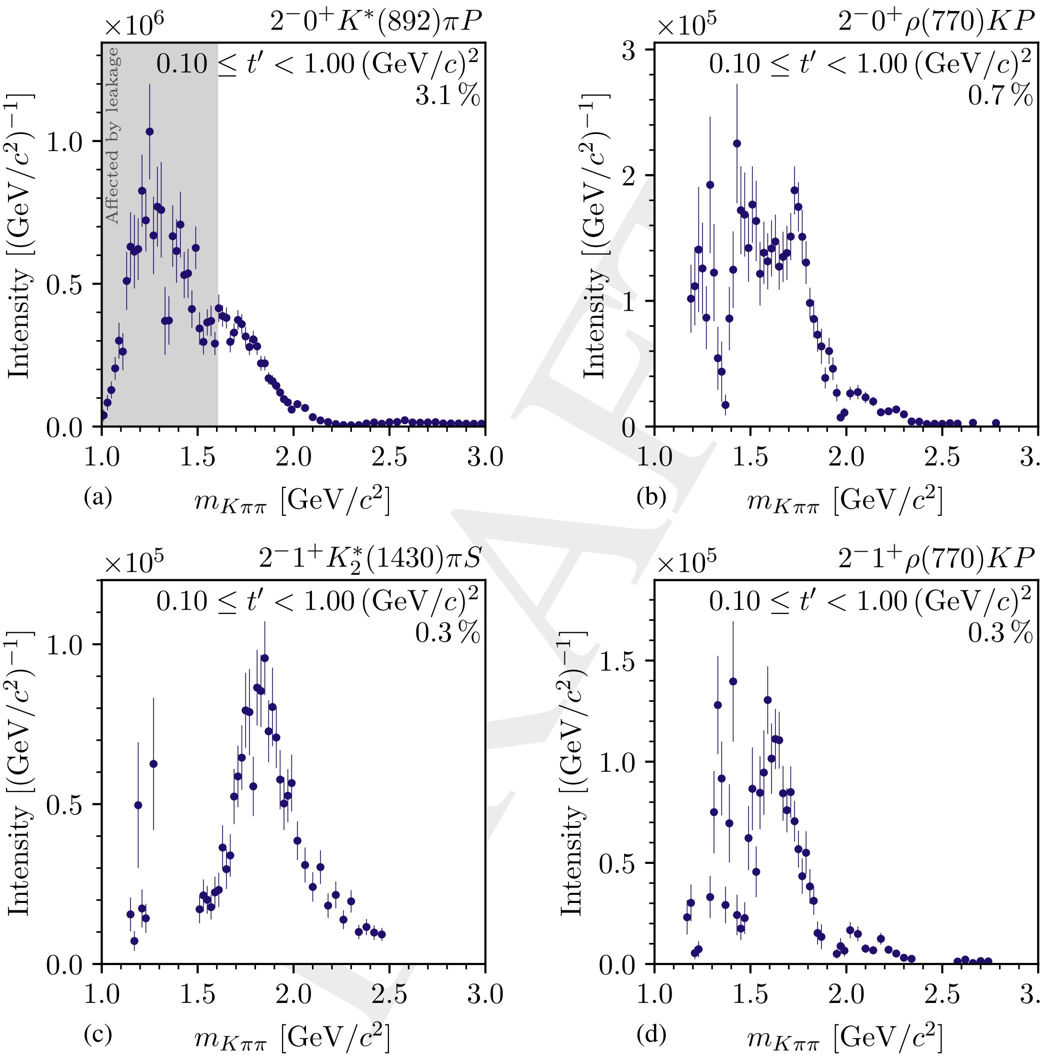

Figure 7.17: Same as figure 7.2, but for four selected partial waves with $J^P = 2^-$ that were not included in the 10-wave RMF.

$2^- 0^+ K^*(892)\,\pi\, F$ wave, which was included in the 10-wave RMF. The intensity of the peak is about twice as large as the intensity of the $1.75\,\mathrm{GeV}/c^2$ peak in the $2^- 0^+ K^*(892)\,\pi\, F$ wave, which is expected because of the higher energy needed to produce the larger orbital angular momentum of the F wave. Also, the $2^- 0^+ \rho(770)\, K\, P$ wave shows a narrow peak between about $1.7\,\mathrm{GeV}/c^2$ and $1.8\,\mathrm{GeV}/c^2$ as shown in figure 7.17b. Similar to the two waves with $K^*(892)$ isobar, the peak in the $2^- 0^+ \rho(770)\, K\, P$ wave has about twice the intensity of the $1.75\,\mathrm{GeV}/c^2$ peak in the $2^- 0^+ \rho(770)\, K\, F$ wave. Although the $2^- 0^+ \rho(770)\, K\, P$ wave does not exhibit artifacts that could directly be related to the leakage effect in our studies, its intensity spectrum exhibits a strongly enhanced intensity for $m_{K\pi\pi} \lesssim 1.6\,\mathrm{GeV}/c^2$, which presumably is an analysis artifact.[r] The $2^- 1^+ \rho(770)\, K\, P$ wave, i.e. the same wave but with $M = 1$, is shown in figure 7.17d. It has about half the intensity of the $M = 0$ wave, which is consistent with the expectation that waves with a higher spin projection M are suppressed. The $2^- 1^+ \rho(770)\, K\, P$ wave exhibits much fewer artifacts in the low-mass region than the $M = 0$ wave. It also exhibits a clear peak, which however sits at a lower mass of about $1.6\,\mathrm{GeV}/c^2$. This shift may be caused by a different composition of the various possible contributions to this wave. A potential origin of this shift could only be studied by including this wave in an RMF, which was not possible here due to the remaining artifacts in this wave. All of these three waves; i.e. the $2^- 0^+ K^*(892)\,\pi\, P$, $2^- 0^+ \rho(770)\, K\, P$, and $2^- 1^+ \rho(770)\, K\, P$ waves; exhibit non-zero intensity for $m_{K\pi\pi} \geq 2\,\mathrm{GeV}/c^2$. However, no clear signal from the $K_2(2250)$ can be observed in any of these three waves. Finally, the t'-summed intensity spectrum of the $2^- 1^+ K_2^*(1430)\,\pi\, S$ wave is shown in figure 7.17c. It has about a quarter of the intensity of its partner wave with $M = 0$ in the 10-wave RMF, which is the $2^- 0^+ K_2^*(1430)\,\pi\, S$ wave. The $2^- 1^+ K_2^*(1430)\,\pi\, S$ wave exhibits a clear peak at about $1.8\,\mathrm{GeV}/c^2$, similar to its $M = 0$ partner wave. However, we do not observe a pronounced high-mass shoulder, which indicates that the $K_2(2250)$ is suppresses in the $M = 1$ wave with respect to $M = 0$ wave. A similar effect was observed for the $\pi_2(2005)$ resonance in the COMPASS $\pi^-\pi^-\pi^+$ analysis in the $2^{-+} 0^+ f_2(1270)\,\pi\, S$ and $2^{-+} 1^+ f_2(1270)\,\pi\, S$ waves [41]. In summary, the 2^- sector compromises many waves with interesting signals in addition to the four wave selected for the 10-wave RMF. However, most of them exhibit artifacts or are small. Hence, they were not included in the 10-wave RMF.

7.4.1 Discussion

The PDG [9] lists three states with $J^P = 2^-$ quantum numbers: the established $K_2(1770)$ and $K_2(1820)$, which are close in mass; and the $K_2(2250)$, which needs further confirmation. Figure 7.18 shows the PDG average values for the masses and widths of these states as blue, red, and green stars, respectively.

[r] For example, the intensity of the $2^- 0^+ \rho(770)\, K\, P$ wave in the region $m_{K\pi\pi} \lesssim 1.6\,\mathrm{GeV}/c^2$ strongly changes in the various systematic studies as shown in figure G.2b. Especially, it seems to be sensitive to the choice of the wave-set.

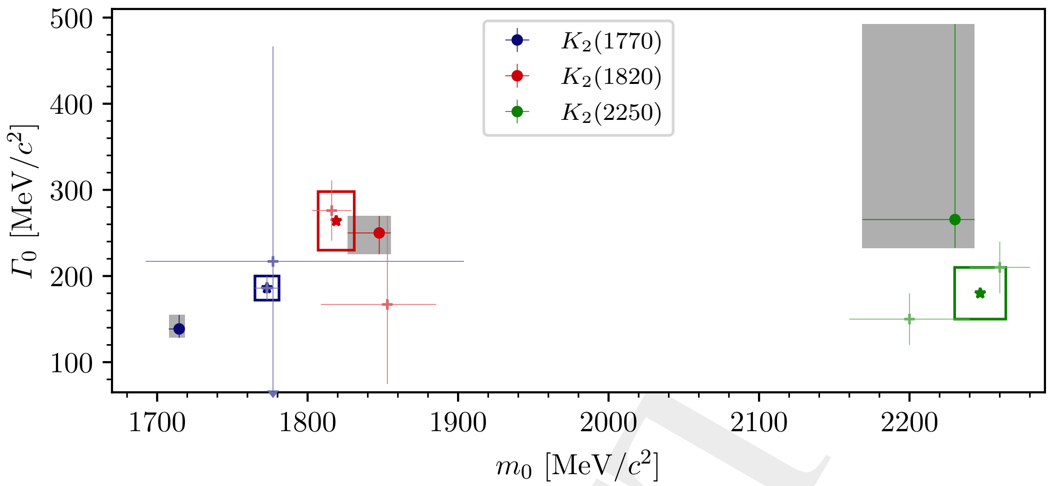

Figure 7.18: Same as figure 7.4, but for the resonance parameters of the K_2 resonances.

4684 **The $K_2(1770)$ and the $K_2(1820)$**

4685 The different signals in the four waves with $J^P = 2^-$ included in the 10-wave RMF, and especially
4686 the large phase motions in the relative phases between these waves indicate a complicated
4687 interference of various components in the 1.8 GeV/c^2 mass region. However, our approach to
4688 simultaneously model these four waves in all t' bins in one RMF gives us the possibility to
4689 reliably separate these contributions and to measure their parameters, i.e. the masses and widths
4690 of the $K_2(1770)$ and $K_2(1820)$.

4691 Our estimate for the mass of the $K_2(1770)$ (blue point) is smaller than the PDG average value.
4692 We also obtained a slightly smaller width compared to the PDG average value. Our estimate
4693 for the width the $K_2(1820)$ (red point) is in good agreement with the PDG average value. Our
4694 estimate for its mass is slightly larger than the PDG average value, but they still agree within
4695 their uncertainties.

4696 Only two measurements entered the PDG averaging for the resonance parameters of the $K_2(1770)$
4697 and the $K_2(1820)$, i.e. the measurement of the LASS experiment of the reaction $K^- p \to$
4698 $K^- \omega p$ [35] and the measurement of the LHCb experiment of the reaction $B^+ \to J/\psi \phi K^+$ [34],
4699 which was already discussed in section 7.1.1. LASS quotes very small uncertainties for their
4700 estimates of the $K_2(1770)$ mass and width. Especially, they are much smaller than the uncer-
4701 tainties of the LHCb measurement. Consequently, the LASS measurement dominates the PDG
4702 average values for the $K_2(1770)$. However, it is not clear whether the uncertainties quoted by
4703 LASS in ref. [35] include systematic effects. Thus, the total uncertainties of the PDG average
4704 values for the resonance parameters of the $K_2(1770)$ might be underestimated. Furthermore, as
4705 discussed in section 6.3, it was not possible to perform a full set of systematic studies within the
4706 scope of this work. Therefore, also our estimate for the systematic uncertainty of the mass of the

$K_2(1770)$ might be underestimated. This may cause the discrepancy between our estimate for the $K_2(1770)$ mass and the PDG average value. It should also be noted that our estimates for the resonance parameters of the $K_2(1770)$ are in agreement with the LHCb measurement within their large uncertainties. In addition, our estimate for the mass of the $K_2(1770)$ is in better agreement with the prediction of 1709 MeV/c^2 from a quark-model calculation in ref. [10] (see figure 1.1), than the PDG average value. This further supports our estimate for this parameter.

There are other previous studies of the 2^- sector in the mass region below about 2 GeV/c^2 [24, 37, 152, 153]. However, they typically considered only one K_2 state, which yielded a mass of this state of about 1770 MeV/c^2, i.e similar to the PDG average value for the $K_2(1770)$. To compare to these results, we performed in systematic study ***E*** an RMF where we included only one K_2 component for the mass region below 2 GeV/c^2 (see section 6.3). This study yielded a mass of this state of about 1740 MeV/c^2, which is more consistent with previous observations (see table 6.4). This demonstrates the sensitivity of the obtained resonance parameters on the employed RMF model. Furthermore, study ***E*** yielded a reduced χ^2 of 0.844, which is slightly worse than the reduced χ^2 value of 0.826 obtained in the main analysis. Hence, our data prefer two K_2 resonances for the mass region below 2 GeV/c^2. However, given the limited precision of our data, we cannot exclude the hypothesis of a single K_2 in the mass region below 2 GeV/c^2. Also, the results from LASS "clearly prefer the model with two $J^P = 2^-$ resonances" [35],[s] while they cannot exclude the single-K_2 hypothesis and LHCb [34] determined the significance of the $K_2(1770)$ to be 5.0σ and that of the $K_2(1820)$ to be 3.0σ. Thus, none of the measurements of the 2^- sector, including our analysis, could individually exclude the single-K_2 hypothesis. However, many analyses prefer the two-K_2 hypothesis. Therefore, $K_2(1770)$ and $K_2(1820)$ are both now considered established states, which is also supported by our measurement. Furthermore, also quark-model calculations predict two K_2 states in this mass region [10].

In addition to the measurements discussed above, also ACCMOR studied four 2^- waves in their analysis of the reaction $K^- + p \to K^-\pi^-\pi^+ + p$ [23]. Analogously to our analysis, they studied the $2^- 0^+ K_2^*(1430)\,\pi\, S$ and $2^- 0^+ f_2(1270)\, K\, S$ waves shown in figures 7.19a and 7.19b, respectively. Both waves exhibit similar signals as found in this analysis (cf. figures 7.13a and d). In addition, ACCMOR studied the $2^- 0^+ K^*(892)\,\pi\, P$ wave shown in figure 7.19c, which is affected by the leakage effect in our analysis. In exchange for this wave, we used the $2^- 0^+ K^*(892)\,\pi\, F$ wave, which exhibits an even clearer signal. The $2^- 0^+ K^*(892)\,\pi\, F$ wave was not considered in the ACCMOR analysis. ACCMOR also included the $2^- 0^+ \rho(770)\, K\, P$ wave in their wave set. However, a signal in this wave "is barely significant" [23] in their data. We observe a peak in this wave (see figure 7.17b) and an even clearer signal in the $2^- 0^+ \rho(770)\, K\, F$ wave (see figure 7.15d), which was also not considered in the ACCMOR analysis. Since the COMPASS $K^-\pi^-\pi^+$ sample is about 3.6 times larger than the one used in the ACCMOR analysis, our parameter estimates are not only more precise, but we were also able to study more waves including waves at the per-mil level such as the $2^- 0^+ K^*(892)\,\pi\, F$ and $2^- 0^+ \rho(770)\, K\, F$ waves. These waves exhibit more clean resonance signals, which also mitigates systematic effects. From their fits, ACCMOR obtained only rough estimates for the resonance parameters of the $K_2(1770)$

[s] In ref. [35], fitting a model with only a single K_2 component to their data yielded a low mass value of the K_2 state of (1728 ± 7) MeV/c^2, which surprisingly is in better agreement with our estimate for the mass of the $K_2(1770)$.

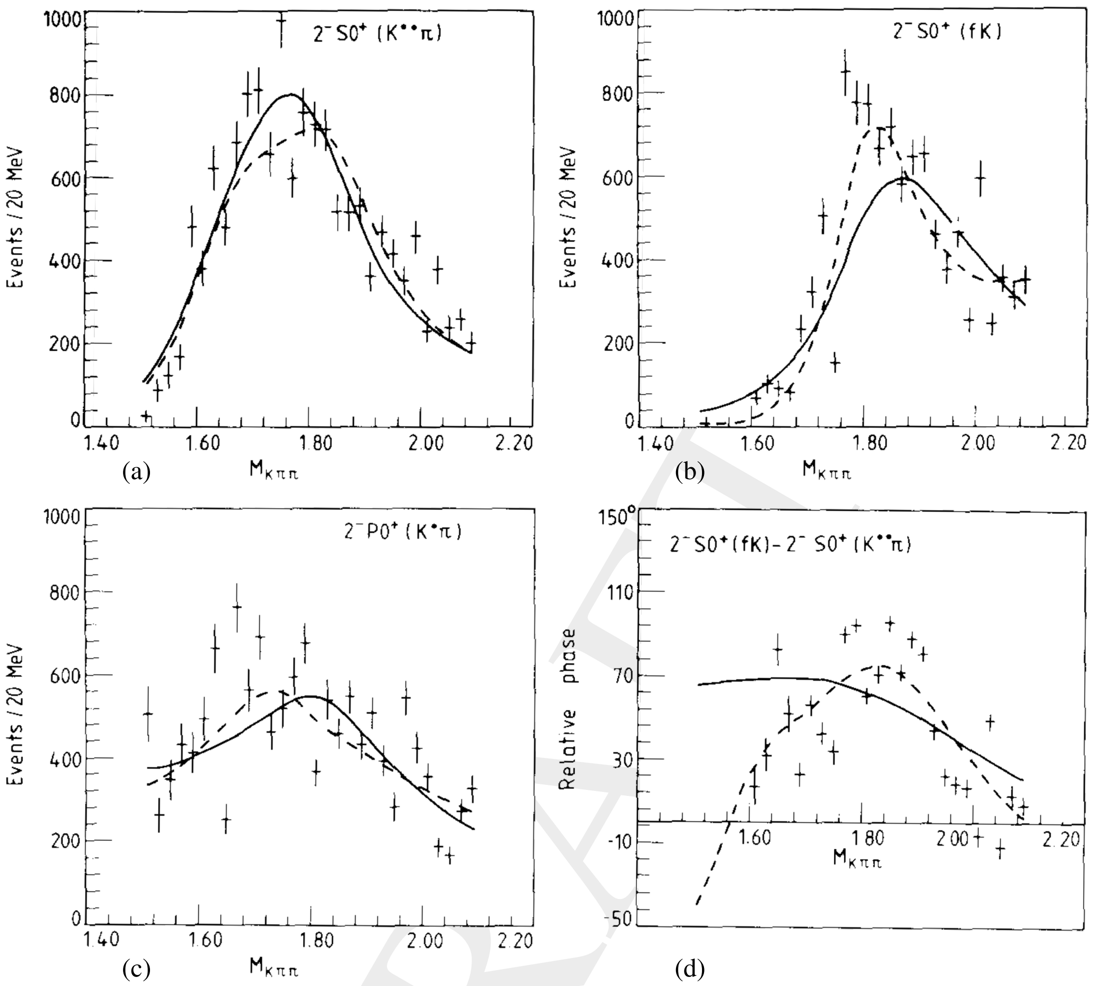

Figure 7.19: Intensities and phases of three 2^- waves as obtained from a partial-wave decomposition performed by the ACCMOR collaboration [23] in the range $0.0 \le t' \le 0.7\,(\mathrm{GeV}/c)^2$ (data points). (a), (b), and (c) show the intensity spectra of the $2^-\,0^+\,K_2^*(1430)\,\pi\,S$, $2^-\,0^+\,f_2(1270)\,K\,S$, and $2^-\,0^+\,K^*(892)\,\pi\,P$ waves, respectively. (d) shows the relative phase between the $2^-\,0^+\,f_2(1270)\,K\,S$ wave and the $2^-\,0^+\,K_2^*(1430)\,\pi\,S$ wave. The solid curves represent the results of an RMF with a single resonance component and a background component to these waves. The dashed curves represent the results of an RMF of two resonance components and a background component to these waves.

and $K_2(1820)$, which were excluded from the PDG averaging. While their estimates for the mass and width of the $K_2(1820)$ are in good agreement with our results, they obtained for the $K_2(1770)$ a larger mass of about $1780\,\mathrm{MeV}/c^2$ and a larger width of about $210\,\mathrm{MeV}/c^2$ with respect to our analysis.

ACCMOR also tested the one-K_2 hypothesis (solid curves in figure 7.19) and the two-K_2 hypothesis (dashed curves in figure 7.19). While models based on both hypotheses reproduce the $2^-\,0^+\,K_2^*(1430)\,\pi\,S$ and $2^-\,0^+\,K^*(892)\,\pi\,P$ waves fairly well (see figures 7.19a and 7.19c), the description of the $2^-\,0^+\,f_2(1270)\,K\,S$ wave is improved when including two K_2 components (see figure 7.19b). In particular, ACCMOR observed a rise in the relative phase between the $2^- 0^+ f_2(1270)\, K\, S$ wave and the $2^- 0^+ K_2^*(1430)\, \pi\, S$ wave in the mass region of the peak (see figure 7.19d), similar to the one observed in our analysis (cf. figure 7.13b). This phase motion cannot be reproduced with only one K_2 component. ACCMOR concluded, that “fits with two resonances are slightly better” [23], but they also could not exclude the one-K_2 hypothesis.

The $K_2(2250)$

In the mass region above $2\,\mathrm{GeV}/c^2$, the PDG lists one state with $J^P = 2^-$, i.e. the $K_2(2250)$. We find a potential signal from the $K_2(2250)$ and no evidence for additional states in this mass region. Our estimate for the mass of the $K_2(2250)$ agrees with the PDG average value and also with the values from previous measurements (see green point, star, and pluses in figure 7.18). However, our estimate for the width of the $K_2(2250)$ is about $90\,\mathrm{MeV}/c^2$ larger than the PDG average value and is also larger than all previous measurements. Still, our estimate for the $K_2(2250)$ width agrees with the PDG average value within two times their uncertainties.[t] Except for the measurement in ref. [152], which did not enter the PDG averaging, all previous measurements studied the $K_2(2250)$ in its decay to the $\Lambda\overline{p}$ or $\overline{\Lambda}p$ final state [30, 31, 36, 154, 155]. However, the $K_2(2250)$ is close in mass to the phase-space threshold of the $\overset{(-)}{\Lambda}\overset{(-)}{p}$ final states and the obtained resonance parameters may be sensitive to the employed model for kinematic effects such as the centrifugal-barrier factors. We studied, for the first time,[u] the $K_2(2250)$ decaying to $K_2^*(1430)\pi$ and $f_2(1270)K$ in a partial-wave analysis. For the first time, we simultaneously studied resonances in the mass regions below and above $2\,\mathrm{GeV}/c^2$ in one RMF. This allowed us to consistently take into account the high-mass tails of the $K_2(1770)$ and $K_2(1820)$ when modeling the mass region of the $K_2(2250)$ and the low-mass tail of the $K_2(2250)$ when modeling the mass region of the $K_2(1770)$ and $K_2(1820)$. In summary, we gained a new view on the $K_2(2250)$ in our analysis, which may contribute to establish this state.

7.5 $J^P = 3^-$ Partial Waves

The main 10-wave RMF does not include waves from the $J^P = 3^-$ sector. However, the $K_3^*(1780)$ with $J^P = 3^-$ is a well-known state. In order to study this state in our data, we present studies extending the 10-wave RMF by 3^- waves. We find potential resonance-like signals only in two 3^- waves, i.e. in the $3^- 1^+ K^*(892)\, \pi\, F$ and $3^- 1^+ \rho(770)\, K\, F$ waves. These waves are small with relative intensities of about $0.3\,\%$ and $0.1\,\%$, respectively, i.e. only at the per-mill level.

[t] In our analysis, the width of the $K_2(2250)$ has a large systematic uncertainty. Further systematic studies, which are missing, might reveal larger uncertainties towards a lower value. This would bring our estimate for the width of the $K_2(2250)$ in better agreement with the PDG average value.

[u] According to the PDG listing [9], the $K_2(2250)$ was studied so far only in $\overset{(-)}{\Lambda}\overset{(-)}{p}$ final states, except for the measurement in ref. [152]. In ref. [152], where the $K_2(2250)$ was studied in the $K_S K_S K_L$ system in the reaction $\pi^- C \to K_S K_S K_L + Y$, no partial-wave analysis was performed, but only a cut-based analysis was performed followed by fitting the mass spectra of the $K_S K_S K_L$ and $K_S K_S$ systems.

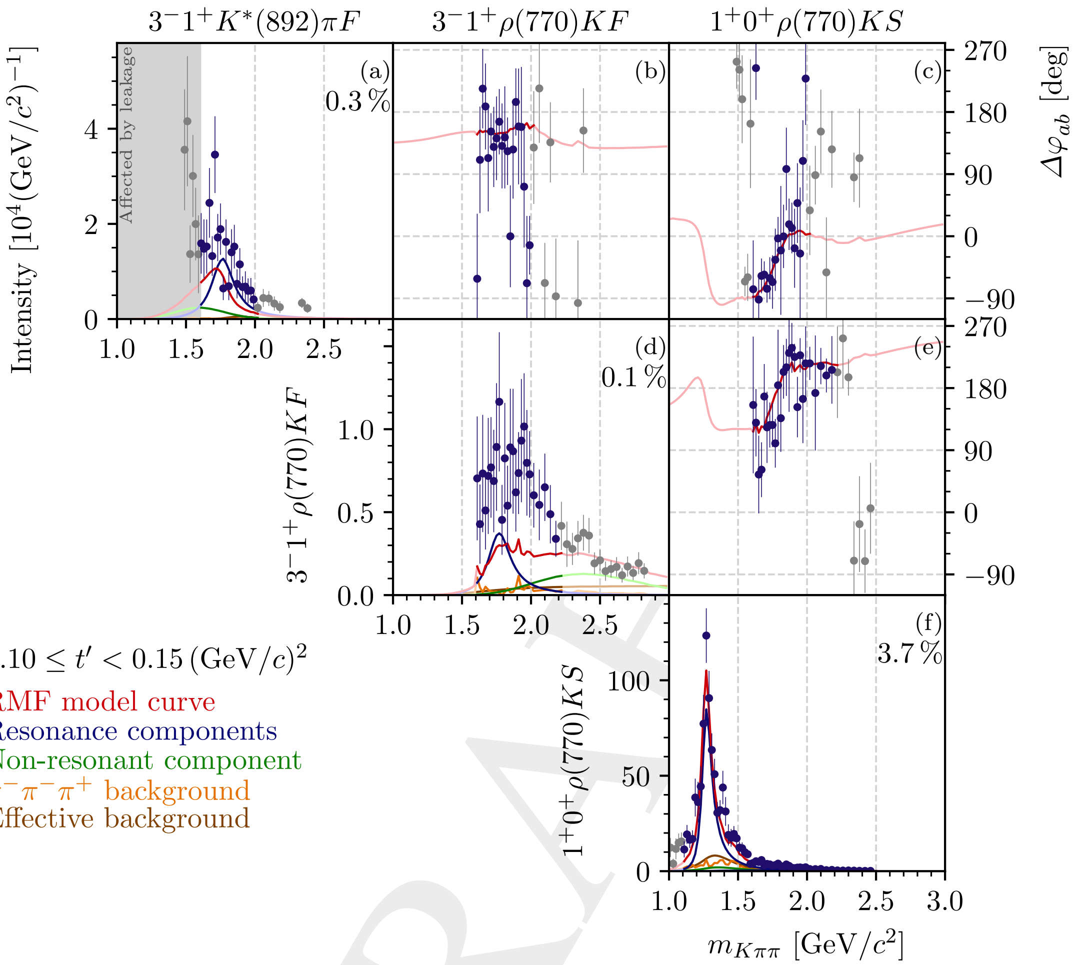

Figure 7.20: Same as figure 7.1, but showing the results of an extended RMF, where the $3^-\,1^+\,K^*(892)\,\pi\,F$ and $3^-\,1^+\,\rho(770)\,K\,F$ waves were included in addition to the waves of the 10-wave RMF. The $1^+\,0^+$ $\rho(770)\,K\,S$ wave serves as phase reference. The lowest t' bin is shown.

As exemplarily shown in figure 7.20a for the lowest t' bin, the intensity spectrum of the $3^-\,1^+$ $K^*(892)\,\pi\,F$ wave exhibits a peak at about $1.8\,\mathrm{GeV}/c^2$ and practically zero intensity above about $2\,\mathrm{GeV}/c^2$. The mass region below $1.6\,\mathrm{GeV}/c^2$ cannot be interpreted in terms of physics signals, because it is affected by the leakage effect. In contrast, the intensity spectrum of the $3^-\,1^+$ $\rho(770)\,K\,F$ wave exhibits a broad bump peaking at about $2.0\,\mathrm{GeV}/c^2$ with a high-mass tail reaching up to almost $3\,\mathrm{GeV}/c^2$ (see figure 7.20d).

The phase of the $3^-\,1^+\,K^*(892)\,\pi\,F$ wave relative to the $1^+\,0^+\,\rho(770)\,K\,S$ wave is shown for the lowest t' bin in figure 7.20c. It rises between 1.5 and $2.0\,\mathrm{GeV}/c^2$ by about 140°, which is consistent with a resonance causing the peak in the intensity spectrum of the $3^-\,1^+\,K^*(892)\,\pi\,F$ wave. Interestingly, also the phase of the $3^-\,1^+\,\rho(770)\,K\,F$ wave relative to the $1^+\,0^+\,\rho(770)\,K\,S$ wave rises in the same mass region by about 120° (see figure 7.20e). The relative phase between the $3^- 1^+ K^*(892)\,\pi\,F$ wave and the $3^- 1^+ \rho(770)\,K\,F$ wave is approximately constant with a phase offset of about 140°. Both observations point towards the same resonance contributing to both 3^- waves, even if their intensity spectra are significantly different.

In order to perform a first study of a possible resonance content in the $3^- 1^+ K^*(892)\,\pi\,F$ and $3^- 1^+ \rho(770)\,K\,F$ waves, we performed an extended RMF including these two waves in addition to the waves of the 10-wave RMF. We modeled the 3^- waves by a $K_3^*(1780)$ component in addition to non-resonant and background components (see appendix E.2 for details). This extended RMF yielded resonance parameters for the K_1, K_2, K_2^*, and K_4^* components that agree with the results from the 10-wave RMF.[v] The extended RMF describes the main features of the intensity spectrum of the $3^- 1^+ K^*(892)\,\pi\,F$ wave reasonably well as shown by the red curve in figure 7.20a. The fit yields a large contribution of the $K_3^*(1780)$ component The extended RMF cannot reproduce the broad bump in the intensity spectrum of the $3^- 1^+ \rho(770)\,K\,F$ wave (see figure 7.20d). However, the extended RMF describes well all the off-diagonal spin-density matrix elements of the $3^- 1^+ K^*(892)\,\pi\,F$ and $3^- 1^+ \rho(770)\,K\,F$ waves as exemplary shown in figure 7.21. The good description of the off-diagonal spin-density matrix elements by the extended RMF can also be seen in the relative phases of the $3^- 1^+ K^*(892)\,\pi\,F$ and $3^- 1^+ \rho(770)\,K\,F$ waves, which are all reproduced well by the RMF (see figures 7.20b, c, and e). The imperfect description of only the intensity spectrum of the $3^- 1^+ \rho(770)\,K\,F$ wave, which is at per-mill level, is similar to the one observed for the 4^+ waves (see section 7.3). Following the same argumentation, we can still use this wave to study the $K_3^*(1780)$. The RMF yields a considerable contribution of the $K_3^*(1780)$ also to the $3^- 1^+ \rho(770)\,K\,F$ wave.

7.5.1 Discussion

The $K_3^*(1780)$ was observed by various previous experiments [22, 97, 156, 157]. Our rough estimate for its mass of $1790\,\mathrm{MeV}/c^2$[w] agrees with the PDG average value of $(1779 \pm 8)\,\mathrm{MeV}/c^2$. Our rough estimate for its with of $210\,\mathrm{MeV}/c^2$ is slightly larger than the PDG average value of $(161 \pm 17)\,\mathrm{MeV}/c^2$ [9]. However, the latter is mainly determined by the measurement in ref. [157], which obtained a width of only $(135 \pm 22)\,\mathrm{MeV}/c^2$. Other measurements, such as a recent study of the decay $\psi(3686) \to K^+K^-\eta$ performed by BES III [156] or a measurement by LASS [97] obtained a width of about $200\,\mathrm{MeV}/c^2$, i.e. in good agreement with our rough estimate. Hence, we conclude that we observe clear indications for the $K_3^*(1780)$ contributing to the $3^- 1^+ K^*(892)\,\pi\,F$ and $3^- 1^+ \rho(770)\,K\,F$ waves consistent with previous observations of this known state. This means, that the $K_4^*(2045)$ is not the only known state at the per-mill level that we can extract, which further supports the robustness of our analysis.

[v] Except for the value of the $K_2(2250)$ width, all resonance parameters obtained from this extended RMF are consistent with the results from the 10-wave RMF within the corresponding uncertainties. The extended RMF yielded a $55\,\mathrm{MeV}/c^2$ smaller width of the $K_2(2250)$. This discrepancy is slightly larger than the corresponding negative uncertainty of $33\,\mathrm{MeV}/c^2$ as obtained from the 10-wave RMF. However, our estimates for the systematic uncertainties may be underestimated (see section 6.3). Thus, we consider the results from this extended RMF to agree with the results from the 10-wave RMF.

[w] As no systematic studies of the extended RMFs were performed, we only quote rough values for our estimates on the resonance parameters rounded to a precision of $10\,\mathrm{MeV}/c^2$, and we do not give the corresponding uncertainties.

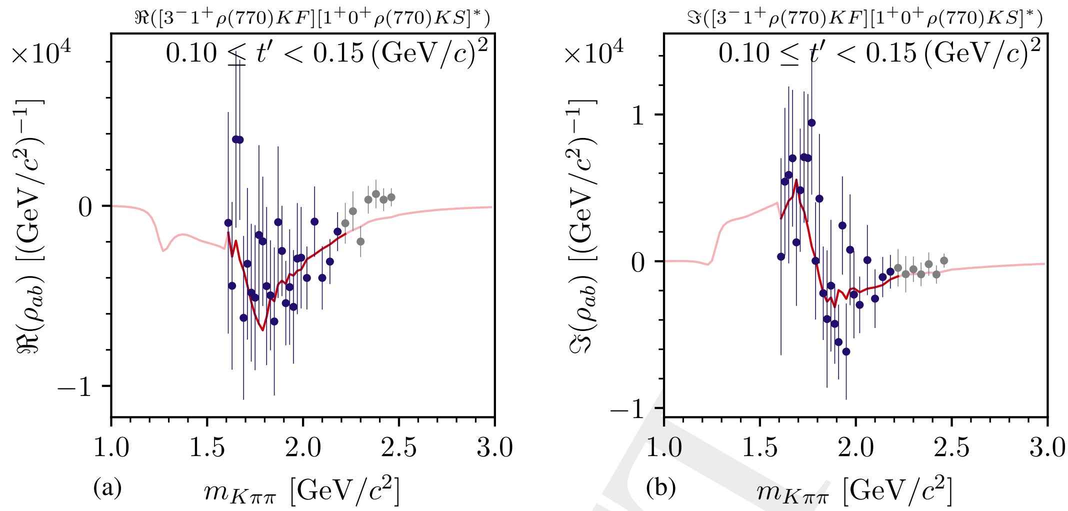

Figure 7.21: Same as figure 7.2, but showing the results of an extended RMF, where the $3^-\,1^+\,K^*(892)\,\pi\,F$ and $3^-\,1^+\,\rho(770)\,K\,F$ waves and the waves of the 10-wave RMF were included, for (a) the real part and (b) the imaginary part of the off-diagonal spin-density matrix element of the $3^-\,1^+\,\rho(770)\,K\,F$ and the $1^+\,0^+\,\rho(770)\,K\,S$ waves in the lowest t' bin.

7.6 $J^P = 0^-$ Partial Waves

Among the 0^- waves included in the 238-wave set, the $0^-\,0^+\,\rho(770)\,K\,P$ wave exhibits the clearest potential signals of excited pseudoscalar kaons. The intensity spectrum of this wave in the second-lowest t' bin, where the interesting features are seen clearly, is shown in figure 7.22a. It exhibits a peak at about $1.4\,\mathrm{GeV}/c^2$ followed by a second peak at about $1.7\,\mathrm{GeV}/c^2$ and a small bump at about $1.9\,\mathrm{GeV}/c^2$. In the $1.4\,\mathrm{GeV}/c^2$ region, the intensities have large uncertainties, which indicates that we cannot reliably determine the contribution of this wave in this mass region. This may be caused by the large leakage effect on other $J^P = 0^-$ waves as discussed below, which may influence also the $0^-\,0^+\,\rho(770)\,K\,P$ wave via its correlation with the other 0^- waves.

The phase of the $0^-\,0^+\,\rho(770)\,K\,P$ wave relative to the $1^+\,0^+\,\rho(770)\,K\,S$ wave is shown in figure 7.22b. Similar to the intensity, it is not well determined in the $1.4\,\mathrm{GeV}/c^2$ region. In the mass region of the $1.7\,\mathrm{GeV}/c^2$ peak, we observe a rise in this relative phase of about 60°. Also the phase of the $0^-\,0^+\,\rho(770)\,K\,P$ wave relative to the $2^+\,1^+\,\rho(770)\,K\,S$ wave rises in this mass region (see figure 7.22c). Together, the peak in the intensity and the rise of the phases of the $0^-\,0^+\,\rho(770)\,K\,P$ wave relative to various other waves indicate the presence of a resonance at about $1.7\,\mathrm{GeV}/c^2$. We do not observe a clear phase motion in the relative phases of the $0^-\,0^+\,\rho(770)\,K\,P$ wave in the mass region of the $1.9\,\mathrm{GeV}/c^2$ bump. However, in this mass region there are also resonances in the reference waves, such as the K_1', which may partly compensate the phase motion caused by a potential K resonance at about $1.9\,\mathrm{GeV}/c^2$.

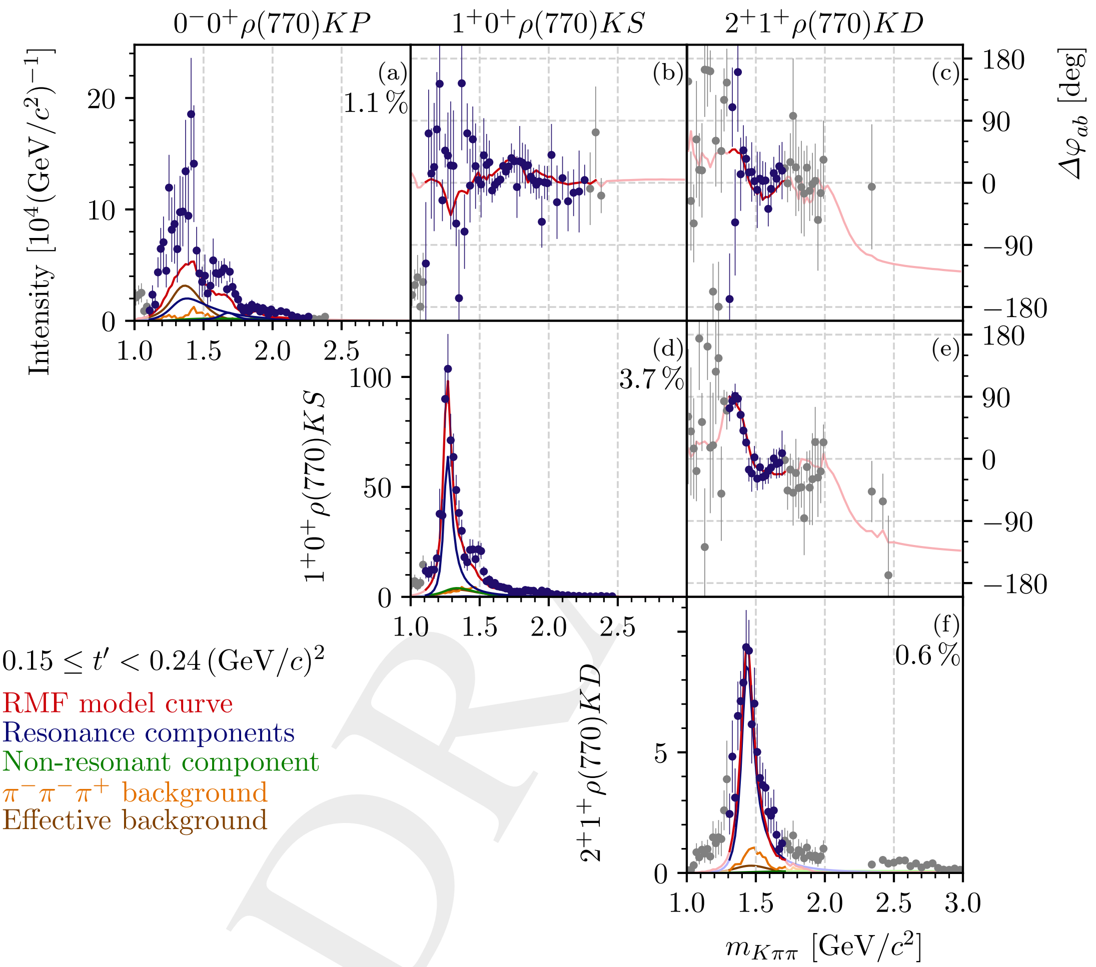

Figure 7.22: Same as figure 7.1, but showing the results of an extended RMF, where the $0^-\,0^+\,\rho(770)\,K\,P$ wave was included in addition to the waves of the 10-wave RMF. The $1^+\,0^+\,\rho(770)\,K\,S$ and $2^+\,1^+\,\rho(770)\,K\,D$ waves serve as phase references. The second-lowest t' bin is shown.

In order to perform a first study of a possible resonance content in the $0^-\,0^+\,\rho(770)\,K\,P$ wave, we performed an extended RMF including this wave in addition to the waves of the 10-wave RMF. We modeled this 0^- wave by three K resonance components; i.e. the $K(1460)$, the $K(1630)$, and the $K(1830)$; in addition to non-resonant and background components (see appendix E.2 for details). This extended RMF yielded resonance parameters for the K_1, K_2, K_2^*, and K_4^* components that agree with the results from the 10-wave RMF.[x] While this extended RMF reproduces reasonably well the off-diagonal spin-density matrix elements of the $0^-\,0^+\,\rho(770)\,K\,P$ wave, the description of the intensity spectrum of this wave by the RMF is imperfect. In particular, it fails to reproduce the overall magnitude of the intensity in this wave, similar to the results for the 3^- waves (see section 7.5) and for the 4^+ waves (see section 7.3). Given the small yield of the potential $K(1830)$ signal, we performed another extended RMF where we omitted the $K(1830)$ component from the RMF model. This RMF yielded an only slightly worse reduced χ^2 value of 0.840 compared to 0.837 when including the $K(1830)$ component. Also, the resonance parameters of the $K(1460)$ and $K(1630)$ components are not strongly affected when omitting the $K(1830)$ component. Hence, the $K(1830)$ component describes an only weak signal in the $0^-\,0^+\,\rho(770)\,K\,P$ wave.

The largest wave of the 0^- sector is the $0^-\,0^+\,K^*(892)\,\pi\,P$ wave. Its t'-summed intensity spectrum is shown in figure 7.23a. The $m_{K\pi\pi} \lesssim 1.6\,\mathrm{GeV}/c^2$ region of this wave is affected by the leakage effect. Hence, we cannot study the $K(1460)$ in this wave. At about $1.6\,\mathrm{GeV}/c^2$, the $0^-\,0^+\,K^*(892)\,\pi\,P$ wave exhibits a shoulder, which may arise from the $K(1630)$. However, as this shoulder is just at the border of the mass region affected by the leakage effect, we cannot draw hard conclusions on a $K(1630)$ signal in the $0^-\,0^+\,K^*(892)\,\pi\,P$ wave. The intensity spectrum of the $0^-\,0^+\,K^*(892)\,\pi\,P$ wave also exhibits a bump between $1.8\,\mathrm{GeV}/c^2$ and $1.9\,\mathrm{GeV}/c^2$, which may arise from the $K(1830)$. In order to validate this hypothesis, the $0^-\,0^+\,K^*(892)\,\pi\,P$ wave would have to be included in an RMF, but the leakage effect prohibits this.

The last 0^- wave in our analysis that exhibits potential resonance-like signals is the $0^-\,0^+\,[K\pi]_S^{K\pi}\,\pi\,S$ wave shown in figure 7.23b. Also in this wave, the $m_{K\pi\pi} \lesssim 1.6\,\mathrm{GeV}/c^2$ region of is affected by the leakage effect. Above this mass region, its intensity spectrum exhibits a broad peak at about $1.7\,\mathrm{GeV}/c^2$ with a long high-mass tail that extends beyond $2\,\mathrm{GeV}/c^2$. This peak may arise from the $K(1630)$ and the $K(1830)$ may contribute to the high-mass tail. However, we were not able to describe the $0^-\,0^+\,[K\pi]_S^{K\pi}\,\pi\,S$ wave together with the $0^-\,0^+\,\rho(770)\,K\,P$ wave in one RMF. Hence, the signals in both waves may not be fully compatible within the limitations of our Breit-Wigner RMF model.

[x] Except for the value of the $K_1(1270)$ width, all resonance parameters obtained from this extended RMF are consistent with the results from the 10-wave RMF within the corresponding uncertainties. The extended RMF yielded a $12\,\mathrm{MeV}/c^2$ smaller width of the $K_1(1270)$. This deviation is slightly larger than the corresponding negative uncertainty of $6\,\mathrm{MeV}/c^2$ as obtained from the 10-wave RMF. However, our estimates for the systematic uncertainties may be underestimated (see section 6.3). Thus, we consider the results from this extended RMF to agree with the results from the 10-wave RMF.

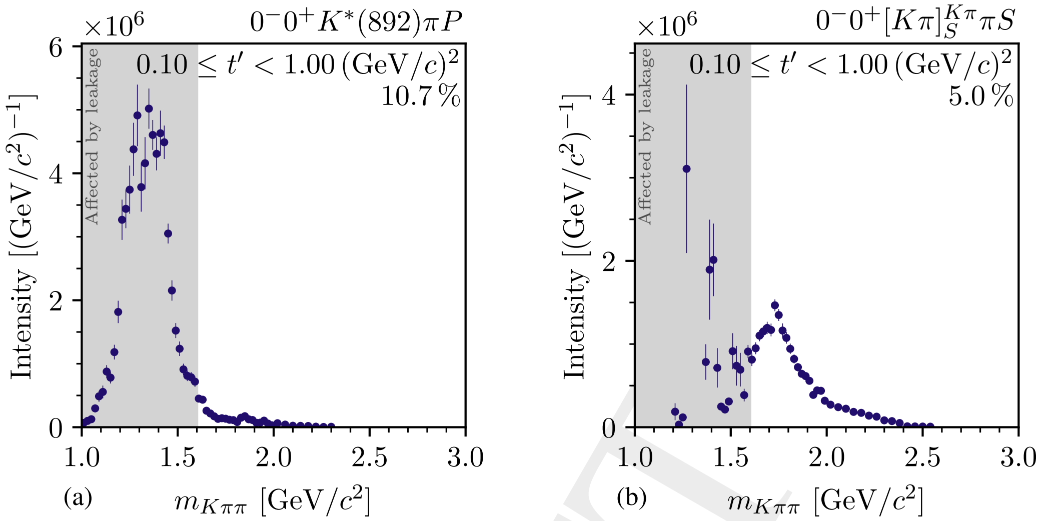

Figure 7.23: Same as figure 7.2, but showing the t'-summed intensity spectra of (a) the $0^-\,0^+\,K^*(892)\,\pi\,P$ wave and (b) the $0^-\,0^+\,[K\pi]^{K\pi}_S\,\pi\,S$ wave.

7.6.1 Discussion

Unfortunately, many of the $J^P = 0^-$ waves are affected by the leakage effect. Consequentially, we can study excited pseudoscalar states reliably only in the $0^-\,0^+\,\rho(770)\,K\,P$ wave. The PDG lists three excited pseudoscalar states: the $K(1460)$, the $K(1630)$, and the $K(1830)$. While the $K(1460)$ is considered an established state, the $K(1830)$ and the $K(1630)$ still need further confirmation.

The $K(1460)$

The $K(1460)$ has been studied in an analysis of the decay $D^0 \to K^\mp\pi^\pm\pi^+\pi^-$ by LHCb [26], as well as in the ACCMOR analysis [23] and in the analysis of data from SLAC in ref. [158], which both analyzed the same reaction as in our work. The PDG does not provide average values for the $K(1460)$ resonance parameters. Our rough estimate for its mass of $1360\,\mathrm{MeV}/c^2$ is smaller than the masses observed by the previous experiments, which are in the range of 1400 to $1480\,\mathrm{MeV}/c^2$ [9]. Our rough estimate for its width of $420\,\mathrm{MeV}/c^2$ is larger than the widths observed by previous experiments, which are in the range of 250 to $340\,\mathrm{MeV}/c^2$ [9]. However, given the large uncertainties of measured spin-density matrix elements of the $0^-\,0^+\,\rho(770)\,K\,P$ wave in the $1.4\,\mathrm{GeV}/c^2$ mass region and the fact that we considered only one 0^- wave, our estimates for the $K(1460)$ resonance parameters have large statistical uncertainties and may have systematic uncertainties. Hence, we consider our results on the $K(1460)$ to not contradict the previous measurements.

The $K(1830)$

So far, the $K(1830)$ has been studied by the CERN Ω' spectrometer in the reaction $K^- p \to K^- K^- K^+ p$ [37] and by LHCb in the analysis of the decay $B^+ \to J/\psi \phi K^+$ [34]. Our rough estimate for the $K(1830)$ mass of $1870\,\mathrm{MeV}/c^2$ is in good agreement with the mass estimate by LHCb. Our rough estimate for its width of $80\,\mathrm{MeV}/c^2$ is smaller than the width estimate of $(168 \pm 90\,^{+280}_{-104})\,\mathrm{MeV}/c^2$ by LHCb, but still consistent within their large uncertainties. CERN Ω' gives only rough estimates for the resonance parameters of the $K(1830)$ without uncertainties. Hence, our rough estimates for the $K(1830)$ resonance parameters are consistent with the results from the limited set of previous studies of this state.

The $K(1630)$

While the PDG lists three exited pseudoscalar states, quark-model calculations [10, 159] predict only two states (see figure 1.1). The lower-mass quark-model state can be associated with the $K(1460)$, and the higher-mass quark-model state can probably be associated with the $K(1830)$. Hence, the $K(1630)$ is a candidate for a supernumerary state with respect to the quark model, which points towards a possible exotic nature of the $K(1630)$.

The $K(1630)$ was studied so far only in the reaction $\pi^- p \to (K^0_S \pi^+ \pi^-) X^+ \pi^- X^0$ by a single bubble-chamber experiment at CERN [160, 161]. While the PDG lists the $K(1630)$ as a K state, i.e. with $J^P = 0^-$, its quantum numbers are not jet well determined [161]. Our rough estimate of $1680\,\mathrm{MeV}/c^2$ for the $K(1630)$ mass is similar to the value of $(1629 \pm 7)\,\mathrm{MeV}/c^2$ obtained in ref. [160]. However, we obtained a larger value of $150\,\mathrm{MeV}/c^2$ for its width compared to the $16^{+19}_{-16}\,\mathrm{MeV}/c^2$ [9] obtained in ref. [160]. However, one would expect a much larger width for an excited pseudoscalar state.

In the ACCMOR analysis, a model consisting of a single Breit-Wigner component for the $K(1460)$ and a simple background component was fitted to the $0^-\,0^+\,\rho(770)\,K\,P$, $0^-\,0^+\,K^*(892)\,\pi\,P$, and $0^-\,0^+\,[\pi\pi]_S\,K\,S$ waves [23]. While their model reproduces well the $0^-\,0^+\,K^*(892)\,\pi\,P$ and $0^-\,0^+\,[\pi\pi]_S\,K\,S$ intensities and relative phases, it is not able to perfectly reproduce the intensity and the relative phase of the $0^-\,0^+\,\rho(770)\,K\,P$ wave at a mass of about $1.7\,\mathrm{GeV}/c^2$, i.e. in the mass region in which we potentially observe the $K(1630)$ in the same wave (cf. curve and data points in figure 7.24a). For example, ACCMOR also observed a rise in the relative phase of the $0^-\,0^+\,\rho(770)\,K\,P$ wave around about $1.7\,\mathrm{GeV}/c^2$ similar to what we find in our analysis. However, their model with only the $K(1460)$ could not reproduce this rise. Thus, it seems that signs of the $K(1630)$ are visible already in the ACCMOR analysis, but they did not consider this state in their RMF.

In the LHCb analysis in ref. [26], the authors performed a model-independent partial-wave analysis (MIPWA), which is similar to our so-called freed-isobar analysis that is presented in chapter 8 and which allowed them to extract the amplitude for the $J^P = 0^-$ $K^-\pi^-\pi^+$ system in

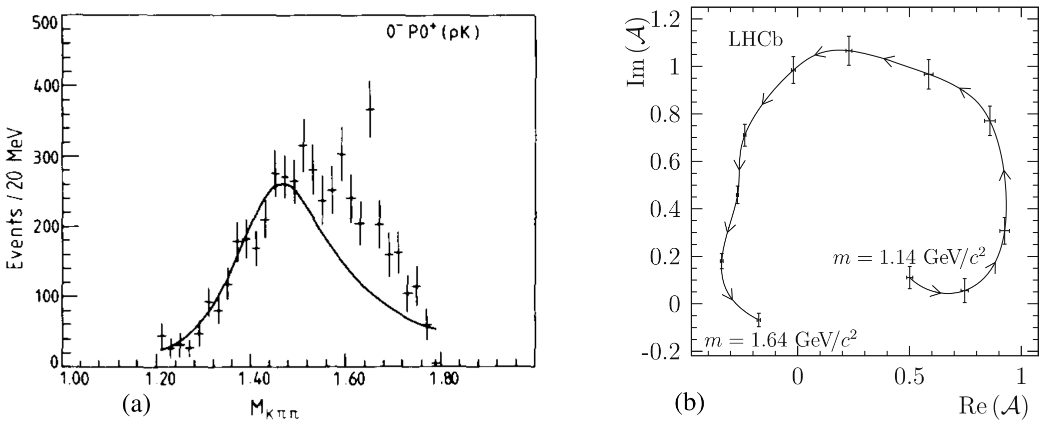

Figure 7.24: Results from previous studies of excited pseudoscalar resonances. (a) shows the intensity spectrum of the $0^- 0^+ \rho(770)\, K\, P$ wave as obtained in the ACCMOR analysis in the range $0 \leq t' \leq 0.7\,(\text{GeV}/c)^2$ [23]. The curve represents the results of a fit of a model consisting of one Breit-Wigner component and a simple background component to this wave and to the $0^- 0^+ K^*(892)\, \pi\, P$ and $0^- 0^+ [\pi\pi]_S\, K\, S$ waves. (b) shows the Argand diagram of the amplitude for the $K^-\pi^-\pi^+$ system being in a $J^P = 0^-$ state as obtained from a model-independent partial-wave analysis by LHCb [26]. The curve shows a cubic spline that interpolates between the data points.

bins of $m_{K\pi\pi}$ instead of imposing a Breit-Wigner shape for it. They used this approach to confirm the resonance nature of the $K(1430)$. Figure 7.24b shows the Argand diagram as obtained from their MIPWA. In addition to the clear circle caused by the $K(1460)$, the last three data points might indicate the beginning of another circle at about $1.6\,\text{GeV}/c^2$, which might be related to the $K(1630)$. Unfortunately, LHCb could not study the 0^- amplitude beyond $1.64\,\text{GeV}/c^2$ because of the limited kinematic reach of their analysis given by the D^0 mass. This clearly shows the advantage of studying strange mesons in diffractive production where the full mass range and hence the complete spectrum of strange mesons is accessible in a single self-consistent analysis. Hence, we can directly count the number of appearing states unambiguously, while determining the number of states from multiple measurements that studied only a single state requires assigning these measurements to the corresponding states, which may be ambiguous to the measurement uncertainties. The three signals we observe in the $0^- 0^+ \rho(770)\, K\, P$ wave point towards a supernumerary, excited pseudoscalar state in the $1.7\,\text{GeV}/c^2$ mass region. However, further systematic studies are needed in order to establish this state.

7.7 $J^P = 3^+$ Partial Waves

Among the waves with $J^P = 3^+$, the $3^+ 0^+ K_3^*(1780)\, \pi\, S$ and $3^+ 1^+ K_2^*(1430)\, \pi\, P$ waves exhibit the clearest signals of a potential K_3 resonance. Both waves have a relative intensity at the per-mill level of only about 0.1 %. The intensity spectrum of the $3^+ 0^+ K_3^*(1780)\, \pi\, S$ wave in the second-lowest t' bin, where the interesting features are seen clearly, is shown in figure 7.25a. It exhibits a narrow peak at about $2.1\,\text{GeV}/c^2$ with a high-mass shoulder at about $2.5\,\text{GeV}/c^2$.

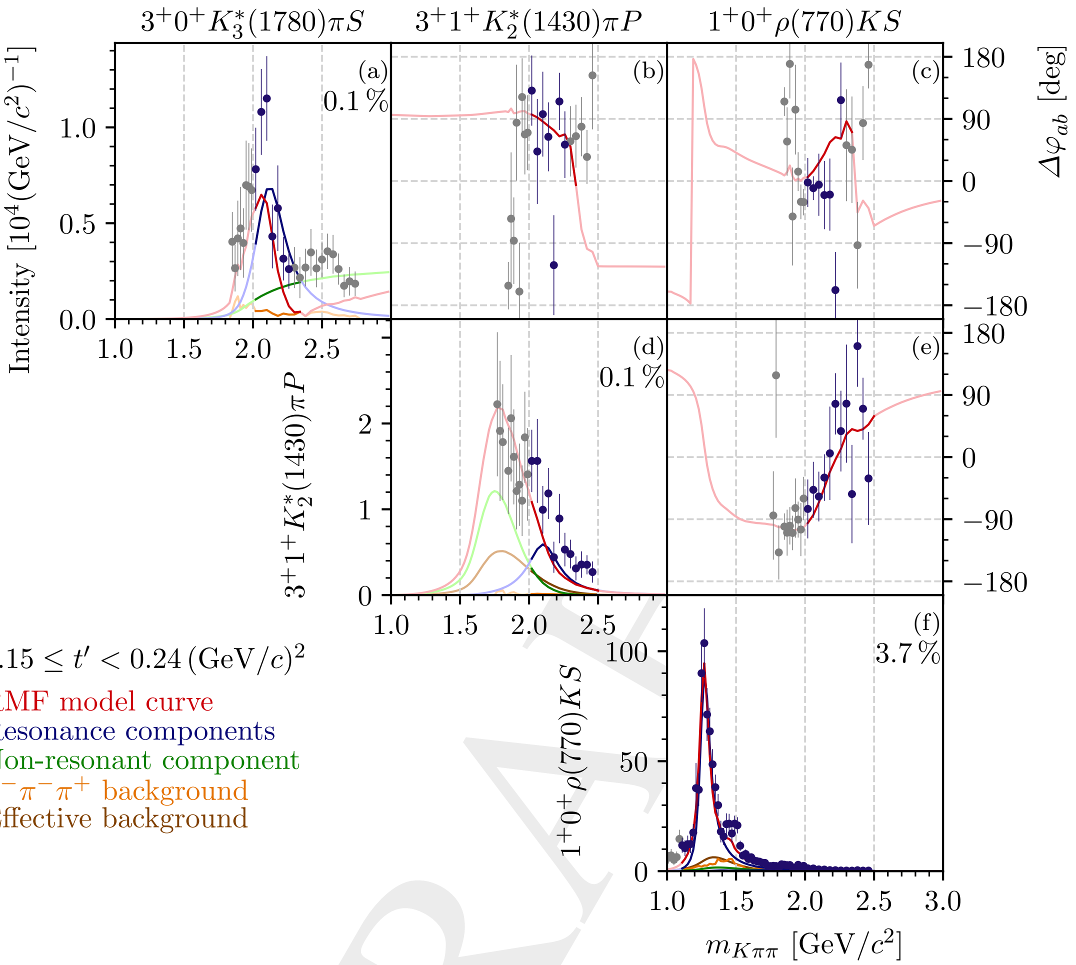

Figure 7.25: Same as figure 7.1, but showing the results of an extended RMF, where the $3^+\,0^+\,K_3^*(1780)\,\pi\,S$ and $3^+\,1^+\,K_2^*(1430)\,\pi\,P$ waves were included in addition to the waves of the 10-wave RMF. The $1^+\,0^+$ $\rho(770)\,K\,S$ wave serves as phase reference. The second-lowest t' bin is shown.

The intensity spectrum of the $3^+\,1^+\,K_2^*(1430)\,\pi\,P$ wave continuously falls from about 1.8 to $2.5\,\mathrm{GeV}/c^2$, i.e. in the mass region in which this wave was included in the 238-wave set (see figure 7.25d).

Figure 7.25e shows the phase of the $3^+\,1^+\,K_2^*(1430)\,\pi\,P$ wave relative to the $1^+\,0^+\,\rho(770)\,K\,S$ wave in the second-lowest t' bin. We observe a clear rise by about 130° between about 1.9 and $2.4\,\mathrm{GeV}/c^2$, even though there is no clear peak visible in the corresponding intensity spectrum. The phase of the $3^+\,0^+\,K_3^*(1780)\,\pi\,S$ wave relative to the $1^+\,0^+\,\rho(770)\,K\,S$ wave exhibits large fluctuations (see figure 7.25c). Overall, it exhibits only the tendency of a rise between 2.0 and $2.4\,\mathrm{GeV}/c^2$, even though there is a clear peak visible in the corresponding intensity spectrum. Hence, we find indications for a resonance at about $2.1\,\mathrm{GeV}/c^2$ in both 3^+ waves, i.e. in the intensity of the $3^+\,0^+\,K_3^*(1780)\,\pi\,S$ wave and in the relative phase of the $3^+\,1^+\,K_2^*(1430)\,\pi\,P$

wave. The relative phase between the $3^+\,0^+\,K_3^*(1780)\,\pi\,S$ wave and the $3^+\,1^+\,K_2^*(1430)\,\pi\,P$ wave in the second-lowest t' bin is shown in figure 7.25b. It exhibits no clear phase motion below $2.2\,\mathrm{GeV}/c^2$, as expected if both waves are dominated by the same resonance.

In order to perform a fist study of a possible resonance content in the $3^+\,0^+\,K_3^*(1780)\,\pi\,S$ and $3^+\,1^+\,K_2^*(1430)\,\pi\,P$ waves, we performed an extended RMF including both 3^+ waves in addition to the waves of the 10-wave RMF. We modeled the 3^+ waves by the $K_3(2320)$ component in addition to non-resonant and background components (see appendix E.2 for details). The extended RMF yielded resonance parameters for the K_1, K_2, K_2^*, and K_4^* components that are consistent with the results from the 10-wave RMF. The model curve of the extended RMF has a peak in the intensity spectrum of the $3^+\,0^+\,K_3^*(1780)\,\pi\,S$ wave, similar to the one observed in the measured intensity spectrum (see figure 7.25a). This peak is dominated by the $K_3(2320)$ component. The continuously falling intensity spectrum of the $3^+\,1^+\,K^*(892)\,\pi\,P$ wave is reproduced by the extended RMF by large contributions of the non-resonant and effective background components together with the $K_3(2320)$ component. Also, the relative phases of both 3^+ waves are reproduced well by the extended RMF.[y]

7.7.1 Discussion

The PDG lists one strange meson with $J^P = 3^+$, the $K_3(2320)$, which is not considered an established state [9]. So far, it has been seen by only two experiments in the $\Lambda\overline{p}$ and $\overline{\Lambda}p$ final states [30, 31].[z] The analysis in ref. [30] yielded a width of $(150 \pm 30)\,\mathrm{MeV}/c^2$ and the analysis in ref. [31] yielded a width of about $250\,\mathrm{MeV}/c^2$.[aa] The latter one agrees well with our rough estimate of $270\,\mathrm{MeV}/c^2$. On average, both experiments measured a $K_3(2320)$ mass of $(2324 \pm 24)\,\mathrm{MeV}/c^2$ [9], which is slightly larger than our rough estimate of $2120\,\mathrm{MeV}/c^2$. Interestingly, the mass of the $K_3(2320)$ as obtained from the $\Lambda\overline{p}$ and $\overline{\Lambda}p$ final states agrees with the quark-model prediction from ref. [10] for the first excitation of the K_3 spectrum, while our estimate from $K_3^*(1780)\,\pi$ and $K_2^*(1430)\,\pi$ final states is in good agreement with the predicted ground states (see figure 1.1). Hence, different states may appear in our analysis and in the analyses in refs. [30, 31], due to the different decay modes that are studied. However, the assignment of our measurement and of the measurements in refs. [30, 31] to the corresponding quark-model states may be ambiguous, because the systematic uncertainties on our estimates for the $K_3(2320)$ resonance parameter may be large. Also, the systematic uncertainties on the estimates for the $K_3(2320)$ resonance parameter from refs. [30, 31] may be large, because it is not clear whether the authors of refs. [30, 31] used centrifugal-barrier factors to model the threshold behavior.[ab] Omitting the centrifugal-barrier factors biases the mass estimates towards larger

[y] In general, the extended RMF reproduces well the off-diagonal spin-density matrix elements of the $3^+\,0^+\,K_3^*(1780)\,\pi\,S$ and $3^+\,1^+\,K_2^*(1430)\,\pi\,P$ waves (not shown).

[z] According to the PDG listing [9].

[aa] In ref. [31], the value of the $K_3(2320)$ width was not optimized in a fit to data, but tuned by hand.

[ab] The authors of refs. [30, 31] only give the statement that they fit a relativistic Breit-Wigner to the partial waves, but they do not give the exact formula. Hence, it is not clear whether their model includes centrifugal barrier factors. Ref. [30] does not make any statement about centrifugal barrier factors and ref. [31] only states that they "have imposed correct threshold behavior by drawing smooth curves $\propto p^L$ through the moments ..." [31].

values, in particular for the $K_3(2320)$, because its mass is close to the phase-space threshold of the $\overset{(-)}{\Lambda}\overset{(-)}{p}$ final state and because of the large orbital angular momentum involved in the $\overset{(-)}{\Lambda}\overset{(-)}{p}$ decay.

7.8 $J^P = 4^-$ Partial Waves

The $4^- \, 0^+ \, K_2^*(1430) \, \pi \, D$ wave exhibits the cleanest resonance-like signal with $J^P = 4^-$. This wave has a relative intensity of only about 0.1 %. The corresponding intensity spectrum is shown in figure 7.26a exemplarily for the lowest t' bin. It exhibits a broad peak at about $2.3\,\mathrm{GeV}/c^2$. In the same mass region, we observe a rise by about 100° of the phase of the $4^- \, 0^+ \, K_2^*(1430) \, \pi \, D$ wave relative to the $1^+ \, 0^+ \, \rho(770) \, K \, S$ wave as shown in figure 7.26b. Both, the intensity peak and the rise of the relative phase, indicate the presence of a K_4 resonance at about $2.3\,\mathrm{GeV}/c^2$.

In order to perform a first study of a possible resonance content in the $4^- \, 0^+ \, K_2^*(1430) \, \pi \, D$ wave, we performed an extended RMF including this 4^- wave in addition to the waves of the 10-wave RMF. We modeled this 4^- wave by one resonance component, i.e. the $K_4(2500)$, in addition to non-resonant and background components (see appendix E.2 for details). This extended RMF yielded resonance parameters for the K_1, K_2, K_2^*, and K_4^* components that are consistent with the results from the 10-wave RMF. The model curve of extended RMF has a peak in the intensity spectrum of the $4^- \, 0^+ \, K_2^*(1430) \, \pi \, D$ wave similar to the one observed in the measured intensity spectrum (see figure 7.26a). However, the RMF underestimates the total intensity in this wave, similar to other waves at the per-mill level (see section 7.3). In addition to a broad effective background component, the RMF assigns a large intensity to the $K_4(2500)$ component. The rise in the phase of the $4^- \, 0^+ \, K_2^*(1430) \, \pi \, D$ wave relative to the $1^+ \, 0^+ \, \rho(770) \, K \, S$ wave is reproduced well by the extended RMF.

7.8.1 Discussion

The PDG lists the $K_4(2500)$ as a not-established state [9]. So far, it has been seen by only a single experiment in the reaction $K^+ p \to \overline{\Lambda} p p$ [31].[ac] They measured a mass of $(2490 \pm 20)\,\mathrm{MeV}/c^2$, which is larger than our rough estimate of $2260\,\mathrm{MeV}/c^2$, and a width of about $250\,\mathrm{MeV}/c^2$ similar to our rough estimate of $300\,\mathrm{MeV}/c^2$.[ad] Similar to the discussion of the $K_3(2320)$ in section 7.7, the mass of the $K_4(2500)$ as obtained from the $\overline{\Lambda} p$ final state agrees better with a quark-model prediction from ref. [10] for the first excitation of the K_4 spectrum, while our estimate is in good agreement with the predicted ground states. However, the assignment of our measurement and of the measurement in refs. [31] to the corresponding quark-model states may be ambiguous, as already discussed for the $K_3(2320)$.

[ac] According to the PDG listing [9].
[ad] In ref. [31], the value of the $K_4(2500)$ width was not optimized in a fit to data, but tuned by hand.

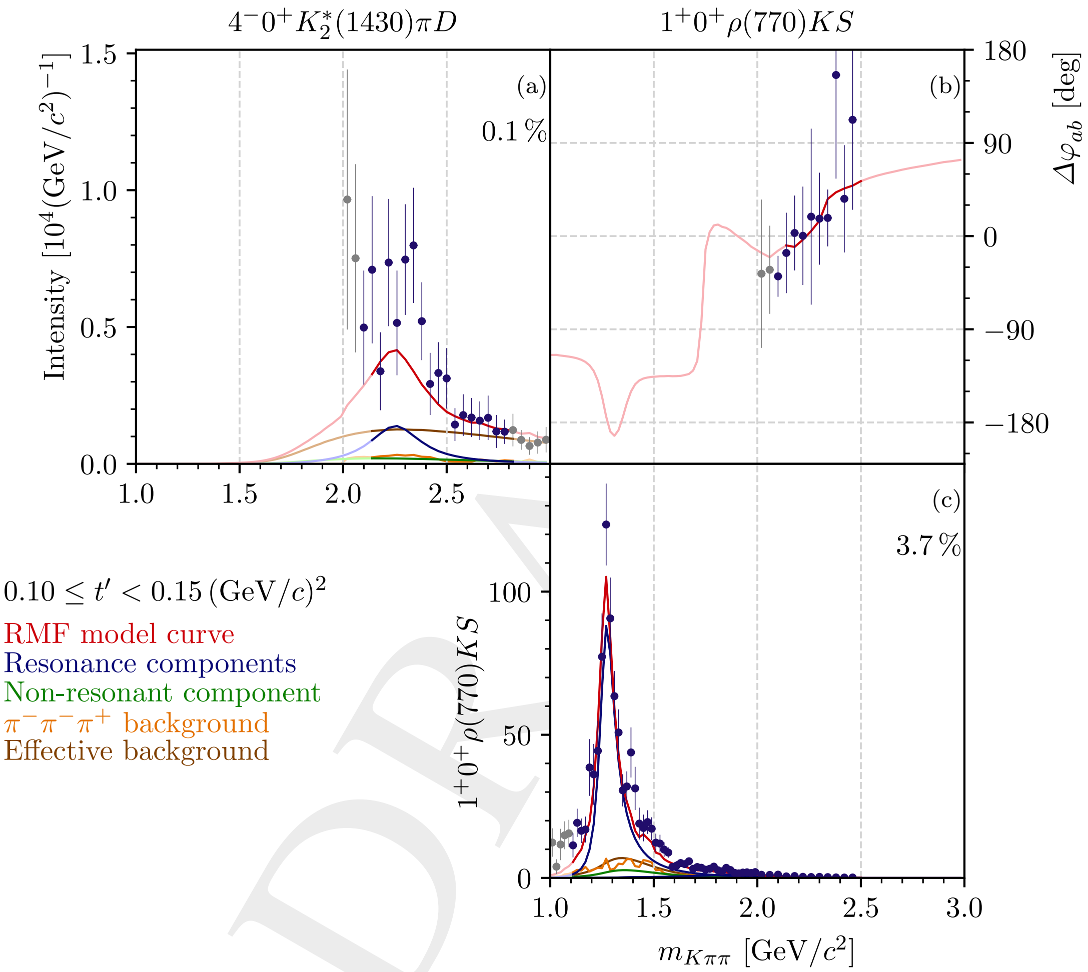

Figure 7.26: Same as figure 7.1, but showing the results of an extended RMF, where the $4^-\,0^+\,K_2^*(1430)\,\pi\,D$ wave was included in addition to the waves of the 10-wave RMF. The $1^+\,0^+\,\rho(770)\,K\,S$ wave serves as phase reference. The lowest t' bin in shown.

7.9 Further Interesting Partial Waves

In this section we summarize or findings in partial waves with J^P quantum numbers that are not discussed in sections 7.1 to 7.8. The PDG lists two excited K^* state, i.e. the $K^*(1410)$ and the $K^*(1680)$ [9]. Both are considered as established states.[ae] In our analysis, the 1^- waves are strongly affected by the leakage effect. Thus, we cannot study the $K^*(1410)$ in our analysis as it lies in the affected mass region. Figure 7.27a exemplarily shows the t'-summed intensity spectrum of the $1^- \, 1^+ \, \rho(770) \, K \, P$ wave. It exhibits an enhancement between about 1.6 and $1.9\,\mathrm{GeV}/c^2$, i.e. in the mass region of the $K^*(1680)$. However, this enhancement is not accompanied by a clear rise of the relative phases of this wave (not shown), which would indicate a $K^*(1680)$ signal in this wave. In general, we do not observe any clear resonance-like signals in $J^P = 1^-$ waves in our data. Hence, we did not study 1^- waves in RMFs.

The last group of partial waves that were not yet discussed are waves with high spins os $J \geq 5$. The PDG lists only one state with $J \geq 5$, the $K_5^*(2380)$, which has been seen so far only by the LASS experiment in the $K^-\pi^+$ final state [122]. In our analysis, we observe in all corresponding 5^- waves negligible intensity over the analyzed mass range (not shown). Hence, we do not observe a $K_5^*(2380)$ in our data. In general, the partial waves with $J \geq 5$ that were selected by the wave-set selection procedure in section 5.2 have only small intensity at the per-mill level. Most of these high-spin waves have a $K^-\pi^+$ isobar such as the $K^*(892)$. Figures 7.27b to 7.27d show exemplarily the t'-summed intensity spectra of three selected waves. Typically, the $m_{K\pi\pi} \lesssim 2\,\mathrm{GeV}/c^2$ regions exhibit a noncontinuous intensity spectrum, e.g. at about $1.9\,\mathrm{GeV}/c^2$ in figure 7.27c. We assume this mass region of the high-spin waves to be dominated by artifacts, because of three reasons: (i) it is partly affected by the leakage effect, (ii) the intensity spectra are sensitive to systematic effects, and (iii) we do not expect a state with $J \geq 5$ in this low-mass region. Above about $2\,\mathrm{GeV}/c^2$, the high-spin waves typically exhibit a broad bump in their intensity spectra. These broad intensity bumps are not accompanied by any clear phase motions. In general, we observe no evidence for resonances in the high-spin waves. However, more detailed studies might be able to reveal small resonance signals.

A possible explanation for the broad intensity bumps in the high-spin waves is that these waves are dominated by non-resonant contributions such as contributions from Deck-like reactions, which are described in section 2.1.1. We discussed the importance of high-spin waves to describe non-resonant contributions already when discussing the narrow peaks at $\cos\theta_{\mathrm{GJ}}^{K\pi} = +1$ and $\cos\theta_{\mathrm{GJ}}^{\pi\pi} = -1$ shown in figure 5.24. From the COMPASS $\pi^-\pi^-\pi^+$ analysis, where similar Deck-like non-resonant contributions appear, it is known that these contributions cause broad bumps in the intensity spectra of partial waves with high spin, which are not accompanied by pronounced phase motions [11, 124]. We expect qualitatively similar contributions from Deck-like reactions also in our analysis. Furthermore, given the much larger mass of the K^- compared to the π^-, we assume the contributions from Deck-like reactions with pion exchange shown in figure 2.2a to be dominant compared to the ones with kaon exchange shown in figure 2.2b. Deck-like reactions

[ae] Waves with $J^P = 1^-$ would be interesting to study, not only because they may exhibit excitations of the $K^*(892)$ ground state, but also because one of these excited states may be the strange partner of the spin-exotic $\pi_1(1600)$ resonance, which was observed e.g. in the COMPASS $\pi^-\pi^-\pi^+$ analysis [41].

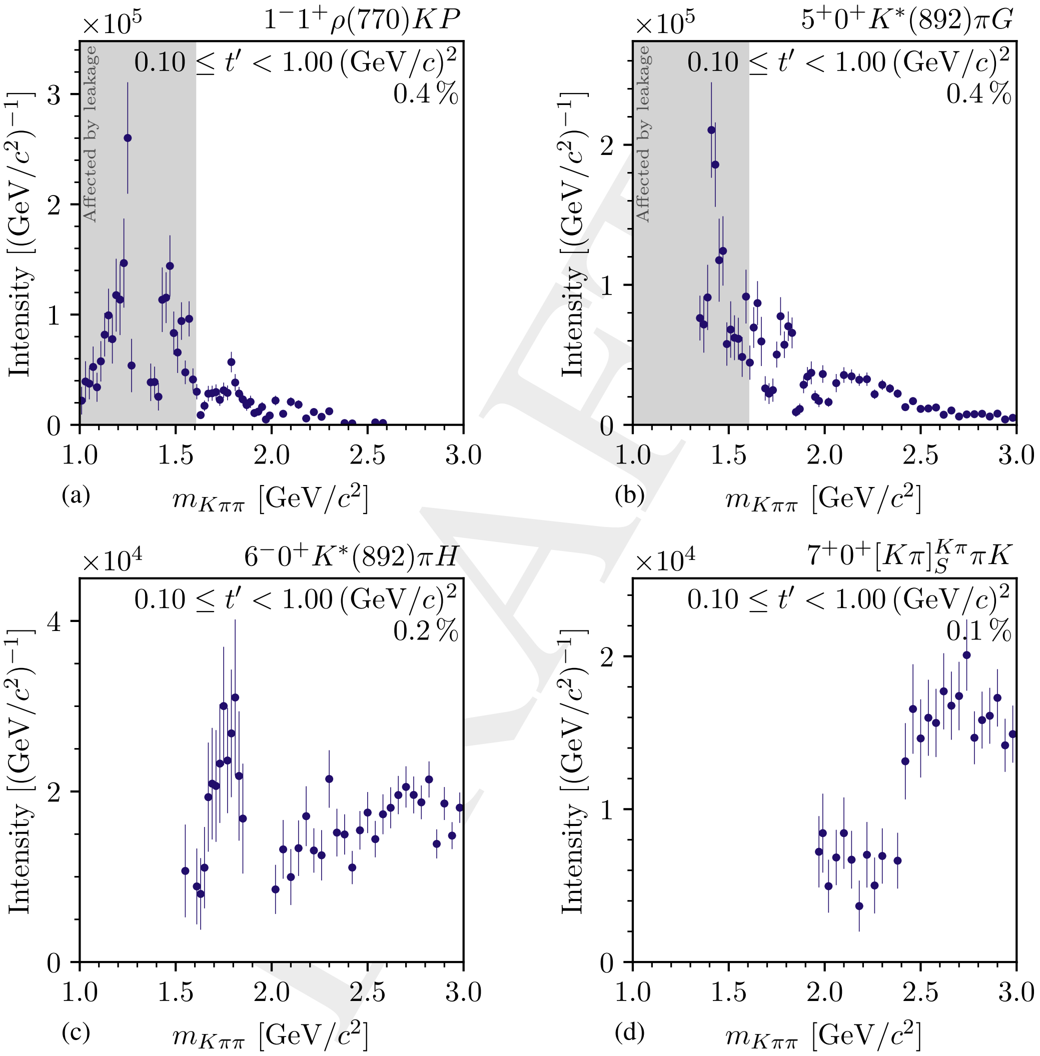

Figure 7.27: Same as figure 7.2, but showing the t'-summed intensity spectra of the $1^-\,1^+\,\rho(770)\,K\,P$ wave and of three high-spin waves with $J \geq 5$.

with pion exchange proceed via $K^{-}\pi^{+}$ isobars. Hence, the fact the most of the high-spin waves have a $K^{-}\pi^{+}$ isobar supports the hypothesis that the high-spin waves are dominated by Deck-like reactions.

8 The Freed-Isobar Analysis

The main focus of our analysis is the study of strange mesons appearing in the $K^-\pi^-\pi^+$ system as it was done in the conventional PWD and in the RMFs discussed in chapters 5 to 7. However, non-strange and strange light mesons appear also as isobars in the $\pi^-\pi^+$ and $K^-\pi^+$ subsystems, respectively. So far, this fact was used in the conventional PWD to disentangle the various decay modes of the strange mesons into the $K^-\pi^-\pi^+$ system by employing fixed parameterizations for the dynamic amplitudes of the corresponding isobars (see section 5.1.4). However, the appearance of light mesons in the $\pi^-\pi^+$ and $K^-\pi^+$ subsystems allows us to also study these states. Therefore, we performed so-called freed-isobar PWD fits. The freed-isobar approach was developed and successfully applied already in the COMPASS $\pi^-\pi^-\pi^+$ analysis [11, 39, 42, 125] and is similar to approaches called (Quasi-)Model-Independent-Partial-Wave-Analysis (Q)MIPWA applied in the analysis of multi-body heavy-meson and τ decays [26, 162].

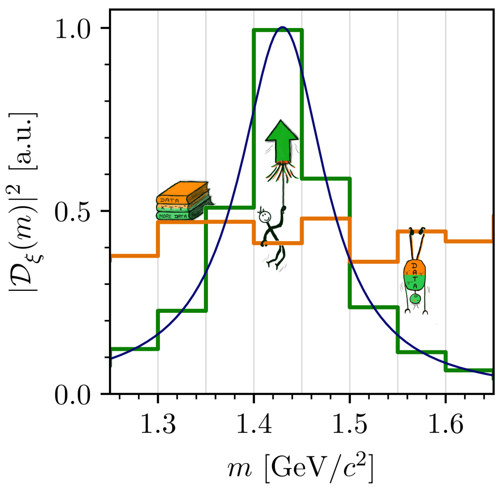

Figure 8.1: Schematic illustration of the freed-isobar method. The blue curve shows the intensity of a relativistic Breit-Wigner amplitude as used for the fixed isobar dynamic amplitudes as a function of the two-body mass. The horizontal orange lines represent the piecewise constant functions before the PWD fit to the data. The vertical gray lines indicate the mass bins. The horizontal green lines represent the piecewise constant functions after the PWD fit. In this illustration, the bins were chosen to be much wider than in the acutal analysis for better visualisation. From ref. [163].

In the freed-isobar PWD the fixed parameterizations for the dynamic amplitudes of the isobars (blue curve in figure 8.1) are replaced by piecewise constant functions in the two-body mass (orange lines in figure 8.1). The function values in the two-body mass bins are adopted to the data during the PWD fit. This parameterization is hence very flexible and does not make any assumptions on the resonance content in the particular two-body subsystem. In this way, we measure the amplitudes of $\pi^-\pi^+$ and $K^-\pi^+$ subsystems in the freed-isobar PWDs (green lines in figure 8.1). Although the dynamic amplitudes of the isobars are free in the freed-isobar PWDs, still the isobar model is employed. This means we consider the decay of a $K^-\pi^-\pi^+$ intermediate state with well-defined quantum numbers $J^P\, M^\varepsilon$ into a bachelor particle and into a $\pi^-\pi^+$ or $K^-\pi^+$ isobar two-body subsystem, which has a well-defined relative orbital angular momentum l between both particles. The species of isobar resonances appearing in the studied $\pi^-\pi^+$ and $K^-\pi^+$ subsystems are fully determined by l, i.e. their spin equals to l; their parity equals to $(-1)^l$; and their isospin equals to $1/2$ for $K^-\pi^+$ isobars, 1 for $\pi^-\pi^+$ isobars with odd spin, and 0 for $\pi^-\pi^+$ isobars with even spin. The bachelor particle and the isobar system have a well-defined relative orbital angular momentum L. Thus, in a freed-isobar PWD, we measure the $[\pi\pi]_l$ and $[K\pi]_l$ isobar amplitudes as a function of the invariant mass, i.e. $m_{\pi^-\pi^+}$ and $m_{K^-\pi^+}$, respectively, of the isobar system in a certain partial wave. We do this independently for each $(m_{K\pi\pi}, t')$ cell. This means, for each $(m_{K\pi\pi}, t')$ cell we measure an independent isobar amplitude. The formalism of the freed-isobar PWD is presented in appendix F.

As the freed-isobar approach increases drastically the number of free parameters of the PWD model, its application is possible only for high-precision data samples as it is the case for the COMPASS $\pi^-\pi^-\pi^+$ sample. Compared to the COMPASS $\pi^-\pi^-\pi^+$ sample, our $K^-\pi^-\pi^+$ sample is about 70 times smaller.[a] Hence, we cannot free the dynamic amplitudes of multiple isobars simultaneously as it was done in the COMPASS $\pi^-\pi^-\pi^+$ analysis [125]. Still, our $K^-\pi^-\pi^+$ sample is sufficiently large to perform proof-of-principle tests of the freed-isobar approach for single isobars. We performed four independent freed-isobar PWDs. In each, we freed only a single isobar dynamic amplitude; i.e. the $[\pi\pi]_P$, $[K\pi]_P$, $[K\pi]_D$, and $[K\pi]_S$ amplitudes; in a single partial wave, while keeping the other partial waves as in the conventional 238-wave PWD. Finally, we performed RMFs to the two-body mass dependence of the measured freed-isobar amplitudes in order to study their resonance content. As we performed no systematic studies yet, we cannot give systematic uncertainties for the parameter estimates of the isobar resonance. Hence, we give no uncertainties, and we quote the resonance parameters only rounded to a precision of 1 MeV$/c^2$. The results of the four freed-isobar analyses are discussed in sections 8.1 to 8.4.

[a] Here, we refer to the size of the COMPASS $\pi^-\pi^-\pi^+$ sample as used for the first freed-isobar PWD presented in ref. [39]. Compared to the COMPASS $\pi^-\pi^-\pi^+$ sample that was obtained in the improved analysis that will be presented in ref. [43], our $K^-\pi^-\pi^+$ sample is about 150 times smaller.

8.1 The $[\pi\pi]_P$ Amplitude

Among the isobars resonances that were considered in the conventional PWD (see table 5.2), the $\rho(770)$ is one of the best known states. Thus, studying the corresponding dynamic amplitude in the freed-isobar analysis and comparing the results to previous measurements of the $\rho(770)$ parameters allows us to verify the freed-isobar approach for our $K^-\pi^-\pi^+$ sample. The $\rho(770)$ dominantly decays to two pions, where the pion pair is in a P wave, i.e. the pions have one unit of orbital angular momentum. Hence, our goal is to determine the $[\pi\pi]_P$ amplitude by employing the freed-isobar PWD. The largest partial-wave with a $\rho(770)$ isobar is the $1^+\,0^+\,\rho(770)\,K\,S$ wave (see section 7.1). Thus, we performed a freed-isobar PWD, where we replaced the $1^+\,0^+\,\rho(770)\,K\,S$ wave included in the conventional 238-wave PWD by a freed $1^+\,0^+\,[\pi\pi]_P\,K\,S$ wave.

Figure 8.2 shows the measured $[\pi\pi]_P$ freed-isobar amplitude in two exemplarily selected $m_{K\pi\pi}$ bins in the lowest t' bin. The intensity spectrum of the $[\pi\pi]_P$ freed-isobar amplitude in the $m_{K\pi\pi}$ region of the K_1 double peak exhibits a clear pear at $m_{\pi^-\pi^+} \approx 0.75\,\text{GeV}/c^2$ (see figure 8.2a). The high-mass part of the peak is cut off by the phase-space border. As shown in figure 8.2b, the corresponding Argand diagram of the real and imaginary parts of the $[\pi\pi]_P$ freed-isobar amplitude exhibits a circle, which is characteristic for a Breit-Wigner like resonance. Figure 8.2c exemplarily shows the intensity spectrum of the $[\pi\pi]_P$ freed-isobar amplitude at higher $m_{K\pi\pi}$. It also exhibits a peak at $m_{\pi^-\pi^+} \approx 0.75\,\text{GeV}/c^2$, which is, however, more noisy. The corresponding Argand diagram does not show a clear circle starting at the origin. However, a circle-like shape may be recognized, whose starting point is shifted away from the origin. Such a shift may be caused by a background contribution to this amplitude.

The red curves in figure 8.2 represent the result of an RMF to the measured $[\pi\pi]_P$ freed-isobar amplitude, which we modeled by a single Breit-Wigner component. The RMF reproduces well the $[\pi\pi]_P$ amplitude in the $m_{K\pi\pi}$ region of the K_1 double peak. We obtained a mass of about $766\,\text{MeV}/c^2$ and a $\rho(770)$ width of about $148\,\text{MeV}/c^2$. Both values are close to the corresponding PDG average values of $(769.0 \pm 0.9)\,\text{MeV}/c^2$ and $(150.9 \pm 1.7)\,\text{MeV}/c^2$ [9]. In the higher $m_{K\pi\pi}$ region shown in figures 8.2c and 8.2d, the RMF cannot reproduce the $[\pi\pi]_P$ freed-isobar amplitude as the RMF model consists of only a Breit-Wigner resonance component without a background component. However, one should note that the $m_{\pi^-\pi^+}$ position of the peak in the intensity spectrum agrees well with the expected position of the $\rho(770)$ peak also in the higher $m_{K\pi\pi}$ region shown in figures 8.2c and 8.2d. Furthermore, the agreement between the RMF and the measured $[\pi\pi]_P$ freed-isobar amplitude is better again for $m_{K\pi\pi} \gtrsim 1.7\,\text{GeV}/c^2$. We cannot observe clear indications for excited ρ states in the measured $[\pi\pi]_P$ freed-isobar amplitude.

In summary, the $[\pi\pi]_P$ freed-isobar amplitude from the $1^+\,0^+\,[\pi\pi]_P\,K\,S$ partial wave exhibits a clear $\rho(770)$-like signal, whose mass and width agree with previous measurements. This proves that the freed-isobar approach works in principle, even for our comparatively small $K^-\pi^-\pi^+$ sample. Furthermore, this demonstrates the applicability of the isobar model and of the $\rho(770)$ Breit-Wigner parameterization with mass and width taken from the PDG in the conventional

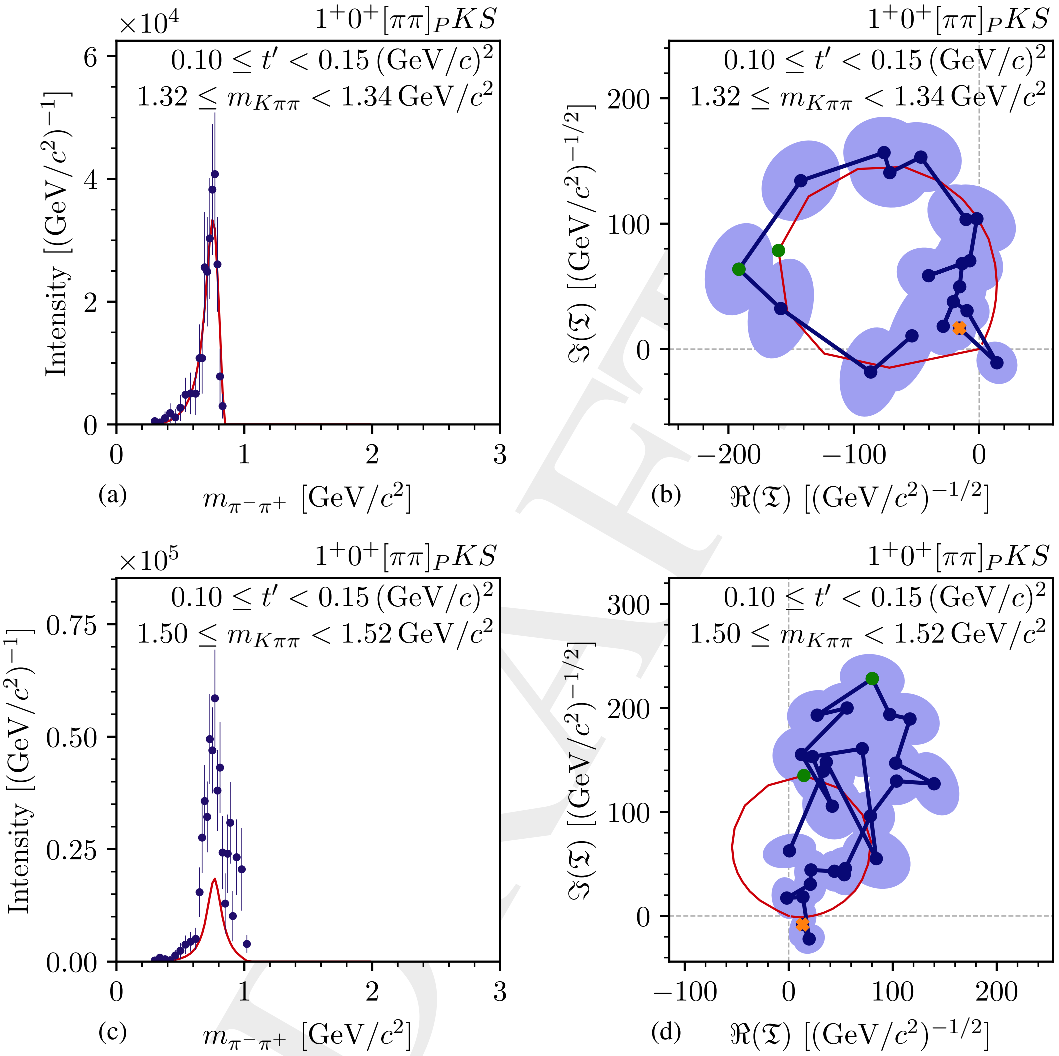

Figure 8.2: Intensities (left column) and Argand diagram (right column), i.e. real vs. imaginary parts of the $[\pi\pi]_P$ freed-isobar amplitude in the $1^+\,0^+\,[\pi\pi]_P\,K\,S$ wave at $m_{K\pi\pi} \approx 1.33\,\mathrm{GeV}/c^2$ (top row) and $m_{K\pi\pi} \approx 1.51\,\mathrm{GeV}/c^2$ (bottom row) in the lowest t' bin. The blue data points represent the result of the freed-isobar PWD. In (b) and (d), the blue shaded areas represent the corresponding uncertainty ellipses and the orange crosses indicate the data point that corresponds to the lowest $m_{\pi^-\pi^+}$ bin, i.e. the start point of the Argand diagram. The red curves are the model curves from an RMF to the measured $[\pi\pi]_P$ freed-isobar amplitude. The green data points and the corresponding green points on the model curves indicate the $m_{\pi^-\pi^+}$ bin that is closest to the nominal mass of the $\rho(770)$ resonance as obtained in the RMF.

fixed-isobar PWD. Additional effects, such as final-state interactions, i.e. rescattering within the three-body final state,[b] seem to have only a minor influence on the dynamic amplitude of the isobars in the reaction $K^- + p \to K^-\pi^-\pi^+ + p$. Hence, the freed-isobar analysis of the $[\pi\pi]_P$ amplitude confirms in a model-independent way our observation of the $K_1(1270)$ and K_1' decays to the $\rho(770)K$ final state, which are discussed in section 7.1.

8.2 The $[K\pi]_P$ Amplitude

Besides the $\rho(770)$, also the $K^*(892)$ is a well-known state, which decays dominantly to the $K^-\pi^+$ final state where both are in a P wave. We study the corresponding $[K\pi]_P$ freed-isobar amplitude in the largest partial wave with a $K^*(892)$ isobar, which is the $1^+\,0^+\,K^*(892)\,\pi\,S$ wave. Hence, we performed a freed-isobar PWD, where we replaced the $1^+\,0^+\,K^*(892)\,\pi\,S$ and $1^+\,0^+\,K^*(1680)\,\pi\,S$ waves included in the conventional 238-wave PWD by a freed $1^+\,0^+\,[K\pi]_P\,\pi\,S$ wave. However, one should note that both replaced waves are affected by the leakage effect in the conventional PWD. Thus, the leakage effect may also bias the results of the freed-isobar PWD for the $[K\pi]_P$ amplitude.

Figure 8.3 shows the measured $[K\pi]_P$ freed-isobar amplitude in two exemplarily selected $m_{K\pi\pi}$ bins in the lowest t' bin. The intensity spectrum of the $[K\pi]_P$ freed-isobar amplitude exhibits a clear narrow peak at $m_{K^-\pi^+} \approx 0.9\,\text{GeV}/c^2$ as shown in figure 8.3a for the $m_{K\pi\pi}$ region of the $K_1(1400)$. The corresponding Argand diagram exhibits a circle as expected for the $K^*(892)$ resonance (see figure 8.3b). Figures 8.3c and 8.3d show the $[K\pi]_P$ amplitude in a higher $m_{K\pi\pi}$ bin. Also here, we observe a clear $K^*(892)$ peak in the intensity spectrum and a circle in the Argand diagram. In addition, we observe a small high-mass shoulder at $m_{K^-\pi^+} \approx 1.2\,\text{GeV}/c^2$.

The red curves in figure 8.3 represent the result of an RMF to the measured $[K\pi]_P$ freed-isobar amplitude, which we modeled by a single Breit-Wigner component. The RMF reproduces well the intensity spectra of the $[K\pi]_P$ freed-isobar amplitude over the analyzed $m_{K\pi\pi}$ range. Also, the Argand diagrams are overall reproduced well. However, at higher $m_{K\pi\pi}$, the Argand diagram of the $[K\pi]_P$ freed-isobar amplitude appears to be rotated and shifted with respect to the RMF curve (see figure 8.3d). As for the $[\pi\pi]_P$ freed-isobar amplitude discussed in section 8.1, this rotation and shift may indicate small background contributions to the measured $[K\pi]_P$ freed-isobar amplitude. For $m_{K^-\pi^+} > 1\,\text{GeV}/c^2$, the $[K\pi]_P$ intensity exhibits an enhancement over the RMF curve, which includes only the $K^*(892)$. However, in additional RMFs we could not model sufficiently well this $m_{K^-\pi^+}$ region by the excited $K^*(1410)$ and $K^*(1680)$, which are both listed as established states by the PDG [9]. Hence, we do not observe clear signals of excited K^* states in the measured $[K\pi]_P$ freed-isobar amplitude. We obtained a mass for the $K^*(892)$ component of about $895\,\text{MeV}/c^2$ and a width of about $49\,\text{MeV}/c^2$. Both values agree well with the corresponding PDG average values of $(895.55 \pm 0.20)\,\text{MeV}/c^2$ and $(47.3 \pm 0.5)\,\text{MeV}/c^2$, respectively.

[b] See ref. [164] for a discussion on effects from final-state interactions on the amplitudes of two-body subsystems in three-body decays of heavy mesons.

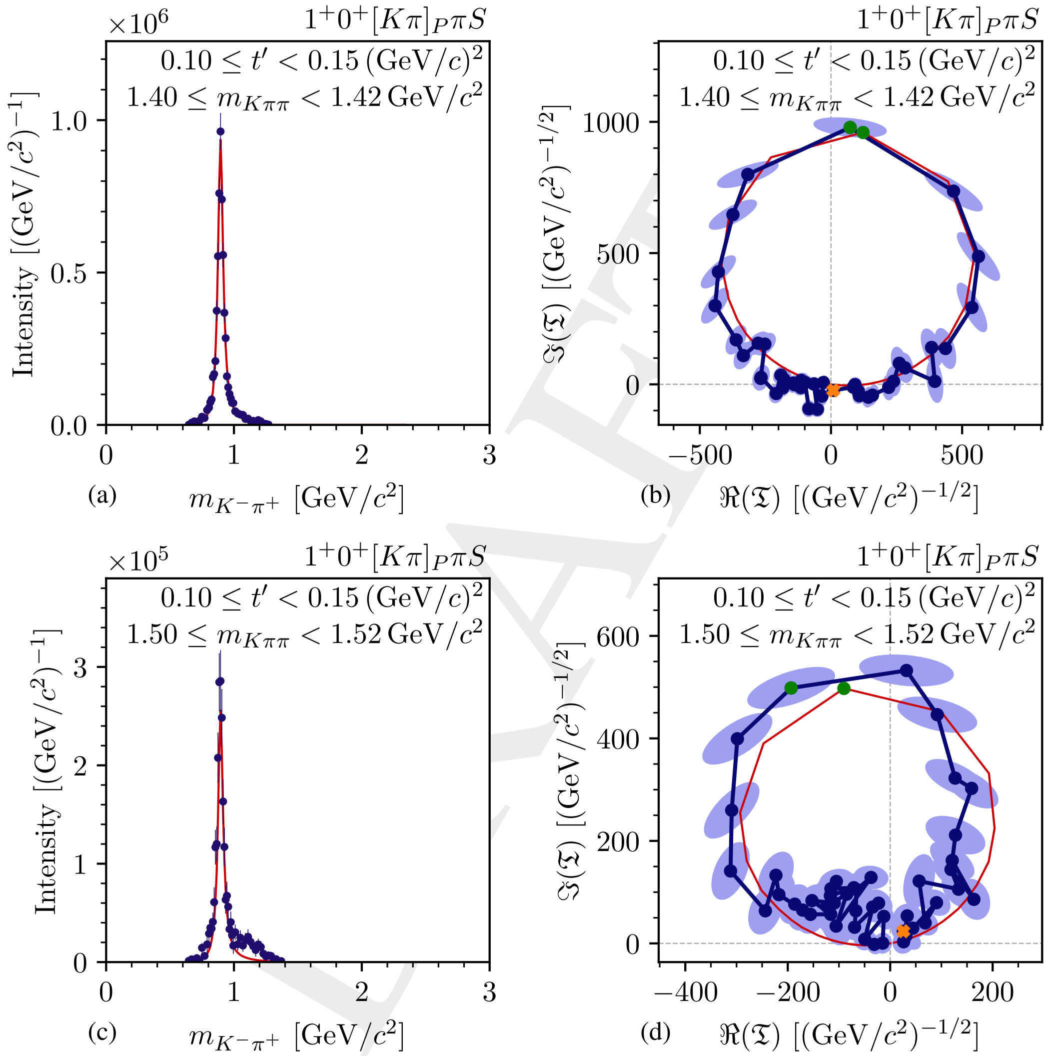

Figure 8.3: Same as figure 8.2, but showing the $[K\pi]_P$ freed-isobar amplitude from the freed $1^+\,0^+$ $[K\pi]_P\,\pi\,S$ wave at $m_{K\pi\pi} \approx 1.41\,\mathrm{GeV}/c^2$ (top row) and $m_{K\pi\pi} \approx 1.51\,\mathrm{GeV}/c^2$ (bottom row) in the lowest t' bin.

In summary, we observe a clear $K^*(892)$ signal in the $[K\pi]_P$ freed-isobar amplitude as determined from the freed-isobar PWD, whose mass and width agree with previous measurements, and we do not observe pronounced signals from excited $K^*(1410)$ or $K^*(1680)$. This further confirms the applicability of the freed-isobar approach to our $K^-\pi^-\pi^+$ sample and demonstrates that the PDG average values for the $K^*(892)$ mass and width used in the conventional PWD are consistent with our data. This good agreement is somewhat surprising and means that the leakage effect does not seem to induce a large bias on the shape of the measured $[K\pi]_P$ freed-isobar amplitude.

8.3 The $[K\pi]_D$ Amplitude

In our analysis, the $K_2^*(1430)$ appears not only in the $K^-\pi^-\pi^+$ system in partial waves with $J^P = 2^+$ (see section 7.2), but also in the $K^-\pi^+$ subsystem as an isobar. In order to study the $K_2^*(1430)$ also in the $K^-\pi^+$ subsystem, we measured the $[K\pi]_D$ amplitude in a freed-isobar analysis. The largest wave in the 238-wave set with a $K_2^*(1430)$ isobar is the $2^-\,0^+\,K_2^*(1430)\,\pi\,S$ wave. However, it still has a small relative intensity of only 1.2 %. We performed a freed-isobar PWD, where we replaced the $2^-\,0^+\,K_2^*(1430)\,\pi\,S$ wave included in the conventional 238-wave PWD by a freed $2^-\,0^+\,[K\pi]_D\,\pi\,S$ wave.

Figure 8.4 shows the measured $[K\pi]_D$ freed-isobar amplitude in an exemplarily selected $m_{K\pi\pi}$ bin at the $K_2(1770)$ in the lowest t' bin. The intensity spectrum of the $[K\pi]_D$ freed-isobar amplitude exhibits a clear peak at $m_{K^-\pi^+} \approx 1.4\,\mathrm{GeV}/c^2$. The corresponding Argand diagram show a circle as expected for the $K_2^*(1430)$ resonance.

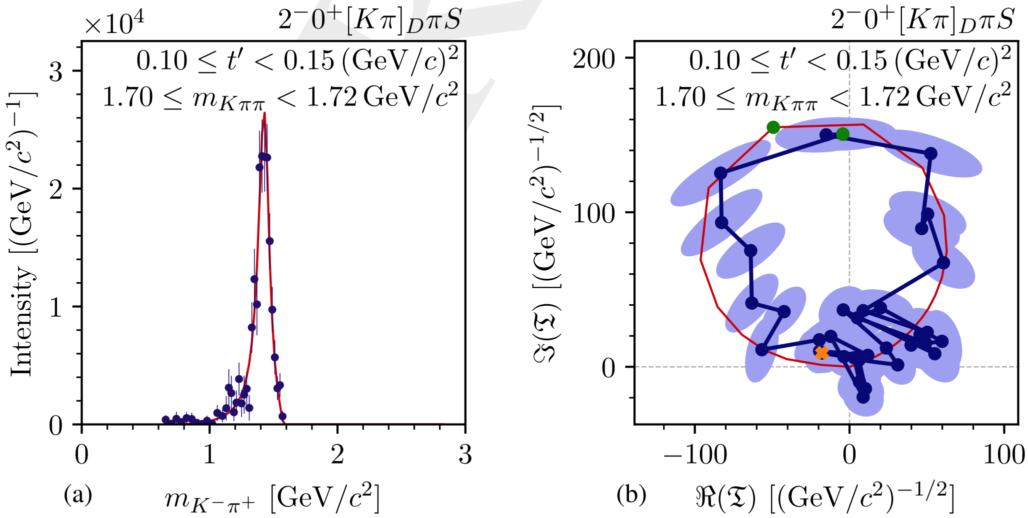

Figure 8.4: Same as figure 8.2, but showing the $[K\pi]_D$ freed-isobar amplitude from the freed $2^-\,0^+$ $[K\pi]_D\,\pi\,S$ wave at $m_{K\pi\pi} \approx 1.73\,\mathrm{GeV}/c^2$ in the lowest t' bin.

The red curves in figure 8.4 represent the result of an RMF to the measured $[K\pi]_D$ freed-isobar amplitude, which we modeled by a single Breit-Wigner component. The RMF reproduces well the intensity spectra of the $[K\pi]_D$ freed-isobar amplitude over the analyzed $m_{K\pi\pi}$ range as exemplarily shown in figure 8.4a. Also, the Argand diagrams are reproduced well. From the freed-isobar analysis, we obtained a mass of the $K_2^*(1430)$ component of about $1430\,\mathrm{MeV}/c^2$ and a width of about $106\,\mathrm{MeV}/c^2$, which are in good agreement with our estimates for the mass and width of the $K_2^*(1430)$ in the $K^-\pi^-\pi^+$ decay as obtained from the conventional PWD (see section 7.2). Given that we study the neutral $K_2^*(1430)$ in the $K^-\pi^+$ decay and the charged $K_2^*(1430)$ in the $K^-\pi^-\pi^+$ decay and considering that both measurements yielded the same mass, we do not observe a significant mass difference between the neutral and the charged $K_2^*(1430)$ as indicated by the PDG average values (see discussion in section 7.2). We do not observe any pronounced signal from an excited $K_2^*(1980)$ in our data.

In summary, the $[K\pi]_D$ freed-isobar amplitude exhibits a clear $K_2^*(1430)$ signal. This demonstrates that the freed-isobar approach works even for small waves at the percent level, such as the $2^-\,0^+\,K_2^*(1430)\,\pi\,S$ wave, and confirms the partial waves with a $K_2^*(1430)$ resonance in the conventional PWD.

8.4 The $[K\pi]_S$ Amplitude

Among the isobar subsystems that can be studied in the freed-isobar analysis, the $[K\pi]_S$ freed-isobar amplitude is of special interest. It plays a major role in multi-body final states with a $K\pi$ subsystem as the $K^-\pi^-\pi^+$ final state studied here, but also in many other analyses [26, 162, 165, 166]. At the same time, the analytical structure of the $[K\pi]_S$ amplitude is complicated and not yet well-known. It is hence in the focus of theoretical investigations [98, 101, 167].

The largest wave in the 238-wave set with a $[K\pi]_S^{K\pi}$ isobar is the $0^-\,0^+\,[K\pi]_S^{K\pi}\,\pi\,S$ wave with a relative intensity of 5.0 %. Hence, we performed a freed-isobar PWD, where we replaced the $0^-\,0^+\,[K\pi]_S^{K\pi}\,\pi\,S$ and $0^-\,0^+\,[K\pi]_S^{K\eta}\,\pi\,S$ waves included in the conventional 238-wave PWD by a freed $0^-\,0^+\,[K\pi]_S\,\pi\,S$ wave.

Figure 8.5 shows the measured $[K\pi]_S$ freed-isobar amplitude in three exemplarily selected $(m_{K\pi\pi}, t')$ cells. At $m_{K\pi\pi} \approx 1.73\,\mathrm{GeV}/c^2$, the $[K\pi]_S$ intensity spectrum shown in figure 8.5a exhibits a peak at $m_{K^-\pi^+} \approx 1.4\,\mathrm{GeV}/c^2$ with a pronounced low-mass shoulder reaching down to the phase-space border. The corresponding Argand diagram is shown in figure 8.5b. It exhibits a deformed half-circle in the $m_{K^-\pi^+}$ region of the $1.4\,\mathrm{GeV}/c^2$ peak. In the $m_{K^-\pi^+}$ region of the low-mass shoulder, the amplitude in the Argand diagram moves only slowly with a bulge. Both, the intensity spectrum and the Argand diagram show similarities to the fixed $[K\pi]_S^{K\pi}$ isobar dynamic amplitude used in the conventional PWD (see figure 5.5).[c] Hence, the $1.4\,\mathrm{GeV}/c^2$

[c] The measured $[K\pi]_S$ freed-isobar amplitude also includes phase-space effects, in contrast to the fixed $[K\pi]_S^{K\pi}$ isobar dynamic amplitude shown in figure 5.5. However, these phase-space effects are only slowly changing with mass and not introduce peaks.

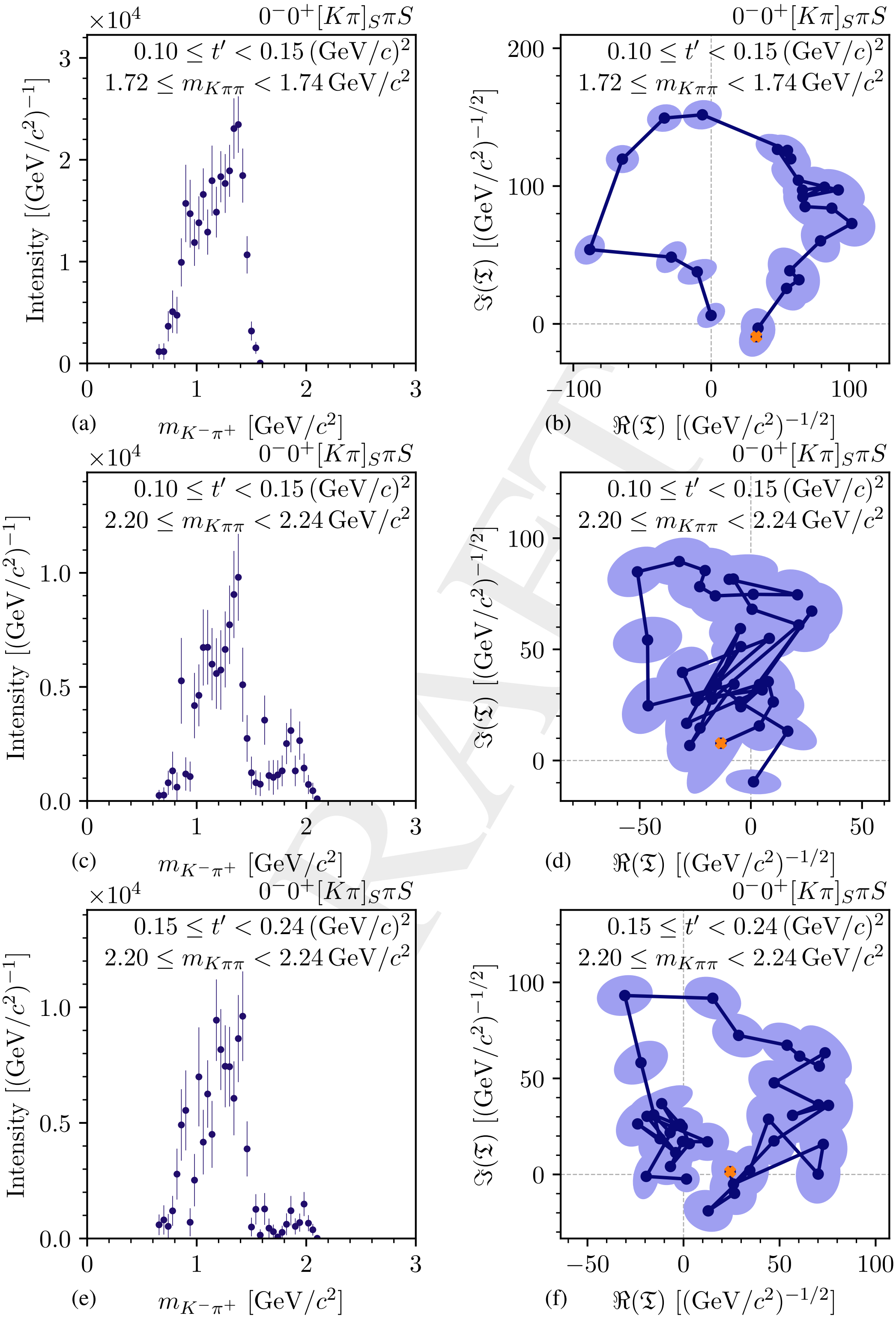

Figure 8.5: Same as figure 8.2, but showing the $[K\pi]_S$ freed-isobar amplitude in the $0^-\,0^+\,[K\pi]_S\,\pi\,S$ wave at $m_{K\pi\pi} \approx 1.73\,\mathrm{GeV}/c^2$ (top row) and $m_{K\pi\pi} \approx 2.22\,\mathrm{GeV}/c^2$ (middle row) in the lowest t' bin and at $m_{K\pi\pi} \approx 2.22\,\mathrm{GeV}/c^2$ in the second-lowest t' bin (bottom row).

peak indicates a $K_0^*(1430)$ signal in our data and the low-mass shoulder is presumably driven by the $K_0^*(700)$.

At higher $m_{K\pi\pi}$, we still observe the same features in the intensity spectra and the Argand diagram for $m_{K^-\pi^+} \lesssim 1.6\,\text{GeV}/c^2$ as exemplarily shown in figures 8.5c to 8.5f for $m_{K\pi\pi} \approx 2.22\,\text{GeV}/c^2$ in the two lowest t' bins. In the—now accessible—$m_{K^-\pi^+} \gtrsim 1.6\,\text{GeV}/c^2$ region, the intensity spectra of the $[K\pi]_S$ freed-isobar amplitude exhibit another peak at about $1.9\,\text{GeV}/c^2$ (see figures 8.5c and 8.5e). This peak is accompanied by structures at the end of the Argand diagrams, which are clearest in the $(m_{K\pi\pi}, t')$ cell shown in figure 8.5f. However, due to the limited precision of our $K^-\pi^-\pi^+$ sample, we cannot resolve a clear circle at $m_{K^-\pi^+} \approx 1.9\,\text{GeV}/c^2$, which would clarify the resonance character of the intensity peak. Still, the peak at $m_{K^-\pi^+} \approx 1.9\,\text{GeV}/c^2$ is an indication for a possible $K_0^*(1950)$ isobar signal in our data.

In summary, the similarities of the measured $[K\pi]_S$ freed-isobar amplitude to the fixed model used for the $[K\pi]_S^{K\pi}$ and $[K\pi]_S^{K\eta}$ dynamic amplitudes indicate the observation of $K_0^*(700)$, $K_0^*(1430)$, and possibly $K_0^*(1950)$ signals in our data. Since in particular the $K_0^*(700)$ and $K_0^*(1430)$ are overlapping due to their large widths, the modeling of the $[K\pi]_S$ freed-isobar amplitude would require a more elaborate RMF model than a simple sum of Breit-Wigner amplitudes. With the help of such a more elaborate model, we could also measure the properties of the K_0^* sates, i.e. their pole parameters. Furthermore, the freed $0^-\,0^+\,[K\pi]_S\,\pi\,S$ wave has an isotropic distribution in all decay angles.[d] As an isotropic distribution is less characteristic and thus harder to distinguish, e.g. from background, we expect the $[K\pi]_S$ wave to be more likely affected by systematic effects or analysis artifacts. This would need to be studied in dedicated systematic and pseudodata studies, which are beyond the scope of this work. However, the first glimpse on the $[K\pi]_S$ freed-isobar amplitude presented in this section, as well as the consistent results from the three other freed-isobar analyses, demonstrate that the COMPASS $K^-\pi^-\pi^+$ sample has the potential to also deepen our knowledge about the $[\pi\pi]_P$, $[K\pi]_P$, $[K\pi]_D$, and $[K\pi]_S$ systems.

[d] The orbital angular momentum L in the isobar-bachelor system is 0 as well as the orbital angular momentum in the $K^-\pi^+$ isobar subsystem.

9 Conclusions and Outlook

We employed the diffractive-scattering reaction $K^- + p \to K^-\pi^-\pi^+ + p$ to explore the excitation spectrum of strange mesons based on a data sample that was collected during the 2008 and 2009 diffraction data-taking campaigns of the COMPASS experiment. The event selection was based on an unpublished study of this reaction at COMPASS [44] and was considerably improved. One of the major challenges of this event selection is the separation of beam kaons from the about 36 times larger pion contribution in the beam. To this end, we developed a novel likelihood-based approach that exploits the full information from both CEDAR detectors. Our approach yields an excellent performance for beam-kaon identification with an efficiency of about 85 %—about twice as large as the efficiency of the previously used method—while maintaining a low impurity from pions of about 3 %. Our optimized event selection yields the so far world's largest $K^-\pi^-\pi^+$ sample of 720 949 events, which is about 3.6 times larger than the previously world's largest $K^-\pi^-\pi^+$ sample obtained by the WA3 experiment at CERN [23].

Based on this data sample, we performed a partial-wave decomposition (PWD), where we extract the $m_{K\pi\pi}$ and t' dependence of the transition amplitudes of partial waves with well-defined quantum numbers and decay modes of the $K^-\pi^-\pi^+$ system. We inferred the set of partial waves that need to be included in the PWD model from the data. To this end, we started with a large pool of 596 allowed waves considering spins up to $J = 7$. To select those waves that significantly contribute to the data, we added regularization terms to the likelihood function that are based on model-selection techniques to select those waves that significantly contribute to the data. In comparison to previous analyses applying model-selection techniques [67, 108], we extended the approach by incorporating effects from the experimental acceptance in the regularization terms and by imposing continuity in $m_{K\pi\pi}$ for the selected wave sets. Both extensions clearly improved the selected wave sets. Furthermore, we improved the estimates for the parameter values and their uncertainties determined from the PWD by using Bootstrapping techniques starting at the event-sample level. In addition, we performed first studies of applying the freed-isobar technique, which allowed us to study for the first time the amplitudes of the $K^-\pi^+$ and $\pi^-\pi^+$ subsystems in the diffractively produced $K^-\pi^-\pi^+$ final state.

We observe artificially enhanced partial-waves intensities in a limited set of partial waves for $m_{K\pi\pi} \lesssim 1.6\,\mathrm{GeV}/c^2$. These artifacts are caused by the loss of information due to the limited kinematic coverage of our final-state particle identification. This so-called leakage effect limits the physics reach of our analysis. However, we could clearly identify waves affected by the leakage effect using three different approaches, which yielded consistent results. This allowed us to still study strange mesons in the large set of non-leakage waves, which covers a variety of J^P sectors and decay modes.

We searched for strange mesons and measured their masses and widths by performing resonance-model fits (RMFs) to the spin-density matrix elements of selected waves, which were extracted by the conventional and the freed-isobar PWDs. For the main analysis, we selected a subset of 10 partial waves, which included 7 resonance components. We extended this 10-wave RMF model in dedicated studies of further resonances. To construct the RMF models, we employed Breit-Wigner amplitudes. It is worth stressing that we obtained our estimates for the masses and widths of the strange mesons by fitting simultaneously a large set of partial waves from different J^P sectors taking into account all interference terms between these partial waves. We also freed the mass and width parameters for all studied strange-meson resonances,[a] in contrast to many previous analyses [23, 24, 26, 27, 30].

One of the major challenges of our analysis is the treatment of incoherent background in our $K^-\pi^-\pi^+$ sample. We developed an ansatz where we effectively treat these incoherent background contributions at the level of the PWD and explicitly model them in the RMFs. The largest incoherent background of about 6.7 % arises from events of the reaction $\pi^- + p \to \pi^-\pi^-\pi^+ + p$. We take into account this background component by employing a high-quality model obtained by the analysis of the COMPASS $\pi^-\pi^-\pi^+$ sample [43].

Finally, we performed extensive studies to verify our analysis approach and to estimate systematic effects. We performed a variety of pseudodata studies of the PWD and RMF. With these studies we showed the self-consistency of our analysis. For example, we performed an input-output studied by applying our full analysis chain to a pseudodata sample that includes resonances with known masses and widths. Then we measured these masses and widths again in the RMF. Especially noteworthy, we demonstrated that we can separate $K^-\pi^-\pi^+$ signals from $\pi^-\pi^-\pi^+$ background by mixing pure $K^-\pi^-\pi^+$ and $\pi^-\pi^-\pi^+$ pseudodata samples. We performed also a first set of systematic studies covering potential influences from the event selection, the PWD model, and the 10-wave RMF model. From these studies, we obtained lower bounds for systematic uncertainties, which are typically of comparable size as the statistical uncertainties.

In summary, we performed the so-far most comprehensive analysis of the $K^-\pi^-\pi^+$ final state. We determined the parameters of 7 strange mesons by simultaneously fitting the intensities and interference terms of 10 selected waves. The parameters of 6 further strange mesons were determined in dedicated studies. Finally, the $\rho(770)$, $K^*(892)$, and $K_2^*(1430)$ mesons appearing in the $\pi^-\pi^+$ and $K^-\pi^+$ subsystems were studied in freed-isobar analyses. In total, the extracted resonances cover almost all J^P sectors as shown in figure 9.1. This way we obtained the so-far most complete picture of the strange-meson spectrum coming from a single analysis.

We observe signals of well-known strange mesons, such as the $K_1(1270)$ and the K_J^* states, but also of states that need further confirmation, such as the $K_2(2250)$, in the partial-wave intensities and in the interference terms represented by the relative phases. Given the large size of our $K^-\pi^-\pi^+$ sample we could study small signals down to the per-mil level such as the $K_4^*(2045)$. By binning our data in t', we also studied the t' dependencies of the extracted resonances,

[a] The $K_1(1400)$ could not be studied, because it is only a very small signal in the analyzed 1^+ waves. We had to fix the parameters of the corresponding component to the PDG average values in the RMFs.

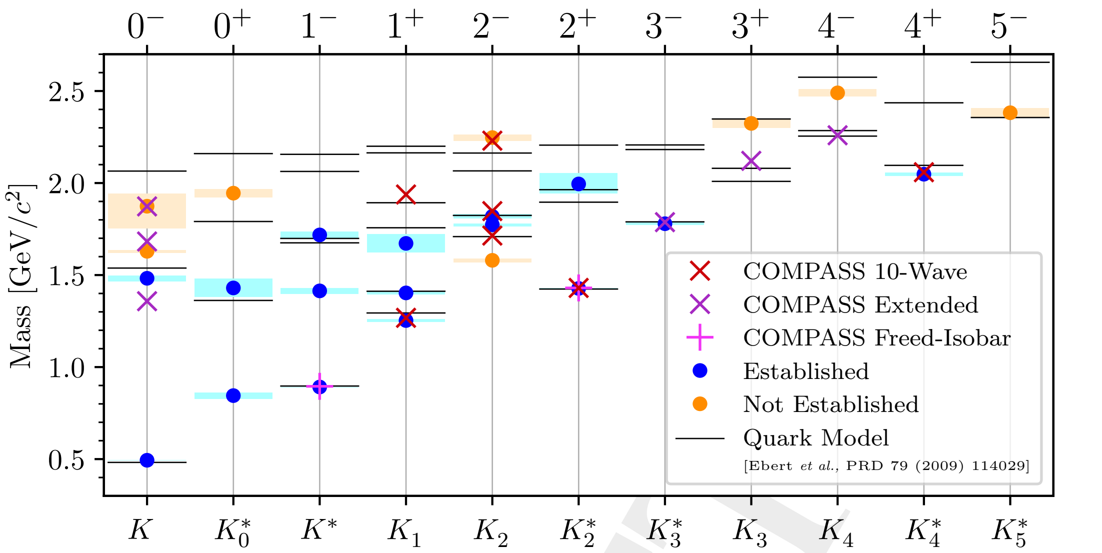

Figure 9.1: Spectrum of strange mesons, i.e. nominal masses of strange mesons grouped by their J^P quantum numbers. The crosses represented our measured mass values as obtained from the 10-wave RMF (red) or from the corresponding dedicated studies (violet) (see chapter 7). The magenta pluses represent our measured mass values as obtained from the freed-isobar analysis (see chapter 8). Analogously to figure 1.1, the blue data points show the masses of established states, the orange data points those of not established states as listed by the PDG [9]. The similarly colored boxes represent the corresponding uncertainties. The black horizontal lines show the masses of states as predicted by the quark-model calculation in ref. [10]. As we show only masses below 2.7 GeV/c^2 for a better visualization, the not-established $K(3100)$ is omitted here.

which typically show the expected behavior. This supports the resonance nature of the observed signals. In most cases, our estimates for the masses and widths of the 14 studied strange mesons agree with previous measurements and with quark-model calculations (see figure 9.1). Our uncertainties for most of the measured masses and widths are competitive with the corresponding so far best measurements of these parameters. For the widths of the $K_4^*(2045)$ and $K_2(1820)$, we obtained even the so far smallest uncertainties.[b]

Our analysis not only provides a high-precision measurement of the masses and widths, but also adds complementary information. For example, we performed the first search[c] for the $K_2(2250)$ in final states other than $\overset{(-)}{\Lambda}\overset{(-)}{p}$. In contrast to previous analyses of the $J^P = 2^-$ sector [24, 30, 31, 34–37, 152–155], we studied a wide mass range in a single self-consistent analysis by including three K_2 states and by simultaneously fitting four 2^- partial waves, which represent different decay modes. Similarly, we also studied the $K_3(2320)$ and $K_4(2500)$ for the first time in final states other than $\overset{(-)}{\Lambda}\overset{(-)}{p}$.

[b] Disregarding measurements that were not included in the corresponding PDG average and measurements for which it is not clear whether their uncertainties include systematic uncertainties, we obtained in addition the so far smallest uncertainties for the masses of the K_1', $K_2(1770)$, $K_2(1820)$, and $K_4^*(2045)$, and for the widths of the K_1' and $K_2(1770)$.

[c] According to the PDG listing [9].

Furthermore, we performed a first study of excited pseudoscalar kaons over a wide mass range in a single analysis. We find indications for three excited pseudoscalar kaons; i.e. the $K(1460)$, the $K(1630)$, and the $K(1830)$; while quark-model calculations predict only two states in this mass region. Especially, the $K(1630)$ signal is the clearest among these three signals and is least compatible with the two quark-model states (see figure 9.1). This suggests that the $K(1630)$ is a supernumerary state and thus a candidate for a crypto-exotic state.

Another way to represent our results is in the form of a Chew-Frautschi plot as shown in figure 9.2. As first discussed by Chew and Frautschi [45], mesons group into families, which lie on so-called Regge trajectories. It is a long-known experimental observation that these Regge trajectories correspond to approximately straight lines in the Chew-Frautschi plot [46].[d]

Also, our measurements of strange mesons nicely group into three families in the Chew-Frautschi plot, i.e. the K_J^* ground states, the K_J ground states, and the K_J excited states. The members of these three families follow approximately linear Regge trajectories,

$$J(m_0) = \alpha_0 + \alpha' m_0^2, \tag{9.1}$$

which are represented by the orange, green, and blue lines in figure 9.2.[e] Table 9.1 lists the parameters of all three Regge trajectories.[f] Our estimates for the parameters of the Regge trajectories are in agreement with those determined from a quark-model calculation in ref. [10] and with those determined from previous measurements in ref. [170], except for the trajectory of the K_J excited states, which has a slightly smaller slope value in our case and a larger intersect.[g] In summary, our analysis yields a Chew-Frautschi plot with three Regge trajectories up to high meson spins of $J = 4$, and gives a consistent picture of the strange-meson spectrum. This again demonstrates that we explored a large fraction of the known strange-meson spectrum at COMPASS using data from only a single reaction $K^- + p \to K^-\pi^-\pi^+ + p$.

9.1 Outlook and Further Prospects

In this work, we performed a first set of systematic studies. In order to obtain estimates for the full systematic uncertainties, a complete set of systematic studies has to be performed in a further analysis. Obtaining such a complete set of systematic studies was not possible within the

[d] Also, QCD string models [168] and calculations using Salpeter equations [169] predict linear Regge trajectories. More detailed studies allow for a non-zero curvature of the Regge trajectories, from which conclusions on the "appropriate dynamic equation and potential to describe mesons" [170] can be drawn.

[e] Our estimate for the $K_4(2500)$ mass (violet point for $J = 4$) might be too low to fit onto the corresponding linear Regge trajectory (green line). This may indicate a non-zero curvature of the Regge trajectory as observed in e.g.ref. [170]. However, since we do not yet have systematic uncertainties for this mass estimate, we cannot make a clear statement on the curvature of the Regge trajectories here.

[f] See caption of figure 9.2 for details on the fitting of the three Regge trajectories.

[g] The smaller slope value for trajectory of the K_J excited states can partly be explained by our comparably low mass estimate for the $K(1460)$, for which we have, however, no systematic uncertainty. This may also explain the larger intersect.

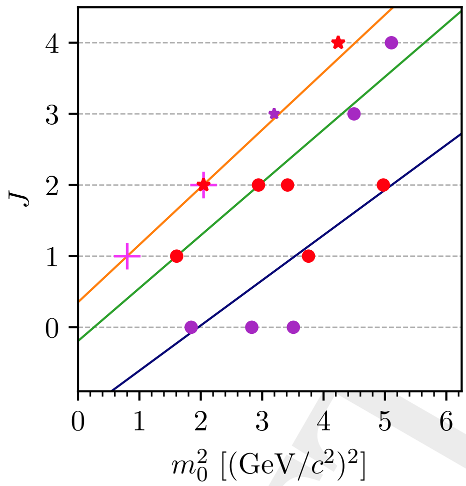

Figure 9.2: Chew-Frautschi plot of strange mesons, i.e. spin J of the state versus its nominal-mass squared as obtained from our analysis. The stars represent K_J^* ground states, the dots represent K_J states. The red stars and dots show the results obtained from the 10-wave RMF, the violet stars and dots show the results of the corresponding extended RMF. The magenta pluses show the results for the $K^*(892)$ and $K_2^*(1430)$ as obtained from the freed-isobar analyses. The orange, green, and blue lines represent fits of Regge trajectories to the K_J^* states, K_J ground states, and K_J excited states, respectively. The $K_2(1820)$ is not considered for the green Regge trajectory of the K_J ground states. The $K(1460)$ is considered for the blue Regge trajectory of the excited K_J states. The $K(1630)$ and $K(1830)$ were not considered for the fit, because they belong to higher excitations or are potential supernumerary states. In order to obtain the linear Regge trajectories, we performed χ^2 fits where we took into account only the statistical uncertainties of our mass estimates and where we neglected all correlations for simplicity.

Table 9.1: Intersects α_0 and slopes α' of the three Regge trajectories of the K_J^* ground states, K_J ground states, and K_J excited states (K_J'). The first line lists our rough estimates for the parameters of the Regge trajectories, the second line lists the parameters as obtained from a quark-model calculation in ref. [10], the third line lists the parameters as obtained from previous measurements (prev. meas.) in ref. [170]. As we do not yet have systematic uncertainties for the parameter estimates from the extended RMFs and the freed-isobar analyses, we cannot give systematic uncertainties for our parameters of the Regge trajectories. Hence, we quote here only rough estimates without uncertainties. Also, in ref. [170] no uncertainties are quoted and we do not list the uncertainties from ref. [10] for a clear arrangement.

	K_J^*		K_J		K_J'	
	α_0	α' [(GeV/c^2)$^{-2}$]	α_0	α' [(GeV/c^2)$^{-2}$]	α_0	α' [(GeV/c^2)$^{-2}$]
COMPASS	0.35	0.81	−0.19	0.74	−1.24	0.64
Quark model	0.318	0.839	−0.197	0.780	−2.240	0.964
Prev. meas.	0.25	0.89	−0.15	0.69	−2.1	0.97

scope of this work. For example, systematic effects from the choice of partial waves and model components included in the RMFs have to be studied. Nonetheless, we expect our first estimates for the systematic uncertainties to not drastically underestimate the full systematic uncertainties. Also, systematic studies of the extended RMFs and the freed-isobar analyses still have to be performed.

There are also aspects of our analysis that may be improved in the future in order to reduce systematic uncertainties. Furthermore, by comparing the results of improved analyses to our results, our results could be further scrutinize. While we used a rank=3 model in the final 238-wave PWD, we performed the wave-set selection using only a rank=1 model, because a wave-set selection using a rank=3 model is computationally and technically much more demanding. This in principle can lead to a too large wave set. However, we do not find artifacts that hint at a too large wave set in the results of the 238-wave PWD. In a future analysis, performing the wave-set selection using a rank=3 model could validate our results. Also, Breit-Wigner models as used in our RMFs are good approximations only in the case of narrow isolated resonances. In cases of overlapping resonances, such as the $K_2(1770)$ and $K_2(1820)$, more elaborate models that incorporate constraints imposed by unitarity and analyticity may in principle improve the RMF results. In particular, such elaborate models would allow a future analysis to determine the pole parameters and couplings, which—in contrast to Breit-Winger parameters and branching fractions—represent the actual, fundamental, and process-independent properties of a resonance. A step in this direction was achieved by the authors of ref. [134], who developed such a model for the $\eta^{(\prime)}\pi$ final state. However, three-body final states, such as the $K^-\pi^-\pi^+$ final state analyzed in our work, are much more complicated and there are no already applicable models for them available. Developing such models for three-body final states requires close collaboration between experimentalists and theorists.

At COMPASS, the $K^-\pi^-\pi^+$ final state is the flag-ship channel for strange-meson spectroscopy. The COMPASS samples for other charge combinations such as the $K^-\pi^0\pi^0$ or the $K^0_\mathrm{S}\pi^-\pi^0$ final states are expected to be significantly smaller due to the smaller experimental acceptance for detecting and reconstructing a π^0. However, as the π^0 and the K^0_S are identified by their reconstruction, the charged particles in these final states do not need to be positively identified by the RICH. Thus, in contrast to our analysis, these two channels do not suffer from acceptance effects from the RICH particle identification. Therefore, the study of the $K^-\pi^0\pi^0$ and $K^0_\mathrm{S}\pi^-\pi^0$ final states may give complementary information to our analysis.

While the $K\pi\pi$ final state allows us to study in principle the full strange-meson spectrum, strange mesons can be studied at COMPASS also in other final states, which provide additional information on parts of the strange-meson spectrum. For example, an analysis of the $K^0_\mathrm{S}\pi^-$ final state, in which K^*_J states can be studied with high precision, is currently ongoing [65, 171].[h] States at higher masses can be addressed in final states with heavier particles such as $K^-\phi$, $K^-\omega$, and $\Lambda\bar{p}$. At COMPASS, also these final states can in principle be studied. Hence, COMPASS will contribute further to improve our understanding of the strange-meson sector.

[h] Unfortunately, K^*_0 states, i.e. the $[K\pi]_S$ amplitude, cannot be studied in this final state, because states with $J^P = 0^+$ cannot be produced in diffractive scattering of a kaon beam.

Furthermore, strange mesons will be studied in the decays of heavy mesons and τ leptons using upcoming high-precision data from currently running experiments such as Belle II, BES III, and LHCb. For example, strange mesons can be studied in the decay $\tau^- \to K^-\pi^-\pi^+\nu_\tau$, for which Belle II will measure a large sample. However, τ decays are dominated by only K_1 states. Also, often only a limited mass range is accessible in the decays of heavy mesons and τ leptons, as discussed, for example, in section 7.1.1 for the $B^+ \to J/\psi\phi K^+$ decay studied by LHCb at CERN [34]. Still, with continuously growing data samples, we can expect more precise studies of the strange-meson sector form decays of heavy mesons or τ leptons.

Another laboratory to study strange mesons are photo-production reactions. There are plans [172, 173] to study final states with strange mesons such as $KK\pi\pi$ at the GlueX experiment at Jefferson Lab by employing an upgraded final-state particle identification based on a DIRC detector originally used by the BaBar experiment [25, 174]. This would allow GlueX to study strange mesons appearing in the $K\pi\pi$ and $K\pi$ subsystems using methods similar to our freed-isobar approach. Also at Jefferson Lab, a proposal for strange-hadron spectroscopy with a secondary K^0_L beam using the GlueX spectrometer was recently approved [175]. The meson spectroscopy part of the physics program focuses mainly on the $K\pi$ final state, with the goal to study K^*_J states with high precision.

While the spectroscopy program of the PANDA experiment, which is currently under construction at GSI, focuses on mainly charm and hyperon physics, PANDA can in principle also study strange mesons in reactions such as $\bar{p}p \to K^+K^0\pi^-\pi^+\pi^-$ [176].

Finally, there is a letter of intent for a new QCD facility at CERN's M2 beam line called AMBER [177]. A pilot run for the first phase of this experiment using the existing M2 beam line has already been approved by CERN [178]. The second phase of this experiment proposes to upgrade the M2 beam line in order to allow radio-frequency separation of the beam particles and thereby drastically increasing the antiproton and kaon fraction in the hadron beam. The very broad physics program of the second phase includes strange-meson spectroscopy. The goal is to collect a $K^-\pi^-\pi^+$ sample of more than 10×10^6 events, i.e. roughly 10 times larger than our existing COMPASS $K^-\pi^-\pi^+$ sample. With such a data sample, AMBER could map out the strange-meson spectrum with unprecedented detail and precision, similar to what the analysis of the large COMPASS $\pi^-\pi^-\pi^+$ sample did for the non-strange light-meson sector [39, 41]. With our work, we prepared the road map for such an analysis by applying sophisticated techniques such as the wave-set selection, the correction for the $\pi^-\pi^-\pi^+$ background, and the freed-isobar analysis.

In summary, with our results from the $K^-\pi^-\pi^+$ final state at COMPASS and with many upcoming results from various experiments, strange-meson spectroscopy is entering a high-precision era. This will lead to a more precise and in particular a more complete picture of the excitation spectrum of strange mesons. It will deepen our understanding of the strong interaction, which forms these mesons, and it will also have an impact on other fields of physics, such as the search for CP violation in multi-body decays of heavy mesons, where these strange mesons appear as well.

A Particle Identification

A.1 Beam-Particle Identification

A.1.1 Calibration Data Sample

In section 3.1.4, we developed a method for beam-particle identification using the information of both CEDAR detectors, based on a likelihood ansatz. The parameters of the corresponding likelihood function in equation (3.13) can be determined by any calibration sample containing a mixture of the different beam-particle species. The only requirement for this calibration samples is that it needs to be sufficiently large to perform a time-dependent calibration.

Preselection

First, a preselection was performed, which is common to the calibration sample and the performance validation samples discussed in appendix A.1.2. The following cuts were applied:

- DT0 trigger
- Exactly one candidate for the interaction vertex of the beam particle was reconstructed
- Beam track was measured with the silicon detectors of the beam telescope[a]
- The beam track coincides with the event in time: $|t_{\mathrm{Beam}}| < 5\,\mathrm{ns}$[b]

Final Selection

To obtain a large calibration sample with good quality, we used an event sample with three charged hadrons in the final state. In addition, this sample has a similar resolution of the measured beam-particle inclination as the $K^-\pi^-\pi^+$ sample, which important for the likelihood calibration as discussed in section 3.1.4 of the main text. The following cuts were applied:

[a] This is done by requiring that the last measured z position of the beam track was at most 200 cm upstream of the target.

[b] The time of the event, i.e. the time of the trigger signal is by construction $t_{\mathrm{trigger}} = 0\,\mathrm{ns}$.

- Preselection as discussed above
- Three charged tracks leave the interaction vertex
- Vertex z position in the target region: $-65\,\text{cm} < z_{\text{PV}} < -30\,\text{cm}$
- Exclusivity: $|E_{\text{sum}} - 191\,\text{GeV}| < 8\,\text{GeV}$ with $E_{\text{sum}} = \sum_{\text{i}=1}^{3} E_{\text{track},i}$

It is very important to use the DT0 trigger. Otherwise, the CEDAR trigger, which was tuned to trigger on events with incoming beam kaons, heavily biases the result of the calibration.

A.1.2 Validation Data Samples

To study the properties of the likelihood-based beam-particle identification and to determine its efficiency and impurity, clean pion-beam and kaon-beam samples are needed.

A pion-beam sample with small kaon contribution was obtained by selecting events of the reaction $\pi^- + p \to \pi^-\pi^0\pi^0 + p$. In this channel, the complete final state can be identified. The π^0 were identified via their decay $\pi^0 \to \gamma\gamma$ using the ECALs and the π^- was identified using the RICH detector. The following selection cuts were applied to the events:

- Preselection (see appendix A.1.1)
- One charged track leaving the interaction vertex
- Vertex z position in the target region: $-65\,\text{cm} < z_{\text{PV}} < -30\,\text{cm}$
- Exactly four ECAL clusters without associated charged track called <u>neutral clusters</u> with: (see ref. [179] for details)
  - $E_{\text{Cluster}} > 0.6\,\text{GeV}$ for ECAL1 or $E_{\text{Cluster}} > 1.2\,\text{GeV}$ for ECAL2
  - $|t_{\text{Cluster}} - t_0(E_{\text{Cluster}})| < 3\sigma_{\text{ECAL}}(E_{\text{Cluster}})$[c]
- Exactly one combination of these four clusters to build two π^0 candidates that each fulfills $|m_{\gamma_i\gamma_j} - 135\,\text{MeV}/c^2| < 11\,\text{MeV}/c^2$
- Exclusivity: $|E_{\pi^-\pi^0\pi^0} - 191\,\text{GeV}| < 10\,\text{GeV}$
- The charged outgoing particle was identified as a pion using the RICH detector
  - Particle momentum in the range $10\,\text{GeV}/c < p_{\pi^-} < 30\,\text{GeV}/c$
  - RICH likelihood: $\mathcal{L}^{\text{RICH}}(\pi) \geq 1.4\mathcal{L}^{\text{RICH}}(K)$ and $\mathcal{L}^{\text{RICH}}(\pi) \geq 1.4\mathcal{L}^{\text{RICH}}(p)$

Applying these cuts, we obtained pion-beam samples of 1 223 190 events for the 2008 and 1 159 220 events for the 2009 diffraction data set, which are large enough to make reliable statements about efficiency and impurity. Figure A.1a shows the ratio of the distribution of the beam-particle inclinations for this pion-beam sample and the corresponding distribution of the three-hadron sample used to calibrate the likelihood parameterization (see section 3.1.4). Both distributions are normalized to their data set size. In the important central region, the ratio is

[c] This cut was applied only to the 2008 diffraction data set, because there is no calibration of the time resolution available for the 2009 diffraction data set.

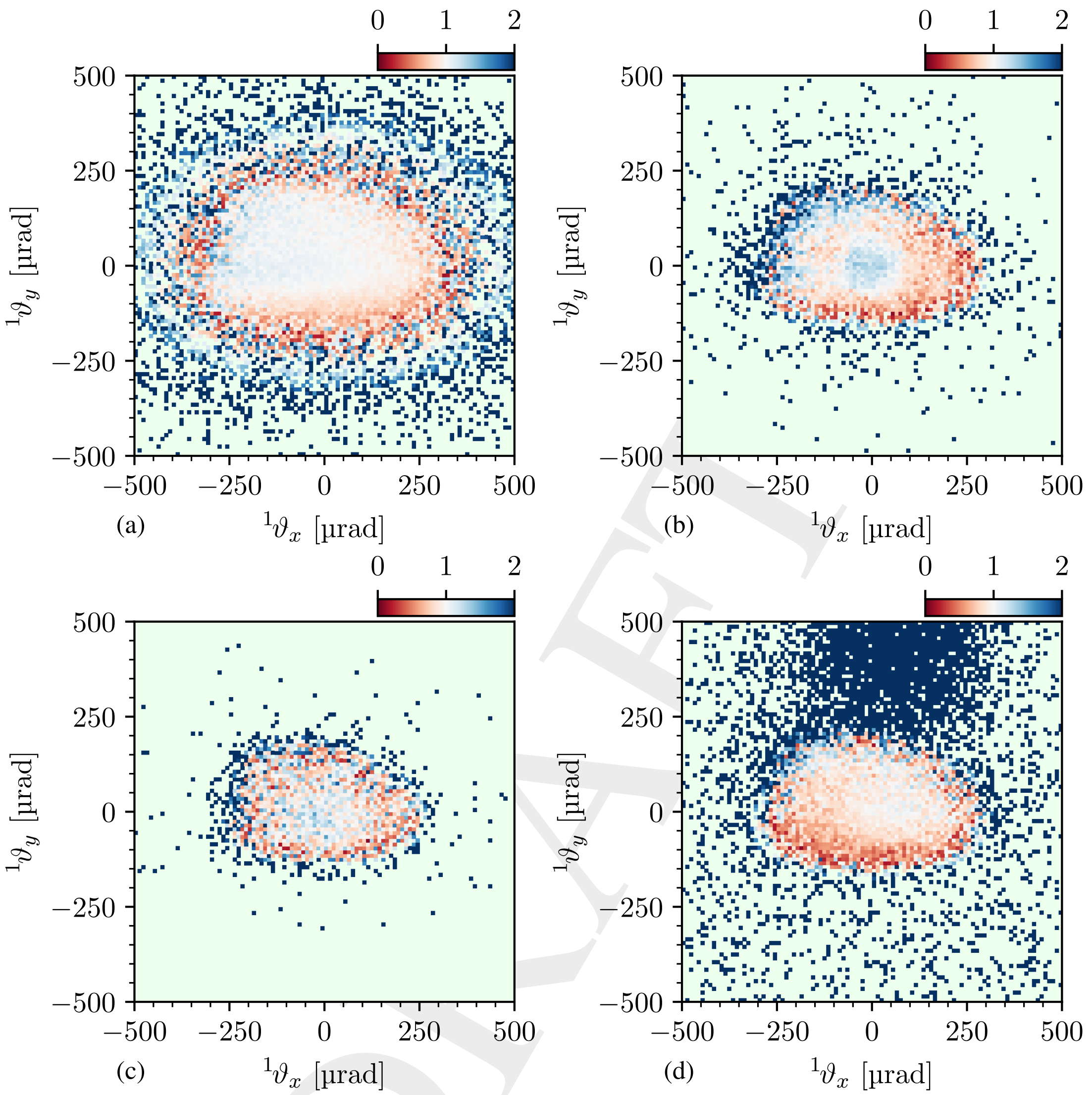

Figure A.1: Ratios of the beam inclination distribution for the various validation samples and the three-hadron sample used for calibration. Before calculating the ratio, each distribution was normalized to the number of events in the corresponding data sample. (a) shows the pion-beam sample and (b), (c), and (d) show the kaon-beam samples from the $K^- \to \mu^-\bar{\nu}_\mu$, $\pi^-\pi^-\pi^+$, and $\pi^-\pi^0$ decays, respectively.

around one, which means that the pion-beam sample illuminates the CEDARs in a similar way as the three-hadron sample. Therefore, the efficiency and impurity values we obtained from the pion-beam sample are expected to be comparable to the ones for the three-hadron sample and thus to the ones for the $K^-\pi^-\pi^+$ data.

We obtained a clean kaon-beam sample by selecting decays of beam kaons into various final states. The first kaon-beam sample is based on the decay $K^- \to \mu^-\bar{\nu}_\mu$, where the following cuts were applied:

- Preselection (see appendix A.1.1)
- One charged track leaving the reconstructed vertex
- Vertex z position upstream of the target: $-270\,\mathrm{cm} < z_{\mathrm{PV}} < -70\,\mathrm{cm}$
- Sum of energies deposited into both ECALs $< 5\,\mathrm{GeV}$
- Outgoing track is identified as a muon: Track traversed > 60 radiation lengths
- Momentum of the outgoing muon track $p_\mu < 180\,\mathrm{GeV}/c$
- Reconstructed beam-particle mass $|m_{\mu\bar{\nu}} - 493.677\,\mathrm{MeV}/c^2| < 42\,\mathrm{MeV}/c^2$[d] (see figure A.2b)

Applying the above cuts, we obtained a $K^- \to \mu^-\bar{\nu}_\mu$ sample of 84 313 events for the 2008 and 71 274 events for the 2009 diffraction data set. In contrast to the pion-beam sample, the beam inclination distribution of the $K^- \to \mu^-\bar{\nu}_\mu$ sample has relatively more events in the center as compared to the three-hadron sample (see figure A.1b). This may slightly bias the efficiency towards larger values as the efficiency for kaon identification is higher for kaons traversing the CEDARs parallel to their optical axes. Similarly, also the impurity value determined from this sample may be slightly biased.

To overcome this problem and to get an estimate for the systematic uncertainty of the efficiency and impurity values, two further kaon-beam samples were used. The second kaon-beam sample is based on the kaon decay $K^- \to \pi^-\pi^-\pi^+$. The following cuts were applied:

- Preselection (see appendix A.1.1)
- Three charged tracks leaving the interaction vertex
- Vertex z position upstream of the target: $-270\,\mathrm{cm} < z_{\mathrm{PV}} < -70\,\mathrm{cm}$
- Exclusivity: $|E_{\pi^-\pi^-\pi^+} - 191\,\mathrm{GeV}| < 8\,\mathrm{GeV}$
- Reconstructed mass $|m_{\pi^-\pi^-\pi^+} - 493.677\,\mathrm{MeV}/c^2| < 14\,\mathrm{MeV}/c^2$ (see figure A.2a)

With only 15 212 events for the 2008 and 14 969 events for the 2009 diffraction data set, this kaon-beam sample is significantly smaller than the $K^- \to \mu^-\bar{\nu}_\mu$ sample. This is mainly due to the smaller branching fraction of the $K^- \to \pi^-\pi^-\pi^+$ decay. The beam inclination distribution is not in perfect agreement with the one of the three-hadron sample, but more similar than the $K^- \to \mu^-\bar{\nu}_\mu$ sample (see figure A.1c). Thus, this kaon-beam sample can be used to obtain a better estimated for the efficiency and impurity values.

The third kaon-beam sample is based on the kaon decay $K^- \to \pi^-\pi^0$. The following cuts were applied:

- Preselection (see appendix A.1.1)
- One charged tracks leaving the reconstructed vertex
- Vertex z position upstream of the target: $-270\,\mathrm{cm} < z_{\mathrm{PV}} < -70\,\mathrm{cm}$

[d] The neutrino momentum is given by $\vec{p}_{\bar{\nu}} = \vec{p}_{\mathrm{Beam}} - \vec{p}_\mu$, where $\vec{p}_{\mathrm{beam}} = 190\,\mathrm{GeV}/c \cdot (\mathrm{d}x/\mathrm{d}z, \mathrm{d}y/\mathrm{d}z, 1)$ using the measured beam inclination and an average beam momentum of approximately $190\,\mathrm{GeV}/c$. The neutrino energy is $E_{\bar{\nu}} = |\vec{p}_{\bar{\nu}}|c$.

- Neutral ECAL cluster with the largest energy must have an energy of at least 10 GeV
- Exactly one combination of the highest-energy neutral ECAL cluster with another neutral ECAL cluster, where
  - * Energy of the second neutral ECAL cluster was larger than 2 GeV
  - * $|m_{\gamma_i \gamma_j} - 135\,\text{MeV}/c^2| < 10\,\text{MeV}/c^2$
- Energy of the second neutral ECAL cluster with lower energy larger than 8 GeV[e]
- Exclusivity: $|E_{\pi^-\pi^0} - 191\,\text{GeV}| < 8\,\text{GeV}$

Applying the above cuts we obtained 94 890 events for the 2008 and 93 639 events for the 2009 diffraction data set. However, in the kaon peak, we find only approximately 7500 events in the 2008 and 6300 events in the 2009 diffraction data set (see figure A.2c). Therefore, the $K^- \to \pi^-\pi^0$ sample is the smallest of all validation samples. Compared to the three-hadron sample, the beam inclination distribution exhibits an increased number of events above the main beam spot for ${}^1\vartheta_y > 200\,\mu\text{rad}$ and therefore a reduced number of events for ${}^1\vartheta_y \lesssim 0\,\mu\text{rad}$ (see figure A.1d). The reason for this could be the comparably large background below the kaon peak (see figure A.2c). Also, the distribution within the main beam spot is different from that of the three-hadron sample.

Each of the kaon-beam samples has some caveats. However, comparing the results from all three samples provides a handle on the systematic uncertainties of the efficiency and impurity values and yields more reliable results.

A.1.3 Determination of Efficiency and Purity

To determine the efficiency $P_{\text{ID}}(K \to K)$ for kaon identification, we applied the CEDAR particle identification cut for kaons, i.e. the log-likelihood different smaller than $\mathcal{T}_{\text{C}}(K)$ [see equation (3.15)], to all three kaon-beam samples. We estimated the efficiency as the ratio of the event numbers before and after applying the CEDAR particle identification cut. Due to the pion contamination of the kaon-beam sample, this approach only gives a lower limit for the efficiency. For the $K^- \to \pi^-\pi^0$ and $K^- \to \mu^-\bar{\nu}_\mu$ valiation samples, the kaon peak sits on a considerable background (see figures A.2b and A.2c). To extract the efficiency also from these samples, we fitted a Gaussian signal function plus a second-order background polynomial to the $\pi^-\,\pi^0$ and $\mu^-\bar{\nu}_\mu$ mass spectra. Then, we calculated the efficiency as the ratio of the integrals of the Gaussian signal functions before (figure A.2c) and after (figure A.2d) applying the CEDAR particle identification cut for kaons. Similarly, the efficiency for pion identification is the ratio of the pion-beam sample before and after applying the CEDAR particle identification cut for pions.

[e] First, we applied the more relaxed constrained of a cluster energy larger than 2 GeV in order to allow for more combinations of neutral clusters in one event. Then we required that exactly one of these combinations exist. This reduced combinatorial background.

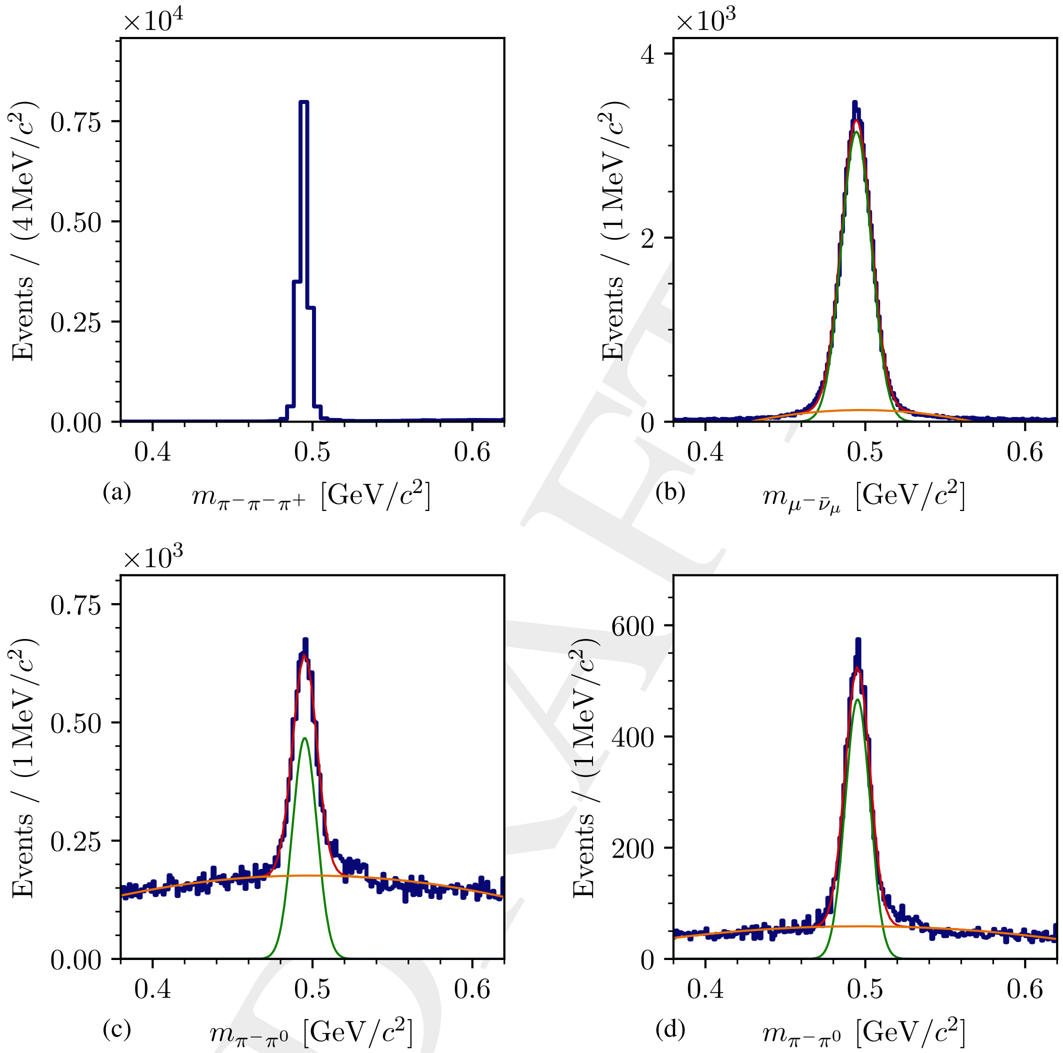

Figure A.2: Kaon peak in the invariant mass spectra of the kaon-beam samples. (a) $\pi^-\pi^-\pi^+$ invariant mass spectrum of the $K^- \to \pi^-\pi^-\pi^+$ sample, (b) $\mu^-\bar{\nu}_\mu$ invariant mass spectrum of the $K^- \to \mu^-\bar{\nu}_\mu$ sample, and (c) π^- π^0 invariant mass spectrum of the $K^- \to \pi^-\pi^0$ sample before applying the CEDAR particle identification cut for kaons. (d) π^- π^0 invariant mass spectrum of the $K^- \to \pi^-\pi^0$ sample after applying the CEDAR particle identification cut for kaons. The dark blue histogram represents the data. In (b)-(d), the red curve is the result of a fit with a the Gaussian signal function plus a second-order background polynomial. The green curve is the Gaussian signal function, and the orange curve is the background polynomial. The sample of the decay $K^- \to \pi^-\pi^-\pi^+$ shown in (a) is background free. Therefore, we did not perform a fit to extract the number of kaon decays, but we directly used the number of selected events.

To estimate the probability $P_{\mathrm{ID}}(\pi \to K)$ to misidentify a pion as a kaon, we applied the CEDAR particle identification cut for kaons on the pion-beam sample and calculated the ratio of the remaining events and the total number of events of the pion-beam sample. Similarly, the probability to misidentify a kaon as a pion was obtained from each kaon-beam sample by applying the cut on the CEDAR particle identification for a pion.

To determine the purity of the identified-kaon sample, the impurity from pions, muons, electrons, and antiprotons in the beam had to be determined. The total impurity is dominated by the impurity from misidentified pions in the identified-kaon sample, which was calculated in the following way

$$\mathrm{Impurity}(K) = \frac{N_{K\to\pi}}{N_{K\to K} + N_{\pi\to K}} = \frac{P_{\mathrm{ID}}(\pi \to K)\cdot R_{\pi K}}{P_{\mathrm{ID}}(K \to K) + P_{\mathrm{ID}}(\pi \to K)\cdot R_{\pi K}}, \tag{A.1}$$

taking into account the number ratio of pions to kaons $R_{\pi K} = 35.9 \pm 1.0$ in the beam [63]. The impurity of an identified-pion sample from misidentified kaons was calculated in an analogous way.

A.2 Final-State Particle Identification

A.2.1 The Likelihood Approach

The likelihood for a given particle-species hypothesis S for a final-state particle is formulated in terms of the probability of the observed hit pattern of individual Cherenkov photons, j, in the RICH. The distribution of measured Cherenkov angle θ_j of a single photon is modeled by a Gaussian function with width σ_θ. A uniform distribution of emitted Cherenkov photons is assumed in the azimuthal angle φ_j around the direction of the particle. Finally, the total probability to observe a photon in the RICH detector under the Cherenkov angle θ_j is modeled in ref. [64] as:

$$f(\theta_j, \varphi_j|S) = \frac{A}{\sqrt{2\pi}\sigma_\theta}\exp\left[-\frac{(\theta_j - \theta^S_{\mathrm{Ch}})^2}{2\sigma^2_\theta}\right]\epsilon(\theta_j, \varphi_j) + b(\theta_j, \varphi_j). \tag{A.2}$$

Here, $A = A_0 \sin^2\theta^S_{\mathrm{Ch}}$ is the expected number of Cherenkov photons, $\epsilon(\theta_j, \varphi_j)$ the probability that a photon emitted with the angles (θ_j, φ_j) reaches the photon detector and is detected, and $b(\theta_j, \varphi_j)$ is the strength of background contributions[f] that are uncorrelated with the final-state particle.

[f] The strength of the background can be computed as a function of the photon position in the photon-detector plane as explained in ref. [64].

The information from all N measured photons is combined in one extended likelihood:[g]

$$\tilde{\mathcal{L}}(S) = e^{-F(S)} \prod_{j=1}^{N} f(\theta_j, \varphi_j; S). \tag{A.3}$$

Here, $F(S)$ is the expected number of photons. It is calculated by integrating $f(\theta_j, \varphi_j; S)$ over the (θ_j, φ_j) reference region defined by the RICH acceptance (see ref. [64]).

The likelihood is normalized to the number of photons:

$$\mathcal{L}(S) = \sqrt[N]{\tilde{\mathcal{L}}(S)}. \tag{A.4}$$

This allows to consistently tune the likelihood-ratio threshold for particles with different number of photons.

A.2.2 Validation Samples

In order to estimate the performance of the RICH particle identification; i.e. the efficiency $P(S \to S)$ to identify a particle and the misidentification probability $P(S \to S')$ to assign the wrong particle hypothesis S', validation samples of final-state particles are required. These samples need to contain particles that were identified without using the RICH information. We determined efficiency and misidentification probability separately for π^+, K^+, p and π^-, K^-, $\bar{p}$. We also treated the 2008 and 2009 diffraction data sets individually.

Kaon Validation Sample

We used $\phi(1020) \to K^-K^+$ decays as source of kaons. As the $\phi(1020)$ is very short-lived, we cannot separate its decay vertex from the interaction vertex where the $\phi(1020)$ was produced, which is the point of interaction of the beam particle with the target. Therefore, we considered only events where the interaction vertex is within the region of the target, i.e. $-65 \leq Z_{\text{Vtx}} < -30\,\text{cm}$. For all events with at least two charged particles leaving the interaction vertex, we considered all possible combinations of two oppositely charged particle pairs. Assuming the kaon hypothesis, we calculated the mass of the K^-K^+ system and required that it is around the $\phi(1020)$ mass, i.e. $0.98 \leq m_{KK} < 1.07\,\text{GeV}/c^2$.[h] To keep the signal-to-background ratio of the $\phi(1020)$ ignal sufficently large, we required that one of the two kaons was identified by the RICH.

[g] For each final-state particle, all photons with $\theta_j < 70\,\text{mrad}$ were considered in equation (A.3). This threshold of 70 mrad is lager than the maximum possible Cherenkov angle. For final states with more than one particle, there can be ambiguities in the association of Cherenkov photons to particles. This combinatorial background was accounted for by $b(\theta_j, \varphi_j)$.

[h] We estimated the combinatorial background below the $\phi(1020)$ peak. For about 5 % of all K^- K^+ combinations whose invariant mass lies within five standard deviations around the $\phi(1020)$ peak, one of the two kaons was used multiple times also in other combinations.

Thus, when selecting the K^+ validation sample, we identified the K^- via the RICH information using a likelihood-ratio threshold of $\mathcal{T}_\mathrm{R} = 1$ and vice versa.[i] For the 2008 diffraction data set, we obtained 44 059 131 events for the K^- and 40 828 357 events for the K^+ validation sample. For the 2009 diffraction data set, we obtained 35 105 832 events for the K^- and 31 887 217 events for the K^+ validation sample. However, only 3.6 % of these events come from $\phi(1020) \to K^-K^+$ decays.

From these data samples, we can determine the probability that a particle hypothesis S is assigned to a kaon by the RICH:

$$P(K \to S) = \frac{N_{K\to S}}{N_\mathrm{tot}}, \tag{A.5}$$

where N_tot is the total number of kaons in the validation sample and $N_{K\to S}$ is the number of kaons that were identified as species S. The probability $P(K \to K)$ is the kaon identification efficiency and $P(K \to S)$ with $S \neq K$ are the misidentification probabilities.

Figure A.3a shows the invariant mass spectrum of the K^-K^+ system for the K^- validation sample, i.e. when identifying the K^+. It exhibits a clear peak at about $1.02\,\mathrm{GeV}/c^2$ from the decay $\phi(1020) \to K^-K^+$. However, the $\phi(1020)$ peak sits on a large background. Thus, in equation (A.5) we could not directly use the numbers of particles in the data sample, but we had to determine the number of $\phi(1020)$ decays in the peak. Therefore, we modeled the m_{KK} distribution as a sum of signal functions for the $\phi(1020)$ decays and a smooth background component, which was modeled by a second-order polynomial in m_{KK}. The measurement resolution in m_{KK} of about $1.5\,\mathrm{MeV}/c^2$ is at the same order of magnitude as the total decay width of the $\phi(1020)$ of $4.249\,\mathrm{MeV}/c^2$ [9]. Therefore, we used a Voigt function [180], which is a convolution of a non-relativistic Breit-Wigner shape with FWHM Γ and a Gaussian function with standard deviation σ to parameterize the signal component. In total, our model function is given by

$$\frac{\mathrm{d}N}{\mathrm{d}m_{KK}} = A\,\mathrm{Voigt}(m_{KK} - m_0; \sigma, \Gamma) + a + b(m_{KK} - m_0) + c(m_{KK} - m_0)^2. \tag{A.6}$$

Here; A, m_0, σ, a, b, and c are free parameters that were determined by a fit to the data. We fixed the width, Γ, of the Breit-Wigner term to its know value from ref. [9]. We determined the number of $\phi(1020)$ decays by integrating the signal function over the range $1.0 \leq m_{KK} < 1.05\,\mathrm{GeV}/c^2$.[j] By performing this fit individually for the total data sample and for the subsamples where the kaon was assigned the hypothesis S, we can determine N_tot and $N_{K\to S}$, respectively.[k] The results are discussed in appendix A.2.3. Figure A.3b shows exemplarly the m_{KK} distribution in a selected $(|\vec{p}_\mathrm{R}|, \sqrt{\theta_\mathrm{R}})$ cell. The red curve represents a fit of the model function in equation (A.6) to the distribution. It reproduces well the data with a p-value of 0.73.

[i] The identification of both particles is independent. Thus, identifying one kaon using the RICH does not bias the identification probabilities of the other one. However, the kinematic range of the other particle might be limited.

[j] In practice we, calculated the integral of the histogram and the integral of the background function, because this method has proven to be more robust with respect to systematic effects.

[k] As m_0 and σ should be the same for the subsamples, we fixed these parameters in the fits to the subsamples to the values obtained in the fit to the full sample. This improved the fit stability and thereby reduced systematic effects.

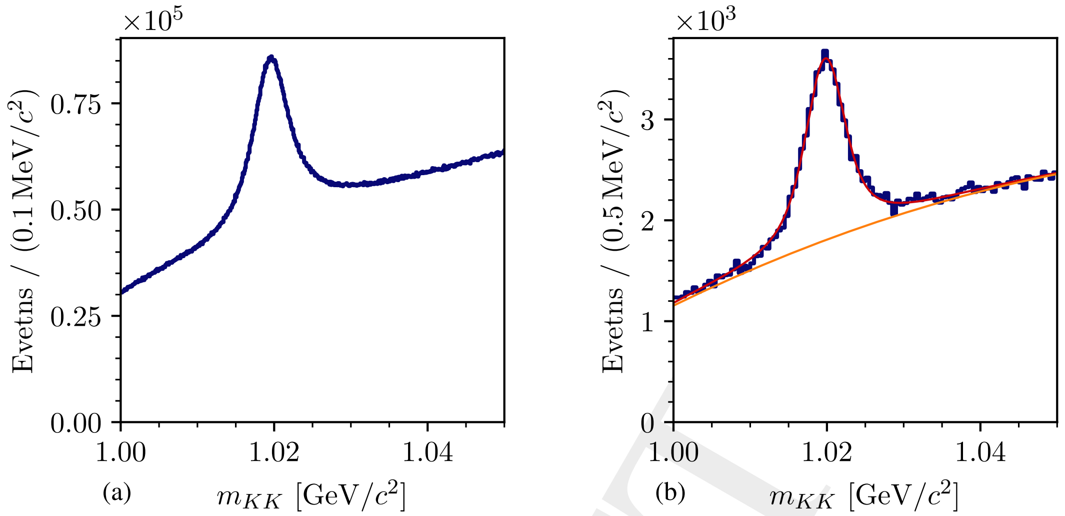

Figure A.3: Invariant mass spectrum of the K^-K^+ system in the 2008 K^- validation sample, i.e. after identifying the positive particle as a K^+ (see text). (a) shows the complete data set. (b) shows a subset of the data in a $(|\vec{p}_\mathrm{R}|, \sqrt{\theta_\mathrm{R}})$ cell around $(18.75\,\mathrm{GeV}/c, 0.19\,\sqrt{rad})$. The blue histograms represents the data. The red curve in (b) represents the result of a fit of equation (A.6) to the data. The orange curve shows the background component in equation (A.6).

Preselection for Pion and Proton Validation Samples

We used $K^0_\mathrm{S} \to \pi^-\pi^+$, $\Lambda \to \pi^- p$, and $\bar{\Lambda} \to \pi^+\bar{p}$ decays as a sources of pions and (anti)protons. As the decay of these neutral particles, which are commonly caleld V^0 particles, proceeds via the weak interaction, the V^0 particles have long lifetimes. Thus, their decay vertex is displaced from the interaction vertex where they were produced. These displaced vertices of V^0 decays were reconstructed from the two measured charged daughter particles.

We considered all displaced decay vertices with two oppositely charged tracks leaving the vertex within the region $-28 \leq Z_\mathrm{ddv} < 150\,\mathrm{cm}$ after the target.[l] We required that the decaying V^0 particle was produced in a interaction vertex. To do so, we reconstructed the direction of the V^0 particle by summing the measured momenta of the two daughter particles. We required, that the distance of closest approach between the direction of the reconstructed V^0 track and the interaction vertex that is closest to this track is smaller than 3 mm. Finally, we ensured that none of the two daughter tracks was associated with this closest interaction vertex.

This sample contains contributions from two-body decays of K^0_S, Λ, and $\bar{\Lambda}$; which appear as arks with only little background in the Armenteros plot in figure A.4.[m]

[l] We excluded the target region to exclude vertices from beam interactions that were erroneously reconstructed as displaced decay vertices.

[m] The Armenteros plot shows the momentum component, p_T, of one of the daughter particles that is transversal to the V^0 momentum, p_T, versus the assymmetry of the longitudinal momentum components, $p_\mathrm{L}^\pm$, of the positive and negative daughter particles. By construction, p_T is the same for both daughter particles.

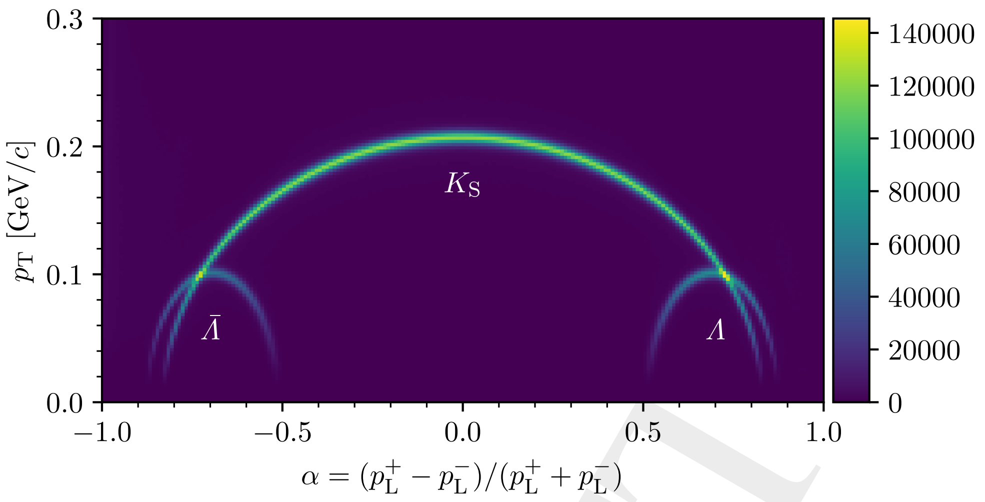

Figure A.4: Armenteros plot[m] of the V^0 data sample of the 2008 diffraction data set.

Pion Validation Sample

In order to obtain a clean pion sample from $K_S^0 \to \pi^-\pi^+$ decays, we needed to reject background contributions from Λ and $\bar{\Lambda}$ decays from teh V^0 sample. Therefore, we calculated the invariant pion-proton mass and rejected events in the range within $\pm 7\,\mathrm{MeV}/c^2$ around the peak position of $1116.1\,\mathrm{GeV}/c^2$, which is consistent with the nominal Λ mass [9].[n] For the 2008 diffraction data set, we obtained 72 608 756 K_S^0 decay candidates (see figure A.5). For the 2009 diffraction data set, we obtained 60 865 406 K_S^0 decay candidates.

The K_S^0 sample exhibits only little background in the signal region of the $m_{\pi^-\pi^+}$ spectrum, in contrast to the kaon valdidation sample discussed above. Therefore, we performed only a side-band subtraction to account for the background when determining the number of K_S^0 decays. We used a signal region of $450 \le m_{\pi\pi} < 550\,\mathrm{MeV}/c^2$ and sideband regions of $420 \le m_{\pi\pi} < 450\,\mathrm{MeV}/c^2$ and $550 \le m_{\pi\pi} < 580\,\mathrm{MeV}/c^2$.

Using this sample, we determined efficiency and misidentification probability for negative and positive pions using equation (A.5) in the same way as discussed for negative and positive kaons.

[n] The peak position was determined from a fit of a sum of two Gaussian and a second-order polynomial to the mass spectrum.

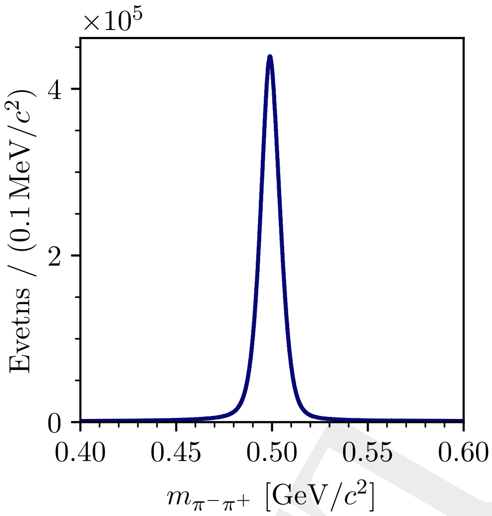

Figure A.5: Invariant mass distribution of the $\pi^-\ \pi^+$ system for the V^0 sample from the 2008 diffraction data set.

Proton Validation Sample

We used the decays $\Lambda \to \pi^- p$ and $\bar{\Lambda} \to \pi^+ \bar{p}$ as sources of protons and antiprotons. To reject the K^0_S background contribution in the V^0 sample, we rejected events where the invariant $\pi^-\ \pi^+$ mass, $m_{\pi^-\pi^+}$, is within 20 MeV/c^2 around the K^0_S peak at 499 MeV/c^2, which is consistent with the nominal K^0_S mass [9].[n]

Λ decays are well separated from $\bar{\Lambda}$ decays in the Armenteros plot (see figure A.4). In order to obtain a clean proton sample from Λ decays and a clean antiproton sample from $\bar{\Lambda}$ decays, we selected evetns with $\alpha > 0$ and $\alpha < 0$, respectively. For the 2008 diffraction data set, we obtained 10 930 951 Λ decay candidates (see figure A.6a) and 11 825 422 $\bar{\Lambda}$ decay candidates (see figure A.6b). For the 2009 diffraction data set, we obtained 10 038 288 Λ decay candidates and 11 256 626 $\bar{\Lambda}$ decay candidates. Analogous to the pion validaiton sample, we determine the number of Λ and $\bar{\Lambda}$ decays from a side-band subtraction of the $m_{\pi^- p}$ and $m_{\pi^+ \bar{p}}$ spectra, respectively. The signal region is $1100 \leq m_{\pi^\pm \overset{(-)}{p}} < 1130$ MeV/c^2. The sideband regions are $1080 \leq m_{\pi^\pm \overset{(-)}{p}} < 1100$ MeV/c^2 and $1130 \leq m_{\pi^\pm \overset{(-)}{p}} < 1150$ MeV/c^2.

Using this sample, we determined efficiency and misidentification probability for protons and antiprotons using equation (A.5) in the same way as discussed for negative and positive kaons.

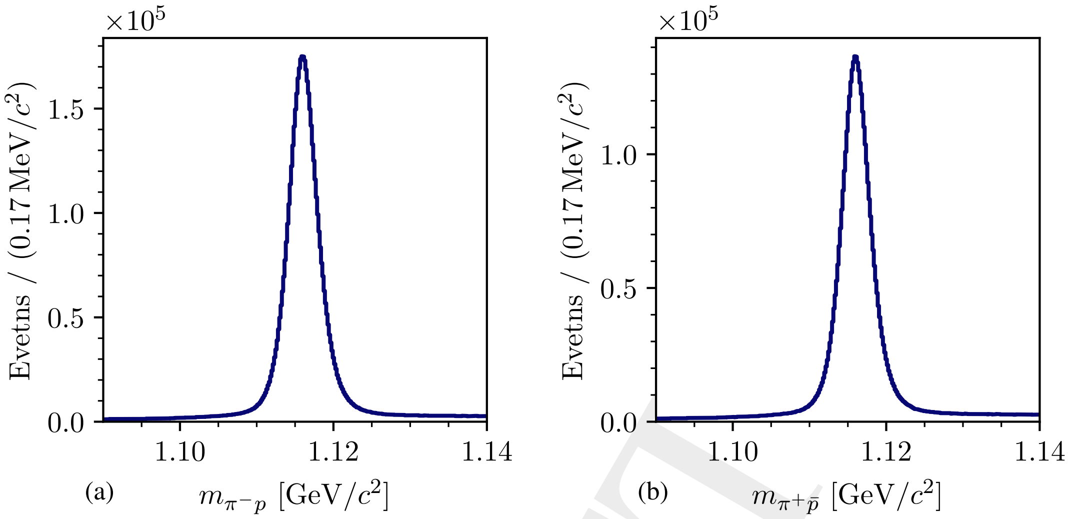

Figure A.6: Invariant mass distribution of the pion-proton system. (a) shows the $m_{\pi^- p}$ distribution for the Λ decay assumption. (b) shows the $m_{\pi^+ \bar{p}}$ distribution for the $\bar{\Lambda}$ decay assumption. Both plots show the 2008 diffraction data set.

A.2.3 RICH Particle-Identification Performance

In this section, we present the results of the RICH performance studies, i.e. the efficiency and misidentification probabilities shown in figures A.7 to A.9 for the 2008 diffraction data set and a threshold of $\mathcal{T}_\mathrm{R} = 1.15$ of the RICH likelihood ratio in equation (3.19). The same threshold value was used for the event selection of the reaction $K^- + p \to K^-\pi^-\pi^+ + p$ discussed in section 4.1. Here, we will discuss technical aspects of the RICH performance matrices. The main aspects of the RICH performance are discussed in the main text in section 3.2.2.

Figure A.7 shows the efficiency and misidentification probabilities for negative kaons. Figure A.7a shows the sum over all probabilities in each $(|\vec{p}_\mathrm{R}|, \sqrt{\theta_\mathrm{R}})$ cell. It is in good agreement with one, except at the kinematic borders of the kaon validation sample, were the number of events becomes small. It is not exactly one as we estimated $N_{K\to S}$ and N_tot in equation (A.5) from independent fits. The overall good agreement with one proves, that we are able to reliably estimate efficiencies and impurities from fits to the m_{KK} spectrum.

Figure A.8 shows the efficiency and misidentification probabilities for negative pions.Since the pion validation sample is much larger than the kaon validation sample, we used a finer binning in $(|\vec{p}_\mathrm{R}|, \sqrt{\theta_\mathrm{R}})$. Also here, sum over all probabilities is in good agreement with one, showing that the side-band subtraction approach introduces only small systematic effects.

Figure A.9 shows the efficiency and misidentification probabilities for antiprotons. As for the pion validation sample, the sum over all probabilities is in good agreement with one. Due to the higher antiproton mass, we can identify antiprotons only above about 18 GeV/c. The upper

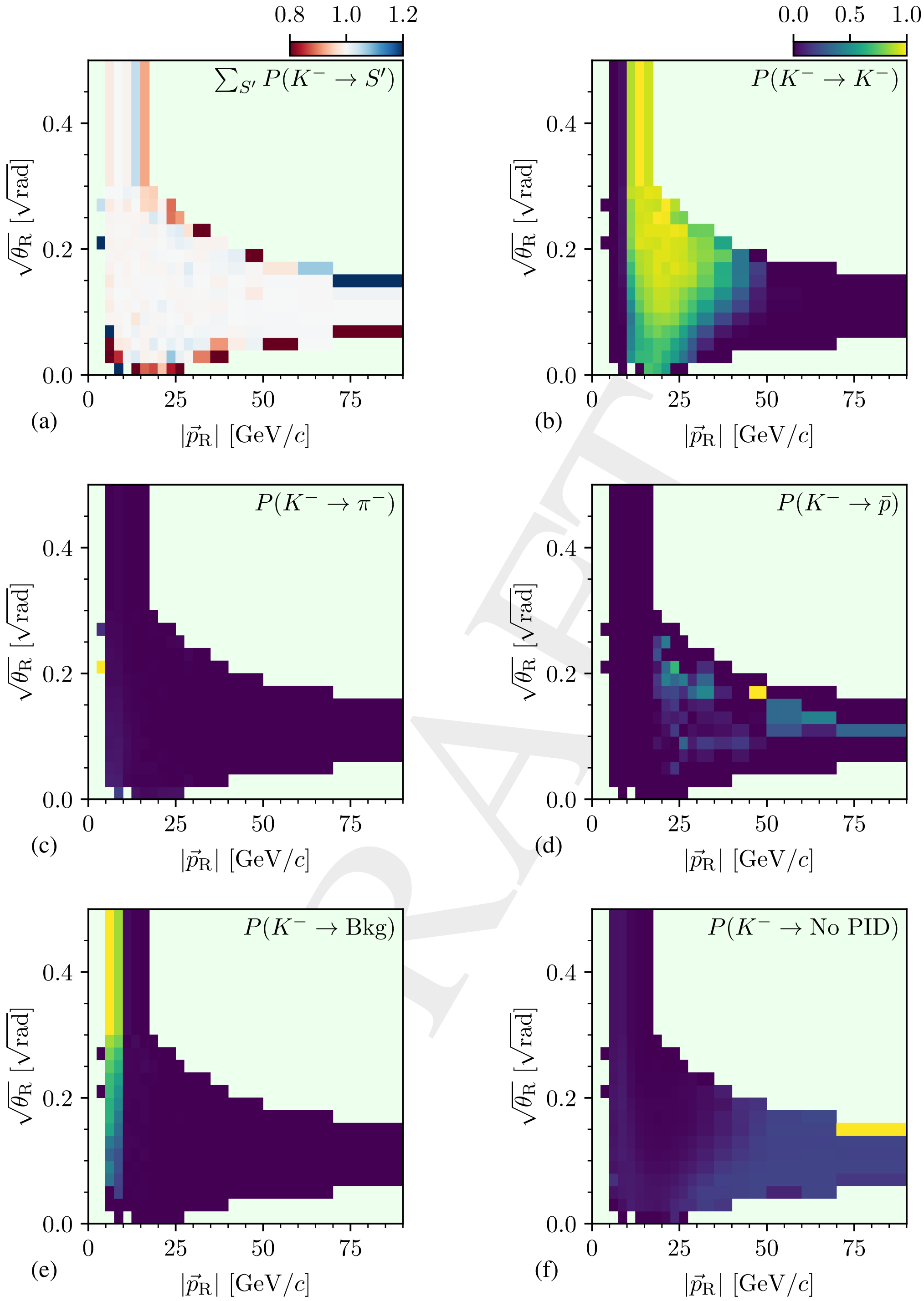

Figure A.7: RICH efficiency and misidentification probability for negative kaons in cells of the particle momentum $|\vec{p}_R|$ and the square-root of the track angle θ_R at the RICH position for the 2008 diffraction data set using a likelihood-ratio threshold of $\mathcal{T}_R = 1.15$. (b) shows the identification efficiency. (c) to (e) show the probability to misidentify the kaon as a pion, antiproton, or as background, respectively. (f) shows the probability to not identify a kaon. (a) shows the sum over (b) to (f). (b) to (f) have the same color scale. Regions without calibration data are drawn in light green.

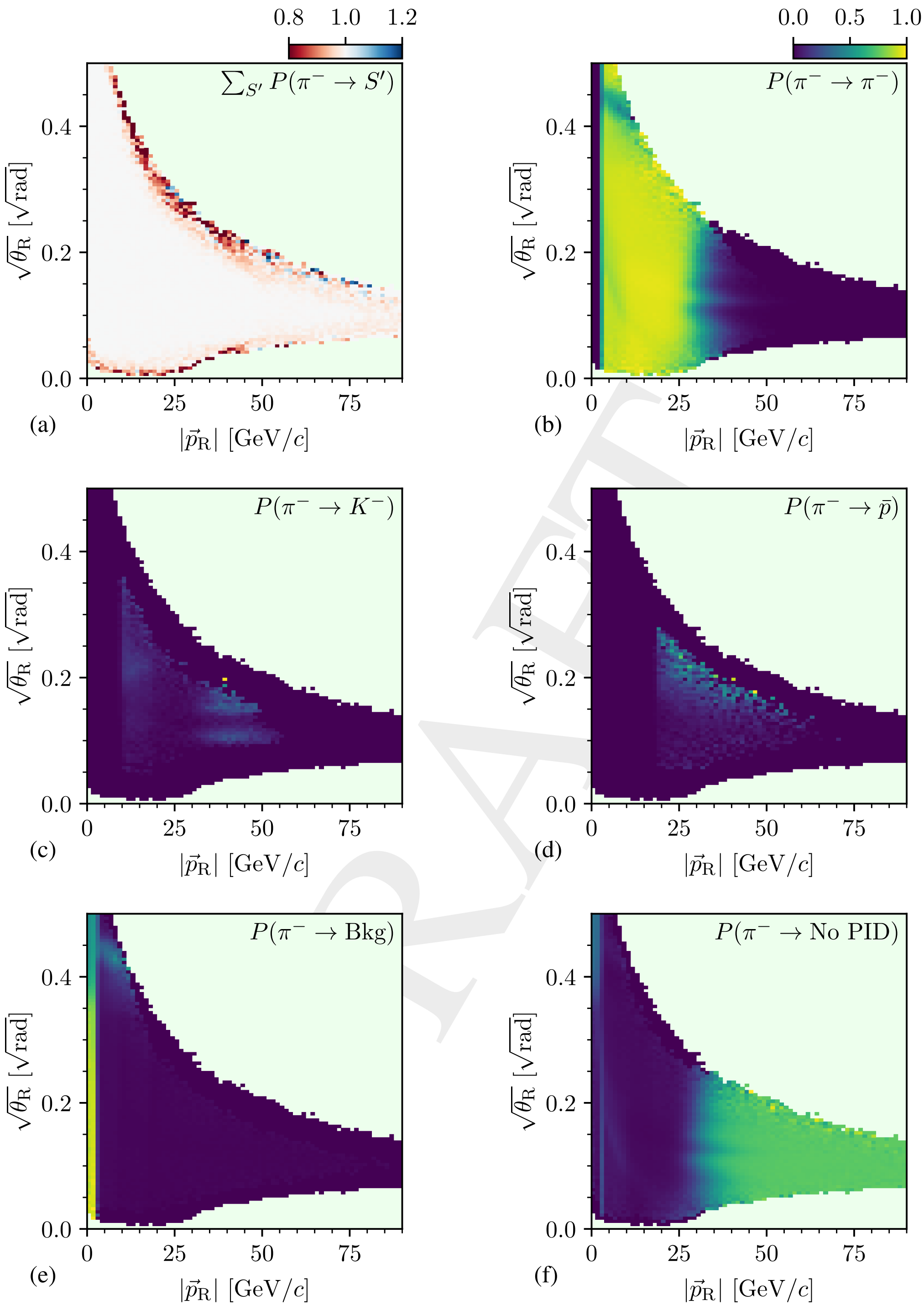

Figure A.8: RICH efficiency and misidentification probability for negative pions in cells of the particle momentum $|\vec{p}_{\mathrm{R}}|$ and the square-root of the track angle θ_{R} at the RICH position for the 2008 diffraction data set using a likelihood-ratio threshold of $\mathcal{T}_{\mathrm{R}} = 1.15$. (b) shows the identification efficiency. (c) to (e) show the probability to misidentify the pion as a kaon, antiproton, or as background, respectively. (f) shows the probability to not identify a pion. (a) shows the sum over (b) to (f). (b) to (f) have the same color scale. Regions without calibration data are drawn in light green.

momentum limit depends on the track angle and reaches up to 75 GeV/c. In the center of the distribution, we achieve a high antiproton identification efficiency of about 86 %.

The RICH efficiencies and misidentification probabilities for positive kaons, pions, and protons are in good agreement with those for the corresponding negative particle species discussed above, except for small differences between the efficiency of negative and positive pions at the kinematic borders of the validation sample. As those differences are the borders, they are not important here.

The RICH performance studies for the 2009 diffraction data set yielded similar results as those for the 2008 diffraction data set. Figure A.10 shows as an example the efficiencies for negative pions and kaons. Nonetheless, we still threat the RICH performance separately for both years as the experimental setup for both years was slightly different.

A.2.4 RICH Threshold Tuning for the $K^-\pi^-\pi^+$ Final State

We estimated the efficiency to identify the $K^-\pi^-\pi^+$ final state for a given $\mathcal{T}_\mathrm{R}$ by comparing the number of events that pass the $K^-\pi^-\pi^+$ event selection described in section 4.1, relative to the number of selected $K^-\pi^-\pi^+$ events for $\mathcal{T}_\mathrm{R} = 1.00$. The blue curve in figure 3.14 shows the efficiency determined from the 2008 diffraction data set.

The purity (orange curve in figure 3.14) is the fraction of events where the K^- and π^- hypotheses were correctly attribute to the final-state particles. As the determination of the purity requires knowledge about the true particle species, we used a pseudodata sample of $K^-\pi^-\pi^+$ events that is uniformly distributed in the $K^-\pi^-\pi^+$ phase space to estimate the purity. The Monte Carlo method used to obtain such a pseudodata sample is described in appendix C. This estimate may be biased, because in the measured data $K^-\pi^-\pi^+$ events are not uniformly distributed in phase space. However, at this stage of the analysis, i.e. before the partial-wave decomposition, this was the best approximation which could be employed. Furthermore, here we are not interested in the absolute value of the purity, but we are mainly interested in its $\mathcal{T}_\mathrm{R}$ dependence, which is less sensitive to the distribution of the final-state particles.

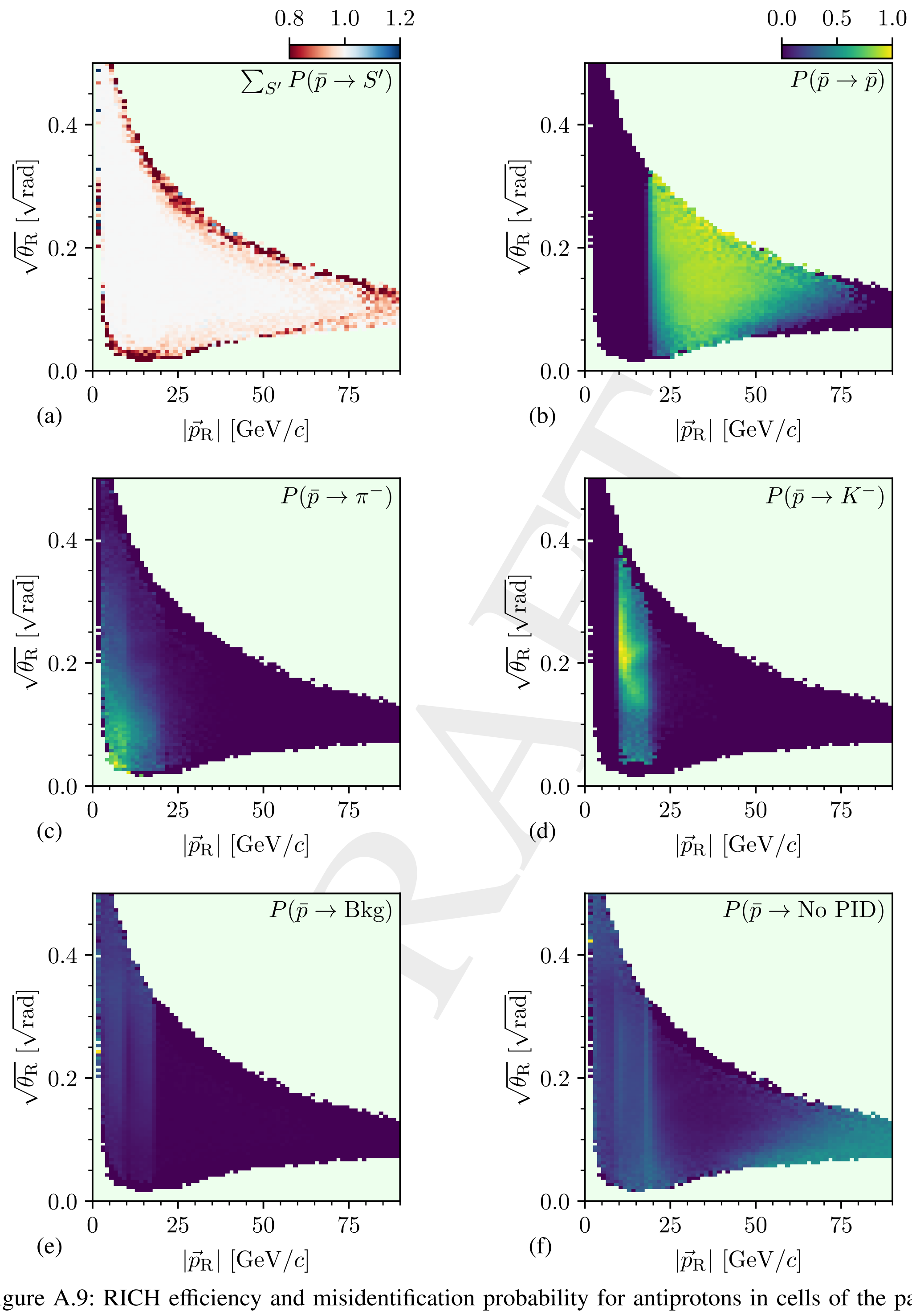

Figure A.9: RICH efficiency and misidentification probability for antiprotons in cells of the particle momentum $|\vec{p}_R|$ and the square-root of the track angle θ_R at the RICH position for the 2008 diffraction data set using a likelihood-ratio threshold of $\mathcal{T}_R = 1.15$. (b) shows the identification efficiency. (c) to (e) show the probability to misidentify the antiproton as a pion, kaon, or as background, respectively. (f) shows the probability to not identify a antiproton. (a) shows the sum over (b) to (f). (b) to (f) have the same color scale. Regions without calibration data are drawn in light green.

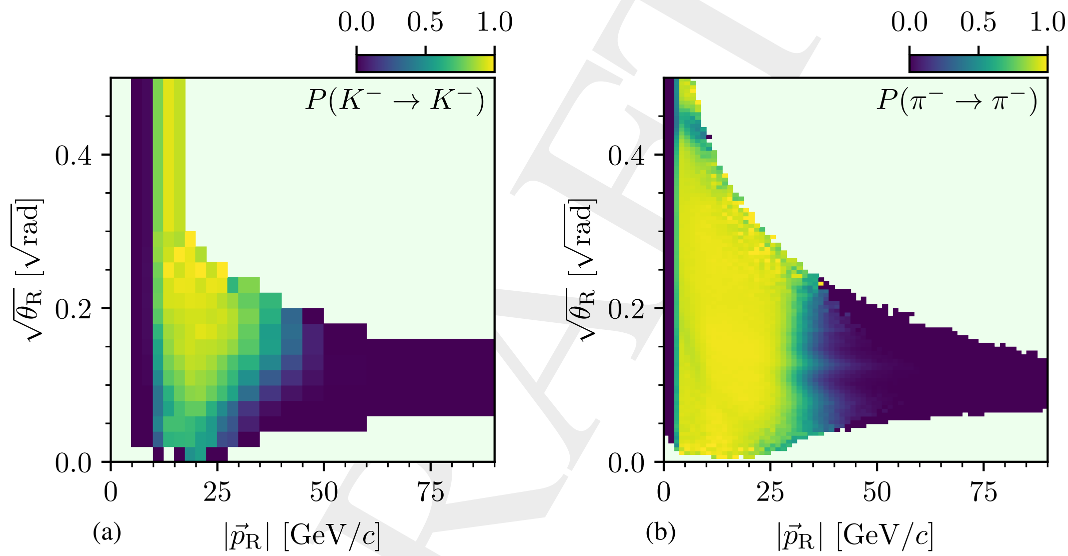

Figure A.10: RICH efficiency for (a) kaons and (b) pions in cells of the particle momentum $|\vec{p}_R|$ and the square-root of the track angle θ_R at the RICH position for the 2009 diffraction data set using a likelihood-ratio threshold of $\mathcal{T}_R = 1.15$. Compare figures A.7b and A.8b, respectively.

B Event Selection

B.1 Reconstruction of Beam Energy

At COMPASS, the energy of the beam particle was not directly measured by the experimental setup. However, we reconstructed it from the measured three-momenta of the $K^-\pi^-\pi^+$ final-state particles and the measured inclination of the beam particle track; assuming an exclusive event, assuming the target particle to be a proton, and assigning the beam and final-sate particle masses according to the CEDAR and RICH information, respectively. The energy of the beam particle reconstructed in this way is an important quantity to ensure the exclusivity of an event. It was used to suppress background events where not all final-state particles were detected.

To calculate the energy E_{beam} of the beam kaon we used the following approach. First, we determine the magnitude $|\vec{p}_{\text{beam}}|$ of its three-momentum. From the four-momenta p_i of the final-state particles we calculate the total four-momentum,

$$p_X = (E_X, \vec{p}_x) = \sum_{i=1}^{3} p_i, \tag{B.1}$$

of the final-state system X.

The Mandelstam variable t can be calculated in two different ways (see figure B.1): (i) from the kinematics of the beam vertex in the laboratory frame, i.e.

$$t = (p_{\text{beam}} - p_X)^2 = m_{\text{beam}}^2 + m_X^2 - 2\left(E_{\text{beam}} E_X - |\vec{p}_{\text{beam}}|\,|\vec{p}_X| \cos\theta\right), \tag{B.2}$$

where θ is the scattering angle, i.e. the angle between the momentum of the X-system and of the beam particle. It is calculated from $\vec{p}_X$ in equation (B.1) and the measured beam-particle inclination; (ii) from the kinematics of the target vertex, i.e.

$$t = (p_{\text{target}} - p_{\text{recoil}})^2 = 2m_{\text{target}}(m_{\text{target}} - E_{\text{recoil}}) = 2m_{\text{target}}(E_X - E_{\text{beam}}), \tag{B.3}$$

where we use that the target proton is at rest in the laboratory frame and where we assume that the target proton stays intact in the scattering reaction. Therefore, the energy transferred between the upper and lower vertex is $(m_{\text{target}} - E_{\text{recoil}}) = (E_X - E_{\text{beam}})$.

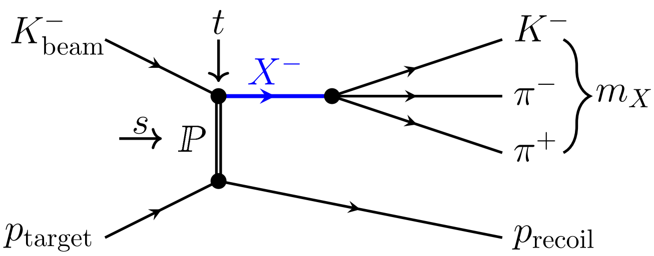

Figure B.1: Schematic view of the diffractive scattering reaction $K^- + p \to K^-\pi^-\pi^+ + p$ with the kinematic variables of interest. s is the total center-of-momentum energy of the $K^-_{\mathrm{beam}} p_{\mathrm{target}}$ system; t is the squared four-momentum transferred between the beam kaon and the target proton; and m_X is the invariant mass of the $K^-\pi^-\pi^+$ final state.

Combining equations (B.2) and (B.3)

$$m^2_{\mathrm{beam}} + m^2_X - 2\left(E_{\mathrm{beam}}E_X - |\vec{p}_{\mathrm{beam}}|\,|\vec{p}_X|\cos\theta\right) = 2m_{\mathrm{target}}(E_X - E_{\mathrm{beam}}) \tag{B.4}$$

and substituting the beam energy by the beam momentum via $E_{\mathrm{beam}} = \sqrt{m^2_{\mathrm{beam}} + |\vec{p}_{\mathrm{beam}}|}$ yields

$$m^2_{\mathrm{beam}} + m^2_X - 2\left(E_{\mathrm{beam}}E_X - |\vec{p}_{\mathrm{beam}}|\,|\vec{p}_X|\cos\theta\right) = 2m_{\mathrm{target}}(E_X - E_{\mathrm{beam}}) \tag{B.5}$$

$$2m_{\mathrm{target}}E_X - m^2_{\mathrm{beam}} - m^2_X - 2|\vec{p}_{\mathrm{beam}}||\vec{p}_X|\cos\theta = -2(E_X - m_{\mathrm{target}})\sqrt{m^2_{\mathrm{beam}} + |\vec{p}_{\mathrm{beam}}|^2}. \tag{B.6}$$

By taking the square of equation (B.6) and sorting the result by powers of $|\vec{p}_{\mathrm{beam}}|$, we obtain a quadratic equation in $|\vec{p}_{\mathrm{beam}}|$:

$$\begin{aligned} 0 = &\overbrace{\left[4(|\vec{p}_X|\cos\theta)^2 - 4(E_X - m_{\mathrm{target}})^2\right]}^{\equiv a}|\vec{p}_{\mathrm{beam}}|^2 \\ &+ \underbrace{\left[4(m^2_{\mathrm{beam}} + m^2_X - 2m_{\mathrm{target}}E_X)|\vec{p}_X|\cos\theta\right]}_{\equiv b}|\vec{p}_{\mathrm{beam}}| \\ &+ \underbrace{\left[(m^2_{\mathrm{beam}} + m^2_X - 2m_{\mathrm{target}}E_X)^2 - 4(E_X - m_{\mathrm{target}})^2 m^2_{\mathrm{beam}}\right]}_{\equiv c} \end{aligned} \tag{B.7}$$

Solving equation (B.7) allows to calculate the beam momentum from measured quantities:[a]

$$|\vec{p}_{\mathrm{beam}}| = \frac{-b + \sqrt{b^2 - 4ac}}{2a}. \tag{B.8}$$

[a] Only one of the two solutions of the quadratic equation in equation (B.7) is physical, i.e. yields a positive momentum.

Finally, the beam energy is calculated from the beam momentum via

$$E_{\text{beam}} = \sqrt{m_{\text{beam}}^2 + |\vec{p}_{\text{beam}}|^2}. \tag{B.9}$$

B.2 Estimation of the Non-Exclusive Background

In order to estimate the non-exclusive background in the final $K^-\pi^-\pi^+$ sample, we needed to separate exclusive from non-exclusive contributions in the distribution of the reconstructed beam energy E_{beam} shown in figure B.2.

The finite width of the peak in the beam-energy distribution of exclusive events arises from the intrinsic energy spread of the resolution of the apparatus. As a rough approximation, we parameterized the peak by a sum of two Gaussian functions $\mathcal{N}$ with different means μ_i and widths σ_i.

As there are many possible sources for non-exclusive events contributing to our data, there is no physics model for their E_{beam} distribution. We assumed that the E_{beam} distribution of non-exclusive events has a non-peaking shape in the energy region around the nominal beam energy and that it vanishes above this region, because the total energy in any reaction is limited by the beam energy. We parameterize the non-exclusive contributions by an arcus-tangents function, which models the vanishing background above the peak region, multiplied by a fourth order polynomial in the beam energy. The full model reads:

$$\begin{aligned} f(E_{\text{beam}}) = &\mathcal{N}(E_{\text{beam}}, \mu_1, \sigma_1) + \mathcal{N}(E_{\text{beam}}, \mu_2, \sigma_2) \\ &+ \underbrace{\left[\sum_{i=0}^{4} a_i \left(E_{\text{beam}} - \mu_1 - \varDelta E\right)^i\right] \cdot \left[\frac{\pi}{2} - \arctan\left\{b\left(E - \mu_1 - \varDelta E\right)\right\}\right]}_{\text{BG}(E_{\text{beam}})}, \end{aligned} \tag{B.10}$$

where μ_i, σ_i, a_i, b, $\varDelta E$ are the free parameter, which we fit to the data.

Figure B.2 shows the result of a fit[b] of equation (B.10) to the distribution after applying all cuts, except for the cut on E_{beam}. The non-exclusive contribution, $\text{BG}(E_{\text{beam}})$ shown by the orange curve, drops quickly above the nominal beam energy of about 191 GeV.

Using this fit result we estimated the total number of events and the number of non-exclusive events in our selected data sample by integrating the red and orange curves over the selected E_{beam} range. We obtained 402 051 events for the total number of events, which deviates only slightly from the measured number of 397 701 events in this energy region. This shows, that the model

[b] We performed a binned maximum-likelihood fit using a Poisson assumption for the distribution of the number of events in each bin. We fit a wide energy region from 155 to 221 GeV, to determine the parameters especially of the non-exclusive background term.

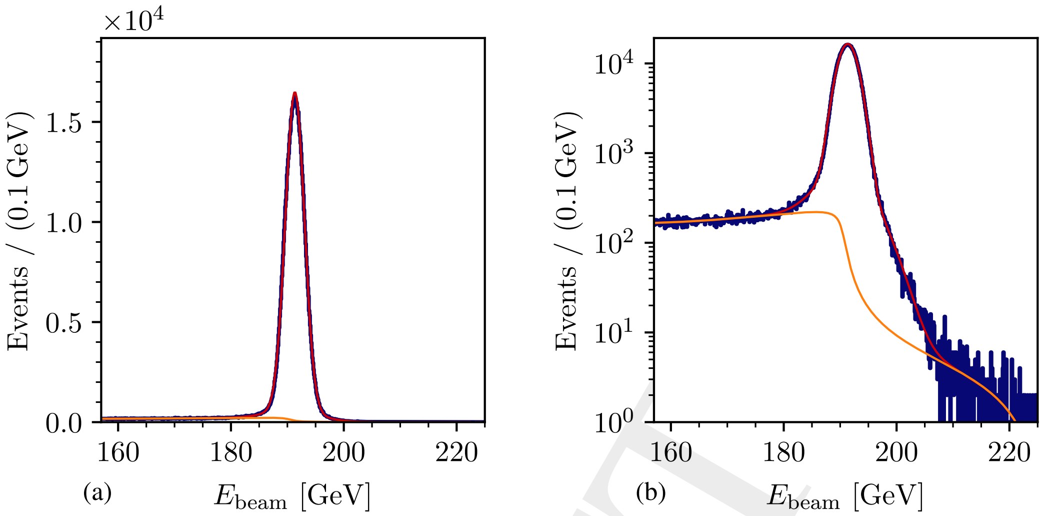

Figure B.2: Distribution of the reconstructed beam energy of the $K^{-}\pi^{-}\pi^{+}$ sample (blue histogram) after applying all cuts, except for the cut on E_{beam}, (a) in linear scale and (b) in logarithmic scale. The red curves show the fit of equation (B.10) to the distribution. The orange curves show the non-exclusive contributions $\text{BG}(E_{\text{beam}})$ [see equation (B.10)].

describes the data well. Given the ad-hoc nature of our parameterization $\text{BG}(E_{\text{beam}})$ for the non-exclusive contributions, the result may depend on this choice. To investigate this, we performed systematic studies were we reduced and increased the order of the background polynomial in equation (B.10). We also tested other fit ranges. Finally, we estimated a contribution of non-exclusive events to our data sample of $(2 \pm 1\,(\text{sys.}))\,\%$.

B.3 Fit of t' Spectra

In section 4.2, we qualitatively discuss the t' distribution. In this section, we parameterize the shape of the t' distribution and determine its parameters and its $m_{K\pi\pi}$ dependence. The shape of the t' distribution is also required as input to generate pseudodata (see appendix C). Since this is done independently for the years 2008 and 2009, we studied the t' distribution independently for both years. Here, we discuss only the results for 2008. The results for 2009 are similar.

The slope of the t' spectrum is steeper in the low- than in the high-t' region. In order to describe the full t' spectrum with one parameterization, we modeled it by a double-exponential distribution

$$\frac{\mathrm{d}\widehat{N}_{\text{ev}}(t';\, m_{K\pi\pi})}{\mathrm{d}t'} = A(m_{K\pi\pi})\left[e^{-b_1(m_{K\pi\pi})t'} + R(m_{K\pi\pi})e^{-b_2(m_{K\pi\pi})t'}\right], \tag{B.11}$$

where $b_i(m_{K\pi\pi})$ are the slope parameters and R is the ratio between the strength of second and first exponential contribution. b_1, b_2, A, and R depend on $m_{K\pi\pi}$.

The measured t' spectrum is distorted by acceptance effects caused by the experimental setup. In order to take these effects into account, we approximated the acceptance in two-dimensional cells of $m_{K\pi\pi}$ and t' based on a Monte Carlo sample that is uniformly distributed in the phase space (see appendix C for details).[c] We parameterized the t' dependence of the acceptance η in a given $m_{K\pi\pi}$ bin by

$$\eta(t'; m_{K\pi\pi}) = \eta_0 + \frac{1}{(t' - t'_0)^\alpha} \left[a + bt' + ct'^2 \right], \tag{B.12}$$

where η_0, t'_0, α, a, b, and c are free parameters. These free parameters are determined from a fit of equation (B.12) to the acceptance obtained from the Monte Carlo sample. The fit was performed in the t' range $0.08 \leq t' < 2.0\,(\mathrm{GeV}/c)^2$. Figure B.3a shows the result of such a fit in the range $1.2 \leq m_{K\pi\pi} < 1.4\,\mathrm{GeV}/c^2$. In the shown and in all other $m_{K\pi\pi}$ ranges, the used parameterization describes the acceptance well.

Finally, we modeled the measured t' spectrum as

$$\begin{aligned} \frac{\mathrm{d}\widehat{\widehat{N}}_\mathrm{ev}(t'; m_{K\pi\pi})}{\mathrm{d}t'} &= \eta(t'; m_{K\pi\pi}) \cdot \frac{\mathrm{d}\widehat{N}_\mathrm{ev}(t'; m_{K\pi\pi})}{\mathrm{d}t'} \\ &= \eta(t'; m_{K\pi\pi}) \cdot A(m_{K\pi\pi}) \left[e^{-b_1(m_{K\pi\pi})\, t'} + R(m_{K\pi\pi})\, e^{-b_2(m_{K\pi\pi})\, t'} \right]. \end{aligned} \tag{B.13}$$

We fitted equation (B.13) to the t' spectrum in the range $0.1 \leq t' < 2.0\,(\mathrm{GeV}/c)^2$ independently in $400\,\mathrm{MeV}/c^2$ wide bins of $m_{K\pi\pi}$ to determine the $m_{K\pi\pi}$ dependence of the free parameters b_i, A, and R.[d] Figure B.3b shows, for example, the t' spectrum in the range $1.2 \leq m_{K\pi\pi} < 1.6\,\mathrm{GeV}/c^2$. Our model (red curve) reproduces the measured t' spectrum well. This also holds for all other $m_{K\pi\pi}$ ranges.

Figure B.4a shows the slope parameters as a function of $m_{K\pi\pi}$. The first exponential term exhibits a steeper slope, i.e. a larger slope parameter, than the second exponential by construction of the fitting procedure. The steeper exponential becomes shallower with increasing $m_{K\pi\pi}$, while the slope of the shallower exponential stays almost constant with a maximum at about $m_{K\pi\pi} \approx 2\,\mathrm{GeV}/c^2$. The low-$m_{K\pi\pi}$ region is dominated by the steeper exponential as shown by the ratio of their strength in figure B.4b. In the high-$m_{K\pi\pi}$ region at about $3\,\mathrm{GeV}/c^2$ the shallower exponential becomes more significant, but its contribution stays below about 11 %. We observed qualitatively similar features in the COMPASS data of the reaction $\pi^- + p \to \pi^-\pi^-\pi^+ + p$ [39].

B.4 Time Stability

In order to reject data where some of the detectors were malfunctioning, we tested the time stability of the data taking. Therefore, we studied the change of various kinematic distributions with time for the reactions $K^- + p \to K^-\pi^-\pi^+ + p$ and $\pi^- + p \to \pi^-\pi^-\pi^+ + p$ [43]. We mainly

[c] Doing so, we neglected the non-uniform distribution of the measured events in the phase space. However, this has only a minor effect on the acceptance in t' and hence, it does not strongly influence the extracted slope parameters.

[d] We performed a binned maximum-likelihood assuming a Poisson distribution for the number of events in each bin.

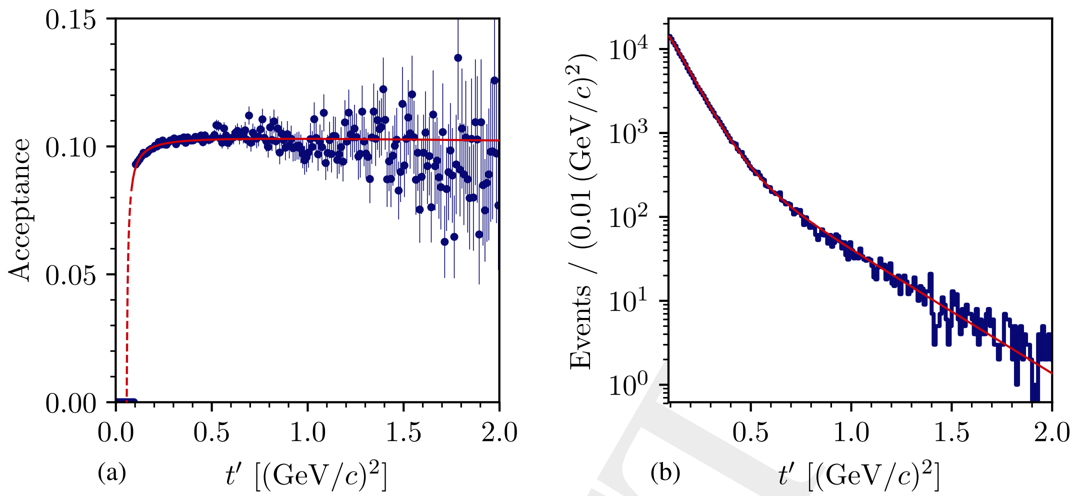

Figure B.3: Result of fits to extract the t' slope parameters form the 2008 diffraction data set. (a) shows the experimental acceptance as a function of t' in the range $1.2 \leq m_{K\pi\pi} < 1.4\,\mathrm{GeV}/c^2$ (blue points) together with a fit of equation (B.12) (solid red curve). The dashed red curve shows the extrapolation beyond the fitted t' range. (b) shows the measured t' spectrum in the range $1.2 \leq m_{K\pi\pi} < 1.6\,\mathrm{GeV}/c^2$ (blue histogram) together with a fit of equation (B.13) (red curve).

studied distributions in final-state kinematic variables, which are analyzed in the partial-wave decomposition (see section 5.1). As a simple test to check for changes in the distributions, we determined the moments of the distributions as a function of time and check for deviations from the average value of the corresponding moment.

Figure B.5 shows the mean value, i.e. first moment, of the $m_{K\pi\pi}$ distribution as a function of time represented by the run number. Outliers, i.e. data points that significantly deviate from the average value, in this or one of the other studied kinematic distributions that could be correlated to problems in the experimental setup were removed from the final data sample (see section 4.1). These data are shown as gray points. The remaining data, shown as blue points, exhibit no significant time dependence. Using a χ^2 test,[e] for example the time dependence of the mean value of $m_{K\pi\pi}$ is consistent with a constant with a p-value of 0.7. With this approach, we were able to clean up our data sample from artifacts caused by problems during the data taking.

[e] See sections 4.5 and 4.7 in ref. [119] for details on the χ^2 test.

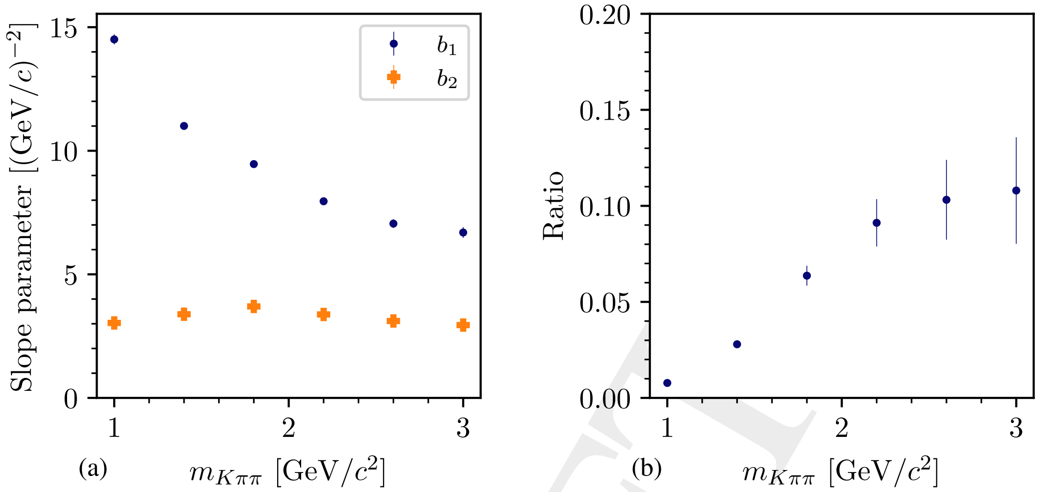

Figure B.4: Results of fitting equation (B.13) to the measured t' spectra in bins of $m_{K\pi\pi}$ as obtained from the 2008 diffraction data set. (a) shows the slope parameters of the first (blue) and second (orange) exponential. (b) shows the ratio of the strength of the second and the first exponential term in equation (B.13). The uncertainties are smaller than the marker size for most of the data points.

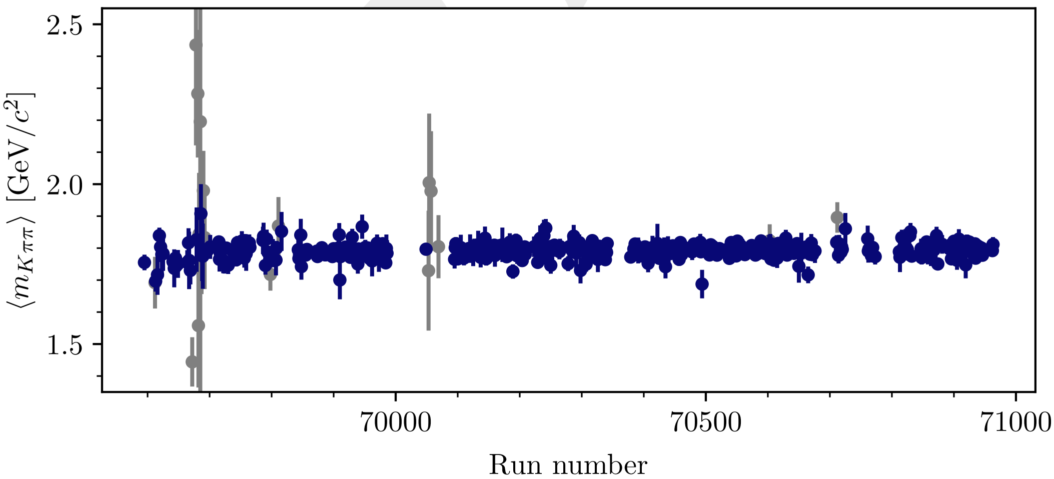

Figure B.5: Time stability of the $m_{K\pi\pi}$ distribution. The mean mass $\langle m_{K\pi\pi} \rangle$ per chunk of data in time, called run, is shown, versus the number of the run ordered in time. The blue points show the selected data, the gray points show the rejected data. The errors bars represent the statistical uncertainty of the mean values.

C Monte Carlo Simulation

Monte Carlo simulations are an important tool in partial-wave analyses. They allow us to verify the applied analysis methods or to trace the origin of some systematic effects. In addition, they are necessary to study effects caused by the finite probability to experimentally observe a produced event, i.e. by the acceptance.

We performed Monte Carlo simulations by generating so-called produced pseudodata samples of events that are randomly distributed according to a certain model input. We used different physics models or generated samples that are uniformly distributed in the phase-space variables. The procedure is described in appendix C.1.

To study the experimental acceptance and resolution and to take the effects they cause into account when comparing models to measured data, we applied both to the produced pseudodata samples. The procedure is described in appendix C.2. Thereby, we obtained so-called reconstructed pseudodata samples.

The distributions of the reconstructed pseudodata, called reconstructed distributions, mimic the measured distributions of data recorded by the experiment, which we refer to as measured data in the following. The distributions of produced pseudodata events, called produced distributions, are the "true" distribution of the underlying physics process, i.e. without acceptance and resolution effects. We also call the "true" distributions of the underlying physics process of measured data produced distributions of produced events. Finally, the reconstructed values of kinematic variables of reconstructed pseudodata mimic measured values of measured data and the produced values are the true values of the kinematic variable with which the event was produced.

As the measurement effects induced by the apparatus can be different for the diffraction data taking campaigns in 2008 and 2009, we treated both years separately. In this chapter, we discuss the main features of the measurement effects exemplarily for the 2008 setup. The measurement effects of the 2009 setup show similar features.

C.1 Generating Pseudodata of Diffractive Scattering Reactions

In this section, we will briefly summarize how to generate pseudodata samples of diffractive scattering reactions. The generic topology of these reactions is depicted in figure C.1. An example of such a reaction is the reaction $K^- + p \to K^-\pi^-\pi^+ + p$ analyzed in this work.

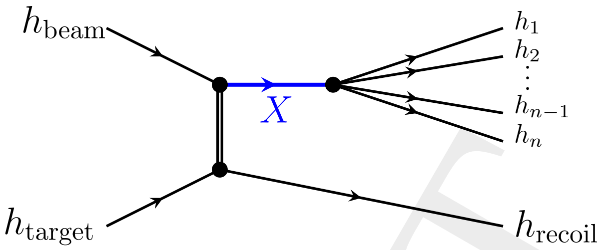

Figure C.1: Schematic view of diffractive scattering of a high-energy hadronic beam particle h_{Beam} off some hadronic target particle h_{target}. In this process, the target particle scatters elastically and the beam particle gets excited into some intermediate state X, which further decays into a hadronic n-body final state.

As we analyzed our data independently in kinematic cells of the invariant mass m_X of the X system and of the reduced four-momentum transfer squared t', we generate pseudodata samples independently in (m_X, t') cells. For fixed m_X and t', the probability of an event is proportional to the decay rate of the intermediate state X to the n-body final state, which is proportional to two factors (see equation (43.10) in ref. [9]): (i) the matrix element squared $|\mathcal{M}|^2$ and (ii) the differential n-body phase-space volume $\mathrm{d}\Phi_n$. The first one encodes the properties of the physical process, the latter one is a purely kinematic factor.

In order to generate events that are distributed according to their reaction cross-section, we first generated a sample of events that is uniformly distributed in the n-body phase space, i.e. the probability to produce an event is proportional only to $\mathrm{d}\Phi_n$.

Second, we obtained a produced pseudodata sample of a given model for $|\mathcal{M}|^2$ by randomly accepting events from the phase-space distributed sample according to their probability, which is proportional to $|\mathcal{M}|^2$.[a] For example, when generating a pseudodata sample from the results of a partial-wave decomposition, i.e. from the modeled intensity distribution $\mathcal{I}(\tau, m_{K\pi\pi}, t')$ [see equation (5.16)], we used $|\mathcal{M}(\tau, m_{K\pi\pi}, t')|^2 \propto \mathcal{I}(\tau, m_{K\pi\pi}, t')$. The m_X and t' dependence is accounted for by generating a number of events in each (m_X, t') cell that is proportional to the number of events predicted by the model.

A special case are pseudodata samples that are distributed uniformly in the n-body phase space of the final-state particles, i.e. $|\mathcal{M}|^2 = 1$. For example, such so-called phase-space pseudodata samples were used to accounting for acceptance effects in the partial-wave decomposition. For these samples, we drew m_X uniformly in the analyzed mass range and t' according to the t'

[a] See [181, 182] for details on this accept-reject method.

spectra we observed in the corresponding measured sample (see appendix B.3 for the t' spectra of the $K^-\pi^-\pi^+$ sample).

C.2 Monte Carlo Simulation of the Experimental Setup

Although, the COMPASS experimental setup covers a wide kinematic range, its acceptance and measurement resolution are finite. These measurement effects distort the distribution of produced events. Thus, they have to be taken into account when comparing measured distributions to, e.g. model expectations. The dominant effect for the $K^-\pi^-\pi^+$ final state is the limited momentum range of the final-state particle identification.

In order to obtain a reconstructed pseudodata sample that incorporates acceptance and resolutions effects, we processed the events of the produced pseudodata sample through a Monte Carlo simulation of the full COMPASS setup. Then, we applied the same event reconstruction algorithm [53] to the simulated detector responses, as applied to measured data. Finally, only those events entered the reconstructed pseudodata sample that survived the same event-selection criteria as applied to measured data. Following this approach, a reconstructed pseudodata sample is distributed as if it had been measured by the experimental apparatus.

The Monte Carlo simulation of the COMPASS setup is described in section 10 of ref. [49]. In the following, we describe aspects of the Monte Carlo simulation that were improved in this analysis (appendix C.2.1) or that are particular to this analysis (appendices C.2.2 and C.2.3).

C.2.1 Simulation of the Beam and Vertex Distribution

In order to simulate the experimental setup, we transformed the event kinematics from the center-of-momentum system of the reaction to the laboratory frame. This required the distribution of beam particle momentum to be known. In addition, the interaction vertex had to be placed within the target volume. The spatial distribution of the interaction vertices is given by the distribution of the beam particles in the plane transverse to the beam direction and by the target material (see figure 4.2). In total, the six-dimensional beam-particle distribution is required to generate pseudodata, i.e. the vertex position $(X_{\text{Vtx}}, Y_{\text{Vtx}}, Z_{\text{Vtx}})$ and the beam momentum. The latter one is expressed in terms of the beam energy E_{beam} and in terms of the inclinations $\frac{p_x}{|\vec{p}|}$ and $\frac{p_y}{|\vec{p}|}$ of the beam track in horizontal and vertical direction, respectively. The orientation angle of the production plane of the reaction (see section 5.1.1) around the direction of the beam particle is uniformly distributed, due to ration symmetry.

The beam-particle distribution is high-dimensional, complicatedly correlated, and thus hard to model. Therefore, we generated the beam-particle distribution of pseudodata events by using the beam-particle kinematics from randomly chosen events of a measured beam sample.

In total, we generated about 200 times more pseudodata events than measured events, which required a large beam sample. In order to obtain a beam sample, we selected events with three charged particles in the final state, because measuring three charged tracks allows for a precise reconstruction of the interaction vertex, which reduces systematic effects from the beam sample. Simulating resolution effects at the borders of the kinematic regions that were selected for the measured $K^-\pi^-\pi^+$ sample requires generating pseudodata events also outside these regions. Therefore, the cuts to select the beam sample were chosen to be wider compared to the ones for the measured $K^-\pi^-\pi^+$ sample. Starting from the same preselection as for the $K^-\pi^-\pi^+$ final state (see section 4.1 for details), we applied the following additional cuts:

- Signal from the diffraction trigger DT0
- Interaction vertex position along the beam direction: $-70 \leq Z_{\mathrm{Vtx}} < -27\,\mathrm{cm}$
- Interaction vertex position in the plane transverse to the beam direction: $\sqrt{X_{\mathrm{Vtx}}^2 + Y_{\mathrm{Vtx}}^2} < 1.9\,\mathrm{cm}$
- Momentum conservation in $\Delta\phi_{\mathrm{recoil}}$ using the measured recoil proton (see section 4.1)
- Reconstructed beam-particle energy $|E_{\mathrm{beam}} - 191.35\,\mathrm{GeV}| < 17.95\,\mathrm{GeV}$
- Uncertainty in the reconstructed beam energy[b] is less than 20 GeV

The kinematic distributions of this beam sample are distorted by acceptance and resolution effects. However, the physical distributions are needed as input to the Monte Carlo simulation. Therefore, we had to correct the beam sample for these effects.

The strongest acceptance effect is in the Z_{Vtx} distribution. Final-state particles produced in reactions at the upstream end of the target have to fly a long path through the target and thereby undergo multiple scattering.[c] Thus, the acceptance is lower for events with an interaction vertex located at the upstream end of the target. In the other variables of the beam sample the acceptance is approximately uniform in the range of interest. To correct for the acceptance in Z_{Vtx}, we determined the acceptance in bins of Z_{Vtx} from a reconstructed phase-space pseudodata sample of the reaction $\pi^- + p \to \pi^-\pi^-\pi^+ + p$, which is the dominant contribution to the beam sample. Then, the acceptance was parameterized by a third-order polynomial in Z_{Vtx}:

$$\eta(Z_{\mathrm{Vtx}}) = A\left[1 + a(Z_{\mathrm{Vtx}} + 50\,\mathrm{cm}) + b(Z_{\mathrm{Vtx}} + 50\,\mathrm{cm})^2 + c(Z_{\mathrm{Vtx}} + 50\,\mathrm{cm})^3\right], \qquad \text{(C.1)}$$

where A, a, b, and c are free parameters we fitted to the acceptance in bins of Z_{Vtx}. Using the parameterization in equation (C.1),we corrected the beam sample for acceptance effects in the

[b] We calculated the uncertainty in E_{beam} using linear error propagation of equation (B.9). We used the uncertainties of the measured momenta of the final-state particles and of the measured beam-particle inclination. We also took into account the correlations between these measured quantities from the event-reconstruction fit [53].

[c] The material thickness of the liquid-hydrogen target along the beam axis corresponds to 4.5 % of a radiation length and 5.5 % of a nuclear interaction length [49].

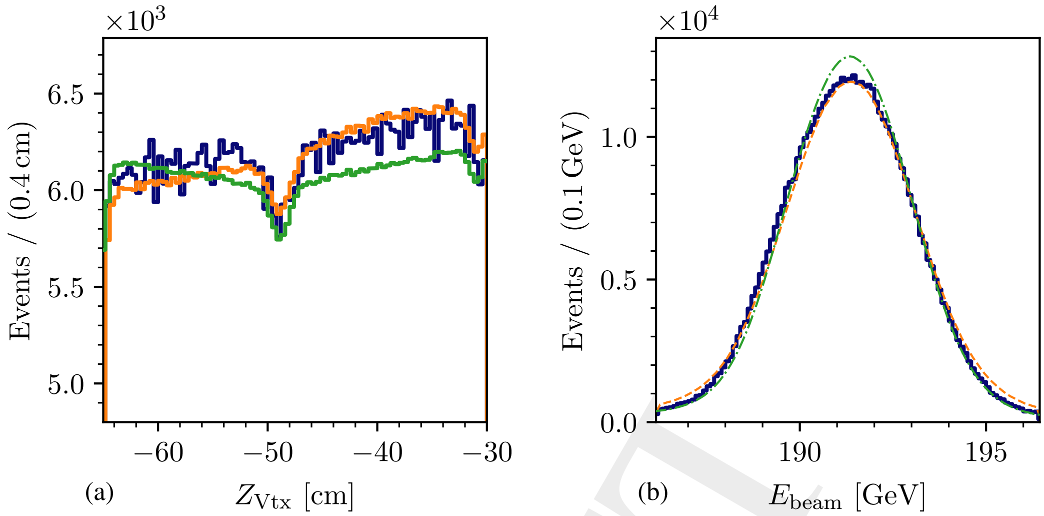

Figure C.2: (a) Interaction vertex position along the beam axis and (b) beam energy of a reconstructed $K^-\pi^-\pi^+$ phase-space pseudodata sample for the 2008 diffraction data taking (orange histograms). The blue histograms show the corresponding measured distributions of the $K^-\pi^-\pi^+$ sample from the 2008 diffraction data set. The green histograms show the distributions of the beam sample extracted from the 2008 diffraction data set corrected for the dominant acceptance and resolution effects (see text). The corrected beam sample is used as input to the Monte Carlo simulation. The histograms are normalized to the same integral as the measured $K^-\pi^-\pi^+$ data histograms in the shown ranges.

Z_{Vtx} distribution by randomly accepting events with a probability proportional to the weight[d]

$$w(Z_{\mathrm{Vtx}}) = \frac{1}{1 + a(Z_{\mathrm{Vtx}} + 50\,\mathrm{cm}) + b(Z_{\mathrm{Vtx}} + 50\,\mathrm{cm})^2 + c(Z_{\mathrm{Vtx}} + 50\,\mathrm{cm})^3}. \tag{C.2}$$

Thereby, we accepted a large fraction of the beam sample of about 94 %.

Figure C.2a shows the Z_{Vtx} distribution of the beam sample after this acceptance correction (green histogram). It disagrees with the measured Z_{Vtx} distribution of the $K^-\pi^-\pi^+$ sample (blue histogram) due to the acceptance effects. The orange histogram shows the reconstructed Z_{Vtx} distribution of a reconstructed $K^-\pi^-\pi^+$ phase-space pseudodata sample. This sample was generated using the acceptance-corrected beam sample as input. Then, it was processed through the detector Monte Carlo simulation. Thereby, acceptance effects were applied to this reconstructed $K^-\pi^-\pi^+$ phase-space pseudodata sample. It is in fair agreement wit the measured $K^-\pi^-\pi^+$ distribution, which demonstrates that our acceptance correction of the beam sample works. Using the Z_{Vtx} distribution from the beam sample to generate events allows us to take into account effects that are not modeled in the detector Monte Carlo simulation. For example, the dip in the Z_{Vtz} distribution at about −48 cm, which is caused by inefficient areas of the RPD scintillator slabs due to connectors for the calibration laser [183].

[d] As we were interested only in the deviation from a flat acceptance and not in an absolute normalization, we dropped the A parameter here, which is the acceptance at $Z_{\mathrm{Vtx}} = -50\,\mathrm{cm}$. As $A \approx 0.5$, this drastically improved the efficiency of the acceptance correction.

The strongest resolution effect is in the measured beam-particle energy E_{beam}. As for the acceptance effects in Z_{Vtx}, we needed to correct the beam sample for this resolution effect in order to use it as input to the Monte Carlo simulation. Using Bayes' formula, the probability that the beam particle was produced with energy $\tilde{E}_{\text{beam}}$ given that we measured E_{beam} is

$$P(\tilde{E}_{\text{beam}}|E_{\text{beam}}) = \frac{P(E_{\text{beam}}|\tilde{E}_{\text{beam}})\,P(\tilde{E}_{\text{beam}})}{P(E_{\text{beam}})}. \tag{C.3}$$

Here, $P(E_{\text{beam}})$ is the probability distribution of the measured energy, $P(\tilde{E}_{\text{beam}})$ is the probability distribution of the produced beam energy, i.e. without resolution effects, and $P(E_{\text{beam}}|\tilde{E}_{\text{beam}})$ is the probability to measure an energy E_{beam} if the event was produced with an energy $\tilde{E}_{\text{beam}}$, i.e. it encodes the smearing effect due to the resolution.

We modeled the resolution function, $P(E_{\text{beam}}|\tilde{E}_{\text{beam}})$, by a Gaussian function centered around zero with standard deviation σ_{R}.[e] We approximated the distribution $P(\tilde{E}_{\text{beam}})$ of the produced energy of the beam particle also by a Gaussian function with mean $\tilde{\mu}$ and standard deviation $\tilde{\sigma}$. This is only a rough approximation, e.g. it neglects the weak correlation between the beam-particle energy and other kinematic variables of the beam particle introduced by the beam-line optics.

The energy resolution $\sigma_{\text{R}} = 0.78\,\text{GeV}$[f] was taken from the detector Monte Carlo simulation.[g] The mean and standard deviation of the produced-energy distribution $P(\tilde{E}_{\text{beam}})$ were calculated from the measured energy distribution $P(E_{\text{beam}})$ of the beam sample. Under the assumptions made here, $P(E_{\text{beam}})$ is a Gaussian distribution with standard deviation $\sigma = \sqrt{\tilde{\sigma}^2 + \sigma_{\text{R}}^2}$ and mean $\mu = \tilde{\mu}$. We determined $\sigma = 1.82\,\text{GeV}$ and $\mu = 191.35\,\text{GeV}$[f] by fitting a Gaussian function plus a second-order background polynomial to the E_{beam} distribution of the beam sample.

Using the assumptions made above and equation (C.3), $P(\tilde{E}_{\text{beam}}|E_{\text{beam}})$ becomes a Gaussian shape with mean and standard deviation of

$$\hat{\mu} = \frac{\tilde{\sigma}^2}{\sigma_{\text{R}}^2 + \tilde{\sigma}^2} E_{\text{beam}} + \frac{\sigma_{\text{R}}^2}{\sigma_{\text{R}}^2 + \tilde{\sigma}^2} \tilde{\mu} \qquad \text{and} \qquad \hat{\sigma} = \sqrt{\frac{1}{\frac{1}{\sigma_{\text{R}}^2} + \frac{1}{\tilde{\sigma}^2}}}. \tag{C.4}$$

In order to correct for the E_{beam} resolution when generating a pseudodata event from the beam sample, we randomly drew the energy $\tilde{E}_{\text{beam}}$ of the pseudo beam particle according to $P(\tilde{E}_{\text{beam}}|E_{\text{beam}})$ using the measured energy E_{beam} of a randomly chosen event from the beam sample.[h]

[e] Thereby, we neglected a potential energy dependence of the energy resolution.

[f] Here, we give the values for the 2008 setup. The values for the 2009 setup are similar.

[g] We fit a Gaussian function with standard deviation σ_{R} to the distribution of the differences between the physical and the reconstructed energy of beam particles from the reconstructed phase-space pseudodata sample of the reaction $\pi^- + p \to \pi^-\pi^-\pi^+ + p$ discussed above.

[h] Note that we used E_{beam} from the beam sample, and we used $P(\tilde{E}_{\text{beam}}|E_{\text{beam}})$ only to correct for the energy resolution. The reason for this is, that E_{beam} form the beam sample is distributed according to the physical distribution, which

The green histogram in figure C.2b shows the distribution of the resolution-corrected beam-particle energy $\tilde{E}_{\text{beam}}$ of the beam sample. It is narrower than the measured E_{beam} distribution of the $K^-\pi^-\pi^+$ sample shown by the blue histogram. The orange histogram shows the reconstructed beam-particle energy from a reconstructed $K^-\pi^-\pi^+$ phase-space pseudodata sample, which was generated using the resolution-corrected beam sample as input. It is in good agreement with the measured $K^-\pi^-\pi^+$ data in the peak region. This shows, that the correction of the resolution effects works well. Only in the tails of the distribution, where the Gaussian assumption is not a good approximation anymore, the reconstructed $K^-\pi^-\pi^+$ phase-space pseudodata sample slightly deviates from the measured sample.

C.2.2 Modeling the CEDAR Acceptance

The likelihood approach discussed in section 3.1 is able to identify the beam particles in a wide kinematic range. Figure C.3a shows that the acceptance, i.e. the efficiency to identify a beam kaon, is above about 95 % for small beam-particle inclinations. However, it drops to about 60 % for inclination angles above about 100 mrad.

A full simulation of the CEDAR response in the detector Monte Carlo simulation is not feasible as it is computationally too expensive.[i] Therefore, we incorporated the CEDAR acceptance effect in the detector Monte Carlo simulation in an approximate way by randomly accepting a pseudodata event with beam-particle inclination $({}^1\vartheta_x, {}^1\vartheta_y)$ with the probability given by the acceptance as shown in figure C.3a.[j] When simulating events with beam pions, but still applying an event selection for beam kaons as done in section 5.10, we randomly accepted pseudodata events with beam-particle inclination $({}^1\vartheta_x, {}^1\vartheta_y)$ with the misidentification probability as shown in figure C.3b.[j]

C.2.3 Modeling the RICH Acceptance

A full simulation of the RICH response in the detector Monte Carlo simulation is not feasible for the same reasons as for the CEDAR response. Following ref. [49], we inferred the RICH response from data. As shown in section 3.2.2, we determined for a given RICH likelihood-ratio threshold $\mathcal{T}_{\text{R}}$ the final-state particle identification probabilities $P(X \to S)$ independently in

is only roughly approximated by a Gaussian function and which includes all correlations with other kinematic variables. In our approach, the Gaussian approximation is used only for the resolution correction, while generating events directly according to $P(\tilde{E}_{\text{beam}})$ would imply a Gaussian approximation for the energy distribution.

[i] A full simulation of the CEDAR response would require to simulate each single Cherenkov photon including its path through the CEDAR optics and its detection in the PMTs. This is difficult to implement and computationally very expensive. As we do not expect large influence of the CEDAR acceptance on the kinematic distribution of the final-state particles, which is studied in the partial-wave decomposition, a full simulation of the CEDAR response would be inadequately time-consuming.

[j] Doing so, we linearly interpolated between the $({}^1\vartheta_x, {}^1\vartheta_y)$ cells. In the green regions in figure C.3 without calibration data, we never identified the beam kaon. However, only a negligible fraction of pseudodata events has beam-particle inclinations in these regions.

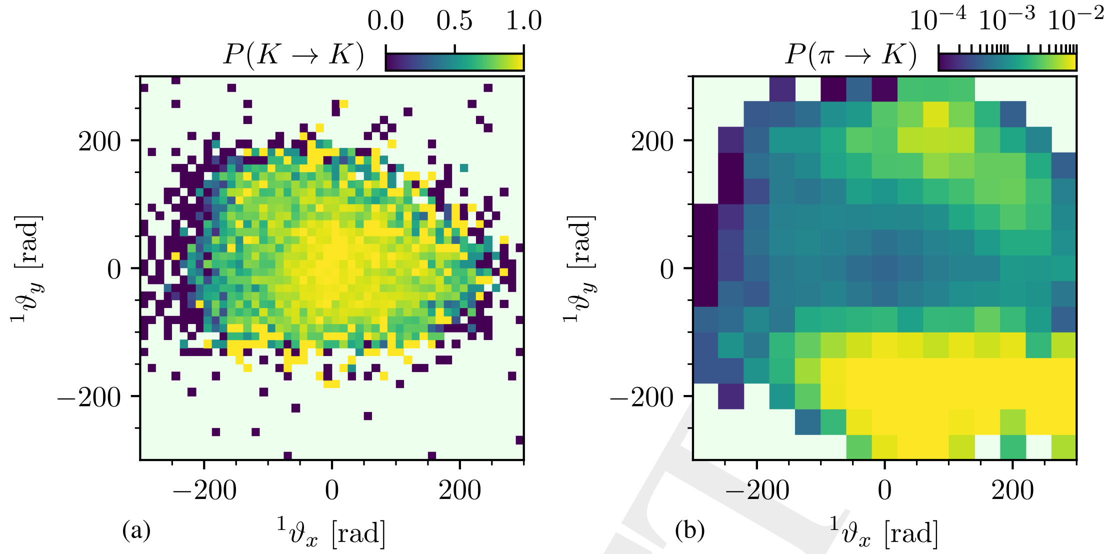

Figure C.3: (a) acceptance for the identification of beam kaons and (b) misidentification probability to identify a beam pion as a kaon by the CEDAR detectors as a function of the inclination of the beam-particle track with respect to the optical axis of CEDAR1. The acceptance was determined from the $K \to \pi^-\pi^-\pi^+$ validation sample of the 2008 diffraction data set and the misidentification probability was determined from the pion-beam validation sample of the 2008 diffraction data set (see appendix A.1.2). Given the small fraction of misidentified beam pions, we chose a more coarse binning in (b). We chose the reference system of CEDAR1 for the beam-particle inclination. Regions without calibration data are drawn in light green.

cells of the particle momentum $|\vec{p}_\mathrm{R}|$ and the square-root of its track angle θ_R with respect to the nominal beam axis, both defined at the RICH position, for the different particle species X and for the different particle-species hypotheses S. Using these probabilities, we simulated the RICH response to a particle of species X by randomly drawing a particle-species assignment S by the RICH according to $P(X \to S)$.[k] As muons and pions are very close in mass, we approximated the probability to identify a muon as particle species S using the pion validation sample, i.e. we assumed $P(\mu \to S) \approx P(\pi \to S)$.[l]

C.3 Predictions for Kinematic Distributions from the Partial-Wave Decomposition

In order to study kinematic distributions as predicted by some model for $|\mathcal{M}|^2$, e.g. for the comparison of the PWD result with measured data discussed in section 5.6, we generated phase-space pseudodata samples and assigned a weight w_i to each event that is proportional to $|\mathcal{M}|^2$

[k] Doing so, we linearly interpolated between the $(|\vec{p}_\mathrm{R}|, \sqrt{\theta_\mathrm{R}})$ cells and normalized the sum over all probabilities to be one.

[l] Muons can appear in the simulation, e.g. from decays of final-state kaons. However, these contributions are negligible for the reactions simulated in this work.

of the event (cf. appendix C.1).[m] When weights are assigned to a reconstructed phase-space pseudodata sample, the obtained distribution resembles the distribution of measured events. When weights are assigned to a produced phase-space pseudodata sample, the obtained distribution resembles true physical distribution. We chose the normalization of the weights such that the sum over all weights is the model prediction for the total number of events. This means that

$$\sum_i w_i \equiv \widehat{\widehat{N}}_{\text{ev}} \qquad \text{or} \qquad \sum_i w_i \equiv \widehat{N}_{\text{ev}} \tag{C.5}$$

for the distribution of reconstructed or produced events, respectively. Thus, histograms filled with these weights of reconstructed pseudodata events can be directly compared to histograms from measured data.

When predicting distributions of a data sample that consists of different sub-samples,[n] we first obtained the distributions for the individual sub-samples following the approach described in the previous paragraph. As these distributions are normalized to the expected number of events in each sub-sample according to equation (C.5), we simply added them to obtain the distributions of the total sample.

When predicting distributions based on the result of a PWD fit, we used $|\mathcal{M}(\tau, m_{K\pi\pi}, t')|^2 \propto \mathcal{I}(\tau, m_{K\pi\pi}, t')$, where $\mathcal{I}(\tau, m_{K\pi\pi}, t')$ is the model intensity [see equation (5.16)] evaluated using the maximum-likelihood estimates of the transition amplitudes and data-set fraction parameters from the fit.

When predicting distributions based on the results of a Bootstrapping of the PWD, as done in section 5.6, we used $|\mathcal{M}(\tau, m_{K\pi\pi}, t')|^2 \propto \mathcal{I}(\tau, m_{K\pi\pi}, t')$, where we evaluated the model intensity using the Bootstrapping estimates for the spin-density matrix elements and data-set fraction parameters. To this end, we used the formulation of $\mathcal{I}(\tau, m_{K\pi\pi}, t')$ in terms of spin-density matrix elements as given in equation (5.19).[o]

[m] For the same number of generated phase-space events, using weights leads to a slightly reduced variance from the Monte Carlo sampling of the predicted quantities, compared to the accept-reject algorithm described in appendix C.1.

[n] For example, the $K^-\pi^-\pi^+$ sample consists of three sub-samples from the 2008, the 2009W2X, and the 2009W35 diffraction data taking campaigns with slightly different acceptances.

[o] In ROOTPWA, which is our PWD software framework, $\mathcal{I}(\tau, m_{K\pi\pi}, t')$ is implemented in terms of transition amplitudes as input parameters. Thus, in order to use the Bootstrapping estimates for the spin-density matrix elements, the corresponding spin-density matrix has to be decomposed into a set of transition amplitudes. Although we used a rank=3 spin-density matrix in the PWD model, the spin-density matrix obtained from Bootstrapping has maximum rank. This is because its elements are calculated individually by calculating the mean values of the corresponding estimates from the independent Bootstrapping fits. These mean values do not have the constraint of a rank=3 matrix implemented. In principle, a Cholesky decomposition of the spin-density matrix obtained from Bootstrapping could be used, which would yield a set of tranition amplitudes that is similar to the Chung and Trueman parameterization [73]. However, the Cholesky decomposition yielded numerically unstable result. Thus, we used an eigenvalue decomposition, which yielded a set of transition amplitudes that given the same $\mathcal{I}(\tau, m_{K\pi\pi}, t')$ as directly using the Bootstrapping estimates for the spin-density matrix elements in equation (5.19).

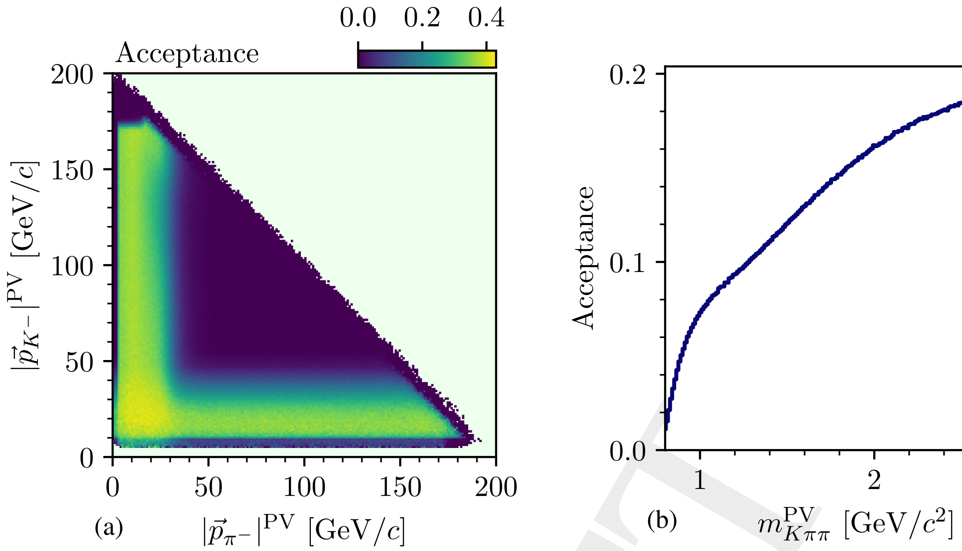

Figure C.4: Acceptance of the 2008 experimental setup as determined from a reconstructed $K^-\pi^-\pi^+$ phase-space pseudodata sample as a function of (a) the momenta of the two identified negative final-state particles and (b) the invariant mass of the $K^-\pi^-\pi^+$ system. The physical values (PV) of the kinematic variables with which the event was produced are shown, which do not involve smearing due to the detector resolution or misidentification of the final-stat particle species. Both figures show the acceptance for events that were produced uniformly in the $K^-\pi^-\pi^+$ phase space, which is different from the distribution with which the measured events were produced.

C.4 Acceptance and Resolution for the $K^-\pi^-\pi^+$ Sample

Using the approach discussed in appendices C.1 and C.2, we generated a reconstructed phase-space pseudodata sample of the reaction $K^- + p \to K^-\pi^-\pi^+ + p$. Based on this sample, we performed first studies of acceptance and resolution effects on different kinematic variables. One should keep in mind, that considering individual variables implies a marginalization over all other kinematic variables. Here, we marginalized using a sample that was generated uniformly in phase space. The events produced in the physical reaction follow a different distribution, which can be taken into account only using the model from the partial-wave decomposition (see section 5.6).

The strongest acceptance effects originate from the limited momentum range of the RICH final-state particle identification (see section 3.2.2). The acceptance of the reconstructed phase-space pseudodata shows the same bands in the momentum distribution of the two identified negative final-state particles as the measured distribution (cf. figures 4.3 and C.4a). The acceptance is vanishing in the inner triangular region where both momenta are above about 50 GeV/c. This supports the statements about the experimental acceptance in section 4.1.

The above discussed acceptance effects lead to a non-uniform acceptance also in other kinematic variables. For example, the acceptance as a function of $m_{K\pi\pi}$ drops towards lower masses as

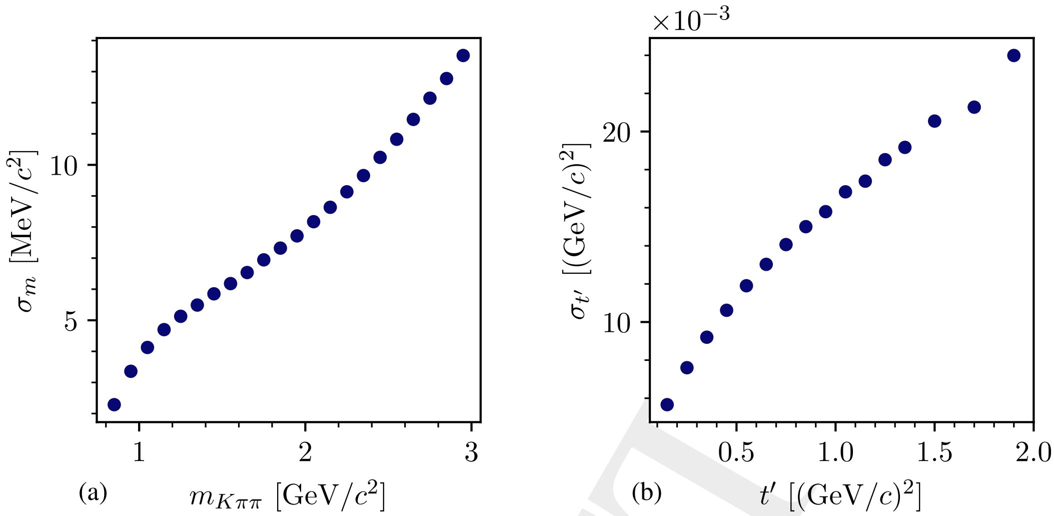

Figure C.5: Resolution of the 2008 experimental setup as determined from a reconstructed $K^-\pi^-\pi^+$ phase-space pseudodata sample. (a) shows the resolution σ_m in the invariant mass of the $K^-\pi^-\pi^+$ system as a function of $m_{K\pi\pi}$. (b) shows the resolution $\sigma_{t'}$ in t' as a function of t'. We determined the resolution from a fit of a Gaussian function plus a constant background to the distribution of the differences between the reconstructed and the produced value. As the pseudodata falls exponentially with t', we used a coarser binning at high-t' to compensate for the smaller amount of data.

shown in figure C.4b for the phase-space pseudodata sample. This demonstrates how crucial an accurate treatment of the acceptance is. Fortunately, the acceptance exhibits no peaking structures in $m_{K\pi\pi}$. Therefore, the structures observed in the measured $m_{K\pi\pi}$ distribution shown in figure 4.6a can still be interpreted on a qualitative level.

The reconstructed phase-space pseudodata sample also allows us to determine the experimental resolution of the detector setup. The resolution in $m_{K\pi\pi}$ worsens continuously with increasing $m_{K\pi\pi}$ from about $3\,\text{MeV}/c^2$ at $m_{K\pi\pi} = 0.8\,\text{GeV}/c^2$ to about $14\,\text{MeV}/c^2$ as $m_{K\pi\pi} = 3\,\text{GeV}/c^2$ (see figure C.5a). However, as most of the strange-meson resonances have widths of above $100\,\text{MeV}/c^2$, the resolution in $m_{K\pi\pi}$ will have a negligible influence on the width measurement of resonances.

Also, the resolution in t' worsens from about $6 \times 10^{-3}\,(\text{GeV}/c)^2$ at $t' = 0.1\,(\text{GeV}/c)^2$ to about $24 \times 10^{-3}\,(\text{GeV}/c)^2$ at $t' = 2\,(\text{GeV}/c)^2$ as shown in figure C.5b. The resolution in t' is sufficiently high to perform a partial-wave analysis in narrow t' bins. In this analysis, the narrowest t' bin at $t' = 0.125\,(\text{GeV}/c)^2$ has a width of $50 \times 10^{-3}\,(\text{GeV}/c)^2$, which is much larger than the resolution.

D Partial-Wave Decomposition

D.1 Wave-Set Selection

D.1.1 Determination of Intensity Thresholds

In order to determine the intensity threshold above which waves were included in the wave set, we studied the partial-waves intensities obtained from the wave-set selection fits in individual $(m_{K\pi\pi}, t')$ cells. Figure D.1a exemplarily shows the partial waves ordered by intensity, i.e. the so-called ordered-intensity distribution. As discussed in section 5.2.5, ordered-intensity distributions exhibit jumps. The intensities at which those jumps appear determine the thresholds above which waves were selected for the wave set. In order to automatically determine the threshold for each $(m_{K\pi\pi}, t')$ cell, we searched for all jumps in the ordered-intensity distribution of the $(m_{K\pi\pi}, t')$ cell. We defined a jump as a discontinuity where the intensity changes by more than a factor eight, i.e. where the intensity of a wave is smaller than $1/8$ of the intensity of the next lager wave.[a] If we found no discontinuity by at least a factor eight, the position where the relative change of wave intensities in the ordered-intensity distribution is largest was used as jump, exemplarily shown in figure D.1b where the change in intensity was smaller than a factor eight everywhere. The threshold (black horizontal lines in figure D.1) was given by the intensity at the position of the jump. If there were multiple jumps, we used the jump in the region of the highest intensity to define the threshold, i.e. the leftmost jump found in the ordered-intensity distribution. In order to avoid too small or too large wave sets, we did not consider jumps at the position of the two waves with the largest intensity and the ten waves with the smallest intensity. For example, jumps at waves with large intensity may be physical, as individual partial waves may dominate the physical distribution of the data.

Figure D.2 shows the thresholds for all 300 $(m_{K\pi\pi}, t')$ cells that were determined as explained above. For 129 cells, the threshold determination yielded thresholds in the reasonable range between about 1 and 20. In the remaining cells, the automatic threshold determination failed. The obtained thresholds were either too low, i.e. below 1, leading to a too large wave set, or too large, i.e. above 20, leading to a too small wave set. Additionally, we considered the threshold determination to be failed if the number of waves selected by the automatically determined threshold was larger than 150 or, for cells with $m_{K\pi\pi} > 2\,\mathrm{GeV}/c^2$,[b] smaller than 5. For these

[a] We chose the minimal required intensity change to be a factor eight in order to be much larger than the average intensity fraction of subsequent waves in the ordered-intensity distribution.

[b] For $m_{K\pi\pi} \leq 2\,\mathrm{GeV}/c^2$, we allowed wave sets with less than 5 waves, e.g. in the lowest $m_{K\pi\pi}$ bins.

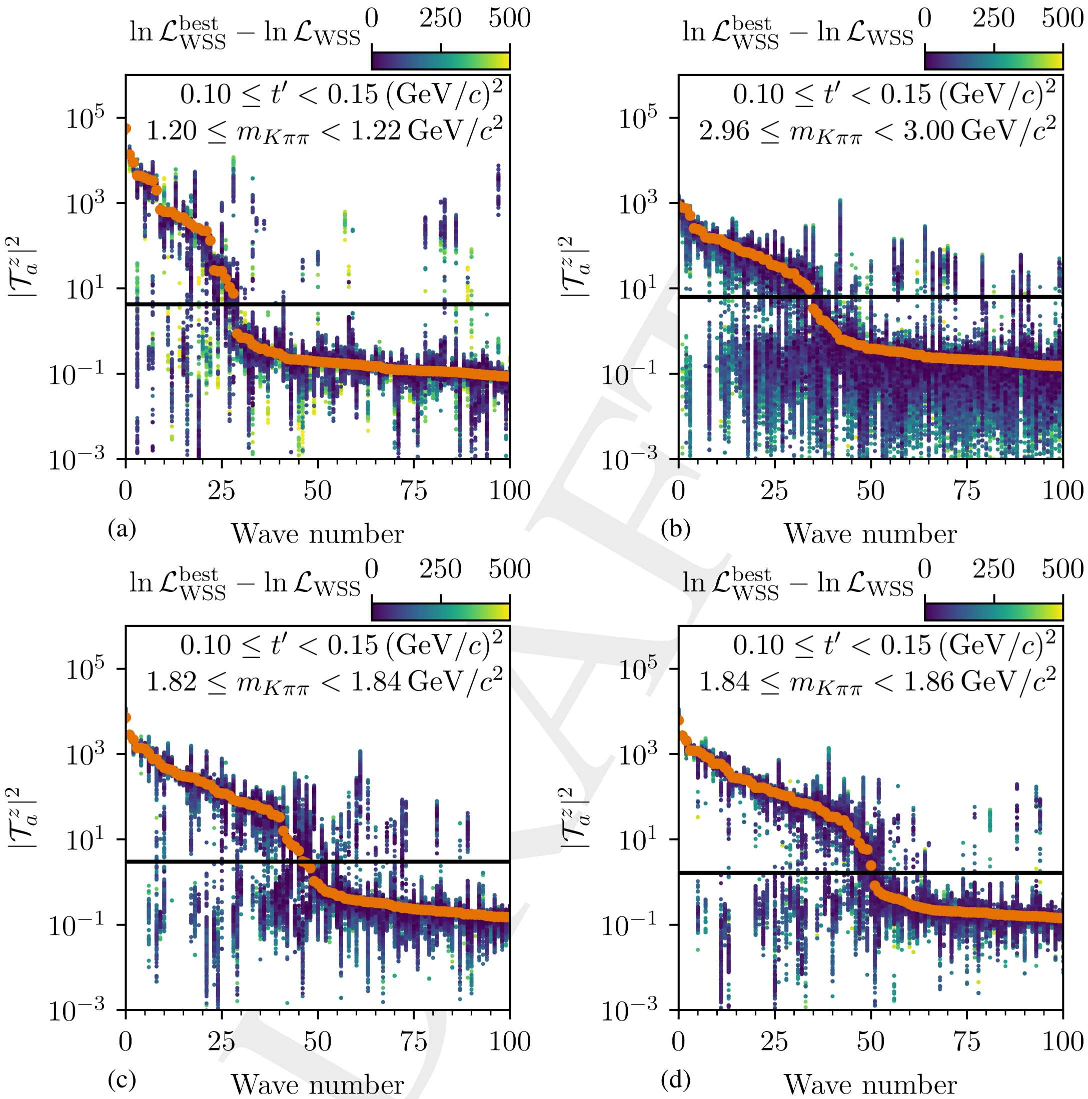

Figure D.1: Partial waves ordered by their intensity in the lowest t' bin in four different $m_{K\pi\pi}$ bins. The waves are ordered by intensity as obtained from the best result in each cell and numbered accordingly. The orange points show the best result out of 700 fit attempts. The other colored points show the results from the other fit attempts. Their color represents $\ln \mathcal{L}_{\mathrm{WSS}}^{\mathrm{best}} - \ln \mathcal{L}_{\mathrm{WSS}}$. Only results where this difference is smaller than 500 units are plotted. Only the 100 waves with the largest intensity are shown. The black horizontal line marks the threshold, above which waves were selected for the wave set (see text). (b) are the same as figures 5.9a and 5.9b in the main text, respectively.

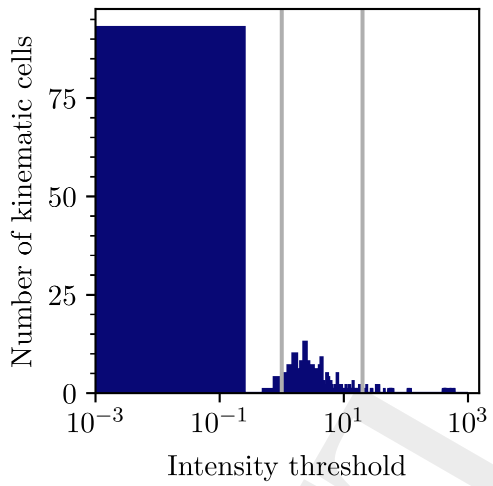

Figure D.2: Distribution of the automatically determined thresholds for all 300 $(m_{K\pi\pi}, t')$ cells. Only thresholds within the vertical gray lines are used to define the wave set.

cells, we fixed the threshold to a value of 3, which corresponds to the peak in the distribution of thresholds from cells where the automatic threshold determination worked (see figure D.2). Figure D.1c shows the partial waves ordered by intensity in a $(m_{K\pi\pi}, t')$ cell where the automatic threshold determination failed, because the distribution exhibits a smooth transition from waves with large to waves with low intensities instead of a sudden jump.[c] Still the manually defined threshold of 3 agrees with the distribution. In the neighboring $(m_{K\pi\pi}, t')$ cell shown in figure D.1d, the intensity distribution showed again a clear jump and the threshold could be determined automatically.

[c] We observed such a "smearing" of the jump in a few cells. This behavior seems to be caused by slightly different jump positions in neighboring $m_{K\pi\pi}$ cells via the continuity term in equation (5.57).

D.1.2 Manually Selected Waves

Table D.1: Waves that were included in the wave sets over the corresponding $m_{K\pi\pi}$ range given below independent of the result of the wave-set selection fits (see section 5.2.6). Waves and mass ranges were chosen that show interesting signals worth being studied in the resonance-model fit (see chapters 6 and 7). These waves were already selected in most $(m_{K\pi\pi}, t')$ cells in the given $m_{K\pi\pi}$ range by the wave-set selection fits. We only ensured that these waves are included in the waves sets in all $(m_{K\pi\pi}, t')$ cells in the given $m_{K\pi\pi}$ range.

Wave	$m_{K\pi\pi}$ Range Start [GeV/c^2]	$m_{K\pi\pi}$ Range End [GeV/c^2]
$0^- \, 0^+ \, [K\pi]_S^{K\pi} \, \pi \, S$	1.6	2.4
$0^- \, 0^+ \, \rho(770) \, K \, P$	1.0	2.4
$1^+ \, 0^+ \, K^*(892) \, \pi \, S$	1.0	2.5
$1^+ \, 0^+ \, \rho(770) \, K \, S$	1.0	2.5
$1^+ \, 1^+ \, \rho(770) \, K \, S$	1.0	2.5
$2^+ \, 1^+ \, K^*(892) \, \pi \, D$	1.0	2.0
$2^+ \, 1^+ \, \rho(770) \, K \, D$	1.0	2.0
$2^- \, 0^+ \, K^*(892) \, \pi \, F$	1.5	3.0
$2^- \, 0^+ \, K_2^*(1430) \, \pi \, S$	1.4	3.0
$2^- \, 0^+ \, \rho(770) \, K \, F$	1.5	3.0
$2^- \, 0^+ \, f_0(980) \, K \, D$	1.5	3.0
$2^- \, 0^+ \, f_2(1270) \, K \, S$	1.5	3.0
$2^- \, 1^+ \, K_2^*(1430) \, \pi \, S$	1.5	2.5
$3^+ \, 0^+ \, K_3^*(1780) \, \pi \, S$	2.0	2.5
$3^+ \, 1^+ \, K_2^*(1430) \, \pi \, P$	2.0	2.5
$3^- \, 1^+ \, K^*(892) \, \pi \, F$	1.5	2.2
$3^- \, 1^+ \, \rho(770) \, \pi \, F$	1.6	2.5
$4^+ \, 1^+ \, K^*(892) \, \pi \, G$	1.6	3.0
$4^+ \, 1^+ \, \rho(770) \, K \, D$	1.6	3.0
$4^- \, 0^+ \, K^*(892) \, \pi \, F$	1.8	3.0
$4^- \, 0^+ \, K_2^*(1430) \, \pi \, D$	2.0	3.0
$4^- \, 0^+ \, \rho(770) \, K \, F$	1.8	3.0
$4^- \, 1^+ \, K^*(892) \, \pi \, F$	1.5	3.0

6153 ### D.1.3 The 238-Wave Set

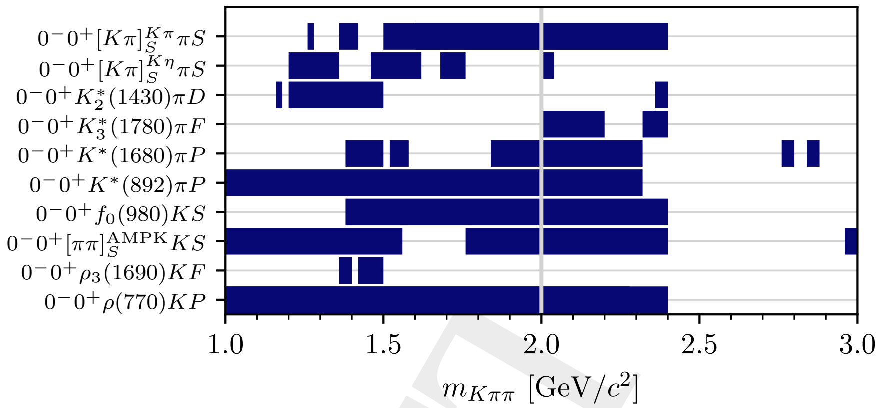

Figure D.3: Mass ranges of selected waves with $J = 0$ in the range $0.10 \leq t' < 0.15\,(\mathrm{GeV}/c)^2$. The gray vertical line indicates the mass where the $m_{K\pi\pi}$ binning changes from 20 MeV/c^2 to 40 MeV/c^2 wide bins.

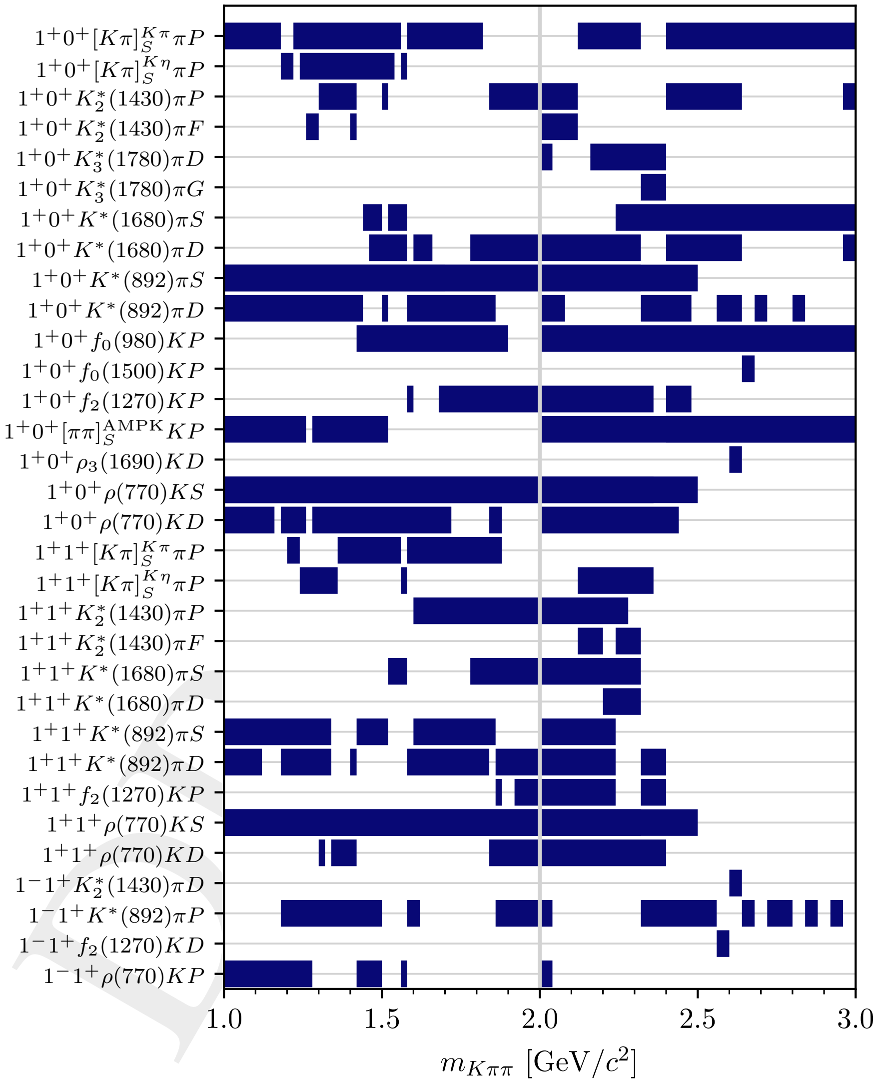

Figure D.4: Mass ranges of selected waves with $J = 1$ in the range $0.10 \leq t' < 0.15\,(\mathrm{GeV}/c)^2$. The gray vertical line indicates the mass where the $m_{K\pi\pi}$ binning changes from $20\,\mathrm{MeV}/c^2$ to $40\,\mathrm{MeV}/c^2$ wide bins.

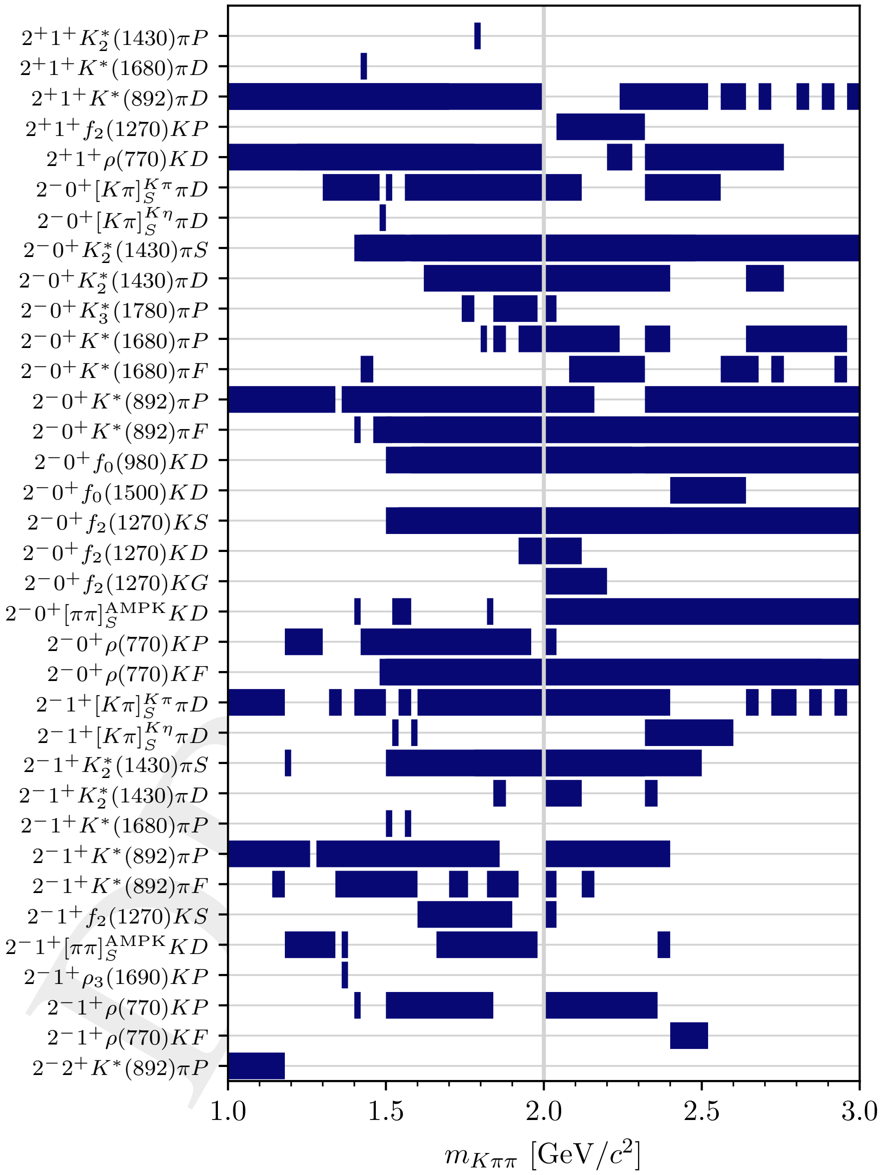

Figure D.5: Mass ranges of selected waves with $J = 2$ in the range $0.10 \leq t' < 0.15\,(\mathrm{GeV}/c)^2$. The gray vertical line indicates the mass where the $m_{K\pi\pi}$ binning changes from $20\,\mathrm{MeV}/c^2$ to $40\,\mathrm{MeV}/c^2$ wide bins.

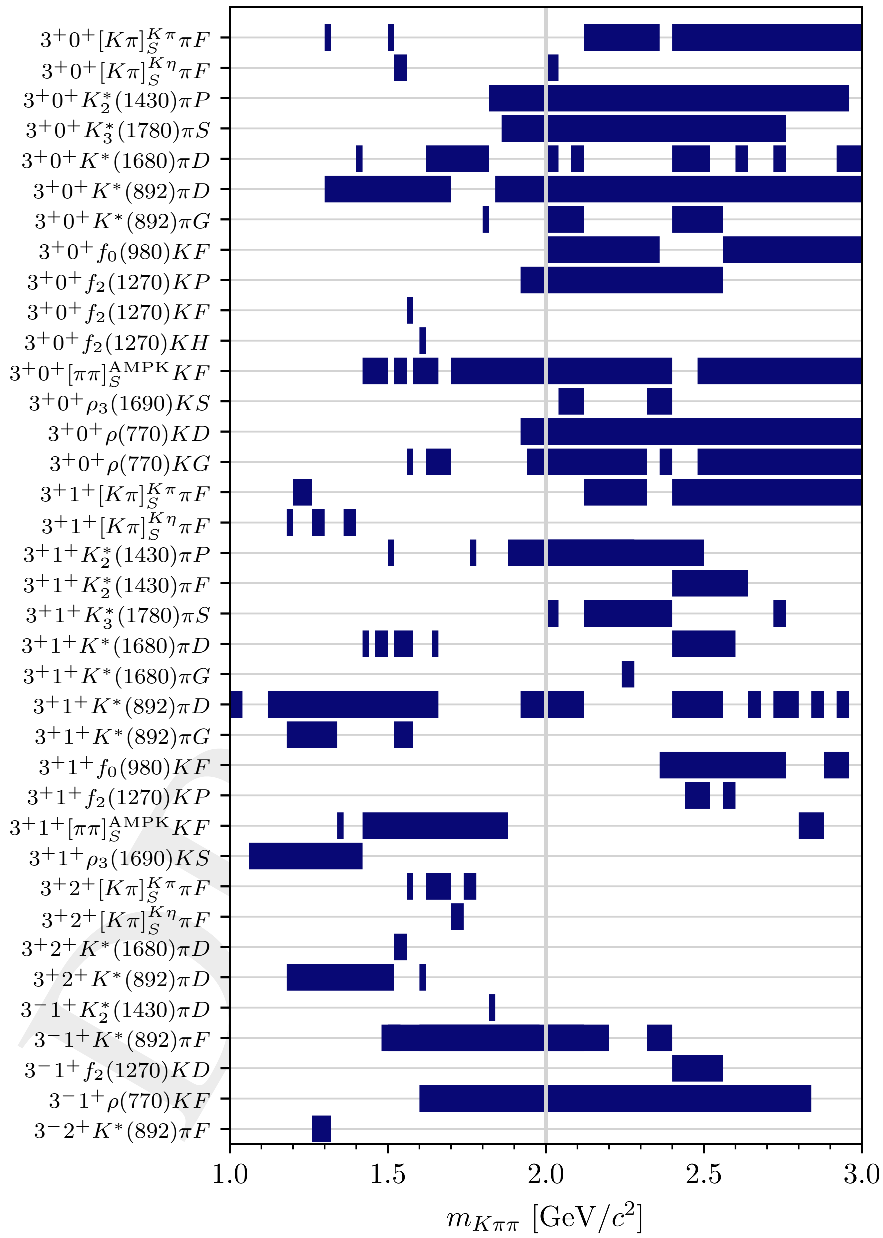

Figure D.6: Mass ranges of selected waves with $J = 3$ in the range $0.10 \leq t' < 0.15\,(\mathrm{GeV}/c)^2$. The gray vertical line indicates the mass where the $m_{K\pi\pi}$ binning changes from $20\,\mathrm{MeV}/c^2$ to $40\,\mathrm{MeV}/c^2$ wide bins.

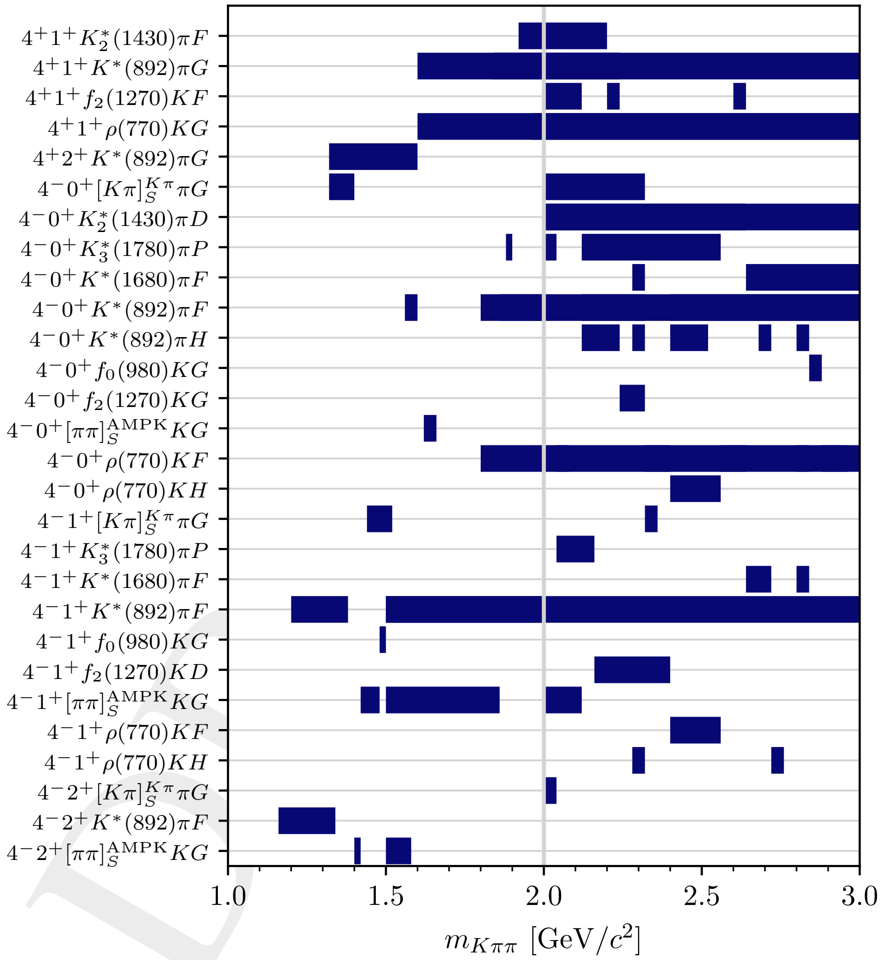

Figure D.7: Mass ranges of selected waves with $J = 4$ in the range $0.10 \leq t' < 0.15\,(\mathrm{GeV}/c)^2$. The gray vertical line indicates the mass where the $m_{K\pi\pi}$ binning changes from $20\,\mathrm{MeV}/c^2$ to $40\,\mathrm{MeV}/c^2$ wide bins.

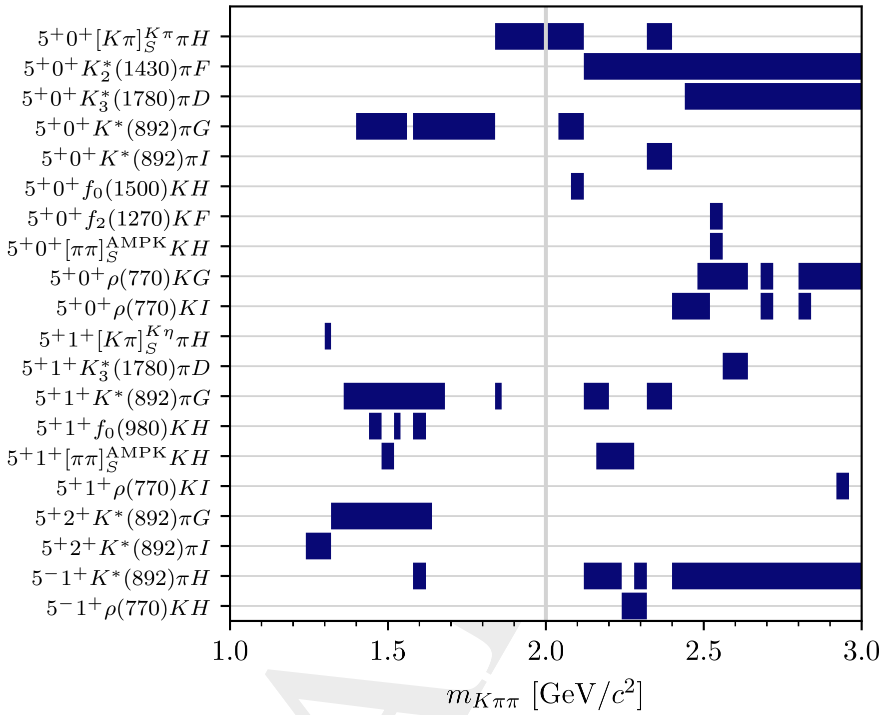

Figure D.8: Mass ranges of selected waves with $J = 5$ in the range $0.10 \leq t' < 0.15\,(\mathrm{GeV}/c)^2$. The gray vertical line indicates the mass where the $m_{K\pi\pi}$ binning changes from $20\,\mathrm{MeV}/c^2$ to $40\,\mathrm{MeV}/c^2$ wide bins.

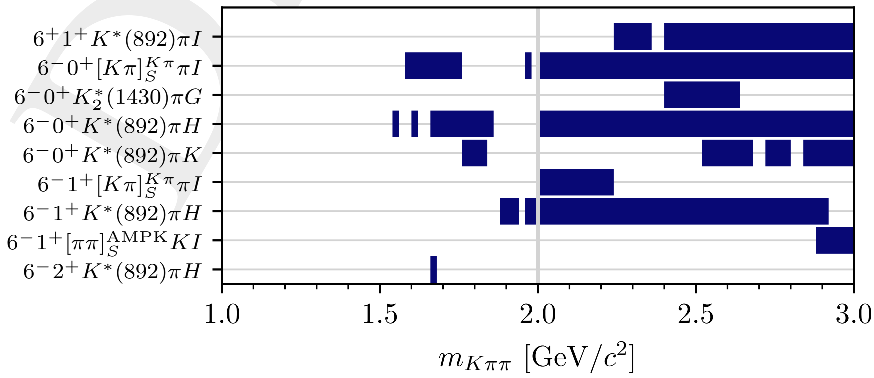

Figure D.9: Mass ranges of selected waves with $J = 6$ in the range $0.10 \leq t' < 0.15\,(\mathrm{GeV}/c)^2$. The gray vertical line indicates the mass where the $m_{K\pi\pi}$ binning changes from $20\,\mathrm{MeV}/c^2$ to $40\,\mathrm{MeV}/c^2$ wide bins.

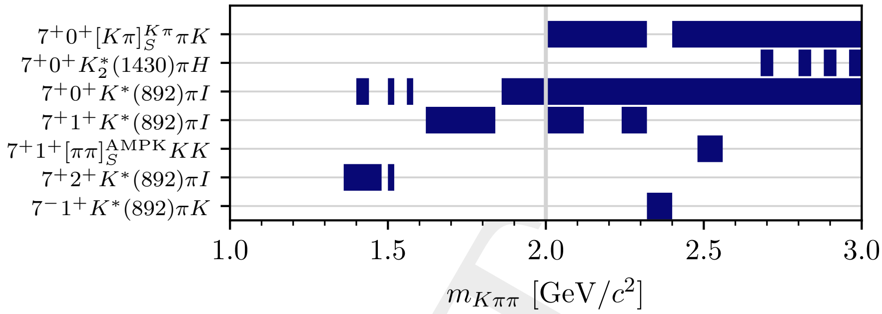

Figure D.10: Mass ranges of selected waves with $J = 7$ in the range $0.10 \leq t' < 0.15\,(\mathrm{GeV}/c)^2$. The gray vertical line indicates the mass where the $m_{K\pi\pi}$ binning changes from $20\,\mathrm{MeV}/c^2$ to $40\,\mathrm{MeV}/c^2$ wide bins.

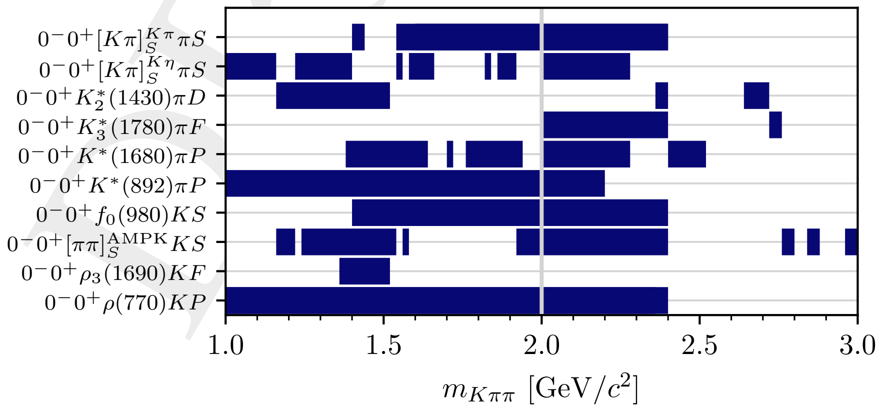

Figure D.11: Mass ranges of selected waves with $J = 0$ in the range $0.15 \leq t' < 0.24\,(\mathrm{GeV}/c)^2$. The gray vertical line indicates the mass where the $m_{K\pi\pi}$ binning changes from $20\,\mathrm{MeV}/c^2$ to $40\,\mathrm{MeV}/c^2$ wide bins.

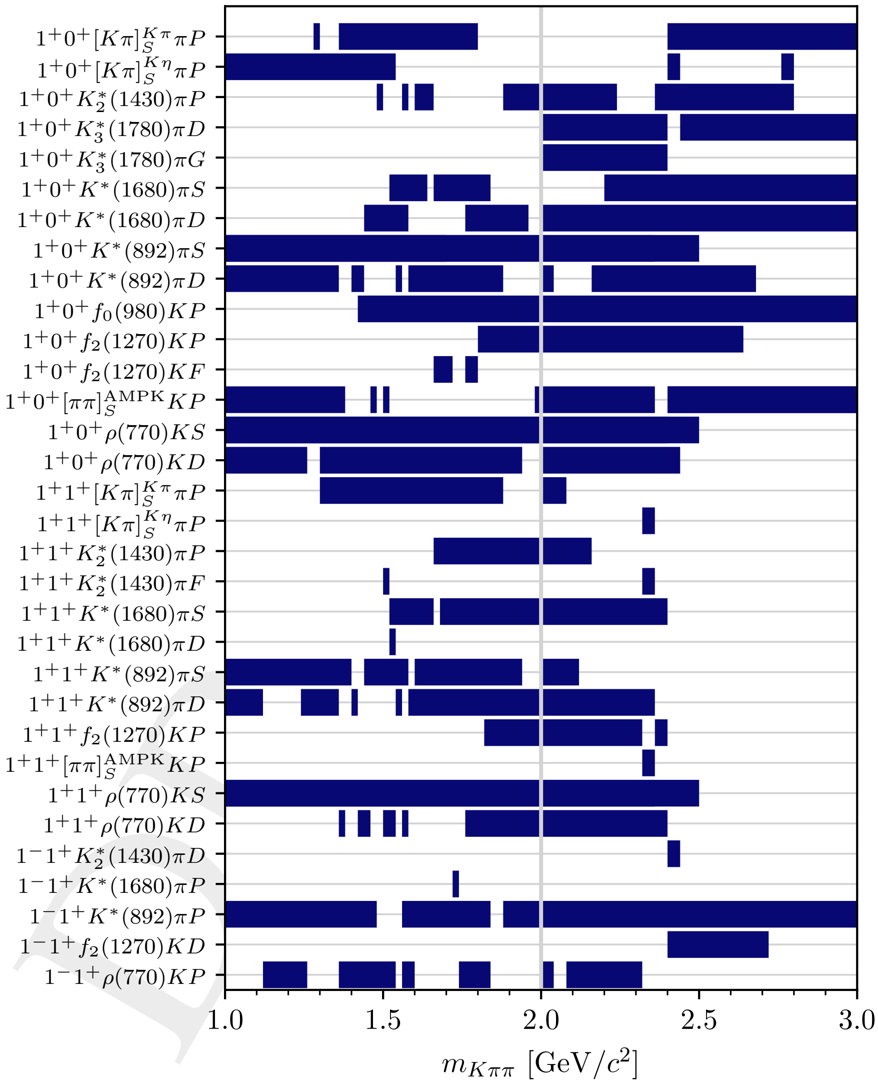

Figure D.12: Mass ranges of selected waves with $J = 1$ in the range $0.15 \leq t' < 0.24\,(\mathrm{GeV}/c)^2$. The gray vertical line indicates the mass where the $m_{K\pi\pi}$ binning changes from $20\,\mathrm{MeV}/c^2$ to $40\,\mathrm{MeV}/c^2$ wide bins.

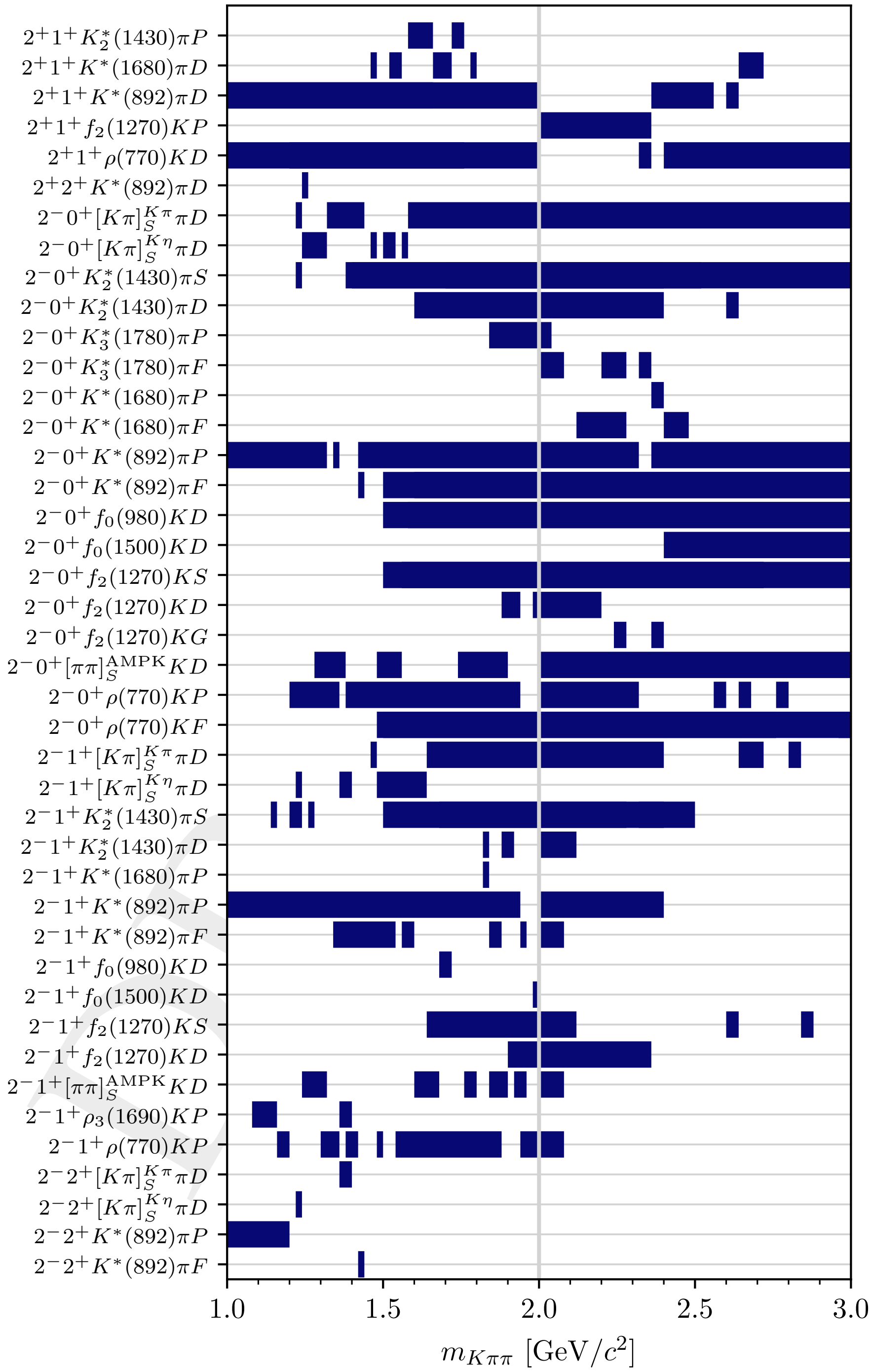

Figure D.13: Mass ranges of selected waves with $J = 2$ in the range $0.15 \le t' < 0.24\,(\mathrm{GeV}/c)^2$. The gray vertical line indicates the mass where the $m_{K\pi\pi}$ binning changes from $20\,\mathrm{MeV}/c^2$ to $40\,\mathrm{MeV}/c^2$ wide bins.

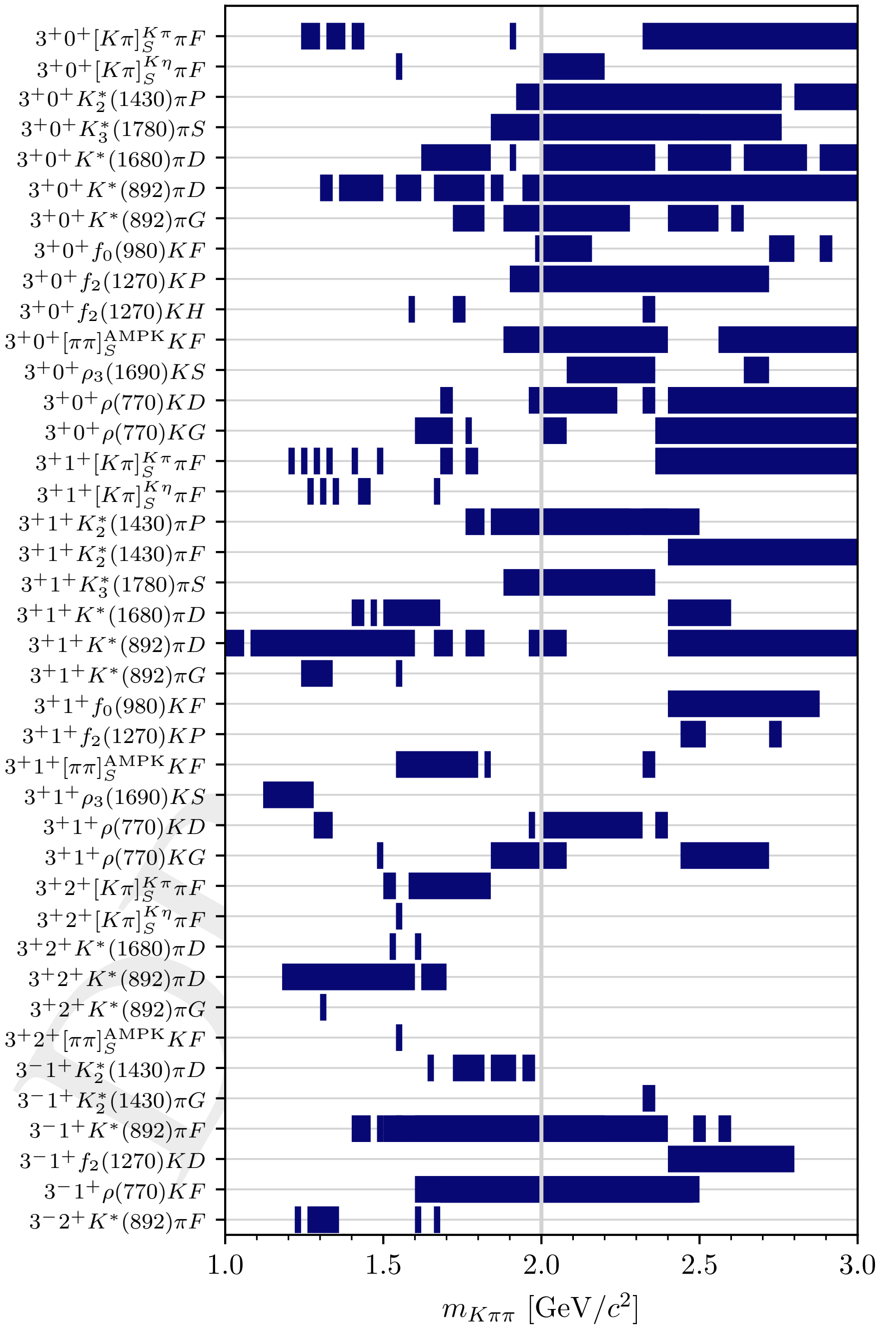

Figure D.14: Mass ranges of selected waves with $J = 3$ in the range $0.15 \leq t' < 0.24\,(\mathrm{GeV}/c)^2$. The gray vertical line indicates the mass where the $m_{K\pi\pi}$ binning changes from 20 MeV/c^2 to 40 MeV/c^2 wide bins.

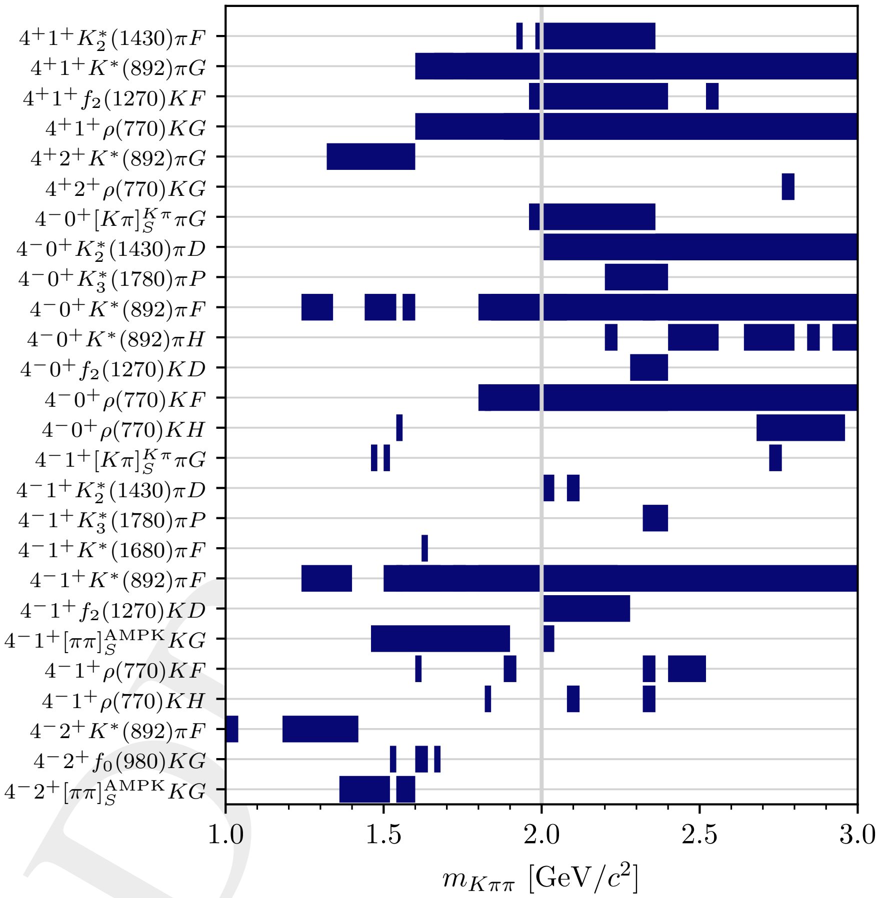

Figure D.15: Mass ranges of selected waves with $J = 4$ in the range $0.15 \leq t' < 0.24\,(\mathrm{GeV}/c)^2$. The gray vertical line indicates the mass where the $m_{K\pi\pi}$ binning changes from $20\,\mathrm{MeV}/c^2$ to $40\,\mathrm{MeV}/c^2$ wide bins.

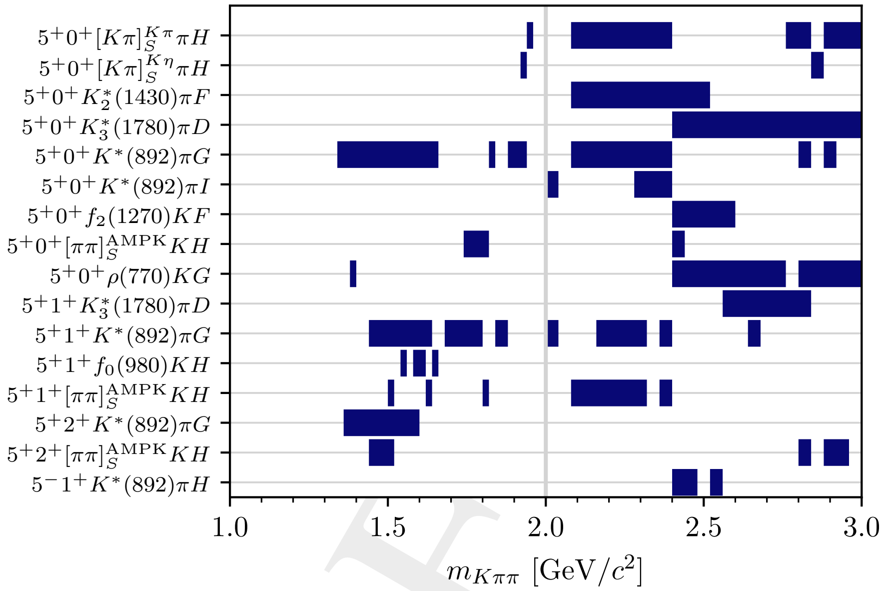

Figure D.16: Mass ranges of selected waves with $J = 5$ in the range $0.15 \leq t' < 0.24\,(\mathrm{GeV}/c)^2$. The gray vertical line indicates the mass where the $m_{K\pi\pi}$ binning changes from $20\,\mathrm{MeV}/c^2$ to $40\,\mathrm{MeV}/c^2$ wide bins.

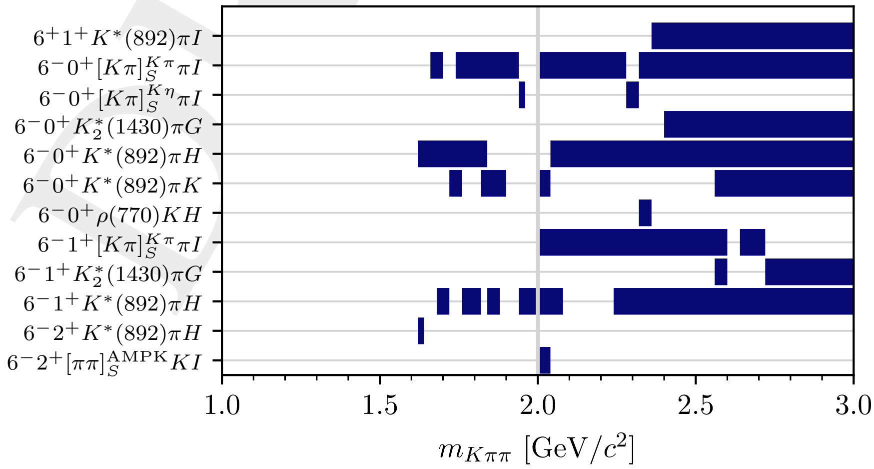

Figure D.17: Mass ranges of selected waves with $J = 6$ in the range $0.15 \leq t' < 0.24\,(\mathrm{GeV}/c)^2$. The gray vertical line indicates the mass where the $m_{K\pi\pi}$ binning changes from $20\,\mathrm{MeV}/c^2$ to $40\,\mathrm{MeV}/c^2$ wide bins.

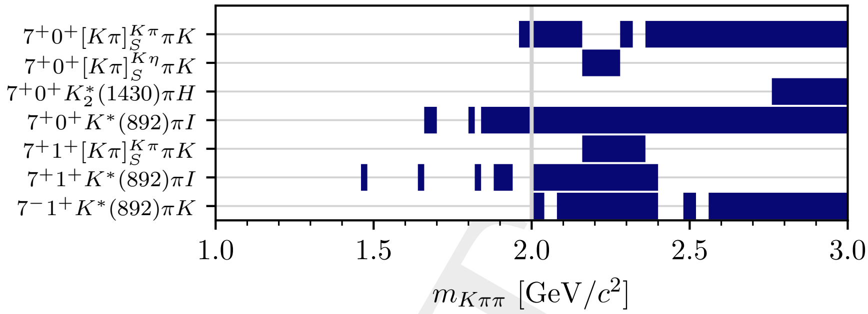

Figure D.18: Mass ranges of selected waves with $J = 7$ in the range $0.15 \leq t' < 0.24\,(\mathrm{GeV}/c)^2$. The gray vertical line indicates the mass where the $m_{K\pi\pi}$ binning changes from $20\,\mathrm{MeV}/c^2$ to $40\,\mathrm{MeV}/c^2$ wide bins.

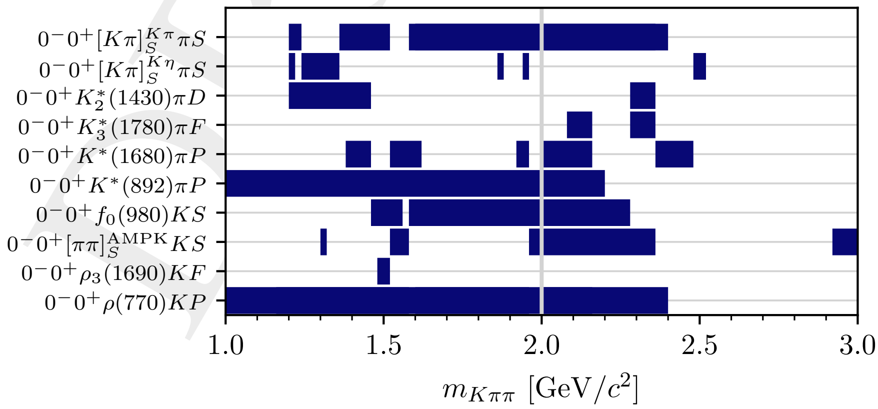

Figure D.19: Mass ranges of selected waves with $J = 0$ in the range $0.24 \leq t' < 0.34\,(\mathrm{GeV}/c)^2$. The gray vertical line indicates the mass where the $m_{K\pi\pi}$ binning changes from $20\,\mathrm{MeV}/c^2$ to $40\,\mathrm{MeV}/c^2$ wide bins.

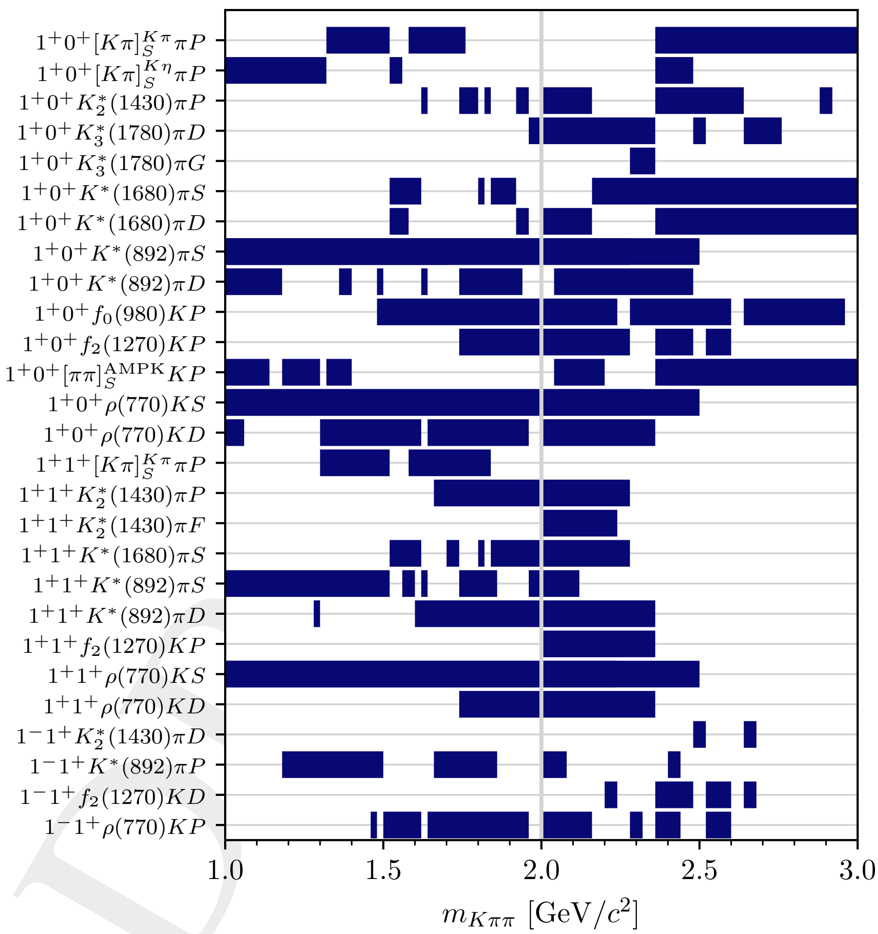

Figure D.20: Mass ranges of selected waves with $J = 1$ in the range $0.24 \leq t' < 0.34\,(\mathrm{GeV}/c)^2$. The gray vertical line indicates the mass where the $m_{K\pi\pi}$ binning changes from $20\,\mathrm{MeV}/c^2$ to $40\,\mathrm{MeV}/c^2$ wide bins.

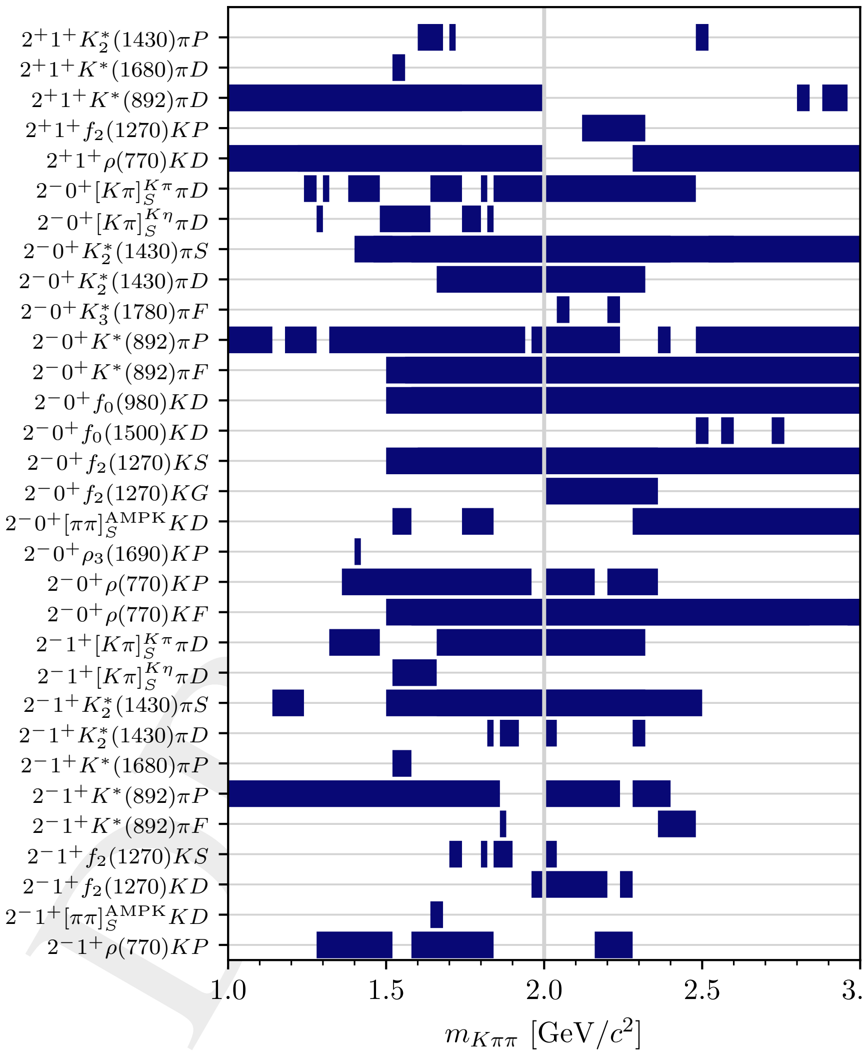

Figure D.21: Mass ranges of selected waves with $J = 2$ in the range $0.24 \le t' < 0.34\,(\mathrm{GeV}/c)^2$. The gray vertical line indicates the mass where the $m_{K\pi\pi}$ binning changes from $20\,\mathrm{MeV}/c^2$ to $40\,\mathrm{MeV}/c^2$ wide bins.

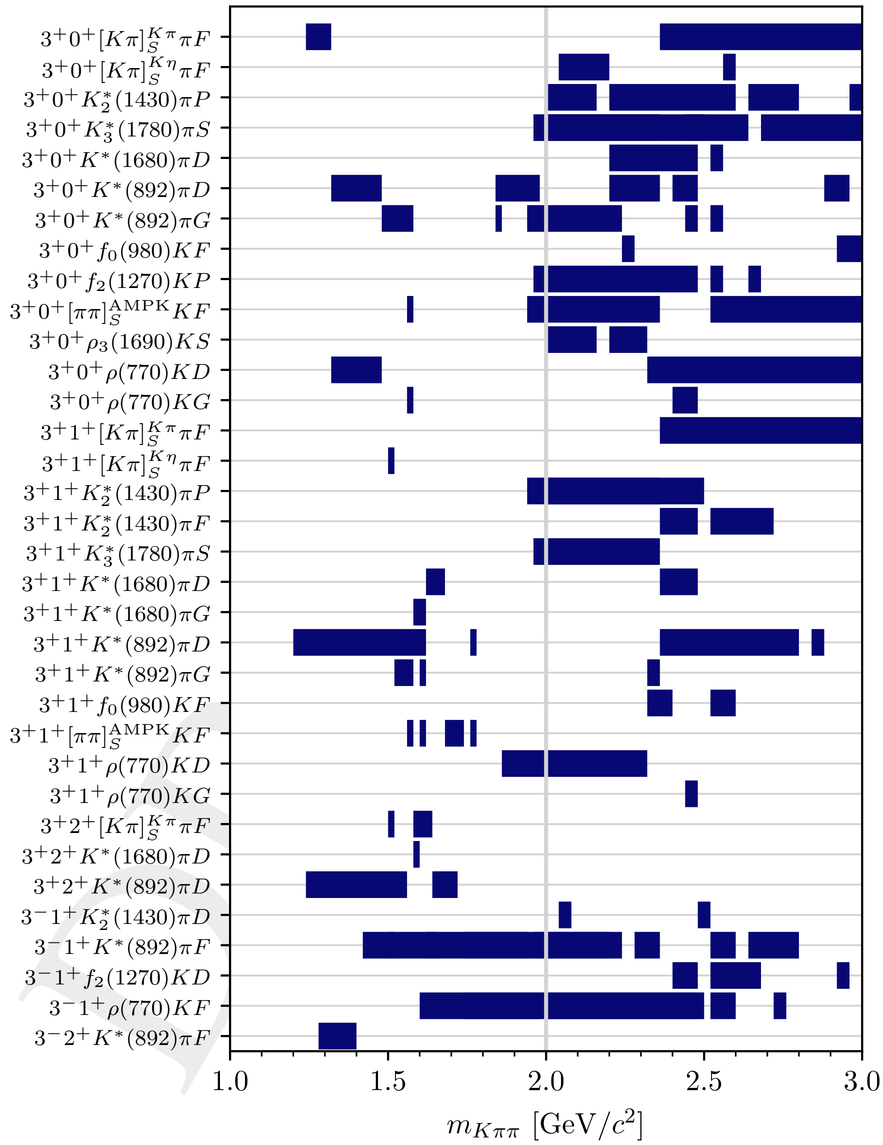

Figure D.22: Mass ranges of selected waves with $J = 3$ in the range $0.24 \le t' < 0.34\,(\mathrm{GeV}/c)^2$. The gray vertical line indicates the mass where the $m_{K\pi\pi}$ binning changes from $20\,\mathrm{MeV}/c^2$ to $40\,\mathrm{MeV}/c^2$ wide bins.

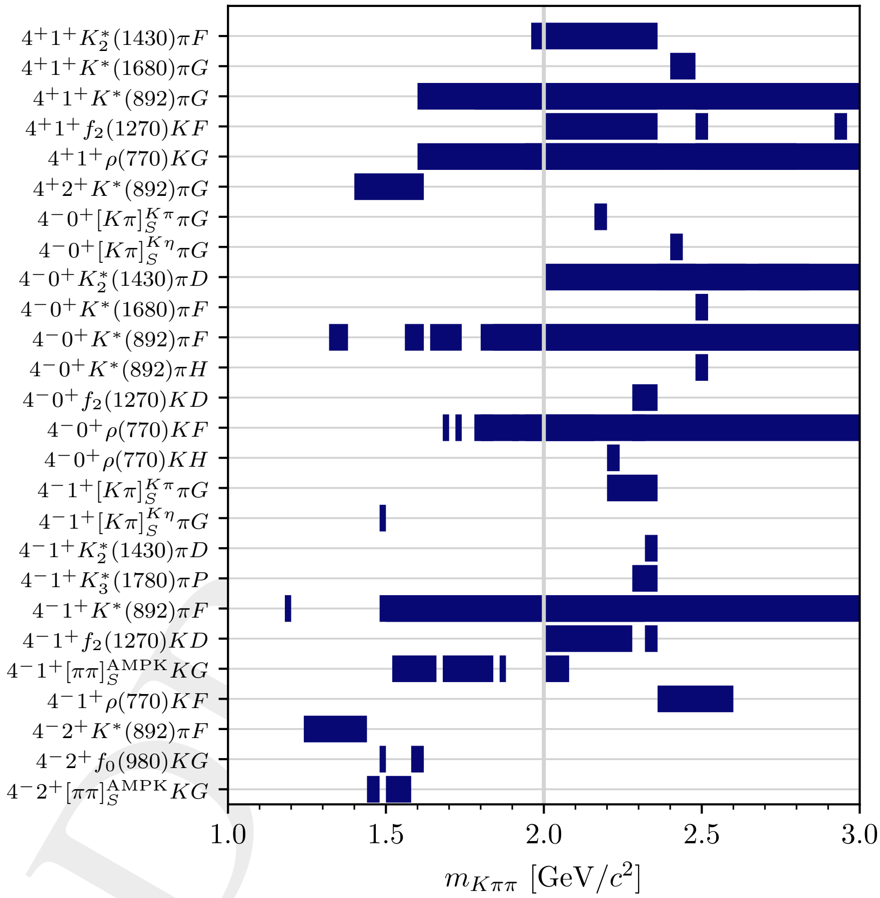

Figure D.23: Mass ranges of selected waves with $J = 4$ in the range $0.24 \le t' < 0.34\,(\mathrm{GeV}/c)^2$. The gray vertical line indicates the mass where the $m_{K\pi\pi}$ binning changes from $20\,\mathrm{MeV}/c^2$ to $40\,\mathrm{MeV}/c^2$ wide bins.

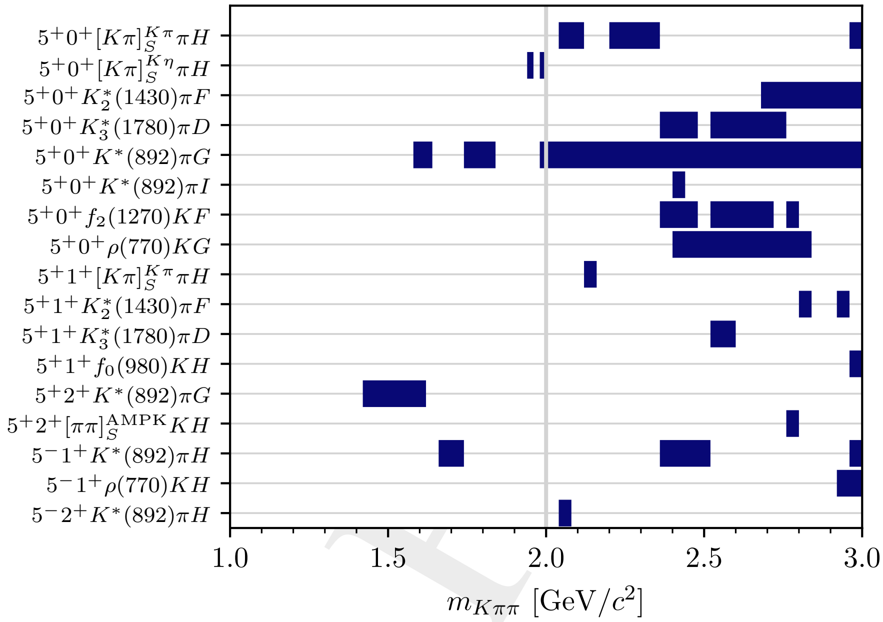

Figure D.24: Mass ranges of selected waves with $J = 5$ in the range $0.24 \leq t' < 0.34\,(\mathrm{GeV}/c)^2$. The gray vertical line indicates the mass where the $m_{K\pi\pi}$ binning changes from $20\,\mathrm{MeV}/c^2$ to $40\,\mathrm{MeV}/c^2$ wide bins.

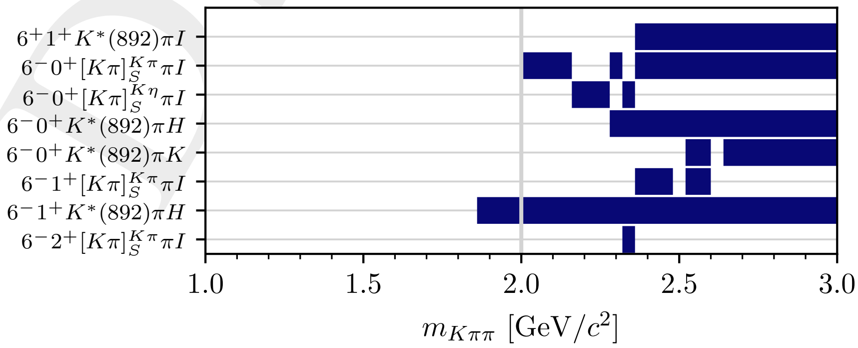

Figure D.25: Mass ranges of selected waves with $J = 6$ in the range $0.24 \leq t' < 0.34\,(\mathrm{GeV}/c)^2$. The gray vertical line indicates the mass where the $m_{K\pi\pi}$ binning changes from $20\,\mathrm{MeV}/c^2$ to $40\,\mathrm{MeV}/c^2$ wide bins.

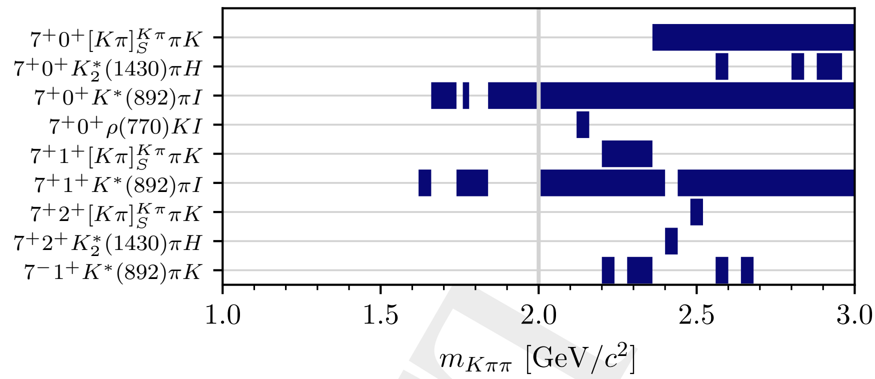

Figure D.26: Mass ranges of selected waves with $J = 7$ in the range $0.24 \leq t' < 0.34\,(\text{GeV}/c)^2$. The gray vertical line indicates the mass where the $m_{K\pi\pi}$ binning changes from $20\,\text{MeV}/c^2$ to $40\,\text{MeV}/c^2$ wide bins.

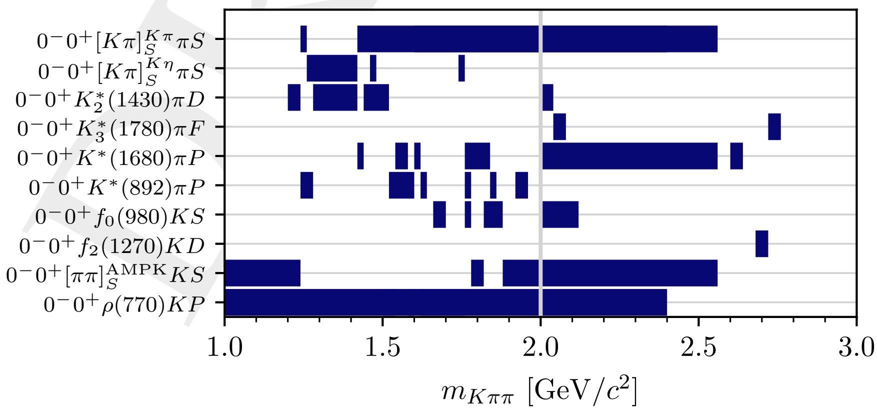

Figure D.27: Mass ranges of selected waves with $J = 0$ in the range $0.34 \leq t' < 1.00\,(\text{GeV}/c)^2$. The gray vertical line indicates the mass where the $m_{K\pi\pi}$ binning changes from $20\,\text{MeV}/c^2$ to $40\,\text{MeV}/c^2$ wide bins.

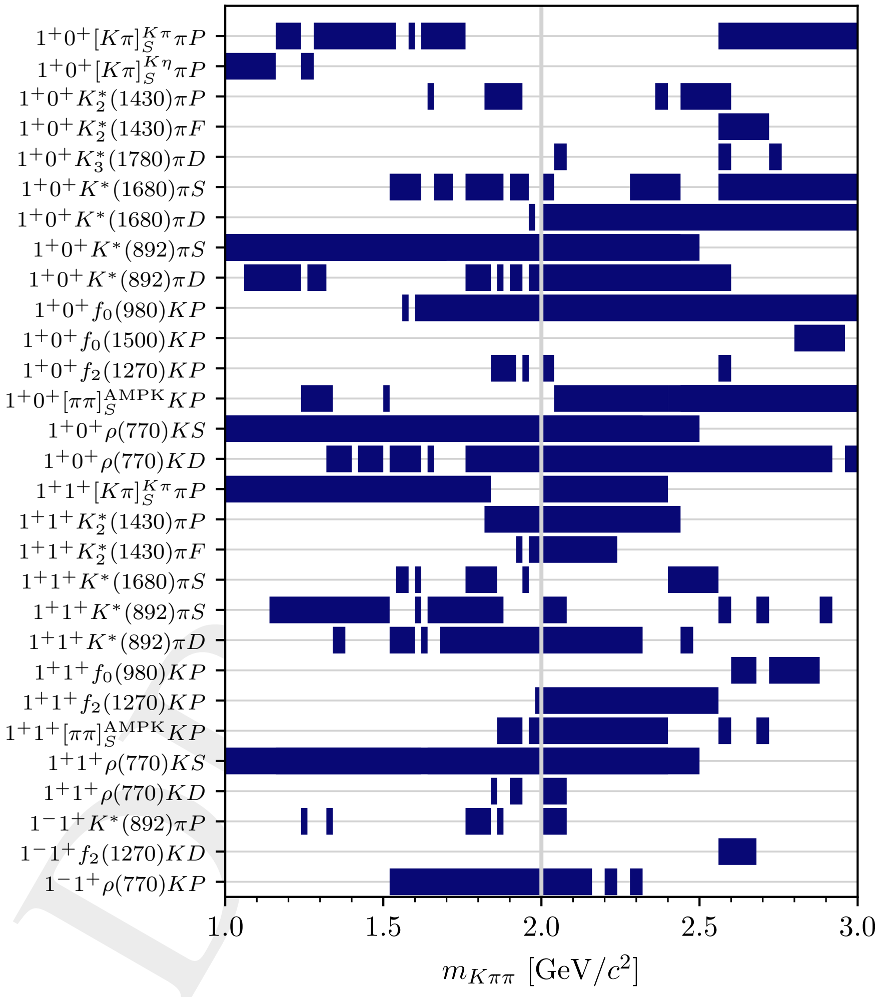

Figure D.28: Mass ranges of selected waves with $J = 1$ in the range $0.34 \leq t' < 1.00\,(\mathrm{GeV}/c)^2$. The gray vertical line indicates the mass where the $m_{K\pi\pi}$ binning changes from 20 MeV/c^2 to 40 MeV/c^2 wide bins.

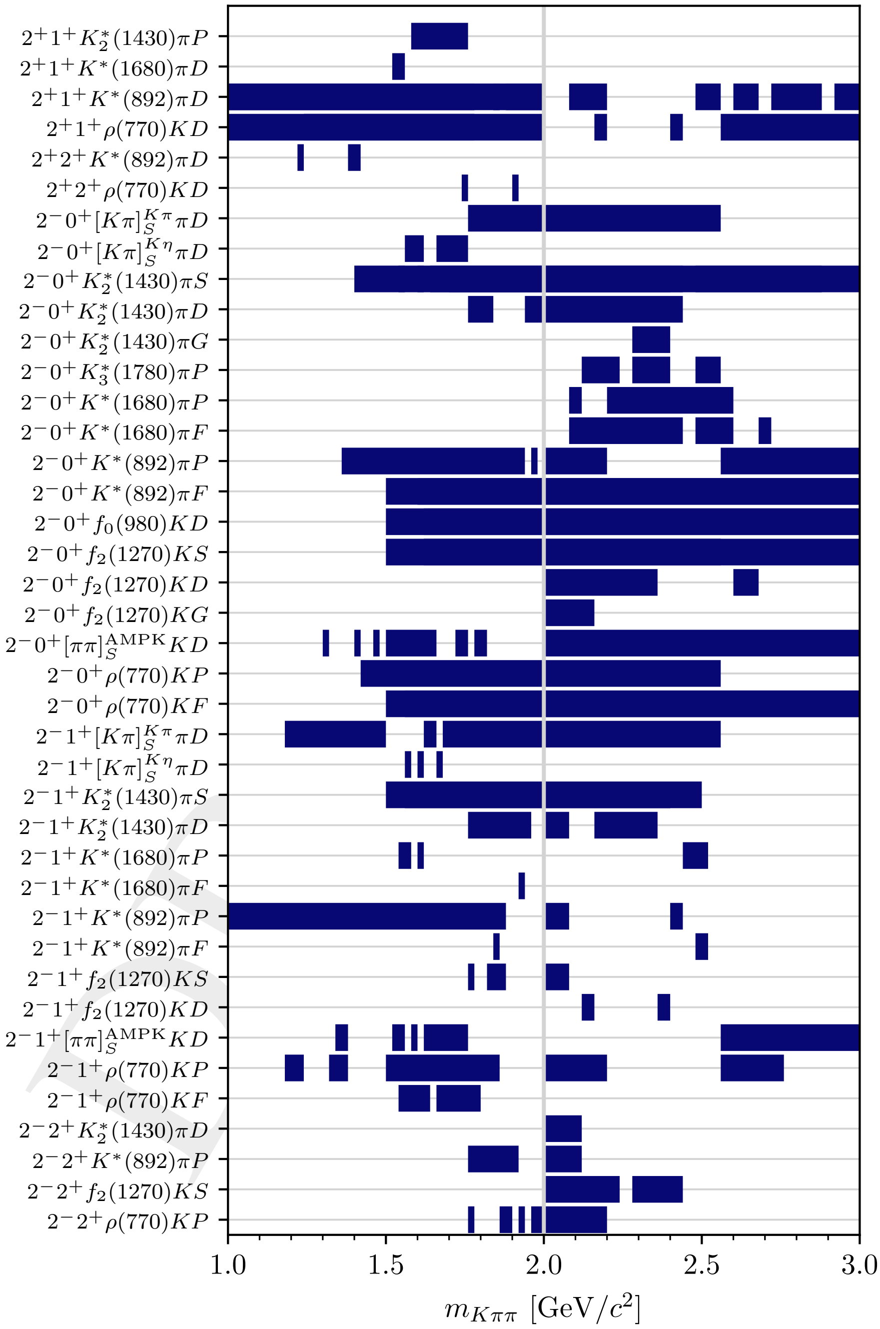

Figure D.29: Mass ranges of selected waves with $J = 2$ in the range $0.34 \leq t' < 1.00\,(\mathrm{GeV}/c)^2$. The gray vertical line indicates the mass where the $m_{K\pi\pi}$ binning changes from $20\,\mathrm{MeV}/c^2$ to $40\,\mathrm{MeV}/c^2$ wide bins.

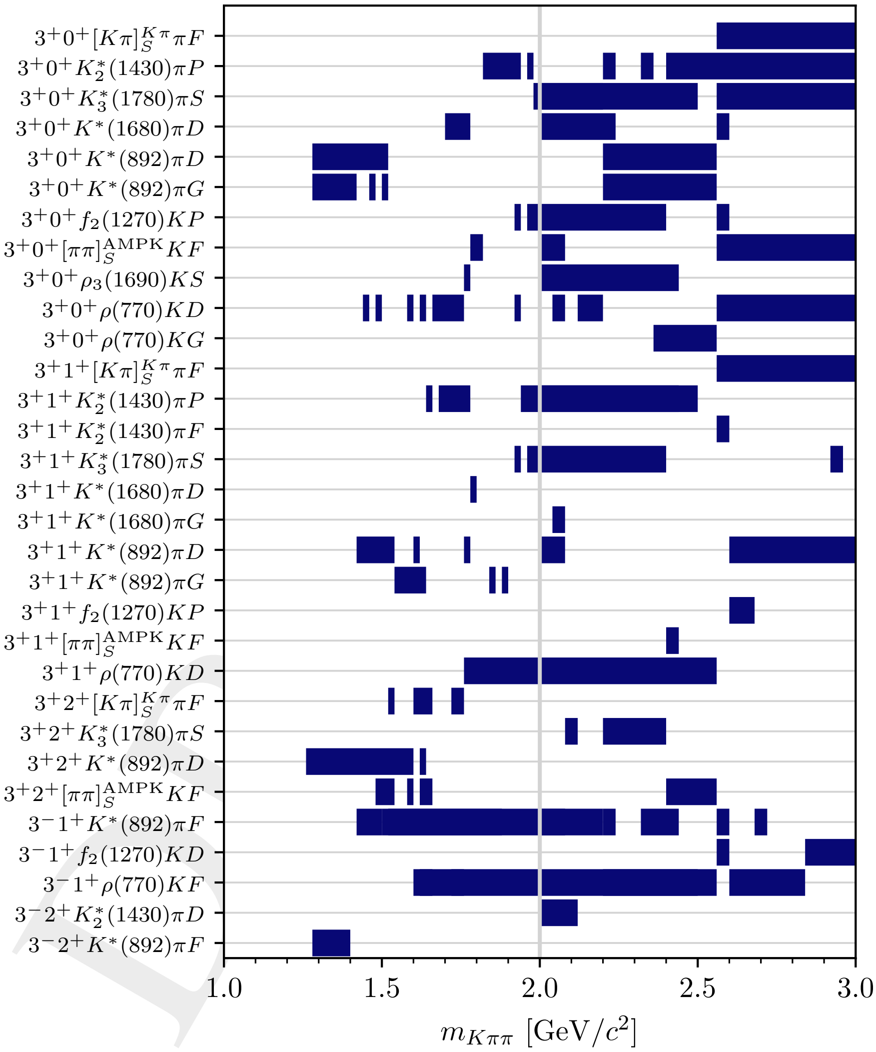

Figure D.30: Mass ranges of selected waves with $J = 3$ in the range $0.34 \le t' < 1.00\,(\mathrm{GeV}/c)^2$. The gray vertical line indicates the mass where the $m_{K\pi\pi}$ binning changes from $20\,\mathrm{MeV}/c^2$ to $40\,\mathrm{MeV}/c^2$ wide bins.

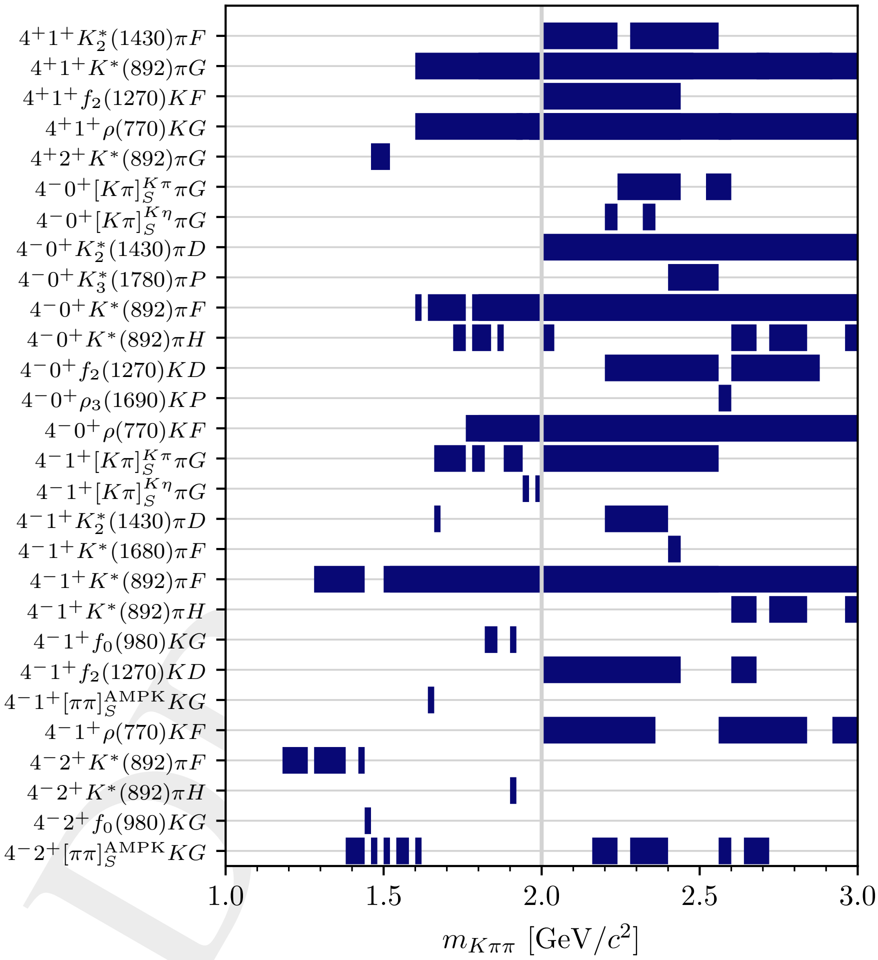

Figure D.31: Mass ranges of selected waves with $J = 4$ in the range $0.34 \leq t' < 1.00\,(\mathrm{GeV}/c)^2$. The gray vertical line indicates the mass where the $m_{K\pi\pi}$ binning changes from $20\,\mathrm{MeV}/c^2$ to $40\,\mathrm{MeV}/c^2$ wide bins.

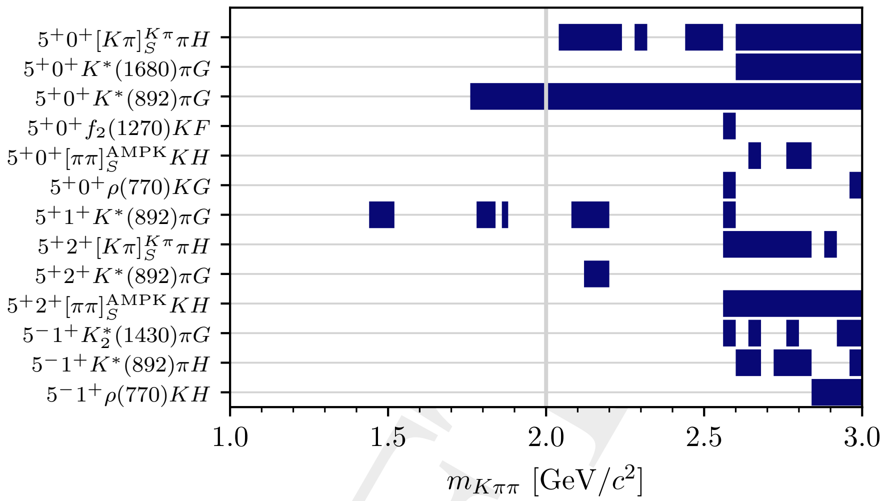

Figure D.32: Mass ranges of selected waves with $J = 5$ in the range $0.34 \leq t' < 1.00\,(\mathrm{GeV}/c)^2$. The gray vertical line indicates the mass where the $m_{K\pi\pi}$ binning changes from $20\,\mathrm{MeV}/c^2$ to $40\,\mathrm{MeV}/c^2$ wide bins.

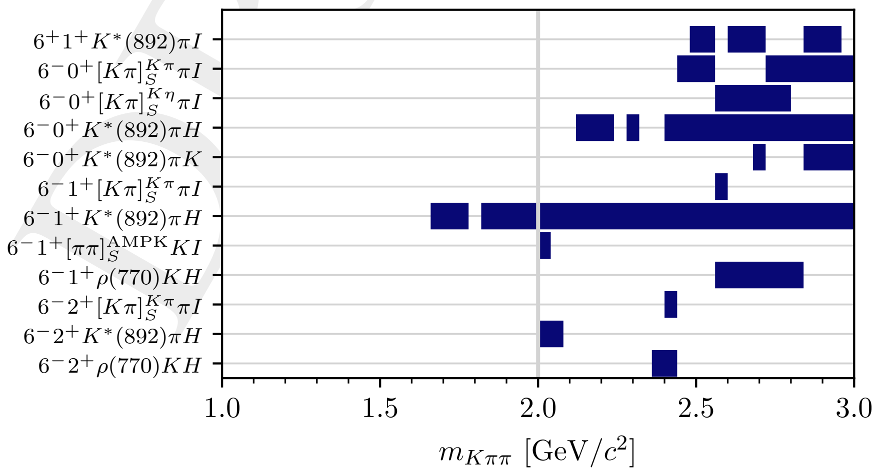

Figure D.33: Mass ranges of selected waves with $J = 6$ in the range $0.34 \leq t' < 1.00\,(\mathrm{GeV}/c)^2$. The gray vertical line indicates the mass where the $m_{K\pi\pi}$ binning changes from $20\,\mathrm{MeV}/c^2$ to $40\,\mathrm{MeV}/c^2$ wide bins.

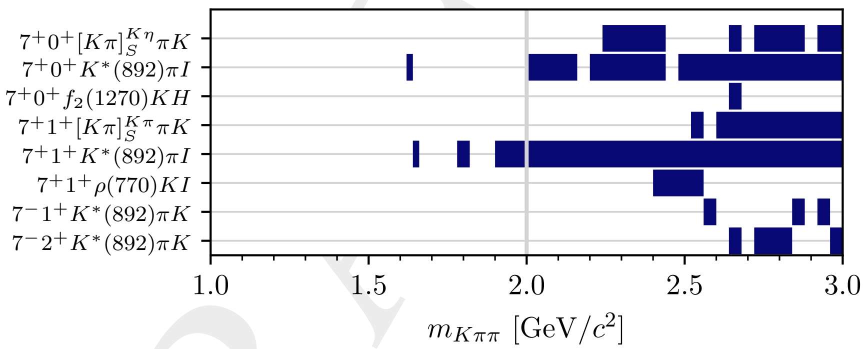

Figure D.34: Mass ranges of selected waves with $J = 7$ in the range $0.34 \leq t' < 1.00\,(\text{GeV}/c)^2$. The gray vertical line indicates the mass where the $m_{K\pi\pi}$ binning changes from $20\,\text{MeV}/c^2$ to $40\,\text{MeV}/c^2$ wide bins.

D.2 Experimental Acceptance and Agreement between Partial-Wave Model and Data

In this section, we present plots to show the acceptance in the kinematic variables of the reaction $K^- + p \to K^-\pi^-\pi^+ + p$ and the agreement between the results of the PWD fit, i.e. PWD predictions for the kinematic distributions in the $K^-\pi^-\pi^+$ phase-space variables, and the measured data. Details on how we determined the PWD predictions can be found in section 5.6 and appendix C.

The five-dimensional phase space of the $K^-\pi^-\pi^+$ final state can be represented by four angles and the invariant mass of one of the three two-body subsystems. Different representations are possible (see sections 5.1.1 and 5.6 for details). In figures D.36 to D.41, we consider the $\pi^-\pi^+$ isobar system. In figures D.42 to D.47, we consider the $K^-\pi^+$ isobar system. Table D.2 gives an overview over these figures. We split the analyzed $m_{K\pi\pi}$ range into three sub-ranges: (i) the mass range of the K_1 double-peak, $1.0 \leq m_{K\pi\pi} < 1.5\,\text{GeV}/c^2$; (ii) the mass range of the peak of the K_2 resonances, $1.5 \leq m_{K\pi\pi} < 2.0\,\text{GeV}/c^2$; and (iii) the high-mass range, $2.0 \leq m_{K\pi\pi} < 3.0\,\text{GeV}/c^2$. The agreement between PWD model and data is discussed in section 5.6.

Table D.2: Figures showing the agreement between the results of the PWD and the measured data as a function of individual phase-space variables and as a function of two two-body decay angles. In addition, we show the acceptance as a function of the two-body decay angles using a common scale for the acceptance.

	$m_{K\pi\pi}$ range in GeV/c^2	[1.0, 1.5]	[1.5, 2.0]	[2.0, 3.0]
$\pi^-\pi^+$ isobar system	individual phase-space variables	D.36	D.38	D.40
	correlation of decay angles	D.37	D.39	D.41
$K^-\pi^+$ isobar system	individual phase-space variables	D.42	D.44	D.46
	correlation of decay angles	D.43	D.45	D.47

In addition, we present estimates of the experimental acceptance as a function of different kinematic variables. The acceptance is strongly modulated in particular in the Gottfried-Jackson angles as, for example, shown in figure D.39e. Furthermore, the acceptance strongly depends on $m_{K\pi\pi}$ (compare, for example, figures D.39e and D.41e). This strong modulation of the acceptance is caused by the limited momentum range of the final-state particle identification by the RICH detector (see section 3.2.2).

The acceptance depends on all kinematic variables. Showing the acceptance as a function of only a subset of the kinematic variables implies marginalization over the not shown kinematic variables. For example, showing the acceptance as a function of $m_{K\pi\pi}$ in figure D.35a implies marginalization over t' and the five phase-space variables of the $K^-\pi^-\pi^+$ system. As, the acceptance depends in a correlated way on $m_{K\pi\pi}$, t', and on the $K^-\pi^-\pi^+$ phase-space variables, the marginalized acceptance at a given $m_{K\pi\pi}$ depends on the distributions in t' and the $K^-\pi^-\pi^+$

phase-space variables used for the marginalization. As we want to show the acceptance for the reaction $K^- + p \to K^-\pi^-\pi^+ + p$, we used for the acceptance plots shown in figures D.35 to D.47 and in figure 5.23b the physical kinematic distribution as predicted by the PWD model for the reaction $K^- + p \to K^-\pi^-\pi^+ + p$ for the marginalization. The acceptance is calculated as the ratio of the number of reconstructed events and the number of produced events as predicted by the PWD model.[d]

Figure D.35a shows the average acceptance for the reaction $K^- + p \to K^-\pi^-\pi^+ + p$ as a function of $m_{K\pi\pi}$. In the region $m_{K\pi\pi} < 1.6\,\mathrm{GeV}/c^2$, the acceptance is approximately constant and has a low value of about 2 %. Compared to the acceptance for a sample that is distributed uniformly in phase-space, the acceptance for the reaction $K^- + p \to K^-\pi^-\pi^+ + p$ as predicted using the PWD model is lower in this $m_{K\pi\pi}$ region (cf. figures C.4b and D.35a). The $m_{K\pi\pi}$ region below about $1.6\,\mathrm{GeV}/c^2$ is affected by the leakage effect discussed in section 5.9, which leads to an overestimation of the number of produced events and thus to a strong bias for the estimate of the average acceptance towards smaller values in this $m_{K\pi\pi}$ region. The PWD prediction for the distributions of reconstructed events is not affected by the leakage effect. Above about $1.6\,\mathrm{GeV}/c^2$, the acceptance rises steeply to a value of about 10 % in the mass region of the K_2 ground states around $1.8\,\mathrm{GeV}/c^2$. After this region, the rise is less steep. Above $2.5\,\mathrm{GeV}/c^2$, the acceptance starts to saturate at a value of about 22 %, which is slightly higher than the acceptance of about 19 % for a sample that is distributed uniformly in phase-space. The distribution in $\cos\theta_{\mathrm{GJ}}^{K\pi}$ strongly peaks at 1 in this $m_{K\pi\pi}$ region (see figure 5.24a). For this kinematics, the bachelor π^- goes in backward direction with respect to the direction of the beam K^- in the Gottfried-Jackson frame. This translates to a slow π^- in the laboratory frame which is more likely identified by the RICH. Thus, the acceptance for the reaction $K^- + p \to K^-\pi^-\pi^+ + p$ is higher in this mass region compared to a sample that is distributed uniformly in phase-space, i.e. whose $\cos\theta_{\mathrm{GJ}}^{K\pi}$ distribution is flat.

The average acceptance as a function of $m_{\pi^-\pi^+}$ shown in figure D.35b is roughly constant, but exhibits structures in the mass regions of some of the $\pi^-\pi^+$ resonances that we observe in this distribution (see figure 4.7b). For example, the acceptance exhibits a dip in the $m_{\pi^-\pi^+}$ region of the $f_0(980)$ isobar resonance at about $1\,\mathrm{GeV}/c^2$ and rises again in the mass region of the $f_2(1270)$ isobar resonance at about $1.3\,\mathrm{GeV}/c^2$. As both isobar resonances have different spin, the correspondingly different angular distributions of their decay and the strong modulation of the acceptance in the decay angles can explain the different average acceptances.

The acceptance effects discussed above show, that the measured distributions can be interpreted only at a qualitative level. An acceptance correction that takes into account the full high-dimensional dependence of the acceptance on all kinematic variables is mandatory in order to interpret the data on a quantitative level as done in the partial-wave analysis.

[d] The PWD prediction for the number of reconstructed events was obtained by weighting reconstructed phase-space pseudodata. The number of produce events as predicted by the PWD model was obtained by weighting produced phase-space pseudodata. The weights are proportional to the model intensity in equation (5.16) using the results of the PWD fit to the $K^-\pi^-\pi^+$ sample. See appendix C for details.

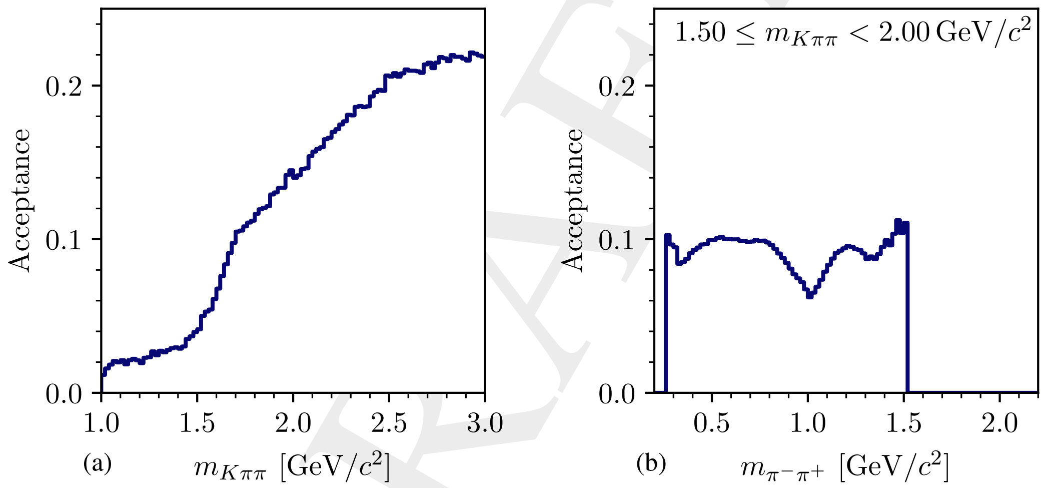

Figure D.35: Marginalized acceptance for the reaction $K^- + p \to K^-\pi^-\pi^+ + p$. (a) shows the acceptance as a function of $m_{K\pi\pi}$. (b) shows the acceptance as a function of $m_{\pi^-\pi^+}$ in the range $1.5 \leq m_{K\pi\pi} < 2.0\,\mathrm{GeV}/c^2$.

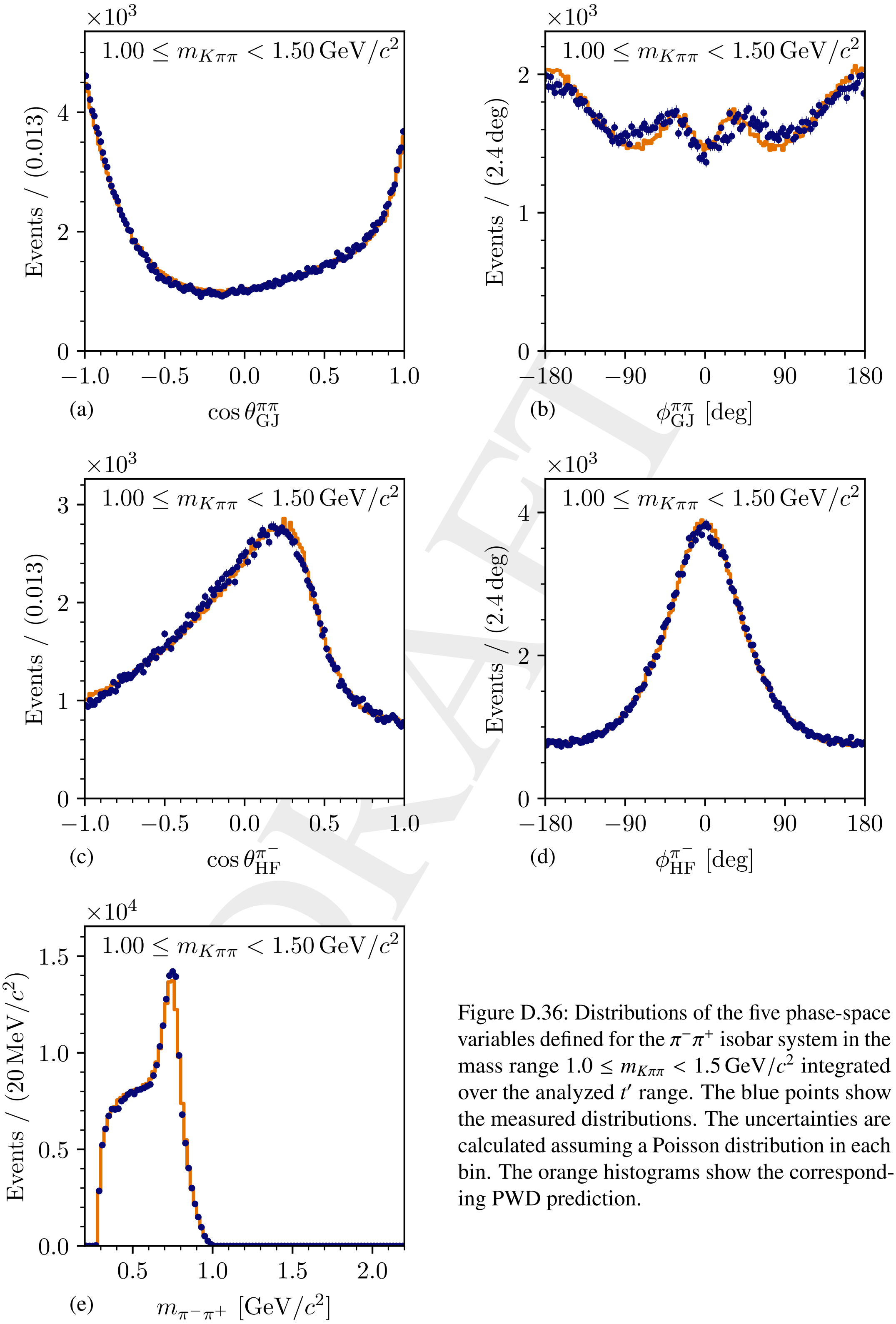

Figure D.36: Distributions of the five phase-space variables defined for the $\pi^-\pi^+$ isobar system in the mass range $1.0 \leq m_{K\pi\pi} < 1.5\,\mathrm{GeV}/c^2$ integrated over the analyzed t' range. The blue points show the measured distributions. The uncertainties are calculated assuming a Poisson distribution in each bin. The orange histograms show the corresponding PWD prediction.

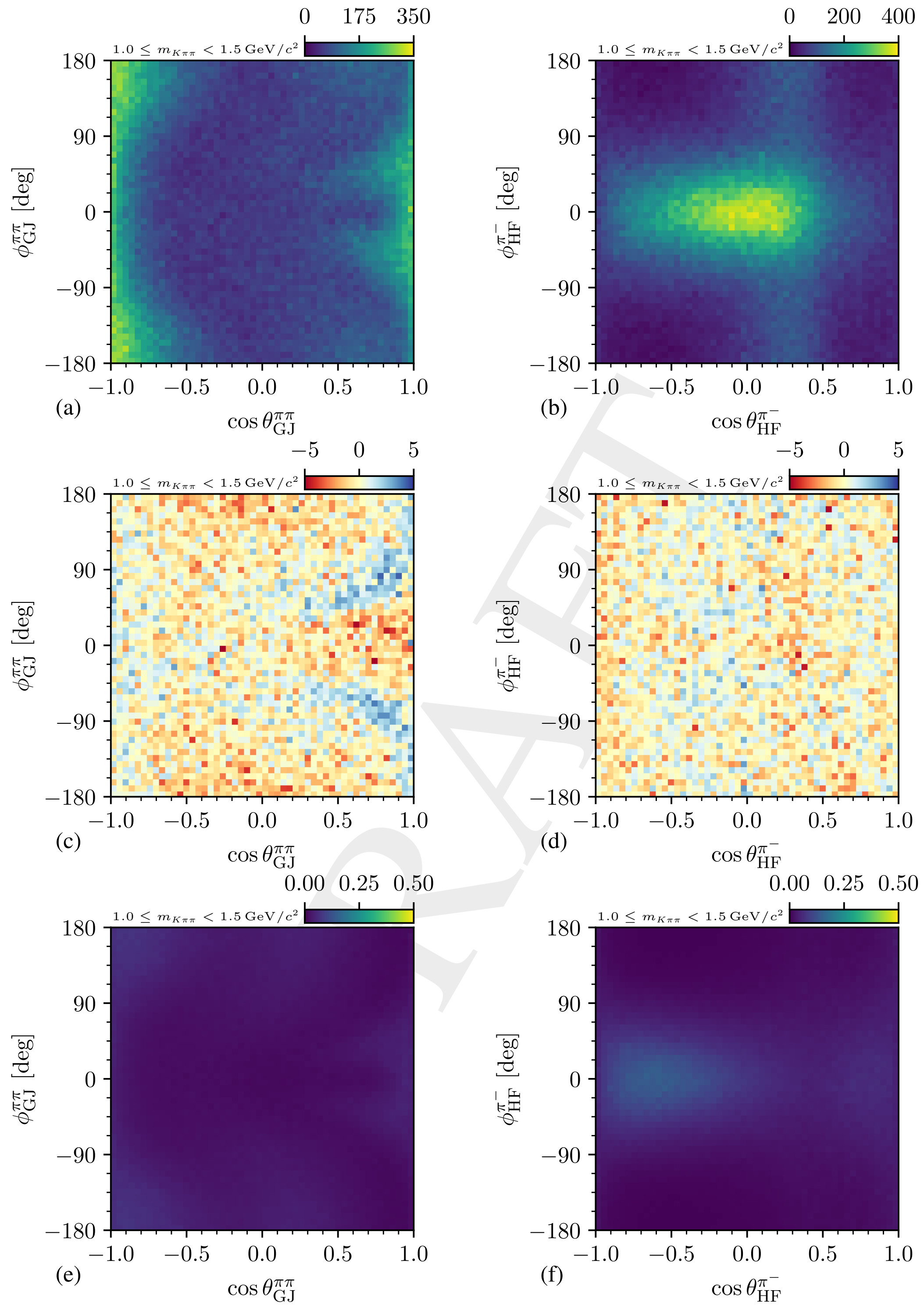

Figure D.37: Distributions of the four two-body decay angles defined for the $\pi^-\pi^+$ isobar system in the mass range $1.0 \leq m_{K\pi\pi} < 1.5\,\mathrm{GeV}/c^2$ integrated over the analyzed t' range. The top row shows the measured distributions, the middle row shows the difference between the measured number of events and the corresponding PWD prediction divided by the square root of the PWD prediction, and the lower row shows the acceptance.

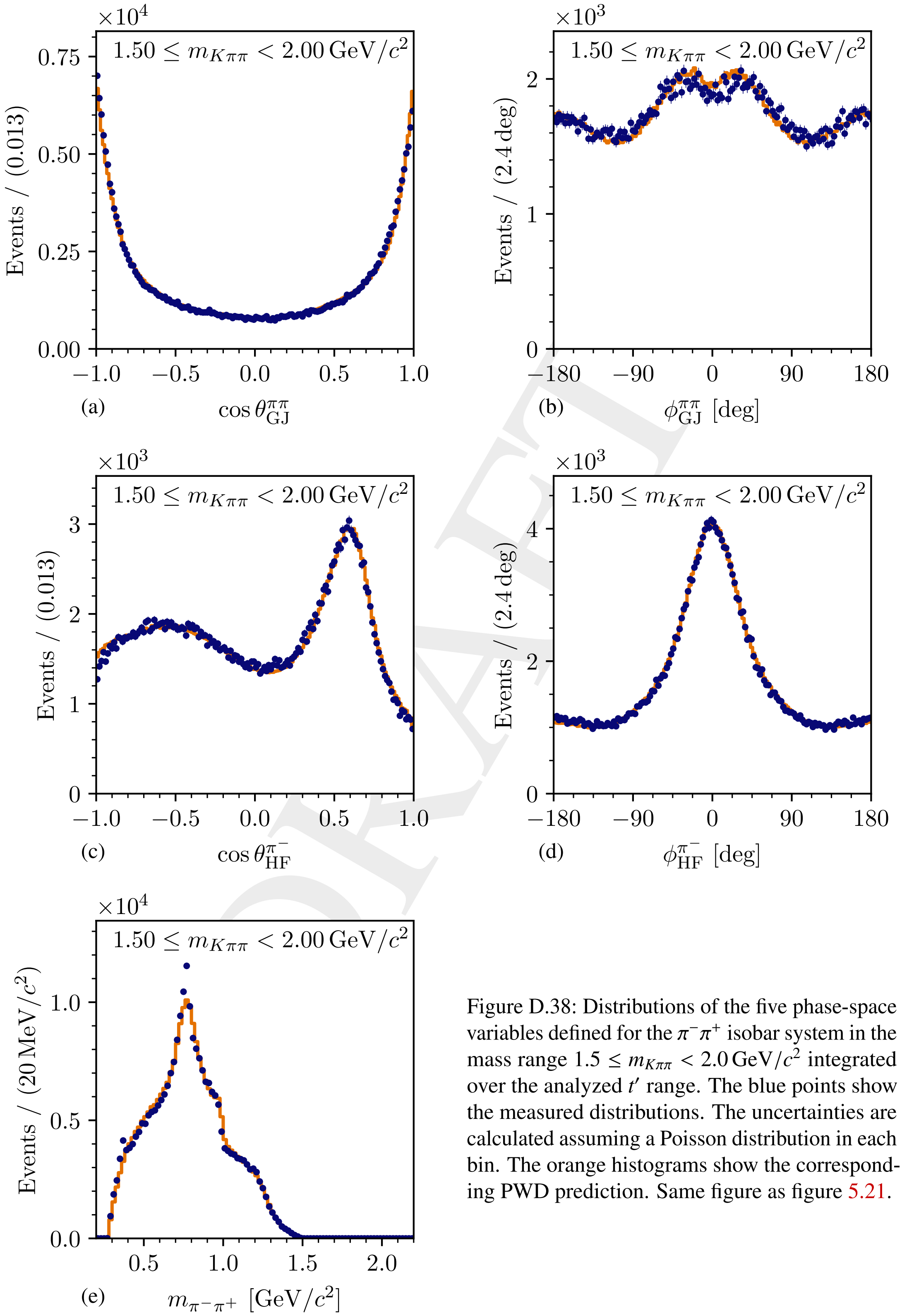

Figure D.38: Distributions of the five phase-space variables defined for the $\pi^-\pi^+$ isobar system in the mass range $1.5 \leq m_{K\pi\pi} < 2.0\,\mathrm{GeV}/c^2$ integrated over the analyzed t' range. The blue points show the measured distributions. The uncertainties are calculated assuming a Poisson distribution in each bin. The orange histograms show the corresponding PWD prediction. Same figure as figure 5.21.

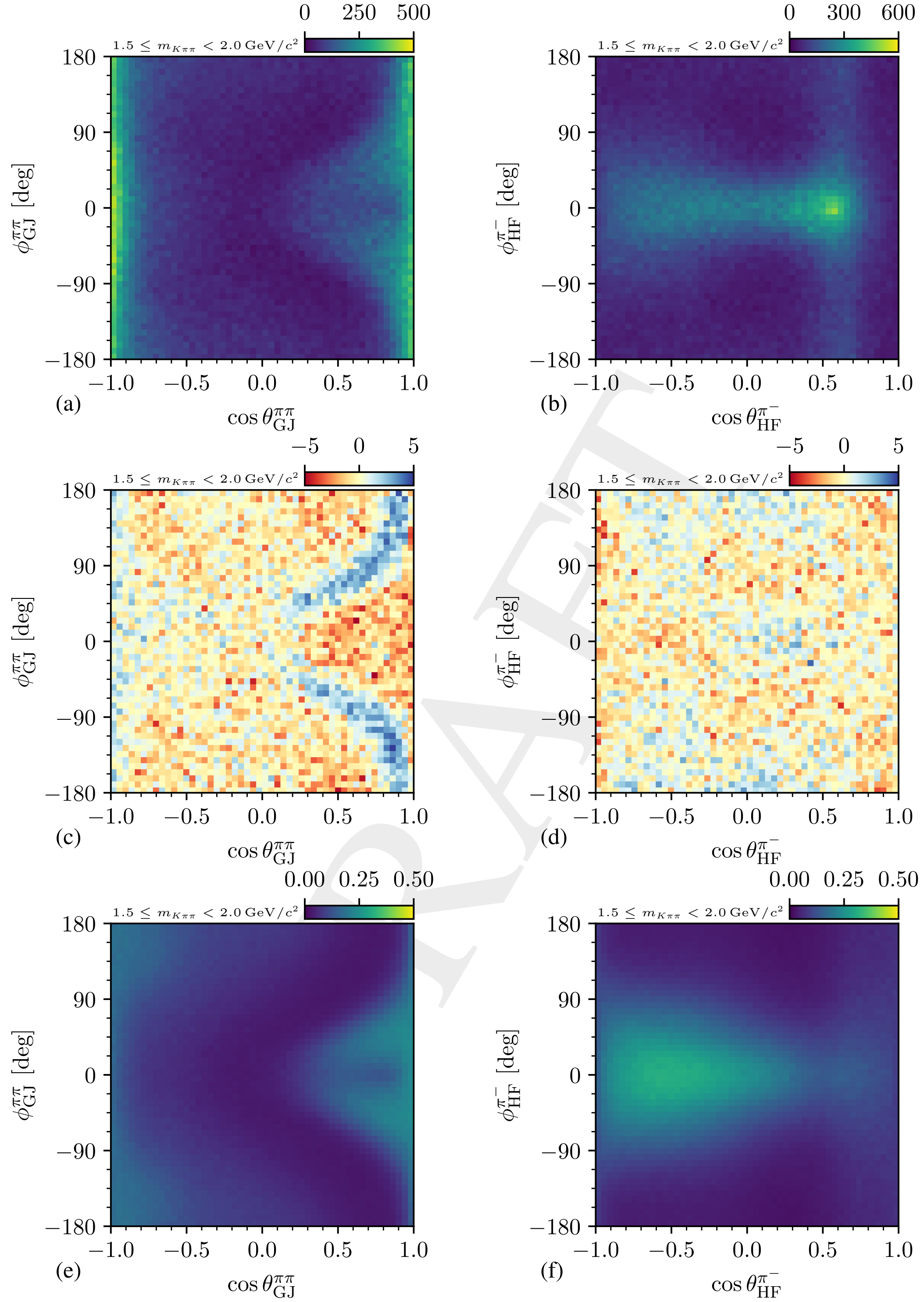

Figure D.39: Distributions of the four two-body decay angles defined for the $\pi^-\pi^+$ isobar system in the mass range $1.5 \leq m_{K\pi\pi} < 2.0\,\mathrm{GeV}/c^2$ integrated over the analyzed t' range. The top row shows the measured distributions, the middle row shows the difference between the measured number of events and the corresponding PWD prediction divided by the square root of the PWD prediction, and the lower row shows the acceptance.

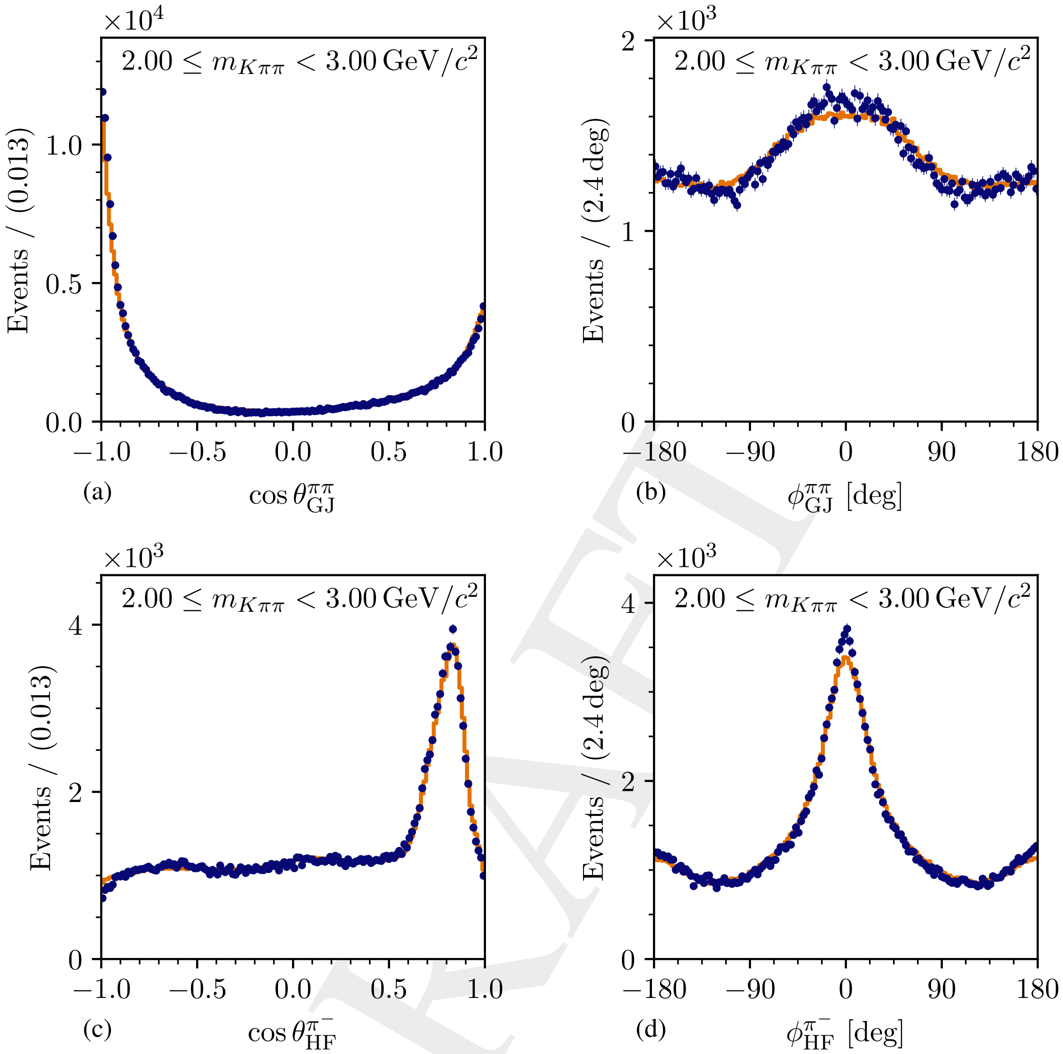

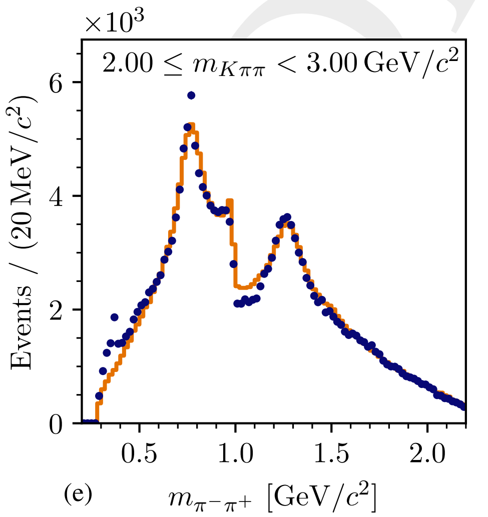

Figure D.40: Distributions of the five phase-space variables defined for the $\pi^-\pi^+$ isobar system in the mass range $2.0 \le m_{K\pi\pi} < 3.0\,\mathrm{GeV}/c^2$ integrated over the analyzed t' range. The blue points show the measured distributions. The uncertainties are calculated assuming a Poisson distribution in each bin. The orange histograms show the corresponding PWD prediction.

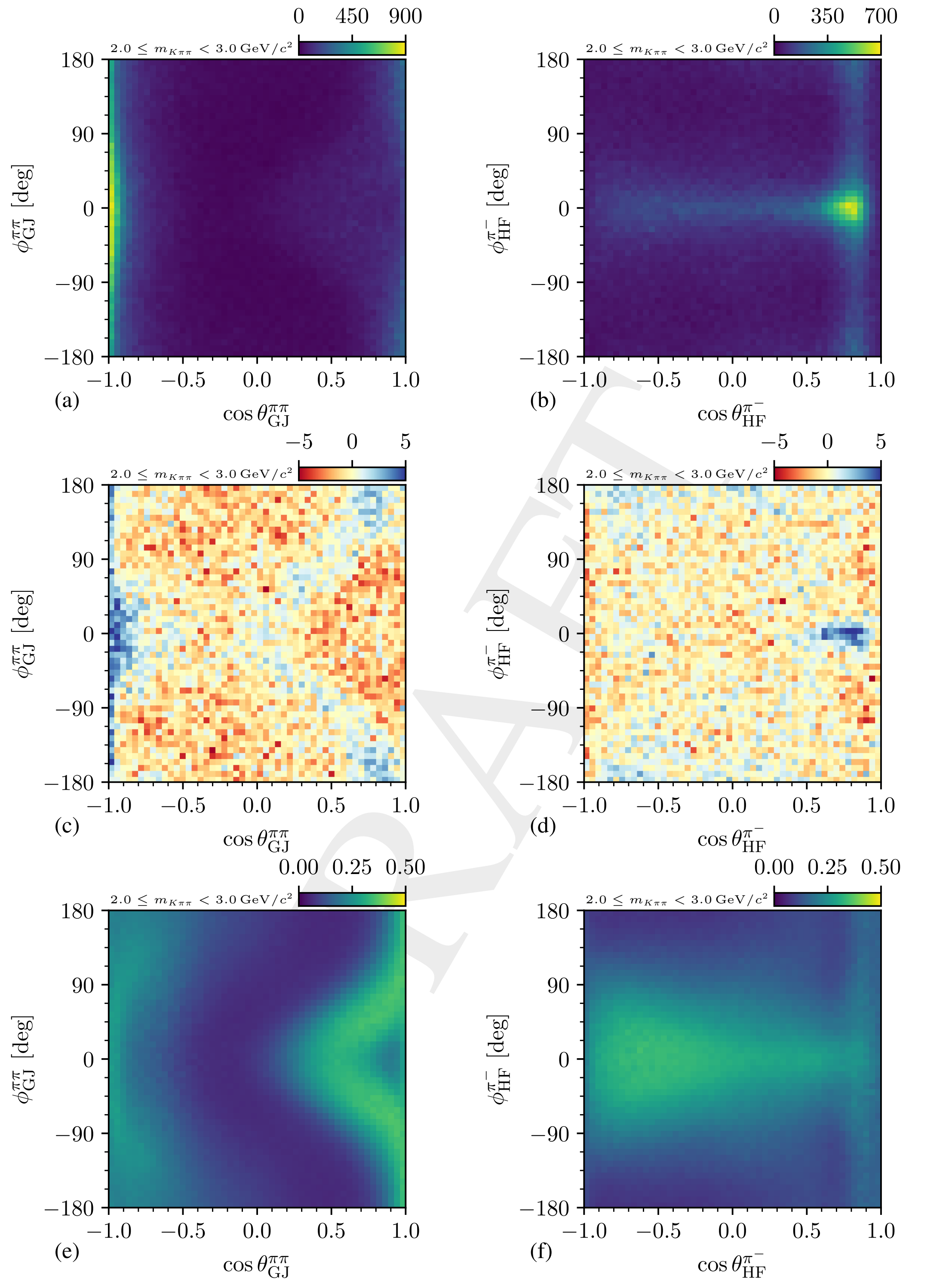

Figure D.41: Distributions of the four two-body decay angles defined for the $\pi^-\pi^+$ isobar system in the mass range $2.0 \le m_{K\pi\pi} < 3.0\,\mathrm{GeV}/c^2$ integrated over the analyzed t' range. The top row shows the measured distributions, the middle row shows the difference between the measured number of events and the corresponding PWD prediction divided by the square root of the PWD prediction, and the lower row shows the acceptance.

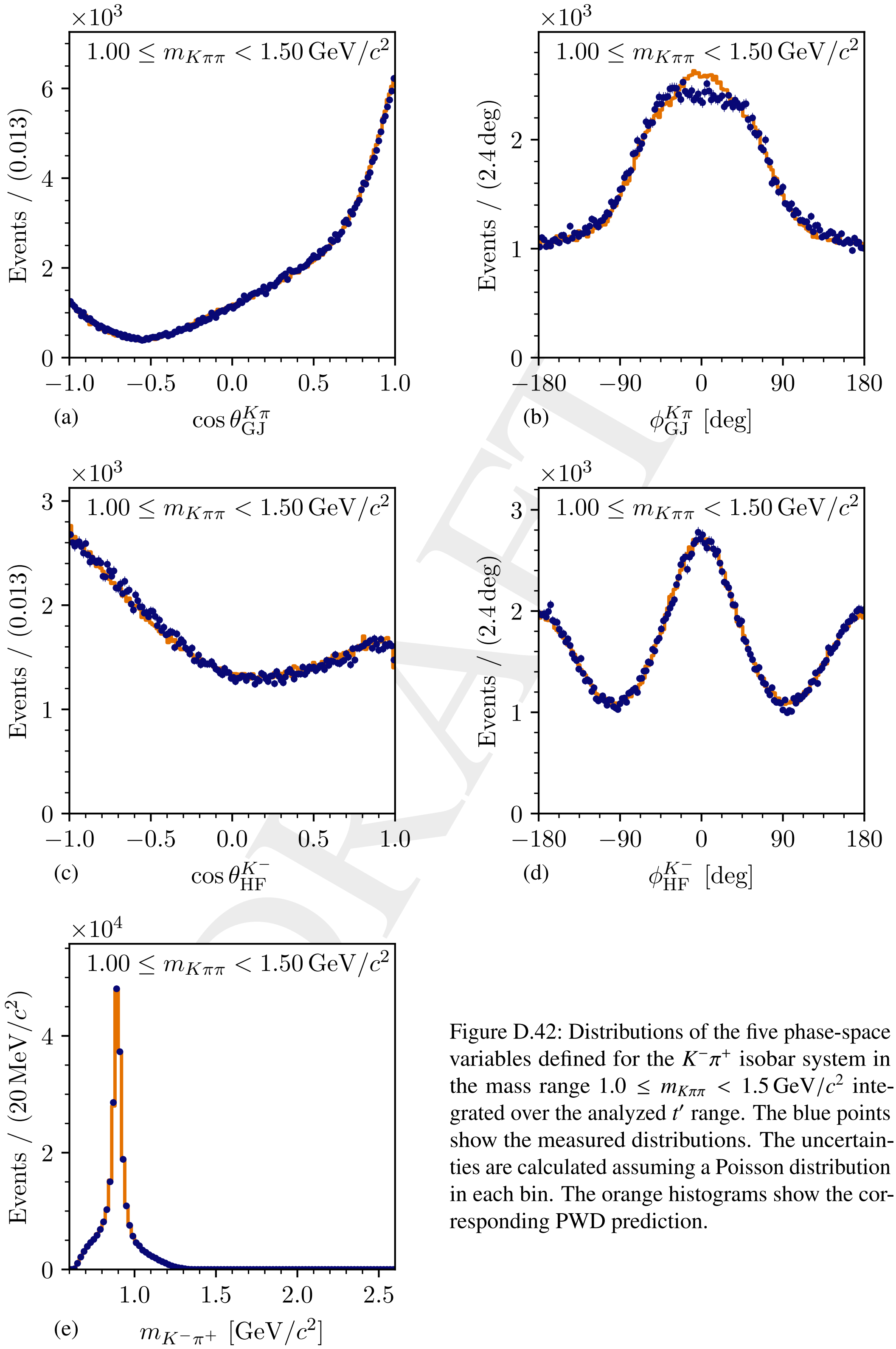

Figure D.42: Distributions of the five phase-space variables defined for the $K^-\pi^+$ isobar system in the mass range $1.0 \le m_{K\pi\pi} < 1.5\,\mathrm{GeV}/c^2$ integrated over the analyzed t' range. The blue points show the measured distributions. The uncertainties are calculated assuming a Poisson distribution in each bin. The orange histograms show the corresponding PWD prediction.

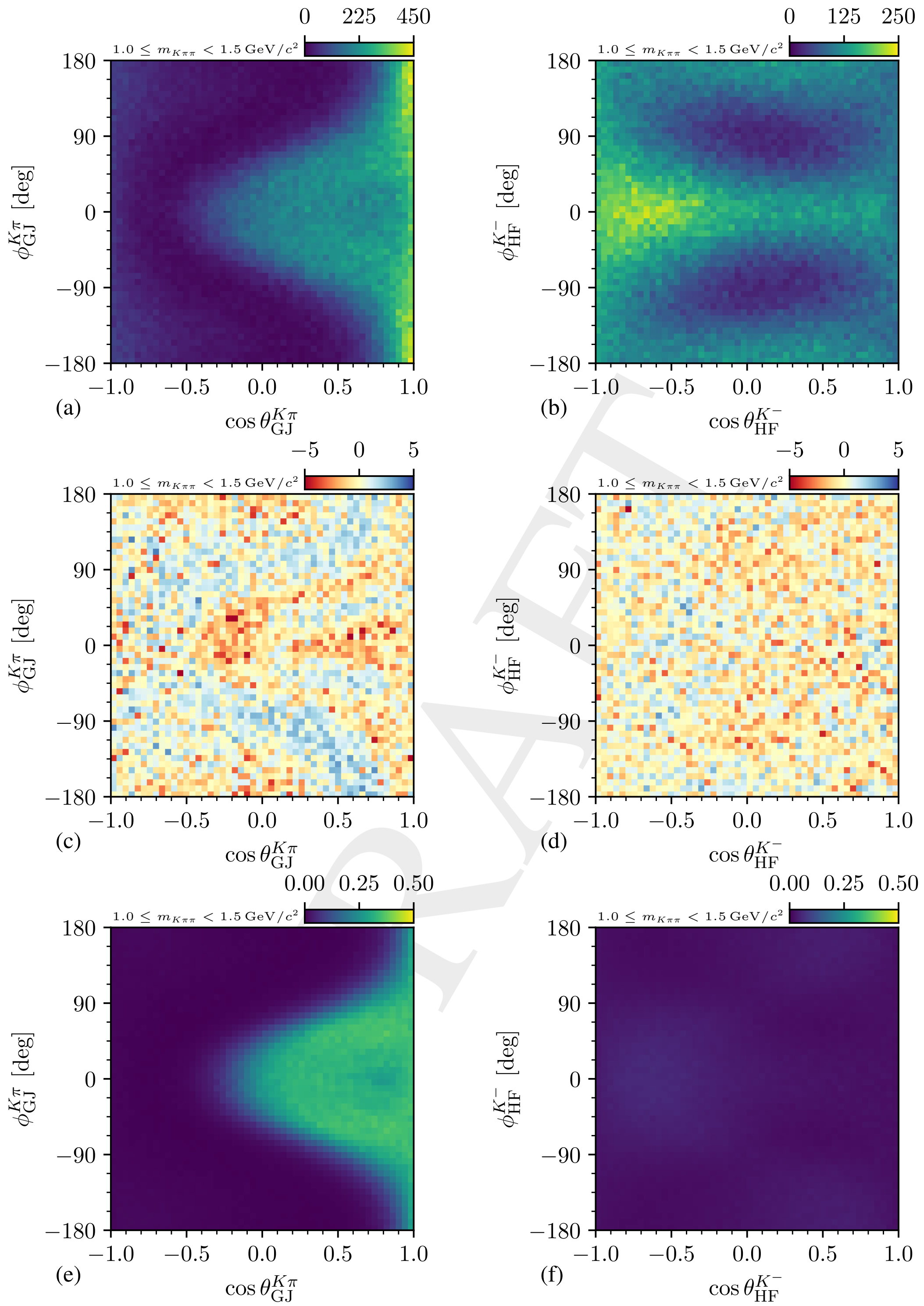

Figure D.43: Distributions of the four two-body decay angles defined for the $K^-\pi^+$ isobar system in the mass range $1.0 \le m_{K\pi\pi} < 1.5\,\mathrm{GeV}/c^2$ integrated over the analyzed t' range. The top row shows the measured distributions, the middle row shows the difference between the measured number of events and the corresponding PWD prediction divided by the square root of the PWD prediction, and the lower row shows the acceptance.

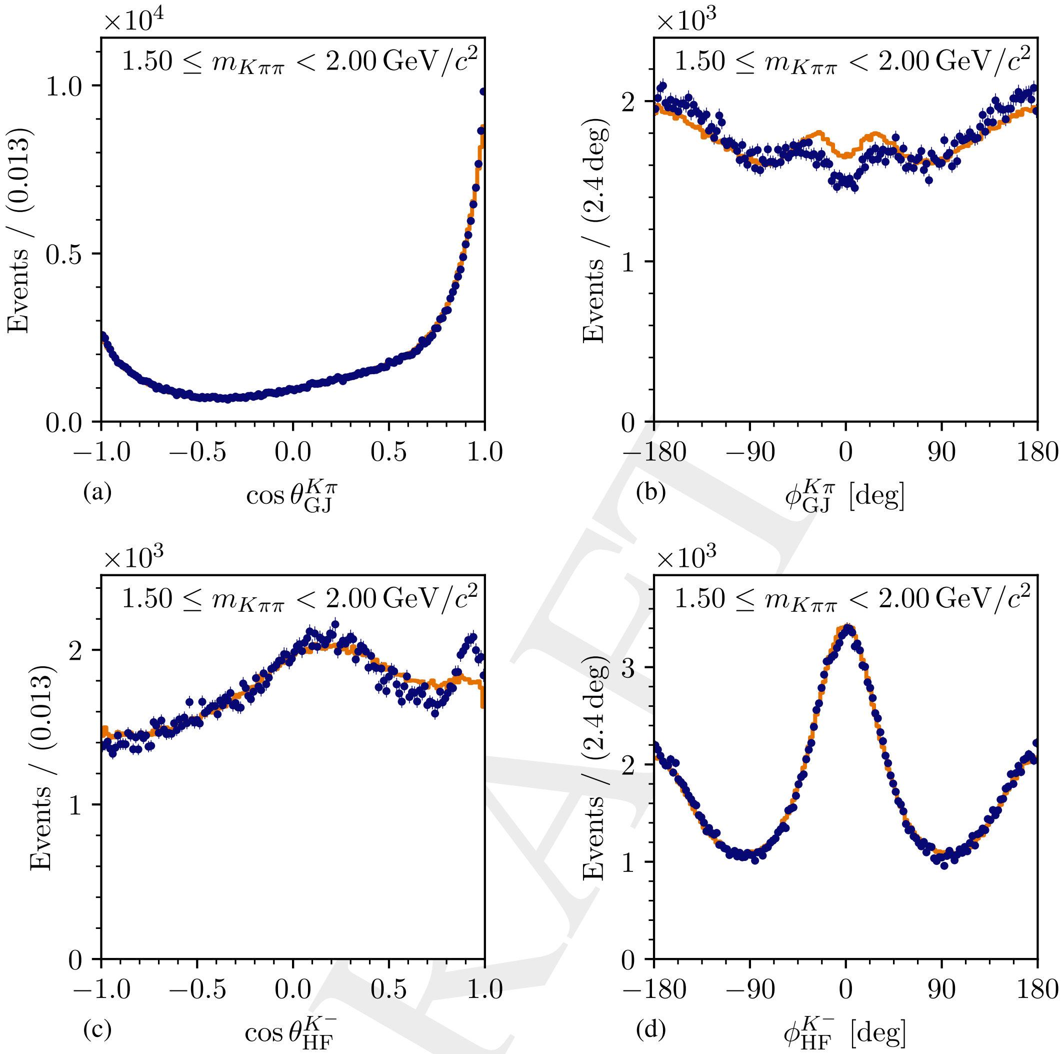

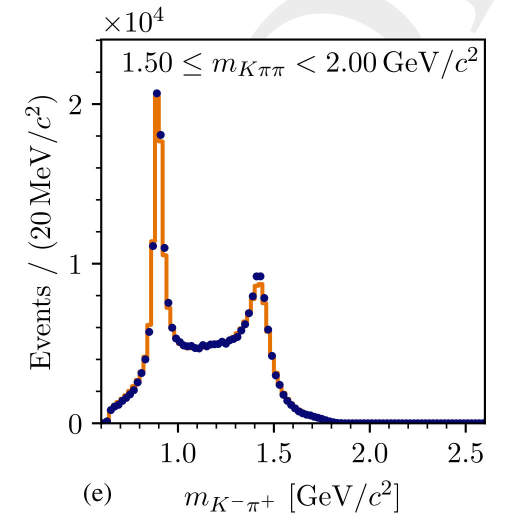

Figure D.44: Distributions of the five phase-space variables defined for the $K^-\pi^+$ isobar system in the mass range $1.5 \leq m_{K\pi\pi} < 2.0\,\mathrm{GeV}/c^2$ integrated over the analyzed t' range. The blue points show the measured distributions. The uncertainties are calculated assuming a Poisson distribution in each bin. The orange histograms show the corresponding PWD prediction.

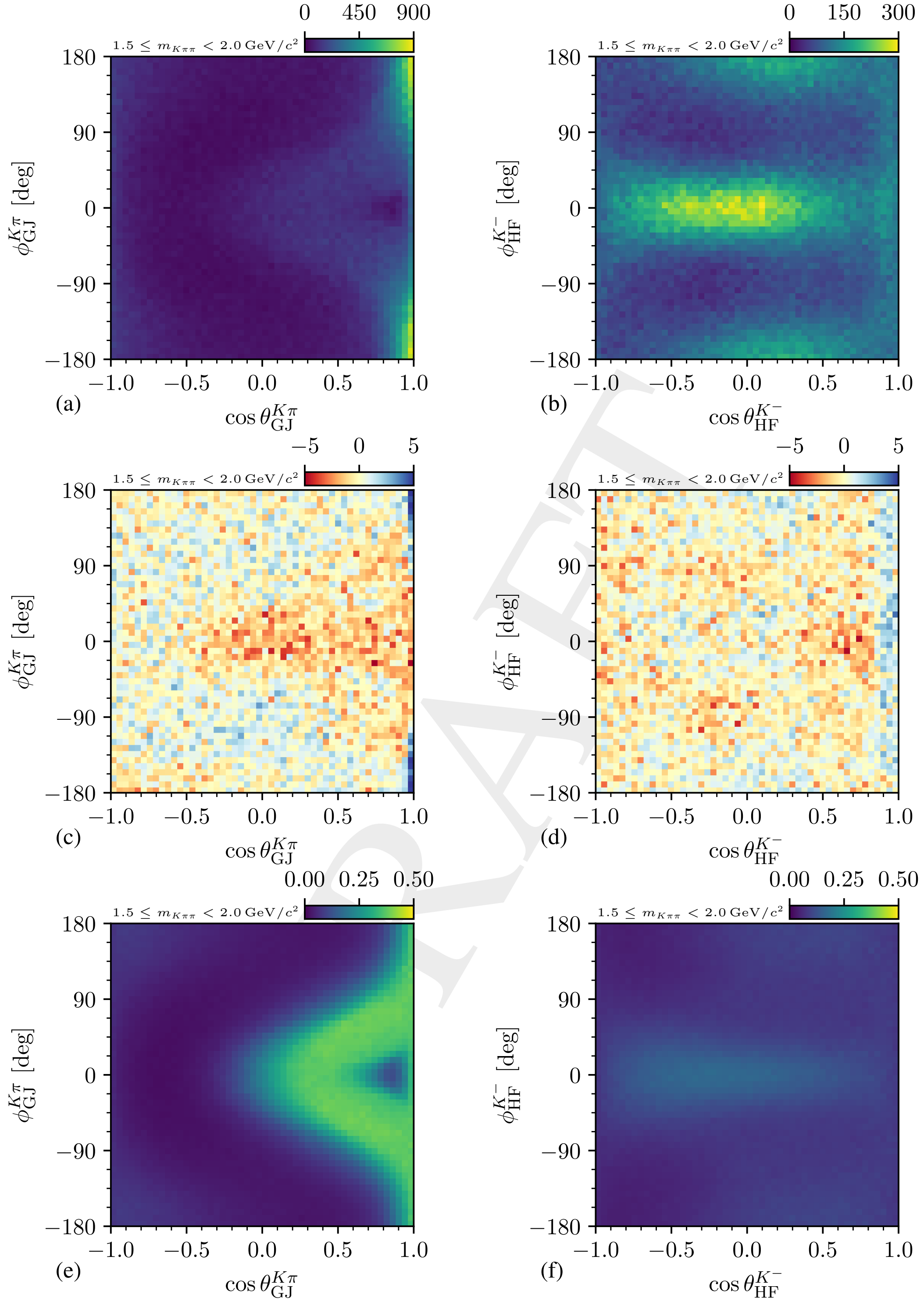

Figure D.45: Distributions of the four two-body decay angles defined for the $K^-\pi^+$ isobar system in the mass range $1.5 \leq m_{K\pi\pi} < 2.0\,\mathrm{GeV}/c^2$ integrated over the analyzed t' range. The top row shows the measured distributions, the middle row shows the difference between the measured number of events and the corresponding PWD prediction divided by the square root of the PWD prediction, and the lower row shows the acceptance.

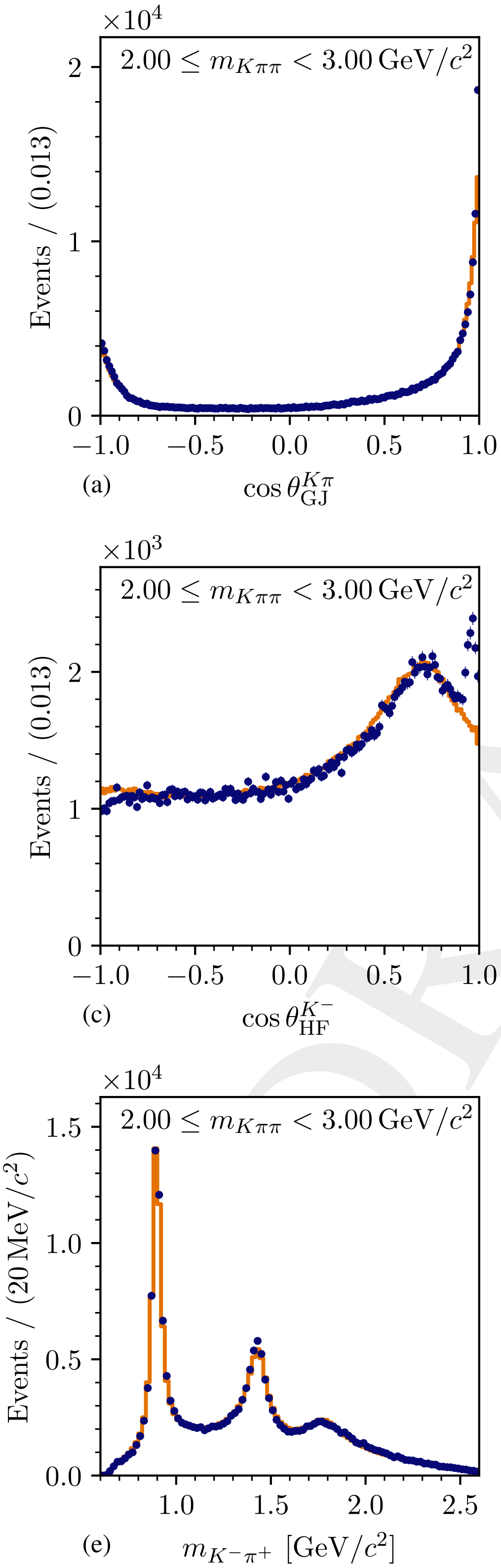

Figure D.46: Distributions of the five phase-space variables defined for the $K^-\pi^+$ isobar system in the mass range $2.0 \leq m_{K\pi\pi} < 3.0\,\mathrm{GeV}/c^2$ integrated over the analyzed t' range. The blue points show the measured distributions. The uncertainties are calculated assuming a Poisson distribution in each bin. The orange histograms show the corresponding PWD prediction.

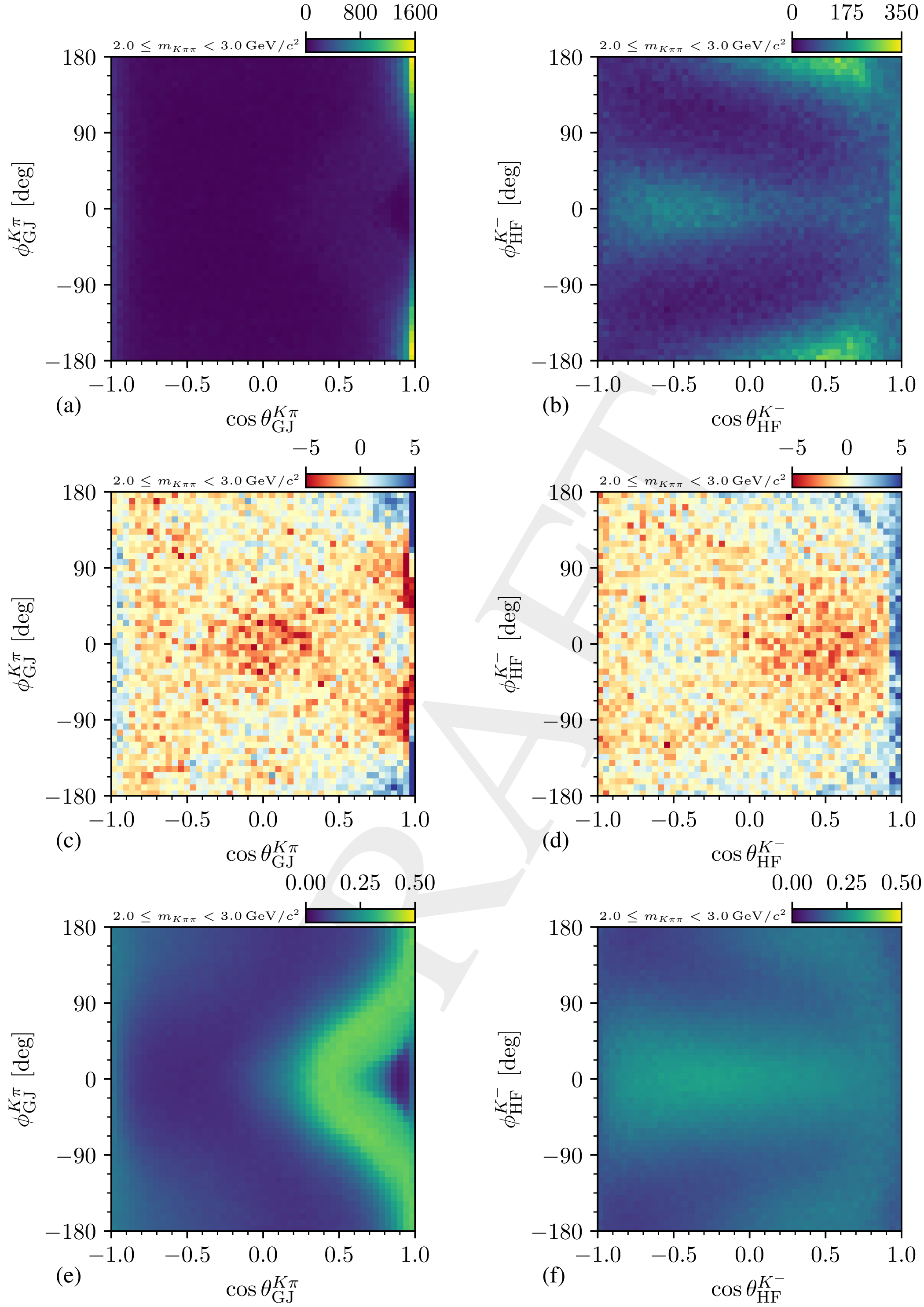

Figure D.47: Distributions of the four two-body decay angles defined for the $K^{-}\pi^{+}$ isobar system in the mass range $2.0 \leq m_{K\pi\pi} < 3.0\,\mathrm{GeV}/c^2$ integrated over the analyzed t' range. The top row shows the measured distributions, the middle row shows the difference between the measured number of events and the corresponding PWD prediction divided by the square root of the PWD prediction, and the lower row shows the acceptance.

D.3 Phase-Space Integral Matrix and Overlaps

Figure D.48a shows the magnitude of the elements of the phase-space integral matrix as given in equation (5.22) at $m_{K\pi\pi} = 1.31\,\mathrm{GeV}/c^2$ in the lowest t' bin. As stated in section 5.9, for most waves we observe only small overlaps (dark blue regions) due to the orthogonality of the Wigner D-functions. However, there are some exceptions. For example, the $0^-\,0^+\,[K\pi]_S^{K\pi}\,\pi\,S$ and $0^-\,0^+\,[\pi\pi]_S^{\mathrm{AMPK}}\,K\,S$ waves have an overlap close to one (see (i) in figure D.48a). As the spins as well as the orbital angular momenta of both waves are the same, i.e. zero, they differ only by the different isobar amplitudes that correspond to $[K\pi]_S^{K\pi}$ and $[\pi\pi]_S^{\mathrm{AMPK}}$. In the low $m_{K^-\pi^+}$ and $m_{\pi^-\pi^+}$ ranges kinematically accessible at $m_{K\pi\pi} = 1.31\,\mathrm{GeV}/c^2$, these isobar amplitudes are similar (see figures 5.4 and 5.5). Thus, the decay amplitudes become similar and the corresponding overlap becomes large. A similar case are the $1^+\,0^+\,[K\pi]_S^{K\pi}\,\pi\,P$ and $1^+\,0^+\,[K\pi]_S^{K\eta}\,\pi\,P$ waves, where we observe a large overlap marked by (ii).

Also, we find modest overlaps of about 0.5 between various waves marked by (iii) and (iv), e.g. between the $1^+\,0^+\,[K\pi]_S^{K\pi}\,\pi\,P$ and $1^+\,0^+\,\rho(770)\,K\,S$ waves. Both have the same $J^P\,M^\varepsilon$ quantum numbers. For the $1^+\,0^+\,[K\pi]_S^{K\pi}\,\pi\,P$ wave, the $K^-\pi^+$ system is in an S wave and the π^--isobar system is in a P wave. For the $1^+\,0^+\,\rho(770)\,K\,S$ wave, the K^--isobar system is in an S wave and the $\pi^-\pi^+$ system is in a P wave. Thus, the angular distribution of both waves are similar. However, they are not identical and both waves clearly differ in the isobar amplitude. Thus, the overlap is smaller than one, which means that the waves can be separated in principle in the PWD. This holds for all waves with similar overlap values.

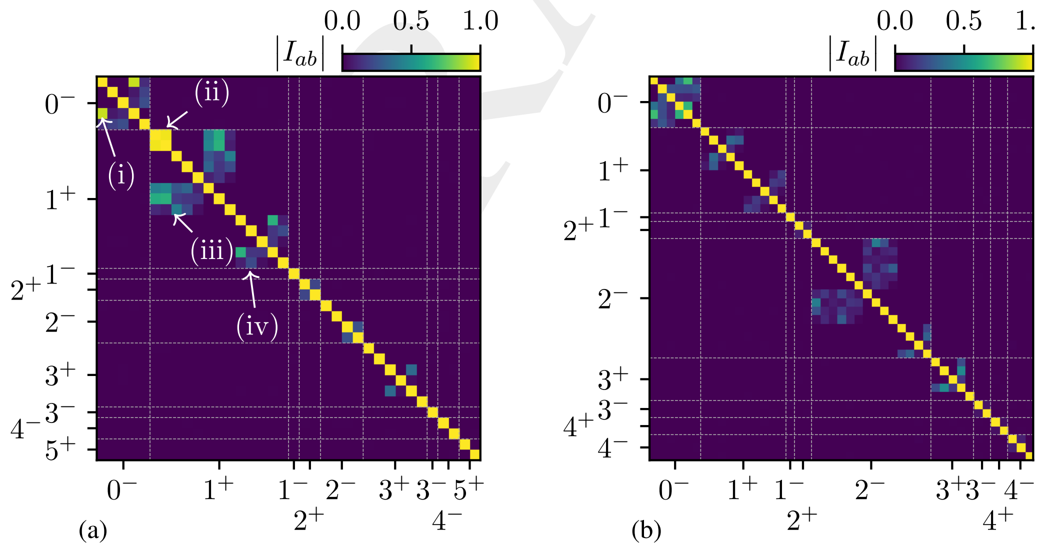

Figure D.48: Magnitude of the elements of the phase-space integral matrix for the wave set in the kinematic cell at (a) $m_{K\pi\pi} = 1.31\,\mathrm{GeV}/c^2$ and (b) $m_{K\pi\pi} = 1.91\,\mathrm{GeV}/c^2$ in the lowest t' bin. For simplicity, the incoherent flat wave is not shown and in (b) we show only waves with $J \leq 4$.

Figure D.48b shows the magnitude of the elements of the phase-space integral-matrix at a higher mass of $m_{K\pi\pi} = 1.91\,\mathrm{GeV}/c^2$ in the lowest t' bin. Overall, the overlaps are smaller in the high-$m_{K\pi\pi}$ region than in the low-$m_{K\pi\pi}$ region and we do not observe overlaps as large as those marked with (i) and (ii) in figure D.48a. The reason for this is, that at higher $m_{K\pi\pi}$ the phase-space is larger, i.e. a larger range in $m_{\pi^-\pi^+}$ and $m_{K^-\pi^+}$ is kinematically accessible. Thus, we explore more of the isobar amplitude in the PWD, which improves the separation of, e.g., the $0^- \, 0^+ \, [K\pi]_S^{K\pi} \, \pi \, S$ and $0^- \, 0^+ \, [\pi\pi]_S^{\mathrm{AMPK}} \, K \, S$ waves. Similar to some 1^+ waves in the low-$m_{K\pi\pi}$ region, we find modest overlaps between some 2^- waves in the high-$m_{K\pi\pi}$ region. The latter one is dominated by 2^- resonances and thus more 2^- waves were selected for the wave set in the shown $(m_{K\pi\pi}, t')$ cell.

Partial waves with large overlaps can lead to artifacts, i.e. wrong estimates for the spin-density matrix elements in the PWD. This is because the decay amplitudes, which are similar for overlapping waves, may cancel each other via destructive interference in a large region of the phase space in the coherent sum of the model intensity given by equation (5.16). Although the intensities of the partial waves in such a destructive interference may become artificially large, they change the model intensity only marginally. Thus, destructive interference may be misused by the PWD fit to describe statistical fluctuations or small imperfections in the model.

Such destructive interference effects from overlapping waves are know, e.g. from the COMPASS $\pi^-\pi^-\pi^+$ analysis [43]. We do not observe large destructive interference effects from overlapping waves in the partial waves shown in this work. A reason is that the wave set obtained from the wave-set selection described in section 5.2 was designed to disfavor overlapping waves by imposing $m_{K\pi\pi}$ thresholds for waves with heavy isobars (see section 5.2.4).

D.4 $\pi^-\pi^-\pi^+$ Pseudodata Studies

D.4.1 The $\pi^-\pi^-\pi^+$ Pseudodata Model

The PWD model used to generate the $\pi^-\pi^-\pi^+$ pseudodata sample was obtained from the so-far world's largest sample of the reaction $\pi^- + p \to \pi^-\pi^-\pi^+ + p$ collected by COMPASS during the 2008 diffraction data taking.[e] This $\pi^-\pi^-\pi^+$ sample was first analyzed and published in ref. [39]. Based on these results, an improved analysis was performed and will be presented in ref. [43].[f] An improved event reconstruction of the raw data with a refined time-resolved detector alignment. Also, the event selection was fine-tuned; i.e. some cut parameters were optimized for the updated data sample, the cut to suppress central-production reactions was

[e] The 2009 diffraction data set was not used in the $\pi^-\pi^-\pi^+$ analysis when obtaining the model for the $\pi^-\pi^-\pi^+$ pseudodata, yet.

[f] As the analysis of ref. [43] was not finished when obtaining the model for the $\pi^-\pi^-\pi^+$ pseudodata, the final results that will be shown in ref. [43] may slightly differ from the model for the $\pi^-\pi^-\pi^+$ pseudodata sample. However, the description of the measured $\pi^-\pi^-\pi^+$ sample by the PWD model, which is the property of the PWD model that is important for generating pseudodata from, it should remain basically unchanged.

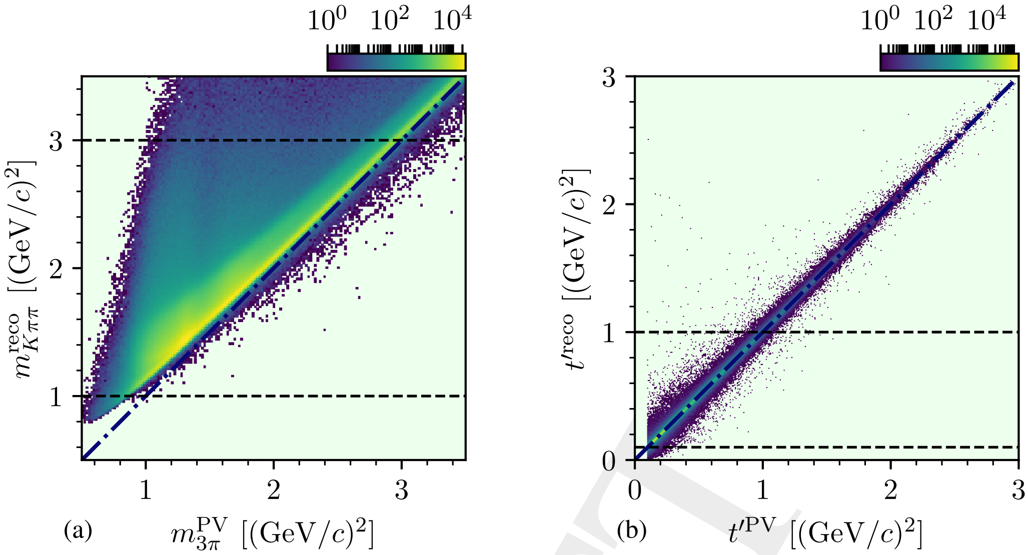

Figure D.49: Reconstructed versus true physical values (PV) for the $\pi^-\pi^-\pi^+$ pseudodata sample reconstructed as $K^-\pi^-\pi^+$ events: (a) for $m_{K\pi\pi}$ and (b) for t'. The dashed horizontal black lines show the $m_{K\pi\pi}$ and t' ranges analyzed in this work. The dash-dotted blue lines represents $m^{\text{reco}}_{K\pi\pi} = m^{\text{PV}}_{3\pi}$ and $t'^{\text{reco}} = t'^{\text{PV}}$, respectively. The reconstructed sample without the beam-particle identification cut is shown. Regions without events are shown in light green.

not applied, and the particle identification cuts to suppress beam kaons and final-state particles other than pions were improved using the methods developed in this work (see sections 3.1, 3.2, and 4.1). This yielded a measured $\pi^-\pi^-\pi^+$ sample of about 70.4×10^6 events in the kinematic region $0.5 \le m_{3\pi} < 3.5\,\text{GeV}/c^2$ and $0.1 \le t' < 3.0\,(\text{GeV}/c)^2$. This sample is significantly larger and covering a wider kinematic region as the one used ref. [39].

Based on this $\pi^-\pi^-\pi^+$ sample, a PWD was performed using the same approach as presented in section 5.1. The same wave set as in ref. [39] was used, which consists of 88 partial waves. The corresponding PWD model was formulated in terms of a rank=1 spin-density matrix for the positive-reflectivity waves, a rank=2 spin-density matrix for the negative-reflectivity waves, and an incoherent flat wave. A fine binning in $m_{3\pi}$ and t' was used, i.e. the sample was split in 300 $m_{3\pi}$ bins with a width of $10\,\text{MeV}/c^2$ and 33 non-equidistant t' bins, which were chosen such that a similar number of events enters each t' bin.

We used the results of this PWD as an input to generate a $\pi^-\pi^-\pi^+$ pseudodata sample in the kinematic ranges $0.5 \le m_{3\pi} < 3.5\,\text{GeV}/c^2$ and $0.1 \le t' < 3.0\,(\text{GeV}/c)^2$. Then, we reconstructed this produced $\pi^-\pi^-\pi^+$ pseudodata sample as $K^-\pi^-\pi^+$ events in order to study the $\pi^-\pi^-\pi^+$ contamination of the measured $K^-\pi^-\pi^+$ sample (see section 5.10). To test whether the $\pi^-\pi^-\pi^+$ kinematic range is sufficient to cover the analyzed $K^-\pi^-\pi^+$ range of $1.0 \le m_{K\pi\pi} < 3.0\,\text{GeV}/c^2$ and $0.1 \le t' < 1.0\,(\text{GeV}/c)^2$, we show in figure D.49 the reconstructed values (reco) under the $K^-\pi^-\pi^+$ event hypothesis versus the true physical values (PV) with which the $\pi^-\pi^-\pi^+$ pseudodata event was produced.

The reconstructed value for $m_{K\pi\pi}$, i.e.

$$m_{K\pi\pi}^{\text{reco}} = \sqrt{\left(p_{K^-}^{\text{reco}} + p_{\pi^-}^{\text{reco}} + p_{\pi^+}^{\text{reco}}\right)^2}, \tag{D.1}$$

is given by the reconstructed three-momenta of the final-state particles and their mass assumptions, which yields the four-momenta $p_{h^\pm}^{\text{reco}}$ of the final-state particles. For the final-state π^- that was erroneously identified as K^- in the reconstructed $\pi^-\pi^-\pi^+$ pseudodata sample, this mass assumption is wrong. Typically, $m_{K\pi\pi}^{\text{reco}}$ is as large or larger than the value $m_{3\pi}^{\text{PV}}$ with which the event was produced (see figure D.49a). Just above the $\pi^-\pi^-\pi^+$ threshold at about $m_{3\pi}^{\text{PV}} = 0.5\,\text{GeV}/c^2$, the difference between $m_{K\pi\pi}^{\text{reco}}$ and $m_{3\pi}^{\text{PV}}$ is given mainly by the mass difference between the final-state K^- and π^-, because of the wrong mass assumption for one of the final-state π^-. With increasing $m_{3\pi}^{\text{PV}}$, this relation is smeared out, because of the larger momenta of the final-state particles, which have a larger influence on $m_{K\pi\pi}^{\text{reco}}$ (see equation (D.1)). From the distribution in figure D.49a we do not expect events with $m_{3\pi}^{\text{PV}} < 0.5\,\text{GeV}/c^2$ or $m_{3\pi}^{\text{PV}} > 3.5\,\text{GeV}/c^2$ to enter the analyzed $m_{K\pi\pi}^{\text{reco}}$ region (dashed horizontal lines). Thus, the $m_{3\pi}^{\text{PV}}$ range in which we generated pseudodata events is sufficient to cover the analyzed $m_{K\pi\pi}^{\text{reco}}$ range.

As expected, the reconstructed squared four-momentum transfer t'^{reco} scatters around the true physical value t'^{PV} with which the event was produced (see figure D.49b), as expected. We do not expect events with $t'^{\text{PV}} > 3.0\,(\text{GeV}/c)^2$ to enter the analyzed t'^{reco} region (dashed horizontal lines). However, the lower limit of the analyzed t' range of $0.1\,(\text{GeV}/c)^2$ is the same for both analysis. It is given by the minimum energy necessary for the recoil proton to produce a signal in the recoil-proton detector (see section 2.2). Due to the finite resolution in t'^{reco} of about $0.006\,(\text{GeV}/c)^2$ (see figure C.5b), a small fraction of events with $t'^{\text{PV}} < 0.1\,(\text{GeV}/c)^2$ may enter the analyzed t'^{reco} range. However, we do not have a PWD model for $t'^{\text{PV}} < 0.1\,(\text{GeV}/c)^2$ and thus we cannot generate pseudodata for this range. Hence, we neglect these events in the low t'^{reco} region of the reconstructed $\pi^-\pi^-\pi^+$ pseudodata sample. Due to the exponential shape of the t'^{PV} distribution, this bin-migration effect may lead to a slight underestimation of the number of $\pi^-\pi^-\pi^+$ background events in the lowest t' bin. However, given the good resolution in t'^{reco}, we expect this effect to be negligible.

In conclusion, the PWD model from the COMPASS $\pi^-\pi^-\pi^+$ analysis is well suited to generate a realistic pseudodata sample for the reaction $\pi^- + p \to \pi^-\pi^-\pi^+ + p$, which allows us to study the $\pi^-\pi^-\pi^+$ background in the $K^-\pi^-\pi^+$ sample. The results of this study are discussed in sections 5.10.1 and 5.10.2.

D.4.2 Acceptance of the $K^-\pi^-\pi^+$ Event Selection for $\pi^-\pi^-\pi^+$ Events

As discussed in section 5.10.1, we expect about 6.7 % $\pi^-\pi^-\pi^+$ background in the $K^-\pi^-\pi^+$ sample. This amount of $\pi^-\pi^-\pi^+$ background is given by the beam-particle miss-identification probability; the acceptance of the final-state event selection, i.e. the $K^-\pi^-\pi^+$ event selection without the beam-particle identification; and potentially different cross-sections for the reactions

$K^- + p \to K^-\pi^-\pi^+ + p$ and $\pi^- + p \to \pi^-\pi^-\pi^+ + p$. The amount of $\pi^-\pi^-\pi^+$ background is about twice as large as the expected impurity from beam pions in a kaon-beam sample selected by the CEDARs, which is about 3 % (see section 3.1.6). By comparing the acceptance of the $K^-\pi^-\pi^+$ final-state event selection for $\pi^-\pi^-\pi^+$ pseudodata events and for $K^-\pi^-\pi^+$ pseudodata events, we found that the acceptance for $\pi^-\pi^-\pi^+$ events is about twice as large as the acceptance for $K^-\pi^-\pi^+$ events. This explains the two-times larger amount of $\pi^-\pi^-\pi^+$ background compared to the naïve expectation from the impurity from beam pions in a kaon-beam sample.

The main reason for the comparably high acceptance of the final-state event selection for $\pi^-\pi^-\pi^+$ events is that in the $K^-\pi^-\pi^+$ event selection we required only one of the two negative final-state particles to be identified. The π^- is identified for most of the events (see figure 4.3). Events of the reaction $K^- + p \to K^-\pi^-\pi^+ + p$ have one final-state π^- to be identified, while events of the reaction $\pi^- + p \to \pi^-\pi^-\pi^+ + p$ have two π^- and thus a higher probability to be accepted. In principle, the final-state particle identification veto should reject $\pi^-\pi^-\pi^+$ events (see section 4.1). However, only few $\pi^-\pi^-\pi^+$ events are rejected, because the positive final-state particle is a π^+ in both reactions and because it is kinematically very improbable to simultaneously identify both negative final-state particles (see section 4.1). Also, the other event selection cuts do not suppress $\pi^-\pi^-\pi^+$ events with respect to $K^-\pi^-\pi^+$ events. Figure D.50 shows the distributions of the $\pi^-\pi^-\pi^+$ pseudodata sample reconstructed as $K^-\pi^-\pi^+$ events (red histograms) in the kinematic variables used to impose energy and momentum conservation in the event selection as discussed in section 4.1. They exhibit peaks that are similar to those of the measured $K^-\pi^-\pi^+$ sample (blue histograms). Thus, also the cuts (gray vertical lines) on energy conservation, i.e. on E_{beam}, and on momentum conservation, i.e. on $\Delta\phi_{\text{recoil}}$, do not suppress the $\pi^-\pi^-\pi^+$ background in the $K^-\pi^-\pi^+$ sample.

In summary, the amount of $\pi^-\pi^-\pi^+$ background is mainly caused by the limited kinematic range of the final-state particle identification. Since the relative amount of $\pi^-\pi^-\pi^+$ background in the $K^-\pi^-\pi^+$ sample is dominantly explained by acceptance effects, the cross-sections of the reactions $K^- + p \to K^-\pi^-\pi^+ + p$ and $\pi^- + p \to \pi^-\pi^-\pi^+ + p$ have a similar scale. This is consistent with measurements of the total Kp and πp cross-sections [9].

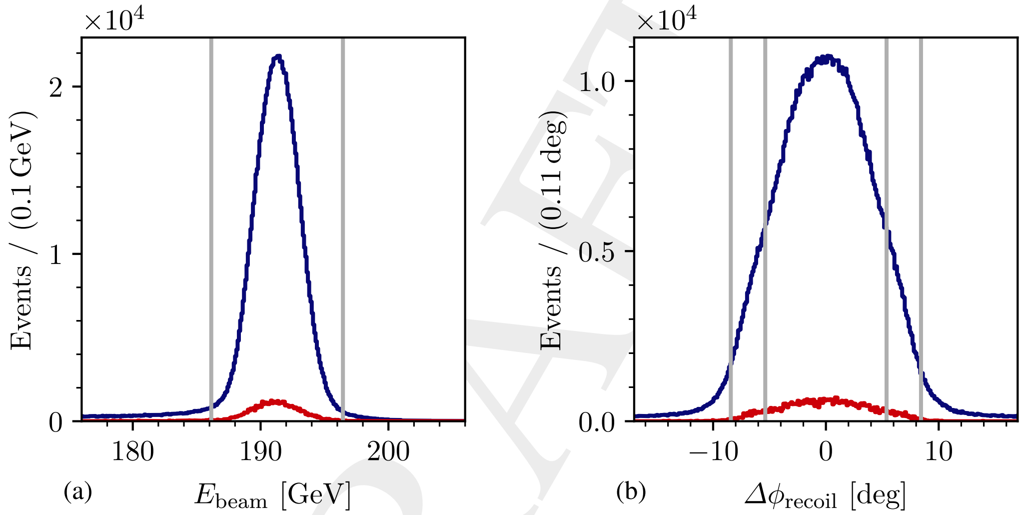

Figure D.50: Distribution of the kinematic variables used to select exclusive events. The red histograms show the $\pi^-\pi^-\pi^+$ pseudodata sample reconstructed as $K^-\pi^-\pi^+$ events (see section 5.10) and scaled such that the number of reconstructed $\pi^-\pi^-\pi^+$ pseudodata events corresponds to the predicted amount of $\pi^-\pi^-\pi^+$ background in the $K^-\pi^-\pi^+$ sample. The blue histograms show the measured $K^-\pi^-\pi^+$ sample (same as figure 4.4). (a) shows the distribution of the reconstructed beam energy after all cuts except for the cut on E_{beam}. (b) shows the distribution of $\Delta\phi_{\mathrm{recoil}}$, which is a measure of momentum conversation (see section 4.1), after all cuts except for the cut on $\Delta\phi_{\mathrm{recoil}}$. The gray lines represent the applied cuts.

E The Resonance Model Fit

E.1 The 10-Wave RMF

E.1.1 The 10-Wave RMF Model

An overview over the 10-wave RMF model is given in section 6.2.1 and it is also summarized in table 6.1. Here, we provide additional, mainly technical details of the 10-wave RMF model.

Table E.1 lists the eight resonance components included in the 10-wave RMF. For all resonance components, we used the relativistic Breit-Wigner amplitude given in equation (5.39) with a dynamic width that takes into account a single decay channel given in the last column in table E.1. The same decay channel is used for all resonances that belong to the same J^P sector, i.e. the dominant decay channel of the dominant resonance. We chose the parameter limits for the m_0 and Γ_0 parameters (second column in table E.1) to be as little restrictive as possible in order to prevent the results ending up on these limits, which would bias our results. Resonance components representing ground or excited states of the same J^P sector have non-overlapping m_0 limits. For example, this prevents interchange of resonance components, which would lead to ambiguities in the RMF. The upper limit for Γ_0 of $600\,\text{MeV}/c^2$ is the same for all resonance components. It is much larger than the width of the broadest of the included resonances as measured by previous experiments, which is the $K_2(1820)$ with a width of about $276\,\text{MeV}/c^2$ [91]. The lower limits for the Γ_0 parameters were optimized for each resonance to suppress solutions with unrealistically small widths. We chose these limits to be smaller than any previous Γ_0 measurement of the corresponding state. Furthermore, we selected the start-parameter ranges for m_0 and Γ_0 such that their cover a reasonable range including previous measurements [91] plus a safety margin. Hence, we do not expect bias from the choice of the start-parameter ranges. As the $K_1(1400)$ is only a small signal in the two included 1^+ waves, we could not determine its mass and width reliably (see section 6.3.3). Thus, we fixed the m_0 and Γ_0 parameters of the $K_1(1400)$ component to the corresponding PDG average values [91] as listed in table E.1.

For the non-resonant and effective background components, we used in most of the waves the simplified shape given in equations (6.11) and (6.17) as listed in table 6.1. The parameter limits of $-0.1 \leq b_k < 130.0\,(\text{GeV}/c)^{-2}$ were chosen to be much larger than the expected range of b_k, e.g. larger than the typical values for b_k obtained in the COMPASS $\pi^-\pi^-\pi^+$ analysis [41]. The start parameter range was chosen to be $1.0 \leq b_k < 10.0\,(\text{GeV}/c)^{-2}$. For those components that are parameterized by extended non-resonant and effective background shapes in equations (6.8)

Table E.1: Resonance components included in the set $\mathbb{S}_a$ in equation (6.6) for the 10 partial waves listed in table 6.1. In addition, we list the fit-parameter limits and the start-parameter ranges (see text) for the mass parameters m_0 and width parameters Γ_0. The resonance parameters of the $K_1(1400)$ component were fixed in the RMF to the PDG average values [91]. The last column shows the decay mode that we assumed when calculating the dynamic width of the resonance in equation (5.40).

Resonance	Parameter	Limits [MeV/c^2]		Start Ranges [MeV/c^2]		Fixed Values [MeV/c^2]	Decay Mode for $\Gamma(m)$
$K_1(1270)$	m_0	1200	1500	1270	1290	—	$K^*(892)\,\pi\,S$
	Γ_0	50	600	80	130	—	
$K_1(1400)$	m_0	—	—	—	—	1403	$K^*(892)\,\pi\,S$
	Γ_0	—	—	—	—	174	
$K_1(1630)$	m_0	1550	2300	1600	1900	—	$K^*(892)\,\pi\,S$
	Γ_0	50	600	120	350	—	
$K_2^*(1430)$	m_0	1300	1500	1425	1435	—	$K\,\pi\,S$
	Γ_0	80	600	105	115	—	
$K_2(1770)$	m_0	1700	1790	1700	1790	—	$K^*(892)\,\pi\,P$
	Γ_0	100	600	150	250	—	
$K_2(1820)$	m_0	1800	2000	1820	1850	—	$K^*(892)\,\pi\,P$
	Γ_0	100	600	150	250	—	
$K_2(2250)$	m_0	2100	2450	2200	2280	—	$K^*(892)\,\pi\,P$
	Γ_0	50	600	150	250	—	
$K_4^*(2045)$	m_0	2000	2400	2050	2080	—	$K^*(892)\,\pi\,G$
	Γ_0	100	600	150	250	—	

and (6.18), respectively, we chose the parameter limits $-5.0 \leq a_k < 30.0$ and $-500.0 \leq c_k < 500.0$, and the start-parameter ranges $0.1 \leq a_k < 1.0$ and $-3.0 \leq c_k < 3.0$.

There are a few exceptions from these parameter limits and start-parameter ranges that we had to introduce to improve the fit stability and convergence rate:

- The non-resonant components in the 2^+ waves turned out to be small (see section 7.2). In combination with the rather narrow $m_{K\pi\pi}$ fit ranges, in which we considered data from these 2^+ waves, we were not able to reliably determine the shape parameter b_k of the non-resonant components in these waves. In most of the cases, our estimates for the b_k ended up at the lower parameter limit of $-0.1\,(\mathrm{GeV}/c)^{-2}$. Hence, we fixed the b_k parameters of the non-resonant components in the 2^+ waves to $b_k = -0.1\,(\mathrm{GeV}/c)^{-2}$.

- Similarly, the b_k parameter of the non-resonant component in the $2^-\,0^+\,K^*(892)\,\pi\,F$ wave could not be determined from the limited $m_{K\pi\pi}$ fit range of this wave. In order to obtain an estimate for b_k, we performed an RMF with an extended upper $m_{K\pi\pi}$ fit range for this wave. This fit yielded a value of $b_k = 1.616\,(\mathrm{GeV}/c)^{-2}$. Then, we fixed b_k to this value in all others RMFs.[a]

- We fine-tuned some start-parameter ranges and parameter limits based on the results of first RMFs in order to improve the speed of convergence of the fit and thereby reduce the computational costs:
  - We changed the start-parameter ranges of the non-resonant component of the $2^-\,0^+\,K_2^*(1430)\,\pi\,S$ wave to $3.0 \leq a_k < 5.0$ and $2.0 \leq c_k < 3.0$.
  - We changed the start-parameter ranges of the effective background component of the $2^-\,0^+\,K_2^*(1430)\,\pi\,S$ wave to $7.0 \leq a_k < 8.0$ and $3.3 \leq c_k < 3.4$.
  - We changed the start-parameter ranges of the effective background component of the $4^+\,1^+\,K^*(892)\,\pi\,G$ wave to $4.0 \leq a_k < 6.0$ and $1.5 \leq c_k < 1.6$.
  - We changed the parameter limits of the effective background component of the $2^-\,0^+\,K_2^*(1430)\,\pi\,S$ wave to $-0.5 \leq a_k < 30.0$.
  - We changed the parameter limits of the effective background component of the $2^-\,0^+\,f_2(1270)\,\pi\,S$ wave to $-0.1 \leq b_k < 200\,(\mathrm{GeV}/c)^{-2}$.
- The intensity spectrum of the $4^+\,1^+\,K^*(892)\,\pi\,G$ wave exhibits an enhanced low-mass tail below $m_{K\pi\pi} \approx 2\,\mathrm{GeV}/c^2$ as shown in figure 5.20b. As the pre-factor in equation (6.6), which encodes the $m_{K\pi\pi}$ dependence of the production and the phase space, suppresses the transition amplitude at low $m_{K\pi\pi}$, the RMF yielded very large values for a_k in equation (6.8) to compensate for the suppression when trying to reproduce this enhanced low-mass tail. To take this into account we dropped this pre-factor in the model of the effective background in the $4^+\,1^+\,K^*(892)\,\pi\,S$ wave in equation (6.16), i.e. we used the following modified version of equation (6.18):

$$\mathcal{D}_k^{\mathrm{eBKG}}(m_{K\pi\pi}; a_k, c_k) = \frac{\mathcal{D}_k^{\mathrm{NR}}(m_{K\pi\pi}; a_k, c_k)}{\sqrt{\mathfrak{N}_a(m_{K\pi\pi})}\, m_{K\pi\pi}\, \mathcal{P}_{\mathbb{P}}(m_{K\pi\pi}, t')}. \tag{E.1}$$

  As a_k has a different meaning in this parameterization, we applied different parameter limits of $-5.0 \leq a_k < 60.0$.

[a] As the RMF does not describe well the region $m_{K\pi\pi} > 2\,\mathrm{GeV}/c^2$ in the $2^-\,0^+\,K^*(892)\,\pi\,F$ wave, we did not use the extended $m_{K\pi\pi}$ fit range in the main analysis.

E.1.2 Results from the 10-Wave RMF

In this section, we summarize additional results from the 10-wave RMF that are not shown in the main text in section 6.2. The parameter estimates for the shape parameters of the non-resonant and effective background terms are listed in tables E.2 and E.3, respectively. The spin-density matrices of the 10-wave RMF from the four analyzed t' bins are shown in figures E.1 to E.4.

Table E.2: Estimates for the shape parameters of the non-resonant components as obtained from the 10-wave RMF described in section 6.2. The statistical and systematic uncertainties are not given. Values of shape parameters that were fixed in the RMF (see appendix E.1.1) are marked by $^{(*)}$.

Partial wave	Parameter	Value
$2^-0^+\bar{K}_2^*(1430)\pi S$	c	3.00
	a	11.0
$1^+0^+\rho^0(770)KS$	b [(GeV/c)$^{-2}$]	4.03
$1^+1^+\rho^0(770)KS$	b [(GeV/c)$^{-2}$]	3.39
$2^+1^+\bar{K}^*(892)\pi D$	b [(GeV/c)$^{-2}$]	$^{(*)}-0.1$
$2^+1^+\rho^0(770)KD$	b [(GeV/c)$^{-2}$]	$^{(*)}-0.1$
$2^-0^+\bar{K}^*(892)\pi S$	b [(GeV/c)$^{-2}$]	$^{(*)}$ 1.616
$2^-0^+\rho^0(770)KF$	b [(GeV/c)$^{-2}$]	8.6
$2^-0^+f_2(1270)KS$	b [(GeV/c)$^{-2}$]	7.4
$4^+1^+\bar{K}^*(892)\pi G$	b [(GeV/c)$^{-2}$]	19
$4^+1^+\rho^0(770)KG$	b [(GeV/c)$^{-2}$]	3.1

Table E.3: Estimates for the shape parameters of the effective background components as obtained from the 10-wave RMF described in section 6.2. The statistical and systematic uncertainties are not given.

Partial wave	Parameter	Value
$2^-0^+\bar{K}_2^*(1430)\pi S$	c	3.88
	a	12.91
$4^+1^+\bar{K}^*(892)\pi G$	c	2.05
	a	7
$1^+0^+\rho^0(770)KS$	b [(GeV/c)$^{-2}$]	5.7
$1^+1^+\rho^0(770)KS$	b [(GeV/c)$^{-2}$]	13.01
$2^-0^+\bar{K}^*(892)\pi F$	b [(GeV/c)$^{-2}$]	7
$2^-0^+f_2(1270)KS$	b [(GeV/c)$^{-2}$]	0.1
$2^-0^+\rho^0(770)KF$	b [(GeV/c)$^{-2}$]	3.5
$2^+1^+\bar{K}^*(892)\pi D$	b [(GeV/c)$^{-2}$]	8.4
$2^+1^+\rho^0(770)KD$	b [(GeV/c)$^{-2}$]	10.7
$4^+1^+\rho^0(770)KG$	b [(GeV/c)$^{-2}$]	0.1

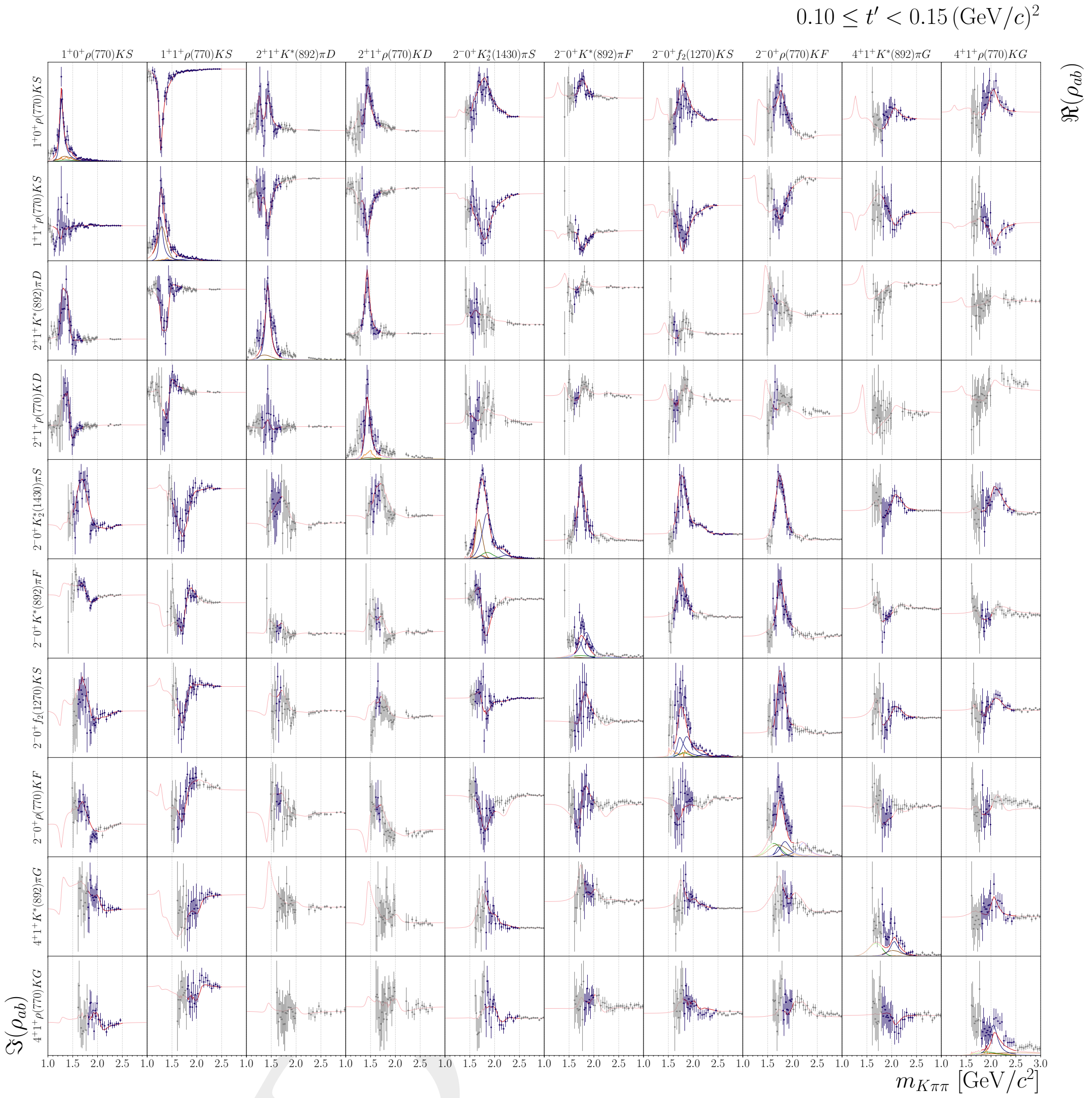

Figure E.1: Same figure as figure 6.2: Real and imaginary parts of the spin-density matrix elements, i.e. $\Lambda_{ab}(m_{K\pi\pi}, t')$ in equation (6.19), as a function of $m_{K\pi\pi}$ in the lowest of the four t' bins for the 10 partial waves that were included in the 10-wave RMF. The figures on the diagonal show the intensity spectra. The upper-right and lower-left off-diagonal figures show the real and imaginary parts of the off-diagonal elements of the spin-density matrix, respectively. The blue data points represent the measured spin-density matrix elements. The curves represent the result of the 10-wave RMF to these data points. The red curves represent the total RMF model. The blue curves represent the individual resonance components, the green curves the non-resonant components, the orange curves the $\pi^-\pi^-\pi^+$ background components, and the brown curves the effective background components. The extrapolations beyond the $m_{K\pi\pi}$ fit ranges are shown in lighter colors. The corresponding data points are shown in gray. The ranges of the vertical axes are different for each subplot. They are adjusted to the data shown in each subplot. Hence, we do not show tick marks for the vertical axes.

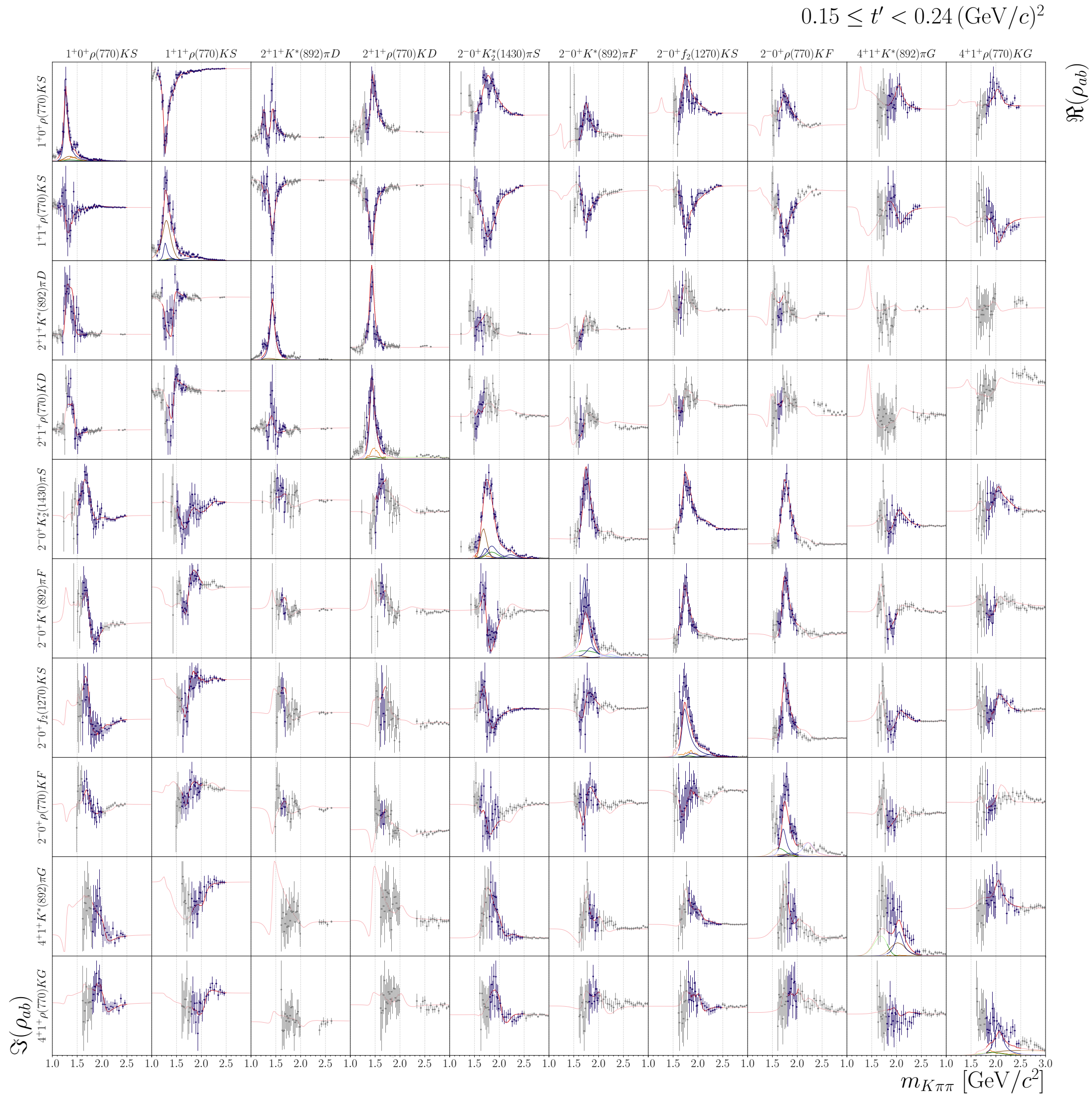

Figure E.2: Same as figure E.1 but for the second t' bin.

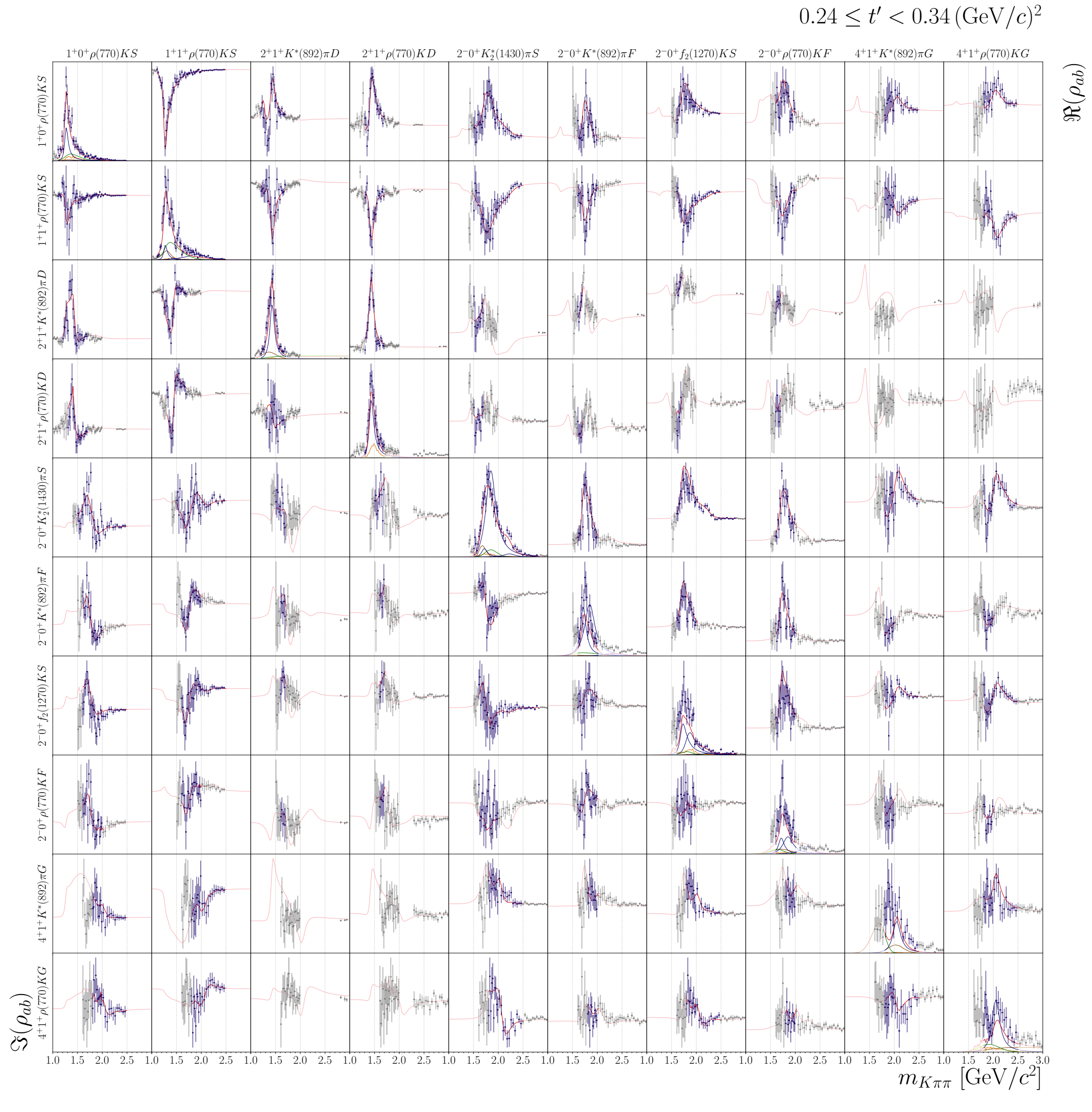

Figure E.3: Same as figure E.1 but for the third t' bin.

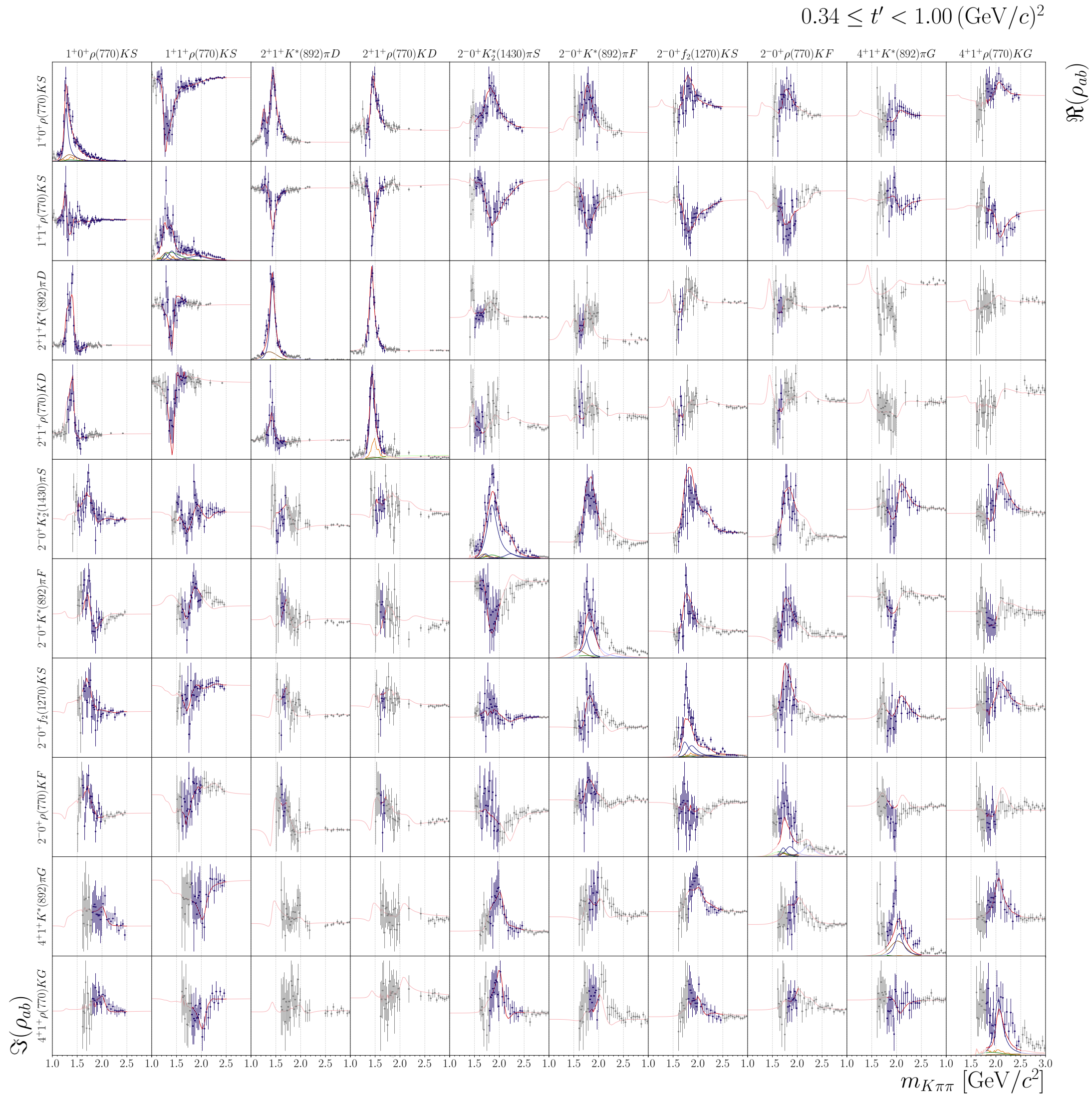

Figure E.4: Same as figure E.1 but for the fourth t' bin.

E.2 Extended Resonance-Model Fits of Waves with $J^P = 0^-$, 3^+, 3^-, and 4^-

In order to also study the resonance content of waves with $J^P = 0^-, 3^+, 3^-$, and 4^-; which were not included in the 10-wave RMF; we performed four extended RMFs, one per J^P sector. In these extended RMFs, we added waves of further interest to the 10-wave RMF model, which is described in section 6.2.1. The modeling of these additional waves and the fitting procedure is the same as used for the 10-wave RMF and described in section 6.1. Table E.4 lists the additional partial waves that were used in the extended RMFs and their model components. Table E.5 lists the additional resonance components in these waves. The results of the extended RMFs for the 0^-, 3^+, 3^-, and 4^- waves are discussed in sections 7.5, 7.6, 7.7, and 7.8, respectively.

Table E.4: List of partial waves and model components included in the extended RMFs in addition to the waves and components of the 10-wave RMF, which are listed in table 6.1. The first column gives the J^P sectors, for which the extended RMF was performed. The second column lists the corresponding wave names. The third column lists the resonance components included in $\mathbb{S}_a$ in equation (6.6). They are specified in table E.5. The forth column lists the parameterization used for the dynamic amplitudes of the non-resonant components (NR). The fifth column lists the model for the $\pi^-\pi^-\pi^+$ background components. The sixth column lists the parameterizations used for the dynamic amplitudes of the effective background components (eBKG) in equation (6.16). The last two columns list the $m_{K\pi\pi}$ range, in which data from this partial wave is considered in the RMF.

RMF	Partial Wave	Resonances	NR	$\pi^-\pi^-\pi^+$	eBKG	$m_{K\pi\pi}$ Range [GeV/c^2]	
0^-	$0^-\,0^+\,\rho(770)\,\pi\,P$	$\{K(1460), K(1630), K(1830)\}$	(6.11)	(6.15)	(6.17)	1.1	2.3
3^+	$3^+\,0^+\,K_3^*(1780)\,\pi\,S$	$\{K_3(2320)\}$	(6.11)	(6.15)	—	2.0	2.3
	$3^+\,1^+\,K_2^*(1430)\,\pi\,P$		(6.11)	(6.15)	(6.17)	2.0	2.5
3^-	$3^-\,1^+\,K^*(892)\,\pi\,F$	$\{K_3^*(1780)\}$	(6.11)	(6.15)	(6.18)	1.6	2.0
	$3^-\,1^+\,\rho(770)\,K\,F$		(6.8)	(6.15)	(6.17)	1.6	2.2
4^-	$4^-\,1^+\,K_2^*(1430)\,\pi\,D$	$\{K_4(2500)\}$	(6.11)	(6.15)	(6.17)	2.1	2.8

Table E.5: Resonance components included in $\mathbb{S}_a$ in equation (6.6) for the extended RMFs (labeled by the first column) in addition to the resonances listed in table E.1. The columns 4 and 5 list the parameter limits and start-parameter ranges (see text in section 6.1.6) for the mass and width parameters, m_0 and Γ_0, respectively. The last column lists the decay mode that we assumed for the dynamic width of the resonance in equation (5.40).

RMF	Resonance	Parameter	Limits $[\mathrm{MeV}/c^2]$		Start Ranges $[\mathrm{MeV}/c^2]$		Decay
0^-	$K(1460)$	m_0	1300	1500	1400	1450	$K^*(892)\,\pi\,P$
		Γ_0	10	500	50	200	
	$K(1630)$	m_0	1500	1700	1600	1650	$K^*(892)\,\pi\,P$
		Γ_0	10	350	150	200	
	$K(1830)$	m_0	1800	1930	1820	1860	$K^*(892)\,\pi\,P$
		Γ_0	10	400	130	200	
3^+	$K_3(2320)$	m_0	2100	2500	2200	2450	$K_2^*(1430)\,\pi\,P$
		Γ_0	100	600	100	300	
3^-	$K_3^*(1780)$	m_0	1600	2000	1750	1820	$K_2^*(1430)\,\pi\,P$
		Γ_0	100	600	100	300	
4^-	$K_4(2500)$	m_0	2100	2650	2200	2450	$K^*(892)\,\pi\,F$
		Γ_0	100	600	100	300	

F The Freed-Isobar Analysis

F.1 Method

In this section, we summarize the most important formulas for the freed-isobar PWD (see appendix F.1.1) and for the corresponding RMF (see appendix F.1.2). More detailed explanations of the freed-isobar analysis can be found in refs. [39, 42, 125].

F.1.1 Freed-Isobar Partial-Wave Decomposition

As already discussed in chapter 8, the goal of the freed-isobar PWD is to determine the dynamic amplitudes of selected isobars from data by parameterizing them using piecewise constant functions, i.e.

$$\mathcal{D}_\xi^{\text{free}}(m_{h^-h^+}) = \sum_i \mathfrak{D}_\xi^{\text{free}}(m^i_{h^-h^+})\,\Theta(m_{h^-h^+}; m^i_{h^-h^+}). \tag{F.1}$$

Here, $m_{h^-h^+}$ is the invariant mass of the isobar system, i.e. $m_{K^-\pi^+}$ or $m_{\pi^-\pi^+}$, the window functions $\Theta(m_{h^-h^+}; m^i_{h^-h^+})$ are one within the bin i around $m^i_{h^-h^+}$ and zero everywhere else, and $\mathfrak{D}_\xi^{\text{free}}(m^i_{h^-h^+})$ are the values of the dynamic amplitude $\mathcal{D}_\xi^{\text{free}}(m_{h^-h^+})$ within the bin i around $m^i_{h^-h^+}$, which are free parameters.

Using equation (F.1) as parameterization for the dynamic amplitudes of the isobar yields for decay amplitudes defined in equation (5.9)

$$\begin{aligned}\tilde{\Psi}_a(\tau, m_{K\pi\pi}) = \sum_{\lambda_\xi} \alpha_{X\to\xi bL}\sqrt{\frac{2L+1}{4\pi}}\left[{}^{\varepsilon}D^J_{M\lambda_\xi}(\phi_{\text{GJ}}, \theta_{\text{GJ}}, 0)\right]^* F_L(m_{K\pi\pi})\left(L, 0; J_\xi, \lambda_\xi \middle| J, \lambda_\xi\right)\\ \times \sum_i \mathfrak{D}_\xi^{\text{free}}(m^i_{h^-h^+})\,\Theta(m_{h^-h^+}; m^i_{h^-h^+})\\ \times\ \alpha_\xi\sqrt{\frac{2J_\xi+1}{4\pi}}\left[D^{J_\xi}_{\lambda_\xi 0}(\phi_{\text{HF}}, \theta_{\text{HF}}, 0)\right]^* F_{J_\xi}(m_{h^-h^+}).\end{aligned} \tag{F.2}$$

One should note that $m_{h^-h^+}$ is included in τ. Exchanging the sums $\sum_{\lambda_\xi}$ and $\sum_i$, F.2 can be interpreted as a sum,

$$\tilde{\Psi}_a(\tau, m_{K\pi\pi}) = \sum_i \tilde{\Psi}_{a,i}(\tau, m_{K\pi\pi}), \tag{F.3}$$

over individual decay amplitudes for each $m_{h^-h^+}$ bin

$$\begin{aligned}\tilde{\Psi}_a(\tau, m_{K\pi\pi}; m^i_{h^-h^+}) \equiv \tilde{\Psi}_{a,i}(\tau, m_{K\pi\pi})& \\ \equiv \sum_{\lambda_\xi} \alpha_{X\to\xi bL} \sqrt{\frac{2L+1}{4\pi}} \left[{}^{\varepsilon}D^{J}_{M\lambda_\xi}(\phi_{\mathrm{GJ}}, \theta_{\mathrm{GJ}}, 0)\right]^* & F_L(m_{K\pi\pi}) \left(L, 0; J_\xi, \lambda_\xi | J, \lambda_\xi\right) \\ \times\ \mathfrak{D}^{\mathrm{free}}_\xi(m^i_{h^-h^+}) \Theta(m_{h^-h^+}; m^i_{h^-h^+})& \\ \times\ \alpha_\xi \sqrt{\frac{2J_\xi+1}{4\pi}} \left[D^{J_\xi}_{\lambda_\xi 0}(\phi_{\mathrm{HF}}, \theta_{\mathrm{HF}}, 0)\right]^* F_{J_\xi}(m_{h^-h^+}).&\end{aligned} \tag{F.4}$$

The $\tilde{\Psi}_a(\tau, m_{K\pi\pi}; m^i_{h^-h^+})$ encode the dependence of the decay amplitude on the angles of the $X^- \to \xi^0 b^-$ and the $\xi^0 \to h^-h^+$ decays, where h^-h^+ is either $K^-\pi^+$ or $\pi^-\pi^+$. In addition, $\tilde{\Psi}_a(\tau, m_{K\pi\pi}; m^i_{h^-h^+})$ includes the centrifugal barrier factors $F_L(m_{K\pi\pi})$ and $F_{J_\xi}(m_{h^-h^+})$. The $m_{h^-h^+}$ dependence given by the dynamic amplitude $\mathcal{D}_\xi(m_{h^-h^+})$ of the isobar resonance, which is model dependent, is removed from $\tilde{\Psi}_a(\tau, m_{K\pi\pi}; m^i_{h^-h^+})$.

The same normalization scheme given in equation (5.10) as for the conventional decay amplitudes is applied, which yields the so-called freed decay amplitudes

$$\Psi_a(\tau, m_{K\pi\pi}; m^i_{h^-h^+}) \equiv \frac{\tilde{\Psi}_a(\tau, m_{K\pi\pi}; m^i_{h^-h^+})}{\mathfrak{D}^{\mathrm{free}}_\xi(m^i_{h^-h^+})\, \alpha_{X\to\xi bL}\, \alpha_\xi\, \sqrt{\mathfrak{N}_a(m_{K\pi\pi}; m^i_{h^-h^+})}}. \tag{F.5}$$

Here, also the unknown value of the dynamic amplitude $\mathfrak{D}^{\mathrm{free}}_\xi(m^i_{h^-h^+})$ within the $m_{h^-h^+}$ bin i is removed, in addition to the unknown couplings $\alpha_{X\to\xi bL}$ and α_ξ. The freed wave-normalization integral reads

$$\mathfrak{N}_a(m_{K\pi\pi}; m^i_{h^-h^+}) = \int_{(m_{K\pi\pi}, t')} \mathrm{d}\tilde{m}_{K\pi\pi} \mathrm{d}\tilde{t}' \int \mathrm{d}\Phi_3(\tau) \left| \frac{\tilde{\Psi}_a(\tau, \tilde{m}_{K\pi\pi}; m^i_{h^-h^+})}{\mathfrak{D}^{\mathrm{free}}_\xi(m^i_{h^-h^+})\, \alpha_{X\to\xi bL}\, \alpha_\xi} \right|^2. \tag{F.6}$$

One should note that due to the window function in $\tilde{\Psi}_a(\tau, m_{K\pi\pi}; m^i_{h^-h^+})$, the integral $\int \mathrm{d}\Phi_3(\tau)$, which also includes integration over $m_{h^-h^+}$ as $m_{h^-h^+}$ is included in τ, does not run over the full $K^-\pi^-\pi^+$ phase space, but only over the range of the $m_{h^-h^+}$ bin i.

Analogously to the definition of the transition amplitudes in the conventional PWD, we combine all terms that appear in the model intensity [cf. equation (5.14)], except for the known freed decay amplitudes, to the so-called freed-isobar amplitudes

$$\begin{aligned}\mathfrak{T}^z_a(m_{K\pi\pi}, t'; m^i_{h^-h^+}) &\equiv \mathcal{T}^z_{a,i}(m_{K\pi\pi}, t') \\ &\equiv \overbrace{\sqrt{\frac{\mathscr{L}}{(2\pi\mathfrak{F})^2}}\,\sqrt{m_{K\pi\pi}}\left\{\sum_{k\in\mathbb{S}_a}\mathcal{P}^z_{k,a}(m_{K\pi\pi}, t')\,\mathcal{D}_k(m_{K\pi\pi})\alpha_{k\to\xi bL}\right\}\alpha_\xi}^{=\,\mathcal{T}^z_a(m_{K\pi\pi},t')/\sqrt{\mathfrak{N}_a(m_{K\pi\pi})}} \\ &\quad\times\sqrt{\mathfrak{N}_a(m_{K\pi\pi}; m^i_{h^-h^+})} \\ &\quad\times\,\mathfrak{D}^{\text{free}}_\xi(m^i_{h^-h^+}).\end{aligned} \tag{F.7}$$

One should note that in contrast to the transition amplitude $\mathcal{T}^z_a(m_{K\pi\pi}, t')$ defined in equation (5.15), $\mathfrak{T}^z_a(m_{K\pi\pi}, t'; m^i_{h^-h^+})$ also includes the dynamic amplitude $\mathfrak{D}^{\text{free}}_\xi(m^i_{h^-h^+})$ of the isobar resonance and hence also depends on $m_{h^-h^+}$. This means that at fixed $(m_{K\pi\pi}, t')$, $\mathfrak{T}^z_a(m_{K\pi\pi}, t'; m^i_{h^-h^+})$ mainly[a]encodes the $m_{h^-h^+}$ dependence of the dynamic amplitude of the isobar resonance times an $(m_{K\pi\pi}, t')$ dependent scale and phase.

In order to determine the freed-isobar amplitudes $\{\mathfrak{T}^z_a(m_{K\pi\pi}, t'; m^i_{h^-h^+})\}$ from data, they are parameterized by complex-valued piecewise functions, which are constant within each $(m_{K\pi\pi}, t', m_{h^-h^+})$ cell. We used the same binning in $m_{K\pi\pi}$ and t' as used in the conventional PWD (see chapter 5). The bin widths in $m_{h^-h^+}$ are given by the window functions $\Theta(m_{h^-h^+}; m^i_{h^-h^+})$ and listed in appendix F.2.

In the conventional PWD, formulating $\mathcal{T}^z_a(m_{K\pi\pi}, t')$ as piecewise constant functions in $(m_{K\pi\pi}, t')$ allowed us to analyze our data independently in $(m_{K\pi\pi}, t')$ cells, because amplitudes from different $(m_{K\pi\pi}, t')$ cells do not interfere. Here, the amplitudes of partial waves with isobars in different subsystems interfere at fixed $m_{h^-h^+}$. For example, amplitudes of partial waves with $K^-\pi^+$ isobar interfere at fixed $m_{K^-\pi^+}$ with the amplitudes of partial waves with $\pi^-\pi^+$ isobar at all $m_{\pi^-\pi^+}$, because fixing $m_{K^-\pi^+}$ does not fix $m_{\pi^-\pi^+}$. Hence, the freed PWD cannot be performed independently in $m_{h^-h^+}$ bins, but the full $m_{h^-h^+}$ range of a given $(m_{K\pi\pi}, t')$ cell has to be fit simultaneously in one PWD fit.

The sum over the $m_{h^-h^+}$ bins i and the sum over the partial waves a in the model intensity can be merged to one sum that runs over (a, i), such that the model intensity of the freed isobar PWD reads[b]

$$\mathcal{I}^{\text{free}}(\tau, m_{K\pi\pi}, t') = \sum_z\left|\sum_{a,i}\mathcal{T}^z_{a,i}(m_{K\pi\pi}, t')\,\Psi_{a,i}(\tau, m_{K\pi\pi})\right|^2. \tag{F.8}$$

[a] The wave-normalization integral $\mathfrak{N}_a(m_{K\pi\pi}; m^i_{h^-h^+})$ introduces only a smooth $m_{h^-h^+}$ dependence in the freed-isobar amplitudes, e.g. the centrifugal-barrier factor $F_{J_\xi}(m^i_{h^-h^+})$ is included in $\mathfrak{N}_a(m_{K\pi\pi}; m^i_{h^-h^+})$, because $F_{J_\xi}(m^i_{h^-h^+})$ is appearing in the corresponding freed decay amplitude.

[b] As discussed below, we freed only a single wave per freed-isobar PWD fit. Hence there is only one wave a where we additionally sum over i.

$\mathcal{I}^{\text{free}}(\tau, m_{K\pi\pi}, t')$ has the same structure as $\mathcal{I}(\tau, m_{K\pi\pi}, t')$ in the conventional PWD [see equation (5.16)]. Therefore, the same likelihood formalism is used for the freed-isobar PWD as used for the conventional PWD and described section 5.1. However, because there is one freed-isobar amplitude per $m_{h^-h^+}$ bin of each freed partial wave, the number of free parameters is drastically increased in the freed-isobar PWD.

Given the limited size of our $K^-\pi^-\pi^+$ sample, compared to e.g. the COMPASS $\pi^-\pi^-\pi^+$ sample, we could not free the dynamic amplitudes of isobars in multiple partial waves in a single fit. Still, in order to perform proof-of-principle tests of the freed-isobar approach, we performed four independent freed-isobar PWDs, in which we studied the $[\pi\pi]_P$ (see section 8.1), $[K\pi]_P$ (see section 8.2), $[K\pi]_D$ (see section 8.3), and $[K\pi]_S$ (see section 8.4) amplitudes.

In order to keep the number of free parameters at a manageable size, which still can be determined with our $K^-\pi^-\pi^+$ sample of limited size, we used a spin-density matrix with rank=1 for this proof-of-principle tests of the freed-isobar PWD. Also, we did not perform Bootstrapping of the freed-isobar PWDs to keep the computational costs low, i.e. we used the maximum-likelihood estimates for the freed-isobar amplitudes and the corresponding covariance matrix in the RMFs discussed in appendix F.1.2.

F.1.2 Resonance-Model Fit of Freed-Isobar Amplitudes

In order to study the resonances appearing in the isobar subsystems and to measure their masses and widths, we performed RMFs of the extracted freed-isobar amplitudes. To this end, the $m_{h^-h^+}$ dependence of the freed-isobar amplitudes is modeled.

The freed-isobar amplitudes are modeled using only resonance components. Analogously to equation (6.6), the corresponding modeled amplitudes read

$$\hat{\mathfrak{T}}^z_a(m_{K\pi\pi}, t'; m^i_{h^-h^+}) = \sqrt{\mathfrak{N}_a(m_{K\pi\pi}; m^i_{h^-h^+}) m_{K\pi\pi}}\, \mathcal{P}_{\mathbb{P}}(m_{K\pi\pi}, t') \sum_{k\in\mathbb{S}_a} {}^k\mathcal{C}^z_a(m_{K\pi\pi}, t')\, \mathcal{D}_k(m^i_{h^-h^+}; \zeta_k). \tag{F.9}$$

We used relativistic Breit-Wigner amplitudes according to equation (5.39) for the dynamic amplitudes $\mathcal{D}_k(m^i_{h^-h^+}; \zeta_k)$ (see tables F.3 and F.4). Analogously to the t' dependence in the conventional RMF, the $m_{K\pi\pi}$ and t' dependence is not explicitly modeled here, but the coupling amplitudes ${}^k\mathcal{C}^z_a(m_{K\pi\pi}, t')$ are modeled by piecewise constant functions in $m_{K\pi\pi}$ and t', i.e. there is an independent complex-valued parameter for each $(m_{K\pi\pi}, t')$ cell for each coupling amplitude.

In the χ^2 optimization, the modeled amplitude $\hat{\mathfrak{T}}^z_a(m_{K\pi\pi}, t'; m^i_{h^-h^+})$ is directly compared to the measured amplitude $\mathfrak{T}^z_a(m_{K\pi\pi}, t'; m^i_{h^-h^+})$. To this end, the real-valued vector $\vec{\mu}$ of the freed-isobar amplitudes is constructed. Its elements,

$$\mu_i(m_{K\pi\pi}, t') = \begin{cases} \Re\left(\mathfrak{T}^z_a(m_{K\pi\pi}, t'; m^i_{h^-h^+})\right) & \text{, if } i \text{ is even} \\ \Im\left(\mathfrak{T}^z_a(m_{K\pi\pi}, t'; m^i_{h^-h^+})\right) & \text{, if } i \text{ is odd,} \end{cases} \tag{F.10}$$

represent different $m_{h^-h^+}$ bins.[c] Analogously, the corresponding RMF model quantities read

$$\hat{\mu}_i(m_{K\pi\pi}, t') = \begin{cases} \Re\left(\hat{\mathfrak{T}}^z_a(m_{K\pi\pi}, t'; m^i_{h^-h^+})\right) & \text{, if } i \text{ is even} \\ \Im\left(\hat{\mathfrak{T}}^z_a(m_{K\pi\pi}, t'; m^i_{h^-h^+})\right) & \text{, if } i \text{ is odd} \end{cases} . \tag{F.11}$$

We fit the freed-isobar amplitudes from all four t' bins and from a chosen range in $m_{K\pi\pi}$ (see table F.3) simultaneously in one RMF. With the above definitions, the corresponding χ^2 function reads

$$\chi^2_{\text{freed}} = \sum_{t', m_{K\pi\pi}} \sum_{i,j} \varDelta\mu_i(m_{K\pi\pi}, t')\, \text{Prec}\left[\mu_i(m_{K\pi\pi}, t'), \mu_j(m_{K\pi\pi}, t')\right] \varDelta\mu_j(m_{K\pi\pi}, t'). \tag{F.12}$$

Here,

$$\varDelta\mu_i(m_{K\pi\pi}, t') = \mu_i(m_{K\pi\pi}, t') - \hat{\mu}_i(m_{K\pi\pi}, t') \tag{F.13}$$

is the residual between the measured freed-isobar amplitude and the corresponding RMF model quantity, and $\text{Prec}[\mu_i, \mu_j]$ is the precision matrix, i.e. the inverse of the covariance matrix of the freed-isobar amplitudes as obtained from the freed-isobar PWD.[d]

F.2 Bin Widths used in the Freed-Isobar Partial-Wave Decomposition

Table F.1 lists the bin widths in two-body mass $m_{h^-h^+}$ of the piecewise constant freed-isobar amplitudes in the various two-body mass ranges as used in the freed-isobar analysis discussed in chapter 8. The lowest and highest $m_{h^-h^+}$ bins are chosen wider than the bin width given in table F.1, so that the analyzed range corresponds to the full $m_{h^-h^+}$ range. The lower border of the lowest $m_{h^-h^+}$ bin is given by the sum of the masses of the two final-state particles in the isobar

[c] We dropped the partial wave label a and the coherent sector label z for μ_i, because we freed only one partial wave per freed-isobar fit, and because we used a rank=1 model in the freed PWDs.

[d] We used the maximum-likelihood estimates for the freed-isobar amplitudes and the corresponding covariance matrix. As the real and imaginary parts of the freed-isobar amplitudes are the free parameters in the PWD fits, error propagation is not necessary to obtain the corresponding covariance matrix, in contrast to the covariance matrix of the spin-density matrix elements. Hence, Bootstrapping is not essential for the freed-isobar PWDs.

system, i.e. $m^{\text{min}}_{K^-\pi^+/\pi^-\pi^+} = m_{K^-/\pi^-} + m_{\pi^+}$, rounded down to a precision of three decimal digits. The upper border of the highest $m_{h^-h^+}$ bin is given by the upper border of the analyzed $m_{K\pi\pi}$ range minus the mass of the bachelor particle, i.e. $m^{\text{max}}_{K^-\pi^+/\pi^-\pi^+} = 3\,\text{GeV}/c^2 - m_{\pi^-/K^-}$, rounded up to a precision of three decimal digits. This rounding ensures that the bins cover the full analyzed two-body mass range including numerical effects. For example, the first bin for the $[\pi\pi]_P$ isobar amplitude (see table F.2a) ranges from 0.279 to 0.320 GeV/c^2 and the last bin ranges from 2.440 to 2.506 GeV/c^2.

F.3 Isobar Resonances included in the Resonance-Model Fits

In order to study the resonance content of the measured freed-isobar amplitudes we performed independent RMFs of the $[\pi\pi]_P$, $[K\pi]_P$, and $[K\pi]_D$ isobar amplitudes. Table F.3 lists the resonance components and fit ranges used in these RMFs. The lower limits for the $m_{\pi^-\pi^+}$ and $m_{K^-\pi^+}$ fit ranges are given by the corresponding phase-space border. The upper limits are chosen to include only the $m_{\pi^-\pi^+}$ or $m_{K^-\pi^+}$ range of the corresponding ground state isobar resonance. Table F.4 lists the mass and width parameter limits and start parameter ranges of the resonance components included in these RMFs.

Table F.1: Bin widths of the piecewise constant freed-isobar amplitudes in the various two-body mass ranges for (a) the $[\pi\pi]_P$, (b) the $[K\pi]_P$, (c) the $[K\pi]_D$, and (d) the $[K\pi]_S$ isobar amplitudes as used in the freed-isobar analyses discussed in chapter 8. Note that the lowest and highest $m_{h^-h^+}$ bins are wider than the given bin width (see text).

(a) $[\pi\pi]_P$

$m_{\pi^-\pi^+}$ Range	$m_{\pi^-\pi^+}$ Bin Width
0.279 to 0.640 GeV/c^2	40 MeV/c^2
0.640 to 0.920 GeV/c^2	20 MeV/c^2
0.920 to 2.506 GeV/c^2	40 MeV/c^2

(b) $[K\pi]_P$

$m_{K^-\pi^+}$ Range	$m_{K^-\pi^+}$ Bin Width
0.633 to 0.800 GeV/c^2	20 MeV/c^2
0.800 to 1.000 GeV/c^2	10 MeV/c^2
1.000 to 1.720 GeV/c^2	20 MeV/c^2
1.720 to 2.861 GeV/c^2	40 MeV/c^2

(c) $[K\pi]_D$

$m_{K^-\pi^+}$ Range	$m_{K^-\pi^+}$ Bin Width
0.633 to 1.120 GeV/c^2	40 MeV/c^2
1.120 to 1.720 GeV/c^2	20 MeV/c^2
1.720 to 2.861 GeV/c^2	40 MeV/c^2

(d) $[K\pi]_S$

$m_{K^-\pi^+}$ Range	$m_{K^-\pi^+}$ Bin Width
0.633 to 2.861 GeV/c^2	40 MeV/c^2

Table F.3: Model components and fit ranges of the RMFs to the freed-isobar amplitudes. The first column lists the freed-isobar amplitude. The second column lists the isobar resonance components included in the RMF model. They are specified in table F.4. The next double-column lists the $m_{\pi^-\pi^+}$ or $m_{K^-\pi^+}$ range in which the data from this partial wave are considered in the RMF. The last double-column lists the $m_{K\pi\pi}$ range in which the data from this partial wave is considered in the RMF.

Isobar Amplitude	Resonance	$m_{\pi^-\pi^+/K^-\pi^+}$ Range [GeV/c^2]		$m_{K\pi\pi}$ Range [GeV/c^2]	
$[\pi\pi]_P$	$\rho(770)$	0.279	1.000	1.1	2.5
$[K\pi]_P$	$K^*(892)$	0.633	1.100	1.1	2.5
$[K\pi]_D$	$K_2^*(1430)$	0.633	1.600	1.4	3.0

Table F.4: Resonance components included in the RMFs of the freed-isobar amplitudes (given in the first column). Furthermore, we list the fit-parameter limits and start-parameter ranges (see text) for the mass and width parameters. The last column gives the decay mode that we assumed for the dynamic width of the resonance in equation (5.40), where the first two letter give the daughter particles and last letter gives the angular orbital momentum between the daughter particles.

Isobar Amplitude	Resonance	Parameter	Limits [MeV/c^2]		Start Ranges [MeV/c^2]		Decay
$[\pi\pi]_P$	$\rho(770)$	m_0	600	900	765	780	$\pi\,\pi\,P$
		Γ_0	80	600	140	150	
$[K\pi]_P$	$K^*(892)$	m_0	700	1100	850	950	$K\,\pi\,P$
		Γ_0	10	600	40	60	
$[K\pi]_D$	$K_2^*(1430)$	m_0	1300	1500	1425	1435	$K\,\pi\,D$
		Γ_0	80	600	105	115	

G Systematic Studies

G.1 Partial-Wave Decomposition

G.1.1 The Information-Field-Theory Model

In section 5.7.2, we describe a study in which we selected a wave set for the PWD using a method based on information field theory (IFT) in order to suppress insignificant waves and to impose continuity of the wave set in $m_{K\pi\pi}$. This IFT wave-set selection is an alternative to the regularization methods presented in sections 5.2.2 and 5.2.3. In the IFT wave-set selection, the four t' bins were treated independently, as in the main analysis. IFT is a Bayesian probability theory. Therefore, the quantity we determined in each t' bin is the probability distribution of the transition amplitudes $\{\mathcal{T}_a^z(m_{K\pi\pi})\}$ in all $m_{K\pi\pi}$ bins given the measured $K^-\pi^-\pi^+$ sample $\{\upsilon\}$. Using Bayes formula this posterior probability reads[a]

$$P\left(\{\mathcal{T}_a^z(m_{K\pi\pi})\}\,\middle|\,\{\upsilon\}\right) = \frac{P\left(\{\upsilon\}\,\middle|\,\{\mathcal{T}_a^z(m_{K\pi\pi})\}\right)}{P\left(\{\upsilon\}\right)} P_0\left(\{\mathcal{T}_a^z(m_{K\pi\pi})\}\right). \tag{G.1}$$

Here, $P\left(\{\upsilon\}\right)$ is the evidence. The probability $P\left(\{\upsilon\}\,\middle|\,\{\mathcal{T}_a^z(m_{K\pi\pi})\}\right)$ of the measured $K^-\pi^-\pi^+$ sample given the transition amplitudes incorporates the information from the data. It is given by the product over the likelihoods $\mathcal{L}_{\text{PWD}}\left(\{\mathcal{T}_a^z(m_{K\pi\pi})\}; \{\upsilon\}_{m_{K\pi\pi}}\right)$ defined in equation (5.33) of all $m_{K\pi\pi}$ bins:

$$P\left(\{\upsilon\}\,\middle|\,\{\mathcal{T}_a^z(m_{K\pi\pi})\}\right) = \prod_{m_{K\pi\pi}} \mathcal{L}_{\text{PWD}}\left(\{\mathcal{T}_a^z(m_{K\pi\pi})\}; \{\upsilon\}_{m_{K\pi\pi}}\right). \tag{G.2}$$

We considered only the $K^-\pi^-\pi^+$ sample from the 2008 diffraction data set, because handling of multiple data sets was not easily implementable in the IFT framework and thus not feasible in the IFT systematic study.

The prior probability $P_0\left(\{\mathcal{T}_a^z(m_{K\pi\pi})\}\right)$ encodes the prior knowledge about the transition amplitudes. Here, we implemented our knowledge about the continuity of the transition amplitudes as a function of $m_{K\pi\pi}$ and the condition to suppress insignificant waves. We formulated independent prior terms for the transition amplitudes of each wave a, i.e.

$$P_0\left(\{\mathcal{T}_a^z(m_{K\pi\pi})\}\right) = \prod_a P_a\left(\vec{\mathcal{T}}_a^z\right). \tag{G.3}$$

[a] We drop the t' dependence here for simplicity since we treated the four t' bins independently.

Here, $\vec{\mathcal{T}}_a^z$ is the vector of the 100 transition amplitudes in the 100 $m_{K\pi\pi}$ bins of wave a in the coherent sector z,[b] i.e. the kth component of this vector is[c]

$$\left[\vec{\mathcal{T}}_a^z\right]_k = \mathcal{T}_a^z(m_{K\pi\pi,k}), \tag{G.4}$$

where $m_{K\pi\pi,k}$ is the mass at the position of the kth $m_{K\pi\pi}$ bin. As in the main analysis, we used a rank=1 PWD model for the wave-set selection fits in the IFT study. We drop the sector label z from now on, because each transition amplitude is uniquely labeled by the wave label a.

In the prior, the correlation between transition amplitudes of wave a at different $m_{K\pi\pi}$ locations is represented by the covariance matrix:

$$[C_a]_{kl} = \mathfrak{C}_a\left(m_{K\pi\pi,k}, m_{K\pi\pi,l}\right). \tag{G.5}$$

Here, $\mathfrak{C}_a\left(m_{K\pi\pi,k}, m_{K\pi\pi,l}\right)$ is the two-point correlation function.

In order to formulate the prior probability, we perform the Fourier transformation,

$$\vec{\mathcal{T}}'_a = \mathcal{F}\left\{\vec{\mathcal{T}}_a\right\}, \text{with } \left[\vec{\mathcal{T}}'_a\right]_i = \mathcal{T}'_a(\omega_i), \tag{G.6}$$

of the transition amplitudes from the $m_{K\pi\pi}$ space of mass bins to the corresponding Fourier space $\vec{\omega}$. The corresponding probability $P'_a\left(\vec{\mathcal{T}}'_a\right)$ of the Fourier-transformed transition amplitudes has the covariance matrix C'_a. Assuming statistical homogeneity for the transition amplitudes, i.e.

$$\mathfrak{C}_a\left(m_{K\pi\pi,i}, m_{K\pi\pi,j}\right) = \mathfrak{C}_a\left(m_{K\pi\pi,i} - m_{K\pi\pi,j}\right), \tag{G.7}$$

the covariance matrix in the Fourier space,

$$\mathfrak{C}_a\left(\omega_i, \omega_j\right) = \left[C'_a\right]_{ij} = \delta_{ij}\left(\left[\vec{\sigma}_a\right]_i\right)^2, \tag{G.8}$$

is diagonal [184]. This means that the Fourier-transformed transition amplitudes are independent. Hence, they can be expressed in terms of uncorrelated random variables $\vec{\xi}_a$, which have a standard deviation of one, i.e.

$$\left[\vec{\mathcal{T}}'_a\right]_i = \left[\vec{\sigma}_a\right]_i \left[\vec{\xi}_a\right]_i \tag{G.9}$$

The form of the prior probability in terms of $\vec{\xi}_a$ still has to be chosen. The $\vec{\xi}_a$ represent the Fourier-transformed transition amplitudes. Asymptotically, their probability distribution becomes a Gaussian distribution under certain conditions (see Theorem 4.4.2 in ref. [185]). Thus, we used a Gaussian standard distribution,

$$P_0\left(\vec{\xi}_a\right) = \mathcal{N}\left(\vec{\xi}_a; 0, \mathbb{1}\right), \tag{G.10}$$

[b] In this study, we used an equidistant binning in the full $m_{K\pi\pi}$ range with a bin width of $20\,\mathrm{MeV}/c^2$, because using different $m_{K\pi\pi}$ bin widths as done in the main analysis could not easily be implemented in the IFT framework.

[c] In this section, we use the notation of a vector or matrix in rectangular bracket with the index in the subscript to indicate a single element of the vector or matrix that corresponds to the given index.

as prior probability for $\vec{\xi}_a$.[d] This prior probability has a standard deviation of one, as required by the construction of $\vec{\xi}_a$, and a mean of zero in order to suppress insignificant waves.

However, the standard deviations $\left[\vec{\sigma}_a\right]_i$ that correspond to the frequency ω_i in Fourier space need to be constrained. Since we assume continuity of the transition amplitudes in $m_{K\pi\pi}$, high frequencies, which correspond to fluctuations of the transition amplitudes from bin to bin, are less probable in the prior compared to low frequencies. Thus, $\left[\vec{\sigma}_a\right]_i$ should be smaller for larger ω_i. Based on previous experiences from ref. [127], we used a power-law spectrum in order to suppress high frequencies, which reads

$$\left[\vec{\sigma}_a\right]_i = \alpha_a \cdot |\omega_i|^{-\beta_a} \qquad \text{for } i \neq 0. \tag{G.11}$$

As equation (G.11) diverges for $\omega_0 = 0$, we used a constant γ_a for the zeroth component of the standard deviation, i.e.

$$\left[\vec{\sigma}_a\right]_0 = \alpha_a \cdot \gamma_a. \tag{G.12}$$

Here, α_a, β_a, and γ_a are three additional free hyperparameters per partial wave a, which we introduced in our formulation of the prior probability. In contrast to the Cauchy regularization in equation (5.55) and the continuity term in equation (5.57), which each have only one parameter common to all partial waves; in the IFT study the usage of independent parameters for each wave introduces additional adaptability in the wave-set selection. However, a much larger number of hyperparameters needs to be determined. Instead of choosing the hyperparameters, we inferred them from data using hyperpriors to constrain them. For β_a, we used a Gaussian hyperprior, i.e.

$$P_0\left(\beta_a\right) = \mathcal{N}\left(\beta_a; \mu_\beta, \sigma_\beta\right), \tag{G.13}$$

with $\mu_\beta = 0.9$ and $\sigma_\beta = 0.01$ common to all waves. These parameters where chosen based on recommendations from ref. [127]. The parameters α_a set the scales of the standard deviations of the Fourier-transformed transition amplitudes and thus relate to the scales of the transition amplitudes. As discussed in section 5.2.2, the overall scale of the transition amplitudes spans up to five orders of magnitude. To take this into account, we assumed a log-Gaussian hyperprior for α_a, i.e.

$$P_0\left(\ln \alpha_a\right) = \mathcal{N}\left(\ln \alpha_a; \mu_{\ln\alpha}, \sigma_{\ln\alpha}\right), \tag{G.14}$$

with $\mu_{\ln\alpha} = -1.$ and $\sigma_{\ln\alpha} = 0.1$ common to all waves. We fixed the parameter γ_a to a value of 1.0 for all waves. These parameters where chosen based on recommendations from ref. [127]. Tests using a free γ_a with a log-Gaussian hyperprior did not yield improved fit results, but the fits were much more unstable.

[d] Note that $\vec{\xi}_a$ is actually a vector of complex-valued components. We used independent Gaussian priors for the real part and the imaginary part of these components. This can be done, because in the Fourier space the individual components are independent assuming statistical homogeneity, because the Fourier transformation is a linear operation and hence acts individually on the real part and the imaginary part of the transition amplitudes, and because we do not assume any correlation between the real part and the imaginary part of the transition amplitudes in the prior probability.

In summary, we formulated the prior probability in terms of the Fourier-transformed transition amplitudes as a standard Gaussian distribution in $\vec{\xi}_a$ centered around zero. As the prior is centered around zero, it suppresses insignificant waves. The standard deviation of the Fourier-transformed transition amplitudes and thereby the strength of the suppression of the corresponding waves is individually adjusted for each wave to the data, because we modeled the standard deviations by a power-law spectrum with individual hyperparameters for each wave. Therefore, the bias from regularization and imposing continuity in the prior probability is potentially reduced compared to the Cauchy and continuity terms used in the main analysis.

The final posterior probability of the IFT wave-set selection in a given t' bin reads:

$$P\left(\{\mathcal{T}_a(m_{K\pi\pi})\}, \{\ln\alpha_a\}, \{\beta_a\} \,\middle|\, \{\upsilon\}\right) = \frac{P\left(\{\upsilon\} \,\middle|\, \{\mathcal{T}_a^z(m_{K\pi\pi})\}\right)}{P\left(\{\upsilon\}\right)} \prod_a P_0\left(\vec{\xi}_a\right)\, P_0\left(\ln\alpha_a\right)\, P_0\left(\beta_a\right)\, J_a. \tag{G.15}$$

Using equations (G.6), (G.9), (G.11), and (G.12), the transition amplitudes,[e]

$$\vec{\mathcal{T}}_a = \mathcal{F}^{-1}\left\{\vec{\sigma}_a\left(\ln\alpha_a, \beta_a\right) \cdot \vec{\xi}_a\right\}, \tag{G.16}$$

of the N_{waves} partial waves can be expressed in terms of the free parameters of the IFT model, i.e. the number of waves times the number of $m_{K\pi\pi}$ bins parameters $\left[\vec{\xi}_a\right]_i$, which represent the Fourier coefficients; the N_{waves} parameters $\ln\alpha_a$, which give a scale to the standard deviations of the transition amplitudes in the Fourier space; and the N_{waves} parameters β_a, which represent the slope of the power-law spectrum. The Jacobian term J_a appears in equation (G.15) arises from this variable transformation.

We used the Python software NIFTy [129] to implement the posterior probability in equation (G.15). NIFTy allows us to formulate the posterior probability as a generative model, i.e. to construct the transition amplitudes according to equation (G.16) from the free parameters $\{\vec{\xi}_a\}$, $\{\ln\alpha_a\}$, and $\{\beta_a\}$ in a bottom-up approach. The Jacobian J_a from the variable transformation and the prior probabilities are calculated automatically.

Given the complexity of the model and the computational expensive evaluation of the likelihood function in equation (G.2), a full study of the posterior probability distribution in equation (G.15) was not feasible. Thus, we performed a maximum-a-posteriori fit to determine the IFT estimates for the transition amplitudes, i.e. we optimized the free parameters of the IFT model such that they minimize equation (G.15).[f] In addition, it was sufficient to perform only a maximum-a-posteriori fit, because we used the result of the IFT wave-set selection only to determine whether a wave significantly contributes to the data and should be included in the wave set.

[e] Here, we use the short-hand notation $\left[\vec{\sigma}_a\left(\ln\alpha_a, \beta_a\right) \cdot \vec{\xi}_a\right]_i = \left[\vec{\sigma}_a\left(\ln\alpha_a, \beta_a\right)\right]_i \cdot \left[\vec{\xi}_a\right]_i$ for the vector that is Fourier back-transformed.

[f] As the evidence $P\left(\{\upsilon\}\right)$ does not depend on the fit parameters, it was neglected in the maximum a posteriori fits.

G.1.2 Summary of Systematic Studies of the Partial-Wave Decomposition

In this section, we show a comparison of the results from systematic studies and from the main analysis for all partial waves that are discussed in this work. Figure G.1 shows the t'-summed intensity spectra of the partial waves that are included in the 10-wave RMF discussed in section 6.2. Figure G.2 shows further waves that are not affected by the leakage effect. Figure G.3 shows the t'-summed intensity spectra of partial waves that are affected by the leakage effect.

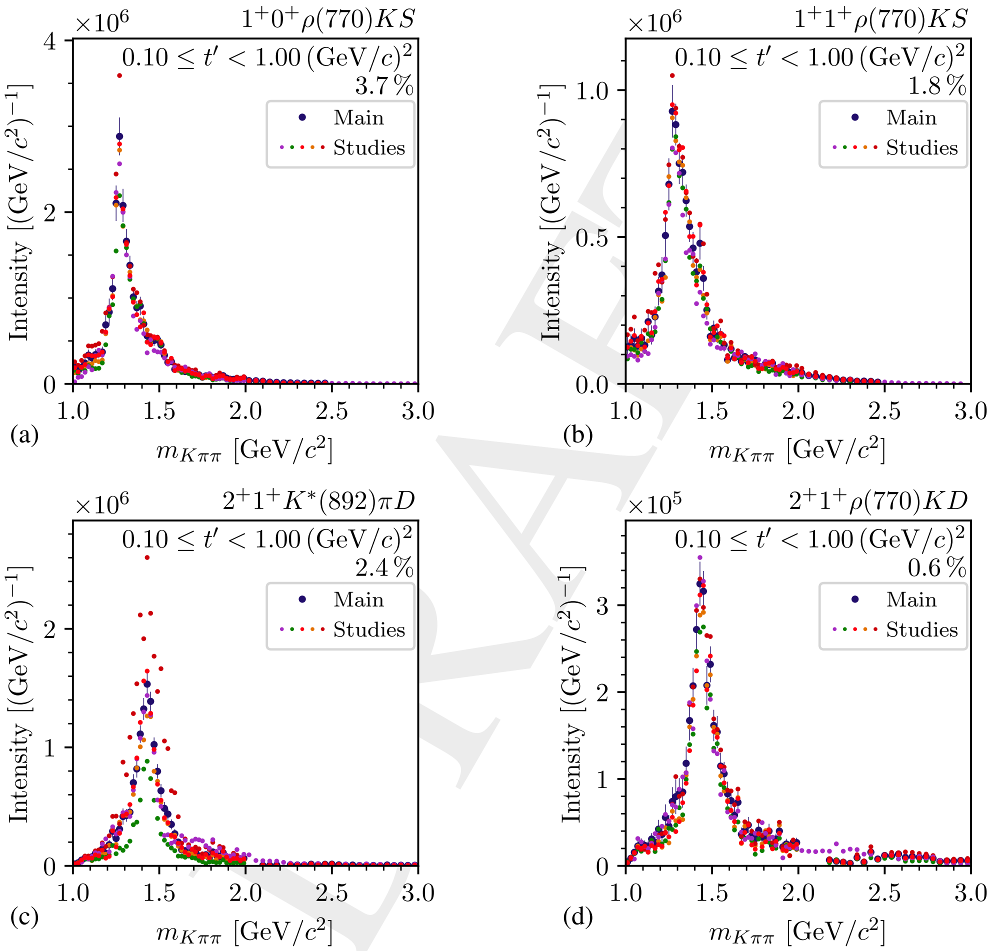

Figure G.1: Comparison of the results from various systematic studies and from the main analysis for partial waves that are included in the 10-wave RMF discussed in section 6.2. The large blue data points show the Bootstrapping estimates from the main analysis. The small differently-colored data points show the maximum-likelihood estimates from the various systematic studies. The violet data points show the study using the wave set constructed from the IFT wave-set selection fits (see section 5.7.2). The light red data points show the study without the $3^+\,1^+\,K^*(892)\,\pi\,D$ wave in the range $m_{K\pi\pi} < 1.7\,\mathrm{GeV}/c^2$ (see section 5.9). The green, red, and orange data points show the studies with a weaker RICH threshold of $\mathcal{T}_\mathrm{R} = 1.05$, with a more restrictive RICH threshold of $\mathcal{T}_\mathrm{R} = 1.30$, and with a more restrictive momentum limit of 40 GeV/c for final-state particle identification; respectively (see section 5.7.1). We do not show uncertainties for the maximum-likelihood estimates from the systematic studies (see section 5.7).

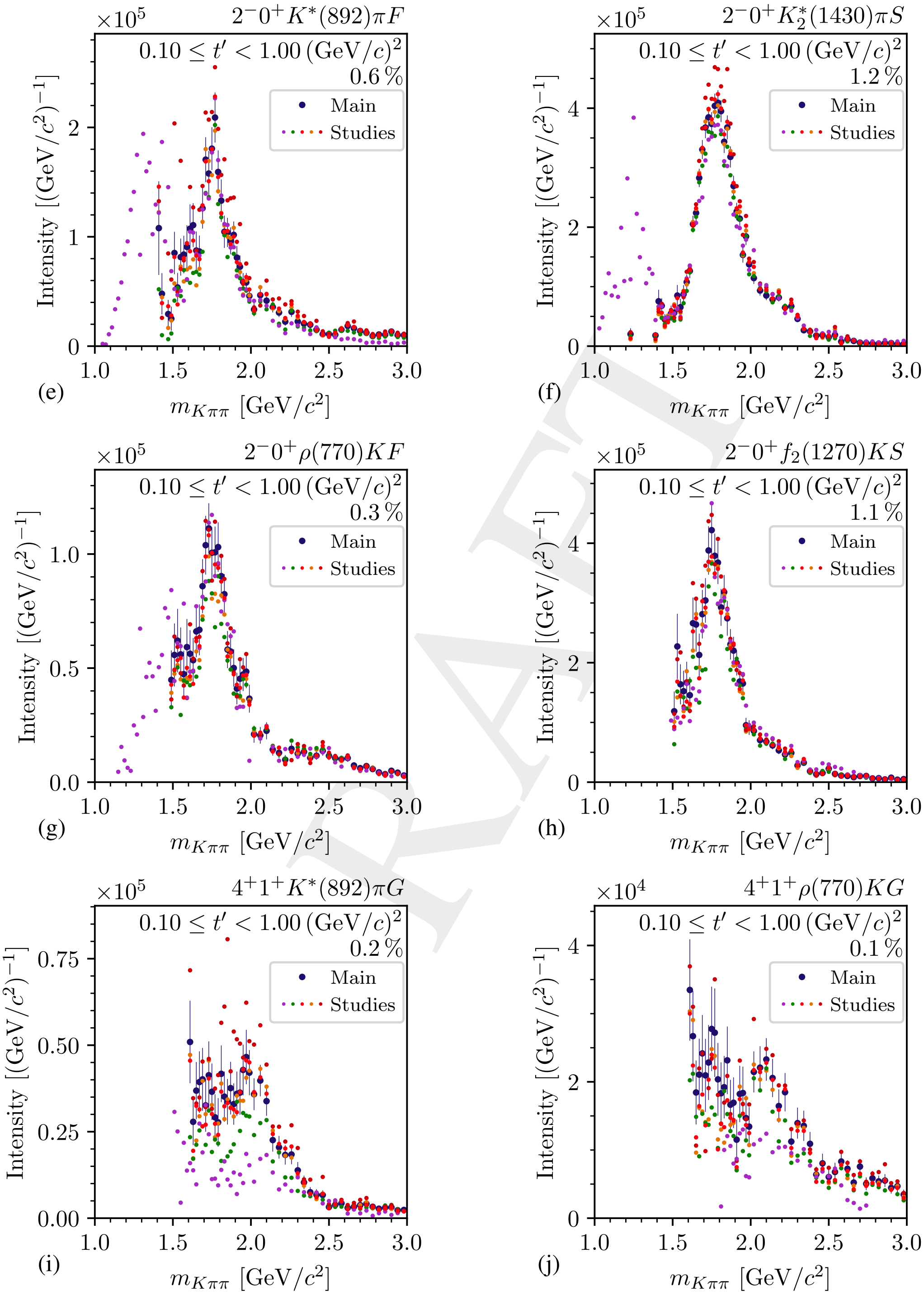

Figure G.1: Continued

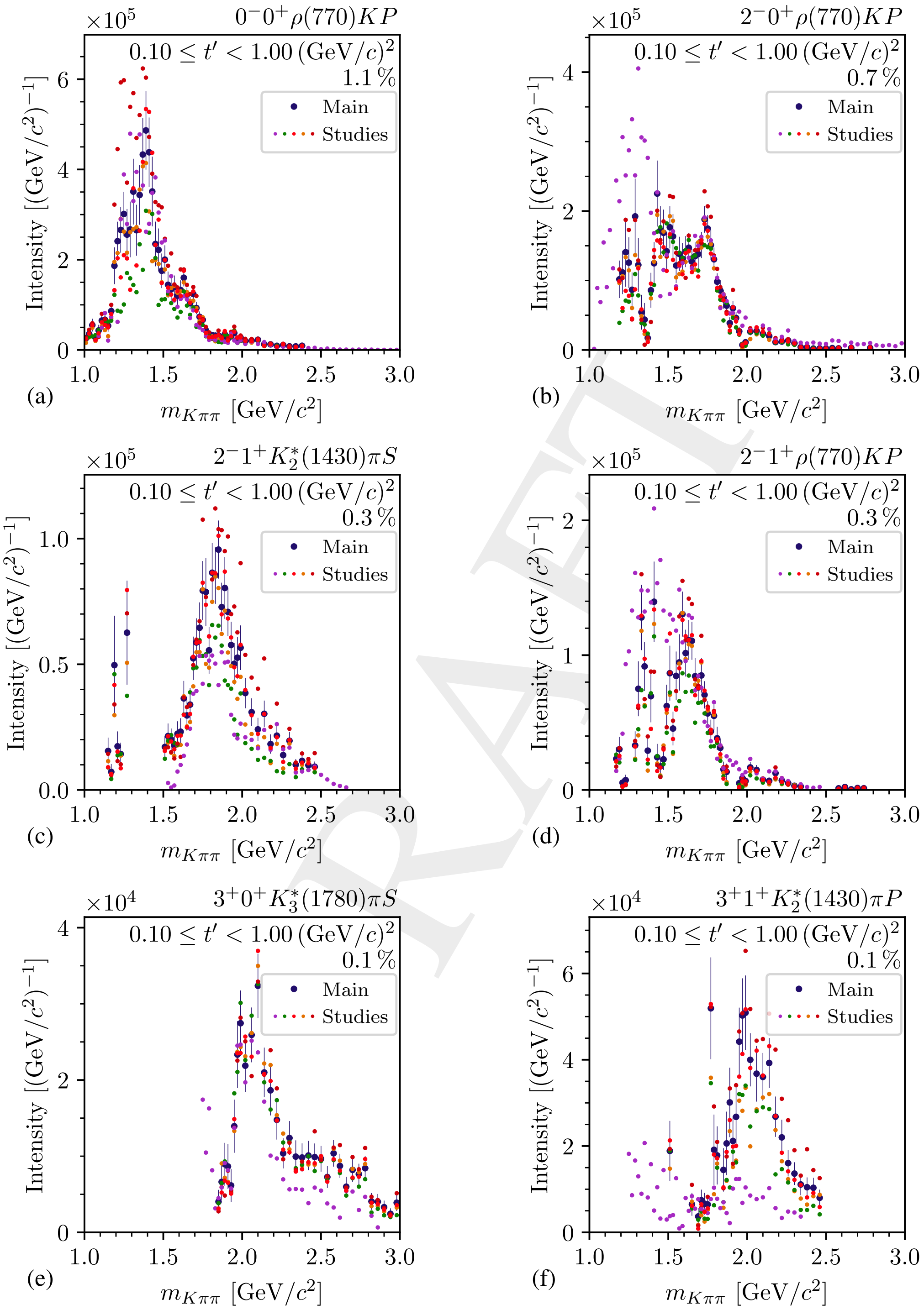

Figure G.2: Same as figure G.1 but for the partial waves that are not included in the 10-wave RMF and not affected by the leakage effect.

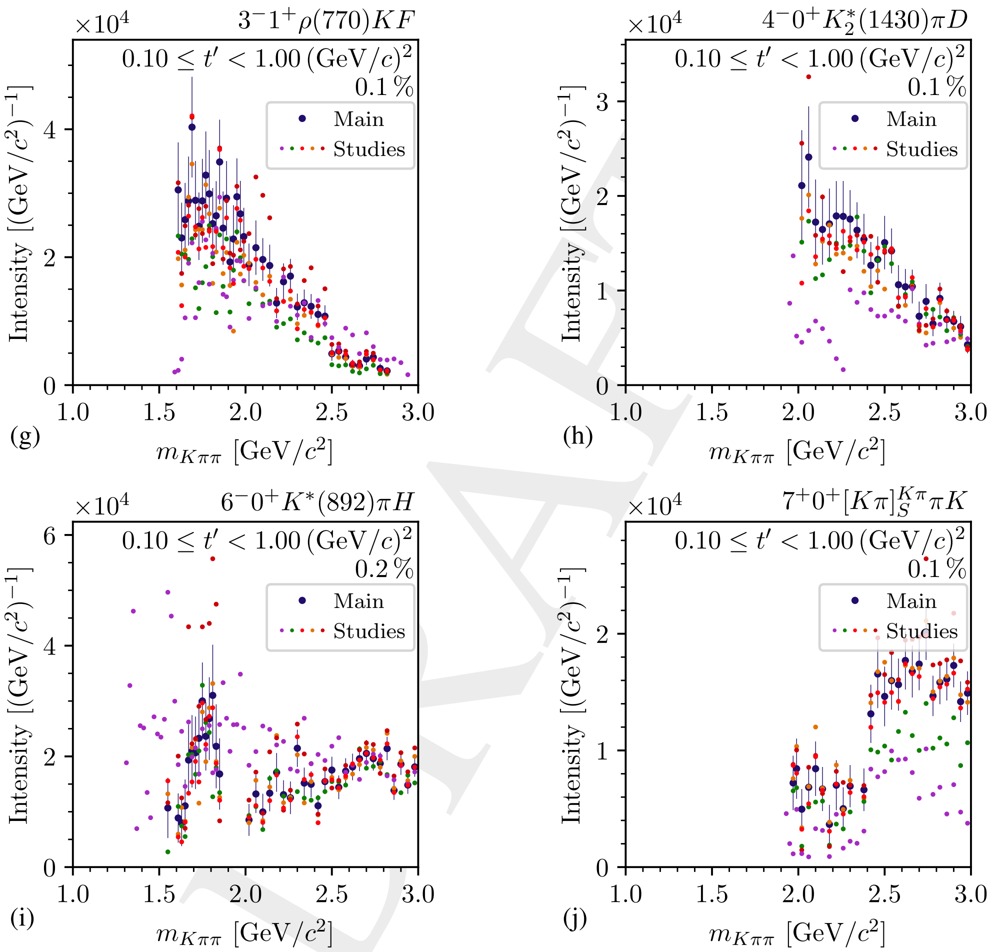

Figure G.2: Continued

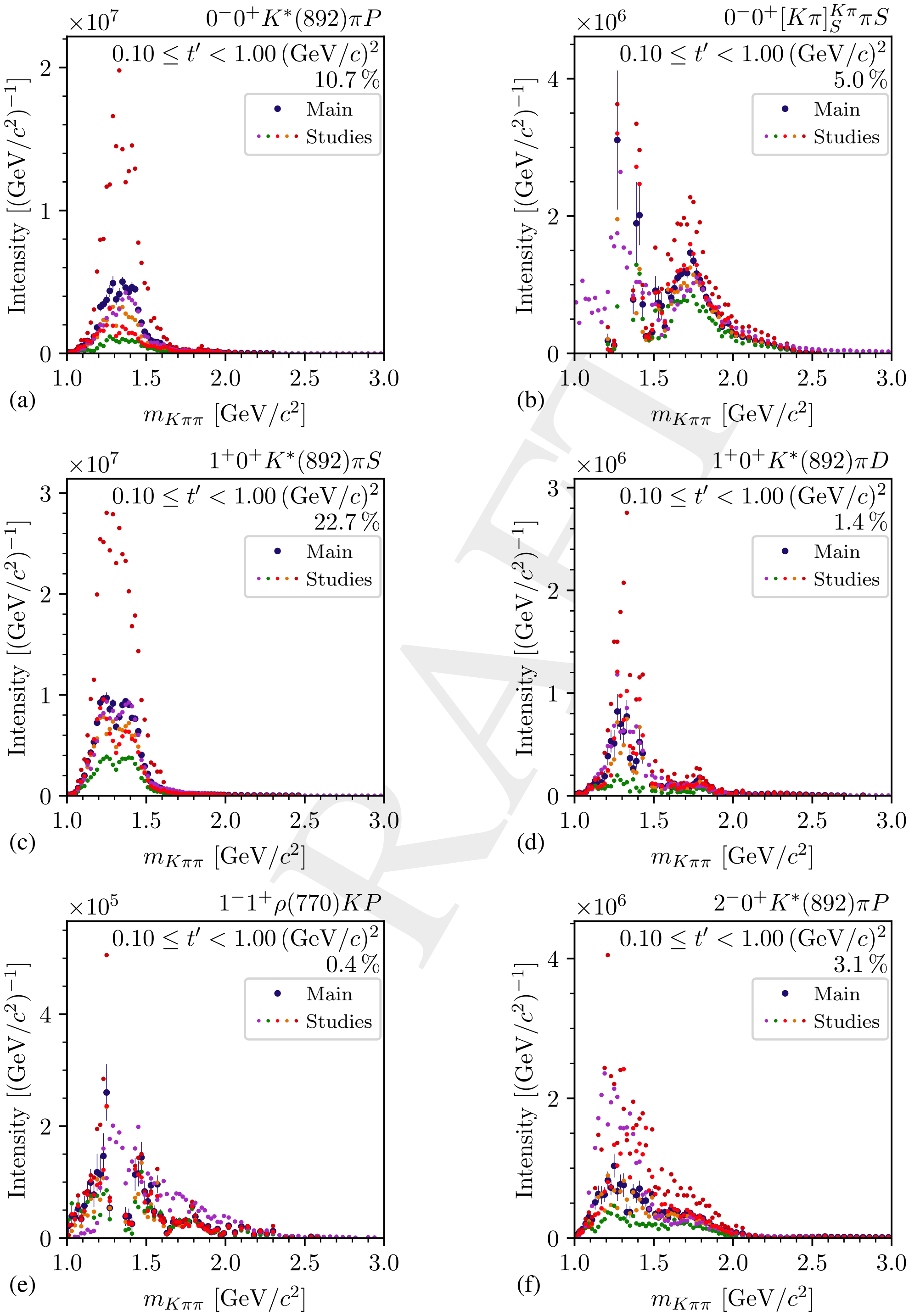

Figure G.3: Same as figure G.1 but for the partial waves that are affected by the leakage effect.

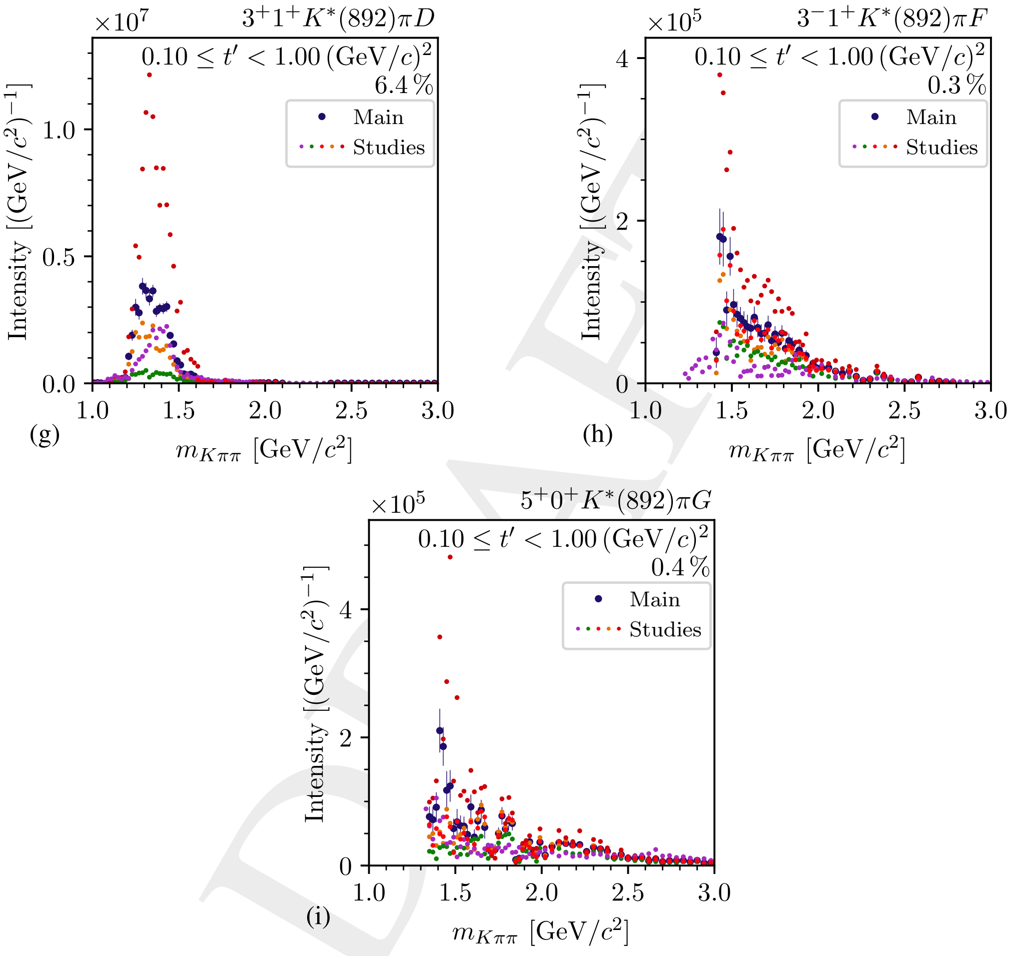

Figure G.3: Continued

H Software Stack

Table H.1: List of the most important software frameworks used in this analysis. The first column gives the name, the second column a short description of the framework. The third column lists the most important sections for which this framework was used. The last column gives the reference to the framework.

Name	Description	See	Ref.
CORAL	COMPASS software for event reconstruction from raw detector data	2.2	[53]
PHAST	Software for event selection used for the preselection	4.1	[186]
Antok	Software for event selection and to create plots of kinematic distributions used for the final $K^-\pi^-\pi^+$ event selection	4.1	[187]
CEDAR Helper	Library for the CEDAR likelihood approach and the corresponding calibration tools	3.1	[188]
RPD Helper	Library to use the information from the recoil-proton detector	4.1	[189]
COMGEANT	COMPASS detector simulation software based on Geant3	C.2	[190]
ROOTPWA	Toolkit for partial-wave analysis of multi-particle final states used for all PWDs, which uses the NLopt package [85] to perform the negative log-likelihood minimization	5, 8	[191]
ROOTPWAtools	Collection of additional tools for PWDs using ROOTPWA	5, 8	[192]
sfitter	Toolkit for resonance-model fits used for all RMFs, which uses `iminuit` [143] to perform the χ^2 minimization	6, 8	[193]
batchelor	Toolkit for job submission on computing clusters	4.1, 5, 6, 8	[194]
modernplotting	Software to create plots for high-energy physics; based on matplotlib [195]	all	[196]
RPWAplotting	Software to create plots of partial-wave analysis results; based on modernplotting	5, 6, 8	[197]

Glossary

Numbers | A | B | C | D | E | F | G | H | I | K | L | M | N | O | P | R | S | T | W

Numbers

10-wave pseudodata sample 176
10-wave pseudodata sample with admixed $\pi^-\pi^-\pi^+$ background 177
10-wave RMF 158
10-wave RMF model 158
238-wave pseudodata model 120
238-wave PWD 96
238-wave set 84

A

acceptance 37
acceptance models 63
acceptance-integral matrix 63

B

bachelor particle 52
$\pi^-\pi^-\pi^+$ background 141
Bootstrapping mean value 90
Bootstrapping samples 90
branching amplitude 154

C

Cauchy regularization 76
centrifugal-barrier factor 57
coherent sectors 59
COMPASS $\pi^-\pi^-\pi^+$ analysis 5
conventional PWD 231
coupling amplitudes 151
cuts 37

D

data-set fraction 62
decay amplitudes 58

Deck-like 8
destructive interference 73
detuned acceptance model 124
diffraction data-taking campaigns 9
DT0 trigger 39
dynamic amplitude 57

E

effective background component (eBKG) 150
enhanced low-mass tails 106
extended RMFs 183

F

final-sate particle ID veto 41
flat wave 59
Flatté parameterization 69
freed decay amplitudes 348
freed-isobar amplitudes 349
freed-isobar PWD fits 231

G

Gottfried-Jackson (GJ) frame 52

H

helicity frame (HF) 53
hit probability 18

I

information field theory 117
intensity of a partial wave 62
intensity spectra 99
interaction vertex 38
isobar 52
isobar model 52

K

$K^-K^-K^+$ **background** 47
$K^-\pi^-\pi^+$ **spin-density matrix** 149

L

leakage artifacts 129
leakage waves 129

low-mass structures 101

M

majority method 14
maximum-likelihood estimates 88
measured data 275
measured distributions 275
measured intensities 161
measured spin-density matrix elements 161
measured values 275
model intensity 59

N

naturality 2
neutral clusters 250
non-leakage waves 129
non-resonant component 150
non-resonant processes 8

O

ordered-intensity distribution 287
overfitting 73
overlaps 129

P

parity 2
partial wave 55
partial-wave analysis (PWA) 51
partial-wave decomposition (PWD) 51
phase motion 103
phase of a wave 103
phase-space integral matrix 62
phase-space pseudodata 276
$\pi^-\pi^-\pi^+$ background PWD 144
$\pi^-\pi^-\pi^+$ pseudodata sample 141
produced distributions 275
produced events 54
produced pseudodata 275
produced values 275
production factor 150
production plane 52
pseudodata studies 120
PWD predictions 107

R

rank of the spin-density matrix 61
real-valued spin-density matrix 155
reconstructed distributions 275
reconstructed pseudodata 275
reconstructed values 275
reduced squared four-momentum transfer 8
reflectivity 56
regularization term 76
relative intensity 104
relative phase 103
resonance components 150
resonance-model fit (RMF) 149
RICH threshold 31
runs 11

S

shape parameters 150
spin-density matrix 60
sub-threshold waves 79

T

t' **spectrum** 167
t'**-summed total intensity spectrum** 99
total model intensity 62
total spin J 2
transition amplitudes 60

W

wave pool 74
wave set 73
wave-normalization integral 58
wave-set selection fit 74

List of Figures

List of Tables

Bibliography

[1] W. E. Lamb and R. C. Retherford, “Fine Structure of the Hydrogen Atom by a Microwave Method,” Phys. Rev. **72** (1947) 241, DOI: 10.1103/PhysRev.72.241. (Cited on page 1)

[2] H. A. Bethe, “The Electromagnetic Shift of Energy Levels,” Phys. Rev. **72** (1947) 339, DOI: 10.1103/PhysRev.72.339. (Cited on page 1)

[3] V. C. Rubin, N. Thonnard, and W. K. Ford Jr., “Rotational properties of 21 SC Galaxies with a Large Range of Luminosities and Rradii, from NGC 4605 (R = 4kpc) to UGC 2885 (R = 122 kpc),” Astrophys. J. **238** (1980) 471, DOI: 10.1086/158003. (Cited on page 1)

[4] P. F. de Salas and A. Widmark, “Dark matter local density determination: recent observations and future prospects,” (2020), arXiv: 2012.11477 [astro-ph.GA]. (Cited on page 1)

[5] N. Loizeau and G. R. Farrar, “Galaxy rotation curves disfavor traditional and self-interacting dark matter halos, preferring a disk component or Einasto function,” (2021), arXiv: 2105.00119 [astro-ph.GA]. (Cited on page 1)

[6] M. Gell-Mann, “A Schematic Model of Baryons and Mesons,” Phys. Lett. **8** (1964) 214, DOI: 10.1016/S0031-9163(64)92001-3. (Cited on page 1)

[7] G. Zweig, “An SU_3 model for strong interaction symmetry and its breaking. Version 1,” (1964), URL: https://cds.cern.ch/record/352337. (Cited on page 1)

[8] G. Zweig, “An SU_3 model for strong interaction symmetry and its breaking. Version 2,” (1964), URL: https://cds.cern.ch/record/570209. (Cited on page 1)

[9] P. A. Zyla et al., [PDG], “Review of Particle Physics 2021 update,” Prog. Theor. Exp. Phys. **2020** (2021) 083C01, DOI: 10.1093/ptep/ptaa104. (Cited on pages 2, 4, 5, 16, 43, 45, 46, 48, 89, 104, 167, 169, 171, 178, 188–192, 210, 214, 216, 220, 221, 224, 225, 227, 233, 235, 243, 257, 259, 260, 276, 335)

[10] D. Ebert, R. N. Faustov, and V. O. Galkin, "Mass spectra and Regge trajectories of light mesons in the relativistic quark model," Phys. Rev. D **79** (2009) 114029, DOI: 10.1103/PhysRevD.79.114029. (Cited on pages 3–5, 194, 212, 221, 224, 225, 243–245)

[11] M. G. Alexeev et al., [COMPASS], "The exotic meson $\pi_1(1600)$ with $J^{PC} = 1^{-+}$ and its decay into $\rho(770)\pi$," (2021), arXiv: 2108.01744. (Cited on pages 3, 5, 101, 152, 227, 231, 399)

[12] R. A. Briceño, J. J. Dudek, and R. D. Young, "Scattering processes and resonances from lattice QCD," Rev. Mod. Phys. **90** (2018) 025001, DOI: 10.1103/RevModPhys.90.025001. (Cited on page 3)

[13] A. J. Woss et al., [HadSpec], "Decays of an exotic 1^{-+} hybrid meson resonance in QCD," Phys. Rev. D **103** (2021) 54502, DOI: 10.1103/PhysRevD.103.054502. (Cited on page 3)

[14] D. J. Wilson et al., [HadSpec], "The quark-mass dependence of elastic πK scattering from QCD," Phys. Rev. Lett. **123** (2019) 42002, DOI: 10.1103/PhysRevLett.123.042002. (Cited on page 3)

[15] R. Brett et al., "Determination of s- and p-wave $I = 1/2$ $K\pi$ scattering amplitudes in $N_f = 2 + 1$ lattice QCD," Nucl. Phys. B **932** (2018) 29, DOI: 10.1016/j.nuclphysb.2018.05.008. (Cited on page 3)

[16] J. J. Dudek et al., [HadSpec], "Resonances in Coupled πK-ηK Scattering from Quantum Chromodynamics," Phys. Rev. Lett. **113** (2014) 182001, DOI: 10.1103/PhysRevLett.113.182001. (Cited on page 3)

[17] A. Poluektov, A. Bondar, and B. D. Yabsley, "Evidence for direct CP violation in the decay $B^- \to D^{(*)}K^\pm$, $D \to K^0_s\pi^+\pi^-$ and measurement of the CKM phase ϕ_3," Phys. Rev. D **81** (2010) 112002, DOI: 10.1103/PhysRevD.81.112002. (Cited on page 4)

[18] R. Aaij et al., [LHCb], "Measurement of the CKM angle γ and B^0_s-$\bar{B}^0_s$ mixing frequency with $B^0_s \to D^\mp_s h^\pm\pi^\pm\pi^\mp$ decays," JHEP **03** (2021) 137, DOI: 10.1007/JHEP03(2021)137. (Cited on page 4)

[19] B. Aubert et al., [BABAR], "Improved measurement of the CKM angle γ in $B^\mp \to D^{(*)}K^{(*)\mp}$ decays with a Dalitz plot analysis of D decays to $K^0_S\pi^+\pi^-$ and $K^0_S K^+K^-$," Phys. Rev. D **78** (2008) 034023, DOI: 10.1103/PhysRevD.78.034023. (Cited on page 4)

[20] S. Bifani et al., “Review of Lepton Universality tests in B decays,” J. Phys. G **46** (2019) 23001, DOI: 10.1088/1361-6471/aaf5de. (Cited on page 4)

[21] M. Algueró et al., “A complete description of P- and S-wave contributions to the $B^0 \to K^+\pi^-\ell^+\ell^-$ decay,” (2021), arXiv: 2107.05301 [hep-ph]. (Cited on page 4)

[22] D. Aston et al., [LASS], “The strange meson resonances observed in the reaction $K^-p \to \bar{K}^0\pi^+\pi^-n$ at 11 GeV/c,” Nucl. Phys. B **292** (1987) 693, DOI: 10.1016/0550-3213(87)90665-1. (Cited on pages 4, 216)

[23] C. Daum et al., [ACCMOR], “Diffractive production of strange mesons at 63 GeV,” Nucl. Phys. B **187** (1981) 1, DOI: 10.1016/0550-3213(81)90114-0. (Cited on pages 4, 45, 47, 49, 75, 150, 189–191, 193, 198, 199, 212–214, 220–222, 241, 242)

[24] D. Frame et al., “A spin-parity analysis of the ϕK^+ system produced in the reaction $K^+p \to \phi K^+p, \phi \to K^+K^-$ at 13 GeV/c,” Nucl. Phys. B **276** (1986) 667, DOI: 10.1016/0550-3213(86)90071-4. (Cited on pages 4, 192, 193, 212, 242, 243)

[25] S. Adhikari et al., [GlueX], “The GLUEX beamline and detector,” Nucl. Instrum. Meth. A **987** (2021) 164807, DOI: 10.1016/j.nima.2020.164807. (Cited on pages 4, 247)

[26] R. Aaij et al., [LHCb], “Studies of the resonance structure in $D^0 \to K^\mp\pi^\pm\pi^\pm\pi^\mp$ decays,” Eur. Phys. J. C **78** (2018) 443, DOI: 10.1140/epjc/s10052-018-5758-4. (Cited on pages 4, 189, 220–222, 231, 238, 242)

[27] H. Guler et al., [Belle], “Study of the $K^+\pi^-\pi^-$ final state in $B^+ \to J/\psi K^+\pi^-\pi^+$ and $B^+ \to \psi' K^+\pi^-\pi^+$,” Phys. Rev. D **83** (2011) 032005, DOI: 10.1103/PhysRevD.83.032005. (Cited on pages 4, 189, 190, 242)

[28] M. Ablikim et al., [BESIII], “Partial-wave analysis of $J/\psi \to K^+K^-\pi^0$,” Phys. Rev. D **100** (2019) 032004, DOI: 10.1103/PhysRevD.100.032004. (Cited on pages 4, 106, 201)

[29] D. M. Asner et al., [CLEO], “Resonance structure of $\tau^- \to K^-\pi^+\pi^-\nu_\tau$ decays,” Phys. Rev. D **62** (2000) 072006, DOI: 10.1103/PhysRevD.62.072006. (Cited on pages 4, 189–192)

[30] T. Armstrong et al., “Evidence for resonant structures in the $\Lambda\bar{p}$ system,” Nucl. Phys. B **227** (1983) 365, DOI: 10.1016/0550-3213(83)90564-3. (Cited on pages 4, 214, 224, 242, 243)

[31] W. E. Cleland et al., "A partial-wave analysis of diffractively produced $\Lambda\bar{p}$ and $\bar{\Lambda}p$ states," Nucl. Phys. B **184** (1981) 1, DOI: 10.1016/0550-3213(81)90206-6. (Cited on pages 4, 214, 224, 225, 243)

[32] G. D. Rochester and C. C. Butler, "Evidence for the Existence of New Unstable Elementary Particles," Nature **160** (1947) 855, DOI: 10.1038/160855a0. (Cited on page 4)

[33] G. F. Bertsch et al., [PDG], "Review of Particle Physics," Phys. Lett. B **239** (1990). (Cited on page 4)

[34] R. Aaij et al., [LHCb], "Observation of $J/\psi\,\phi$ Structures Consistent with Exotic States from Amplitude Analysis of $B^+ \to J/\psi\phi K^+$ Decays," Phys. Rev. Lett. **118** (2017) 022003, DOI: 10.1103/PhysRevLett.118.022003. (Cited on pages 4, 192, 193, 211, 212, 221, 243, 247)

[35] D. Aston et al., [LASS], "Evidence for two $J^P = 2^-$ strange meson states in the $K_2(1770)$ region," Phys. Lett. B **308** (1993) 186, DOI: 10.1016/0370-2693(93)90620-W. (Cited on pages 4, 211, 212, 243)

[36] M. Baubillier et al., "Evidence for a $\Lambda\bar{p}$ resonance with spin-parity 2^-," Nucl. Phys. B **183** (1981) 1, DOI: 10.1016/0550-3213(81)90543-5. (Cited on pages 4, 214, 243)

[37] T. Armstrong et al., "A partial-wave analysis of the $K^-\phi$ system produced in the reaction $K^-p \to K^+K^-K^-p$ at 18.5 GeV$/c$," Nucl. Phys. B **221** (1983) 1, DOI: 10.1016/0550-3213(83)90616-8. (Cited on pages 4, 110, 212, 221, 243)

[38] C. Adolph et al., [COMPASS], "Observation of a New Narrow Axial-Vector Meson $a_1(1420)$," Phys. Rev. Lett. **115** (2015) 82001, DOI: 10.1103/PhysRevLett.115.082001. (Cited on pages 5, 141, 399)

[39] C. Adolph et al., [COMPASS], "Resonance production and $\pi\pi$ S-wave in $\pi^- + p \to \pi^-\pi^-\pi^+ + p_{\text{recoil}}$ at 190 GeV$/c$," Phys. Rev. D **95** (2017) 032004, DOI: 10.1103/PhysRevD.95.032004. (Cited on pages 5, 37, 45, 47, 54, 67, 70, 85, 86, 89, 141, 142, 144, 231, 232, 247, 271, 332, 333, 347, 399)

[40] S. Wallner, "Extraction of Resonance Parameters of Light Meson Resonances in the Charged Three-Pion Final State at the COMPASS Experiment (CERN)," Master thesis: TU München, 2015, URL: https://wwwcompass.cern.ch/compass/publications/theses/2015_dpl_wallner.pdf. (Cited on pages 5, 141, 152, 168, 399, 400)

[41] M. Aghasyan et al., [COMPASS], "Light isovector resonances in $\pi^- p \to \pi^-\pi^-\pi^+ p$ at 190 GeV/c," Phys. Rev. D **98** (2018) 092003, DOI: 10.1103/PhysRevD.98.092003. (Cited on pages 5, 112, 141, 150, 152, 153, 160, 190, 210, 227, 247, 337, 399, 400)

[42] F. Krinner et al., "Ambiguities in model-independent partial-wave analysis," Phys. Rev. D **97** (2018) 114008, DOI: 10.1103/PhysRevD.97.114008. (Cited on pages 5, 231, 347)

[43] F. Kaspar, "Study of the $\pi^-\pi^-\pi^+$ Final State at COMPASS," Ph.D. thesis (in preparation): Technical University of Munich. (Cited on pages 5, 28, 38, 74, 76, 78–80, 112, 141, 142, 232, 242, 271, 332, 399)

[44] P. K. Jasinski, "Analysis of Diffractive Dissociation of K^- into $K^-\pi^+\pi^-$ on a Liquid Hydrogen Target at the COMPASS Spectrometer," CERN-THESIS-2012-191, Ph.D. thesis: Johannes Gutenberg Universität Mainz, 2012, URL: https://cds.cern.ch/record/1493570. (Cited on pages 5, 14, 30, 37, 45, 241, 399)

[45] G. F. Chew and S. C. Frautschi, "Principle of Equivalence for All Strongly Interacting Particles Within the S Matrix Framework," Phys. Rev. Lett. **7** (1961) 394, DOI: 10.1103/PhysRevLett.7.394. (Cited on pages 7, 244)

[46] M. L. Perl, "High energy hadron physics," Wiley, 1974, ISBN: 0-471-68049-4. (Cited on pages 7, 45, 68, 167, 244)

[47] R. T. Deck, "Kinematical Interpretation of the First π-ρ Resonance," Phys. Rev. Lett. **13** (1964) 169, DOI: 10.1103/PhysRevLett.13.169. (Cited on page 8)

[48] L. Bibrzycki et al., [JPAC], "$\pi^- p \to \eta^{(\prime)} \pi^- p$ in the double-Regge region," Eur. Phys. J. C **81** (2021) 647, DOI: 10.1140/epjc/s10052-021-09420-1. (Cited on pages 9, 56)

[49] P. Abbon et al., [COMPASS], "The COMPASS setup for physics with hadron beams," Nucl. Instrum. Meth. A **779** (2015) 69, DOI: 10.1016/j.nima.2015.01.035. (Cited on pages 9–11, 13, 14, 16, 30, 42, 277, 278, 281)

[50] C. Adolph et al., [COMPASS], "Measurement of the Charged-Pion Polarizability," Phys. Rev. Lett. **114** (2015) 062002, DOI: 10.1103/PhysRevLett.114.062002. (Cited on page 9)

[51] V. Y. Alexakhin et al., "First measurement of the transverse spin asymmetries of the deuteron in semi-inclusive deep inelastic scattering," Phys. Rev. Lett. **94** (2005) 202002, DOI: 10.1103/PhysRevLett.94.202002. (Cited on page 9)

[52] P. Abbon et al., [COMPASS], "The COMPASS experiment at CERN," Nucl. Instrum. Meth. A **577** (2007) 455, DOI: 10.1016/j.nima.2007.03.026. (Cited on pages 9, 11)

[53] COMPASS Collaboration, "CORAL," 2019, URL: https://gitlab.cern.ch/compass/comgeant (visited on 07/03/2019). (Cited on pages 11, 277, 278, 365)

[54] S. Wallner et al., "CEDAR PID using the Likelihood Approach for the Hadron-Beam," COMPASS note 2017-1, 2017, URL: https://wwwcompass.cern.ch/compass/notes/2017-1/2017-1.pdf. (Cited on pages 13, 20)

[55] C. Bovet et al., "The Cedar Project. Cherenkov Differential Counters with Achromatic Ring Focus," IEEE Trans. Nucl. Sci. **25** (1978), DOI: 10.1109/TNS.1978.4329375. (Cited on page 13)

[56] C. Bovet et al., "The CEDAR counters for particle identification in the SPS secondary beams : a description and an operation manual," CERN Yellow Reports: Monographs (1982), DOI: 10.5170/CERN-1982-013. (Cited on page 13)

[57] F. Haas, "Two-Dimensional Partial-Wave Analysis of Exclusive 190 GeV $\pi^- p$ Scattering into the $\pi^-\pi^-\pi^+$ Final State at COMPASS (CERN)," CERN-THESIS-2013-277, Ph.D. thesis: TU München, 2014, URL: https://cds.cern.ch/record/1662589. (Cited on pages 14, 30, 39)

[58] J. M. Friedrich, "CEDAR performance 2009," COMPASS note 2010-15, 2010, URL: https://wwwcompass.cern.ch/compass/notes/2010-15/2010-15.pdf. (Cited on pages 15, 28, 30)

[59] T. Weisrock and E.-M. Kabuß, "Using Bayesian Methods for Particle Identification in the CEDARs," COMPASS note 2013-8, 2013, URL: https://wwwcompass.cern.ch/compass/notes/2013-8/2013-8.pdf. (Cited on pages 15, 30)

[60] L. Gatigon, "private communication," 2010. (Cited on page 16)

[61] C. Dittrich, "Selektion des Prozesses $\pi^- + p \to \pi^- + K^- + K^+ + p$ aus COMPASS Daten," Bachelor thesis: TU München, 2019, URL: https://wwwcompass.cern.ch/compass/publications/theses/2019_bac_dittrich.pdf. (Cited on pages 28, 400)

[62] P. Haas, "Analysis of the reaction $\pi^- p \to \omega\pi^-\pi^0 p$ at COMPASS," Master thesis: TU München, 2021. (Cited on pages 28, 38, 399)

[63] M. Krämer, J. M. Friedrich, and S. Huber, "Measurement of the Hadron Beam Composition for the 2009 Primakoff Measurement," COMPASS note 2016-6, 2016, URL: https://wwwcompass.cern.ch/compass/notes/2016-6/2016-6.pdf. (Cited on pages 28, 255)

[64] P. Abbon et al., [COMPASS], "Particle identification with COMPASS RICH-1," Nucl. Instrum. Meth. A **631** (2011) 26, DOI: 10.1016/J.NIMA.2010.11.106. (Cited on pages 31, 32, 255, 256)

[65] J. Beckers, "Search for Light-Meson Resonances in Diffractively Produced $K^-K^+\pi^-$, $K^0_S\pi^-$, and $K^0_S K^-$ Final States Measured at COMPASS," Master thesis: TU München, 2021. (Cited on pages 38, 246, 399, 400)

[66] R. R. Ramos, "Selection of diffractively produced $\eta\pi$ and $\eta'\pi$ final states at the COMPASS experiment," Master thesis: Rheinischen Friedrich-Wilhelms-Universität Bonn, 2018, URL: https://wwwcompass.cern.ch/compass/publications/theses/2018_mst_reyes_ramos.pdf. (Cited on pages 38, 399)

[67] K. A. Bicker, "Model Selection for and Partial-Wave Analysis of a Five-Pion Final State at the COMPASS Experiment at CERN," CERN-THESIS-2016-102, Ph.D. thesis: TU München, 2015, URL: https://cds.cern.ch/record/2215512. (Cited on pages 42, 53, 74, 76, 80, 241, 399)

[68] L. A. Harland-Lang et al., "The phenomenology of central exclusive production at hadron colliders," Eur. Phys. J. C **72** (2012) 2110, DOI: 10.1140/epjc/s10052-012-2110-2. (Cited on page 44)

[69] M. R. Atayan et al., [EHS/NA22], "A study of double pomeron exchange in $\pi^+ p$ and $K^+ p$ interactions at 250 GeV/c," Z. Phys. C **50** (1991) 353, DOI: 10.1007/BF01551447. (Cited on pages 44, 153)

[70] J. D. Hansen et al., "Formalism and assumptions involved in partial-wave analysis of three-meson systems," Nucl. Phys. **B81** (1974) 403, DOI: 10.1016/0550-3213(74)90241-7. (Cited on page 52)

[71] D. Herndon, P. Söding, and R. J. Cashmore, "Generalized isobar model formalism," Phys. Rev. D **11** (1975) 3165, DOI: 10.1103/PhysRevD.11.3165. (Cited on page 52)

[72] B. Ketzer, B. Grube, and D. Ryabchikov, "Light-meson spectroscopy with COMPASS," Prog. Part. Nucl. Phys. **113** (2020) 103755, DOI: 10.1016/j.ppnp.2020.103755. (Cited on pages 54, 56, 57, 61, 104, 141, 153, 167)

[73] S. U. Chung and T. L. Trueman, "Positivity conditions on the spin density matrix: A simple parametrization," Phys. Rev. D **11** (1975) 633, DOI: 10.1103/PhysRevD.11.633. (Cited on pages 55, 56, 61, 283)

[74] K. Gottfried and J. D. Jackson, "On the connection between production mechanism and decay of resonances at high energies," Nuovo Cim. **33** (1964) 309, DOI: 10.1007/BF02750195. (Cited on page 56)

[75] G. Cohen-Tannoudji, P. Salin, and A. Morel, "A simple formulation of high-energy exchange models in terms of direct-channel amplitudes," Nuovo Cim. A **55** (1968) 412, DOI: 10.1007/BF02857563. (Cited on page 56)

[76] V. Mathieu et al., [JPAC], "Moments of angular distribution and beam asymmetries in $\eta\pi^0$ photoproduction at GlueX," Phys. Rev. D **100** (2019) 54017, DOI: 10.1103/PhysRevD.100.054017. (Cited on page 56)

[77] F. Von Hippel and C. Quigg, "Centrifugal-Barrier Effects in Resonance Partial Decay Widths, Shapes, and Production Amplitudes," Phys. Rev. D **5** (1972) 624, DOI: 10.1103/PhysRevD.5.624. (Cited on page 57)

[78] E. P. Wigner, "Gruppentheorie und ihre Anwendung auf die Quantenmechanik der Atomspektren," Braunschweig: Vieweg, 1931, ISBN: 978-3-663-00642-8, URL: https://link.springer.com/book/10.1007%2F978-3-663-02555-9. (Cited on page 57)

[79] E. P. Wigner, "Group theory: and its application to the quantum mechanics of atomic spectra," New York: Academic Press, 1959. (Cited on page 57)

[80] M. G. Alexeev et al., [COMPASS], "Triangle Singularity as the Origin of the $a_1(1420)$," Phys. Rev. Lett. **127** (2021) 82501, DOI: 10.1103/PhysRevLett.127.082501. (Cited on pages 58, 141, 399)

[81] F. Krinner, "private communication," 2021. (Cited on pages 61, 190)

[82] J. Nocedal, "Updating Quasi-Newton Matrices with Limited Storage," Mathematics of Computation **35**.151 (1980) 773, DOI: 10.2307/2006193. (Cited on pages 67, 97)

[83] D. C. Liu and J. Nocedal, "On the limited memory BFGS method for large scale optimization," Mathematical Programming **45**.1-3 (1989) 503, DOI: 10.1007/BF01589116. (Cited on pages 67, 97)

[84] L. Luksan, "Ladislav Luksan — subroutines," URL: https://www.cs.cas.cz/~luksan/subroutines.html (visited on 02/26/2016). (Cited on pages 67, 97)

[85] S. G. Johnson, "The NLopt nonlinear-optimization package," 2017, URL: https://github.com/stevengj/nlopt. (Cited on pages 67, 97, 365)

[86] C. G. Broyden, "The Convergence of a Class of Double-rank Minimization Algorithms 1. General Considerations," J. Inst. Maths Applics **6** (1970) 76, DOI: 10.1093/imamat/6.1.76. (Cited on page 67)

[87] R. Fletcher, "A new approach to variable metric algorithms," The Computer Journal **13** (1970) 317, DOI: 10.1093/comjnl/13.3.317. (Cited on page 67)

[88] D. Goldfarb, "A Family of Variable-Metric Methods Derived by Variational Means," Mathematics of Computation **24**.109 (1970) 23, DOI: 10.2307/2004873. (Cited on page 67)

[89] D. F. Shanno, "Conditioning of Quasi-Newton Methods for Function Minimization," Mathematics of Computation **24**.111 (1970) 647, DOI: 10.2307/2004840. (Cited on page 67)

[90] G. Breit and E. Wigner, "Capture of Slow Neutrons," Phys. Rev. **49** (1936) 519, DOI: 10.1103/PhysRev.49.519. (Cited on page 68)

[91] C. Patrignani et al., [PDG], "Review of Particle Physics," Chin. Phys. C **40** (2016) 100001, DOI: 10.1088/1674-1137/40/10/100001. (Cited on pages 69, 74, 80, 160, 337, 338)

[92] B. Grube et al., "ROOTPWA Particle Data Table," 2019, URL: https://github.com/ROOTPWA-Maintainers/ROOTPWA/blob/master/particleData/particleDataTable2016.txt (visited on 06/21/2019). (Cited on page 69)

[93] S. M. Flatté, "On the nature of 0^+ mesons," Phys. Lett. B **63** (1976) 228, DOI: 10.1016/0370-2693(76)90655-9. (Cited on page 69)

[94] M. Ablikim et al., [BESIII], "Resonances in $J/\psi \to \phi\pi^+\pi^-$ and ϕK^+K^-," Phys. Lett. B **607** (2005) 243, DOI: 10.1016/j.physletb.2004.12.041. (Cited on page 69)

[95] Igor A. Kachaev, "Structure of $\pi\pi$ S-wave in $\pi^+\pi^-\pi^-$ system," *3rd International Conference on Quarks and Nuclear Physics QNP*, Bloomington, IN, U.S.A., 2004. (Cited on page 69)

[96] K. L. Au, D. Morgan, and M. R. Pennington, "Meson dynamics beyond the quark model: Study of final-state interactions," Phys. Rev. D **35** (1987) 1633, DOI: 10.1103/PhysRevD.35.1633. (Cited on page 69)

[97] D. Aston et al., [LASS], "A study of $K^-\pi^+$ scattering in the reaction $K^-p \to K^-\pi^+n$ at 11 GeV/c," Nucl. Phys. B **296** (1988) 493, DOI: 10.1016/0550-3213(88)90028-4. (Cited on pages 69–71, 198, 216)

[98] S. Descotes-Genon and B. Moussallam, "The $K_0^*(800)$ scalar resonance from Roy-Steiner representations of πK scattering," Eur. Phys. J. C **48** (2006) 553, DOI: 10.1140/epjc/s10052-006-0036-2. (Cited on pages 69, 238)

[99] A. J. Bevan et al., "The Physics of the B Factories," Eur. Phys. J. C **74** (2014) 3026, DOI: 10.1140/epjc/s10052-014-3026-9. (Cited on pages 69, 70)

[100] A. Palano and M. R. Pennington, "$K\pi$ $I = 1/2$ S-wave from η_c decay data at BaBar and classic Meson-Meson scattering from LASS," (2017), arXiv: 1701.04881. (Cited on pages 69, 71)

[101] J. R. Peláez and A. Rodas, "Determination of the Lightest Strange Resonance $K_0^*(700)$ or κ, from a Dispersive Data Analysis," Phys. Rev. Lett. **124** (2020) 172001, DOI: 10.1103/PhysRevLett.124.172001. (Cited on pages 69, 238)

[102] W. M. Dunwoodie, "Fits to K pi I=1/2 S-wave Amplitude and Phase Data," 2013, URL: https://www.slac.stanford.edu/~wmd/kpi_swave/kpi_swave_fit.note (visited on 08/08/2017). (Cited on page 70)

[103] R. Aaij et al., [LHCb], "Studies of the resonance structure in $D^0 \to K_S^0 K^\pm\pi^\mp$ decays," Phys. Rev. D **93** (2016) 052018, DOI: 10.1103/PhysRevD.93.052018. (Cited on page 70)

[104] P. Estabrooks et al., "Study of $K\pi$ scattering using the reactions $K^\pm p \to K^\pm\pi^+n$ and $K^\pm p \to K^\pm\pi^-\Delta^{++}$ at 13 GeV/c," Nucl. Phys. B **133** (1978) 490, DOI: 10.1016/0550-3213(78)90238-9. (Cited on page 71)

[105] J. P. Lees et al., “Measurement of the $I = 1/2$ $K\pi$ S-wave amplitude from Dalitz plot analysis of $\eta_c \to K\bar{K}\pi$ in two-photon interaction,” Phys. Rev. D **93** (2016) 012005, DOI: 10.1103/PhysRevD.93.012005. (Cited on page 71)

[106] F. E. Harrell, “Regression Modeling Strategies,” vol. 45, Springer Series in Statistics 2, Springer International Publishing, 2015, DOI: 10.1007/978-3-319-19425-7. (Cited on page 73)

[107] B. Guegan et al., “Model selection for amplitude analysis,” JINST **10** (2015) P09002, DOI: 10.1088/1748-0221/10/09/P09002. (Cited on pages 74, 75)

[108] O. Drotleff, “Model Selection for Partial-Wave Analysis of $\pi^- + p \to \pi^-\pi^+\pi^- + p$ at the COMPASS Experiment at CERN,” Diploma thesis: TU München, 2015, URL: https://wwwcompass.cern.ch/compass/publications/theses/2015_dpl_drotleff.pdf. (Cited on pages 74, 89, 241, 399)

[109] R. Tibshirani, “Regression Shrinkage and Selection Via the Lasso,” J. Royal Stat. Soc. B **58**.1 (1996) 267, DOI: 10.1111/j.2517-6161.1996.tb02080.x. (Cited on page 76)

[110] A. E. Hoerl and R. W. Kennard, “Ridge Regression: Biased Estimation for Nonorthogonal Problems,” Technometrics **12**.1 (1970) 55, DOI: 10.1080/00401706.1970.10488634. (Cited on page 76)

[111] K.-C. Wong, “Evolutionary Multimodal Optimization: A Short Survey,” (2015), arXiv: 1508.00457. (Cited on page 80)

[112] P. Jain and P. Kar, “Non-convex Optimization for Machine Learning,” Foundations and Trends in Machine Learning **10**.3-4 (2017) 142, DOI: 10.1561/2200000058. (Cited on page 80)

[113] M. G. Alekseev et al., [COMPASS], “Observation of a $J^{PC} = 1^{-+}$ Exotic Resonance in Diffractive Dissociation of 190 GeV/c π^- into $\pi^-\pi^-\pi^+$,” Phys. Rev. Lett. **104** (2010) 241803, DOI: 10.1103/PhysRevLett.104.241803. (Cited on page 89)

[114] C. Adolph et al., [COMPASS], “Odd and even partial waves of $\eta\pi^-$ and $\eta'\pi^-$ in $\pi^- p \to \eta^{(\prime)}\pi^- p$ at 191GeV/c,” Phys. Lett. B **740** (2015) 303, DOI: 10.1016/j.physletb.2014.11.058. (Cited on page 89)

[115] B. Efron, “Bootstrap Methods: Another Look at the Jackknife,” Ann. Stat. **7** (1979) 1, DOI: 10.1214/aos/1176344552. (Cited on pages 89, 90)

[116] M. H. Quenouille, "Approximate Tests of Correlation in Time-Series," J. Royal Stat. Soc. B **11** (1949) 68, DOI: 10.1017/s0305004100025123. (Cited on page 90)

[117] J. Shao and D. Tu, "The Jackknife and Bootstrap," vol. 27, Springer Series in Statistics 2, New York: Springer New York, 1995, 83, DOI: 10.1007/978-1-4612-0795-5. (Cited on pages 90, 91)

[118] S. Kullback and R. A. Leibler, "On Information and Sufficiency," Ann. Math. Stat. **22** (1951) 79, DOI: 10.1214/aoms/1177729694. (Cited on page 91)

[119] G. D. Cowan, "Statistical data analysis," Oxford: Clarendon Press, 1998, ISBN: 0-19-850156-0. (Cited on pages 94, 98, 272)

[120] M. Baubillier et al., "Observation of a K^* resonance at 2088 MeV," Phys. Lett. B **118** (1982) 447, DOI: 10.1016/0370-2693(82)90221-0. (Cited on page 106)

[121] W. Cleland et al., "Study of the reactions $K^\pm p \to K^0_S \pi^\pm p$ at 30 and 50 GeV/c: Description of the apparatus and amplitude analysis of the $K^0_S \pi$ system," Nucl. Phys. B **208** (1982) 189, DOI: 10.1016/0550-3213(82)90114-6. (Cited on pages 106, 201, 202)

[122] D. Aston et al., [LASS], "Observation of the leading K^* L-excitation series from $J^P = 1^-$ through 5^- in the reaction $K^- p \to K^- \pi^+ n$ at 11 GeV/c," Phys. Lett. B **180** (1986) 308, DOI: 10.1016/0370-2693(86)90316-3. (Cited on pages 106, 201, 202, 227)

[123] G. Ascoli et al., "Deck-model calculation of $\pi^- p \to \pi^- \pi^+ \pi^- p$," Phys. Rev. D **9** (1974) 1963, DOI: 10.1103/PhysRevD.9.1963. (Cited on page 111)

[124] M. Mikhasenko, "Three-pion dynamics at COMPASS : resonances, rescattering and non-resonant processes," Ph.D. thesis: Rheinische Friedrich-Wilhelms-Universität Bonn, 2019, URL: http://nbn-resolving.de/urn:nbn:de:hbz:5n-56606. (Cited on pages 112, 152, 227)

[125] F. Krinner, "Freed-Isobar Partial-Wave Analysis," CERN-THESIS-2018-492, Ph.D. thesis: TU München, 2018, URL: https://cds.cern.ch/record/2783415. (Cited on pages 112, 231, 232, 347)

[126] T. A. Enßlin, "Information Theory for Fields," Ann. Phys. **531**.3 (2019) 1800127, DOI: 10.1002/andp.201800127. (Cited on page 117)

[127] P. Frank, "private communication," 2019. (Cited on pages 117, 357)

[128] T. A. Enßlin, "private communication," 2019. (Cited on page 117)

[129] P. Arras et al., "NIFTy5: Numerical Information Field Theory v5," Astrophysics Source Code Library (2019), URL: `https://gitlab.mpcdf.mpg.de/ift/nifty`. (Cited on pages 117, 358)

[130] R. A. Horn, "Matrix analysis," ed. by C. R. Johnson, 1st ed., Cambridge: Cambridge Univ. Press, 1985, ISBN: 0521305861. (Cited on page 129)

[131] I. N. Levine, "Quantum chemistry," 5th ed., Upper Saddle River, NJ: Prentice Hall, 2000, ISBN: 0136855121. (Cited on page 129)

[132] D. Ryabchikov, "private communication," 2021. (Cited on page 135)

[133] F. Krinner, [COMPASS], "Freed-isobar analysis of light mesons at COMPASS," *HADRON2019*, Guilin, China, 2020, 465, DOI: `10.1142/9789811219313_0078`. (Cited on page 141)

[134] A. Jackura et al., [JPAC], "New analysis of $\eta\pi$ tensor resonances measured at the COMPASS experiment," Phys. Lett. **779** (2018) 464, DOI: `10.1016/j.physletb.2018.01.017`. (Cited on pages 150, 246)

[135] A. Rodas et al., [JPAC], "Determination of the Pole Position of the Lightest Hybrid Meson Candidate," Phys. Rev. Lett. **122** (2019) 042002, DOI: `10.1103/PhysRevLett.122.042002`. (Cited on page 150)

[136] N. A. Törnqvist, "Understanding the scalar meson $q\bar{q}$ nonet," Z. Phys. C **68** (1995) 35, DOI: `10.1007/BF01565264`. (Cited on page 152)

[137] C. Adloff et al., [H1], "Inclusive measurement of diffractive deep inelastic ep scattering," Z. Phys. C **76** (1997) 613, DOI: `10.1007/s002880050584`. (Cited on page 153)

[138] F. Abe et al., [CDF], "Measurement of small angle $\bar{p}p$ elastic scattering at $\sqrt{s}$ = 546 GeV and 1800 GeV," Phys. Rev. D **50** (1994) 5518, DOI: `10.1103/PhysRevD.50.5518`. (Cited on page 153)

[139] A. Ben-Israel, "Generalized Inverses," ed. by T. N. E. Greville, 2nd ed., CMS Books in Mathematics, New York: Springer, 2003, DOI: `10.1007/b97366`. (Cited on pages 156, 173)

[140] E. H. Moore, "On the reciprocal of the general algebraic matrix," Bulletin of the American Mathematical Society **26**.9 (1920) 394, DOI: 10.1090/S0002-9904-1920-03322-7. (Cited on page 156)

[141] R. Penrose, "A generalized inverse for matrices," Proc. Cambridge Philos. Soc. **51**.3 (1955) 406, DOI: 10.1017/S0305004100030401. (Cited on page 156)

[142] A. Bjerhammar, "Application of Calculus of Matrices to Method of Least Squares: With Special Reference to Geodetic Calculations," Acta polytechnica, Elanders boktr., 1951. (Cited on page 156)

[143] H. Dembinski and P. O. Et al., "scikit-hep/iminuit," (2020), DOI: 10.5281/zenodo.3949207. (Cited on pages 157, 365)

[144] L. S. Geng et al., "Clues for the existence of two $K_1(1270)$ resonances," Phys. Rev. D **75** (2007) 014017, DOI: 10.1103/PhysRevD.75.014017. (Cited on pages 188, 191)

[145] P. Gavillet et al., "Backward production of a spin-parity 1^+ $K\rho$ resonance at 1.28 GeV," Phys. Lett. **76B** (1978) 517, DOI: 10.1016/0370-2693(78)90919-X. (Cited on pages 189, 190)

[146] S. Rodebäck et al., "Q_1 Production by Hypercharge Exchange in $\pi^- p$ Interactions at 3.95 GeV/c," Z. Phys. C **9** (1981) 9, DOI: 10.1007/BF01554104. (Cited on page 189)

[147] A. Astier et al., "Existence and properties of the C-meson as observed in pp annihilations at rest," Nucl. Phys. B **10** (1969) 65, DOI: 10.1016/0550-3213(69)90285-5. (Cited on page 189)

[148] R. Aaij et al., [LHCb], "Amplitude analysis of $B^+ \to J/\psi\phi K^+$ decays," Phys. Rev. D **95** (2017) 012002, DOI: 10.1103/PhysRevD.95.012002. (Cited on page 192)

[149] R. Aaij et al., [LHCb], "Observation of New Resonances Decaying to $J/\psi K^+$ and $J/\psi\phi$," Phys. Rev. Lett. **127** (2021) 082001, DOI: 10.1103/PhysRevLett.127.082001. (Cited on page 192)

[150] M. Baubillier et al., "A partial-wave analysis of the $K\pi\pi$ system produced in the reaction $K^- p \to \overline{K}^0 \pi^+ \pi^- n$ at 8.25 GeV/c," Nucl. Phys. B **202** (1982) 21, DOI: 10.1016/0550-3213(82)90219-X. (Cited on page 197)

[151] D. Aston et al., [LASS], "Observation of new resonant structures in the natural spin-parity strange meson system," Phys. Lett. B **106** (1981) 235, DOI: 10.1016/0370-2693(81)90915-1. (Cited on pages 197, 198)

[152] G. D. Tikhomirov et al., "Resonances in the $K_S K_S K_L$ System Produced in Collisions of Negative Pions with a Carbon Target at a Momentum of 40 GeV," Phys. Atom. Nucl. **66** (2003) 828, DOI: 10.1134/1.1576456. (Cited on pages 212, 214, 243)

[153] S. Chung et al., "Analysis of the $K\omega$ spectrum," Phys. Lett. **51B** (1974) 413, DOI: 10.1016/0370-2693(74)90241-X. (Cited on pages 212, 243)

[154] D. Lissauer et al., "Antihyperon and antiproton production in K^+p interactions at 9 GeV/c," Nucl. Phys. B **18** (1970) 491, DOI: 10.1016/0550-3213(70)90131-8. (Cited on pages 214, 243)

[155] P. V. Chliapnikov et al., "A Study of $\bar{\Lambda}\pi^+$, $\bar{\Lambda}K^+$ and $\bar{\Lambda}p$ Production in 32 GeV/c K^+p Interactions," Nucl. Phys. B **158** (1979) 253, DOI: 10.1016/0550-3213(79)90164-0. (Cited on pages 214, 243)

[156] M. Ablikim et al., [BESIII], "Partial wave analysis of $\psi(3686) \to K^+K^-\eta$," Phys. Rev. D **101** (2020) 032008, DOI: 10.1103/PhysRevD.101.032008. (Cited on page 216)

[157] R. Baldi et al., "Observation of the $K^*(1780)$ in the reaction $K + p \to K^0_S\pi^+p$ at 10 GeV/c," Phys. Lett. **63B** (1976) 344, DOI: 10.1016/0370-2693(76)90279-3. (Cited on page 216)

[158] G. W. Brandenburg et al., "Evidence for a New Strangeness-One Pseudoscalar Meson," Phys. Rev. Lett. **36** (1976) 1239, DOI: 10.1103/PhysRevLett.36.1239. (Cited on page 220)

[159] S. Godfrey and N. Isgur, "Mesons in a relativized quark model with chromodynamics," Phys. Rev. D **32** (1985) 189, DOI: 10.1103/PhysRevD.32.189. (Cited on page 221)

[160] V. M. Karnaukhov, V. I. Moroz, and C. Coca, "A Narrow Structure with $M = 1.63\,\mathrm{GeV}/c^2$ in the Mass Spectrum of $K^0_S\pi^+\pi^-$ System," Phys. Atom. Nucl. **61** (1998) 203. (Cited on page 221)

[161] V. M. Karnaukhov, C. Coca, and V. I. Moroz, "Investigation of the narrow structure $K(1630)$ decaying into the $K^0_S\pi^+\pi^-$ system," Phys. Atom. Nucl. **63** (2000) 588, DOI: 10.1134/1.855673. (Cited on page 221)

[162] G. Bonvicini et al., [CLEO], "Dalitz plot analysis of the $D^+ \to K^-\pi^+\pi^+$ decay," Phys. Rev. D **78** (2008) 052001, DOI: 10.1103/PhysRevD.78.052001. (Cited on pages 231, 238)

[163] V. Blache, "private communication," 2021. (Cited on page 231)

[164] P. C. Magalhães, A. C. dos Reis, and M. R. Robilotta, "Multibody decay analyses: A new phenomenological model for meson-meson subamplitudes," Phys. Rev. D **102** (2020) 076012, DOI: 10.1103/PhysRevD.102.076012. (Cited on page 235)

[165] M. Ablikim et al., [BESIII], "Amplitude analysis of $D^0 \to K^-\pi^+\pi^+\pi^-$," Phys. Rev. D **95** (2017) 072010, DOI: 10.1103/PhysRevD.95.072010. (Cited on page 238)

[166] B. El-Bennich et al., "CP violation and kaon-pion interactions in $B \to K\pi^+\pi^-$ decays," Phys. Rev. D **79** (2009) 094005, DOI: 10.1103/PhysRevD.79.094005. (Cited on page 238)

[167] V. Bernard, D. Boito, and E. Passemar, "Dispersive representation of the scalar and vector $K\pi$ form factors for $\tau \to K\pi\nu_\tau$ and K_{l3} decays," Nucl. Phys. B **218** (2011) 140, DOI: 10.1016/J.NUCLPHYSBPS.2011.06.024. (Cited on page 238)

[168] D. S. Kuzmenko and Y. A. Simonov, "QCD string in Mesons and Baryons," Phys. Atom. Nucl. **64** (2001) 107, DOI: 10.1134/1.1344949. (Cited on page 244)

[169] P. Bicudo, "Large degeneracy of excited hadrons and quark models," Phys. Rev. D **76** (2007) 094005, DOI: 10.1103/PhysRevD.76.094005. (Cited on page 244)

[170] J. K. Chen, "Regge trajectories for the mesons consisting of different quarks," Eur. Phys. J. C **78** (2018) 648, DOI: 10.1140/EPJC/S10052-018-6134-0. (Cited on pages 244, 245)

[171] J. Beckers, "Search for Light-Meson Resonances in Diffractively Produced Final States with K^0_S," Ph.D. thesis (in preparation): TU München. (Cited on page 246)

[172] M. Dugger et al., "A study of meson and baryon decays to strange final states with GlueX in Hall D," (2012), arXiv: 1210.4508. (Cited on page 247)

[173] M. Dugger et al., "A study of decays to strange final states with GlueX in Hall D using components of the BaBar DIRC," (2014), arXiv: 1408.0215. (Cited on page 247)

[174] B. Aubert et al., [BABAR], "The BABAR detector," Nucl. Instrum. Meth. A **479** (2002) 1, DOI: 10.1016/S0168-9002(01)02012-5. (Cited on page 247)

[175] M. Amaryan et al., [KLF], "Strange Hadron Spectroscopy with Secondary K_L Beam in Hall D," (2020), arXiv: 2008.08215. (Cited on page 247)

[176] G. Barucca et al., "PANDA Phase One," Eur. Phys. J. A **57** (2021) 184, DOI: 10.1140/epja/s10050-021-00475-y. (Cited on page 247)

[177] B. Adams et al., [AMBER], "Letter of Intent: A New QCD facility at the M2 beam line of the CERN SPS (COMPASS++/AMBER)," (2018), arXiv: 1808.00848. (Cited on page 247)

[178] B. Adams et al., [AMBER], "COMPASS++/AMBER: Proposal for Measurements at the M2 beam line of the CERN SPS Phase-1: 2022-2024," (2019), URL: https://cds.cern.ch/record/2676885. (Cited on page 247)

[179] S. Uhl and T. Weisrock, "Diffractive Production of Final States decaying to $\pi^-\pi^0\pi^0$ and $\pi^-\eta\eta$," COMPASS release note, 2013, URL: https://wwwcompass.cern.ch/compass/results/2013/february_hadron_2pi0_2eta/suhl_releasenote.pdf. (Cited on page 250)

[180] W. Voigt, "Das Gesetz der Intensitätsverteilung innerhalb der Linien eines Gasspektrums," München, 1912, URL: http://publikationen.badw.de/de/003395768. (Cited on page 257)

[181] J. von Neumann, "Various techniques used in connection with random digits," *Monte Carlo Method*, ed. by A. Germon, G. Forsythe, and H. Germond, National Bureau of Standards Applied Mathematics Series, 12, 1951, 36–38. (Cited on page 276)

[182] S. A. Dupree and S. K. Fraley, "Monte Carlo Sampling Techniques," *A Monte Carlo Primer: A Practical Approach to Radiation Transport*, Boston, MA: Springer US, 2002, 21–56, DOI: 10.1007/978-1-4419-8491-3_2. (Cited on page 276)

[183] C. Dreisbach, "Study of elastic $\pi^- p$ scattering at COMPASS," Master thesis: TU München, 2014, URL: https://wwwcompass.cern.ch/compass/publications/theses/2014_dpl_dreisbach.pdf. (Cited on page 279)

[184] T. Enßlin, "Astrophysical data analysis with information field theory," AIP Conference Proceedings **1636** (2014) 49, DOI: 10.1063/1.4903709. (Cited on page 356)

[185] D. R. Brillinger, "Time series: Data Analysis and Theory," Classics in applied mathematics, Philadelphia, Pa.: Society for Industrial and Applied Mathematics, 2001, ISBN: 9780898719246. (Cited on page 356)

[186] S. Gerassimov and A. Others, "PHysics Analysis Software Tools," 2019, URL: https://ges.home.cern.ch/ges/phast/index.html. (Cited on page 365)

[187] K. Bicker et al., "Antok," 2019, URL: https://github.com/AntokBatchelorMaintainers/antok. (Cited on page 365)

[188] S. Wallner, S. Huber, and C. Dreisbach, "CEDAR Likelihood Helper," 2020, URL: https://gitlab.cern.ch/compass/hadron/cedar-likelihood. (Cited on page 365)

[189] P. Jasinski et al., "RPD Helper," 2019, URL: https://gitlab.cern.ch/compass/hadron/RPD. (Cited on page 365)

[190] COMPASS Collaboration, "COMGEANT," 2019, URL: https://gitlab.cern.ch/compass/comgeant. (Cited on page 365)

[191] B. Grube et al., "RootPWA," 2021, URL: https://github.com/ROOTPWA-Maintainers/ROOTPWA/. (Cited on pages 365, 399)

[192] S. Wallner, J. Beckers, and B. Grube, "ROORPWAtools," 2021, URL: https://gitlab.cern.ch/compass/hadron/ROOTPWAtools. (Cited on page 365)

[193] S. Wallner, "sfitter," 2021, URL: https://gitlab.cern.ch/swallner-pub/sfitter. (Cited on pages 365, 400)

[194] S. Wallner et al., "Batchelor," 2021, URL: https://github.com/AntokBatchelorMaintainers/batchelor. (Cited on page 365)

[195] J. D. Hunter, "Matplotlib: A 2D graphics environment," Comput. Sci. Eng. **9**.3 (2007) 90, DOI: 10.1109/MCSE.2007.55. (Cited on page 365)

[196] S. Wallner et al., "modernplotting," 2021,
URL: https://gitlab.cern.ch/compass/hadron/modernplotting.
(Cited on page 365)

[197] S. Wallner and J. Beckers, "RPWAplotting," 2021,
URL: https://gitlab.cern.ch/compass/hadron/rpwaplotting.
(Cited on page 365)

[198] F. M. Kaspar, "Application and Verification of Model-Selection Techniques for Difractively Produced Three-Pion Final States," Master thesis: TU München, 2017, URL: https://wwwcompass.cern.ch/compass/publications/theses/2017_dpl_kaspar.pdf. (Cited on page 400)

[199] J. Beckers, "Untersuchung der Modellabhängigkeit der Partialwellenanalyse des $K\pi\pi$ -Endzustandes," Bachelor thesis: TU München, 2018, URL: https://wwwcompass.cern.ch/compass/publications/theses/2018_bac_beckers.pdf.
(Cited on page 400)

[200] S. Wallner, [COMPASS],
"Recent Results on Light-Meson Spectroscopy from COMPASS," *HADRON2017*, Salamanca, Spain: PoS, 2018, 032, DOI: 10.22323/1.310.0032. (Cited on page 400)

[201] S. Wallner, [COMPASS], "Light-Quark Resonances at COMPASS," *Confinement2018*, Maynooth, Ireland: PoS, 2018, 097, DOI: 10.22323/1.336.0097. (Cited on page 400)

[202] S. Wallner, [COMPASS], "Strange-Meson Spectroscopy at COMPASS," *HADRON2019*, Guilin, China, 2020, 134, DOI: 10.1142/9789811219313_0019. (Cited on page 400)

[203] S. Wallner, "News from the light and strange meson sector," *HADRON2021*, invited plenary talk, Mexico City, Mexico, 2021,
URL: https://indico.nucleares.unam.mx/event/1541/overview.
(Cited on page 400)

Own Contributions

My analysis of the reaction $K^- + p \to K^-\pi^-\pi^+ + p$ at COMPASS is based on a previous unpublished COMPASS analysis by P. Jasinski [44], where a first event selection and a PWD were performed using only a subset of the COMPASS data. My analysis also relies on the experience gained in the COMPASS $\pi^-\pi^-\pi^+$ analysis [11, 38–41, 80].

I extended, improved, and fine-tuned the existing event selection for the $K^-\pi^-\pi^+$ sample in many regards. For example, I performed a preselection for events with three charged final-state particles, which is used in many other COMPASS analyses [43, 62, 65, 66]. Especially noteworthy, I developed, implemented, and verified a novel approach for beam-particle identification using the full information from both CEDAR detectors, based on first ideas from C. Bicker. To this end, I formulated a coordinate transformation, which is the heart of this approach and which allowed me to calibrate the employed likelihood function without relying on pure beam-kaon and beam-pion calibration samples. Compared to the previously used approach, I doubled the efficiency for beam-kaon identification and thereby doubled the size of the $K^-\pi^-\pi^+$ sample. In addition, I increased the $K^-\pi^-\pi^+$ sample size by almost another factor of two, compared to the existing COMPASS $K^-\pi^-\pi^+$ sample [44], by using the full COMPASS data set, which consists of data from two data taking campaigns (2008 and 2009) with slightly different experimental acceptances, which I had to take into account.

Based on this $K^-\pi^-\pi^+$ sample, I performed a partial-wave decomposition (PWD). I made significant contributions to the PWD software framework ROOTPWA [191]. For the first time for the $K^-\pi^-\pi^+$ sample, I applied model-selection techniques to determine an optimal wave set. In close collaboration with F. Kaspar, who worked on the wave-set selection for $\pi^-\pi^-\pi^+$, I extended the wave-set selection approach developed in previous COMPASS analyses [67, 108] by taking into account acceptance effects and by imposing continuity in $m_{K\pi\pi}$. Furthermore, I applied, for the first time at COMPASS, Bootstrapping techniques starting at the event-sample level to propagate uncertainties up to the PWD level. In addition, I developed and implemented in ROOTPWA an approach to simultaneously fit multiple data samples with different experimental acceptances. To this end, I generated large data samples using the COMPASS detector Monte Carlo simulation.

During the analysis, I observed analysis artifacts in some partial waves. I could trace back the origin of these artifacts to the leakage effect, which is caused by the limited kinematic range of the final-state particle identification. I established three independent approaches to identify the leakage artifacts and I showed that the non-leakage waves are free of these artifacts so that they can be interpreted reliably in terms of physics signals.

A first resonance-model fit (RMF) to the results of the PWD, which was based on an approach similar to the one used in the COMPASS $\pi^-\pi^-\pi^+$ analysis [40, 41], failed. I identified the incoherent background contributions to be the main reason for this failure. Then, I developed an ansatz that effectively handles these incoherent background processes at the stage of the PWD and explicitly models them at the stage of the RMF. Using this ansatz, I developed a RMF model with 10 partial waves. Based on this model, I performed fits in which I studied 7 strange mesons in detail. To this end, I developed a new software for RMFs [193]. Furthermore, I performed a first set of systematic studies, and I performed extensive pseudodata studies to validate my analysis ansatz. In addition, I extended this model to study 7 further strange mesons. Finally, I performed first tests of studying resonances appearing the $K^-\pi^+$ and $\pi^-\pi^+$ subsystems of the $K^-\pi^-\pi^+$ final state, which required further extensions of my RMF software [193]. The physics results presented in this thesis are summarized in figure 9.1.

In addition to the work described in this thesis, I was involved in other COMPASS analyses of bachelor and master students [61, 65, 198, 199]. I also contributed to the COMPASS data taking campaigns in the years 2016, 2017, 2018, and 2021.

I presented various aspects of my analysis in regular meetings within the COMPASS collaboration. Furthermore, I presented my analysis and other COMPASS results at various national and international workshops and conferences. I published some of these results in the corresponding proceedings [200–202]. Finally, I had the honor to be invited to give a plenary talk on news from the light and strange meson sector at the 19th HADRON conference [203].

Acknowledgments—Danksagung

Above all, I would like to thank Prof. Stephan Paul for the opportunity to work on this exciting topic. I greatly appreciate his continued interest in my work, his guidance and support, and the trust he put in me. I am very grateful for the possibilities to peruse my ideas in various areas and for the freedom and flexibility he gave to me. It was a pleasure to work in his group.

I am much obliged to Boris Grube, from whom I learned all about partial-wave analysis. He was and still is a continuous source of advice to me with his kind and patient manner, and he always had the right starting points when I got stuck. I am very grateful for his endurance to proofread this document. I wish you all the best for your future.

Also, I am very thankful for being part of the COMPASS collaboration, for the possibility to work on this grate data sample, and for the many fruitful discussions with my COMPASS colleagues. Especially, I am thankful to Prometeusz Jasinski, who paved the way for this analysis, to Andrii Maltsev and Dmitri Ryabchikov for cross-checking parts of this analysis, and to Mikhail Mikhasenko for his valuable input.

I also want to thank all my colleagues from E18 for an open, enjoyable, and helpful atmosphere. I am grateful for many inspiring discussions with Fabian Krinner, Christian Dreisbach—whom I also thank for proofreading parts of this thesis—, Florian Kaspar, Jan Friedich, Dominik Steffen, Dominik Ecker, Daniel Greenwald, Sebastian Uhl, Markus Krämer, Charly Bicker, Alexander Austregesilo, Stefan Huber, and many others. My special thanks go to Karin Frank for her tireless support in all administrative matters.

Ich möchte meinen Eltern, Alois und Roswitha Wallner, für die stetige Unterstützung während meines gesamten Lebenswegs danken. Ihr habt mich immer darin bestärkt meine eigenen Entscheidungen zu fällen und meinen Interessen nachzugehen. Danke dafür und für alles was ihr für uns getan habt.

Ebenso danke ich Harold und Zdenka Blache für die Unterstützung. Ich danke ebenfalls Petra Werlein für das Korrekturlesen dieser Arbeit.

Most important, I am eternally grateful to Veronika Blache. Without your unconditional support and love this thesis would not have been possible. I dedicate this thesis to you. I am most thankful for being part of our little family.

$$\frac{1}{x^2} \to +\infty^{+\infty}$$

This research was supported by the Excellence Cluster ORIGINS which is funded by the Deutsche Forschungsgemeinschaft (DFG, German Research Foundation) under Germany's Excellence Strategy EXC-2094-390783311. The parts of the computations have been carried out on the computing facilities of the Computational Center for Particle and Astrophysics (C2PAP) and of the Leibniz Supercomputer Center (LRZ).